



National Aeronautics and
Space Administration

R82AEB470
NASA CR-168069

P-530
304585

ENERGY EFFICIENT ENGINE

CORE DESIGN AND PERFORMANCE REPORT

December 1982

AIRCRAFT ENGINE BUSINESS GROUP
ADVANCED TECHNOLOGY PROGRAMS DEPARTMENT
CINCINNATI, OHIO 45215

(NASA-CR-168069) ENERGY EFFICIENT ENGINE
CORE DESIGN AND PERFORMANCE REPORT Report,
Jan. 1978 - Dec. 1982 (GE) 530 p CSCI 21E

N90-28559

Unclass


63/07 0304585

Prepared for

NATIONAL AERONAUTICS AND SPACE ADMINISTRATION
LEWIS RESEARCH CENTER
21000 BROOKPARK ROAD
CLEVELAND, OHIO 44135

These limitations shall be con-
sidered void after two (2) years after date of such data.

NASA - LEWIS RESEARCH CENTER
Contract NAS3-20643

1. Report No. NASA CR-168069		2. Government Accession No.		3. Recipient's Catalog No.	
4. Title and Subtitle Energy Efficient Engine Core Design and Performance Report				5. Report Date December, 1982	
				6. Performing Organization Code	
7. Author(s) E.M. Stearns, et al.				8. Performing Organization Report No. R82AEB470	
9. Performing Organization Name and Address General Electric Company Aircraft Engine Business Group Cincinnati, Ohio 45215				10. Work Unit No.	
				11. Contract or Grant No. NAS3-20643	
12. Sponsoring Agency Name and Address National Aeronautics and Space Administration Lewis Research Center 21000 Brookpark Road Cleveland, Ohio 44135				13. Type of Report and Period Covered Topical January 1978 - December 1982	
				14. Sponsoring Agency Code	
15. Supplementary Notes NASA Project: Mr. C.C. Ciepluch NASA Project Engineer: Mr. A.C. Hoffman GE Project Manager: Mr. R.W. Bucy					
16. Abstract The Energy Efficient Engine (E ³) is a NASA program to develop fuel-saving technology for future large transport aircraft engines. Testing of the General Electric E ³ core has proven that the core component performance and core system performance necessary to meet the program goals have been achieved. The E ³ core design and detailed test results are described and presented in this report.					
17. Key Words (Suggested by Author(s)) Energy Conservation Subsonic Transport Turbine Engine Aircraft Turbine Engine Energy Efficient Engine Core Engine				18. Distribution Statement 	
19. Security Classif. (of this report) Unclassified		20. Security Classif. (of this page) Unclassified		21. No. of Pages	
				22. Price*	

[REDACTED]

[REDACTED]

FOREWORD

This report presents an overview of the design and results of testing the core of General Electric's Energy Efficient Engine (E³). This work was performed for the National Aeronautics and Space Administration (NASA) at the Lewis Research Center under Contract NAS3-20643 as part of the Aircraft Energy Efficiency Program and Energy Efficient Engine Project. Mr. Carl C. Ciepluch is the NASA E³ Project Manager and Mr. Peter G. Batterton is the NASA Assistant Project Manager. Mr. Anthony C. Hoffman is the NASA Project Engineer responsible for the effort associated with the core design and test as reported here. Mr. Raymond W. Bucy is manager of the E³ Project for the General Electric Company. This report was prepared by Mr. E. Marshall Stearns and the General Electric E³ staff.

PRECEDING PAGE BLANK NOT FILMED

TABLE OF CONTENTS

<u>Section</u>		<u>Page,</u>
	SYMBOLS, ABBREVIATIONS, ENGINE STATION DESIGNATIONS	xxiii
1.0	SUMMARY	1
2.0	INTRODUCTION	3
3.0	HARDWARE DESCRIPTION	5
3.1	Front Frame Description	6
3.2	Compressor Description	14
3.2.1	Aerodynamic Design	14
3.2.2	Mechanical Design	19
3.3	Combustor Description	25
3.3.1	Aerodynamic Design	25
3.3.2	Mechanical Design	29
3.4	High Pressure Turbine Description	33
3.4.1	Aerodynamic Design	33
3.4.2	Mechanical Design	39
3.5	Rear Frame and Exhaust Nozzle Description	48
3.6	Sumps, Drives, Gearbox, and Piping Description	53
3.7	Control Description	64
3.8	Instrumentation Description	72
4.0	TEST FACILITY DESCRIPTION	77
5.0	TEST OPERATIONS SUMMARY	87
6.0	TEST RESULTS	122
6.1	Core System Thermodynamic Performance	122
6.1.1	Pretest Predictions	123
6.1.2	Performance Analysis	124
6.1.3	Analysis Results	127
6.2	Compressor Mechanical Performance	159
6.2.1	Clearances	159
6.2.2	Temperatures	159
6.2.3	Frequencies	164
6.2.4	Blade Tip Rubs	185
6.3	Compressor Aerodynamic Performance	186

PRECEDING PAGE BLANK NOT FILMED

TABLE OF CONTENTS (Continued)

<u>Section</u>	<u>Page</u>
6.3.1 Overall Performance Summary	186
6.3.2 Stator Schedules	191
6.3.3 Internal Performance	194
6.3.4 Other Operational Effects	199
6.4 Combustor Mechanical Performance	203
6.4.1 Temperatures	206
6.4.2 Pressures	220
6.4.3 Component Evaluation	220
6.5 Combustor Aerodynamic Performance	220
6.5.1 Instrumentation	221
6.5.2 Testing and Data Acquisition	233
6.5.3 Starting	233
6.5.4 Staging Transition From Pilot-Only to Double-Annular Burning	235
6.5.5 Emissions	237
6.6 High Pressure Turbine Mechanical Performance	284
6.6.1 Instrumentation Status	285
6.6.2 Blade Instrumentation	297
6.6.3 Rotor Metal Temperatures	341
6.6.4 Rotor Cooling Air Delivery System	345
6.6.5 Airfoil Radial Temperature Profiles	354
6.6.6 Stage 1 Nozzle Temperatures	357
6.6.7 Stage 2 Nozzle Temperatures	361
6.6.8 Interstage Seal System Performance	375
6.6.9 Outer Casing Temperatures	386
6.6.10 HP Turbine Clearances and Active Clearance Control	394
6.7 High Pressure Turbine Aerodynamic Performance	426
6.8 Sumps, Drives, Gearbox, and Piping Performance	436
6.8.1 Forward Sump	438
6.8.2 Aft Sump	438
6.8.3 Accessory Drive System	445
6.8.4 Configuration	445
6.8.5 Lube System	447
6.8.6 Core Thrust Bearing Load Analysis	452
6.9 Core System Dynamic Performance	456
6.10 Core Control System Performance	471
6.10.1 Speed Governing	471
6.10.2 Fuel Leak	475
6.10.3 Double-Annular Combustor Control	475
6.10.4 Active Clearance Control	479

TABLE OF CONTENTS (Concluded)

<u>Section</u>		<u>Page</u>
	6.10.5 Start Range Turbine Cooling System	479
	6.10.6 Starting	479
	6.10.7 Subidle Exploration	492
	6.10.8 Sensor Accuracy	492
	6.10.9 FADEC	496
7.0	CONCLUSIONS	498
8.0	REFERENCES	505

LIST OF ILLUSTRATIONS

<u>Figure</u>		<u>Page</u>
1.	E ³ Station Designation.	xxvi
2.	E ³ Flight Propulsion System.	7
3.	E ³ Flight Propulsion System Cross Section.	8
4.	Upper Half of Core Cross Section.	9
5.	Lower Half of Core Cross Section.	11
6.	Photo of Core Test Vehicle.	13
7.	Three-Dimensional Sketch of Compressor Stator No. 6.	18
8.	High Pressure Compressor Rotor Design Features.	20
9.	Photo of Compressor Rotor Hardware.	21
10.	Core and ICLS Compressor Rotor Materials.	23
11.	Compressor Stator Design Features.	24
12.	Compressor Stator Materials.	26
13.	Compressor Bleeds.	27
14.	E ³ Combustor Design Features.	28
15.	Combustor Cross Section With Materials Selection Indicated.	30
16.	Photo of Combustor Dome Assembly, Aft Looking Forward.	31
17.	Photo of Double-Annular Dome and Cowling, Forward Looking Aft.	32
18.	Photo of Combustor Inner Shingle Liner Assembly.	34
19.	HP Turbine Warm Air Rig.	38
20.	HP Turbine Rotor.	41
21.	HP Turbine Static Structures.	42
22.	HP Turbine Stage 1 Nozzle Assembly.	44
23.	HP Turbine Nozzle and Combustor Assembly.	45
24.	HP Turbine Stage 2 Nozzle and Shroud Assembly (Partial).	46
25.	HP Turbine Rotor Assembly.	47
26.	E ³ Core Engine Exhaust System.	49
27.	Turbine Cavity Pressurization and Service Strut Cooling Circuits.	51
28.	Turbine Frame Cooling Circuit.	52
29.	Forward Sump.	54

LIST OF ILLUSTRATIONS (Continued)

<u>Figure</u>		<u>Page,</u>
30.	Aft Sump.	55
31.	Accessory Drive System Cross Section.	57
32.	Accessory Gearbox Cross Section.	59
33.	Schematic of Pneumatic Piping.	60
34.	Major Piping Arrangement of Core Engine.	61
35.	Lube System Schematic.	63
36.	Schematic of Rotor Thrust Balance.	65
37.	Core Engine Control System.	66
38.	E ³ Core Aeroperformance Instrumentation.	74
39.	Core Vibration Monitoring Instrumentation.	76
40.	Core Cell AlW Installation.	78
41.	Facility-Supplied Services.	79
42.	Layout of Cell AlW Control Room.	80
43.	Photo of Cell AlW Control Room Console.	81
44.	Cell Unit Functional System.	84
45.	Site Unit Functional Diagram.	85
46.	Plane 42 Radial Pressure Profile Based on Radial Rakes.	129
47.	Plane 42 Radial Pressure Profile Based on Arc Rakes.	130
48.	Circumferential T42 Profiles for Reading 246.	131
49.	Circumferential T42 Profiles for Reading 250.	132
50.	Circumferential T42 Profiles for Reading 258.	133
51.	Radial Profile of T42 Ring Averaged Data.	134
52.	Core Engine Cooling Flow Schematic Diagram.	136
53.	Total Fifth-Stage Parasitic Cooling Bleed Measured Flows - Compressor ACC Off Versus Compressor ACC On.	138
54.	Total Seventh-Stage Parasitic Cooling Bleed Measured Flows Versus Assumed Flows.	139
55.	Total CDP Chargeable Cooling Bleed Measured Flows Versus Assumed Flows.	140
56.	Phase II Results - Compressor Operating Lines.	141
57.	Phase II Results - Corrected Flow Versus Corrected Speed.	142
58.	Phase II Analysis - Compressor Efficiency Versus Flow.	143

LIST OF ILLUSTRATIONS (Continued)

<u>Figure</u>		<u>Page</u>
59.	Phase II Results - Double-Annular Combustor Pressure Ratio Versus Flow.	145
60.	Phase II Results - Difference Between Measured T42 and T42 Calculated From Emissions Efficiency Data.	147
61.	Phase II Results - Double-Annular Combustor Efficiency Versus Compressor Discharge Temperature.	148
62.	Phase II Results - Combustor Efficiency Emissions Data Delta between Measured and Calculated T42.	149
63.	Phase II Results - Double-Annular HP Turbine Efficiency.	151
64.	High Pressure Turbine Efficiency Scalar.	152
65.	High Pressure Turbine Flow Function Scalar.	154
66.	Core Pumping Characteristics.	157
67.	Corrected Fuel Flow Versus Ideal Gas Power.	158
68.	Compressor Rotor Temperature Comparison.	161
69.	Compressor Stator Temperature Comparison With ACC On.	162
70.	Compressor Stator Temperature Comparison With ACC Off.	163
71.	Inlet Guide Vane Campbell Diagram.	165
72.	Compressor Stage 1 Blade Campbell Diagram.	166
73.	Compressor Stage 1 Vane Campbell Diagram.	167
74.	Compressor Stage 2 Blade Campbell Diagram.	168
75.	Compressor Stage 2 Vane Campbell Diagram.	169
76.	Compressor Stage 3 Blade Campbell Diagram.	170
77.	Compressor Stage 3 Vane Campbell Diagram.	171
78.	Compressor Stage 4 Blade Campbell Diagram.	172
79.	Compressor Stage 4 Vane Campbell Diagram.	173
80.	Compressor Stage 5 Blade Campbell Diagram.	174
81.	Compressor Stage 5 Vane Campbell Diagram.	175
82.	Compressor Stage 6 Blade Campbell Diagram.	176
83.	Compressor Stage 6 Vane Campbell Diagram.	177
84.	Compressor Stage 7 Blade Campbell Diagram.	178
85.	Compressor Stage 7 Vane Campbell Diagram.	179

LIST OF ILLUSTRATIONS (Continued)

<u>Figure</u>		<u>Page</u>
86.	Compressor Stage 8 Blade Campbell Diagram.	180
87.	Compressor Stage 8 Vane Campbell Diagram.	181
88.	Compressor Stage 9 Blade Campbell Diagram.	182
89.	Compressor Stage 9 Vane Campbell Diagram.	183
90.	Compressor Stage 10 Blade Campbell Diagram.	184
91.	HP Compressor Performance Map.	188
92.	Comparison of Compressor Stator Schedule.	192
93.	Core Engine Test Stator Schedule Optimization.	193
94.	Core Compressor Flow Versus Speed.	195
95.	HP Compressor Front Block Performance Map.	197
96.	HP Compressor Rear Block Performance Map.	198
97.	Core Compressor Radial Pressure Distribution.	200
98.	Core Compressor Active Clearance Control Effects (Casing Cooling).	201
99.	Core Compressor Rotor Bore Cooling Effects.	202
100.	Core Compressor Reynolds Number Effects.	204
101.	Combustor Instrumentation.	205
102.	Typical Shingle Backside Thermocouple Attachment.	207
103.	Pilot Zone Shingle Backside Temperatures Compared to Predicted, Mechanical Checkout With Ambient Inlet.	208
104.	Main Zone Shingle Backside Temperatures, Compared to Predicted, Mechanical Checkout With Ambient Inlet.	209
105.	Centerbody Temperatures Compared to Predicted, Mechanical Checkout With Ambient Inlet.	210
106.	Pilot Zone Shingle Backside Temperatures Compared to Predicted, Ram Inlet Conditions.	212
107.	Main Zone Shingle Backside Temperatures Compared to Predicted, Ram Inlet Conditions.	213
108.	Centerbody Temperatures Compared to Predicted, Ram Inlet Conditions.	214
109.	Pilot Zone Shingle Backside Temperatures Compared to Predicted at Test Conclusion.	215

LIST OF ILLUSTRATIONS (Continued)

<u>Figure</u>		<u>Page</u>
110.	Main Zone Shingle Backside Temperatures Compared to Predicted at Test Conclusion.	216
111.	Centerbody Temperatures Compared to Predicted at Test Conclusion.	217
112.	Measured Dome Splash Plate Temperatures.	218
113.	Measured Fuel Nozzle Assembly Temperatures.	219
114.	Combustion System Instrumentation Diagram.	225
115.	Combustor Instrumentation Layout.	226
116.	Combustor Liner Thermocouple Location, Outer Liner Shingles.	227
117.	Combustor Liner Thermocouple Location, Inner Liner Shingles.	228
118.	Main Dome Instrumentation.	229
119.	Centerbody Instrumentation.	231
120.	Combustor Liner Assemblies Pressure Instrumentation.	231
121.	Staging From Pilot-Only to Double-Annular Burning.	238
122.	Combustor Flow Function Versus Corrected Core Speed.	240
123.	Combustor Inlet Temperature Versus Corrected Core Speed.	241
124.	Combustor Inlet Pressure Versus Corrected Core Speed.	242
125.	Combustor Airflow Versus Corrected Speed.	243
126.	Combustor Flow Function Versus Combustor Inlet Temperature.	244
127.	Combustor Inlet Pressure Versus Combustor Inlet Temperature.	245
128.	Combustor Airflow Versus Combustor Inlet Temperature.	246
129.	Combustor Fuel Air Ratio Versus Corrected Core Speed.	247
130.	Combustor Pilot and Main Fuel Flow Versus Corrected Core Speed.	248
131.	Combustor Fuel-Air Ratio Versus Combustor Inlet Temperature.	249
132.	Combustor Pilot and Main Fuel Flow Versus Combustor Inlet Temperature.	250
133.	FPS Adjusted Carbon Monoxide Emissions Versus Compressor Discharge Temperature.	254

LIST OF ILLUSTRATIONS (Continued)

<u>Figure</u>		<u>Page</u>
134.	FPS Adjusted Hydrocarbon Emissions Versus Compressor Discharge Temperature.	255
135.	FPS Adjusted Nitrogen Oxides Emissions Versus Compressor Discharge Temperature.	256
136.	Core Engine Test and FPS Predicted Fuel-Air Ratios Versus Physical Core Speed.	258
137.	Combustor Component Test Idle Emission Results.	259
138.	Measured Smoke Number Versus Compressor Discharge Temperature.	263
139.	Combustion Chemical Efficiency Versus Compressor Discharge Temperature.	264
140.	Combustor System Overall Pressure Losses.	266
141.	Compressor Discharge Total Pressure and Temperature Profiles.	267
142.	Compressor Stage 10 Bleed Manifold Campbell Diagram, Start 2 - Pilot Only.	269
143.	Combustor Campbell Diagram, Start 2 - Pilot Only.	270
144.	Compressor Stage 10 Bleed Manifold, Frequency and Amplitude Versus Time - Start 2 Staging.	271
145.	Combustor Frequency and Amplitude Versus Time, Start 2 Staging.	272
146.	Compressor Stage 10 Bleed Manifold Campbell Diagram, Start 18 Nonaudible Start.	273
147.	Combustor Campbell Diagram, Start 18 Nonaudible Start.	274
148.	Compressor Stage 10 Bleed Manifold Campbell Diagram, Subidle Deceleration Audible Noise.	275
149.	Combustor Campbell Diagram, Subidle Deceleration Audible Noise.	276
150.	Cutaway Showing Passage of Swirl Air to Capped Tube.	277
151.	Compressor Stage 10 Bleed Manifold Spectral Analysis at 7200 RPM.	279
152.	Compressor Stage 10 Bleed Manifold Spectral Analysis at 7690 RPM.	280

LIST OF ILLUSTRATIONS (Continued)

<u>Figure</u>		<u>Page</u>
153.	Compressor Stage 10 Bleed Manifold Spectral Analysis at 8550 RPM.	281
154.	Compressor Stage 10 Bleed Manifold Spectral Analysis at 8650 RPM, No Pipe Blank-Off.	282
155.	HP Turbine Cooling Flows, Temperatures, and Pressures, SI Units.	287
156.	HP Turbine Cooling Flows, Temperatures, and Pressures, English Units.	289
157.	HP Turbine Engine Test Measurement Summary at Maximum Physical Speed and Turbine Efficiency Reading, SI Units.	291
158.	HP Turbine Engine Test Measurement Summary at Maximum Physical Speed and Turbine Efficiency Reading, English Units.	293
159.	HP Turbine Instrumentation and Losses.	295
160.	HP Turbine Strain Gage Locations for Stage 1 and 2 Blades.	298
161.	HP Turbine Stage 1 Blade Strain Gage Identification and Blade Serial Number.	299
162.	HP Turbine Stage 2 Blade Strain Gage Identification and Blade Serial Number.	300
163.	HP Turbine Stage 1 Blade Thermocouple Locations and Identification.	301
164.	HP Turbine Stage 2 Blade Thermocouple Locations and Identification.	302
165.	HP Turbine Stage 1 Blade Thermocouple Identification and Blade Serial Number.	304
166.	HP Turbine Stage 2 Blade Thermocouple Identification and Blade Serial Number.	305
167.	HP Turbine Stage 1 Blade.	306
168.	HP Turbine Stage 2 Blade.	307
169.	HP Turbine Stage 1 Blade Spectrum Frequency Analyzer and Vibration Stress Levels.	309
170.	HP Turbine Stage 1 Blade Vibratory Stress Characteristics (Accel from Idle to 12,800 rpm).	312
171.	HP Turbine Stage 1 Blade Vibratory Stress Characteristics (Accel From 11,550 to 12,450 rpm).	313
172.	HP Turbine Stage 1 Blade Vibratory Stress Characteristics (Decel From 11,850 rpm to Idle).	314

LIST OF ILLUSTRATIONS (Continued)

<u>Figure</u>		<u>Page</u>
173.	HP Turbine Stage 1 Blade Vibratory Stress Characteristics at Maximum Compressor Discharge Pressure.	317
174.	HP Turbine Stage 1 Blade 100-Hour Goodman Diagram at 1000° C (1840° F).	318
175.	HP Turbine Stage 1 Blade Campbell Diagram Showing Measured Vibratory Stresses.	319
176.	HP Turbine Stage 1 Blade Campbell Diagram.	320
177.	HP Turbine Stage 2 Blade Spectrum Frequency Analyzer and Vibration Stress Levels.	322
178.	HP Turbine Stage 2 Blade Vibratory Stress Characteristics (Accel From Idle to 12,350 rpm).	324
179.	HP Turbine Stage 2 Blade Vibratory Stress Characteristics (Accel From 12,050 to 12,810 rpm).	325
180.	HP Turbine Stage 2 Blade Vibratory Stress Characteristics (Decel From 12,810 to 11,800 rpm).	326
181.	HP Turbine Stage 2 Blade Vibratory Stress Characteristics (Decel From 11,800 to 9850 rpm).	327
182.	HP Turbine Stage 2 Blade Vibratory Stress Characteristics (Accel From 10,300 to 12,000 rpm).	328
183.	HP Turbine Stage 2 Blade Vibratory Characteristics at Maximum Compressor Discharge Pressure.	330
184.	HP Turbine Stage 2 Blade 100-Hour Goodman Diagram.	331
185.	HP Turbine Stage 2 Blade Campbell Diagram Showing Measured Vibratory Stresses.	332
186.	HP Turbine Stage 2 Blade Campbell Diagram.	333
187.	HP Turbine Stage 1 Blade Airfoil Temperatures - 25% Span.	335
188.	HP Turbine Stage 1 Blade Airfoil Temperatures - 50% Span.	336
189.	HP Turbine Stage 2 Blade Airfoil Temperatures - 25% Span.	337
190.	HP Turbine Stage 2 Blade Airfoil Temperatures - 50% Span.	338
191.	HP Turbine Stage 1 Blade Temperature Summary.	339
192.	HP Turbine Stage 2 Blade Temperature Summary.	340
193.	HP Turbine Stage 1 Seal Disk Metal Temperatures.	342
194.	HP Turbine Stage 1 Disk Temperatures.	343
195.	HP Turbine Stage 2 Disk Temperatures.	344
196.	HP Turbine Stage 1 Blade Retainer Temperatures.	346

LIST OF ILLUSTRATIONS (Continued)

<u>Figure</u>		<u>Page</u>
197.	HP Turbine Stage 2 Blade Retainer Temperatures.	347
198.	Stage 2 Aft Blade Retainer/Disk Cavity.	348
199.	HP Turbine Expander Cooling Flows.	350
200.	HP Turbine CDP Seal Leakage Flows.	352
201.	HP Turbine Stage 1 Cavity Air Temperature.	353
202.	HP Turbine Airfoil Leading Edge Temperature Profiles.	355
203.	HP Turbine Airfoil Leading Edge Temperature Profiles.	356
204.	HP Turbine Stage 1 Nozzle Band Temperatures.	358
205.	HP Turbine Stage 1 Vane Airfoil Temperatures, 60% Span.	359
206.	HP Turbine Stage 1 Vane Temperatures.	360
207.	HP Turbine Stage 1 Nozzle Temperature Transient.	362
208.	HP Turbine Stage 1 Nozzle Temperature Transient.	363
209.	HP Turbine Stage 2 Nozzle Instrumentation Positions.	364
210.	HP Turbine Stage 2 Nozzle Thermocouple Locations.	365
211.	HP Turbine Stage 2 Nozzle Inner Band Temperatures.	366
212.	HP Turbine Stage 2 Nozzle and Interstage Cavity Pressures and Flows.	368
213.	HP Turbine Stage 2 Vane Temperatures.	369
214.	HP Turbine Stage 2 Nozzle Airfoil Temperatures.	
215.	HP Turbine Stage 2 Nozzle Airfoil Temperatures.	372
216.	HP Turbine Stage 2 Airfoil Temperature Versus Exhaust Area.	373
217.	HP Turbine Stage 2 Nozzle Airfoil Start Transient Temperature.	374
218.	HP Turbine Interstage Cavity Purge System.	376
219.	HP Turbine Interstage Pressures.	377
220.	HP Turbine Interstage Cavity Temperatures.	379
221.	HP Turbine Interstage Forward Cavity Temperatures.	380
222.	HP Turbine Stage 2 Nozzle Band and Interstage Cavity Air Temperatures.	381
223.	HP Turbine Interstage Seal Air Temperatures.	383
224.	HP Turbine Interstage Disk Metal Temperatures.	384

LIST OF ILLUSTRATIONS (Continued)

<u>Figure</u>		<u>Page</u>
225.	HP Turbine Interstage Cavity Air Temperatures.	385
226.	HP Turbine Interstage Seal Forward Air Temperatures.	387
227.	HP Turbine Interstage Seal Aft Air Temperature.	388
228.	HP Turbine Casing Thermocouple Locations.	389
229.	HP Turbine Casing Temperature Distribution (With ACC Cooling, DMS No. 258).	391
230.	HP Turbine Casing Temperature Distribution (With ACC Cooling, DMS No. 256).	392
231.	HP Turbine Shroud Thermocouple Locations.	393
232.	HP Turbine Stage 1 Shroud Temperatures.	395
233.	HP Turbine Stage 2 Shroud Temperatures.	396
234.	HP Turbine Stage 1 Blade Tip Clearance Versus Speed (Prior to Rub), ACC Off.	397
235.	HP Turbine Stage 2 Blade Tip Clearance Versus Speed (Prior to Rub), ACC Off.	398
236.	HP Turbine Stage 1 Casing Temperatures Versus RPM.	399
237.	HP Turbine Stage 2 Casing Temperatures Versus RPM.	400
238.	HP Turbine Anticipated Casing Temperatures Without ACC Cooling or Test Cell Entrainment.	401
239.	HP Turbine Measured Casing Temperatures Without ACC Cooling (DMS No. 256).	402
240.	HP Turbine Best Data Match of Extrapolated Data to Cycle Conditions (No Acc Cooling).	405
241.	HP Turbine Core Cooling Air Piping.	407
242.	HP Turbine Casing Temperatures Versus Speed CDP Supply Pipe Failure Between 93% and 94.6%.	408
243.	HP Turbine Stage 1 Blade Tip Clearance Versus Speed Before and After Rub, ACC Off.	409
244.	HP Turbine Stage 2 Blade Tip Clearance Versus Speed Before and After Rub, ACC Off.	410
245.	HP Turbine Stage 1 Blade Tip Clearance Circumferential Deviation From Average (Initial Test).	411
246.	HP Turbine Stage 2 Blade Tip Clearance Circumferential Deviation From Average (Initial Test).	412

LIST OF ILLUSTRATIONS (Continued)

<u>Figure</u>		<u>Page</u>
247.	HP Turbine Stage 1 Blade Tip Clearance Circumferential Deviation From Average (Final Test).	413
248.	HP Turbine Stage 2 Blade Tip Clearance Circumferential Deviation From Average (Final Test).	414
249.	HP Turbine Stage 1 Blade Tip Clearance Active Clearance Control Effect.	416
250.	HP Turbine Stage 2 Blade Tip Clearance Active Clearance Control Effect.	417
251.	HP Turbine Casing Data Match for Reading 258 Flows and Heat Transfer Coefficient.	418
252.	HP Turbine Casing Measured Temperatures From Reading 258 (Maximum ACC Cooling).	419
253.	HP Turbine Casing Data Match of Reading 258 (Maximum ACC Cooling and Test Cell Air Entrainment).	421
254.	HP Turbine Casing Expected ACC Cooling on Casing for Reading 258 Cycle Conditions (Maximum Cooling and No Test Cell Air Entrainment).	423
255.	Core Turbine Efficiency Shown on Rig Efficiency Map.	429
256.	Core Turbine Flow Function Versus Turbine Corrected Speed.	431
257.	Turbine Exit Pressure Profiles With Speed, Arc Rake Pressure as Measured.	432
258.	Turbine Exit Pressure Profiles With Speed and Corrected Arc Rake Pressure.	433
259.	Comparison of HP Turbine Exit Pressure Profiles, Core Versus Rig.	434
260.	Core Turbine Exit Temperature Profiles.	435
261.	Turbine Static Pressure Distribution.	437
262.	Thrust Bearing Temperature.	439
263.	Thrust Bearing Proximity Probe Output Sensing Radial Motion (Horizontal Plane).	440
264.	Thrust Bearing Proximity Probe Output Sensing Radial Motion (Vertical Plane).	441
265.	Aft Roller Bearing Performance Temperature.	442
266.	Aft Roller Bearing.	444
267.	Aft Roller Bearing Roller Passing Frequency.	446
268.	Start Range Turbine Cooling Pressure.	448

LIST OF ILLUSTRATIONS (Continued)

<u>Figure</u>		<u>Page</u>
269.	Flex Joint Adjacent to Start Range Turbine Cooling Valve.	449
270.	Failed Flex Joint in Start Range Turbine Cooling Piping.	450
271.	Lube Pump Discharge Pressure.	451
272.	Lube Supply and Combined Scavenge Temperatures.	453
273.	Lube System Heat Load.	454
274.	Schematic Showing Addition of Check Valve.	455
275.	Core Thrust Bearing Load Minimum Exhaust Nozzle Area.	457
276.	Core Thrust Bearing Load Maximum Exhaust Nozzle Area.	458
277.	Core System Synchronous Vibration Response, No. 4 Bearing.	460
278.	Core System Transient Vibration 1/Rev Displacement, Bullet Nose.	461
279.	Core System Transient Vibration 1/Rev Displacement, Forward Compressor Case.	462
280.	Core System Transient Vibration 1/Rev Displacement, No. 3 Bearing.	463
281.	Core System Synchronous Vibration Response.	464
282.	Forward Rotor Support and High Load Squeeze Film Damper.	466
283.	System Dynamic Analysis Computer Model Schematic.	467
284.	Modal Deflection for Critical Speed at 3469 RPM.	468
285.	Modal Deflection for Critical Speed at 6911 RPM.	469
286.	Core Engine Subsystems and Connecting Elements Used for Component Mode Analysis of Squeeze Film Damper System Characteristics.	470
287.	Core System Dynamics Response Sensitivity to Damper Oil Film Temperature.	472
288.	No. 3 Bearing Load Computed for Compressor Stage 1 Unbalance Using Direct Damped Solution.	473
289.	No. 4 Bearing Load Computed for Compressor Stage 1 Unbalance Using Direct Damped Solution.	474
290.	Speed Governing Instability.	476
291.	Switch From Single-to-Double-Annular Combustion.	478
292.	Start Time Investigation.	481
293.	Start No. 27 - Transient Plot.	482

LIST OF ILLUSTRATIONS (Concluded)

<u>Figure</u>		<u>Page</u>
294.	Start No. 29 - Transient Plot.	485
295.	Start No. 27 - Sanborn Recording.	488
296.	Core Engine Unbalanced Torque Characteristics.	490
297.	Pretest Predicted Starter Performance.	491
298.	Unbalanced Torque Based on Predicted Starter Performance.	493
299.	Unbalanced Torque Based on Serated Starter Performance.	494
300.	Starting Acceleration Fuel Schedule.	495

LIST OF TABLES

<u>Table</u>	<u>Page</u>
I. E ³ FPS Cycle Characteristics.	5
II. FPS Compressor Aerodynamic Operating Characteristics.	17
III. HP Turbine Aerothermodynamic Design Requirements.	35
IV. Secondary Flow Measurements.	73
V. Aeromechanical Instrumentation.	75
VI. Summary of E ³ Core Tests.	88
VII. Core Test Configuration Changes.	89
VIII. Phase II - Cycle Balance Matrix.	126
IX. Final Calibration Data Points.	128
X. Exhaust System Characteristics.	155
XI. Core HP Compressor Active Clearance Control.	160
XII. HP Compressor Clearance Change With Rotor Bore Cooling at 96% Corrected Speed.	160
XIII. Description of Rubs - Aft Looking Forward.	186
XIV. Maximum Cruise Operating Point.	190
XV. Core Emissions Testing.	222
XVI. Core Engine Test Fuel Sample Analysis.	223
XVII. E ³ Core Engine Test Combustor Instrumentation.	232
XVIII. Automatic Starts.	236
XIX. Emissions Test Operating Line Parameters and Measured Emissions.	239
XX. Emissions Data Corrected to the FPS Cycle.	253
XXI. Core Engine Emissions Levels Corrected for Fuel-Air Ratio Effects.	260

LIST OF TABLES (Concluded)

<u>Table</u>	<u>Page</u>
XXII. Core Emissions Adjusted to FPS Operating Conditions.	262
XXIII. Combustor Aerodynamic Performance Summary.	283
XXIV. Turbine Blade Vibratory Stress Statistical Analysis.	311
XXV. Stage 1 Blade Factors for Projecting Maximum Stress at Life Limiting Location.	315
XXVI. HP Turbine Stage 1 Blade.	315
XXVII. HP Turbine Stage 2 Blade Factors for Projecting Maximum Stress at Life Limiting Location.	321
XXVIII. HP Turbine Stage 2 Blade.	329
XXIX. Core Turbine Operating Parameters Compared to Pretest Cycle.	427
XXX. Core Turbine Parameters Along Operating Line.	428
XXXI. FADEC Sensor Accuracy.	497

LIST OF SYMBOLS, ABBREVIATIONS, AND ENGINE STATION DESIGNATIONS

<u>Symbol or Abbreviation</u>	<u>Definition</u>
A	Area, cm^2 (in^2)
ACC	Active clearance control
Accel	Acceleration
AGB	Accessory gearbox
ALF	Aft looking forward
Amb	Ambient pressure
AMAC	Advanced multistage axial flow core compressor
bhp	Brake horsepower
Btu	British thermal unit
CAFD	Circumferential average flow determination computer program
CDP	Compressor discharge plane, compressor discharge pressure
CF6-50	General Electric commercial turbofan engine family
CRT	Cathode-ray tube
CO	Carbon monoxide
cps	Cycles per second
D	Diameter, m or cm (in.)
Decel	Deceleration
DOC	Direct operating cost
DMS	Data management system
DS	Directionally solidified
D/A	Double annular
E ³	Energy efficient engine
EI	Emissions index
F	Force, N (lbf)
f/a	Fuel-air ratio
FADEC	Full authority digital electronic control
FAR 36	Fuel-air ratio in combustor
FHV	Fuel heating value
F _N	Net thrust
FOD	Foreign object damage

LIST OF SYMBOLS, ABBREVIATIONS, AND ENGINE STATION DESIGNATIONS (Continued)

<u>Symbol or Abbreviation</u>	<u>Definition</u>
FPS	Flight Propulsion System (refers to the fully developed configuration of the energy efficient engine which would be suitable for airframe installation)
G-Idle	Ground idle
h	Heat transfer coefficient, $[W/m^2 \text{ } ^\circ C \text{ (} ^\circ F)]$
Δh	Energy extraction, kJ/kg (Btu/lbm)
HC	Hydrocarbon
HCF	High cycle fatigue
HIP	Hot isostatic pressing (pressed)
HP	Horsepower, high pressure
HPC	High pressure compressor
HPT	High pressure turbine
ICLS	Integrated core/low spool (the complete turbofan test configuration of the E ³)
IGV	Inlet guide vane
KE	Kinetic energy
L	Length, m (in.)
LP	Low pressure
LPT	Low pressure turbine
LCF	Low cycle fatigue
M	Mach number
MXCR	Maximum cruise operating point
MXCL	Maximum climb operating point
N	Speed, rpm
NO _x	Oxides of nitrogen
OGV	Outlet guide vane (compressor or turbine)
P	Pressure, Pa (psi)
PE	Potential energy
PLA	Power lever angle (throttle position)

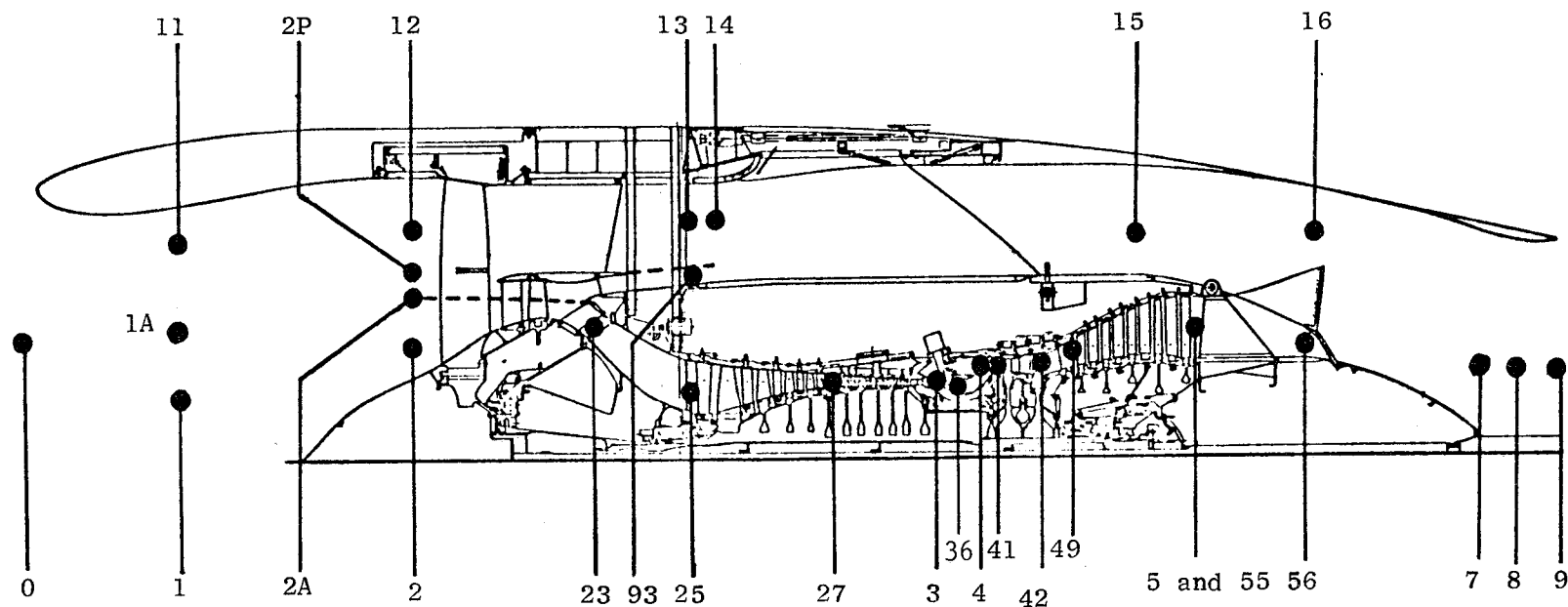
LIST OF SYMBOLS, ABBREVIATIONS, AND ENGINE STATION DESIGNATIONS (Concluded)

<u>Symbol or Abbreviation</u>	<u>Definition</u>
P/A	Force/area (stress), kPa (ksi)
PTO	Power takeoff
rpm	Revolutions per minute
RNI	Reynolds number index
sfc	Specific fuel consumption, kg/N•hr (lbm/lbf•hr)
SLTO	Sea level takeoff
SRTC	Start range turbine cooling
S/A	Single annular
T	Temperature, K (° R)
U	Rotor tangential velocity of the mean radius, m/s (ft/s)
V	Velocity, m/s (ft/s)
W	Weight flow, kg/s (lbm/s)
Γ	Turbine exhaust swirl, degrees
η	Efficiency
θ	Blade tip shroud angle, degrees
σ	Solidity
ϕ	Assembled pretwist rotation angle of blade tip shroud, degrees
Wf/PS3	Unit of fuel flow/unit of compressor discharge pressure, pph/psi

Subscripts

a	Air
C	Coolant, compressor
DT	Dovetail
g	Gas
h	Hub
P	Pitch
t	Tip
S,s	Static

The General Electric mixed-flow engine station designations system is used in this report. Engine station nomenclature is defined in Figure 1.



- | | |
|---|---|
| 0 Ambient | 23 Fan Hub Discharge That Goes to the |
| 1 Inlet Discharge at Fan Hub | Compressor Inlet |
| 1A Flow-Weighted Average at Inlet/Engine | 25 Compressor Inlet |
| Interface | 27 Compressor Interstage Bleed Port (5th Stage) |
| 11 Inlet Discharge at Fan Tip | 3 Compressor Discharge |
| 12 Fan Inlet at Tip | 36 Combustor Inlet |
| 13 Fan Tip OGV Discharge | 4 HP Turbine First Stage Nozzle Inlet |
| 14 Bypass Duct Inlet | 41 HP Turbine First Stage Nozzle Discharge |
| 15 Bypass Duct Exit | 42 HP Turbine Discharge |
| 16 Bypass Stream Mixing Plane | 49 LP Turbine First Stage Nozzle Discharge |
| 2 Fan Inlet at Hub | 5 LP Turbine Discharge |
| 2A Flow-Weighted Average for Total Engine | 55 Core Duct Exit |
| Flow at the Fan Face | 56 Core Duct Exit and Core Stream Mixing Plane |
| 2P Flow-Weighted Average for Total Bypass | 7 Exhaust Nozzle Inlet |
| Flow at the Fan Face | 8 Exhaust Nozzle Throat |
| 93 Fan Hub Discharge That Goes to the | 9 Exhaust Nozzle Discharge |
| Bypass Duct | |

Figure 1. E³ Station Designation.

1.0 SUMMARY

Testing of the Energy Efficient Engine (E³) core, a key element in NASA's E³ program for research into fuel-efficient engine technology, has been concluded. The E³ core used mechanical, aerodynamic, and system technologies advanced beyond current production engine state-of-the-art.

The objectives of the core test program fell into two general categories: First, demonstrate the technology readiness of the technology advancements in the E³ core. Second, learn as much as possible about the core internal mechanical, thermal, and aerodynamic performance.

Core testing was quite successful. Testing was expected to take 60 to 80 hours, but was completed in less than 45 hours. This was indicative of the trouble-free operation of this high-technology engine. No thermal or mechanical problems restricted the planned testing.

Measurements were obtained in the E³ core that were not commonly obtained in tests of other engines. These measurements gave a detailed, accurate assessment of engine operation and performance. For example, accurate core inlet airflow measurements allowed the isolation of combustor performance from turbine performance, something usually deduced analytically. Also, compressor and turbine clearances were accurately measured during engine operation. The 1400 aerodynamic, thermal, and mechanical sensors served to establish a more complete and accurate engine operation data bank than what previously existed, especially for technically advanced hardware. The end result has been a detailed and accurate knowledge of core performance. The core tests advanced the accuracy of correlations between deduced engine performance based on analytical procedures and performance results based on engine testing in real environments. Core tests also allowed accurate correlation of core component rig test results with those of those components operating in the core engine.

When adjusted for interstage instrumentation loss, variable Stators 5 and 6 loss, and Reynolds number effects, core compressor efficiency at the maximum cruise operating point was 85.6%. The goal efficiency for the core compressor was 85.1%.

The diffuser and combustor pressure drop was 5.4% at high power, or 0.4% above goal. This was due to the higher flow function of the core. Goal pressure drop would be met at the Flight Propulsion System (FPS) flow function.

Combustor light-off and staging from single- to double-annular combustion were accomplished successfully. Combustor efficiency was 99.9%, exceeding the goal of 99.6%. Projected to FPS cycle conditions, the core combustor met carbon monoxide and hydrocarbon emissions goals. Oxides of nitrogen emissions were higher than goal. Prior rig testing established design changes which will result in all emissions goals being met in an FPS. Based on measured smoke levels, integrated core/low spool (ICLS) is expected to produce no visible smoke.

Core high pressure turbine efficiency was 92.3%, corrected to FPS tip clearances. When projected to design point conditions, the turbine exceeds the efficiency goal by 0.6%.

The digital electronic control performed well in both automatic and manual modes, thereby providing operational flexibility which was a contributor to expedient engine testing.

Engine starting was accomplished without problems. A total time of under 47 seconds (29 seconds from initiation of fuel flow to reaching idle speed) was achieved without start bleed and with fixed fifth- and sixth-stage compressor stators. Further reductions in start time should be possible in the FPS. Start bleed, start range turbine cooling, and variable Stage 5 and 6 compressor stators will not be used in ICLS testing.

Posttest hardware is in excellent condition. No refurbishment or replacement of parts is necessary for the following ICLS testing. All core hardware is expected to perform satisfactorily during ICLS testing.

2.0 INTRODUCTION

The objective of the E³ Program is the development of technology to improve the energy efficiency of propulsion systems for subsonic commercial aircraft introduced in the late 1980's and early 1990's. The need for the E³ Program was established by shortages of petroleum-based fuels. Since the E³ Program was launched, escalated fuel prices have made improved energy efficiency essential. The E³ Program is a major element of the NASA Aircraft Energy Efficient Program (ACEE).

The following technical goals were established by NASA for the fully developed Flight Propulsion System (FPS):

- Fuel Consumption Minimum 12% reduction in installed sfc compared to a CF6-50C at maximum cruise thrust, M = 0.8 at 10,688 m (35,000 ft) altitude on a standard day.
- Noise Comply with FAR 36 (1978), with provisions for growth.
- Emissions Comply with EPA Proposed (1981) Standards for new engines.
- Performance Retention A 50% reduction in the rate of performance deterioration in-service as compared to the CF6-50C.

To meet and demonstrate the NASA Aircraft Project goals, the E³ Project has four major technical tasks structured as follows:

TASK 1 - PROPULSION SYSTEM ANALYSIS, DESIGN, AND INTEGRATION

This task addresses the design and evaluation of the E³ Flight Propulsion System (FPS), the propulsion system designed for commercial service. The FPS is executed only through the design phase. Task I also establishes the component design and performance requirements to be executed and tested in subsequent tasks. The initial function of Task 1, establishment and evaluation of the FPS design, has been completed. However, it

is periodically upgraded and modified as the technology evolves, as new ideas develop, and as test results become available.

TASK 2 - COMPONENT ANALYSIS, DESIGN, AND DEVELOPMENT

This task consists of the design, fabrication, test, and posttest analysis of the components and includes supporting technology efforts. Task 2 has been completed.

TASK 3 - CORE TEST

This task consists of the design, fabrication, test, and posttest analysis of the core test vehicle which consists of the compressor, combustor, and high pressure turbine. Task 3 is the subject of this report.

TASK 4 - INTEGRATED CORE/LOW SPOOL (ICLS)

This task consists of the design, fabrication, test, and posttest analysis of the ICLS turbofan ground-test vehicle. The core and low pressure components are combined in this vehicle. The ICLS design differs from the FPS in that it does not use a flight design gearbox, controls, nacelle, or fan frame. Design and procurement have been completed. Vehicle buildup and test preparations are underway. Testing is scheduled for the first-half of 1983.

Testing of the E³ core has two general purposes: First, provide for the evaluation of core components operating in the engine environment. Second, allow accurate measurements of those internal conditions that are impractical in a complete turbofan engine. Also, testing identifies hardware and operational problems so that they can be corrected prior to ICLS testing.

This report describes the core design and the test and presents the core test results.

3.0 HARDWARE DESCRIPTION

The General Electric E³ Flight Propulsion System (FPS) achieves high propulsive efficiency by using a low fan pressure and a mixer that combines the fan and core streams (prior to discharging them through a common exhaust nozzle). Higher thermal efficiency is achieved by using a higher engine pressure ratio, matched to high pressure (HP) turbine inlet temperature, and improved component performance compared to current engines such as the CF6-50C. The FPS engine was sized for 162 kN (36,500 lbf) takeoff thrust at sea level static standard day conditions. Characteristic cycle parameters are given in Table I.

Table I. E³ FPS Cycle Characteristics.

Cycle Pressure Ratio at Max Climb ⁽¹⁾	38
Bypass Ratio at Max Climb ⁽¹⁾	6.8
Fan Pressure Ratio at Max Climb ⁽¹⁾	1.65
Turbine Rotor Inlet Temperature at Sea Level Static Warm Day ⁽²⁾ Takeoff Power	1343° C (2450° F)
Specific Fuel Consumption at Max Cruise ⁽³⁾ , Bare Engine	0.0553 kg/(N·hr) ((0.542 lbf/(lbm·hr))
Specific Fuel Consumption at Max Cruise ⁽⁴⁾ , Installed Engine	0.0575 kg/(N·hr) ((0.564 lbf/(lbm·hr))

- (1) Max climb is the aerodynamic design point, M 0.8/10.7 km (35,000 ft), standard day plus 10° C (18° F).
- (2) Sea level static warm day refers to a standard +15° C (27° F).
- (3) Max Cruise is the performance evaluation point, M 0.8/10.7 km (35,000 ft), standard day.

The FPS mechanical layout is compact, thereby contributing to decreased deterioration, allowing simple frame and bearing arrangements, and making the full length fan duct/mixer arrangement practical. The aerodynamic and mechanical designs, the materials and manufacturing techniques are a generation beyond the base engine. The major features of the engine are shown in a sectional view in Figure 2. A cross section of the engine, including the integrated nacelle, is shown in Figure 3.

The core test vehicle, the subject of this report, uses the FPS compressor, combustor, and HP turbine. The frames, gearbox, electronic control, inlet, and exhaust were nonflight designs for ground testing. Some design and material differences in the FPS components were incorporated for economy and practicality and to accommodate extensive instrumentation. Details on the component designs and hardware will be given in the subsequent sections. The upper and lower halves of the core engine are shown in Figures 4 and 5. The assembled core test vehicle is shown in Figure 6.

3.1 FRONT FRAME DESCRIPTION

The core front frame is a nonflight design structure used to simulate the core flowpath of the turbofan frame. The core front frame provides mounting support for the accessory gearbox and for the front of the engine. The forward damper bearing, slipring, and engine thrust bearing are mounted within the front frame hub. Penetrations are provided through eight frame struts for the PTO (power takeoff) shaft and for services equivalent to those required on the turbofan. These include:

- Oil supply for front bearing and gearbox
- Oil supply for bearing damper
- Oil scavenge line
- Seal drain
- Sump vent to air/oil separator
- Oil vent line from gearbox

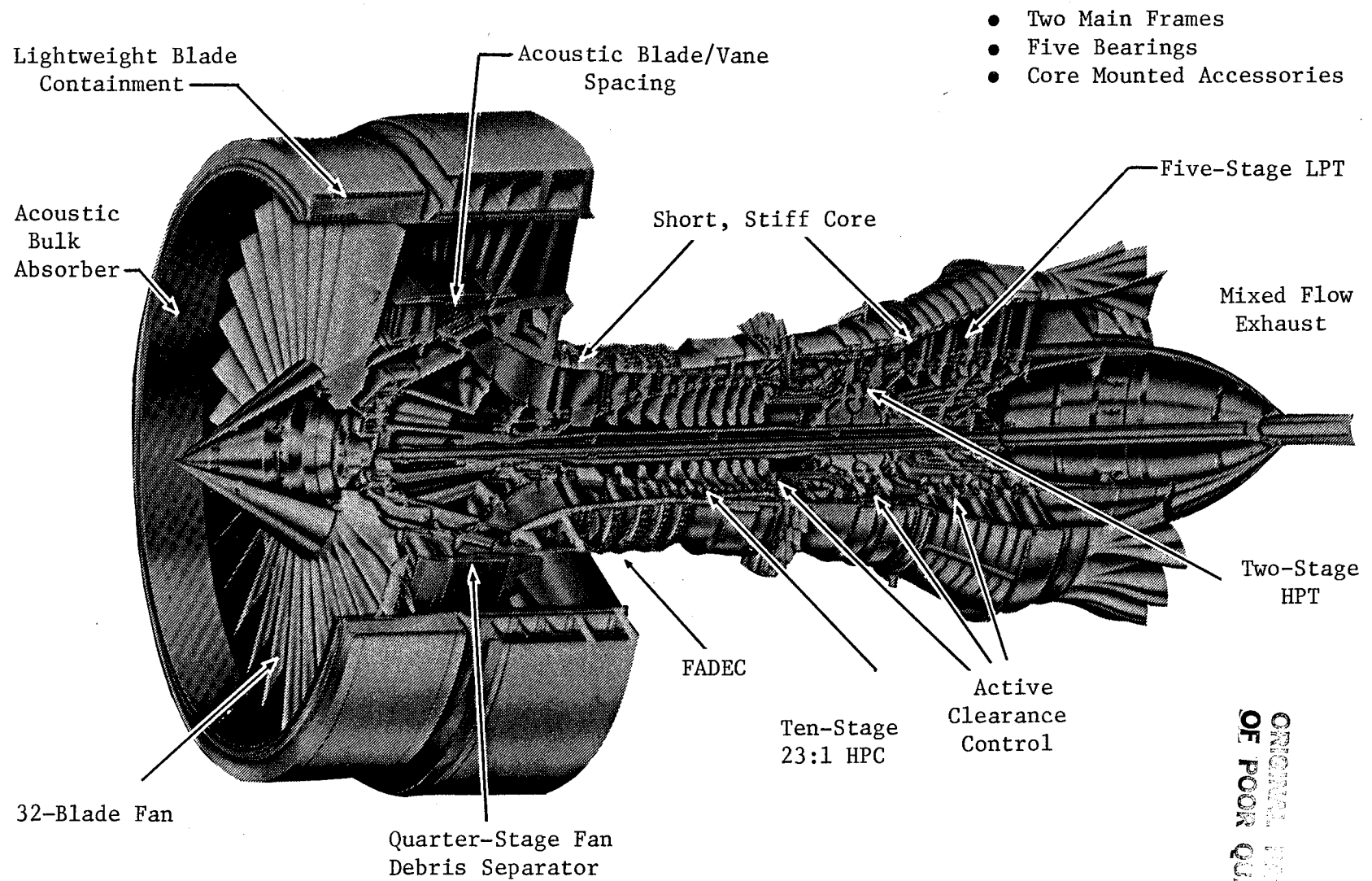


Figure 2. E³ Flight Propulsion System.

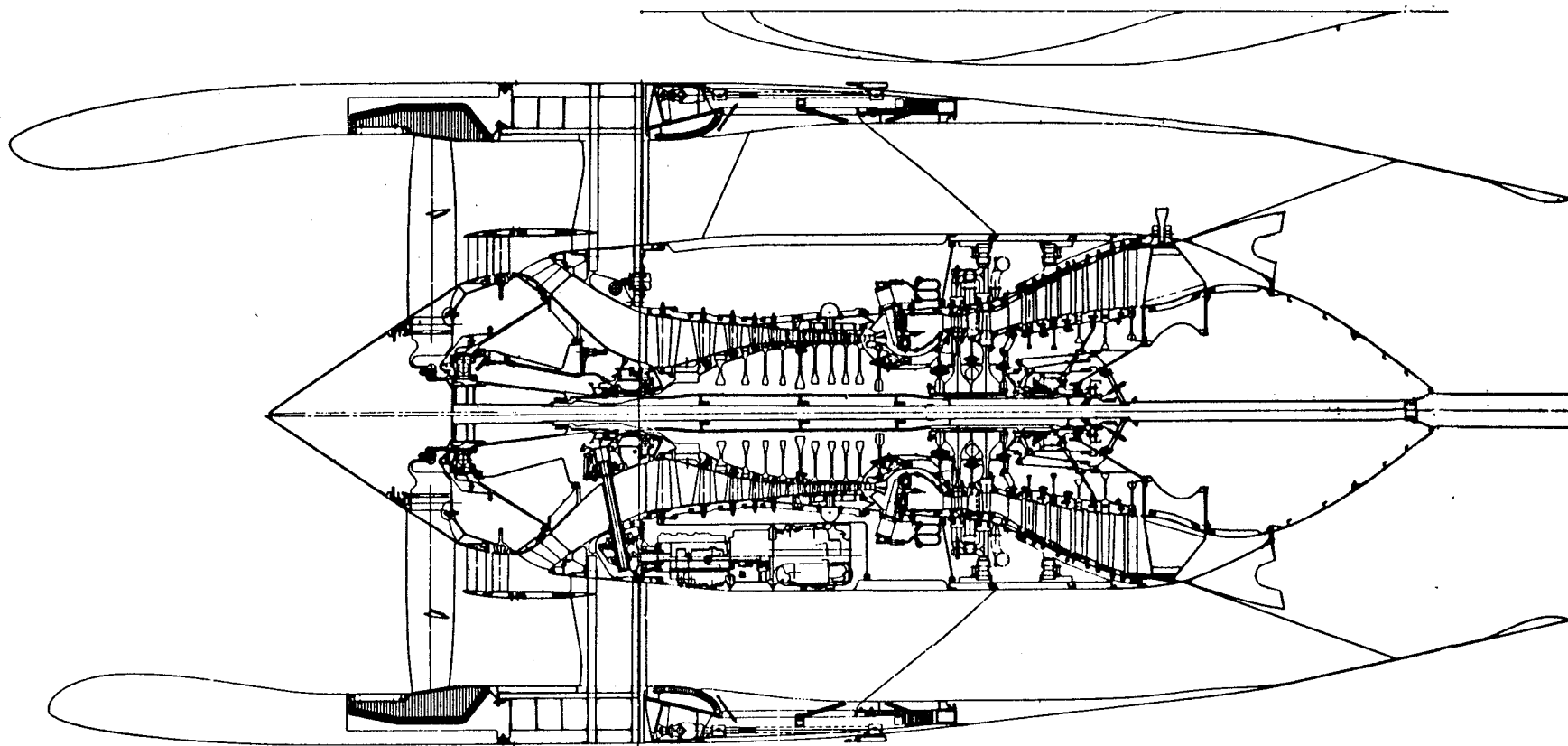


Figure 3. E³ Flight Propulsion System Cross Section.

**NASA
FORMAL
REPORT**

ORIGINAL PAGE IS
OF POOR QUALITY

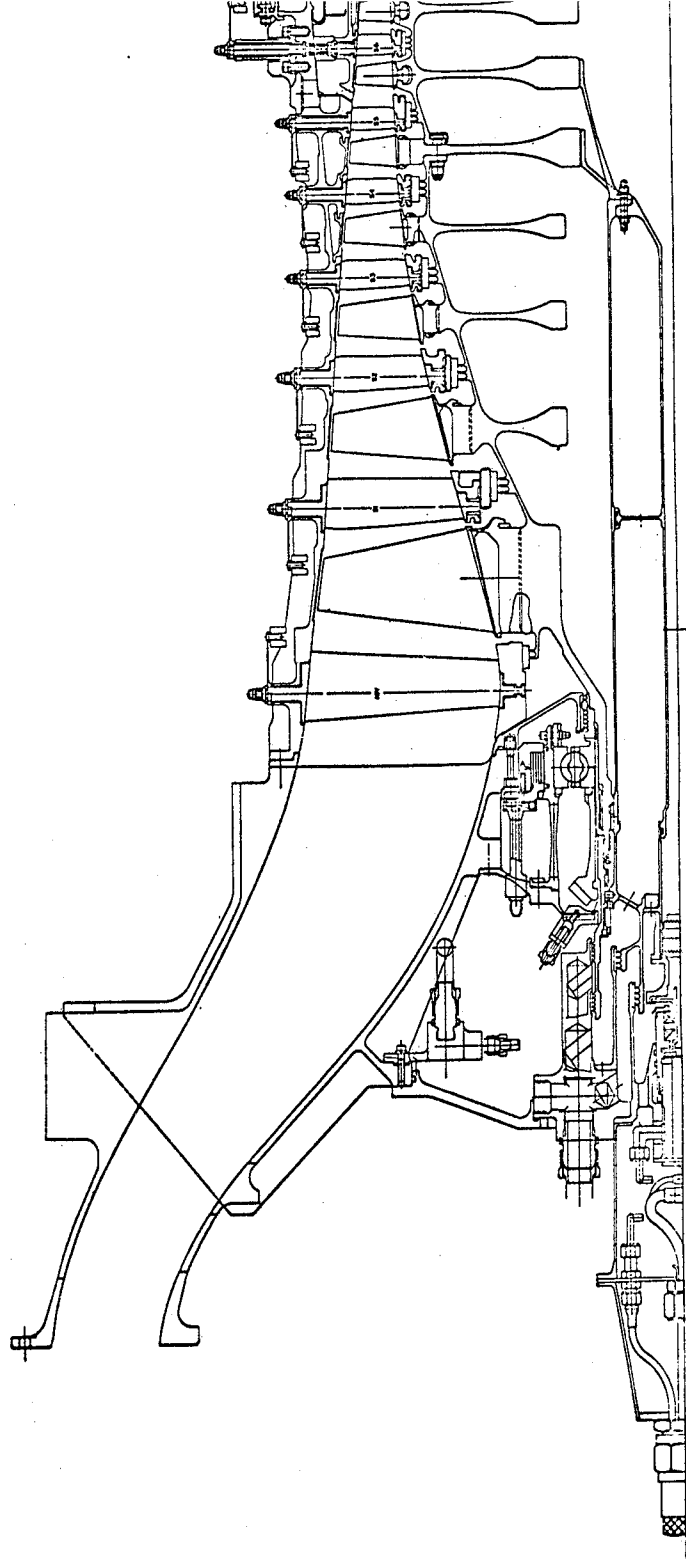
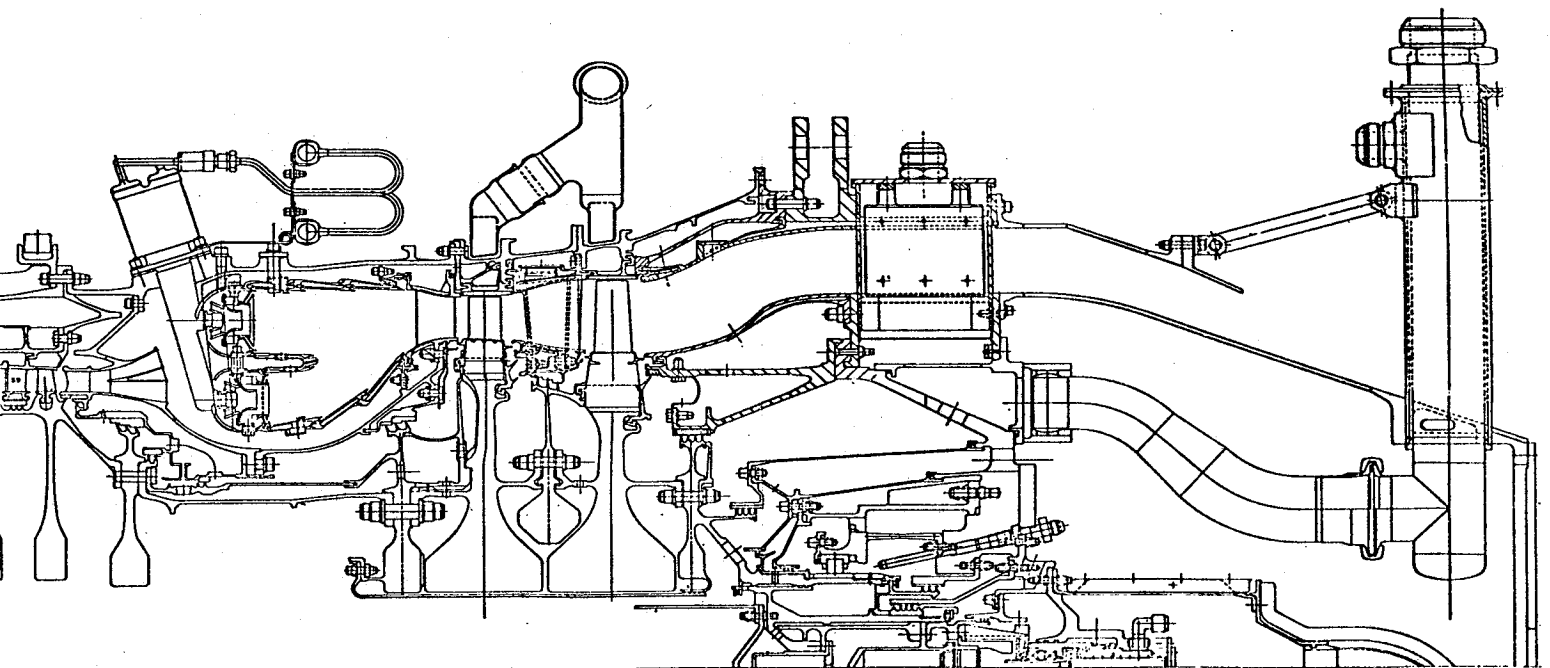


Figure 4. Upper

FOLDOUT FRAME

ORIGINAL PAGE IS
OF POOR QUALITY



f Core Cross Section.

2 FOLDOUT FIGURE

ORIGINAL PHOTO IS
OF POOR QUALITY

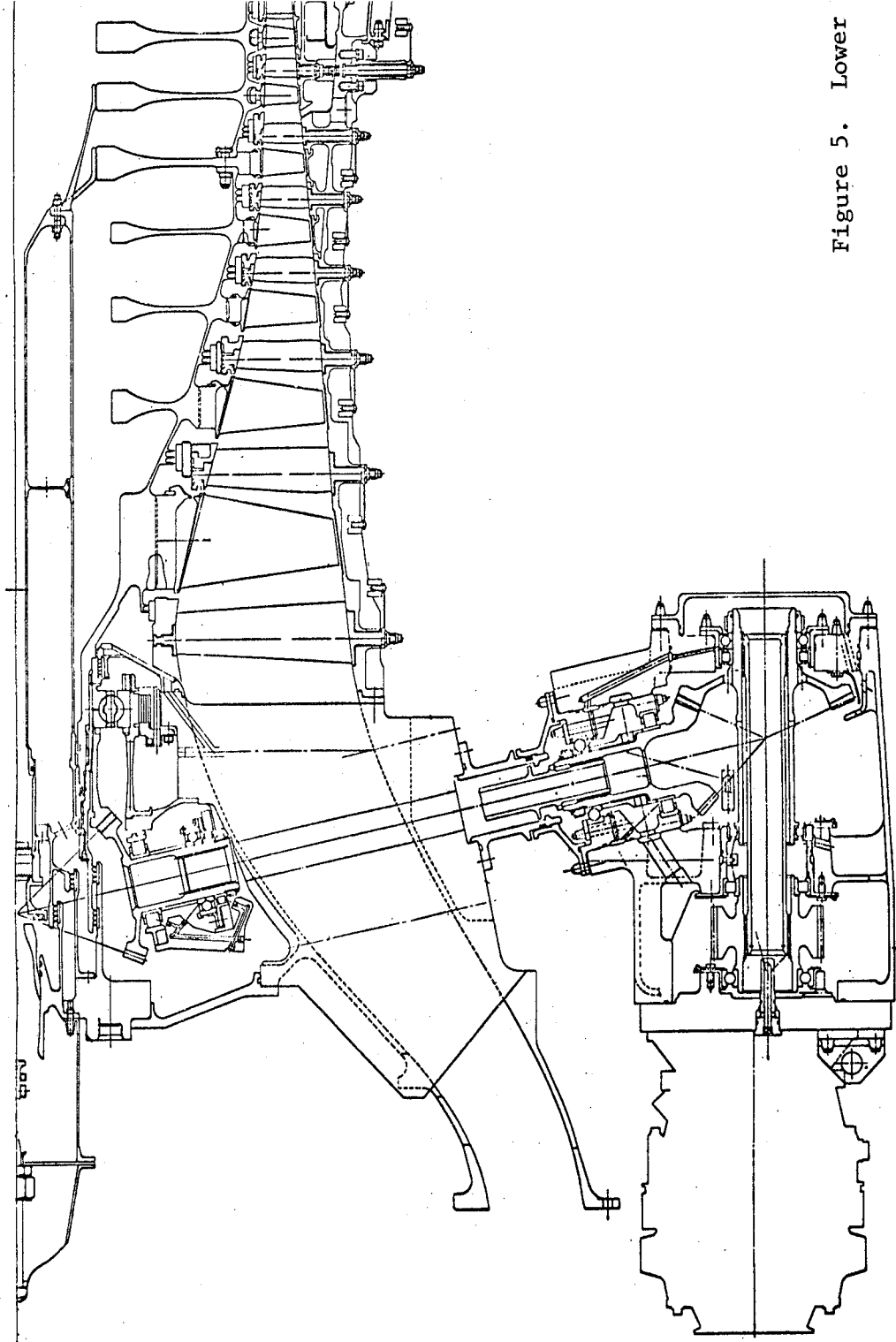
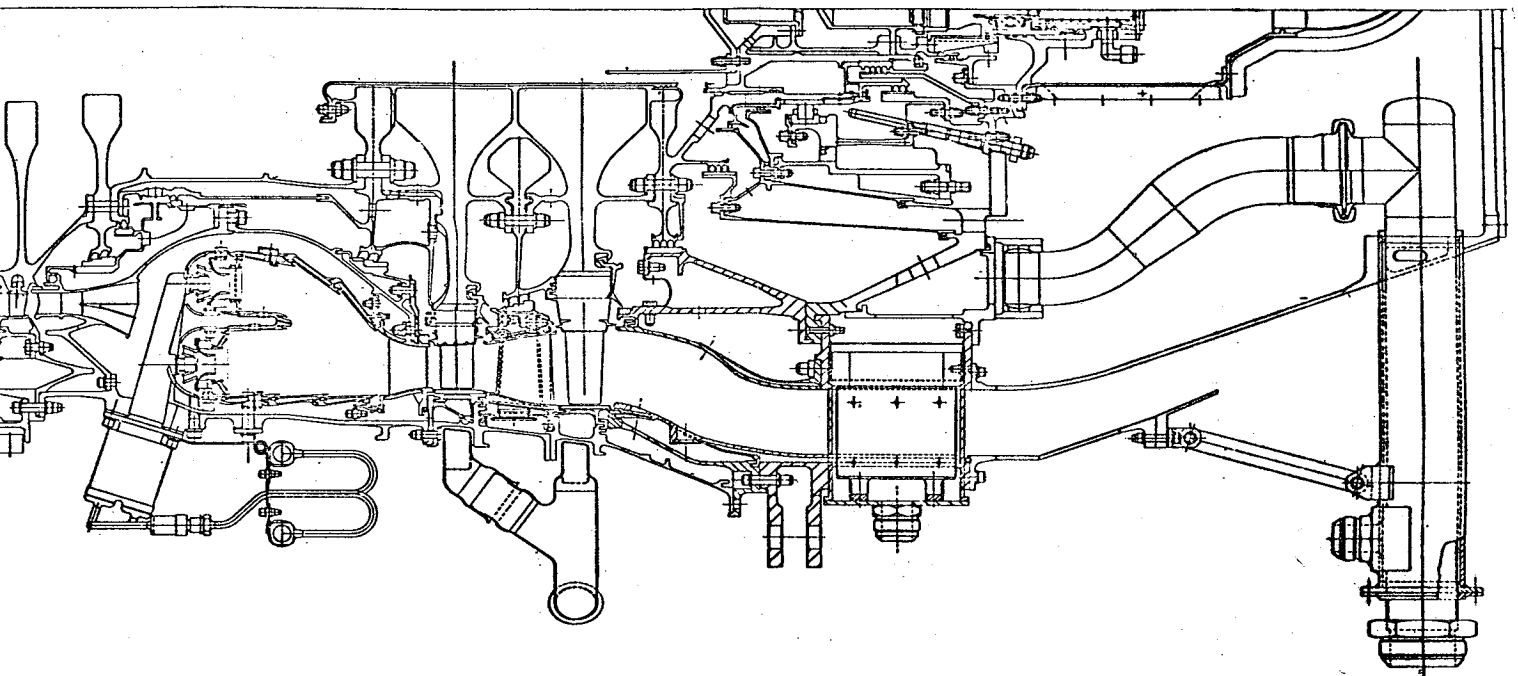


Figure 5. Lower

FOLDOUT FRAME

ORIGINAL PAGE IS
OF POOR QUALITY



Core Cross Section.

2 FOLDBOUT FRAME

ORIGINAL PAGE IS
OF POOR QUALITY

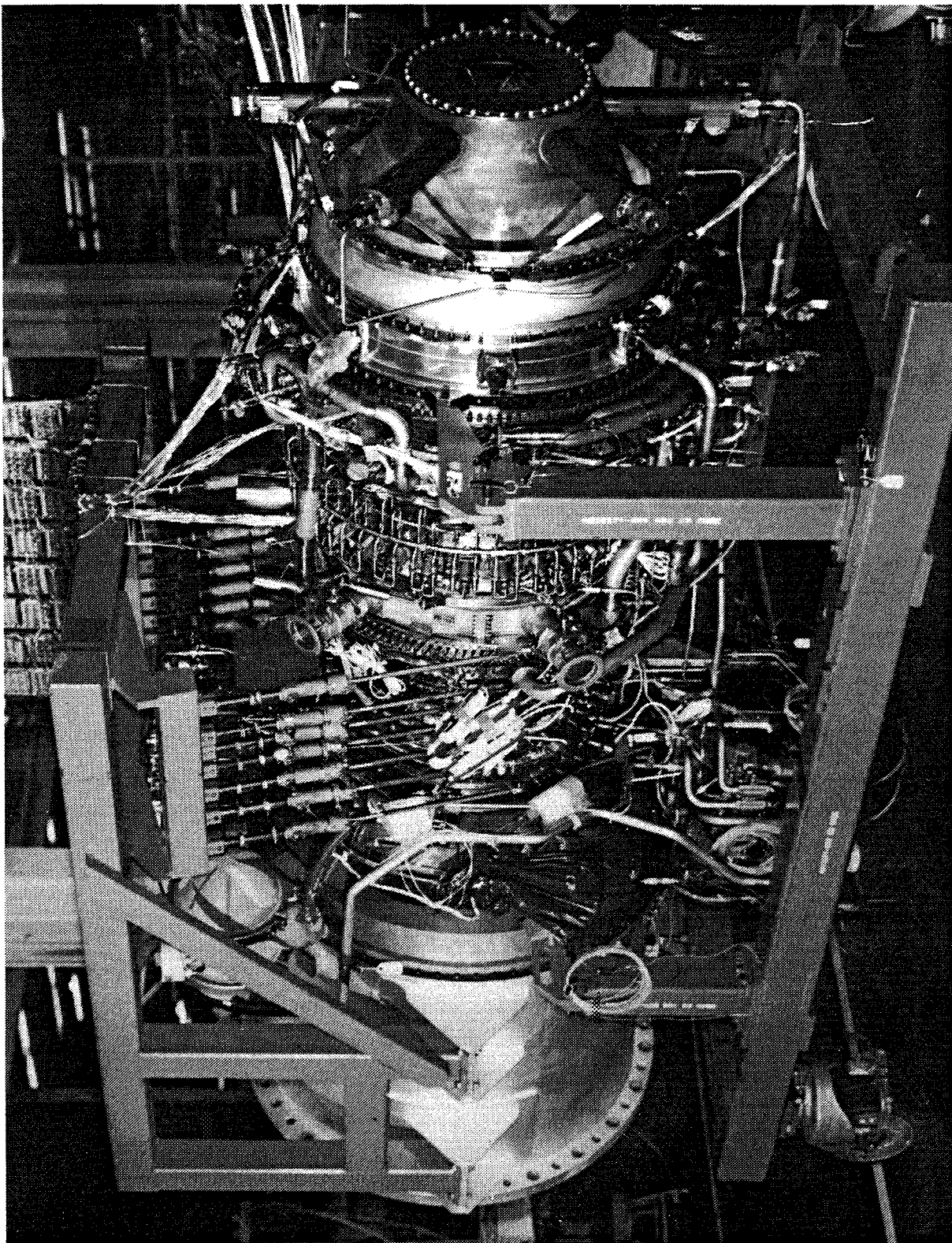


Figure 6. Photo of Core Test Vehicle.

ORIGINAL PAGE
BLACK AND WHITE PHOTOGRAPH

PRECEDING PAGE BLANK NOT FILMED

- Rotating and static instrumentation leadout
- Shop air for rotor bore purge
- Seal pressurization for front sump
- Purge air for seal cavity
- Freon for the slipring, in and out

3.2 COMPRESSOR DESCRIPTION

3.2.1 Aerodynamic Design

The core compressor for the GE/NASA E³ is an advanced technology, 10-stage unit designed to produce an operating line total pressure ratio of 23 at a design corrected tip speed of 456 m/s (1495 ft/s). Because of the high speed, pressure ratio, and aerodynamic loading, it is one of the most technically challenging designs that General Electric has built. The basic configuration was selected during the GE/NASA Advanced Multistage Axial Flow Core Compressor (AMAC) preliminary design studies conducted in 1975-1976 to identify an optimum compressor configuration for use in a low energy consumption, subsonic, commercial turbofan engine.

During the AMAC contract, parametric studies were conducted to determine the influence of the major compressor design features on efficiency, weight, cost, aircraft direct operating cost (DOC), and fuel usage. Those design parameters examined were: aspect ratio, solidity, inlet specific flow, exit Mach number, reaction ratio, inlet radius ratio, exit radius ratio, and number of stages. Compressor speed was set to allow each configuration studied to meet an objective level of stall margin. The studies were conducted for two engine configurations: (1) an engine having a core compressor total pressure ratio of 14 with booster stages on the low pressure spool and (2) an unboosted engine having a core compressor total pressure ratio of 23. The study determined that the best compressor efficiency was obtained by using medium values of average aspect ratio, solidity, and reaction ratio, and by using low values of inlet radius ratio, inlet specific flow, and exit Mach number. Reducing the number of stages by using higher speeds reduced the compressor length and cost, but not necessarily the engine weight. Efficiency was not severely

penalized by using fewer stages, provided that blading Mach numbers did not become excessive. High rear radius ratios were beneficial when used to hold rotor tip Mach numbers of the front stages below the level at which high shock losses would be present. The optimum rear radius ratio tended to increase as the number of stages were reduced and the speed was increased.

At the conclusion of the AMAC study, a 10-stage, 23:1 pressure ratio compressor was recommended for further development. This design incorporated those features mentioned above as contributing to high efficiency. The choice of 10 stages was made because this appeared to offer the best overall combination of desirable features such as compactness, low cost, high efficiency, low engine operating cost, and low fuel usage.

The decision to use the very high (23:1) pressure ratio core compressor in an unboosted engine configuration was made because it gave the lowest fuel consumption which resulted primarily from the use of an efficient two-stage HP turbine. This advantage outweighed the relatively small DOC penalty compared to a boosted engine with a lower core pressure ratio and a less efficient single stage HP turbine.

The technical challenge inherent in such a high pressure ratio for the core compressor was not overlooked. In fact, it is still the highest pressure ratio design that General Electric has ever undertaken; the pressure rise is approximately 30% greater than that of any production single-spool aircraft engine compressor. Both variable stators and starting bleed were provided to aid in achieving adequate low speed stall margin. The challenge of developing stator and bleed schedules that avoid potential starting and idle-to-takeoff acceleration problems was expected to be substantial. Another challenge was to minimize the efficiency penalty that might result from blade shapes compromised for off-design operation. Therefore, detailed performance analyses were made for off-design conditions during the final design process in order to establish design incidence angles and work input distributions that allowed high efficiency near design speed and adequate stall margin at part speed.

Refinements to the core compressor design continued during the E³ preliminary design study. The more significant refinements (1) somewhat increased

the inlet specific flow and the exit Mach number and (2) reduced the speed, average aspect ratio, and average solidity. These changes were made mainly to reduce cost through the use of fewer and longer chord airfoils and to increase blade erosion resistance and general ruggedness. Despite the lower speed, an increase in stall margin potential was predicted, with only a small efficiency penalty.

Many of the advanced features incorporated into the detailed design of the E³ core compressor were developed during a parallel supporting research program - the NASA-sponsored Core Compressor Exit Stage Study. This program utilized a low speed, four stage model of the blading used in the middle and rear E³ compressor stages to develop improved airfoil shapes and vector diagrams. A baseline stage and several modified stages were tested, and worthwhile improvements in efficiency and stall margin were demonstrated by design refinements that improved the flow in the end-wall regions.

Core compressor aerodynamic design requirements were established primarily for the maximum-climb-thrust power setting at a flight condition of Mach 0.8 at 10.67 km (35,000 ft) altitude on a +10° C (+18° F) day. This operating condition places the core compressor at maximum corrected speed, corrected airflow, and total pressure ratio; therefore, it was defined as 100% design corrected speed. However, compressor efficiency requirements were very important at altitude cruise. The performance requirements for these operating conditions, as well as the requirements for sea level takeoff, are listed in Table II. The operating line pressure ratios listed are for zero customer bleed air and zero power extraction. The performance goals in Table II are for the fully developed FPS. The efficiency goal for the core and ICLS engines is one point lower than the FPS goal, reflecting 1980 technology rather than the expected 1986-1990 technology of the full developed FPS product engine.

The basic vector design tool employed was General Electric's Circumferential Average Flow Determination (CAFD) computer program. This program computed the vector diagrams and fluid properties along numerous stream surfaces for a specified flowpath geometry, stage work input distribution, and estimated loss distribution. The resulting axisymmetric, steady-state, circumferential average flow solution included all effects of the full radial equilibrium equation and included internal blade row calculations for some stages.

Table II. FPS Compressor Aerodynamic Operating Requirements.

<u>Parameter</u>	<u>Maximum Climb</u>	<u>Maximum Cruise</u>	<u>Takeoff</u>
Corrected Speed, % Design	100.0	99.5	97.7
Corrected Airflow, kg/s (lbm/s)	54.4 (120.0)	53.5 (118.0)	49.3 (108.7)
Total Pressure Ratio	23.0	22.4	20.1
Adiabatic Efficiency	0.857	0.861	0.865
Polytropic Efficiency	0.903	0.905	0.908
Inlet Temperature, K (° R)	304.4 (547.9)	301.4 (542.5)	327.8 (590.1)
Inlet Pressure, N/m ² (lbf/in ²)	59,641.8 (8.65)	58,055.9 (8.42)	150,586.8 (21.84)

Vector diagrams along blade and vane leading and trailing edges were then used with airfoil section design procedures and cascade analysis computer programs to determine the final blade shapes.

The output data from the CAFD computer program were the vector diagrams at the intersection of the streamlines and the calculation stations. These vector diagrams were used in the design of the E³ blades and vanes as described in the next paragraph. In addition, the vector diagrams were used to calculate blade and vane diffusion factors as an indication of the aerodynamic loading.

The aerodynamic design of the airfoils for the E³ core compressor included the design of transonic and subsonic rotor blades, subsonic stator vanes, and an inlet guide vane (IGV). Fundamentally, the approach utilized for all blade and vane designs was one of tailoring stream surface blade shapes to produce specific airfoil surface velocity distributions. The first four rotors were transonic blade rows and were designed utilizing techniques employed for advanced fan stages. The remaining six stages of rotor blades and all stages of stator vanes were designed to operate in a subsonic flow environment. Figure 7 shows Stator 6, representing a typical stator. In

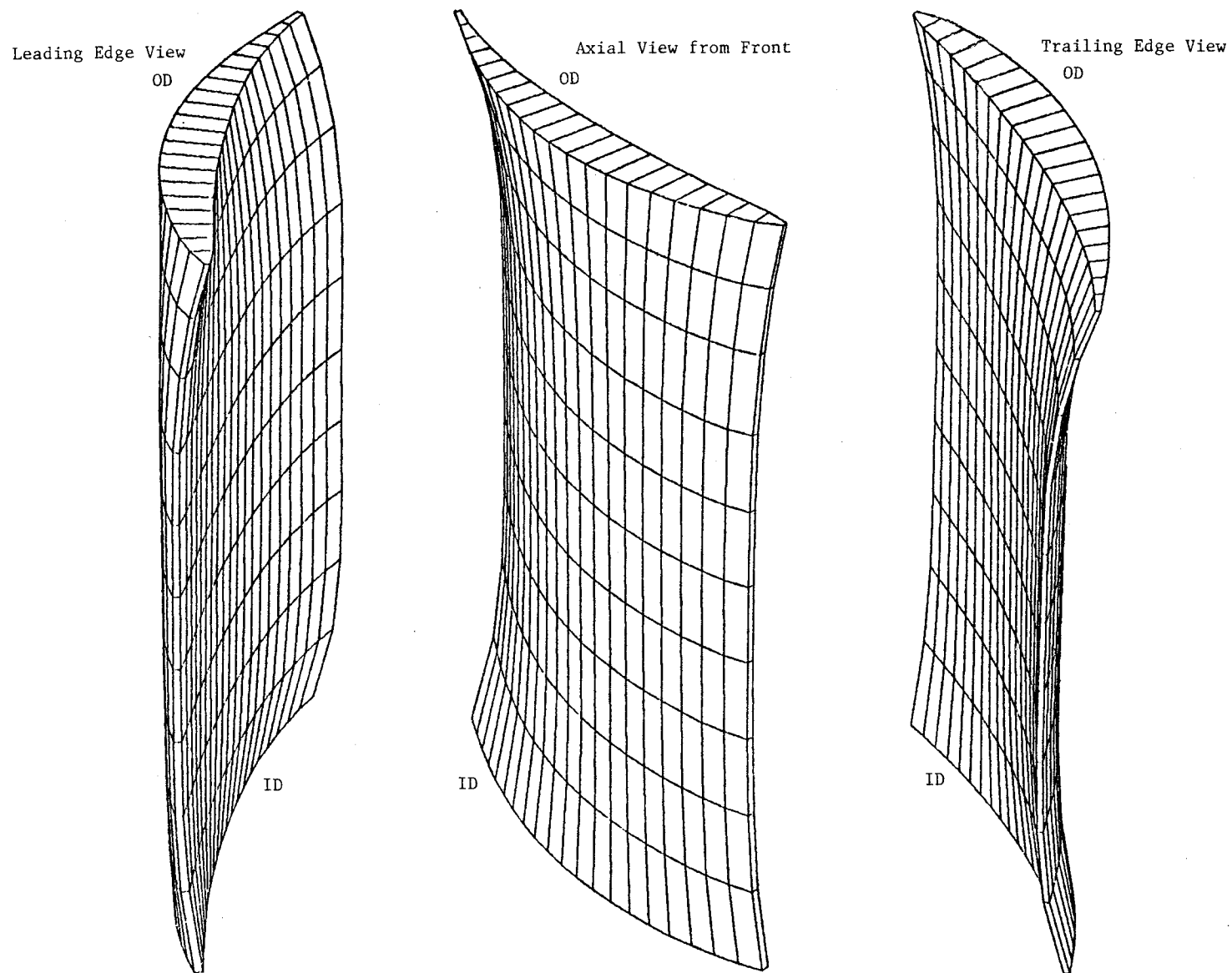


Figure 7. Three-Dimensional Sketch of Compressor Stator 6.

addition, the airfoil section and the unique stagger angle distribution used for the stator vanes are shown.

Casing ports for customer bleed and compressor active clearance control (ACC), used subsequently for low pressure (LP) turbine cooling and purge, were provided at Stator 5 exit. Other casing ports for starting bleed and HP turbine cooling air were located at the Stage 7 exit. While the IGV and the first four stator vane rows are variable in the FPS design, the development rigs and engines incorporate variable Stage 5 and 6 stator vanes. For component and core engine testing, the compressor inlet transition duct was preceded by a bellmouth and bulletnose inlet assembly.

The original aerodynamic design of the core compressor was completed in the second quarter of 1979. Three component tests were conducted: the front six variable stator stages were tested in the first quarter of 1980; the full 10-stage compressor was tested for the first time during the first quarter of 1981; and a second version of the full 10-stage compressor was tested early in 1982. Various design refinements, made as a result of the data obtained during this experimental evaluation, were incorporated into the final compressor version utilized in the E³ core engine.

3.2.2 Mechanical Design

Design requirements for the production engine called for an installed service life of 18,000 hours without engine removal and a total useful life of 36,000 hours. With the exception of some items that were reworked for instrumentation, all components of the core compressor met these requirements.

A cross section of the HP compressor rotor is shown in Figure 8. Unique features contributing to the design objectives of producing a lightweight, rugged, efficient rotor are denoted. Note the use of a single bolt joint at midrotor in order to yield a short, stiff structure. A photograph of the rotor is shown in Figure 9. The use of low aspect ratio airfoils produces a high tolerance to FOD and stalls. Sealing the blade dovetails and polishing the airfoils provides an increase in compressor efficiency. Utilization of fan discharge air to cool the rotor bores helps to optimize rotor-stator

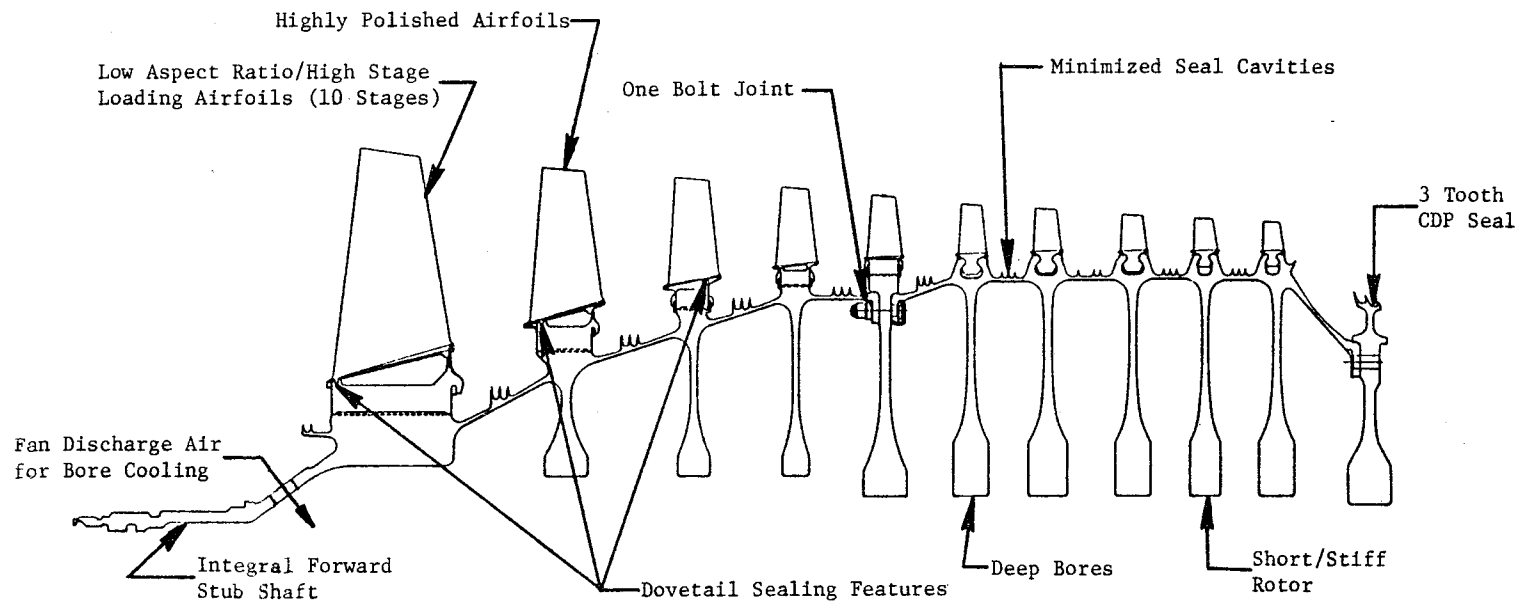


Figure 8. High Pressure Compressor Rotor Design Features.

ORIGINAL PAGE
BLACK AND WHITE PHOTOGRAPH

ORIGINAL PAGE IS
OF POOR QUALITY

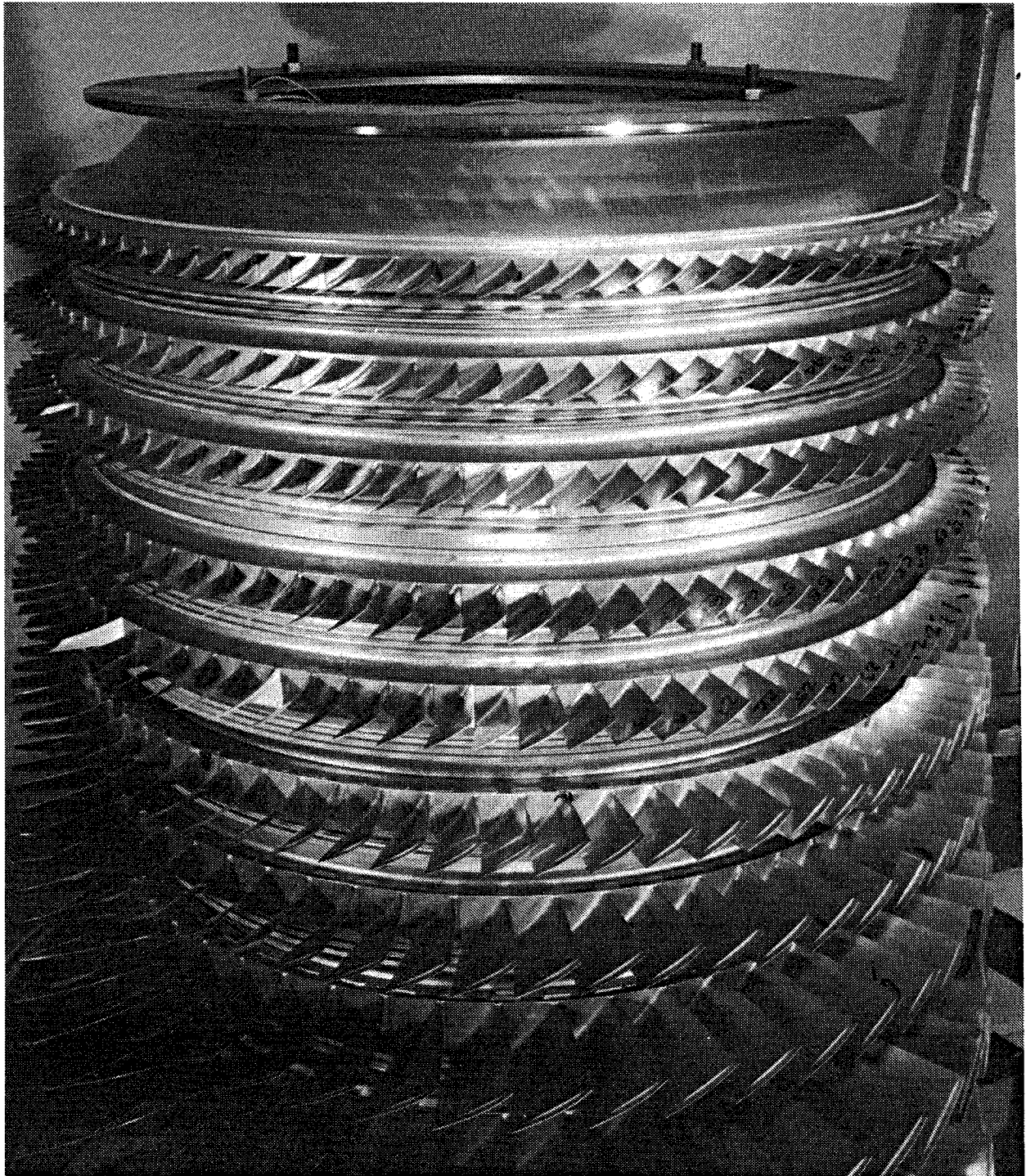


Figure 9. Photo of Compressor Rotor Hardware.

clearances, thus providing additional efficiency gains. The rotor materials selected to achieve a high-strength, cost-effective design are shown on Figure 10.

The compressor stator cross section is shown in Figure 11. Unique features of the design are denoted. The titanium fire prevention requirement is met by the use of nontitanium casings and vanes. To improve compressor cruise performance, the aft case is designed to provide active control of rotor-stator clearances. This is accomplished by isolating the casing structure from the hot flowpath gases and then bathing the structural rings with cooler Rotor 5 discharge air to shrink the casing closer to the rotor blade tips. This cooling air is collected in the annulus over Rotor 10, then is ported through the forward case and is piped aft where it is used to cool the LP turbine and rotor cavity (reference Figure 13). The flow of air is controlled by a fuel-activated valve. The effectiveness of the ACC is discussed in Section 6.2.

Variable vane leading edge tips are covered by the OD/ID trunnions to prevent circumferential crossflow, thereby enhancing performance. Internal GE research tests have shown that small performance gains can result from recessing the flowpath over the blade tips, a feature incorporated on the E³ compressor. End-wall losses are reduced by uniquely contouring the airfoil ends. Because of the end-wall contouring, the fixed geometry vanes could not be fabricated by ordinary methods but had to be cast.

The compressor discharge diffuser is a unique cast structure featuring a flowpath that is split into two annular passages and supported by hollow struts. A portion of the air exhausting at the splitter island is ducted inboard through the hollow struts to provide cooling for the HP turbine. The geometry of the diffuser is so complex that it required an advancement in the state of casting technology in order to be produced. In the early designs, it was planned that the outlet guide vane (OGV) ring would be cast integrally with the diffuser. However, the successful welding of the OGV ring to the diffuser for the core engine has proved this to be a more workable approach.

Inlet guide vanes through Stator 6 were variable on the compressor test rigs and on the core engine to allow for complete performance mapping over the

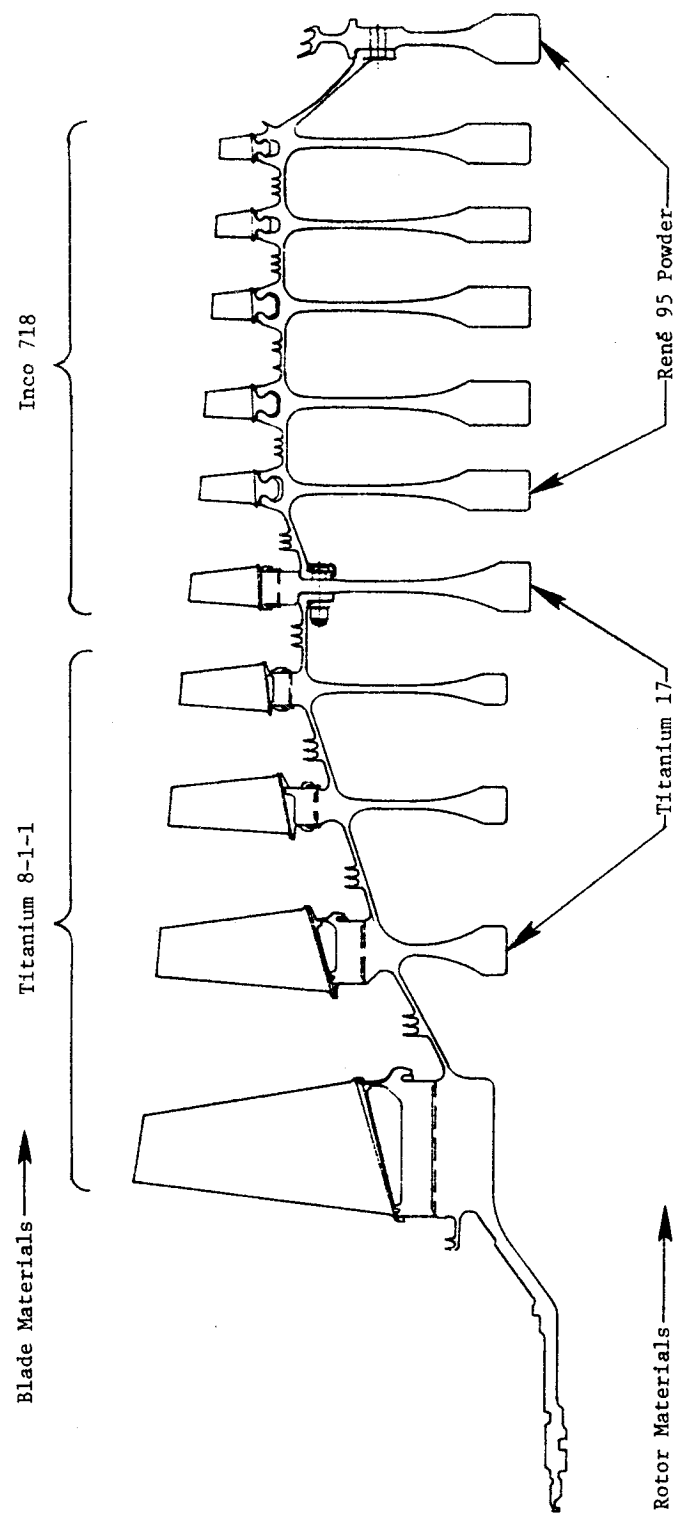


Figure 10. Core and ICLS Compressor Rotor Materials.

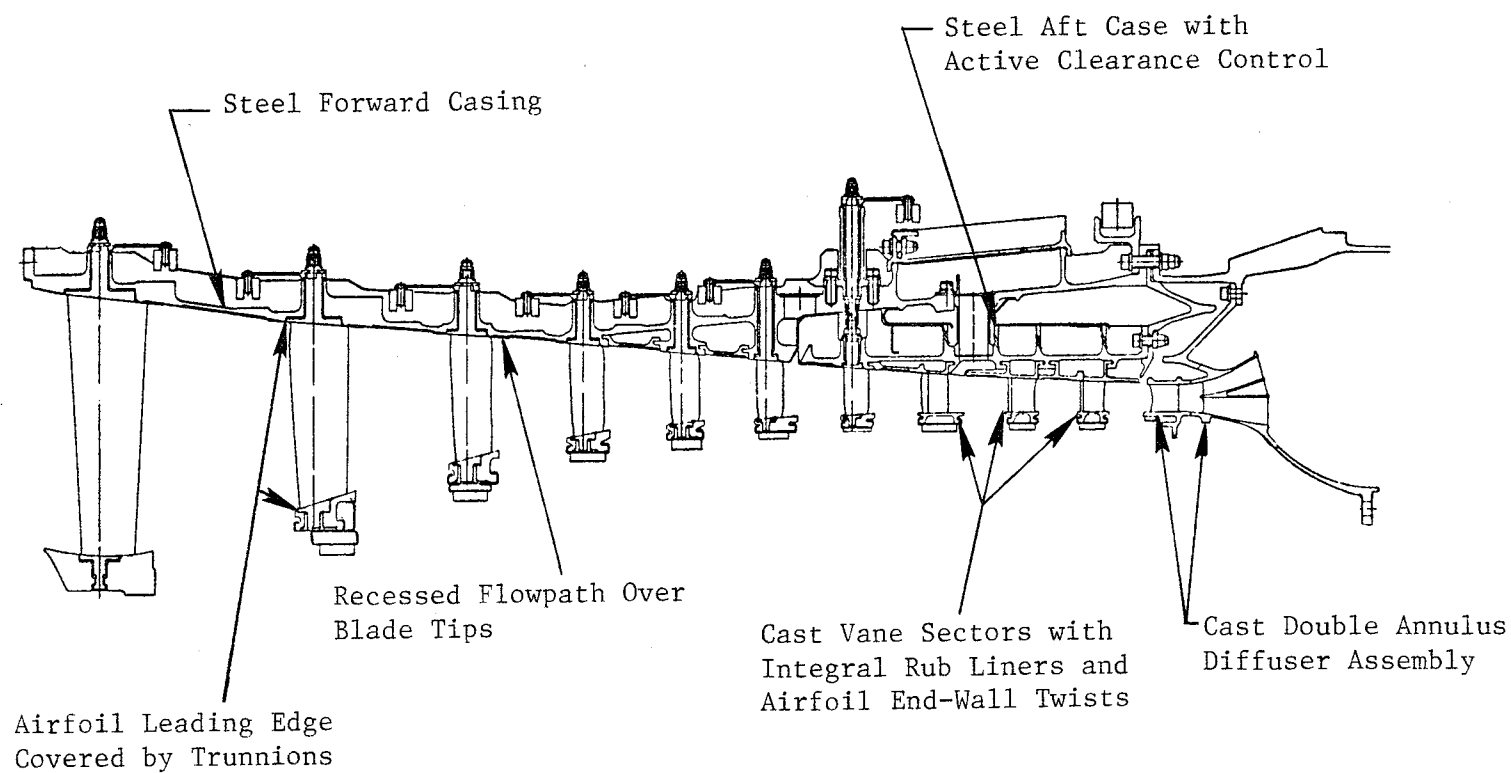


Figure 11. Compressor Stator Design Features.

operating range. Each stage was independently actuated, but had the capability of being ganged to track a specific schedule. It was originally intended that Stators 5 and 6 would be fixed in the product engine; it was demonstrated during the core test that this is acceptable.

Compressor stator materials are listed in Figure 12. The M152 steel alloy was chosen for the casings because its coefficient of expansion closely matched that of the rotor structure, making clearance control easier. Rotor rub lands were coated with current, proven production-engine materials. Variable stator vane bushing materials were chosen after extensive development and test programs to assure they would meet engine life requirements.

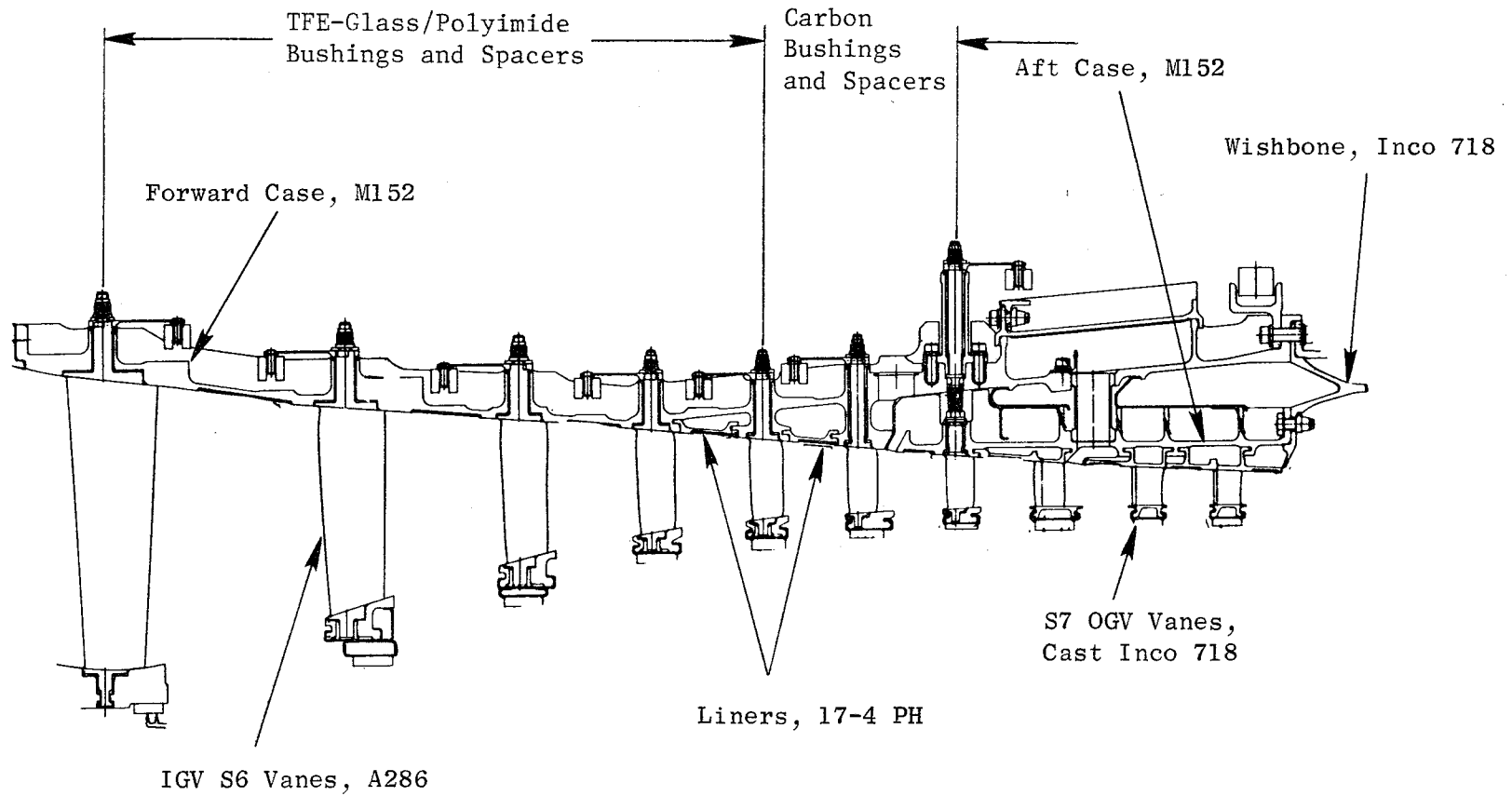
Compressor bleeds, their quantities and their uses, are summarized in Figure 13. During the initial design phases, one area of concern was the starting of a high pressure ratio engine. Provisions were made to bleed up to 30% of Stage 7 air to aid in starting. A portion of the core test was dedicated to investigating engine start characteristics. As a result of these tests, it was determined that the engine could be started without the use of compressor bleed.

3.3 COMBUSTOR DESCRIPTION

3.3.1 Aerodynamic Design

The E³ combustor is the short length, double-annular design shown in Figure 14. The double-annular feature is used to provide low emissions over a wide range of power levels. Only the outer pilot zone is used at low power levels, and it is tuned for low fuel-air ratios. At higher power levels, both zones are used. The inner main zone is tuned for higher fuel-air ratios.

The E³ combustor uses dual cone nozzles for fuel injection. Compressor discharge airflow is directed to the combustor by a split duct prediffuser. Forty-eight percent of the air flows through the outer passage of the prediffuser toward the pilot stage dome, and the remaining 52% is directed toward the main stage dome by the inner passage of the prediffuser. The dome cups of the pilot stage and the main stage are each comprised of axial primary and



Rub Material

Stages 1 - 4, Al-Br-Ni-Cg

Stages 5 - 10, Metco 443
Ni-Cg

Honeycomb

Hastelloy X

Shrouds

IGV and S1, 6061-T6

S2 - S4, 17-4 PH

S5 - S6, Inco 718

Interstage Seals

Inco 600

Figure 12. Compressor Stator Materials.

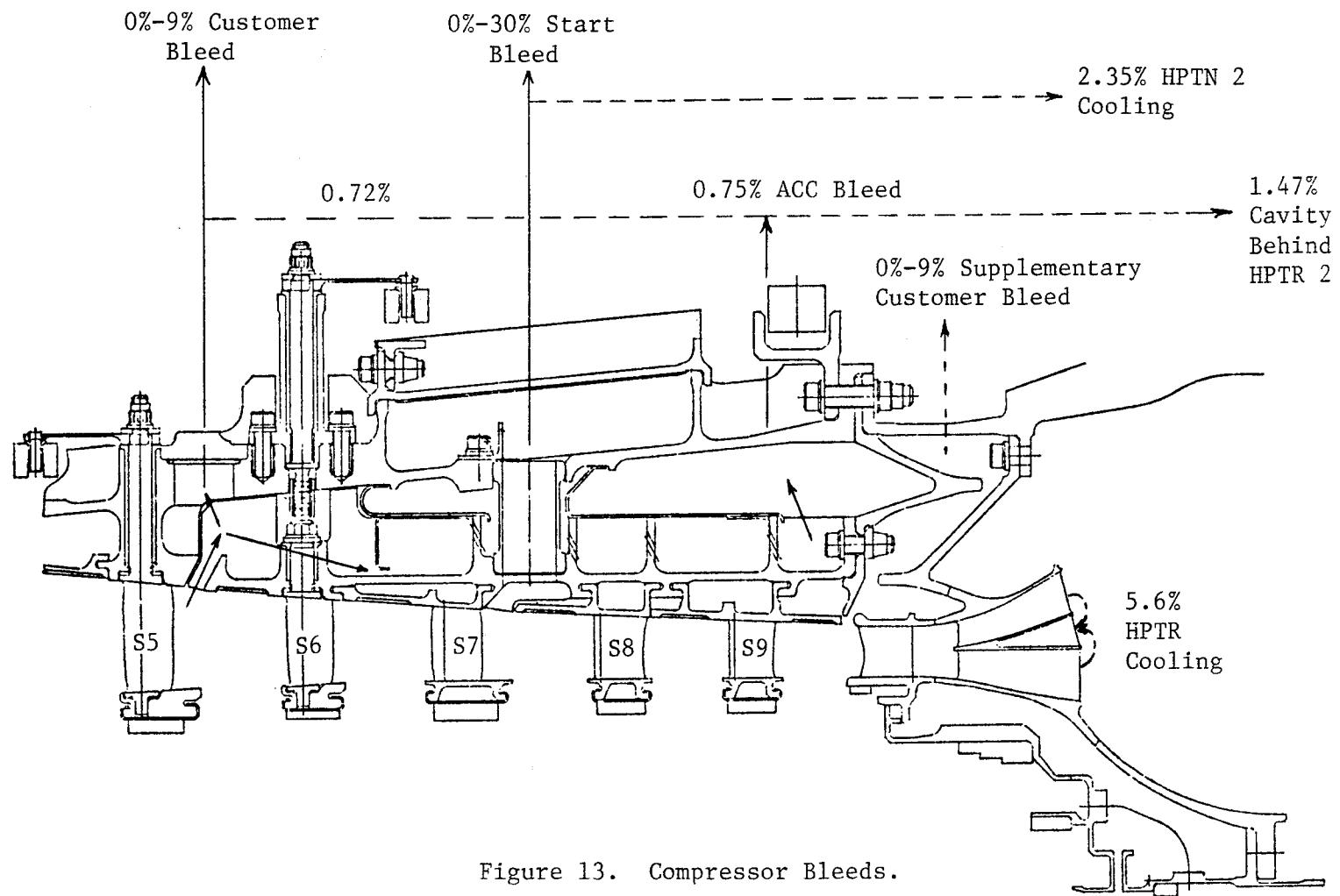


Figure 13. Compressor Bleeds.

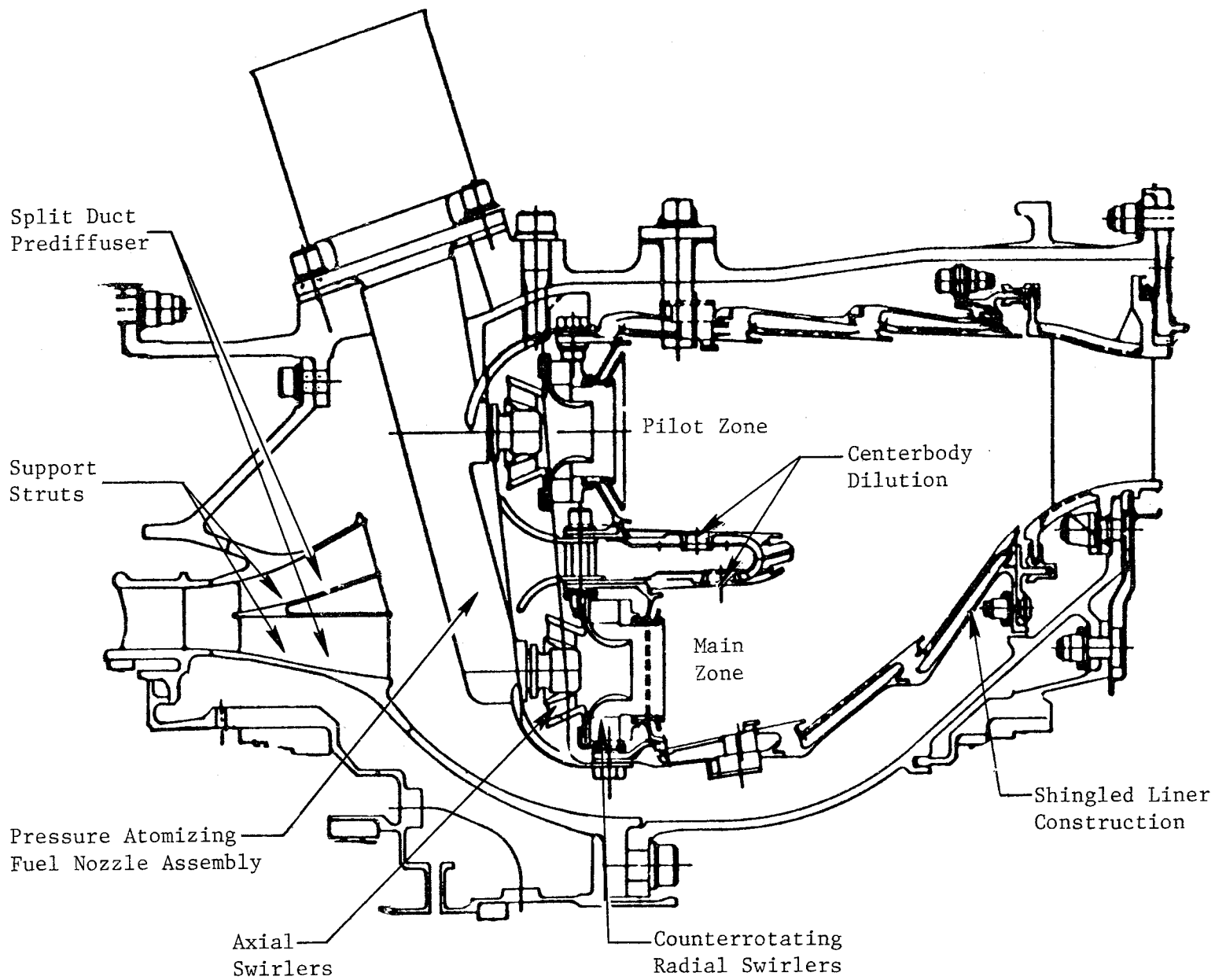


Figure 14. E³ Combustor Design Features.

counterrotating radial secondary airflow swirlers. The liners are of double wall construction and use impingement plus spent-film cooling on the segmented (shingle) section adjacent to the hot gas stream.

Fuel injection for each E³ combustor dome is provided by duplex-type fuel pressure atomizing nozzle tips mounted on a single stem. These fuel nozzles are described in more detail in the Combustor Mechanical Design section which follows. Each of the two tips has a low-fuel-flow primary system for good atomization at low power operating conditions and a high-fuel-flow secondary system to achieve the required fuel flow levels at high power. Fuel flow is supplied to the fuel nozzles by an annular manifold system. Fuel nozzle inlet check valves keep the manifold full and pressurized during shutdown to prevent fuel leakage into the combustor and to reduce start times. Fuel flow to the duplex nozzle tips is controlled by each of two scheduling valves (one for each tip) located in the housing above the stem. The fuel nozzle stem is encased in a heat shield to insulate the fuel from hot compressor gas temperatures. Each fuel-carrying tube within the stem is surrounded by a clearance gap to provide additional insulation. The fuel nozzles are arranged in the combustor to provide the most uniform fuel distribution based on the results of flow calibrations.

3.3.2 Mechanical Design

The E³ combustor with the materials selection called out is illustrated in Figure 15. Photographs of the assembly are shown in Figures 16 and 17. A centerbody structure separates the outer diameter pilot zone from the inner main zone of the combustor. The double annular dome design consists of 60 identical swirl cups. Fuel is injected into the combustor through 30 dual-tip fuel nozzle assemblies. Each nozzle features independent fuel metering. The combustor utilizes a double-wall shingled liner design to provide long life. The combustor assembly is supported at the forward end by 30 support pins positioned radially to transmit all loads from the liners to the outer combustor casing. The combustor-to-stator interface is sealed with fishmouth seals which accommodate axial and radial thermal expansion and assembly clearance stackups between the components.

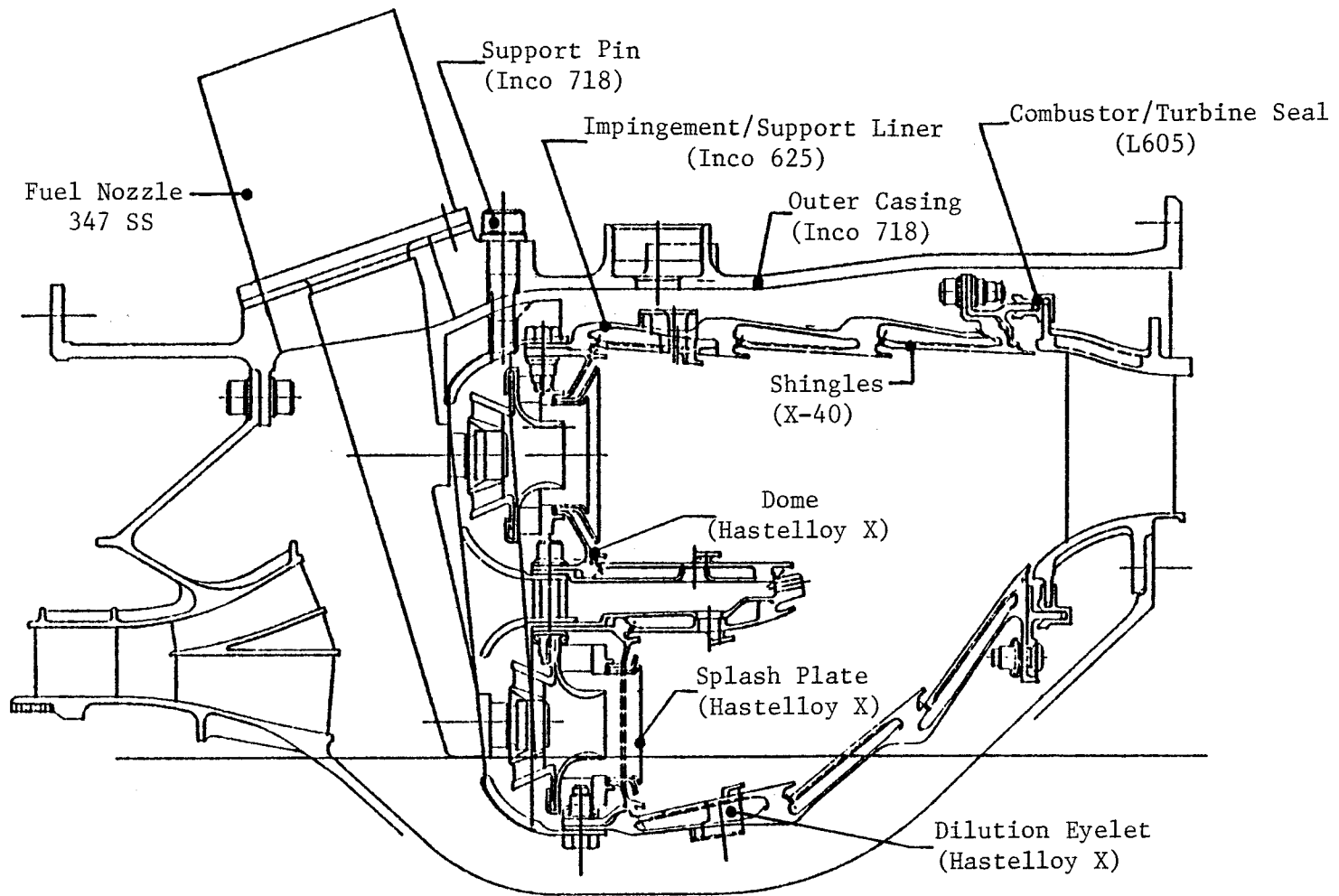


Figure 15. Combustor Cross Section With Materials Selection Indicated.

ORIGINAL PAGE
BLACK AND WHITE PHOTOGRAPH

ORIGINAL PAGE IS
OF POOR QUALITY

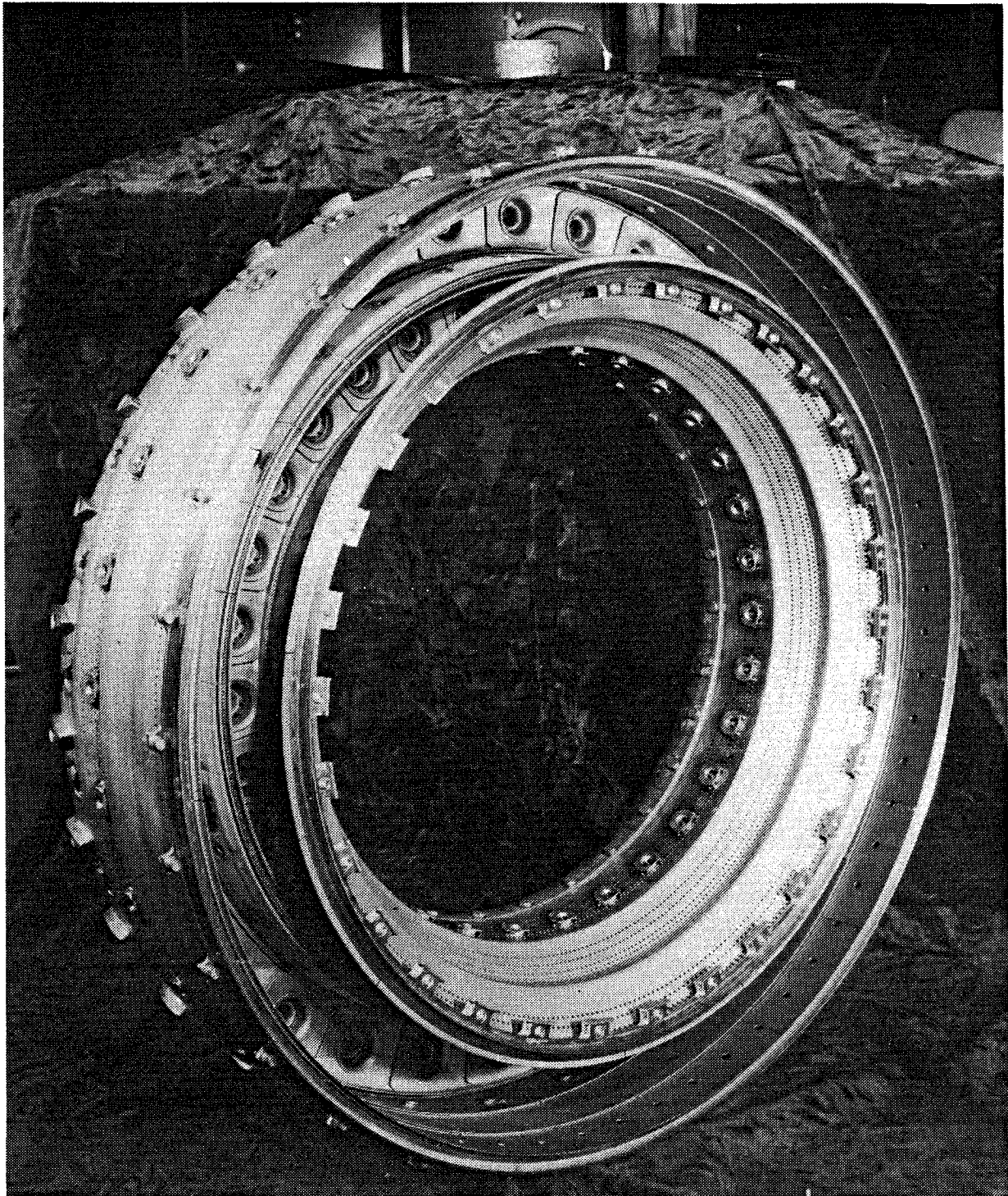


Figure 16. Photo of Combustor Dome Assembly, Aft Looking Forward.

ORIGINAL PAGE
BLACK AND WHITE PHOTOGRAPH

ORIGINAL PAGE IS
OF POOR QUALITY

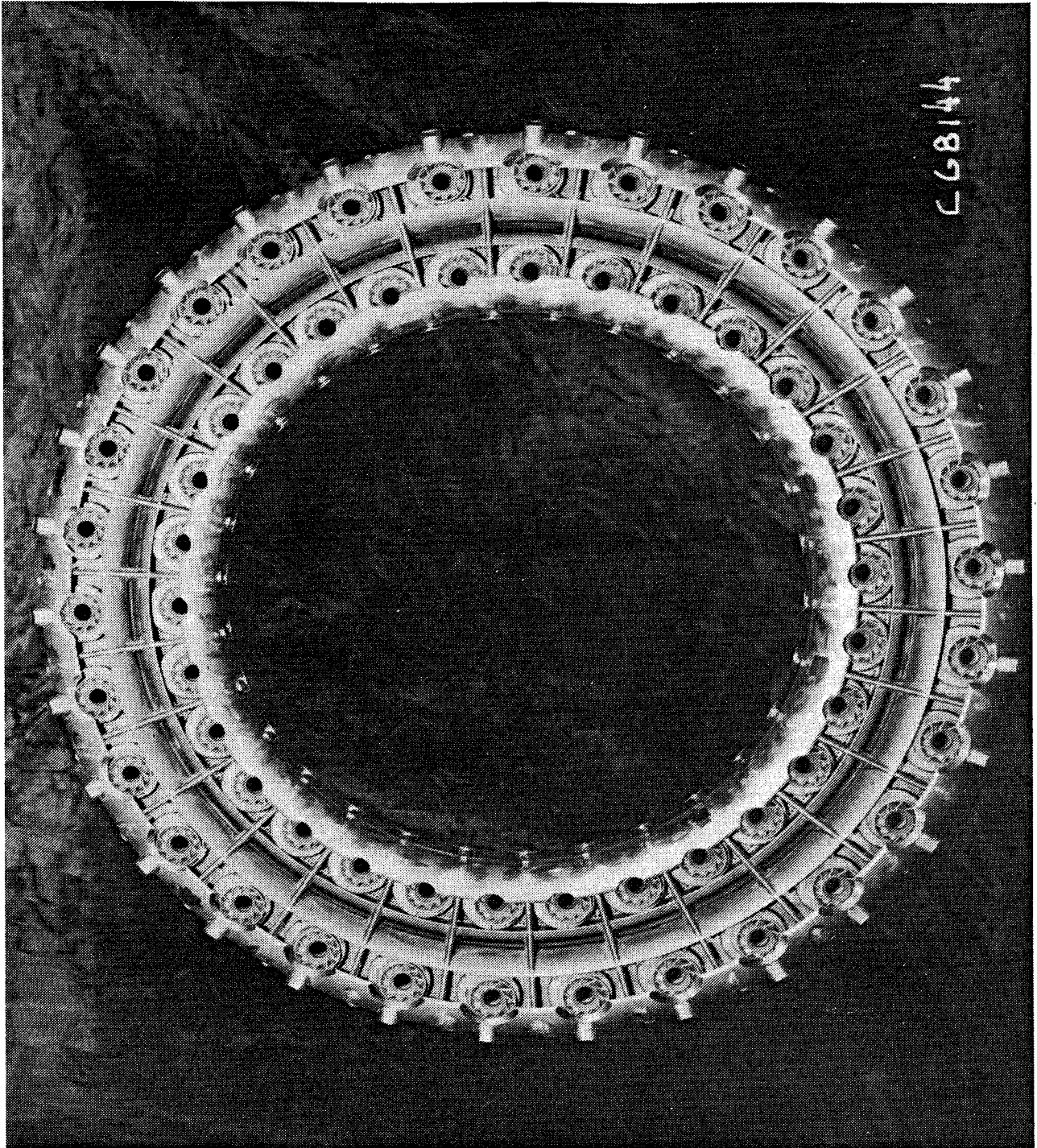


Figure 17. Photo of Double-Annular Dome and Cowling, Forward Looking Aft.

The outer casing supports the combustor assembly, fuel nozzles, fuel delivery system, and ignition system. Ports are provided in the casing for borescope inspection, compressor bleed, and instrumentation leadout.

The liner assembly consists of three axial rows of shingles in the pilot and main zones which are installed in outer/inner support liners. Each row of shingles forms an annular impingement cavity with the support liner. The impingement and dilution holes are laser drilled into the support liners which are machined from forgings. An assembled inner shingle liner is shown in Figure 18.

3.4 HIGH PRESSURE TURBINE DESCRIPTION

3.4.1 Aerodynamic Design

In order to meet the cycle requirements and goals of this program, a two-stage turbine of moderate loading was selected. The aerodynamic design point was chosen to be the maximum climb condition at Mach 0.8 and 10.67 km (35,000 ft), +10° C (+18° F) standard day. This point was determined to be the most stringent, based on a comparison of ICLS and FPS requirements.

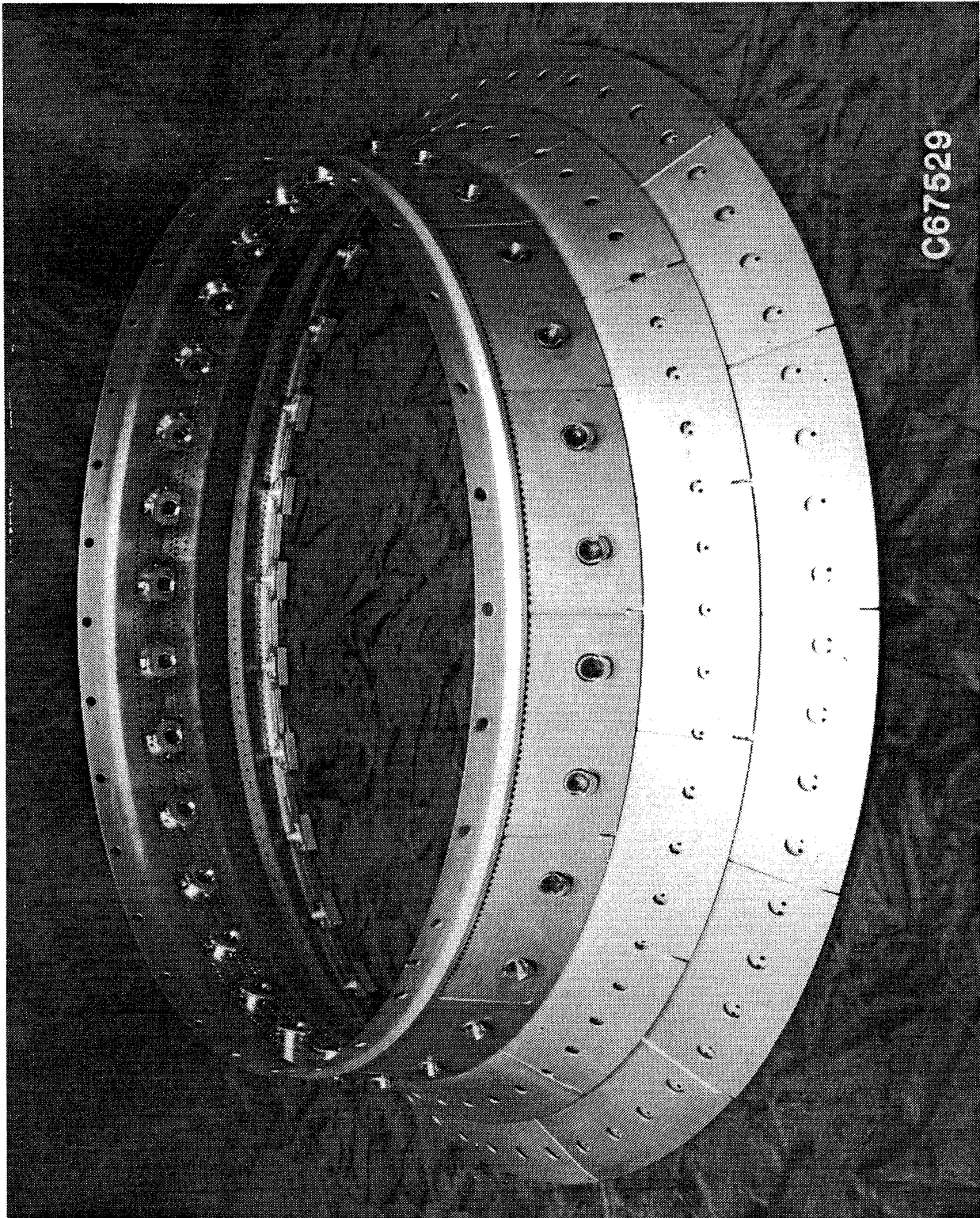
Following completion of the turbine aerodynamic design, early compressor rig testing of the first six stages indicated the potential for a stall margin deficiency relative to pretest prediction. In an effort to reduce this stall margin deficiency, the HP turbine first-stage stator flow area was increased by 4%. This was accomplished by rotating the vane airfoil to the desired throat area.

The significant turbine operating point data are summarized in Table III. The efficiencies presented in this table represent the goals of the program. Note that the open Stage 1 stator flow area is intended only for core and ICLS use.

With minimum cruise specific fuel consumption (sfc) and flight fuel burn as the primary evaluation criteria, a series of system trade studies were performed to identify the turbine configuration and flowpath dimensions for use in subsequent detailed design analyses. Single-stage and two-stage turbines were considered. The two-stage turbine was selected.

ORIGINAL PAGE
BLACK AND WHITE PHOTOGRAPH

ORIGINAL PAGE IS
OF POOR QUALITY



C67529

Figure 18. Photo of Combustor Inner Shingle Liner Assembly.

Table III. HP Turbine Aerothermodynamic Design Requirements.

Parameter	Units	ICLS		FPS		
		Maximum Climb	Max Climb + 4% A41	Maximum Climb	Maximum Cruise	Sea Level Takeoff + 27° F
Inlet Temp., T_{41}	K (° R)	1588 (2858)	1591 (2863)	1557 (2802)	1515 (2728)	1618 (2913)
Energy, $\Delta h/t$	J/kg·K (Btu/lbm·° R)	353.4 0.0844	353.4 (0.0844)	355.5 (0.0849)	353.4 (0.0844)	354.6 (0.0847)
Speed, N/\sqrt{T}	rad/s· \sqrt{K} (rpm/ $\sqrt{° R}$)	33.19 (236.2)	33.78 (240.4)	33.56 (238.9)	33.68 (239.7)	34.22 (243.6)
Corrected Flow, $W\sqrt{T}/P$	$g\sqrt{k}/s\cdot Pa$ (lbm/ $\sqrt{° R}/s\cdot psi$)	0.8648 (17.65)	0.8913 (18.19)	0.8643 (17.64)	0.8638 (17.63)	0.8628 (17.61)
Efficiency, η_T %		91.9	91.9	92.4	92.4	92.1

The turbine pitch-line diameter was established through trade studies which recognized blade loading, blade aspect ratio, weight, tip clearance, and transition to the LP turbine. The resulting diameter was thought to be close to optimum for the overall HP/LP turbine system.

Further trade studies for determining optimum annulus heights were conducted by making vector calculations in which stage exit annulus heights were varied individually. The effects on efficiency of the consequent variation of tip clearance, aspect ratio, edge blockage, aerodynamic loading, and gas deflection were evaluated. Variation in flowpath wetted area and the consequent effect on cooling air consumption and loss were evaluated concurrently and were included in the turbine efficiency evaluation. The design values of annulus area were selected slightly below the aerodynamic optimum in order to minimize the high weight penalty that would be imposed for relatively small gains in efficiency.

Using the flowpath developed in the annulus height studies, further studies were conducted to identify the most appropriate stage energy distribution. The calculations were executed in a manner similar to the annulus height studies, but maintaining constant blade aerodynamic loading. The results of this study indicated that an optimum distribution would exist at approximately 48% to 50% energy extraction in the first stage. However, given the requirement that the second-stage vane coolant supply pressure exceed gas total pressure, it would have been necessary to shift from compressor seventh to eighth-stage cooling air extraction with a net increase in sfc. Consequently, the stage work distribution was selected at 56.5% in the first stage, the minimum consistent with seventh-stage extraction.

The through-flow analysis was executed using a method that solves the full three-dimensional, radial equilibrium equation for circumferentially averaged flow. The procedure accounts for streamline slope and curvature, the effect of radial blade force component due to airfoil sweep and dihedral, airfoil blockage, and radial gradients of flow properties. Calculations were made with radial gradients of blading losses and also with local flow addition to simulate cooling flow injection. Temperature dilution and momentum mixing losses associated with coolant addition were accounted for. The airfoil inlet

angle selection considered mixing between stream tubes, combustor temperature profile, and secondary flow effects.

Airfoil cascade analysis was accomplished by a stream tube curvature method which calculates the compressible flow along a stream surface determined from the through-flow analysis, thus accounting for variations in stream tube thickness.

To verify the design features of the HP turbine, a full scale warm air turbine rig was evaluated. Testing was completed in September 1980. The intent of the rig design was to match the ICLS aerodynamic design with the cooling geometry. Airfoil cooling flows, leakage and purge flows were simulated by including the arrangement and type of seals used. In addition, wheel space geometry was matched in order to simulate windage effects. The cooling system film hole aerodynamic geometry was matched. The inducer (also called expander or tangential accelerator) for rotor coolant delivery was at the same diameter and geometry as in the engine to give similar pumping characteristics. The first-stage stator flow area was not opened 4%. The test rig cross section is shown in Figure 19. Rig tests produced a design point efficiency of 92.5%, which exceeded the ICLS goal by 0.6% and the FPS goal by 0.1%.

The HP turbine for the core engine was basically the same aerodynamic design as the rig-tested turbine; that is, the same flowpath, airfoil count, airfoil shapes, and cooling air delivery system. However, differences existed in Stage 1 flow areas and in the level of cooling flows. These are described as follows:

- As noted previously, the Stage 1 vane flow area was opened 4% relative to the rig area in anticipation of compressor stall margin deficiency.
- During machining of the core engine Stage 1 blade, the trailing edge was inadvertently cut back by 0.127 to 0.1524 cm (0.050 to 0.060 inch). This resulted in an increase in the blade flow area of 2.8%.
- Cooling flow increases were due primarily to hardware deviations and core engine test peculiarities. The following list identifies some of the significant increases. All flows are expressed as a percent of uncorrected core engine flow. Note that a total of 3.5% excess cooling flow, all entering downstream of the first-stage vane, was present in the core engine turbine.

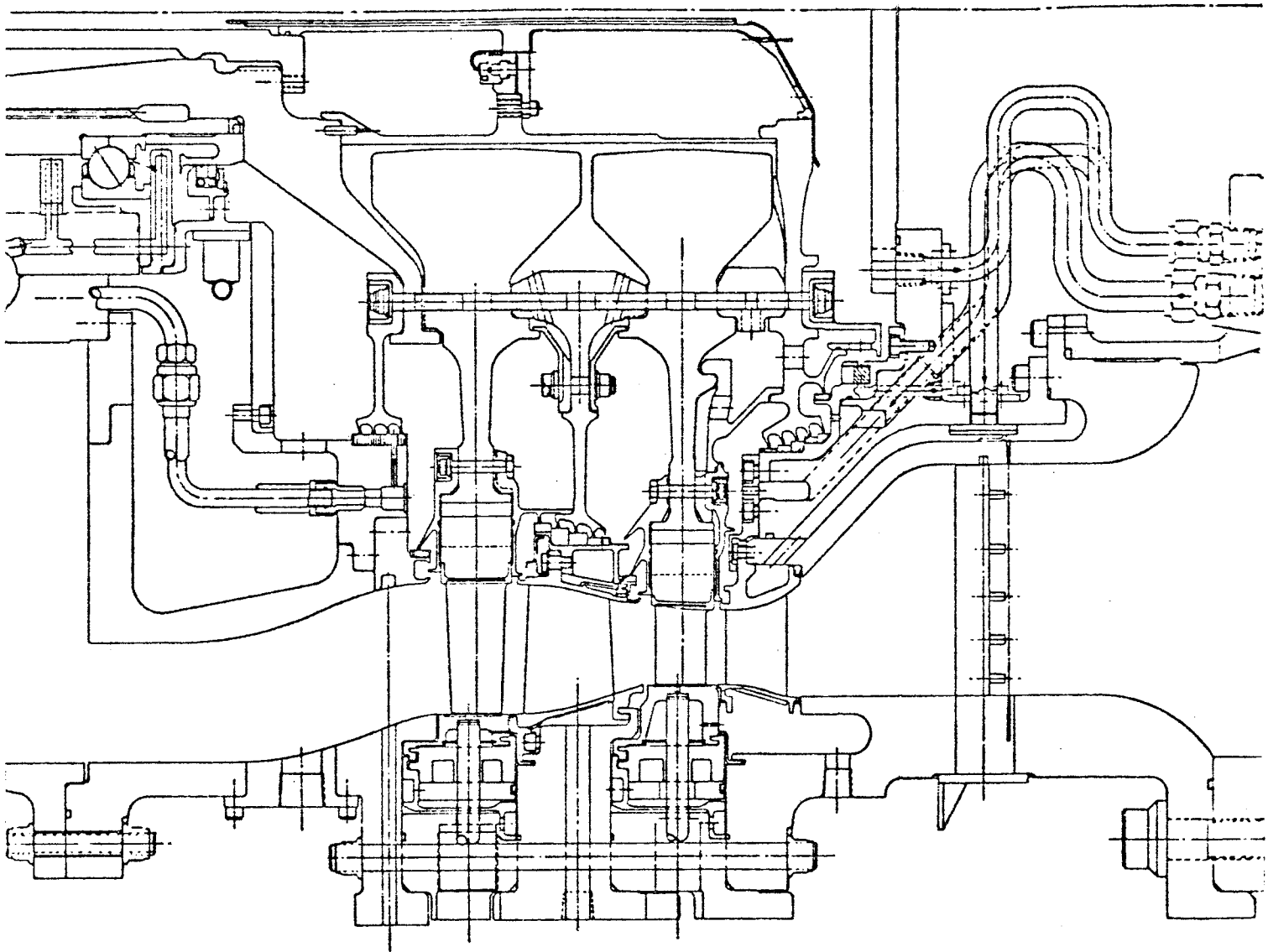


Figure 19. HP Turbine Warm Air Rig.

<u>Item</u>	<u>Excess of Cooling Flow Relative to Design Intent, %</u>	<u>Reason</u>
Stage 1 Shroud	+0.5%	Metal shroud segments for laser clearance probes
Stage 1 Blade	+0.25%	Cutback blade and large trailing edge slots
Stage 2 Vane	+1.0%	Oversized trailing edge slots
Laser Probes	+0.75%	Probe cooling air dumped into flowpath
Aft Cavity Purge and Transition Duct	+1.0%	Peculiar to core, injected upstream of Plane 42 rakes

Core instrumentation for turbine aero performance included cavity static pressures, exit total temperature, and exit total pressure. Primary exit total pressure measurements were obtained with arc rakes located at six centers of equal area. The measuring plane was 5.08 cm (2.0 inches) downstream of the last blade row. Each rake consisted of six elements, for a total of 36. An alternate pressure measurement was obtained with seven radial rakes; each rake had elements located at five centers of equal area. Radial rakes were located nominally at 1.4 inches downstream of the last blade row. Exit temperature measurement was made using seven radial rakes. These were located in the same plane as the radial rakes used for pressure measurement.

3.4.2 Mechanical Design

General Electric's E³ HP turbine represents an advanced technology aimed at achieving high efficiency while still meeting the component life objectives.

The turbine design evolved from the integration of studies conducted by General Electric for NASA. These studies enabled the following advanced

features to be incorporated in the final design: (1) directionally solidified (DS) alloys for blades and Stage 2 vanes, (2) an expander cooling system for the two-stage turbine, (3) active clearance control, (4) ceramic shrouds, and (5) high strength alloys with low coefficients of thermal expansion.

The HP turbine workscope covered all technology disciplines related to high turbine efficiency. These included aerodynamics, heat transfer, metallurgy, mechanical design manufacturing, and test.

The HP turbine mechanical configuration shown in Figures 20 and 21 utilizes a highly efficient two-stage design. The major features are as follows:

1. Inducer System - Reduces the temperature of available air for blade cooling.
2. Impeller - Increases blade coolant air pressure in order to maintain sufficient backflow margin between this air pressure and the hot gas-path pressure.
3. Inner Tube - Separates the compressor rotor purge air from cooling air feeding the Stage 2 blades.
4. Deswirlers - These are rotating vanes built as an integral part of the inducer disk. The purpose of these vanes is to eliminate any potential hazard from acoustic vibration or "vortex whistle."
5. Boltless Blade Retainers - This design requires no bolts through the rim of the disk for support. Elimination of these holes enhances the low cycle fatigue capability of the disk.
6. No Bolts in Disks - The main structural portions of the disks contain no holes. This feature is essential in achieving long disk life.
7. Interstage Disk - Provides better interstage seal clearance control with subsequent reduction of leakage across the interstage seal.
8. Single-Wall Structures - The use of a single-wall casing structure simplifies the geometry configuration for the ACC system. Direct access is provided for the ACC cooling air to impinge on the casing, which directly controls the shroud to blade clearances. No holes penetrate the casing wall.
9. Stage 1 Ceramic Shrouds - Ceramic shrouds require less cooling air compared to other types of shroud material. Cooling air reduction increases thermodynamic efficiency.
10. Stage 2 Solid Shrouds - Use of a solid shroud configuration is expected to improve component life relative to present designs.

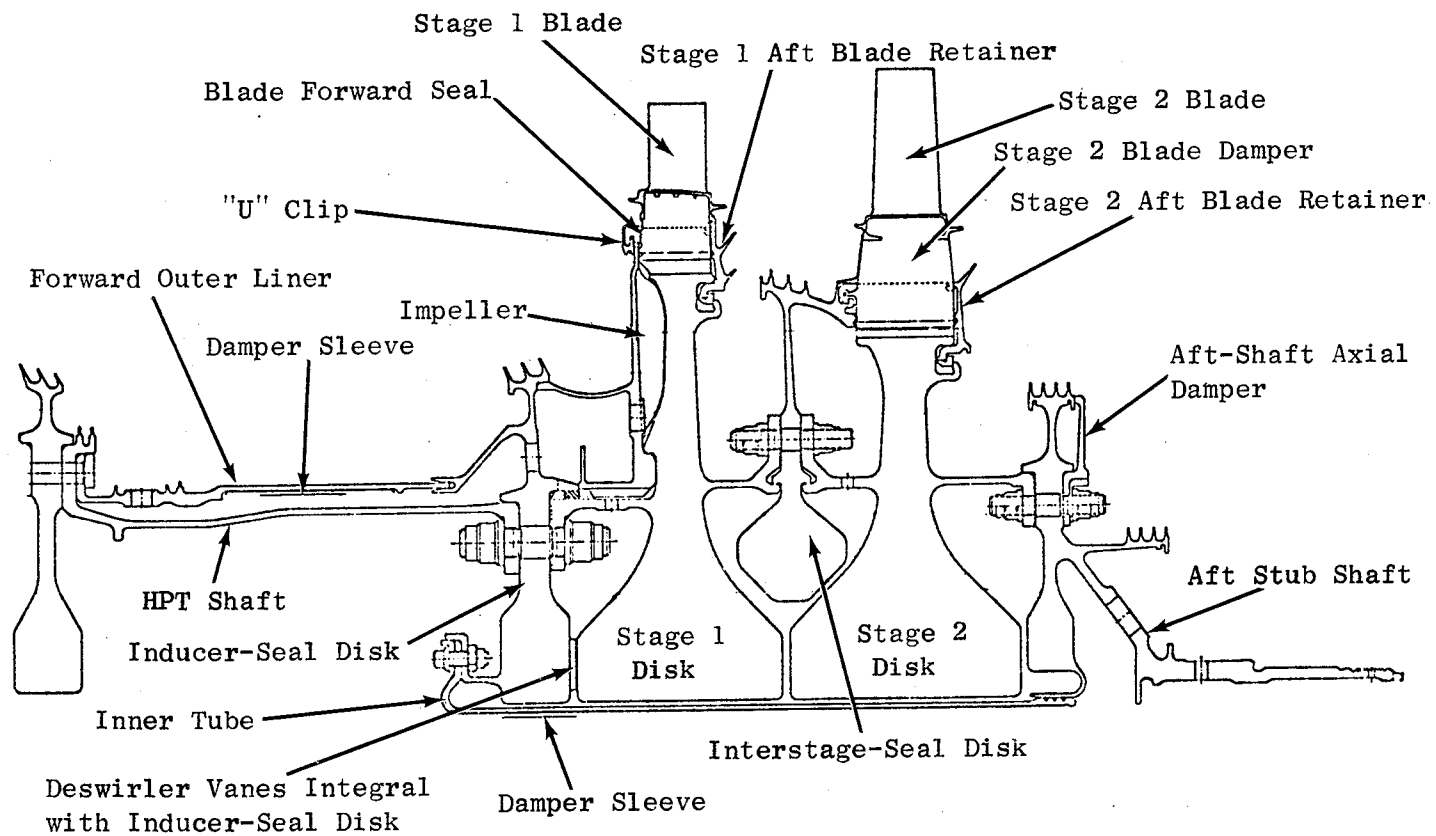


Figure 20. HP Turbine Rotor.

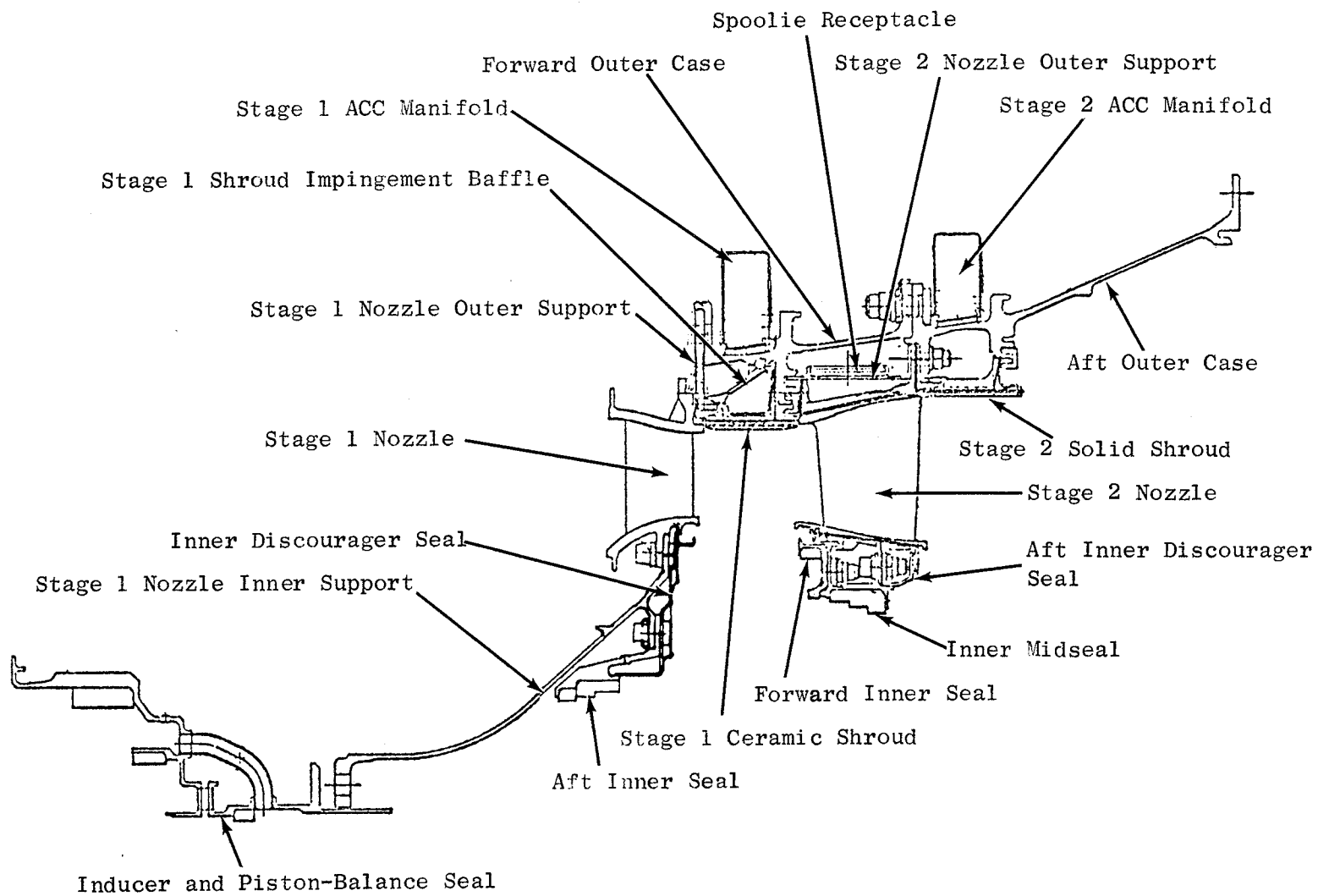


Figure 21. HP Turbine Static Structures.

The core engine turbine is a flight design with the rotor structure sized for growth.

An ACC system is incorporated to impinge cool air on the casing for clearance optimization. The ACC system used facility-supplied air during core testing. In addition, the core engine turbine uses compressor fifth-stage, seventh-stage, and discharge bleed air for cooling. A seventh-stage start bleed system was incorporated to facilitate starting, if needed. If used, seventh-stage start bleed would have depressed the fifth- and seventh-stage turbine cooling air supply pressures. In order to avoid the loss of cooling during the use of start bleed, a start range turbine cooling (SRTC) system was incorporated. This system substituted compressor discharge pressure (CDP) air for fifth- and seventh-stage air if seventh-stage bleed were used for starting. Seventh-stage start bleed air was not necessary for core engine starting, therefore this supplemental cooling circuit was deactivated.

Rework of blades and disks for instrumentation reduced part life, although adequate life exists for core and ICLS testing. Some compromise in Stage 2 vane quality was accepted in order to protect program assets. The effect of this compromise was additional cooling flow through the vanes. Four Stage 1 shroud segments are not of flight design, both in material and configuration, in order to accommodate tip clearance measurement probes. Four Stage 2 shroud segments are also modified to accommodate tip clearance measurement probes. These shroud changes increase cooling air bleed flow from the compressor.

Figure 22 shows the Stage 1 nozzle assembly. The vanes were manufactured from MA754 material. MAR-M-509 was used for the inner/outer bands. This assembly is shown mated with the combustor module in Figure 23.

The Stage 2 nozzle and shroud assembly is shown in Figure 24. The Inco 718 aft casing is clearly shown mated with the Stage 2 nozzles (DS René 150 vanes, René 80 bands) and the Hastelloy X interstage seal.

The HP turbine rotor assembly in Figure 25 clearly shows the cast DS René 150 Stage 1 and 2 turbine blades. Also visible are the seal teeth on the AF115 interstage seal disk and the Inco 718 aft shaft/disk. The Stage 1

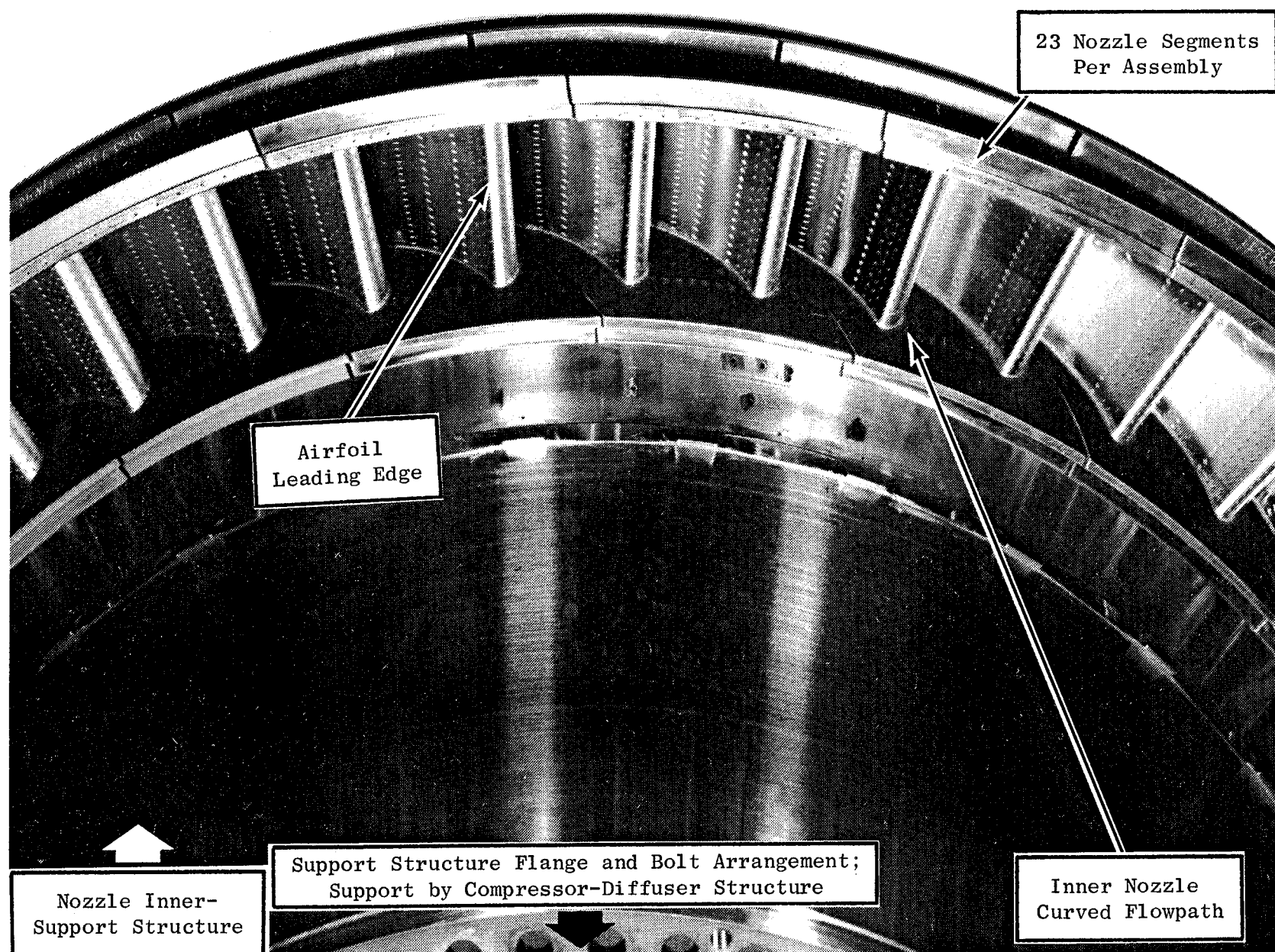


Figure 22. HP Turbine Stage 1 Nozzle Assembly.

ORIGINAL PAGE IS
OF POOR QUALITY

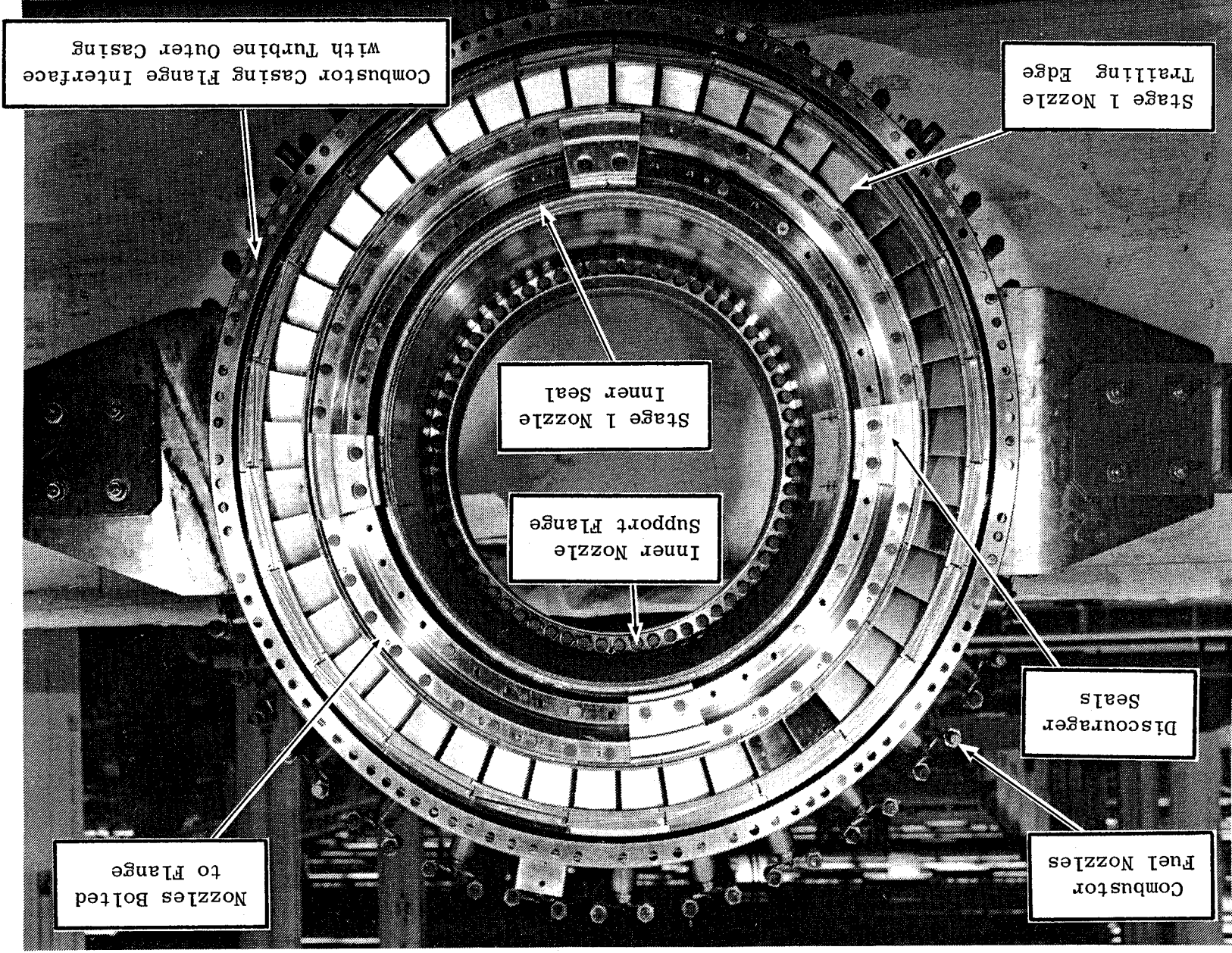
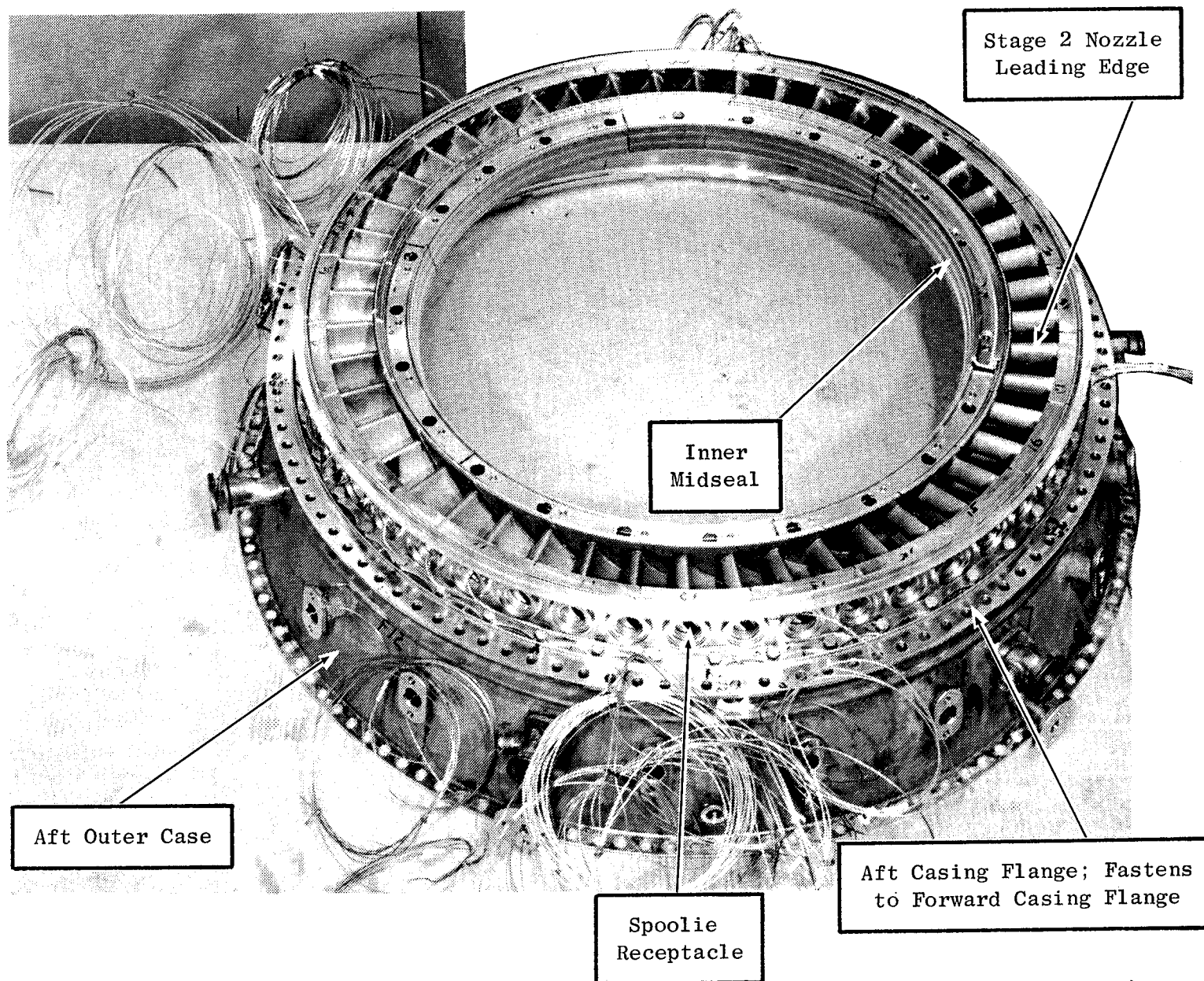


Figure 23. HP Nozzle Turbine and Combustor Assembly.

ORIGINAL PAGE
BLACK AND WHITE PHOTOGRAPH



ORIGINAL PAGE
BLACK AND WHITE PHOTOGRAPH

Figure 24. HP Turbine Stage 2 Nozzle and Shroud Assembly (Partial).

ORIGINAL PAGE
BLACK AND WHITE PHOTOGRAPH

ORIGINAL PAGE IS
OF POOR QUALITY

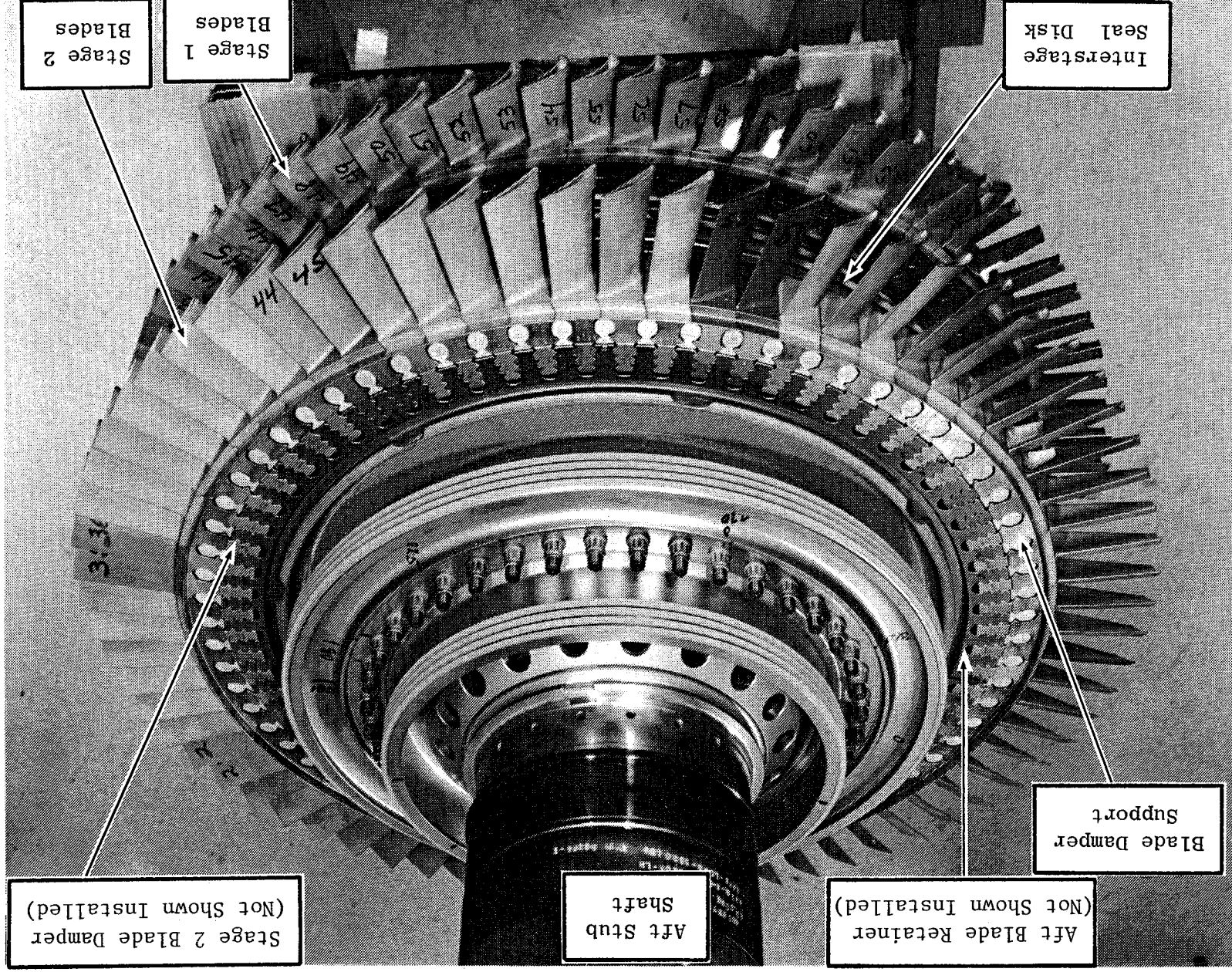


Figure 25. HP Turbine Rotor Assembly.

blade retainer used in the core engine was manufactured from René 95 material because of late delivery of the intended AF115 part. A second part was made, in AF115, but not in time for assembly of the core turbine. The Stage 2 retainer was made from AF115 material.

Turbine Cooling Description

The Stage 1 vane cooling air is extracted from the inner and outer combustor liner cavities. The vanes are partially cooled by two impingement inserts. In addition, film cooling is used around the leading edge and on the pressure side of the vanes. Internal convection cooling is used for the trailing edge portion of the airfoil, with the flow being ejected through slots on the pressure side of the vane trailing edge.

Cooling air for Stage 2 vanes is extracted from Stage 7 of the high pressure compressor. These vanes are cooled by single impingement inserts. Spent impingement air convectively cools the vane trailing edges and is ejected through slots on the pressure side of the vane trailing edge.

Rotor cooling is extracted from the center of the gas flowpath in the combustor diffuser region. It is then accelerated tangentially through an expander nozzle prior to entering the rotor.

Stage 1 blades are cooled by two circuits: The forward circuit uses serpentine convective cooling, impingement cooling against the backside of the leading edge, and leading edge film cooling. The aft circuit uses serpentine convective cooling and trailing edge slot convective cooling which is ejected through the pressure side of the blade trailing edge.

The Stage 2 blade is cooled by two convective circuits; both discharge through slots in the pressure surface near the tips of the blades.

3.5 REAR FRAME AND EXHAUST NOZZLE DESCRIPTION

The slave frame for the core engine is a welded assembly shown in Figure 26. The outer casing was machined from a single forging, while the hub was fabricated by welding the two hub rings to the shear cylinder. The eight radial struts were welded to the hub and the outer casing. The aft engine

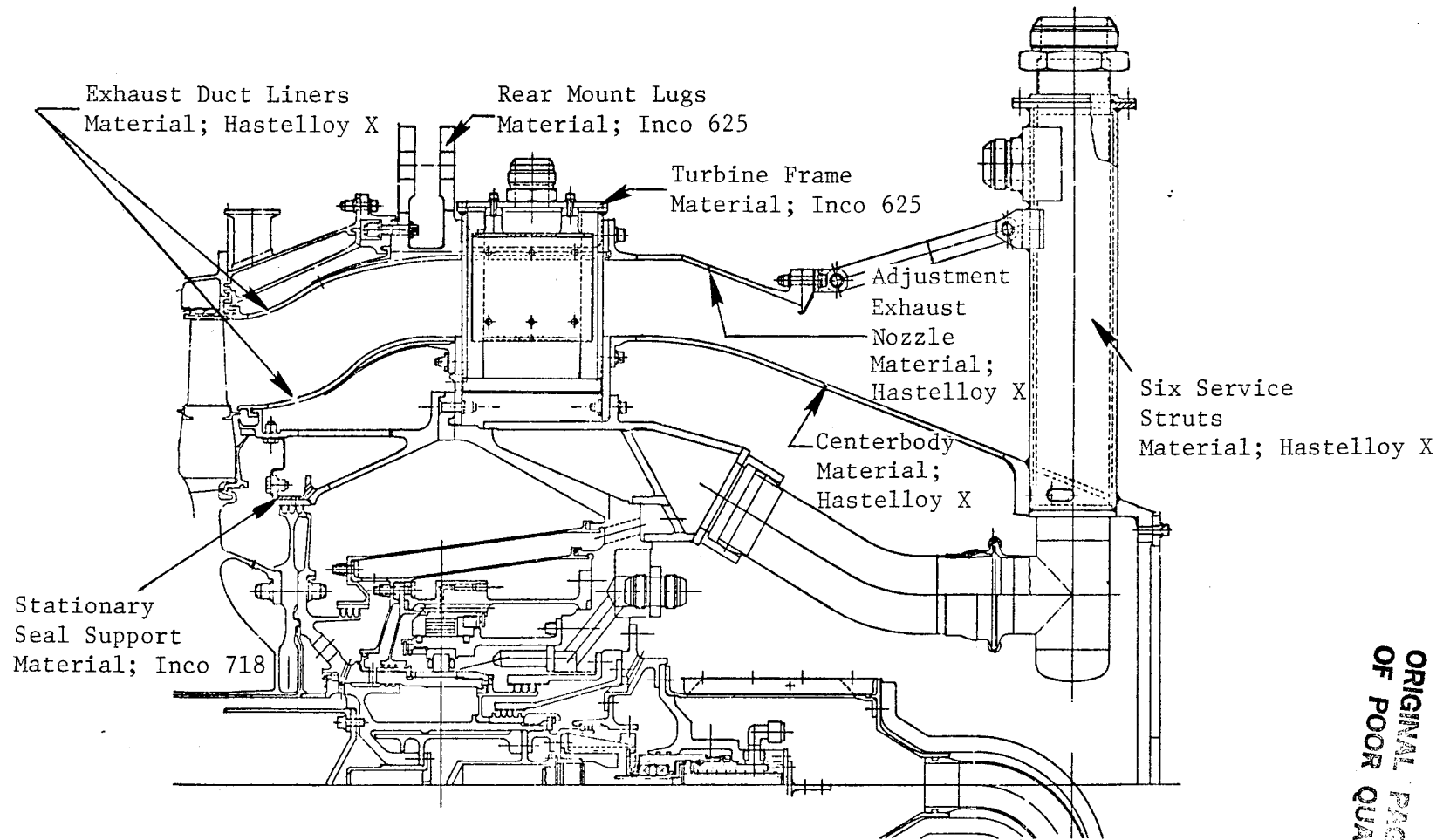


Figure 26. E³ Core Engine Exhaust System.

ORIGINAL PAGE IS
OF POOR QUALITY

mount is located on the turbine frame. In addition, the frame supports the HP turbine exhaust duct liners, exhaust nozzle, centerbody, and number four bearing.

Figure 27 shows the turbine frame cooling air circuit. Shop air enters the frame at the four struts on the vertical and horizontal centerlines. The air then flows between the strut wall and an inner baffle to convection cool the struts and continues between the hub shear cylinder and the hub cooling air baffle to convection cool the hub of the frame. This air then enters the four struts at 45° , 135° , 225° , and 315° ; it convection cools these struts and is dumped overboard to ambient.

In order to provide the same environment on the aft side of the HP turbine disk as will be present on the turbofan engine, fifth-stage bleed air is routed through the frame to pressurize the HP turbine aft cavity. This bleed air, which comes through the first-stage LP turbine vanes on the ICLS engine, enters the four struts at 45° , 135° , 225° , and 315° . Next, the bleed flow passes through tubes into a circumferential cavity in the frame hub, through holes in the forward hub ring, through holes in the seal support structure, and finally leaks through the discourager seal into the flowpath and through the high pressure labyrinth seal to ambient.

The cooling circuit for the six service struts through the centerbody is shown in Figures 27 and 28. These service struts provide the means for leading out the sump and aft slipring service lines (such as oil supply, oil scavenge, oil drain, and instrumentation). The struts are convection cooled with shop air flowing between the outer strut wall and an inner baffle. This air is then dumped into the centerbody and exits to ambient through a hole in the centerbody cover plate.

The exhaust nozzle provides the capability of testing several exhaust nozzle areas for this engine test. The nozzle area was adjusted by replacing nozzle cones of differing lengths. Two nozzle cones were available and could be trimmed to provide the desired areas.

The following effective nozzle areas were supplied. Some warpage altered the flow areas, as discussed further in Section 6.1.

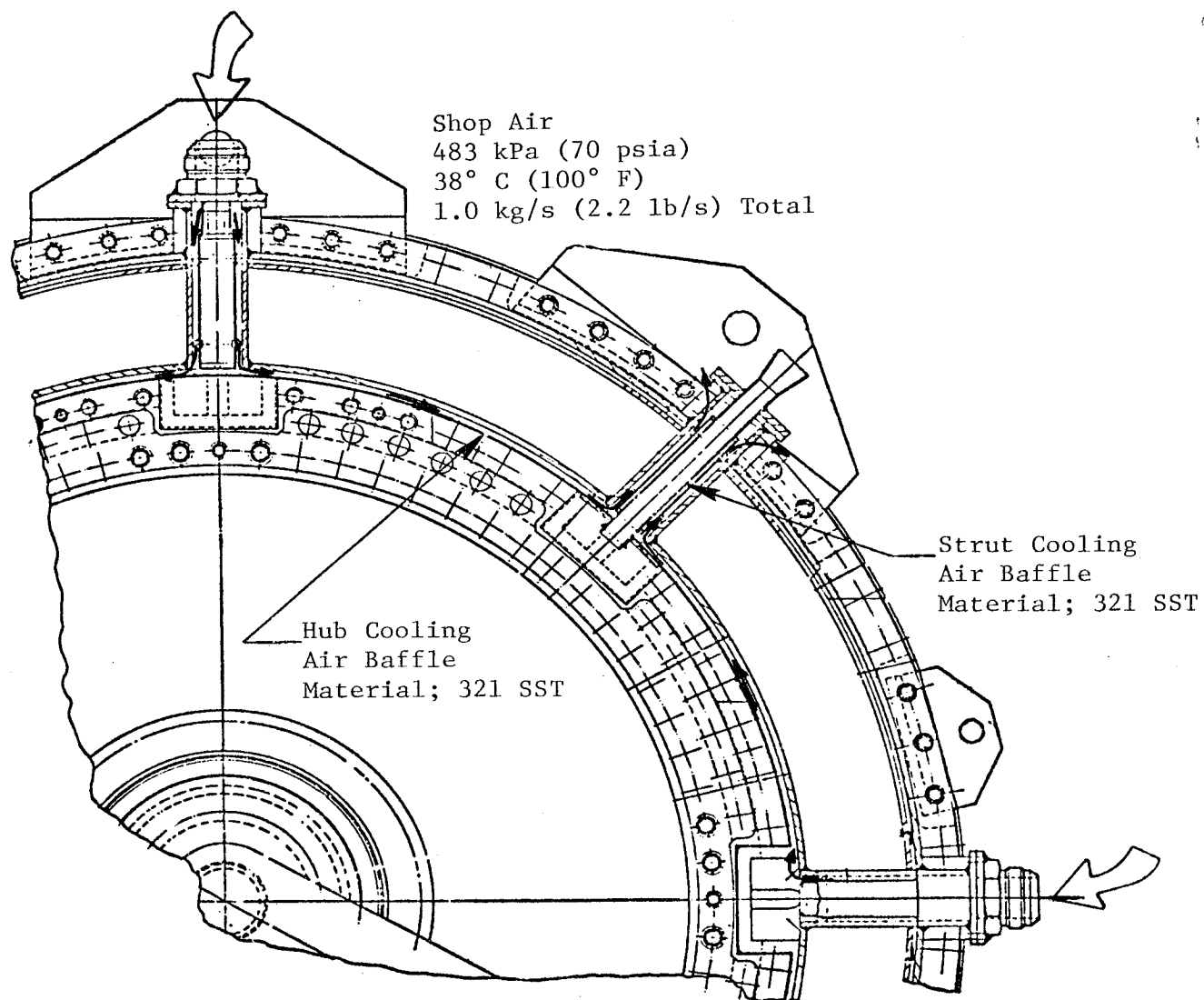


Figure 28. Turbine Frame Cooling Circuit.

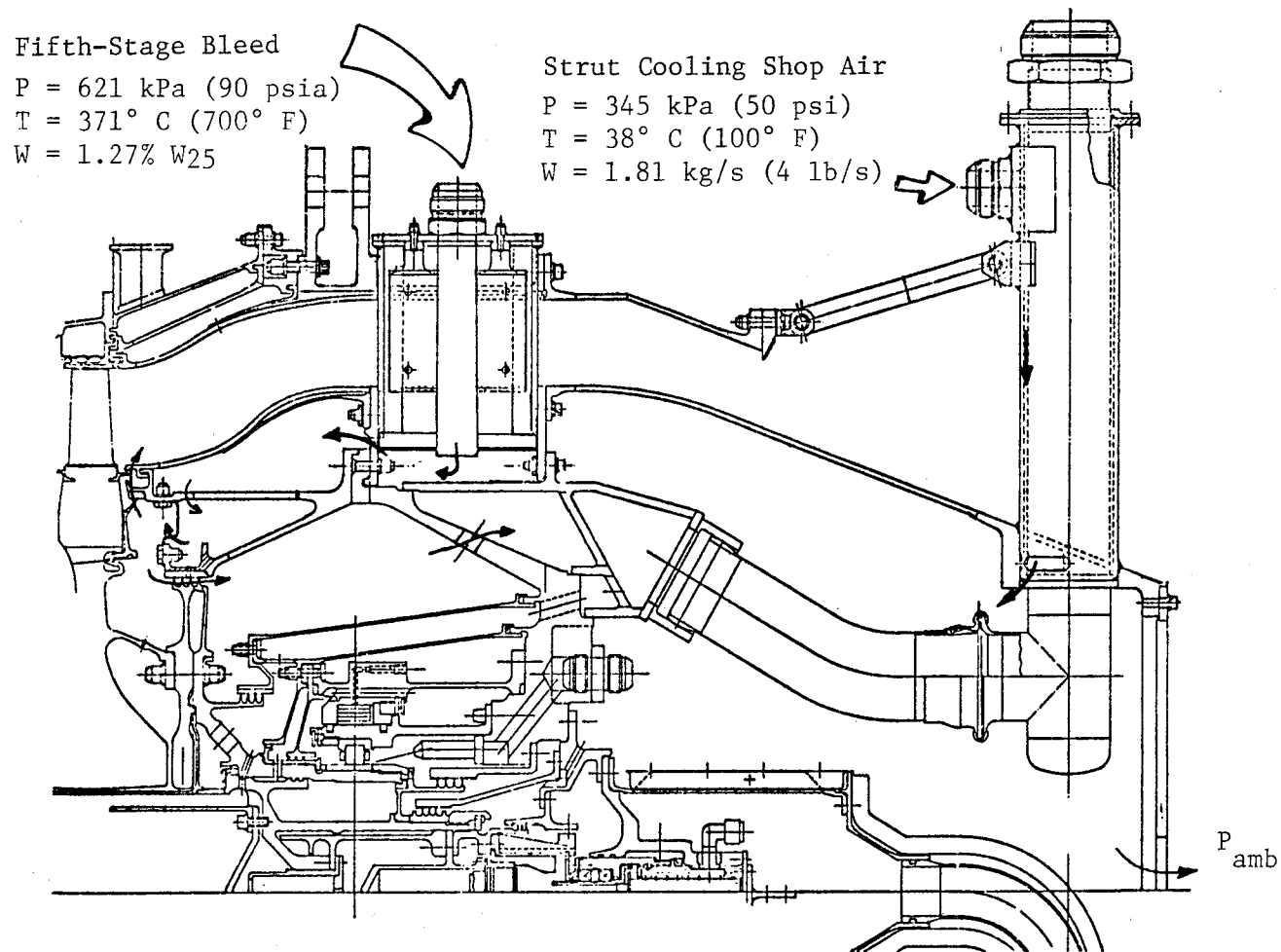


Figure 27. Turbine Cavity Pressurization and Service Strut Cooling Circuits.

ORIGINAL PAGE IS
 OF POOR QUALITY

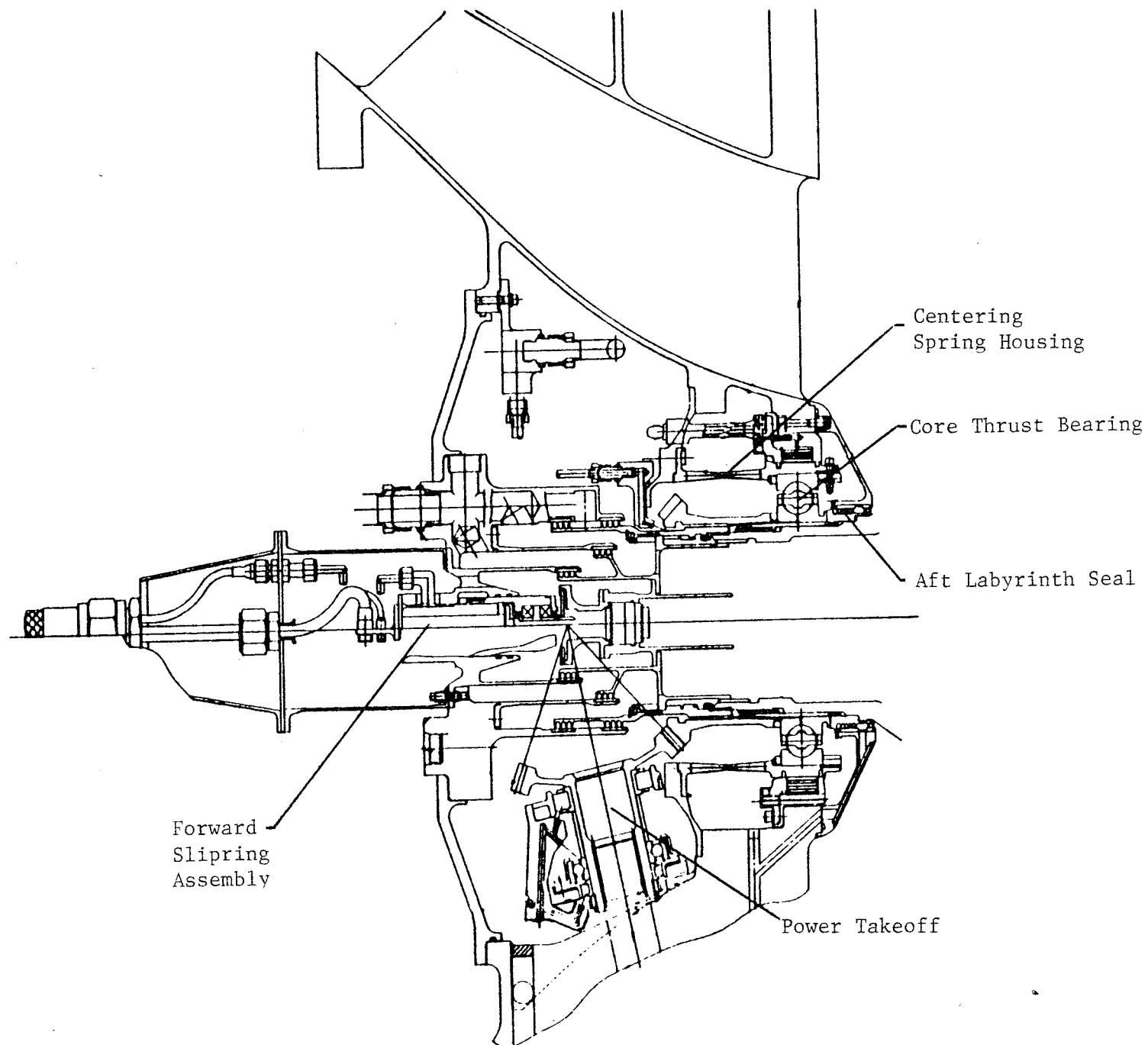


Figure 29. Forward Sump.

946 cm ²	(146.7 in ²)	-10% from Nominal
1052 cm ²	(163 in ²)	Nominal
1093 cm ²	(169.4 in ²)	+4% from Nominal
1219 cm ²	(189 in ²)	+16 from Nominal

3.6 SUMPS, DRIVES, GEARBOX, AND PIPING DESCRIPTION

Forward Sump

The forward sump design for the core engine is shown in Figure 29. Included in this sump is the core thrust bearing which is spring mounted and fluid damped. A PTO gearbox is driven directly from the compressor stub shaft and drives out radially through the bottom strut in the frame.

Just forward of the horizontal PTO gear is a manifold housing which provides the following features:

- Supplies seal pressurization air to the forward sump labyrinth seal.
- Provides a passage for the compressor rotor cooling air which, for the core engine, is obtained from a shop air source.
- Incorporates a purge cavity for slipping cooling air and compressor rotor cooling air.

Also, the forward manifold housing supports the instrumentation slipping assembly that provides the instrumentation leadout from the compressor rotor area. A cover supports the manifold housing and acts as a closure for the forward end of the sump.

Aft Sump

The aft sump design used in the core engine is shown in Figure 30. This sump includes the aft support roller bearing which is mounted in a spring housing similar to that used in the forward sump.

Based on the engine system rotor dynamic analysis, a fluid film damper is not required in the aft sump.

As in the forward sump, labyrinth seals are used for sealing the forward and aft ends of the sumps. These seals are pressurized by shop air supplied

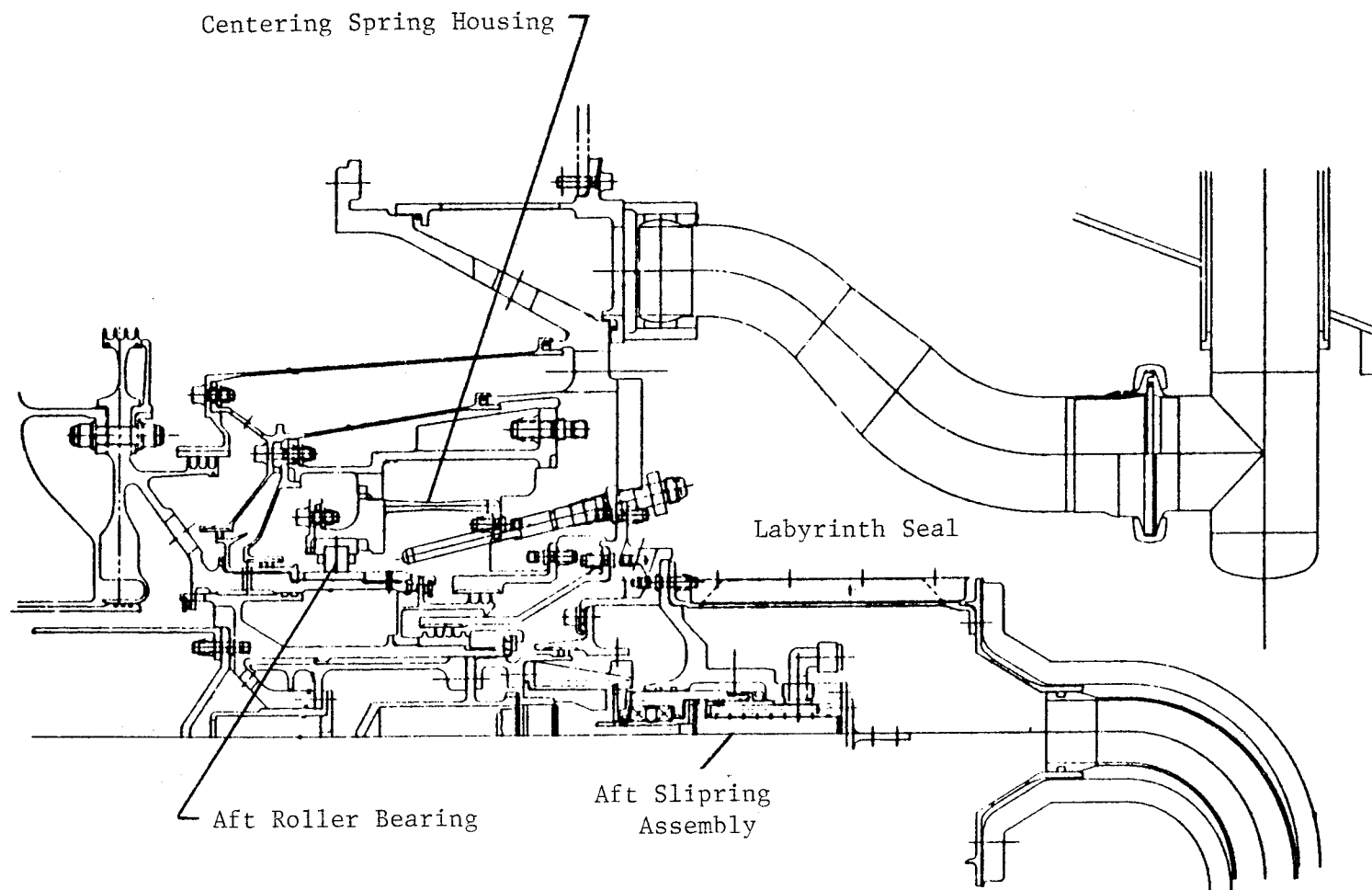


Figure 30. Aft Sump.

ORIGINAL PAGE IS
OF POOR QUALITY

through the support housing. Shop air for seal pressurization surrounds the forward end of the sump with cool air of approximately 93.3° C (200° F).

The cavity outboard of the seal pressurization cavity purges the air, that cools the compressor rotor. This air comes from the forward sump through the compressor rotor and is exhausted to atmospheric pressure through the aft housing. It is expected that this air will be approximately 371.1° C (700° F) maximum. The physical flow area of this cavity is as large as possible to minimize the pressure drop.

A thrust balance cavity is provided between the aft balance piston seal and the stationary structure. This cavity supplies pressurized air through two 50.8-mm (2-inch) diameter pipes. It was planned to maintain this pressure at 344.7 kPa (50 psia) during the majority of the testing. The thrust balance cavity is required to keep the thrust load on the core thrust bearing to levels consistent with long life.

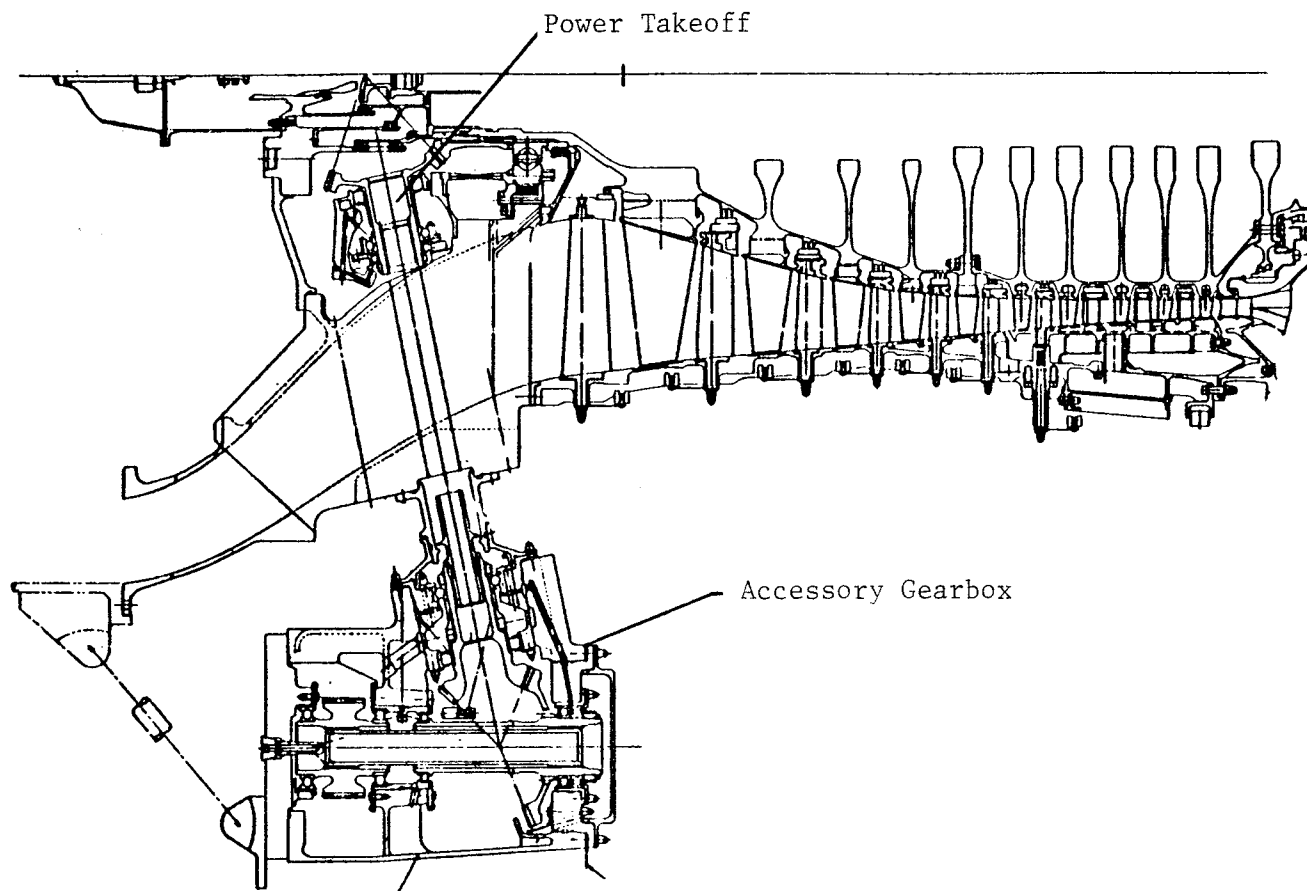
In addition, the aft sump includes an instrumentation slipring assembly. Leadout for the slipring instrumentation is through the aft service struts. Slipring cooling air is purged through the aft housing exhausting to atmospheric pressure.

Accessory Drive System

Figure 31 shows a cross section of the core engine accessory drive system. The accessory gearbox (AGB) is driven by the PTO gearbox located in the forward sump. The AGB provides drive pads for the following accessories:

- Lube and Scavenge Pump
- Two Air Starters
- Control Alternator
- Fuel Pump and Control.

The gearbox is designed for a maximum combined torque from the starters of 1084.6 N.m (800 lb-ft). The maximum accessory horsepower requirement for



ORIGINAL PAGE IS
OF POOR QUALITY

Figure 31. Auxiliary Drive System Cross Section.

the core engine is 53.69 kW (72 hp). Figure 32 shows a cross section of the AGB.

Configuration

The configuration design encompasses the following areas:

- Large pneumatic piping required for active clearance control of compressor and turbine and for turbine cooling
- Manifolds and valving to assist engine starting
- All external lube and fuel lines
- All electrical harnesses required

Figure 33 is a schematic of the pneumatic piping layout, and in Figure 34 this piping is shown configured on the core engine. Much of the configuration hardware for the core engine will also be utilized on the ICLS engine.

Customer air can be extracted at the fifth stage. Piping was provided to a facility valve which will control the amount of air bled. Compressor discharge bleed for customer use is in the FPS design, but is not incorporated into the core engine.

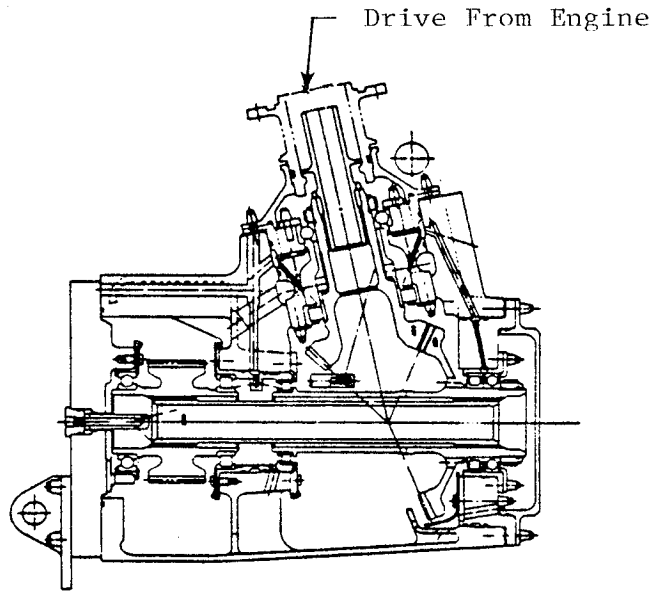
Further, air from the fifth stage is used for ACC and can either be directed over the aft compressor case for cooling to reduce clearance, or through piping outside the compressor to allow clearance increases.

This fifth-stage air flows aft and is used for rear frame cooling in the core engine and for cooling the LP turbine vanes in the ICLS engine.

During starting, provisions are made for seventh-stage air to be bled through four bleed valves. This is vented to the atmosphere in the core engine and to the fan duct in the ICLS engine. This capability was removed early in the test because it was not necessary. Also from the seventh stage, air is piped to the HP turbine second stage for cooling.

Air is piped from the CDP manifold through on-off valves and check valves to the HP turbine second stage to supplement the seventh-stage cooling air during starting, if required.

ORIGINAL PAGE IS
OF POOR QUALITY



Section A-A

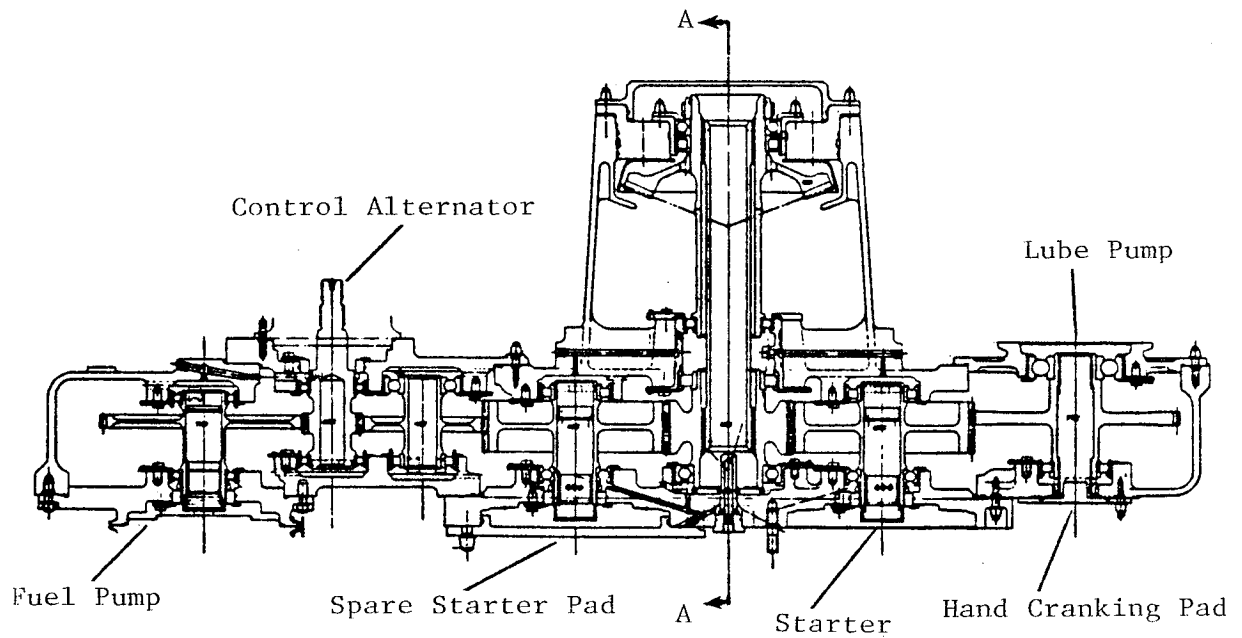


Figure 32. Accessory Gearbox Cross Section.

ENGINE MOUNTED

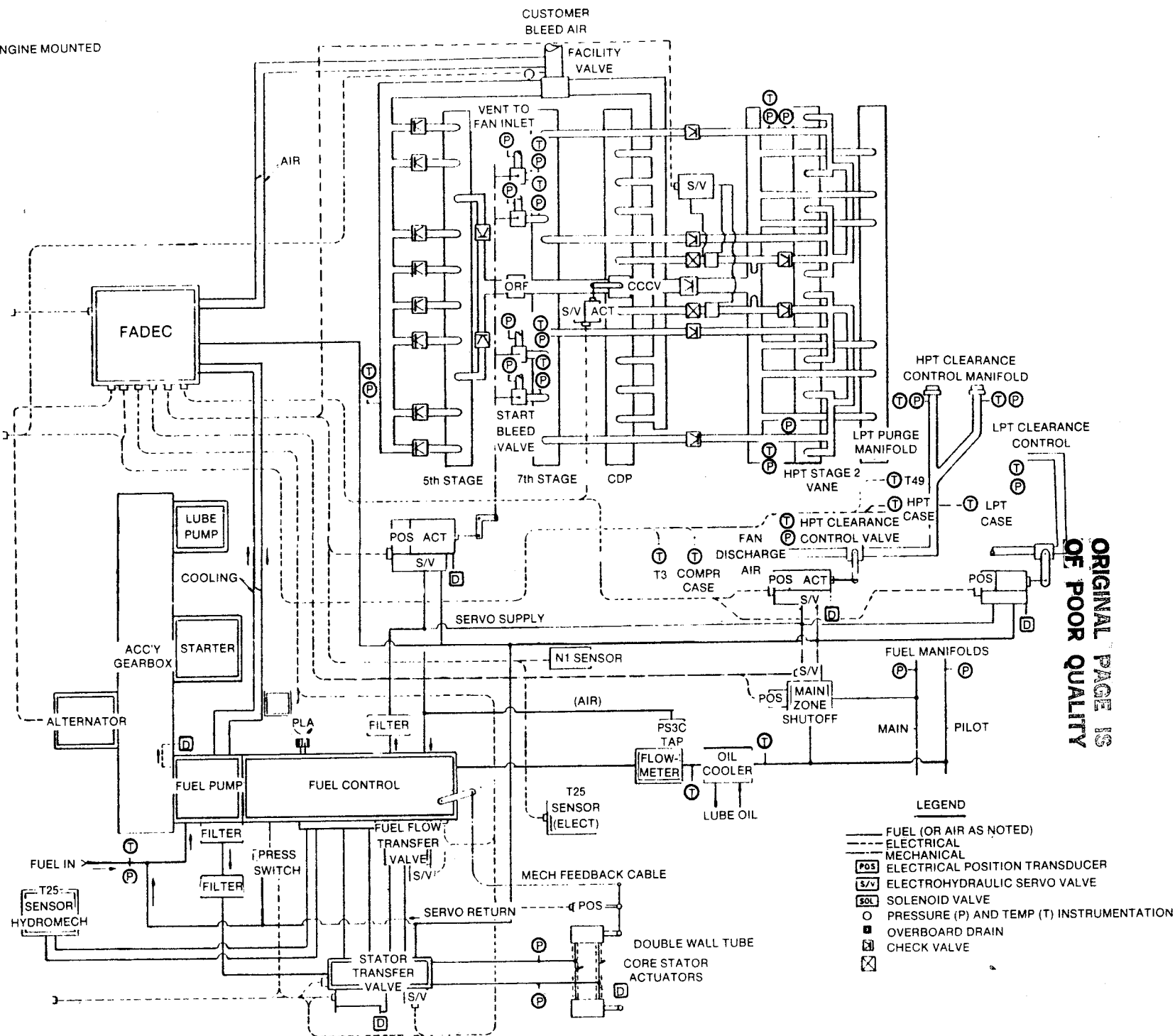
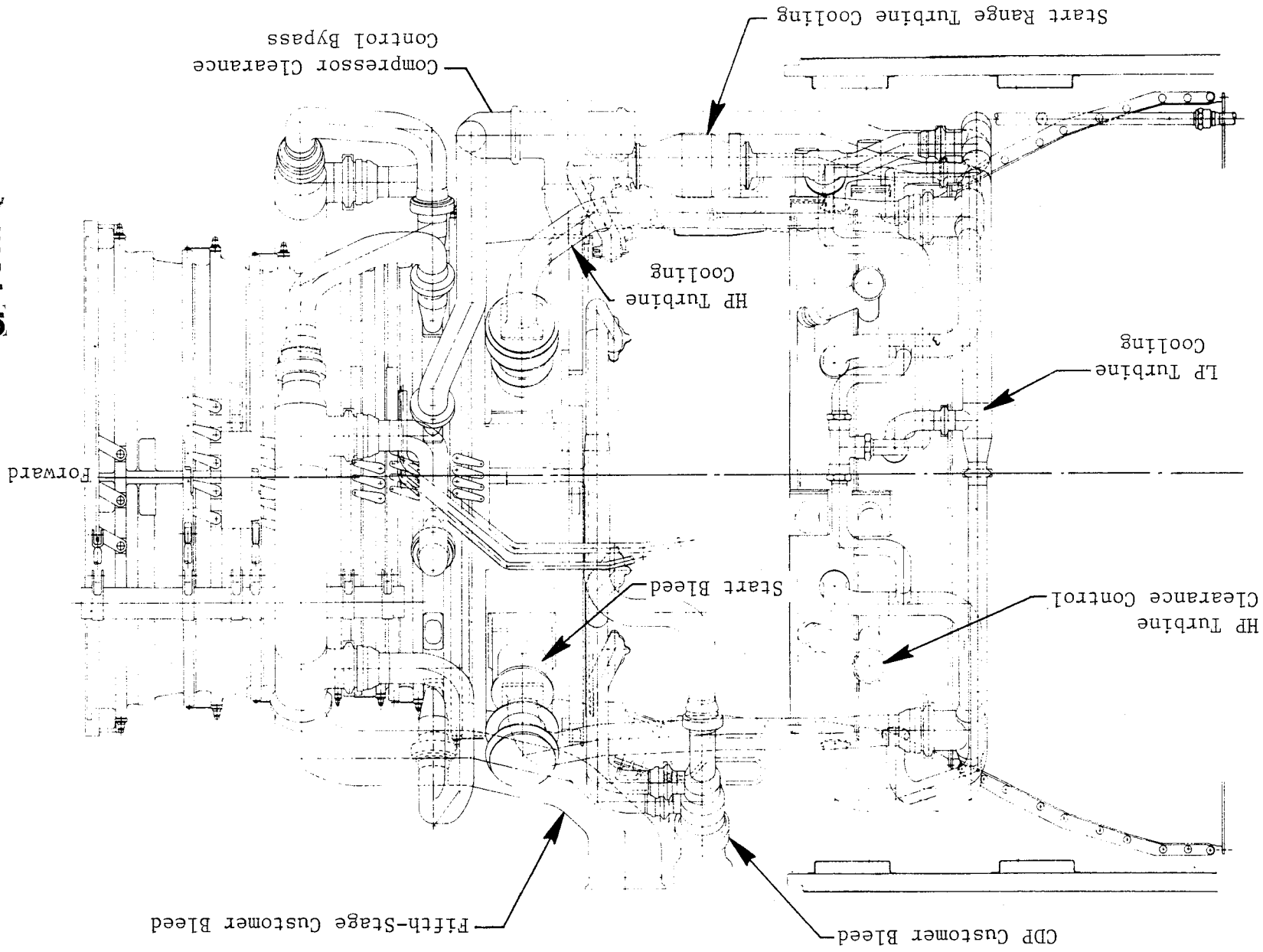

 ORIGINAL PAGE IS
OF POOR QUALITY

Figure 33. Schematic of Pneumatic Piping.

Figure 34. Major Piping Arrangement of Core Engine.



ORIGINAL PAGE IS
OF POOR QUALITY

Lube System

The lube system schematic for the core engine is shown in Figure 35 and is typical of systems used in other GE engines.

Lubrication and cooling oil is supplied to each sump and to the gearbox by a single supply element, then scavenged by utilizing separate scavenge elements.

Oil filters are used on both the supply and scavenge side of the lube system. The supply filter protects the sumps and gearbox from contamination, and the scavenge filter protects the heat exchanger and the lube tank. Each scavenge element has an inlet screen to protect the pumping elements from larger debris.

Both the lube tank and AGB are vented to the forward sump. The AGB vent is used to balance the pressure between the AGB and the forward sump; the vent line from the tank relieves the tank pressure. There is a tank pressurization valve to maintain the tank above ambient pressure.

Check valves are located in the lube and supply side to prevent backflow of oil into the engine sumps, which causes flooding at engine shutdown.

The lube pump used in the core engine is from another engine program and has excessive flow capacity for the core engine. To provide the proper quantity of oil to each component, a bypass orifice is used to return excess oil to the lube pump inlet.

The forward and aft sumps are vented to an externally mounted static air/oil separator. Any oil collected in this separator is pumped back into the system through pumping elements in the scavenge pump. At the outlet of the air/oil separator, an air ejector is used to provide the capability of lowering sump pressure below the engine inlet pressure.

Rotor Thrust

A complex computer model of the secondary air systems, which is pertinent to the calculation of core thrust bearing axial load, was completed as part of

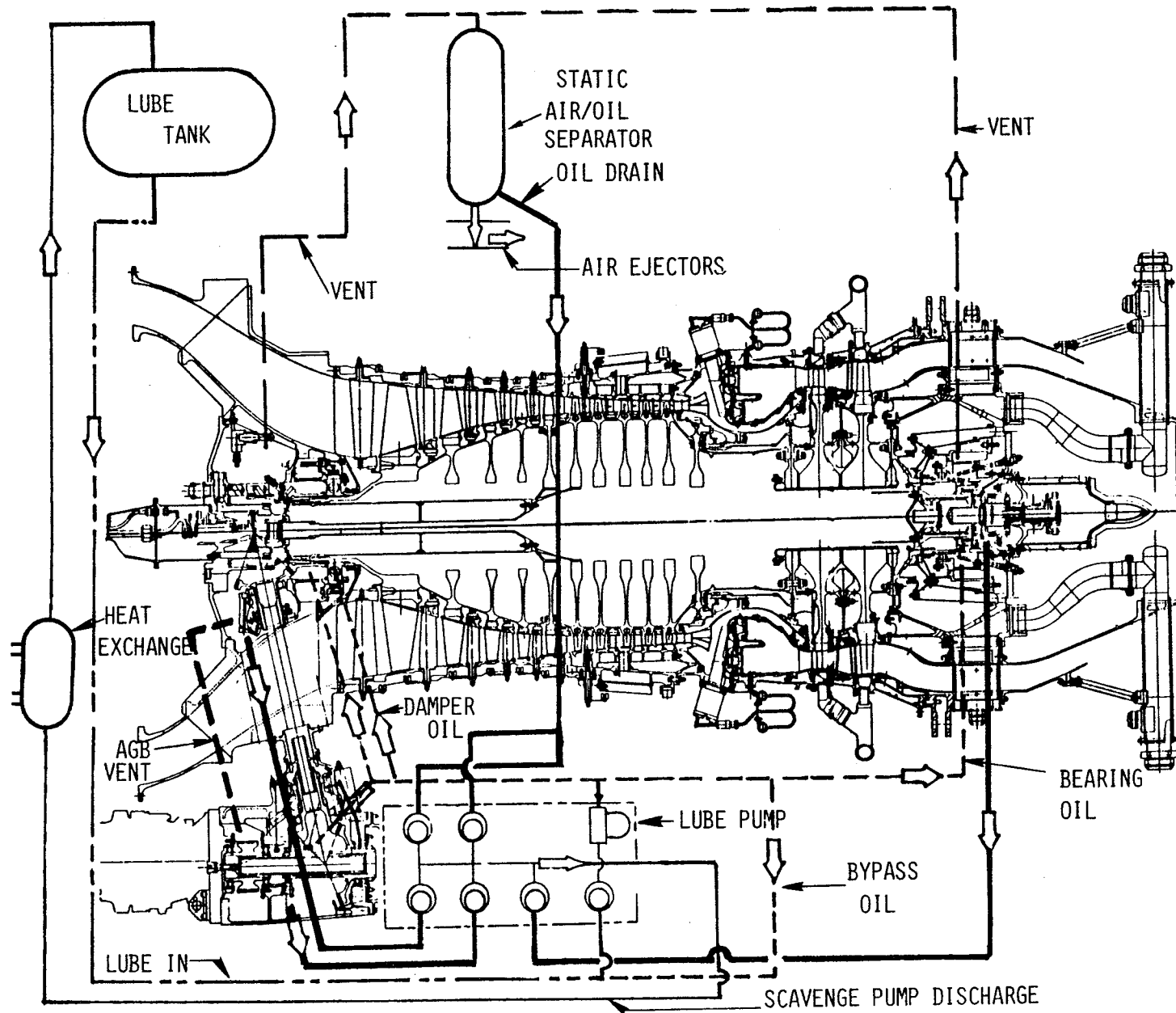


Figure 35. Lube System Schematic.

the design analysis of the core engine system. This computer modeling was used during the design process to evaluate (1) various labyrinth air seal diameters throughout the engine and (2) their effect on the thrust bearing load.

To maintain thrust at an acceptable level and in a forward direction, a pressure balance piston is used. This is shown schematically in Figure 36.

3.7 CONTROL DESCRIPTION

The design of the core engine requires control of the following functions:

- Modulate fuel flow to control thrust.
- Split fuel flow to the two zones of the double-annular combustor.
- Position two air valves for independent ACC of the compressor (Stages 6 through 10) and the HP turbine.
- Position four start bleed valves for control of the core compressor seventh-stage air bleed in the starting region.
- Provide on/off control of two SRTC valves which shift the cooling air source to account for reduced pressure when the starting bleed is used.
- Provide condition monitoring data during core engine operation.

System Structure

The core engine control system is shown schematically in Figure 37. The full authority digital electronic control (FADEC) is the central element in the system. It receives input signals from the control room and from various engine sensors, provides servo signals to control the output devices shown, and receives position feedback signals from the output devices.

Five temperatures are sensed: HP compressor inlet and discharge air; HP turbine discharge gas; engine skin temperatures in the two areas where ACC is provided.

Two pressure inputs to the system are provided - ambient and compressor discharge.

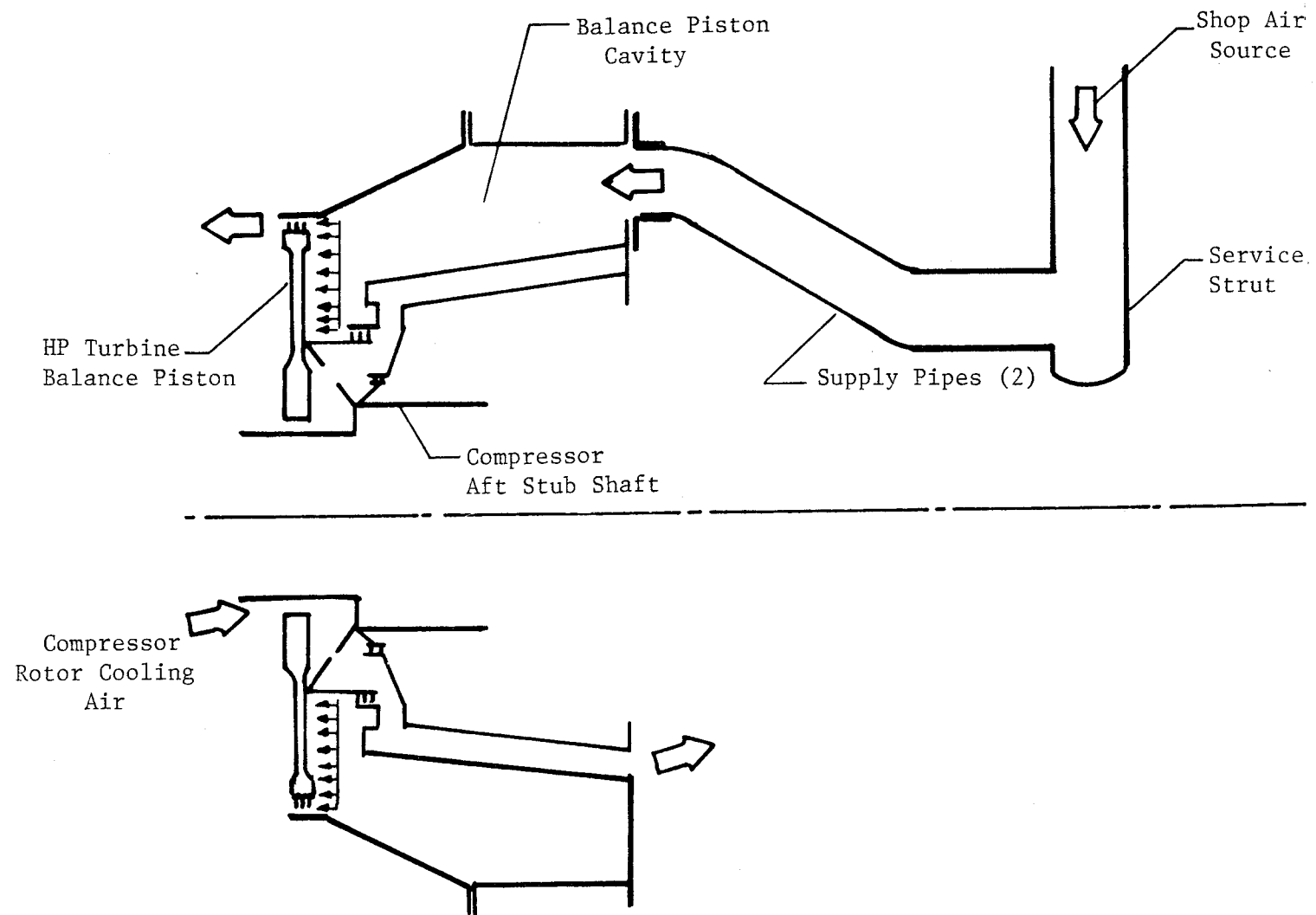


Figure 36. Schematic of Rotor Thrust Balance.

—

Core speed is supplied by an engine mounted and engine driven control alternator which also serves as the primary source of electrical power for the digital control. The control receives 28-volt-d.c. power from an external, source for use during starts and as an alternate power supply in the event of an alternator failure.

Command data are provided to the digital control through a multiplexed digital link which simulated an aircraft interface connection. The primary command input is the position of the engine operator's power lever, but the data link is also used to transmit adjustments and selector switch positions from the control room operator and the control engineering panel to provide experimental flexibility during core engine tests.

The data link also includes a separate channel for transmission of multiplexed digital engine and control system data to the control room, thereby simulating an aircraft engine monitoring connection. These data are displayed on a cathode-ray tube (CRT) and are connected to the cell instrumentation data system.

The control strategy for the various control system functions is contained in the program memory of the digital control. Output signals are generated by the control and transmitted to the various actuation devices in order to control them in accordance with the control strategy. Most of this actuation control is done on a closed loop basis, utilizing electrical position feedback signals from the actuation devices. Virtually all of the action is done with fuel-powered actuators, using excess capacity from the engine fuel pump through electrohydraulic servovalves which respond to the digital control output signals. The only exceptions are the SRTC valves which are air powered through a solenoid valve.

Control output for the fuel valve is handled differently from all others in that it is transmitted to a transfer device capable of providing switchover to hydromechanical control for this variable only. In the event of a digital control malfunction, the electronic fuel control will shift to the hydromechanical backup, and all other controlled variables will be set at safe positions so that the engine can continue to run satisfactorily and can be shut down in a safe manner.

Fuel System Design

An engine-driven, positive displacement vane pump with an integral centrifugal cost element is used. Pump discharge fuel passes through a pump-mounted filter and into the fuel control mounted on the end of the pump.

In the fuel control, fuel metering is accomplished by the combined operation of the metering valve and a bypass valve that returns excess fuel to the inlet of the vane pump element. The bypass valve maintains a fixed differential pressure across the metering valve so that the metering valve area alone determines the amount of fuel flow supplied to the engine combustor. In the primary operating mode, the metering valve is positioned by the digital electronic control; in the backup mode, it is positioned by the hydromechanical control. A transducer provides position feedback to the digital control.

Metered fuel passes out of the fuel control through a pressurizing valve (necessary to maintain sufficient pressure to operate the fuel servos at low flow conditions) and through a cutoff valve which provides a means for positively shutting off fuel to the engine. The fuel then passes through a flowmeter (included to provide experimental test data) and an engine lube/oil cooler. Downstream from the cooler, the fuel flow is split between the pilot zone and the main zone of the combustor. A fully modulated main zone valve and an on-off pilot zone reset valve provide the means for modifying local fuel-air ratios in the combustor.

Fuel Control Strategy

Fuel flow is modulated to control core rotor speed in accordance with the power level angle (PLA) schedule. Limits are imposed on the core speed schedule to prevent excessive engine temperatures and pressures. In addition, transient fuel schedules are included to prevent compressor stall during accelerations and to prevent loss of combustion during decelerations; fuel flow rate-of-change limits are included to limit thermal shocks. The schedules and limits are combined in a selection network which establishes priorities and assures a smooth transition between control modes. A manual input is included to provide the capability of adjusting fuel flow from a control room

potentiometer. This was included primarily to allow the exploration of sub-idle engine characteristics.

Fuel Flow Split Control Strategy

The double annular combustor design requires that fuel from the main metering valve be split between the combustor pilot zone and the main zone. The required flow split characteristics are listed below.

Start Mode - Full fuel flow to the pilot zone only is required to assure ignition and best combustion during acceleration to idle.

Run Mode - Full fuel flow to the pilot zone only is required at idle to provide minimum exhaust emissions. Above idle, fuel is required to both zones.

Decel Mode - The capability to temporarily switch over to pilot-zone-only flow during rapid deceleration is provided in the event that decel blow-out problems are encountered.

Transition - For transition to the double annular burning mode, main zone fuel flow is temporarily held low to prevent pilot starvation as the main fuel nozzles fill.

A manual mode is provided for the main zone shutoff valve and the pilot zone reset valve, allowing each valve to be independently positioned from the control room during engine operation.

The output of the main zone shutoff-logic network operates the main zone valve through a control loop that includes position feedback so that the valve can be set at any position from fully closed to fully open. The pilot zone reset valve control does not include position feedback because the valve is a two-position device (fully open or fully closed) and does not require modulation.

Start Bleed Actuation and Control

The core engine incorporates provisions for controlling bleed air from the compressor seventh stage, in the event that compensation is needed for flow mismatch between the front and rear stages at low speeds during a start. These provisions were disconnected and capped early in the core engine test after it was determined that the bleed was not required and there was some concern over leakage from the system. This bleed flow was to have been

controlled by a set of four butterfly valves connected in parallel to the seventh-stage manifold. The actuation ring connecting the valves was driven by a single fuel-powered servoactuator. The control signal for the servoactuator was provided from the electronic digital control. An electrical position transducer was incorporated in the servoactuator to provide feedback to the control.

Starting Bleed Control Strategy

The automatic control strategy for the starting bleed called for positioning the valves, thus controlling bleed flow as a function of core corrected rpm.

A manual control mode for the start bleed valve was provided to allow experimentation during the engine test program.

Active Clearance Control

There are two separate clearance control systems: one for the compressor, one for the HP turbine.

Compressor clearance control is achieved by passing a variable flow of compressor Stage 5 bleed air over the compressor casing to provide a thermal adjustment of casing dimensions. The Stage 5 air extracted for LP turbine purge (simulated during core test) is ported so that it can flow through the compressor clearance control chamber or through an external bypass pipe. Air from these two flowpaths is ported to a rotary three-way valve (compressor clearance control valve) designed to provide virtually constant LP turbine purge total flow. An electrical transducer within this rotary valve actuator provides position feedback to the control.

Turbine clearance control is achieved by impinging variable amounts of cooling air onto the HP turbine casing, thereby providing thermal control of casing dimensions. Shop air (simulated fan discharge air) was used during core tests and passed through a variable area butterfly valve (HP turbine clearance control valve). This valve is positioned by a fuel-powered actuator similar to the one used for the HP compressor clearance control valve.

Active Clearance Control Strategy

In the automatic clearance control strategy for both the HP compressor and the HP turbine, engine casing temperatures are measured and used to regulate the clearance valves to a scheduled temperature as generated from corrected core speed. A rapid deceleration will cause the clearance control valve to close and to remain closed until the casing has reached its steady-state level. If the engine is reaccelerated before steady-state temperatures are established, the decel override is deactivated and the casing temperature schedule functions normally. The decel override was added to minimize rubs in the event of a hot rotor reburst (that is, a decel followed by an accel before the rotor - which cools slower than the casing - has reached steady-state temperature).

In addition, a manual control mode is provided. When the manual mode is selected, the air valve is positioned as a function of a potentiometer on the electronic digital control operator panel so that clearance control system characteristics can be experimentally evaluated. A decel override is included in the manual mode to preclude a hot rotor reburst with the air valve inadvertently left open after a decel. This override, once activated, remains in effect until manually reset.

The compressor clearance control has an additional feature to maximize clearance during accelerations. Whenever Stage 5 air exceeds the casing temperature, the valve is opened for more rapid casing heating.

Start Range Turbine Cooling

One of the effects of start bleed is to lower pressure levels throughout the compressor. Pressure levels of the parasitic flows extracted from the compressor for turbine cooling and purge are also lowered.

In order to maintain adequate pressure and flow in the parasitic air systems during a start with the start bleed valves open, provisions are made to temporarily connect these systems to a higher pressure source. A pair of air-actuated on-off valves and a system of check valves allow CDP to be applied to the parasitic systems when the start bleed valves are open. Actuation air for the two SRTC valves is controlled by the electronic digital

control through solenoid valves. The SRTC system was disconnected and capped early in the core test when the start bleed provisions were deleted as noted above. A mechanical failure occurred in the system and is described in Section 6.8.

Start Range Turbine Cooling Control Strategy

Two control modes were provided for SRTC, automatic and manual. In the automatic mode, the source for the parasitic air systems was selected as a function of core corrected rpm. Below ground idle power, the systems were connected to CDP; at ground idle and above, they were connected to their normal sources. A slight delay in closing the SRTC valves was provided on reaching ground idle to prevent any undesirable CDP disturbances before steady-state operation was achieved.

In the manual mode, SRTC valves were controlled solely by a switch on the digital electronic control operator panel.

3.8 INSTRUMENTATION DESCRIPTION

The core engine was heavily instrumented to investigate the following areas:

- Aerodynamic performance
- Secondary flows
- Clearances
- Aeromechanical performance
- System vibration
- Operational characteristics

The quantities of instrumentation were as follows:

- 400 Pressures
- 475 Temperatures
- 140 Strain gages
- 20 Accelerometers
- 3 Touch probes
- 6 Clearanceometers

- 8 Laser clearance probes
- 14 Vane angle indicators
- 2 Engine fuel flowmeters

The location and types of aeroperformance instrumentation are shown in Figure 38. Secondary flow determinations were made using pressure and temperature measurements in the flow circuits. External piping flow characteristics had been determined prior to core test. Table IV lists the types of measurements used to determine secondary flows.

Table IV. Secondary Flow Measurements.

<u>Flow System</u>	<u>Method of Measurement</u>
Stage 5 Air for Customer Bleed	Orifice
Stage 5 Air for LPT Purge	Calibrated Piping
Stage 7 Air for Start Bleed	Calibrated Piping
Stage 7 Air for HPT Stage 2 Vane Cooling	Calibrated Piping
CDP Air for Turbine Blade Cooling	Calibrated Inducer
CDP Air for LPT Purge Augmentation	Calibrated Piping
Stage 5 Air for Compressor ACC	Calibrated Piping
Shop Air for Turbine ACC	Calibrated Valve and Calibrated Manifolds
Shop Air for Rotor Bore Cooling	Orifice

Clearances in compressor Stages 3, 5, and 10 were measured by one touch probe and two clearanceometers in each of these stages.

The HP turbine clearances were measured using four laser probes at each stage. At low and medium power levels, the laser probes were purged with high pressure facility air. At high power levels, CDP air was bled from the engine, cooled, and used to purge the laser probes.

The aeromechanical instrumentation is listed in Table V.

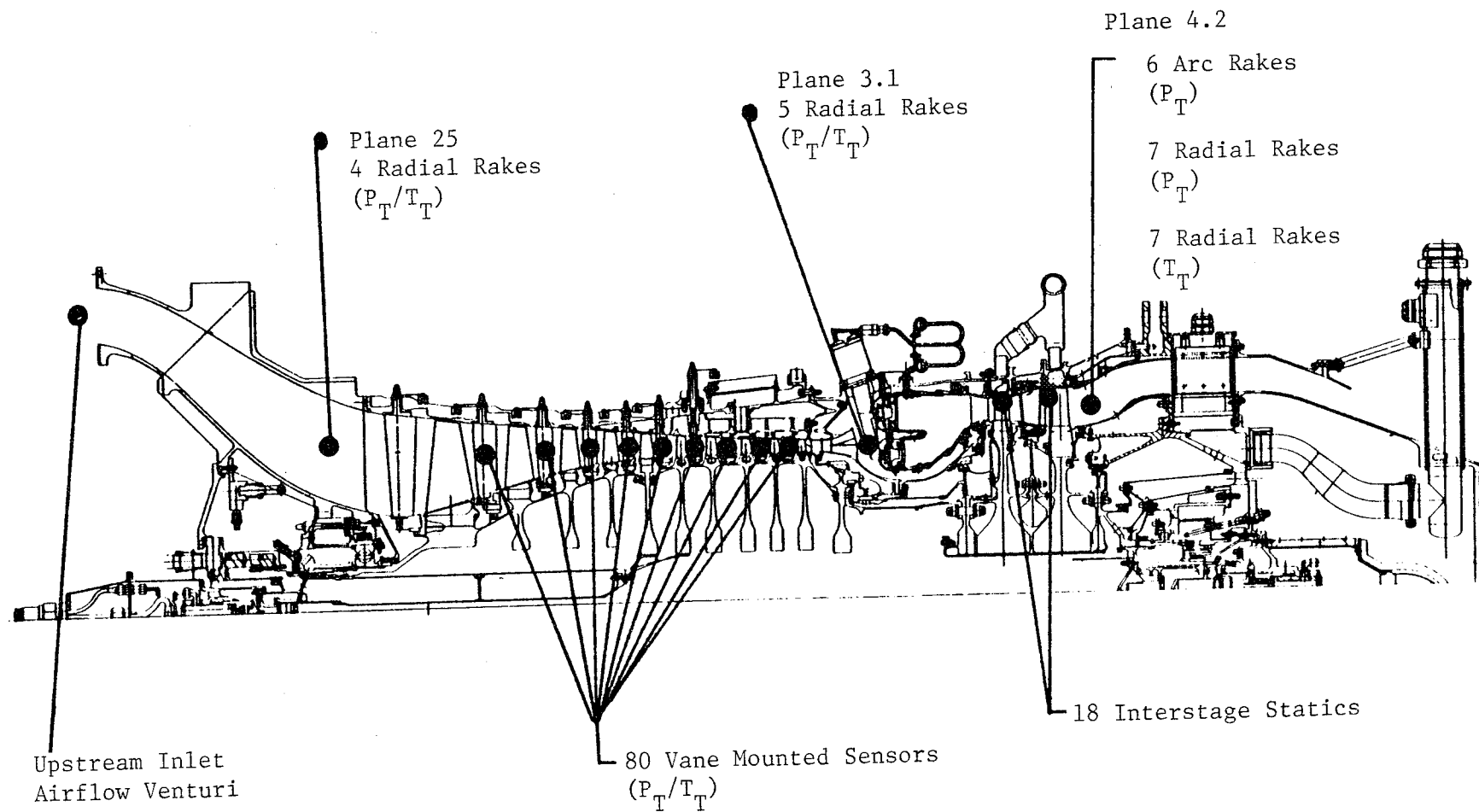


Figure 38. E³ Core Aeroengine Instrumentation.

4.0 TEST FACILITY DESCRIPTION

ore engine was tested in Cell AlW, Building 303, at General Electric, Ohio. Inlet air was supplied to the engine at a controlled temperature through a prefilter, a flow-measuring venturi, and a final pressure. The facility provided for sea level static and ram engine inlet conditions. The engine exhaust was discharged to cell ambient pressure into a duct and through a silencer to ambient.

engine installation is shown in Figure 40. The engine was mounted by a frame connection to the air supply ducting and by a vertical hanger to the engine rear frame. During test, the engine was within the transport dolly but was decoupled from it.

large number of services were provided by the facility. These are shown in Figure 41.

line and facility services were operated from the operations area of the control room. Data acquisition and engineering monitoring occurred in the operator's area of the control room. There the Data Management System recorded, processed, printed, and displayed on computer graphics screens engineering test information. The control room layout is shown in Figure 43 is a photo of the engine operations area.

critical engineering operational data were displayed in real time and recorded by using oscilloscopes, Sanborn strip charts, and tape recorders. Following information was displayed on-line and recorded on Sanborn strip

- Core Speed
- Power Lever Angle
- Fuel Flows
- Compressor Discharge Pressure
- Turbine Discharge Temperature
- Main Zone Fuel Valve Position
- Fuel Flow Control Mode
- Start Bleed Valve Position

shown in
for-
d aft
horizontal

up
Facil-
el
com-
es,

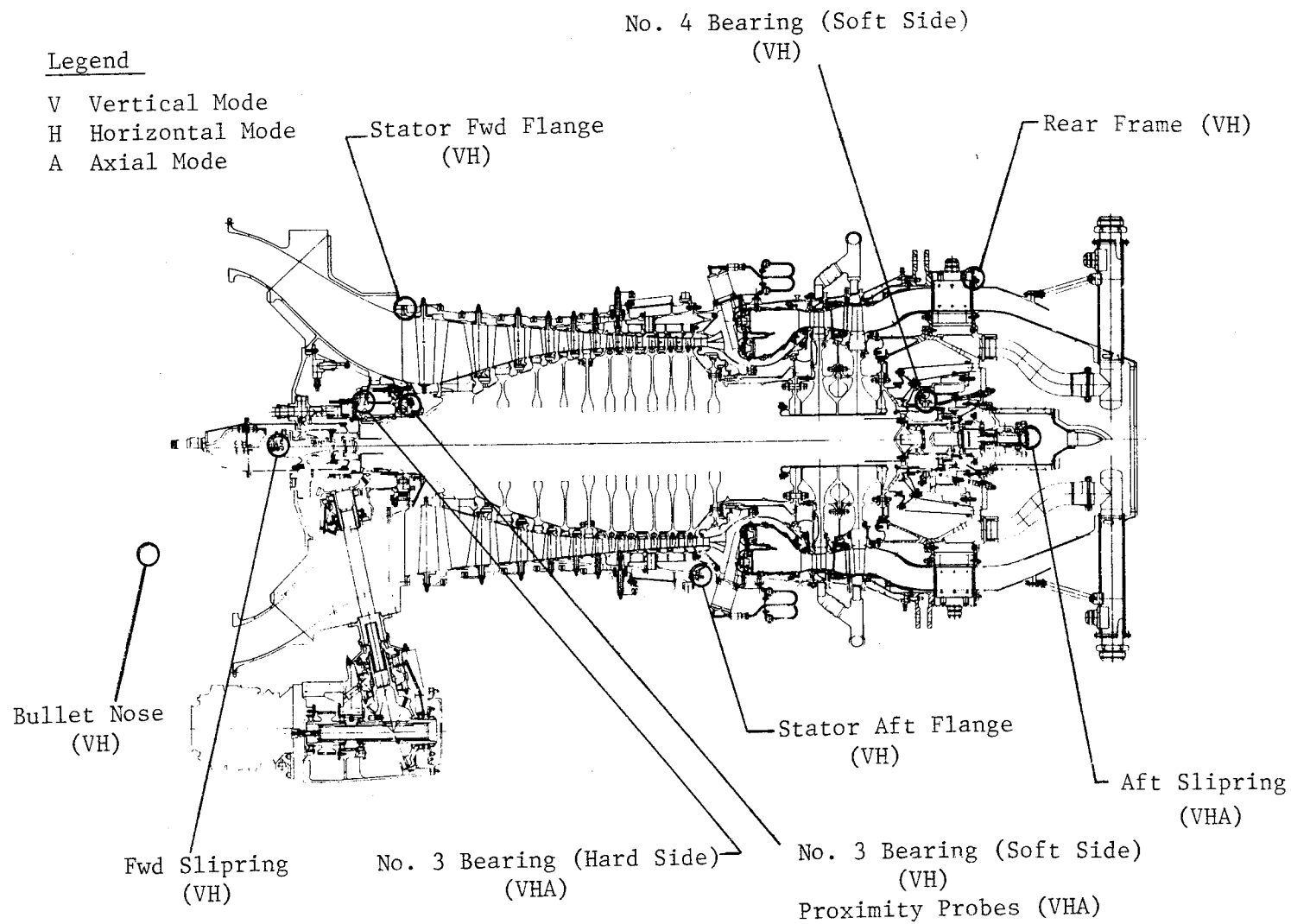


Figure 39. Core Vibration Monitoring Instrumentation.

4.0 TEST FACILITY DESCRIPTION

The core engine was tested in Cell AlW, Building 303, at General Electric, Evendale, Ohio. Inlet air was supplied to the engine at a controlled temperature and pressure through a prefilter, a flow-measuring venturi, and a final filter. The facility provided for sea level static and ram engine inlet conditions. The engine exhaust was discharged to cell ambient pressure into a collector and through a silencer to ambient.

The engine installation is shown in Figure 40. The engine was mounted by a front frame connection to the air supply ducting and by a vertical hanger from the facility to the engine rear frame. During test, the engine was cradled within the transport dolly but was decoupled from it.

A large number of services were provided by the facility. These are shown in Figure 41.

Engine and facility services were operated from the operations area of the control room. Data acquisition and engineering monitoring occurred in the monitor's area of the control room. There the Data Management System (DMS) recorded, processed, printed, and displayed on computer graphics screens the engineering test information. The control room layout is shown in Figure 42; Figure 43 is a photo of the engine operations area.

Critical engineering operational data were displayed in real time and recorded by using oscilloscopes, Sanborn strip charts, and tape recorders. The following information was displayed on-line and recorded on Sanborn strip charts:

- Core Speed
- Power Lever Angle
- Fuel Flows
- Compressor Discharge Pressure
- Turbine Discharge Temperature
- Main Zone Fuel Valve Position
- Fuel Flow Control Mode
- Start Bleed Valve Position

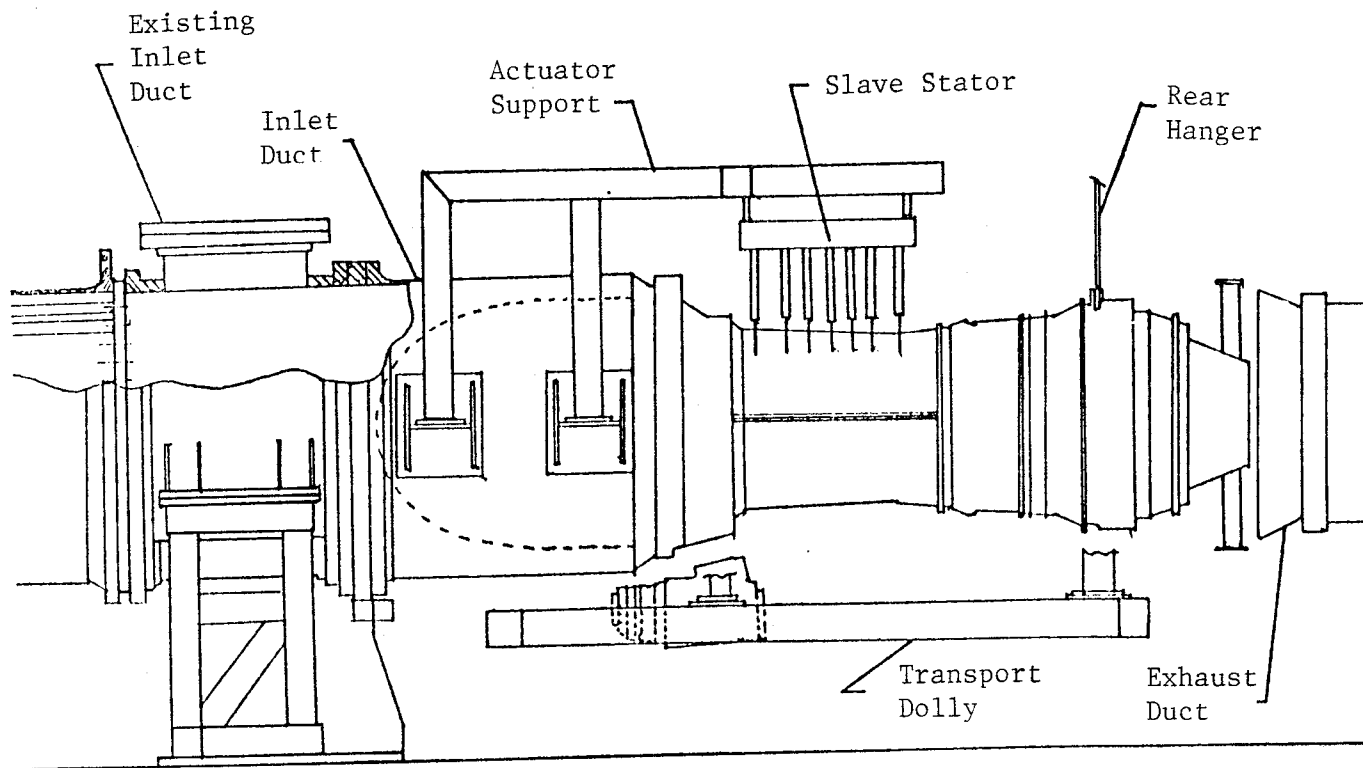


Figure 40. Core Cell AlW Installation.

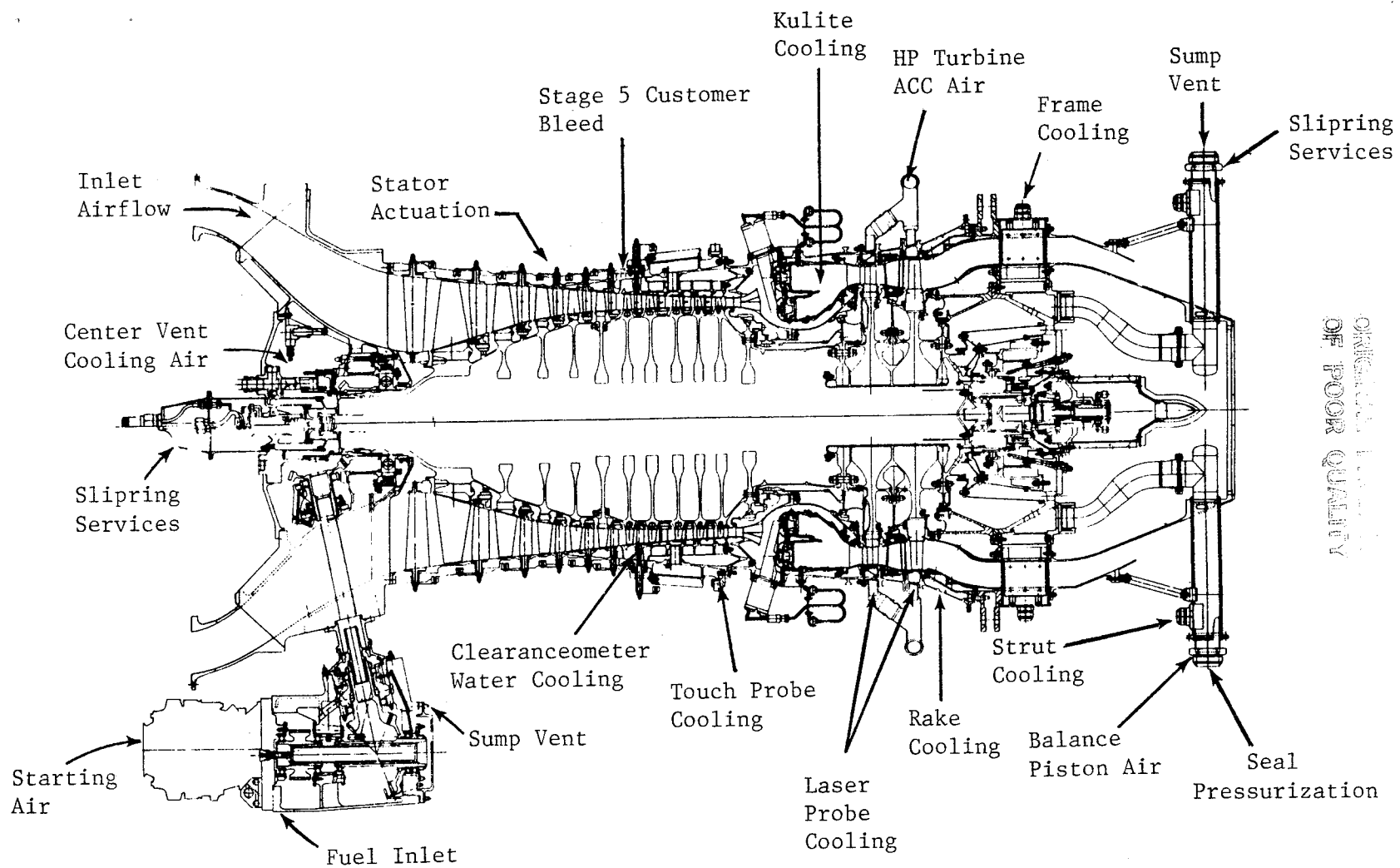


Figure 41. Facility-Supplied Services.

- A. Control Console
- B. FADEC Unit
- C. DMS Cell System
- D. DMS Site System
- E. DMS Graphic Consoles
- F. Printers
- G. Isolation Panel
- H. Tape Recorders
- J. Sanborn Recorders
- K. Traverse Probe Control

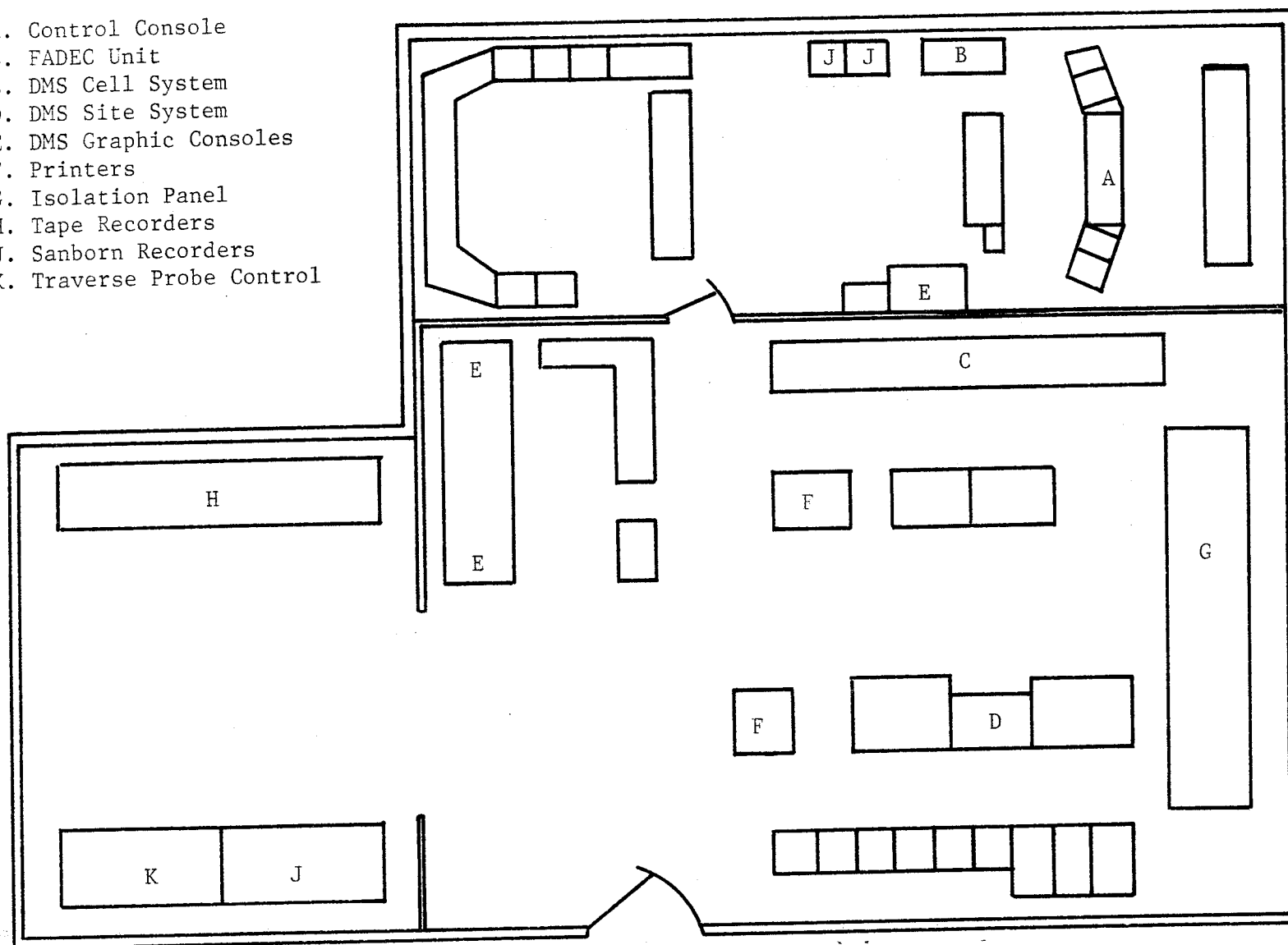


Figure 42. Layout of Cell AlW Control Room.

ORIGINAL PAGE
BLACK AND WHITE PHOTOGRAPH

ORIGINAL PAGE IS
OF POOR QUALITY

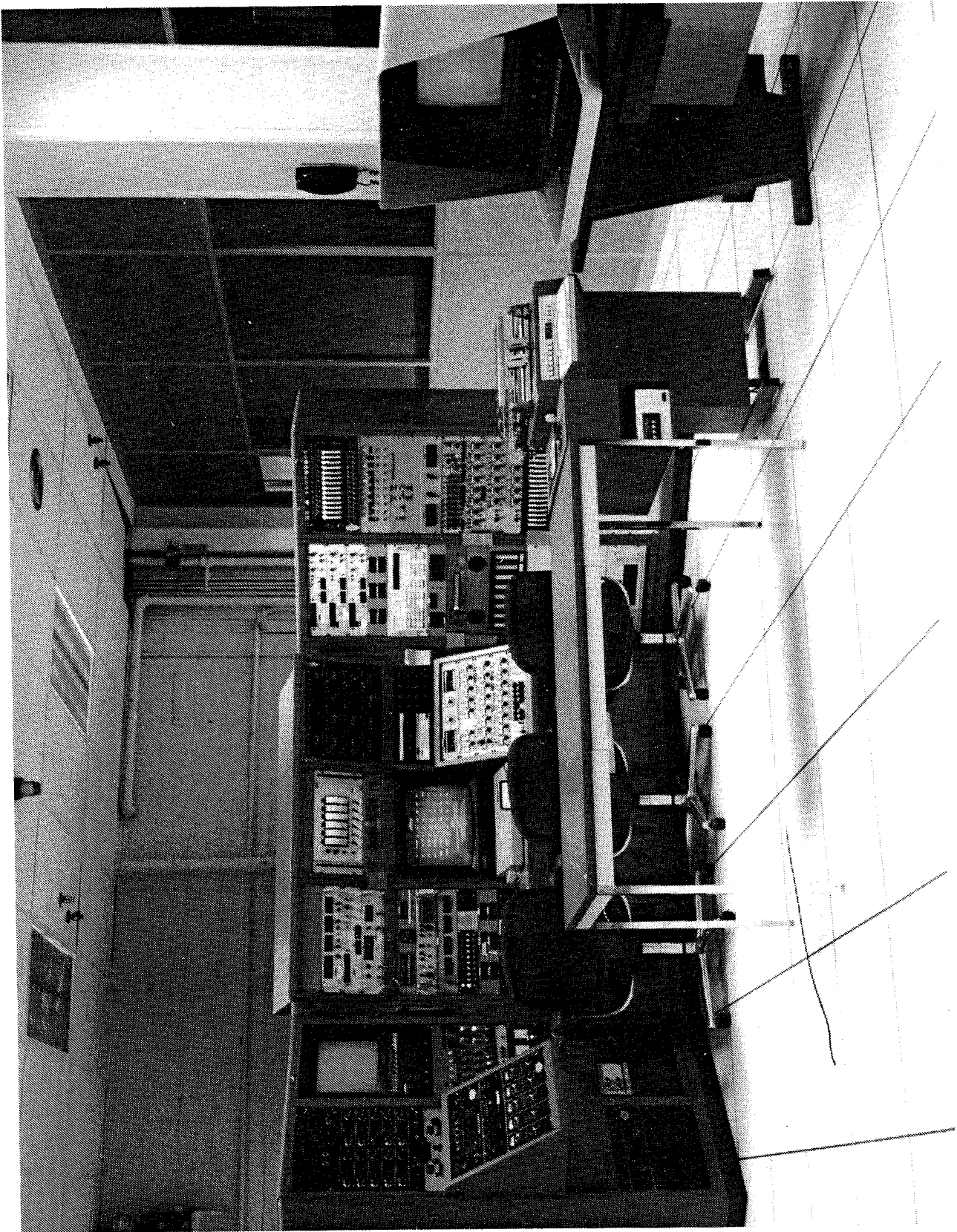


Figure 43. Photo of Cell ALW Control Room Console.

- Compressor Clearance Control Valve Position
- Turbine Clearance Control Valve Position
- Compressor Case Temperature
- Turbine Case Temperature
- Compressor Discharge Temperature
- Start Bleed Valve Position
- Fuel Manifold Pressures
- Combustor Temperature
- Turbine Nozzle Temperatures
- Compressor Clearances
- Turbine Clearances
- Shaft Proximity Probe Axial Location

The following information was recorded on magnetic tapes and displayed on-line on oscilloscopes:

Vibration Recorders

- No. 3 Bearing Support
- No. 4 Bearing Strain Gages
- Proximity Probes
- No. 3 Bearing, Soft Side
- No. 4 Bearing, Soft Side
- No. 3 Bearing, Hard Side
- Bullet Nose
- Turbine Frame
- Stator Case, Forward Flange
- Stator Case, Aft Flange
- Forward Slipring
- Aft Slipring

Strain Gage Recorders

- Turbine Blades
- Plane 2.5 and 3.1 Rakes
- Compressor Blades
- Compressor Vanes

Clearance Recorder

- Laser Probes
- Combustor Kulite Probes
- Clearanceometer Probes

Included on All Recorders

- 1/Rev
- Time Code
- Core Speed
- Voice Commentary

Vibration, turbine strain gage, and rake strain gage recorders and displays were located in the Information Data Room (IDR). Inlet air cleanliness and emissions measuring equipment were located in the test cell adjacent to Cell AlW. All other equipment was located in the control room.

Engineering test data were handled by a DMS which links all GE-Evendale and Peebles engine test sites with a central data processing facility. It operates independent of the real-time systems described above and is designed to perform a number of functions, such as data acquisition, processing, distribution, and graphic presentation of engine test data. It consists of three functional subsystems: Cell Unit, Site Unit, and Communications Controller (C-Con).

The Cell Unit functional subsystem is illustrated in Figure 44 and consists of two minicomputers, analog-to-digital conversion units, a control console, and a hard-copy printer. Its primary functions are data acquisition, system calibration, sample averaging, and engineering units conversion. It interfaces only with the Site Unit for data transfer.

The Site Unit, shown in Figure 45, receives the engineering unit data from the Cell Unit and performs average and error rejection calculations, data quality checks, and engineering calculations. It has a data base storage system and color interactive graphics capability with four consoles.

The C-Con is the coordination unit for data transfer between the Site Unit and the transmission of data to a central Honeywell 6000 computer.

DATA MANAGEMENT SYSTEM (DMS) (EVENDALE, PEEBLES, LYNN)

CELL UNIT

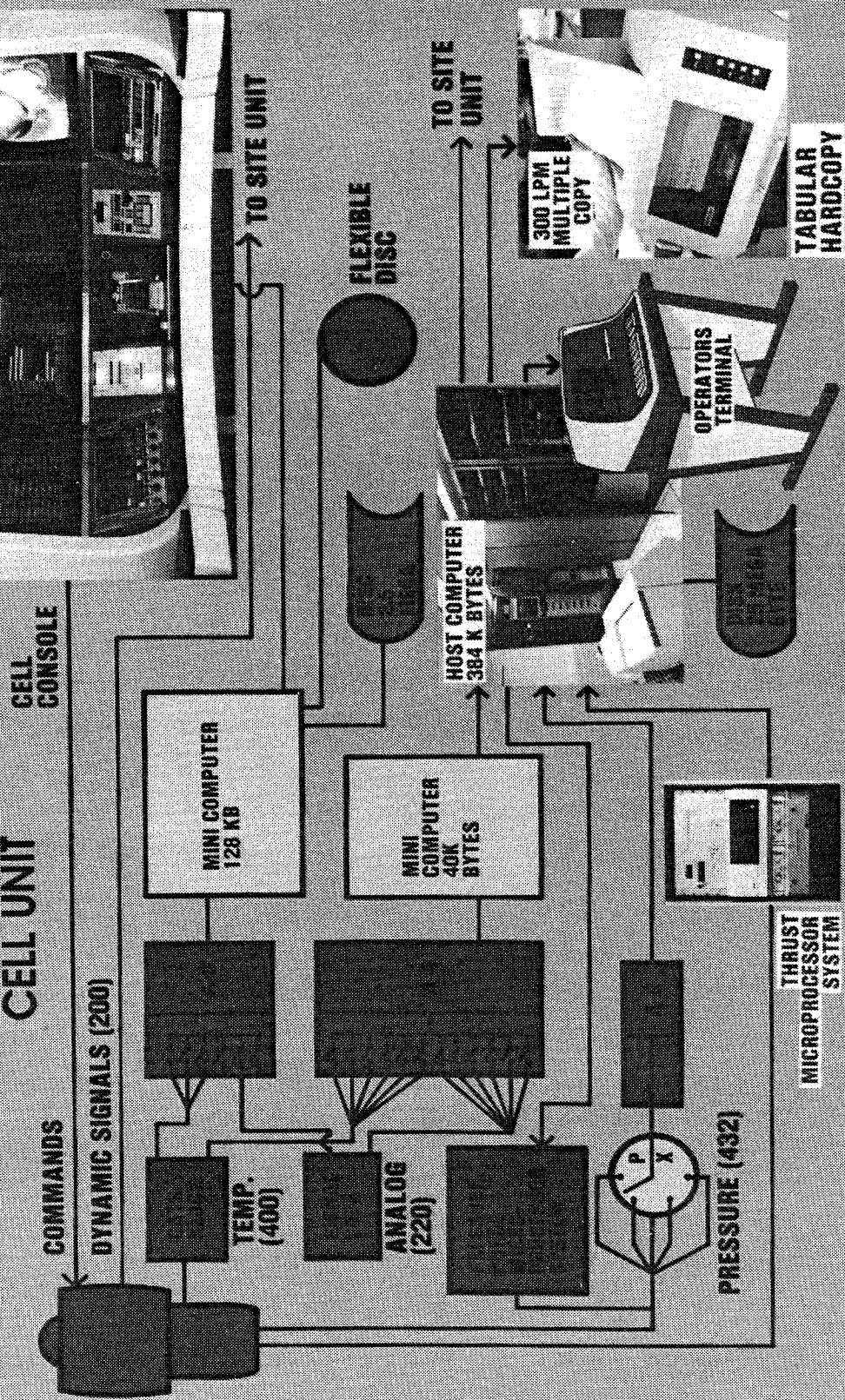


Figure 44. Cell Unit Functional System.

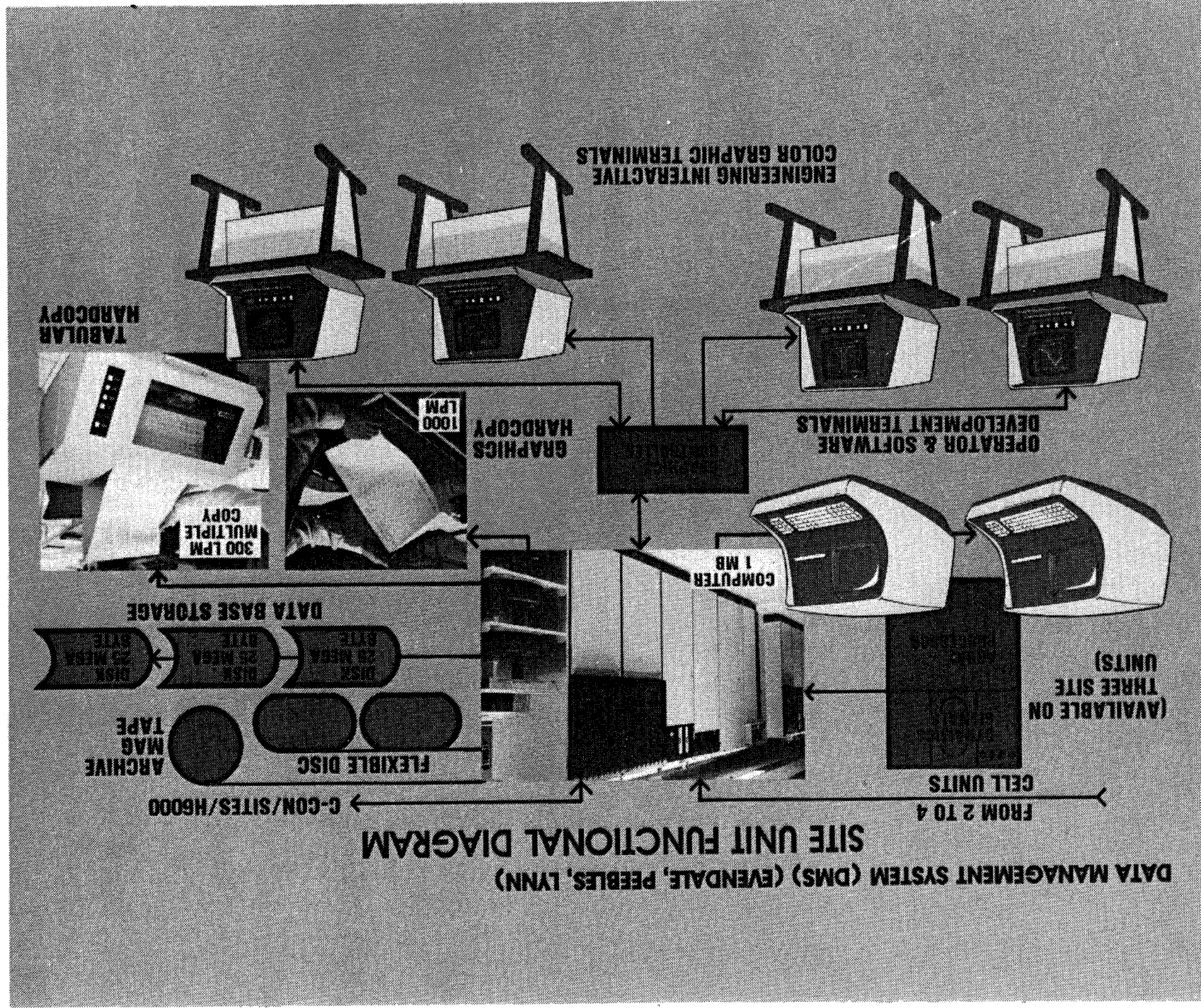


Figure 45. Site Unit Functional Diagram.

The Cell and Site Units were used during the core engine test; they provided on-line performance calculations. All data were stored on the Site Unit data base and later transferred to the Honeywell 6000 computer after reprocessing of known measurement anomalies.

The interactive graphics system permitted an on-line (near real time) comparison of the test data with the pretest data stored in the site computer. The system provided hard copies of the selected data plots, as well as data printouts for each data reading. A dynamic capability of the system also provided transient data processing of the starting, accelerating, and decelerating characteristics of the engine.

5.0 TEST OPERATIONS SUMMARY

This section provides a detailed history of the test activities. It covers configuration changes, test conditions, and details of test cell operations.

The E³ core engine, S/N 531-001/1, completed assembly on 15 July 1982 and was transported to the test cell preparation area. Final preparations were completed and installation in the test cell was initiated on 26 July 1982. Testing began 4 August 1982 and was completed 27 August 1982. Testing was completed in 44.5 hours of fired rotating time. Removal of the engine from the cell began on 30 August 1982; the engine was returned to the assembly area 1 September 1982.

The first portion of the test was a checkout of the engine and test facility. Engine mechanical evaluation over the speed range was completed, and procedures for engine starting and control were developed.

Following engine and facility mechanical checkout, engine performance testing was executed. These tests included compressor stator optimization, emissions evaluation, further start optimization, and operating line migration using three exhaust nozzle areas (A8). Testing was concluded with a final performance calibration.

A summary of the tests conducted is given in Table VI. The term "Run" refers to a specific time period of testing. The term "Test" refers to a specific test activity or test objective.

The engine configuration and some facility hardware and instrumentation were different for some of the tests. A listing of these differences is shown in Table VII.

The following is a history of the test activities from an operational point of view. The test parameters relate to the engine control console readouts, not the Data Management System (DMS) readouts.

Table VI. Summary of E³ Core Tests.

Run	Test	Inlet Pressure	Inlet Temperature	Exhaust Nozzle Area	Venturi Diameter Cm (in.)	No. of Turbine Laser Clearance Probes	Air Starter Motor Used	Compressor Active Clearance Control	Turbine Active Clearance Control	Stage 5 Bleed	Compressor Stator Schedule
1	Pretest Checkout Dry Motor	Ambient	Ambient	Nominal	30.48 (12)	8	Yes	Off	Off	Off	Baseline
2	Wet Motor	Ram	Heated	Nominal	30.48 (12)	8	No	Off/On	Off/On	Off	Baseline
3	Idle Checkout	Ram	Ambient	Nominal	30.48 (12)	8	No	Off	Off	Off	Baseline
4	Mechanical Checkout	Ambient	Ambient	Nominal	30.48 (12)	8	No	Off	Off	Off	Baseline
5	Mechanical Checkout	Ambient/Ram	Ambient	Nominal	30.48 (12)	3	No	Off	Off	Off	Baseline
6	SLS Performance	Ambient	Ambient	Nominal	30.48 (12)	8	No	Off/On	Off/On	Off	Baseline
7	SLS Performance	Ambient	Ambient	Nominal	30.48 (12)	8	No	Off/On	Off/On	Off/On	Base/Optimized
8	SLS Performance	Ambient	Ambient	Nominal	30.48 (12)	4	No	Off/On	Off/On	Off/On	Optimized
9	Start Optimization	Ambient/Ram	Ambient	Nominal	15.24 (6)	0	No/Yes	Off	Off	Off/On	Optimized
10	Emissions	Ambient/Ram	Ambient	Nominal	30.48 (12)	0	No	Off	Off	Off	Optimized
11	A8 Variation	Ambient	Ambient	Minimum/Maximum	30.48 (12)	0	Yes	Off/On	Off	Off	Optimized Stage 5 Locked
12	Final Performance	Ambient	Ambient	Optimized	30.48 (12)	8	No	Off/On	Off/On	Off	Optimized Stage 5 Locked

Table VII. Core Test Configuration Changes.

Run 1

- Blanked off Stage 5 bleed manifold.
- Installed air starter.
- Removed Stage 5 touch probe.
- Nominal A8 exhaust nozzle
- 30.48 cm (12 inch) inlet venturi
- Installed all laser probes.

Run 2

- Installed slave scavenge filter.
- Removed air starter.

Run 3

- Removed fuel control and replaced a defective "O" ring. Reinstalled control.
- Installed Stage 5 bleed manifold.
- Installed Stage 5 touch probe.

Run 4

- Installed stall dump kit.
- Connected air sampling rakes.

Run 5

- Removed and blanked off four Stage 1 and the 6 o'clock Stage 2 laser probes.
- Repaired check valve on laser cooling cart.
- Removed SRTC lines. Blanked off the two CDP bleed ports, two air solenoid lines, and SRTC orifices and check valves.
- Blanked off Stage 5 bleed manifold.

Run 6

- Removed Stage 7 start bleed valves.
- Repaired Stage 1 laser probes. All eight laser probes installed.
- Reconnected Stage 5 customer bleed manifold.

Table VII. Core Test Configuration Changes (Concluded).

Run 7

- Removed slave scavenge system and installed engine scavenge filter.

Run 8

- Removed all four Stage 1 laser probes and installed blank-off pads.

Run 9

- Removed the remaining four Stage 2 laser probes and installed blank-off pads.
- Removed 30.48 cm (12 inch) and installed the 15.24 cm (6 inch) inlet flow venturi.
- Installed the air starter halfway through the run for sea level static starts.

Run 10

- Removed the air starter.
- Disconnected Plane 4.2 radial pressure elements.
- Moved HPT ACC butterfly flow split valves from full open to full closed.
- Installed emissions and smoke measurement hardware.
- Removed 15.24 cm (6 inch) and installed 30.48 cm (12 inch) inlet venturi.

Run 11

- Removed emissions hardware. Reconnected Plane 4.2 radial pressure elements.
- Installed the air starter.
- Exhaust nozzle variations (nominal, maximum, and minimum) were made.

Run 12

- Reinstalled all eight turbine laser probes.
- Capped off the Stage 5 customer bleed manifold.
- Installed the optimized exhaust nozzle.
- Removed the air starter.

E³ Core Test No. 2: Initial Dry Motor
Run No. 1
Date: 4 August 1982
DMS Readings: 1 through 3

Test Conditions

P25 - Ambient
T25 - Ambient
A8 - Nominal [1052 cm² (163 in²) cold-physical]
Venturi - 30.48 cm (12 in.)
Sump Vents - Set at 69 kPa (10 psia)
Seal Pressurization - Vented to ambient
Instrumentation - All eight laser probes installed
Stage 3 and 10 touch probes installed

The engine and facility checklists were completed. Engine rotation was initiated by slowly increasing the starter air pressure to 145 kPa (21 psia), where core speed stabilized at 2100 rpm. A cell inspection identified a fuel leak near the turbine active clearance control (ACC) valve servo line; rotation was stopped. The leak was traced to a loose fitting and was corrected. Dry motoring resumed. Three steady-state DMS readings were recorded at the conditions listed below. The maximum motoring speed obtained was 4000 rpm (32% corrected speed) and was limited by the starter air pressure limit [379 kPa (55 psia)]. The Phase I data reduction program was not functioning correctly throughout this run, so only raw data were recorded. No mechanical or lube system problems were encountered. The maximum starter oil temperature was 82° C (180° F).

Run No. 1

<u>DMS</u>	<u>Core speed, rpm</u>	<u>PCN25R, %</u>	<u>Starter Air Pressure kPa (psia)</u>
1	2100	20	145 (21)
2	3550	30	262 (38)
3	4000	32	372 (54)

Posttest inspections indicated a fuel leak occurring at low pressure around the main fuel control housing. The leak disappeared once the engine began rotating. A small amount of fine metal was found on the magnetic plug

from the accessory gearbox (AGB), which is normal. The forward sump vent line was found to be loose and was tightened. A "green run" fine mesh oil filtration system was installed in place of the oil scavenge filter. The air starter was removed and the pad blank-off installed in preparation for windmill and wet motoring checkout.

E³ Core Test No. 3: Initial Dry Motor
Run No. 2
Date: 5 August 1982
DMS Readings: 4 through 13

Test Conditions

P25 - Ram [Ambient to 180 kPa (26.1 psia)]
T25 - 60°-104° C (140°-220° F)
A8 - Nominal [1052 cm² (163 in²)]
Venturi - 30.48 cm (12 in.)
Sump Vents - 69 kPa (10 psia)
Seal Pressurization - On
Rotor Thrust Balance - 138 kPa (20 psia)
Rotor Bore Cooling - 0.18 kg/s (0.4 lbm/s)
Instrumentation - All eight laser probes installed
Stage 3 and 5 touch probes installed

Engine rotation was initiated by slowly increasing the inlet air pressure. Four speed points were set, with the maximum motoring speed obtained being 3920 rpm. At 3000 rpm, several of the fuel-actuated engine valves, the compressor and turbine ACC's, start bleed, main zone shutoff, and pilot zone reset were successfully exercised. The fuel stopcock was opened and fuel was observed in the engine exhaust; however, there was no indication of fuel flow on the fuel flowmeter. The stopcock was closed and positive fuel shutoff was confirmed. When the fuel flowmeters did not indicate fuel flow when the FADEC (Full Authority Digital Electronic Control) indicated 136 kg/h (300 pph), it was thought that perhaps the flowmeters could not detect such a small flow. Next, a fuel pulse of 454 kg/h (1000 pph) was set by the FADEC, but there was still no indication of fuel flow, although much fuel was seen exiting the exhaust. The problem was later attributed to the electrical wiring of the meter. Several instrumentation faults were defined during the motoring. The coast down of vehicle from 3920 to 0 rpm was observed, with no unusual noises or abnormalities. The following steady-state DMS readings were recorded.

Run No. 2

DMS	Core speed, rpm	P25, kPa (psia)	T25, ° C (° F)	Compressor ACC	Turbine ACC
4	0	Ambient	Ambient	Off	Off
5	2620	139 (20.1)	62 (144)	Off	Off
6	Bad Rdg	--- ---	--- ---	---	---
7	Bad Rdg	---	---	---	---
8	3000	152 (22.1)	74 (165)	Off	Off
9	3000	152 (22.1)	74 (165)	Off	15°
10	3000	152 (22.1)	74 (165)	Full	Full
11	3600	170 (24.6)	104 (220)	Off	Off
12	3920	180 (26.1)	104 (220)	Off	Off
13	0	Ambient	104 (220)	Off	Off

Posttest inspections revealed fuel leaking again from the main fuel control (MFC) in the form of a persistent drip. The MFC was removed, and the leak was located and corrected by replacing a defective "O" ring seal on the housing. The MFC was pressure checked and reinstalled on the vehicle. The facility and instrumentation faults defined during Run 2 were corrected. The facility slave Stage 5 customer bleed system was installed. A recalibration of the throttle rigging was performed, and the Stage 5 touch probe was installed. The facility and engine checklists were completed and the vehicle prepared for the next run.

E³ Core Test No. 3A: Wet Motor Repeat
 No. 4: Initial Start and Idle Checkout
 Run No. 3
 Date: 9 August 1982
 DMS Readings: 14 through 21
 Run Time: 0 hours 26 minutes

Test Conditions

P25 - 179 kPa (26 psia)
 T25 - Ambient
 A8 - Nominal [1052 cm² (163 in²)]
 Venturi - 30.48 cm (12 in.)
 Rotor Thrust Balance - 207 kPa (30 psia) for windmilling
 310 kPa (45 psia) at idle
 Rotor Bore Cooling - 0.27 kg/s (0.6 lbm/s)
 Instrumentation - All eight laser probes installed
 All three touch probes installed

The run began with Test No. 3A, a repeat of the wet motoring. DMS Readings 15 and 16 were zero rpm readings taken with the turbine frame and the aft service strut cooling air turned on to verify the amount of cooling airflow to the struts. The vehicle was windmilled to 30% speed at which time the stop-cock, main zone shutoff, and pilot zone reset valves were successfully exercised.

The first start attempt was made with manual fuel control to the pilot zone while motoring at 30% speed with an inlet pressure of 179 kPa (26 psia) and a starting fuel flow of 136 kg/h (300 pph). No light was detected after 15 seconds of ignition and the start was aborted.

The next start attempt (Start 1) was made under the same conditions. A partial light on one or more burners was indicated by a 40-rpm rise in core speed and a slight increase in EGT to 49° C (120° F). This start was also aborted.

Engine Start 2 was made while motoring at 3820 rpm (30%) with an inlet pressure of 179 kPa (26 psia) and a starting fuel flow of 181 kg/h (400 pph), a 45 kg/h (100 pph) increase. Light-off occurred almost immediately and the vehicle accelerated smoothly to 4780 rpm on starting fuel flow. The fuel flow was then manually increased until a core speed of 7800 rpm (62% corrected) was achieved. The maximum average T42 observed during the two-minute accel to idle was 199° C (390° F). Several DMS readings were recorded at idle. Next, the inlet pressure was lowered to 165 kPa (24 psia) at which time high stress levels on Plane 2 and 3 rakes were observed; the engine was shut down after 26 minutes of run time.

Several instrumentation faults were identified during the idle checkout; however, no other abnormalities were noted. All vibration levels were low, and the lube system performed as expected. The following steady-state DMS readings were recorded.

Run No. 3

DMS	Core speed, rpm	PCN25R, %	P25, kPa (psia)	HPG/HPT ACC	Stage 5 Customer Bleed	Stage 7 Start Bleed
14	0	0	Ambient	Off	0	0
15	0	0	Ambient	Off	0	0
16	0	0	Ambient	Off	0	0
17	3710	30	179 (26.0)	Off	0	0
18	3820	30	179 (26.0)	Off	0	0
19	7780	62	179 (26.0)	Off	0	0
20	7800	62	179 (26.0)	Off	0	0
21	7700	62	179 (26.0)	Off	0	0

Posttest inspections revealed nothing out of the ordinary. The MFC did not leak during the run. Instrumentation faults discovered during the run were corrected. Plane 23 inlet air sampling rakes and the stall dump system were installed. Engine and facility checklists were completed and the engine prepared for mechanical checkout.

The high stress readings indicated on the two instrumentation rakes were found to have been caused by an incorrect calibration of the tape recorder scopes.

E³ Core Test No. 5: Mechanical Checkout
 Run No. 4
 Date: 10 August 1982
 Run Time: 5 hours 0 minutes
 Total Engine Run Time: 5 hours 26 minutes
 DMS Readings: 22 through 55

Test Conditions

P25 - 179 kPa (26 psia) during windmill starts
 - Ambient for steady-state test points
 T25 - Ambient
 A8 - Nominal [1052 cm² (163 in²)]
 Venturi - 30.48 cm (12 in.)
 Rotor Thrust Balance - 310 kPa (45 psia) for ram starts
 - 241 kPa (35 psia) for ambient inlet
 Rotor Bore Cooling - 0.27 kg/s (0.6 lbm/s)
 Instrumentation - All eight laser probes installed
 All touch probes installed

Starting procedure for this test consisted of windmilling the engine to 30% corrected speed with an inlet pressure of 179 kPa (26 psia), then setting 181 kg/h (400 pph) starting fuel flow to the pilot dome. After ignition was observed, the vehicle was accelerated to idle by manually controlling fuel flow.

Mechanical checkout resumed with Start 3. Steady-state DMS readings were taken at 62%, 68.5%, and 76.5% corrected speeds at ambient inlet pressures and with the engine on single-annular (S/A) burning. The stall dump and the automatic fuel control system were activated to check their correct operation. A problem was discovered with the FADEC in the automatic fuel control mode which caused a 68 kg/h (150 pph) oscillation in fuel flow (30 rpm) at all speeds. Although this oscillation was annoying, it did not hinder further testing.

The first switchover to double-annular (D/A) burning was performed at 76% corrected speed without incident. However, while attempting to switch to backup (hydromechanical) control, a combustor blowout was experienced causing an unplanned shutdown. The blowout was attributed to a 3° misadjustment in the hydromechanical power lever angle (PLA) setting and was corrected prior to the next start.

Testing resumed with Start 4. Another uneventful switch from single to double annular burning was made at 76.5% speed. At this time it was first discovered that the start range turbine cooling (SRTC) valves may not have been closed. This was indicated by pressure and temperature levels in the piping downstream of the SRTC valves. There was no valve position feedback to the FADEC. All turbine nozzle temperatures remained within safe operating limits and it was decided to continue testing. Steady-state DMS readings were taken at 76.5%, 83%, and 90% corrected speed without incident.

While attempting to accelerate to 95% speed, a problem developed in the turbine laser probe cooling cart system which prevented the transition from slave air to compressor discharge pressure (CDP) air. This resulted in a backflow condition to the probes and caused an overtemperature failure of all Stage 1 laser probes. Further high-speed testing was deleted to prevent more damage to the Stage 2 probes. The engine was decelerated to 62% speed on

double-annular burning without incident. Also, switch to the backup hydro-mechanical control and back to the primary control was successfully made and the engine shut down.

All vibration, stress, and temperature levels remained within expected safe limits. All clearance measurements were functioning until the time of the laser cart malfunction. Several steady-state DMS readings were recorded and are listed below.

Run No. 4

DMS	Core Speed, rpm	PCN25R, %	P25, kPa (psia)	Combustor Mode	Comments
22	0	0	Ambient	S/A	Zero Reading
23	6,180	62.0	179 (26.0)	S/A	Start 3
24	6,180	62.0	179 (26.0)	S/A	
25	6,180	62.0	179 (26.0)	S/A	
26	7,300	---	152 (22.0)	S/A	
27	8,420	66.0	152 (22.0)	S/A	
28	8,420	66.0	152 (22.0)	S/A	
29	8,480	66.0	Ambient	S/A	
30	9,700	76.5	Ambient	S/A	
31	9,720	76.5	Ambient	S/A	
32	8,640	68.5	Ambient	S/A	Stall Dump
33	9,700	76.5	Ambient	D/A	
34	9,700	76.5	Ambient	D/A	
35	9,700	76.5	Ambient	D/A	
36	9,700	76.5	Ambient	D/A	
					Switch to Hydromechanical Control Blowout
37	9,760	76.5	Ambient	S/A	Start 4
38	9,760	76.5	Ambient	S/A	
39	9,760	76.5	Ambient	D/A	
40	10,450	83.0	Ambient	D/A	
41	10,450	83.0	Ambient	D/A	
42	11,300	90.0	Ambient	D/A	
43	10,520	83.0	Ambient	D/A	
44	10,520	83.0	Ambient	D/A	
45	11,370	90.0	Ambient	D/A	
46	11,370	90.0	Ambient	D/A	
47	11,370	90.0	Ambient	D/A	
48	12,000	93.0	Ambient	D/A	Cart Malfunction
49	8,650	68.5	Ambient	D/A	
50	8,650	68.5	Ambient	D/A	
51	7,760	62.0	Ambient	D/A	
52	0	0	Ambient	D/A	Shutdown Zero Reading

Posttest inspections revealed that a slip joint on one of the two SRTC lines downstream of the SRTC valve had failed, allowing the piping to separate. This permitted engine bleed air (CDP and Stage 5) to dump to ambient. Test data confirmed that between DMS Readings 47 and 48 (the first speed excursion above 90%), air pressure in that line went to ambient. Some distress was observed in the other slip joint and in the CDP bleed piping downstream. It was believed that when the SRTC valves did not close at idle as they should have, a combination of the higher pressure and temperature CDP air distorted the piping, thereby causing the slip joint to fail. Borescope inspections of the compressor, combustor, turbine, and rear frame revealed no problems.

Investigations into the laser probe cooling air supply revealed that one of the check valves in the CDP air circuit did not open as required when the CDP exceeded the slave air supply. This allowed higher pressure gas stream air to backflow into the Stage 1 laser probes and resulted in their failure due to overtemperature of the electronics. All four Stage 1 and one Stage 2 laser probes were removed for inspection and cleaning. The four Stage 1 probes were found to be unusable.

The laser probe cooling cart was completely checked out; the defective check valve was removed and cleaned. The regulating valve used to control the slave high pressure air supply also was repaired and checked out.

On the engine, the SRTC lines were removed, two CDP ports were blanked off, two air solenoid lines were blanked off, and blank offs were substituted for the two orifices and check valves. Four blank-off pads were installed in place of the Stage 1 laser probes. One Stage 2 laser probe hole was plugged, and the Stage 5 customer bleed manifold was blanked off. All instrumentation faults were corrected and the engine prepared for continuation of mechanical check out.

E³ Core Test No. 5A: Continuation of SLS Mechanical Checkout
No. 6: Ram Mechanical Checkout

Run No. 5

Date: 12 August 1982

Run Time: 3 hours 48 minutes

Total Engine Run Time: 9 hours 24 minutes

DMS Readings: 53 through 64

Transients 7001-7004

Test Conditions

P25 - Ambient for sea level static checkout
- 152 kPa (22.0 psia) for ram checkout
T25 - Ambient
A8 - Nominal [1052 cm² (163 in²)]
Venturi - 30.48 cm (12 inch)
Rotor Thrust Balance - 310 kPa (45 psia) for ram inlet
- 241 kPa (35 psia) for sea level static
Rotor Bore Cooling - 0.25 kg/s (0.55 lbm/s)
Instrumentation - No Stage 1 laser probes
- Three Stage 2 laser probes installed

No ACC or overboard bleed were used for this run. Engine starts for this test continued to be made manually with ram inlet air. The first three attempts to transition from single- to double-annular burning were unsuccessful and necessitated three unplanned engine shutdowns from 76.5% speed.

Transient recordings of the main zone fuel manifold pressure revealed that in each case the manifold pressure had not stabilized prior to fully opening the main zone valve, indicating that the manifold and nozzles were not completely filled.

During the starts, several rubs were indicated by the compressor rotor strain gages and were confirmed by the clearanceometers. The rubs were attributed to starting with a "hot" engine, and subsequent starts allowed for at least a 10-minute cool-down before restarting.

During the next staging attempt after Start 8, the manifold pressure was allowed to stabilize (approximately 30 seconds) prior to fully opening the main zone valve, and the switch to double annular was then successful. Next, while accelerating to 11,800 rpm, a facility air valve in the inlet air supply ducting suddenly went full closed, shutting off all air to the vehicle inlet and forcing another emergency shutdown. When the valve closed, T42 spiked at 982° C (1800° F) and the inlet pressure (P25) dropped to about 21 kPa (3 psia).

The problem was traced to a failed coupling between the actuator and the valve stem on facility air valve V126. No apparent damage was done to the vehicle. No rubs were indicated during the deceleration on either the turbine or compressor by the rotor strain gages or clearance probes. The failed facility valve was bypassed in the inlet piping, and testing resumed with Start 9.

The maximum steady-state point recorded was 12,150 rpm (96%), at which time the Stage 2 HP turbine nozzle skin temperature limit was reached. An excursion to 12,810 rpm (100%) was made by locking the compressor stators at their 95% corrected speed value and accelerating until the nozzle temperature limit was reached. Acceleration from 76.5% to 97% and back to 76.5% was made with transient DMS (7003). This concluded E³ Test No. 5, Mechanical Check-out.

The next portion of testing was E³ Test No. 6, the ram mechanical checkout. At flight idle and 76.5% corrected speed, the inlet pressure was increased to 152 kPa (22 psia). An acceleration from 9700 rpm to maximum speed (11,700 rpm) was recorded by transient DMS (7004). Maximum speed was again limited by the Stage 2 turbine nozzle skin temperature. The vehicle was then decelerated to 8700 rpm (68.5%) for a 10-minute cool-down prior to engine shutdown. But, when the change from automatic to manual fuel control was made, it caused a switch from double- to single-annular burning and a combustor blowout occurred, thus ending Run 5. A summary of the DMS points recorded is shown below.

Run No. 5

<u>DMS</u>	<u>Core Speed, rpm</u>	<u>PCN25R, %</u>	<u>P25, kPa (psia)</u>	<u>Combustor Mode</u>	<u>Comments</u>
53	0	0	Transient	---	Zero Reading
	---	30	179 (26)	S/A	Start 5
54	9,630	76.5	Ambient	S/A	
	9,630	76.5	Ambient	D/A	Blowout
	---	30	179 (26)	S/A	Start 6 Aborted

Run No. 5 (Concluded)

DMS	Core Speed, rpm	PCN25R, %	P25, kPa (psia)	Combustor Mode	Comments
	---	30	179 (26)	S/A	Start 7
	9,630	76.5	Ambient	D/A	Blowout
	---	30	179 (26)	S/A	Start 8
55	9,620	76.5	Ambient	D/A	
	11,800	---	Ambient	D/A	Facility Valve Failure
	---	30	179 (26)	S/A	Start 9
56	11,750	93.6	Ambient	D/A	
57	11,750	93.4	Ambient	D/A	
7001	Bad Rdg	---	Ambient	D/A	
7002	Transient	---	Ambient	D/A	Accel 93.4% to 96%
58	12,100	96.0	Ambient	D/A	
59	12,100	96.0	Ambient	D/A	
60	12,340	97.3	Ambient	D/A	Aborted, Stator Stress
61	12,810	100	Ambient	D/A	Locked Stators
7002	Transient	---	Ambient	D/A	76.5% to 97% to 76.5%
62	12,303	97.0	Ambient	D/A	Aborted, Tempera- ture Limit
63	12,150	96.0	Ambient	D/A	
64	9,700	76.5	152 (22)	D/A	
7004	Transient	---	152 (22)	D/A	9,700 to 11,700 to 9,700 rpm
	8,500	68.5	152 (22)	D/A	Blowout

Compressor rotor strain gage signals were unreadable at several speed points during test. The problem occurred during accelerations, with the signals clearing during subsequent decelerations. This was attributed to an intermittent slipping problem.

Posttest borescope inspections revealed the following:

- Several Stage 5 blades showed some indications of rubbing.
- No rub indications were seen on any of the other blades, although the Stage 10 rub lands appeared to be very lightly rubbed.
- Stage 1 turbine blade tips showed some heat discoloration and scale (oxide) buildup on the suction side of the tip. No rubs were noted, although the tip-notched blades [0.076 cm (30 mils) notches] could not be found.

- Stage 2 turbine blades looked alright except, once again, the notched blades could not be located.
- The top-half of the Stage 1 HP turbine shroud segments showed no rubs; the bottom-half was not inspected.
- No other abnormalities were found.

The four Stage 7 start bleed valves were removed and the blank-off pads installed. All laser probes were removed for check out. The spare Stage 2 probes were cannibalized to fabricate two Stage 1 probes. A complete set of Stage 1 and 2 turbine laser probes was reinstalled. The Stage 10 touch probe was repaired, and the Stage 5 customer bleed circuit reconnected. The facility and engine checklists were completed, and the engine was prepared for Run No. 6.

E³ Core Test No. 7: Sea Level Static Performance Optimization
 Run No. 6
 Date: 16 August 1982
 Run Time: 3 hours 55 minutes
 Total Engine Run Time: 13 hours 19 minutes
 DMS Readings: 65 through 75
 Transient 7005

Test Conditions

P25 - Ambient
 T25 - Ambient
 A8 - Nominal [1052 cm² (163 in²)]
 Venturi - 30.48 cm (12 in.)
 Rotor Thrust Balance - 241 kPa (35 psia)
 Rotor Bore Cooling - 0.25 kg/s (0.55 lbm/s)
 Instrumentation - All turbine laser probes installed

Testing resumed with a normal windmilling start (Start 10). At idle, the turbine laser probe cooling cart water pressure indicated the pressure was low. This forced a shutdown in order to identify and correct the problem. The water system was back purged and testing was resumed with Start 11.

The engine was accelerated to flight idle (76.5% speed) and transitioned to double-annular burning without incident. The compressor and turbine ACC valves were exercised at 76.5% to their full-open (minimum clearance) positions. The vehicle was accelerated to 96% speed where the compressor ACC

valve was again fully opened. While preparing to modulate the turbine ACC valve at the same speed, a low-fuel-supply pressure alarm was encountered, and the vehicle was returned to idle and shut down. The alarm was determined to be the result of a faulty transducer signal, since redundant instrumentation indicated no loss of supply pressure. During the run, several other faults in the facility panel pressure readouts were experienced, and it was decided to terminate the night's running to resolve these problems.

Eleven data points were recorded during this run and are listed below. The compressor and turbine clearanceometers functioned without problems, although the turbine clearance was indicated to be 0.076-0.101 cm (0.030-0.040 inch) larger than during Run No. 4.

Run No. 6

DMS	Core Speed, rpm	PCN25R, percent	P25, kPa (psia)	Combustor Mode	Compressor ACC	Turbine ACC	Stage 5 Bleed	Comments
65	0	0	Ambient	-	Off	Off	Off	Zero Reading
66	3,660	30	179 (26)	-	Off	Off	Off	Windmill
67	3,670	30	179 (26)		Off	Off	Off	Windmill
	3,670	30	179 (26)	S/A	Off	Off	Off	Start 10
68	8,750	70	Ambient	S/A	Off	Off	Off	
	---	---	Ambient	S/A	Off	Off	Off	Shutdown, Low Cart Water Pressure
	3,650	30	179 (26)	S/A	Off	Off	Off	Start 11
69	9,570	77	Ambient	D/A	Off	Off	Off	
70	9,570	77	Ambient	D/A	On	Off	Off	
71	9,570	77	Ambient	D/A	Off	30°	Off	
72	9,570	77	Ambient	D/A	Off	Full On	Off	
73	9,570	77	Ambient	D/A	Off	Off	Off	
74	11,960	95.8	Ambient	D/A	Off	Off	Off	
7005	11,970	95.5	Ambient	D/A	On	Off	Off	ACC Transient
75	11,970	95.4	Ambient	D/A	On	Off	Off	Shutdown, Low Fuel Inlet Pressure

The facility pressure transducers were checked out and corrected as required. The slave oil scavenge filter was removed and the engine scavenge filter reinstalled. The Stage 2 6 o'clock laser probe was removed and blade tip clearance measured through the hole. The tip clearance measured 0.251 cm

(0.099 inch) whereas during assembly, the cold buildup tip clearance was 0.165 cm (0.065 inch), an increase of 0.086 cm (0.034 inch). This indicated that a rub had occurred sometime between Run No. 3 and the end of Run No. 6, confirming the laser probe data. The 6 o'clock probe was reinstalled, and the engine was prepared for Run No. 7.

E³ Core Test No. 7: Sea Level Static Performance Optimization
No. 7A: ACC Evaluation
No. 7B: Stator Optimization
No. 7D: Optimized Performance

Run No. 7

Date: 17 August 1982

Run Time: 9 hours 04 minutes

Total Engine Run Time: 22 hours 23 minutes

DMS Readings: 77 through 115

Transient 7006

Test Conditions

P25 - Ambient

T25 - Ambient

A8 - Nominal [1052 cm² (163 in²)]

Venturi - 30.48 cm (12 inch)

Rotor Thrust Balance - 241 kPa (35 psia)

Rotor Bore Cooling - 0.25 kg/s (0.55 lbm/s)

Instrumentation - All turbine laser probes installed

Testing began with a normal windmilling start (No. 12). Several steady-state data points were recorded during this 9-hour run. The compressor and turbine ACC evaluations (Test 7A) were performed at 96.2%, 97.7%, and 98.9% corrected speeds (DMS Readings 77 through 91). The maximum speed obtained was limited by a Stage 2 turbine nozzle limit of 1068° C (1950° F).

The compressor variable stator vane schedule optimization (Test 7B) was performed. Next, up to this point, the baseline stator schedule had been used. Stator optimization was performed at 96% corrected speed by varying the IGV Stage 1 and 3 vane angles from the nominal schedule. The vehicle was then accelerated to the maximum allowable speed (98.2%, as again limited by nozzle temperatures) where another steady-state DMS reading was taken. From these data (DMS Readings 92 through 98), an optimized stator schedule was defined and used during the remainder of the test program. All of the stator optimization work was performed with the compressor and turbine ACC valves fully opened.

Using the optimized stator schedule, the optimized sea level static performance map (Test 7C) was completed at 97.5%, 92.5%, 90%, 85%, 80%, and 76.5% corrected speeds (DMS Readings 99 through 105). At 68.5%, 76.4%, and 89.7% corrected speeds the effects of a locked Stage 5 stator (Test 7C) were investigated (DMS Readings 106 through 115). While attempting to accelerate above 90% speed, a fault in the laser cooling cart recurred which prevented further high-speed testing. Once again, the problem was attributed to a faulty check valve that would not allow a switchover from slave to CDP air. This time no damage occurred to the probes, and a normal shutdown was made. A total of 37 data points were recorded during this run, a summary of which is provided below.

Run No. 7

DMS	Core Speed, rpm	PCN25R, %	P25, kPa (psia)	Combustor Mode	Compressor ACC	Turbine ACC	Comments
77	0	0	Ambient	---	Off	Off	Zero Reading
78	3,660	30	179 (26.0)	---	Off	Off	Windmill
	3,660	30	179 (26.0)	S/A	Off	Off	Start 12
79	8,700	70	Ambient	S/A	Off	Off	
80	9,660	77.6	Ambient	D/A	Off	Off	
81	12,040	95.7	Ambient	D/A	Off	Off	
82	12,040	96.2	Ambient	D/A	On	Off	
83	12,040	96.2	Ambient	D/A	Off	30°	
84	12,040	96.2	Ambient	D/A	Off	Full On	
7006	12,040	96.2	Ambient	D/A	Off	Transient	Closing HPT ACC
85	12,040	96.2	Ambient	D/A	Off	Off	
86	12,210	97.7	Ambient	D/A	Off	Off	
87	12,210	97.7	Ambient	D/A	On	Off	
88	12,210	97.7	Ambient	D/A	On	Full On	
89	12,340	98.7	Ambient	D/A	On	Full On	
90	12,380	98.9	Ambient	D/A	On	Full On	
91	12,210	97.6	Ambient	D/A	On	Full On	
<u>Stator Offset</u>							
92	12,010	96.0	Ambient	D/A	On	Full On	IGV -3°, Stage 1 +2°
93	12,280	98.2	Ambient	D/A	On	Full On	IGV -3°, Stage 1 +2°
94	12,020	96.0	Ambient	D/A	On	Full On	IGV -3°, Stage 1 +2°, -3°
95	12,270	98.2	Ambient	D/A	On	Full On	IGV -3°, Stage 1 +2°, -3°
96	12,020	96.0	Ambient	D/A	On	Full On	IGV -3°, Stage 1 +4°
97	12,303	98.2	Ambient	D/A	On	Full On	IGV -3°, Stage 1 +4°
98	12,020	96.0	Ambient	D/A	Off	Off	Baseline
99	12,170	97.5	Ambient	D/A	On	Off	Optimized
100	11,550	92.5	Ambient	D/A	On	Off	Optimized
101	11,230	90.0	Ambient	D/A	On	Off	Optimized
102	10,610	85.0	Ambient	D/A	70%	Off	Optimized
103	10,600	85.0	Ambient	D/A	70%	Off	Optimized, Stage 5 at 3°
104	9,990	80.0	Ambient	D/A	Off	Off	Optimized
105	9,510	76.5	Ambient	D/A	Off	Off	Baseline

Run No. 7 (Concluded)

DMS	Core Speed, rpm	PCN25R, %	P25, kPa (psia)	Combustor Mode	Compressor ACC	Turbine ACC	Comments
					ACC	Stage 5 Bleed	
106	9,510	76.5	Ambient	D/A	Off	Off	Baseline, Stage 5 at +3°
107	9,510	76.5	Ambient	D/A	Off	Off	Baseline, Stage 5 at 0°
108	11,180	89.7	Ambient	D/A	On	Off	Baseline, Stage 5 at +3°
109	9,540	76.5	Ambient	D/A	Off	Off	Baseline
110	9,540	76.5	Ambient	D/A	Off	9.0%	Baseline
111	8,530	68.5	Ambient	D/A	Off	Off	Baseline
112	8,530	68.5	Ambient	D/A	Off	Off	Baseline, Stage 5 at +9°
113	8,530	68.5	Ambient	D/A	Off	Off	Baseline, Stage 5 at +3°
114	8,530	68.5	Ambient	D/A	Off	Off	Baseline, Stage 5 at 0°
115	0	0	Ambient	---	Off	Off	Zero Reading

Other than the laser cooling cart, no other problem arose during the test. The intermittent noise problem on the compressor strain gages was traced to a faulty ground and was corrected. The clearanceometers continued to function well during the test. A Stage 1 turbine blade rub was predicted and realized at 12,280 rpm. This rub eliminated most of the doubts regarding the accuracy of the optical clearance system, which continued to show a substantially more open clearance on both stages of the turbine.

The Stage 1 laser probes were removed and the turbine borescoped. Static Stage 1 blade clearances were measured and found to be approximately 0.163 cm (0.064 inch), compared to a cold buildup measured clearance of 0.119 cm (0.047 inch), an increase of 0.044 cm (0.017 inch). Once more, the notched blades could not be located. Blank-offs for the four Stage 1 probes were installed, and the vehicle was prepared for Run No. 8.

E³ Core Test No. 7: Sea Level Static Performance Optimization
 No. 7C: Locked Stage 5 Stator
 No. 7E: Customer Bleed and RNI Effects

Run No. 8

Date: 18 August 1982

Run Time: 4 hours 46 minutes

Total Engine Run Time: 27 hours 09 minutes

DMS Readings: 116 through 142

Test Conditions

P25 - Ambient for performance testing
 - Ram for Reynolds number effects
 T25 - Ambient
 A8 - Nominal [1052 cm² (163 in²)]
 Venturi - 30.48 cm (12 inch)
 Rotor Thrust Balance - 241 kPa (35 psia)
 Rotor Bore Cooling - 0.25 kg/s (0.55 lbm/s)
 Instrumentation - All Stage 2 laser probes installed
 Stage 1 probes removed

A windmilling start (No. 13) was made from 25% corrected speed with a starting fuel flow of 181 kg/h (400 pph) without incident. Data were taken at 76.5%, 97.5%, and 96% corrected speeds with 0%, 4.5%, and 9.0% Stage 5 customer bleed. The compressor ACC was also exercised at 40% and 100% flow for the two high-speed points. The locked Stage 5 stator test for 97.5% speed was completed. In all instances the optimized stator schedule was used.

At 96.0% speed, inlet pressure was increased from ambient to 124 and 145 kPa (18 and 21 psia) to determine the Reynolds number effect. No problems were encountered during this run, and a normal shutdown was made. This run completed E³ Test No. 7. The DMS readings are listed below.

Run No. 8

DMS	Core Speed, rpm	PCN25R, %	P25, kPa (psia)	Combustor Mode	Compressor ACC	Turbine ACC	Stage 5 Bleed	Comments
116	0	0	Ambient	---	Off	Off	Off	Zero Reading
117	3,070	25	157 (22.8)		Off	Off	Off	Windmill
	3,070	25	157 (22.8)	S/A	Off	Off	Off	Start 13
118	8,650	70	Ambient	S/A	Off	Off	Off	
119	9,490	76.5	Ambient	S/A	Off	Off	Off	Stage 5 at 8.5°
120	9,490	76.5	Ambient	D/A	Off	Off	4.5%	Stage 5 at 8.5°
121	9,490	76.5	Ambient	D/A	Off	Off	9.0%	Stage 5 at 8.5°
122	12,110	97.5	Ambient	D/A	Off	Off	Off	Stage 5 at 8.5°
123	12,110	97.1	Ambient	D/A	Off	Off	Off	Stage 5 at 1.6°
124	12,180	97.5	Ambient	D/A	40%	Off	Off	Stage 5 at 1.6°
125	12,180	97.5	Ambient	D/A	Full On	Off	Off	Stage 5 at 1.6°
126	12,180	97.5	Ambient	D/A	Full On	Off	Off	Stage 5 at +3°
127	12,180	97.5	Ambient	D/A	Full On	Off	Off	Stage 5 at +9°
128	12,180	97.5	Ambient	D/A	Full On	Off	9.0%	Stage 5 at +1.6°
129	12,180	97.5	Ambient	D/A	Full On	Off	4.5%	Stage 5 at +1.6°
130	12,180	97.5	Ambient	D/A	Full On	Off	4.5%	Stage 5 at +1.6°
131	12,180	97.5	Ambient	D/A	Full On	Full On	4.5%	Stage 5 at +1.6°
132	12,020	96.0	Ambient	D/A	Full On	Off	Off	Stage 5 at -0.8°
133	12,020	96.0	Ambient	D/A	Full On	Off	4.5%	Stage 5 at -0.8°
134	12,020	96.0	Ambient	D/A	Full On	Off	9.0%	Stage 5 at -0.8°

Run No. 8 (Concluded)

DMS	Core Speed, rpm	PCN25R, %	P25, kPa (psia)	Combustor Mode	Compressor ACC	Turbine ACC	Stage 5 Bleed	Comments
135	12,020	96.0	Ambient	D/A	40%	Off	Off	Stage 5 at -0.8°
136	12,020	96.0	Ambient	D/A	Off	Off	Off	Stage 5 at -0.8°
137	12,020	96.0	124 (18.0)	D/A	Off	Off	Off	Stage 5 at -0.8°
138	12,020	96.0	145 (21.0)	D/A	Off	Off	Off	Stage 5 at -0.8°
139	11,770	94.0	145 (21.0)	D/A	Off	Off	Off	Optimized Schedule
140	11,270	90.0	145 (21.0)	D/A	Off	Off	Off	Optimized Schedule
141	8,620	68.5	Ambient	D/A	Off	Off	Off	Optimized Schedule
142	0	0	Ambient	D/A	Off	Off	Off	Zero Reading

After the run, the remaining Stage 2 laser probes were removed and blanked off. The vehicle was borescoped with no problems noted. The 30.48 cm (12 inch) venturi was removed, and the 15.24 cm (6 inch) venturi was installed in the inlet piping. Facility and vehicle checklists were completed and the vehicle prepared for Run No. 9.

E³ Core Test No. 8: Start Optimization
 Run No. 9
 Date: 20 August 1982
 Run Time: 2 hours 40 minutes
 Total Engine Run Time: 29 hours 49 minutes
 DMS Readings: 143 through 184
 Transient 7010-7019

Test Conditions

P25 - Ram for windmill starts
 - Ambient for air starter starts
 T25 - Ambient
 A8 - Nominal [1052 cm² (163 in²)]
 Venturi - 15.24 cm (6 inch)
 Rotor Thrust Balance - 241 kPa (35 psia)
 Rotor Bore Cooling - 0.25 kg/s (0.55 lbm/s)
 Instrumentation - All laser probes removed

The first portion of this test was an evaluation of windmilling characteristics at 5%, 10%, 15%, 20%, 25%, and 30% corrected speeds, with and without Stage 5 customer bleed and a locked stage 5 stator. A summary of the DMS readings is given on the following page.

Run No. 9 - Windmilling Data

DMS	Core Speed, rpm	PCN25R, %	P25 kpa (psia)	HPC/HPT ACC	Stage 5 Bleed	Stage 5 Stator
143	0	0	Ambient	Off	0	Scheduled
144	640	5.0	104 (15.1)	Off	0	Scheduled
145	1370	10.8	112 (16.2)	Off	0	Scheduled
146	1430	11.3	112 (16.2)	Off	Max	Scheduled
147	1360	10.8	112 (16.2)	Off	0	+3°
148	1900	15.0	123 (17.8)	Off	0	Scheduled
149	2520	20.0	138 (20.0)	Off	0	Scheduled
150	2600	20.0	138 (20.0)	Off	Max	Scheduled
151	2540	20.0	138 (20.0)	Off	0	+3°
152	3120	25.0	159 (23.0)	Off	0	Scheduled
153	3740	30.0	183 (26.5)	Off	0	Scheduled
154	3710	30.0	183 (26.5)	Off	Max	Scheduled
155	3700	30.0	183 (26.5)	Off	0	+3°

After windmilling tests were completed, a manual start (No. 14) from 20% windmilling speed was successfully made. Next, two automatic ram starts were made from 20% windmilling speed, with a 20% lean -1 Wf/PS3 unit and a 10% lean accel schedule. After the last start, inlet pressure was reduced to ambient and subidle data were recorded at 60%, 55%, 50%, and 40% corrected speeds, with and without Stage 5 bleed and a locked Stage 5 stator. At 40% speed, a very noticeable combustor "howl" was observed. While trying to set 30% speed, a compressor stall occurred and the engine was shut down. It was later found that the inlet pressure had dropped below ambient, causing the stall. The windmilling starts and subidle data points recorded are listed below.

Run No. 9 - Windmill Starts and Subidle Data

DMS	Core Speed, rpm	PCN25R, %	P25, kPa (psia)	Mode	HPC/HPT ACC	Stage 5 Bleed	Stage 5 Stator	Comments
---	2440	20.0	138 (20)	S/A	Off	0	Sched.	Manual Start 14
156	8670	69.0	138 (20)	S/A	Off	0	Sched.	Manual Start 14
157	7500	60.0	138 (20)	S/A	Off	0	Sched.	Manual Start 14
158	6280	50.0	138 (20)	S/A	Off	0	Sched.	Manual Start 14
159	5010	40.0	138 (20)	S/A	Off	0	Sched.	Manual Start 14
7010	Transient	20.0	138 (20)	S/A	Off	0	Sched.	Automatic Start 15 (20% Lean - 1φ, Time 4:00)
160	8550	76.5	138 (20)	S/A	Off	0	Sched.	
7011	Transient	---	138 (20)	---	Off	0	Sched.	Shutdown
7012	Transient	20.0	138 (20)	S/A	Off	0	Sched.	Auto Start 16 (10% Lean, Time 1:37)

Run No. 9 - Windmill Starts and Subidle Data (Concluded)

DMS	Core Speed, rpm	PCN25R, %	P25, kPa (psia)	Mode	HPC/HPT ACC	Stage 5 Bleed	Stage 5 Stator	Comments
161	8560	68.5	138 (20)	S/A	Off	0	Sched.	
162	8600	69.0	Ambient	S/A	Off	0	Sched.	
163	8540	68.7	Ambient	S/A	Off	0	+3°	
164	8410	67.6	Ambient	S/A	Off	Max	Sched.	
165	7290	60.0	Ambient	S/A	Off	0	Sched.	
166	7220	60.0	Ambient	S/A	Off	0	+3°	
167	6960	55.0	Ambient	S/A	Off	Max	Sched.	
168	6420	51.0	Ambient	S/A	Off	0	Sched.	
169	6290	50.3	Ambient	S/A	Off	0	+3°	
170	5100	41.0	Ambient	S/A	Off	0	Sched.	
171	5060	40.5	Ambient	S/A	Off	0	+3°	
172	2950	30.0	152 (22)	S/A	Off	0	Sched.	Windmill

This completed the windmilling portion of the run. Afterward, the air starter was installed on the accessory gearbox and the starter air line was connected in preparation for ambient inlet starts.

Starter air pressure was slowly increased to initiate engine rotation, then gradually increased to the maximum allowable pressure [379 kPa (55 psia)]. Inlet pressure was maintained at ambient levels and the engine speed stabilized at 4000 rpm (32% corrected speed). A steady-state DMS on point and a transient DMS of the coast down were recorded. A manual start from maximum motoring speed (Start 17) with an inlet pressure of 3.5 kPa (0.5 psia) above ambient was then successfully made.

The next start attempt (No. 18) was made from maximum motoring speed with ambient inlet pressure and a nominal accel fuel schedule. The light-off went well, but after a lengthy acceleration toward idle (in excess of 2 minutes), the air starter oil temperature limit was reached and the starter had to be cut out. The engine, then rotating at about 6400 rpm, could not self-sustain and the start was aborted.

Start 19 was an automatic start from maximum motoring speed with ambient inlet pressure and an accel fuel schedule of nominal +12%. The start went well with a time-to-idle (68.5%) of 1 minute 47 seconds from light-off. One final automatic start (No. 20) was made with an accel fuel schedule of nominal +5 Wf/PS3 unit. (The accel fuel schedule nomenclature is explained in Section 6.5.) The start was without incident and the time to idle was 1 minute. A summary of the ambient inlet starts is given below, along with the DMS readings recorded. Minimum starting fuel flow for all of these starts was 181 kg/h (400 pph).

Run No. 9 - Ambient Inlet Starts With the Air Starter

DMS	Core Speed, rpm	PCN25R, %	P25, kPa (psia)	Start Type	Accel Fuel Schedule	Time to Idle	Comments
173	3430	27.0	Ambient	---	---	---	Dry Motor
7013	Transient	---	Ambient	---	---	---	Coast Down
	4000	32.0	103 (15.0)	---	---	---	Light-Off Condition
7014	Transient	---	103 (15.0)	Manual	Manual	---	Start 17
174	8540	76.5	103 (15.0)	---	---	---	Idle
							Shutdown
	4000	32.0	Ambient	---	---	---	Light-Off Condition
7015	Transient	---	Ambient	Automatic	Nominal	Aborted	Start 18
7016	Transient	---	Ambient	Automatic	Nominal +12%	1:47	Start 19
175	8550	68.5	Ambient	---	---	---	Idle
							Shutdown
	3500	28.0	Ambient	---	---	---	Light-Off Condition
7017	Transient	---	Ambient	Automatic	Nominal +5%	1:00	Start 20
176	8500	68.5	Ambient	---	---	---	Idle
							Shutdown

The final portion of Run No. 9 established dry motoring data to help evaluate starting characteristics. Using the air starter and maintaining an ambient inlet pressure, the vehicle was motored to 10%, 20%, and 33% corrected speeds where steady-state DMS readings were taken with and without a locked Stage 5 stator and 10% customer bleed. Transient DMS recordings of the coast downs from each speed also were taken. A summary of the recorded motoring data points are listed below.

Run No. 9 - Motoring Data With the Air Starter and Ambient Inlet

DMS	Core Speed, rpm	PCN25R, %	P25	Starter Pressure kPa (psia)	Stage 5 Bleed	Stage 5 Stator	Comments
177	1360	9.5	Ambient	124 (18.0)	0	Schedule	
178	1390	9.5	Ambient	124 (18.0)	Max	Schedule	
179	1370	9.5	Ambient	124 (18.0)	0	+3°	
180	2390	20	Ambient	182 (26.4)	0	Schedule	
181	4080	33	Ambient	379 (55.0)	Max	Schedule	
7018	Transient	33	Ambient	0	Max	Schedule	Coast Down
182	4090	33	Ambient	379 (55.0)	0	+3°	
7019	Transient	33	Ambient	0	0	+3°	Coast Down
183	4090	33	Ambient	379 (55.0)	0	+3°	
184	0	-	Ambient	0	0	Schedule	Zero Reading

Posttest inspections revealed nothing abnormal. Plane 4.2 radial pressure rake elements were connected to the emissions sampling manifold. The emissions and smoke sampling and measurement hardware were installed in the

cell and checked out. The air starter was removed and the gearbox pad blanked off. The HP turbine ACC manifold flow-split butterfly valves were moved from their full-open to their full-closed position. The 15.24 cm (6 inch) venturi was removed and the 30.48 cm (12 inch) venturi installed. The facility and vehicle checklists were completed in preparation for Run No. 10.

E³ Core Test No. 9: Emissions
Run No. 10
Date: 23 August 1982
Run Time: 4 hours 31 minutes
Total Engine Run Time: 34 hours 20 minutes
DMS Readings: 185 through 208

Test Conditions

P25 - Ambient to 90% speed
152 kPa (22 psia) above 90% speed
T25 - Ambient
A8 - Nominal [1052 cm² (163 in²)]
Venturi - 30.48 cm (12 inch)
Rotor Thrust Balance - As required
Rotor Bore Cooling - 0.25 kg/s (0.55 lbm/s)
Instrumentation - All laser probes removed

A windmilling automatic start (No. 21) from 25% speed with a nominal -10% accel schedule was made without incident. Emissions data were taken at 76.5%, 83%, 88%, 90%, 94%, and 96% corrected speeds with double-annular burning and at 76.5%, 68.5%, 62%, 58%, and 47% speeds with single-annular burning. And smoke data were recorded at 96.0%, 88%, 68.5%, and 62% speeds.

Emissions data at 62.0%, 68.5%, 76.5%, and 90% were repeated due to residual contamination existing in the sampling pump during the taking of early data points. Smoke data at 96% speed was faulty because of water in the system. No other problems were encountered, and a normal shutdown was made. A summary of the data points recorded is given on the following page. The optimized stator schedule was used during this run with no Stage 5 bleed.

Run No. 10 - Emissions Data

DMS	Core Speed, rpm	PCN25R, %	P25, kPa (psia)	Combustor Mode	HPC/HPT ACC	Emissions	Smoke	Comments
185	0	0	Ambient	---	Off			Zero Reading
186	3,610	29.0	179 (26.0)	---	On	X		Windmill
	3,100	25.0	159 (23.0)	S/A	Off			Start 21 0:40
187	8,550	68.5	Ambient	S/A	Off	X	X	Pump On
188	7,700	61.8	Ambient	S/A	Off	X	X	Pump On
189	9,580	76.5	Ambient	S/A	Off	X		Pump On
190	9,570	76.5	Ambient	D/A	Off	X		Pump On
191	10,320	83.0	Ambient	D/A	Off	X		Pump On
192	10,940	88.0	Ambient	D/A	Off	X	X	Pump On
193	11,220	90.0	Ambient	D/A	Off	X		Pump On
194	11,380	90.0	152 (22.0)	D/A	Off	X		Pump On
195	11,930	94.2	152 (22.0)	D/A	Off	X		Pump Off
196	11,930	94.2	152 (22.0)	D/A	Off	X		Pump On
197	12,130	96.0	151 (21.8)	D/A	Off	X		Bore Cooling = 0.20 kg/s (0.44 pps)
198	12,130	96.0	151 (21.8)	D/A	Off	X	X	= 0.11 kg/s (0.25 pps)
199	12,130	96.0	151 (21.8)	D/A	Off	X	X	= 0.05 kg/s (0.12 pps)
200	11,380	90.0	151 (21.8)	D/A	Off	X		Pump Off
201	9,700	76.5	Ambient	S/A	Off	X		Pump Off
202	9,700	76.5	Ambient	S/A	Off	X		Pump On
203	8,550	68.5	Ambient	S/A	Off	X		Pump On
204	7,760	62.0	Ambient	S/A	Off	X		Pump On
205	7,200	58.0	Ambient	S/A	Off	X		Pump On
206	5,870	47.0	Ambient	S/A	Off	X		Pump On
207	3,670	30.0	179 (26.0)	---	Off	X		Windmill
208	0	0	Ambient	---	Off	X		Zero Reading

Posttest inspections revealed nothing abnormal. No borescope inspections were made so that the setup for the next test could proceed. The emissions equipment was removed and the Plane 4.2 pressure rakes were reconnected. The air starter and starter air supply lines were also reinstalled in preparation for Run No. 11.

E³ Core Test No. 10: Start Optimization
 10A: Max A8 Performance
 10B: Min A8 Performance

Run No. 11
 Date: 24 August 1982
 Run Time: 4 hours 41 minutes
 Total Engine Run Time: 39 hours 1 minute
 DMS Readings: 209 through 232
 Transients 7021-7044

Start Optimization Test Conditions

P25 - Ambient
T25 - Ambient
A8 - Nominal [1052 cm² (163 in²)]
Venturi - 30.48 cm (12 inch)
Rotor Thrust Balance - 241 kPa (35 psia)
Rotor Bore Cooling - 0.25 kg/s (0.55 lbm/s)
Instrumentation - All laser probes removed

Run No. 11 was actually three tests. The first test was to optimize the ambient inlet starting procedure and to evaluate the effects of a locked Stage 5 stator during starts. Eight automatic starts using the air starter were made with ambient inlet condition, 181 kg/h (400 pph) starting fuel flow and various accel fuel schedules, light-off speeds, and Stage 5 stator positions. All starts were successful; it was determined that the Stage 5 stator could be locked at +3° for the remainder of the test program. A summary of the starts is given below. Idle was defined as 62% corrected speed. No bleed air was required.

Run No. 11 - Start Optimization Data

<u>Transient</u> <u>DMS</u>	<u>Light-Off</u> <u>rpm</u>	<u>PCN25R,</u> <u>%</u>	<u>Accel Schedule</u>	<u>Stage 5</u> <u>Stator</u>	<u>Ignition</u> <u>to Idle,</u> <u>seconds</u>	<u>Comments</u>
7021	--		--	--	--	Zero Reading
7030	4200	30	Nominal +20%	Schedule	42	Start 22
7031	3000	25	Nominal +20% + 1φ	Schedule	42	Start 23
7032	3100	25	Nominal +20% + 2φ	Schedule	36	Start 24
7033	7780	62	--	Schedule	--	Coast Down
7034	3000	25	Nominal +20% + 3φ	Schedule	35	Start 25
7035	7790	62	--	Schedule	--	Coast Down
7036	3000	25	Nominal +20% + 4φ	Schedule	31	Start 26
7037	3000	25	Nominal +20% + 5φ	Schedule	31	Start 27
7038	3000	25	Nominal +20% + 5φ	+3°	31	Start 28
7039	7780	62	--	+3°	--	Coast Down
7040	2500	20	Nominal +20% + 5φ	+3°	32	Start 29

As can be seen, an automatic start from 20% speed to 62% was successfully made with the Stage 5 stator locked at +3° using an accel schedule of nominal +20% + 5φ in 32 seconds. Maximum average exhaust temperature (T42) during the start was 560° C (1040° F). This concluded the start optimization test; total run time was 32 minutes. The nominal exhaust nozzle was removed and the engine was prepared for maximum A8 performance testing.

Test No. 10A: Maximum A8 Performance Test Conditions

P25 - Ambient

T25 - Ambient

A8 - Maximum [1219 cm² (189 in²)]

Venturi - 30.48 cm (12 inch)

Rotor Thrust Balance - 379 kPa (55 psia)

Rotor Bore Cooling - 0.25 kg/s (0.55 lbm/s)

Instrumentation - All laser probes removed

Stage 5 stator locked at +3°

Testing with the maximum area nozzle began with Start 30, an automatic start from 25% speed with an accel schedule of nominal +20% + 3φ. Time from ignition to idle was 36 seconds. Steady-state data were taken at 62%, 68.5%, and 76.5% speeds with single-annular burning. While trying to switch to double-annular burning, engine speed dropped dramatically and a blowout occurred. It was reasoned that the fuel flow at idle with the maximum A8 635 kg/h (1400 pph), compared to 862 kg/h (1900 pph) with a nominal A8, was not enough once the fuel split was made to ignite and propagate burning in the main zone. After Start 28, the throttle was advanced until the total fuel flow was close to 862 kg/h (1900 pph), about 81% speed. The switch to double-annular burning was then made smoothly.

Steady-state DMS readings were taken at 76.5%, 85%, 90%, 92.5%, 95%, 97.5%, and 100.4% speeds with the compressor ACC off. Problems with the facility air supply compressors were experienced at high speeds. The engine was decelerated to idle until the troublesome compressor could be brought back online an hour later.

After the steady-state data were taken, a slow 2-minute accel from idle to 100% speed and back to idle was made. The maximum speed obtained was 12,650 rpm (100.4% corrected) and once more was limited by turbine nozzle skin temperatures. No other problems were encountered, and a normal shutdown was made to install the minimum area exhaust nozzle. A summary of maximum nozzle area data points is listed below. Run time with the maximum area nozzle was 2 hours 32 minutes.

Run No. 11 - Maximum A8 Performance

DMS	Core Speed, rpm	PCN25R, %	Combustor Mode	Compressor ACC	HPT ACC/ Stage 5 Bleed	Comments
209	0	0	--	Off	Off	Zero Reading
	3,000	25	S/A	Off	Off	Start Conditions
7041	Transient	--	S/A	Off	Off	Start 30
210	7,780	62.0	S/A	Off	Off	
211	8,560	68.5	S/A	On	Off	
212	9,550	76.5	S/A	On	Off	
			D/A	On	Off	Blowout
	3,000	25.0	S/A	Off	Off	Start 31
213	9,620	76.5	D/A	On	Off	
214	10,620	85.0	D/A	On	Off	
215	11,270	90.0	D/A	On	Off	
216	11,610	92.5	D/A	On	Off	
217	11,930	95.0	D/A	On	Off	
218	11,930	95.0	D/A	Off	Off	
219	12,260	97.5	D/A	On	Off	
220	12,650	100.4	D/A	Off	Off	
221	12,650	100.4	D/A	On	Off	
222	12,480	99.0	D/A	On	Off	
7042	Transient		D/A	Off	Off	2-Minute Decel to Idle

Test No. 10B: Minimum A8 Performance Test Conditions

P25 - Ambient
 T25 - Ambient
 A8 - Minimum [946 cm² (146.7 in²)]
 Venturi - 30.48 cm (12 inch)
 Rotor Thrust Balance - 207 kPa (30 psia)
 Rotor Bore Cooling - 0.25 kg/s (0.55 lbm/s)
 Instrumentation - All laser probes removed

The minimum area nozzle was installed and testing resumed with Start 32. Steady-state data were taken at 62%, 68.5%, 76.5%, 85%, 89%, 92.5%, and 94% corrected speeds. Maximum speed was again limited by turbine nozzle skin temperatures. No problems were encountered during this run of 1 hour 27 minutes. A 2-minute deceleration from maximum to idle speed was made. The data points recorded are listed below. The Stage 5 stator remained locked at +3°.

Run No. 11 - Minimum A8 Performance Data

DMS	Core Speed, rpm	PCN25R, %	Combustor Mode	Compressor ACC	HPT ACC/ Stage 5 Bleed	Comments
	3,000	25.0	S/A	Off	Off	Start 32
223	7,780	62.0	S/A	Off	Off	
224	8,560	68.5	S/A	On	Off	
225	9,550	76.5	S/A	On	Off	
226	9,560	76.5	D/A	On	Off	
227	11,810	94.0	D/A	On	Off	
228	11,600	92.5	D/A	On	Off	
229	11,600	92.5	D/A	Off	Off	
230	11,050	88.0	D/A	On	Off	
231	10,700	85.0	D/A	On	Off	
7043	Transient	85.0	D/A	Off	Off	2-Minute Decel
7044	Transient	94.0	D/A	Off	Off	2-Minute Decel

This completed Run No. 11. Posttest inspections revealed nothing abnormal. The laser probe blank-offs and the 2 o'clock and 10 o'clock Plane 4.2 radial rakes were removed to provide a better access to borescope the turbine. The normal method for rotating the engine for borescope inspections was to turn the gears in the accessory gearbox through an access pad on the housing using a spline adapter tool. After previous tests, the engine would rotate in this manner with very little effort. Following this run, it was found that the rotor would turn 1° to 2° in either direction and then lock. In a few minutes it could be rotated another 1° to 2° before it would lock again. Assuming some kind of hydraulic lock, the fuel line at the pump discharge was disconnected, but with no affect. Next, the line going to the fuel/oil cooler was disconnected. Although this should have had no effect, the rotor could suddenly be turned with as little effort as after previous tests. Neither of the fuel lines appeared to have a great amount of pressure or fuel in them.

Borescope inspections of the compressor, combustor, turbine, and rear frame struts were completed. The inlet sintered-metal filter was removed, cleaned, and reinstalled. All eight laser clearance probes were installed, and the Stage 5 customer bleed manifold was capped off. The nominal area exhaust nozzle was trimmed to give a 4% larger area and then installed in place of the minimum area nozzle. The air starter was removed and the pad

capped. The facility and engine checklists were conducted in preparation for the final performance run.

E³ Core Test No. 11: Final Performance Calibration
Run No. 12
Date: 26 August 1982
Run Time: 5 hours 26 minutes
Total Engine Run Time: 44 hours 27 minutes
DMS Readings: 233 through 259 test data
260 through 276 posttest data
Transients 7045-7050

Test Conditions

P25 - Ambient
T25 - Ambient
A8 - Optimized [target 1093 cm² (169.4 in²)]
Venturi - 30.48 cm (12 inch)
Rotor Thrust Balance - 241 kPa (35 psia)
Rotor Bore Cooling - 0.25 kg/s (0.55 lbm/s)
Instrumentation - All laser probes removed

The first part of this run was used to evaluate windmilling starts. Start 33 was made from a 20% windmilling speed, a minimum fuel flow of 181 kg/h (400 pph), and a nominal accel schedule. The start was sluggish and slow. Start 34 was made from 20% windmilling speed, a minimum fuel flow of 204 kg/h (450 pph), and a nominal accel schedule; this start was much faster. For both starts, the Stage 5 stator was mistakenly locked at +17°.

Performance testing resumed with Start 35. At 62.5% speed the stators were offset to simulate a possible Flight Propulsion System (FPS) condition when speed started to fall off. Speed continued to drop, and the engine was shut down. It was discovered that in the table for stator offsets, several of the Stage 2 and 4 angles were mistakenly interchanged. This resulted in Stage 4 being closed 4° from the optimized schedule, rather than opening 3° as intended, and resulted in the the speed dropoff.

Testing resumed with Start 36. Data were taken at several speed points up to 85% corrected speed. At that point, it was discovered that (1) compressor efficiency was three points lower than in previous tests, and (2) the problem was occurring in Stage 5. Panel readout verified that the Stage 5

stator was locked electronically at $+3^{\circ}$. The engine was shut down to investigate, and it was discovered that although the stator readout indicated $+3^{\circ}$, the Stage 5 stator was actually against its closed stop of $+17^{\circ}$. The problem was traced to a misrigged Stage 5 stator and was corrected. DMS Readings 235 to 244 were in error due to this problem.

Testing resumed with Start 37; a 15% speed windmilling start with a nominal accel schedule and a starting fuel flow of 204 kg/h (450 pph). Data were taken at 68.5%, 76.5%, 85%, 90%, 92.5%, 95%, 97.5%, and 98.3% corrected speed with and without compressor and turbine ACC. The turbine ACC supply air was boosted from the normal 24 kPag (3.5 psig) requirement to 40 kPag (5.8 psig) to increase its effectiveness.

Rotor thrust balance pressure at speeds below 90% was reduced to 172 kPa (25 psia) in an attempt to reduce seal leakages affecting the turbine rotor heat transfer.

At 95% speed, an 8° C (15° F) drop in the FADEC sensor showed only a slight decrease. Stators began to close because the corrected speed calculation was off. The slave stator control was switched from automatic to manual T25 input to bring the stators back on schedule. DMS data revealed that only a small number of the Plane 25 temperatures were reading questionable values. The problem had occurred shortly after bringing another facility inlet air compressor online and was attributed to water in that system affecting certain inlet thermocouples. The stator control remained on manual T25 input for the remainder of the run.

An acceleration from idle to 95.5% speed was made with transient DMS Reading 7048 continuing to record heat transfer data 10 minutes after the acceleration was completed. A similar deceleration (transient DMS Reading 7049) was made from 95.5% to idle. This concluded Run No. 12 and the planned E³ Core Test Program. A normal shutdown was made. Steady-state DMS Readings 260 to 276 continued to be taken at designated time intervals to record soak-back data. A summary of the DMS readings recorded is as follows:

Run No. 12 - Final Performance Calibration

(Stage 5 Stator Locked at +17°)

DMS	Core Speed, rpm	PCN25R, %	P25 kPa (psia)	Combustor Mode	Compressor ACC	Turbine ACC	Stator Schedule	Comments
(Stage 5 = +17°)								
233	0	0	Ambient	—	Off	Off	Optimized	Zero Reading
234	2,950	23	152 (22)	—	Off	Off	Optimized	Windmill
	2,500	20	138 (20)	S/A	Off	Off	Optimized	Start Conditions
7045	Transient	—	138 (20)	S/A	Off	Off	Optimized	Start 33
	2,500	20	138 (20)	S/A	Off	Off	Optimized	Start Conditions
7046	Transient	—	138 (20)	S/A	Off	Off	Optimized	Start 34
	3,120	25	159 (23)	S/A	Off	Off	Optimized	Start 35
235	7,760	62.7	Ambient	S/A	Off	Off	Optimized	
	3,100	25	159 (23)	S/A	Off	Off	Optimized	Start 36
236	7,730	62	Ambient	S/A	Off	Off	FPS	
237	8,530	68.5	Ambient	S/A	Off	Off	Optimized	
238	9,550	76.5	Ambient	S/A	Off	Off	Optimized	
239	9,540	76.5	Ambient	D/A	On	Off	Optimized	
240	9,530	76.5	Ambient	D/A	On	On	Optimized	Turbine ACC = 24 kPag (3.5 psig)
241	9,540	76.5	Ambient	D/A	On	On	Optimized	Turbine ACC = 36 kPag (5.2 psig)
242	10,600	85.1	Ambient	D/A	On	Off	Optimized	
243	10,600	85.1	Ambient	D/A	On	40°	Optimized	Turbine ACC = 24 kPag (3.5 psig)
244	10,600	85.1	Ambient	D/A	On	On	Optimized	Turbine ACC = 37 kPag (5.4 psig)

The Stage 5 stator schedule was recalibrated during the shutdown. The remainder of the test data taken is summarized below.

Run No. 12 - Final Performance Calibration

(Stage 5 Stator Locked at +3°)

DMS	Core Speed, rpm	PCN25R, %	P25 kPa (psia)	Combustor Mode	Compressor ACC	Turbine ACC	Stator Schedule	Comments
	1,860	15	119 (17.2)	S/A	Off	Off	Optimized	Start Conditions
7047	Transient	—	119 (17.2)	S/A	Off	Off	Optimized	Start 37
245	8,520	68.5	Ambient	S/A	Off	Off	Optimized	
246	9,480	76.5	Ambient	D/A	On	On	Optimized	Turbine ACC = 39 kPag (5.6 psig)
247	10,520	85.0	Ambient	D/A	On	On	Optimized	Turbine ACC = 39 kPag (5.6 psig)
248	11,120	90.0	Ambient	D/A	On	Off	Optimized	
249	11,120	90.0	Ambient	D/A	On	Off	Optimized	
250	11,120	90.0	Ambient	D/A	On	On	Optimized	Turbine ACC = 39 kPag (5.6 psig)
251	11,580	92.5	Ambient	D/A	On	Off	Optimized	
252	11,580	92.5	Ambient	D/A	On	On	Optimized	Turbine ACC = 39 kPag (5.6 psig)
253	9,480	76.5	Ambient	D/A	Off	Off	Optimized	T25 Problem
7048	Transient	—	Ambient	D/A	Off	Off	Optimized	76.5 to 95%
254	11,980	95.5	Ambient	D/A	On	Off	Optimized	
255	11,990	95.5	Ambient	D/A	On	On	Optimized	Turbine ACC = 39 kPag (5.6 psig)
256	12,230	97.5	Ambient	D/A	On	Off	Optimized	
257	12,240	97.5	Ambient	D/A	On	On	Optimized	Turbine ACC = 39 kPag (5.6 psig)
258	12,350	98.3	Ambient	D/A	On	On	Optimized	Turbine ACC = 39 kPag (5.6 psig)
7049	Transient	—	Ambient	D/A	Off	Off	Optimized	96-76.5%
259	9,600	76.5	Ambient	D/A	Off	Off	Optimized	
7050	Transient	—	Ambient	D/A	Off	Off	Optimized	Shutdown

Time of shutdown was 03:27 on 27 August 1982. Steady-state DMS Readings 260 to 276 continued to be taken at predetermined time intervals after shutdown. This concluded Run No. 12 and the test.

After the test, the laser probes and borescope plugs were removed for borescope inspection of the rotor and combustor. While trying to rotate the engine, the same problem experienced after the last run (locked rotor) occurred

again. This time, breaking loose the two fuel lines had no effect. In an effort to break the rotor free, balance piston air was turned on to drive the rotor forward. After approximately 124 kPa (18 psia) was supplied to the balance cavity the engine could be freely rotated. The pressure was increased to 172 kPa (25 psia) and the rotor locked. The pressure was decreased to 124 kPa (18 psia), and the rotor was free again. Once more the balance piston pressure was increased, but this time the rotor remained free to turn. The pressure was then gradually decreased, and below 124 kPa (18 psia) the rotor again locked up. The balance piston air was turned off as the possible causes were explored. Thirty minutes later the rotor was free to turn without any balance piston air and remained free thereafter.

Posttest inspections revealed three small pieces of material laying at 6 o'clock directly behind the Stage 2 nozzles. The pieces appeared to be thermal barrier coating from the combustor; no other abnormalities were evident. The oil was drained and measured from the aft and forward sumps, lube pump, accessory gearbox, lube tank, and air/oil separators. This completed all of the core test activities.

6.0 TEST RESULTS

Mechanical and thermodynamic performances were analyzed in detail during and following the core testing. The results of that analysis are presented here. The first section presents overall core thermodynamic performance. This is based on the establishment of component performance levels to achieve a balanced engine cycle which best matches all test measurements. Subsequent sections present the detailed mechanical and thermodynamic performance of each component. Performance of the remaining engine systems are then presented.

6.1 CORE SYSTEM THERMODYNAMIC PERFORMANCE

The objective of the system performance task was to evaluate the performance of the core engine from the compressor inlet through the exhaust nozzle exit plane. Individual component performance was evaluated and compared with the overall core performance while maintaining flow continuity and energy balance. The components evaluated were the high pressure compressor, the combustor, the high pressure (HP) turbine, the exhaust system, and the secondary airflows.

Core engine performance was evaluated during the test using the Data Management System (DMS) Phase I computer program. This program made calculations from direct measurements and compared these with the pretest prediction data stored in the DMS computer. The Phase I calculations helped identify anomalies in the data measurements and provided an assessment of engine condition prior to advancing to the next data measurement point. The Phase I program could not evaluate the indicated component performance relative to the overall performance on a balanced cycle basis. This was accomplished off-line using the Phase II computer program.

The Phase II program was developed from the ICLS (integrated core/low spool) cycle deck which was used in the "core only" mode for core engine data analysis. The Phase II program had iteration capability, permitting performance calculations while maintaining energy balance and flow continuity. The program included subroutines which interacted with the computer databank and

had the capability for data averaging, data editing, and units conversion. The program modified the various components, as modeled in the cycle deck, to match the test data measurements by solving a system of simultaneous equations. Multiple performance calculations were made where redundant data were available, such as HP turbine discharge radial rakes versus arc rakes or facility fuel meter versus engine fuel meters.

This section of the report presents a discussion of the pretest prediction data and the results obtained in Phase II analyses.

6.1.1 Pretest Predictions

Pretest prediction data were generated by using the core engine cycle deck modified to match the engine test configuration. The test configuration modifications included pressure losses for instrumentation, compressor bleed for laser probe cooling, and an exhaust system which included duct and frame losses along with exhaust nozzle coefficients.

The pretest compressor and HP turbine maps were based on rig test data. The compressor efficiency and flow/speed characteristics were based on the 10B rig test. The turbine map was a fit of the rig test data adjusted for a constant blade tip reference clearance of 0.406 mm (0.016 inch).

The cycle deck included logic to adjust the compressor and HP turbine efficiencies as a function of clearance. The compressor adjustment was based on the tenth-stage clearance, whereas the turbine adjustment was based on both first- and second-stage clearances. The clearance models adjusted the cold-build clearance measurements input to the cycle deck and modified them based on rotor speed, gas path pressures, and gas path temperatures.

The secondary or parasitic bleed flows from the fifth stage, seventh stage, and discharge ports of the compressor were set at a constant percentage of compressor airflow. These levels were based on predictions from the flow calibration test data for these circuits (see Section 3.8).

The rake pressure losses used were based on an analytical evaluation of the specific rake designs, except for the turbine discharge radial rakes. The

losses for these rakes were based on measurements made during the low pressure (LP) turbine rig test.

All pretest prediction data were generated by using a standard fuel heating value (FHV) of 427.97×10^5 J/kg (18,400 Btu/lb).

6.1.2 Performance Analysis

The cycle deck performance calculations were based on average pressure and temperature levels at the inlet and exit of each component. Prior to initiating the Phase II analysis, pressure and temperature profiles at the inlet to the compressor (Plane 25) and at the exit of the HP turbine (Plane 42) were evaluated in detail to establish average values. A correlation was established between the indicated average of the rakes and the actual average, including strut and wall effects not detected by the sensors.

The Plane 25 temperatures (T25) used were as indicated by the rake average calculation. The Plane 25 pressure (P25) measurements were adjusted to account for strut and wall pressure losses of the inlet duct. The losses associated with the inlet duct were derived from compressor rig tests and are discussed in Section 6.3.

Evaluation of the HP turbine discharge pressure and temperature was more complex than for the compressor inlet because of the significant variations in radial and circumferential profiles. The data for DMS Readings 246-258 of the final calibration test were evaluated in detail and are discussed in this section.

Two sources of HP turbine discharge pressure (P42) data were available with the multiple radial and arc rake systems installed. The arc rake data was a good indication of the plane average pressure since it included vane wake effects. It also provided a correlation with the rig test data. The radial rake measurements were compared with the arc rake data and will be used to calculate the plane average pressure during the ICLS testing. A detailed comparison of the data from these two rake systems is included in Section 6.7.

Evaluation of the arc rake data indicated the lowest immersion was not reading correctly due to a flow separation problem. A correction factor was

applied to the arc rake average pressure in the off-line computer data bank and is used in the Phase II analysis process.

Two other important pressures used in the Phase II process were the compressor discharge total pressure (P3) and the HP turbine inlet pressure (P4). Plane 3 represents the station between the compressor outlet guide vanes (OGV) and the diffuser inlet. The P3 values were calculated in the Phase I program by two different methods: one for low speed operation and the other for high speed operation. For low speed operation, P3 was calculated from static pressure (PS3) and a flow coefficient determined in compressor rig tests. For high speed operation, P3 was calculated from the measured diffuser exit total pressure, with PS3, and a diffuser loss coefficient determined in compressor rig tests. The P4 values were based on two static pressure measurements in the combustor. This was accurate because of the very low Mach number of the combustor airflow. The difference then between P4 and P3 defines the total pressure drop through the combustor system. The Phase II calculations correlated well with the detailed evaluation provided in Section 6.5.

Cooling airflow measurements from the compressor fifth stage, seventh stage, and compressor discharge ports were reviewed for consistency with the heat transfer assessment of temperatures at the sink locations for these flows. The shapes of the curves for the fifth-stage and seventh-stage flows were not as expected, but these data were used as measured in the final analysis.

Table VIII shows the cycle balance matrix used in the initial Phase II analysis. As previously noted, cycle deck model characteristics are modified to match the measurements shown. The program performs this iterative calculation while matching the input conditions for Plane 25 pressure and temperature, cell barometric pressure, secondary airflows, HP turbine clearances, and core speed.

The facility fuel flowmeter data was chosen for use in the matrix rather than the engine fuel meter data after evaluating the corrections required on both flow measurement systems. The facility fuel readings were taken at pressures and temperatures close to the meter calibration levels. The fuel temperature was within 8.3° C (15° F) of the temperature of the fuel sample taken

for specific gravity evaluation. The temperature correction required for the engine fuel meters was on the order of 83.3° C (150° F), a substantial deviation from the calibration temperature. The engine meters also lacked a pressure correction which could contribute an error of about 0.3 percent. Comparison of the two fuel measurements showed facility measurements were 0.6% higher at high power and 0.3% at low power. Using the facility fuel flow measurement also provided a better match with the HP turbine discharge temperature (T42) at high power where combustion efficiency, and therefore T42, is known with a high level of confidence.

Table VIII. Phase II - Cycle Balance Matrix.

Cycle Deck Modification	Measurements Matched
HP Compressor Flow Versus Speed	Measured Flow
HP Compressor P/P Versus Flow	Phase I Program P3
HP Compressor Efficiency	Measured T3
HP Compressor Efficiency	Measured P42 (Adjusted Arc Rake)
Turbine Map Flow Function	Calculated Flow Function (Phase II)
Combustor Efficiency (0.999 Max)	Measured T42 (Average)
Combustor Fuel-Air Ratio	Measured Fuel Flow (Facility)
Combustor Pressure Loss	Measured P4
Diffuser Pressure Loss	Measured P3.1
Nozzle Flow Coefficient	Calculated Nozzle AE8 (Phase II)
HP Turbine Exit Effective Area	Measured PS42
HP Compressor Inlet Effective Area	Measured PS25
HP Compressor Exit Effective Area	Measured PS3

6.1.3 Analysis Results

Plane 42 Profiles

Table IX shows the compressor corrected airflows and Plane 42 average temperatures and pressures for the final calibration run. It is provided for cross-referencing data presented in this section.

Plane 42 radial and arc rake pressure profiles are presented in Figures 46 and 47 for three selected readings in the final calibration run. Radial profiles are shown for the circumferential ring averages for the radial rakes and the arc rakes. Deviations are shown as a percent of the average pressure of each reading, as noted on the charts.

Examination of the arc rake profile plot shows the problem with the lowest immersion rake: The pressure dropped at the high power points for DMS Readings 250 and 258. This was not consistent with the radial rake profiles. Comparison with the rig arc rake data substantiated a suspected flow separation in the vicinity of this rake.

Figures 48 through 50 show a circumferential plot of the radial rake temperatures for DMS Readings 246, 250, and 258 as a function of relative location to the nearest fuel nozzle. The circumferential location of each rake is identified looking from an aft engine position. Note that the data points for 63B, 197C, and 297D are missing. These were used with the FADEC control system and were not recorded in the DMS data bank. DMS readings for 226A and 226B were missing, but they did not have a significant effect on the ring average calculation.

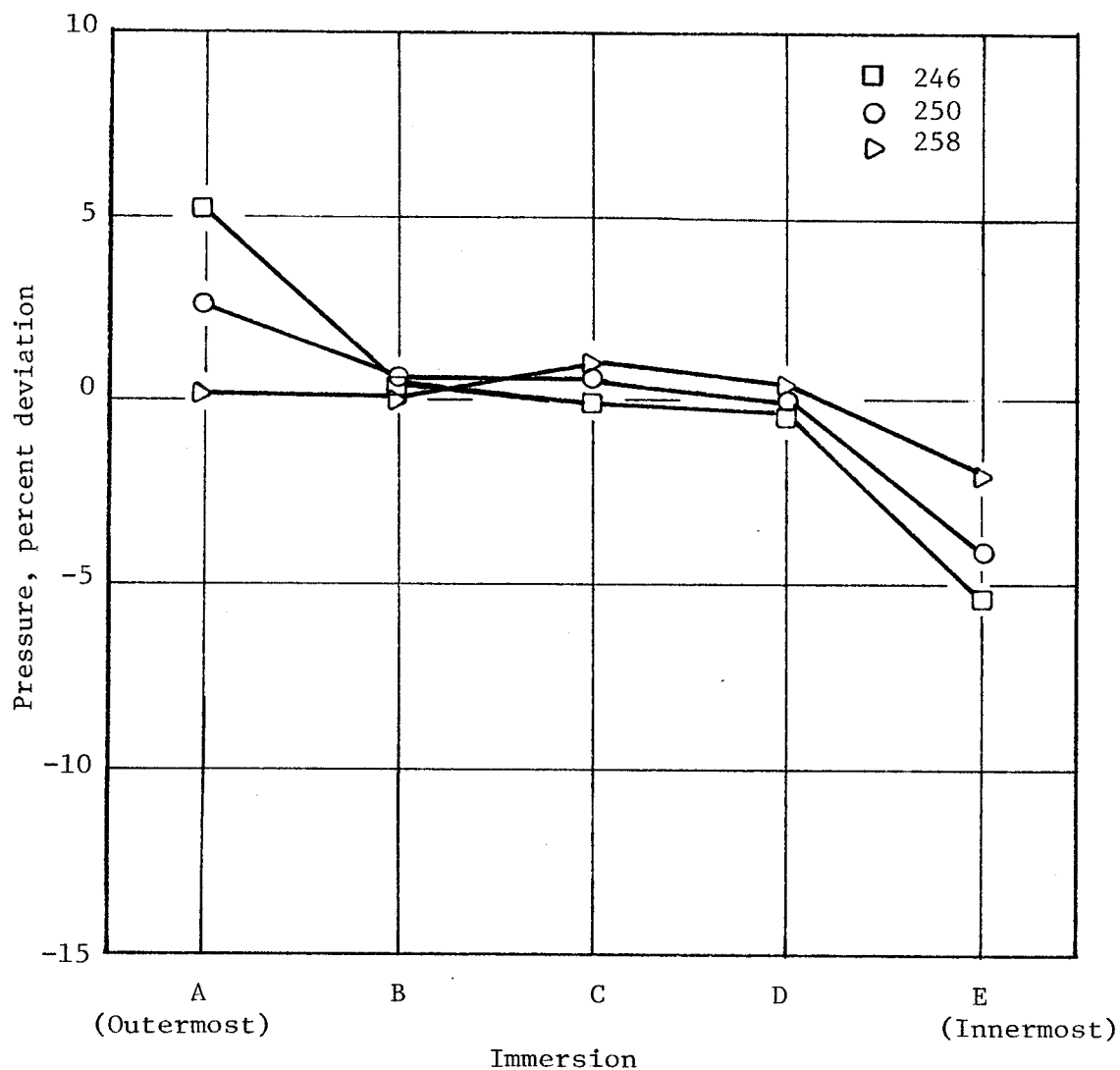
The data plots show the temperature ratio relative to the rake numerical average temperature noted on each figure. A comparison of the ring numerical average and the ring integrated average of the curves was made and found to differ by only a few degrees over the power range shown. Therefore, the average of the ring numerical averages was used in Phase II analyses.

Figure 51 shows a radial profile plot of the ring average temperatures for the final calibration readings. It can be seen that at the high power points (above DMS Reading 252) the temperature decreases toward the walls. This indicates that at high power the average T42 will be less than radial probe calculated average. At low power the profiles are more linear but have a severe

Table IX. Final Calibration Data Points.

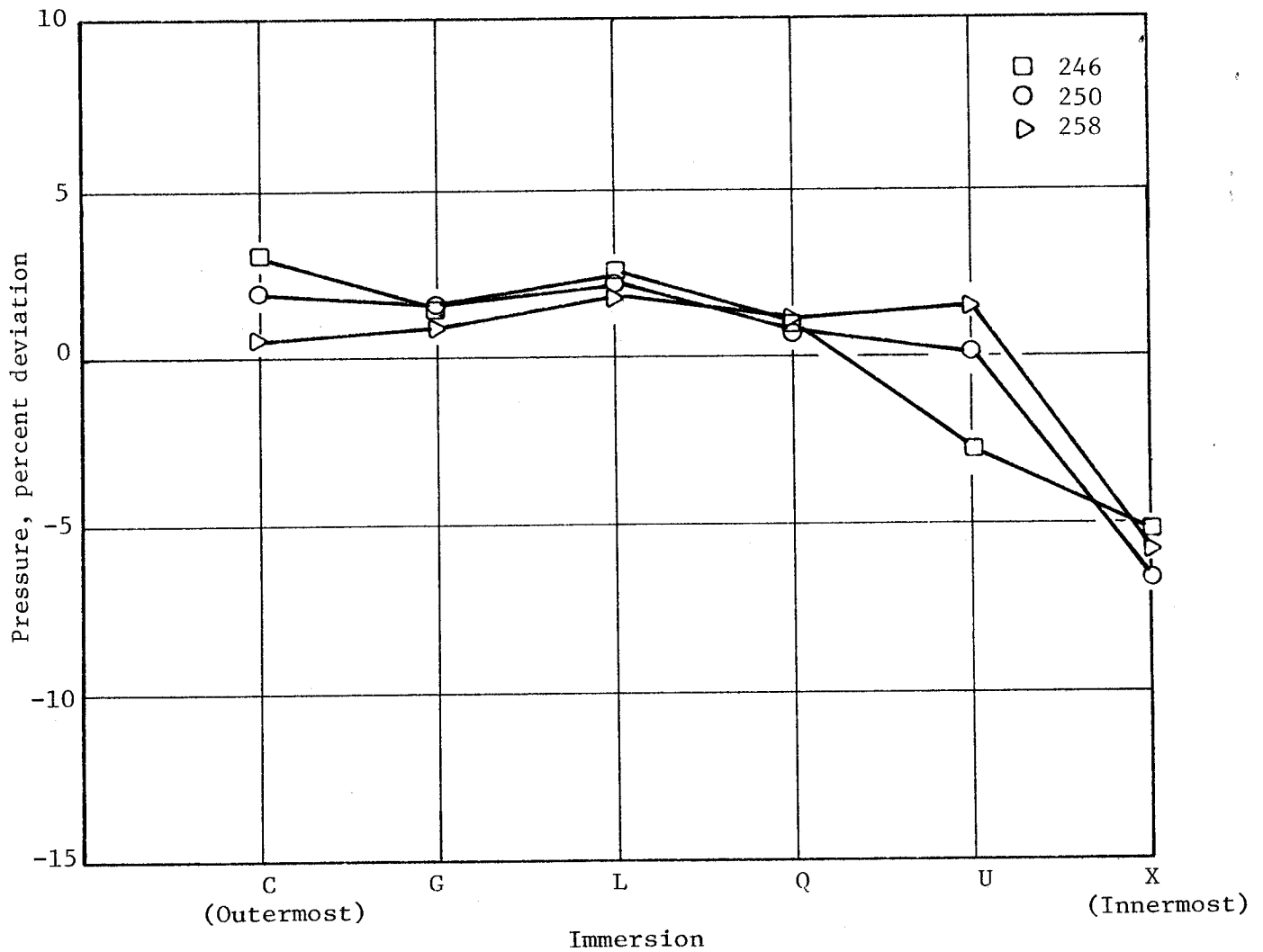
Reading	HPC Corrected Flow kg/s (lbm/s)		HPT ACC (On/Off)	Phase II Calculations				
				Average P42 kN/m ² (psia)		Average T42 K (° R)		P42/P25
246	18.1	(40.0)	On	139.7	(20.26)	675.6	(1216)	
247	25.9	(57.1)	On	183.1	(26.55)	737.8	(1328)	1.81
248	33.1	(73.0)	Off	243.2	(35.27)	850.5	(1531)	2.41
249	32.3	(71.1)	Off	235.3	(34.12)	845.6	(1522)	2.33
250	31.3	(69.1)	On	226.7	(32.88)	825.6	(1486)	2.25
251	38.9	(85.8)	Off	297.2	(43.10)	953.2	(1716)	2.97
252	38.9	(85.8)	On	292.3	(42.39)	930.1	(1674)	2.93
253	17.8	(39.3)*	Off	140.3	(20.36)	709.1	(1276)	1.38
254	47.5	(104.8)	Off	374.8	(54.36)	1076	(1937)	3.84
255	47.9	(105.7)	On	371.8	(53.92)	1054	(1896)	3.81
256	52.4	(115.5)	Off	424.9	(61.63)	1137	(2046)	4.33
257	52.4	(115.5)	On	421.5	(61.14)	1114	(2006)	4.29
258	54.9	(121.0)	On	448.5	(65.05)	1154	(2077)	4.57

*HPC ACC on for All Readings Except 253



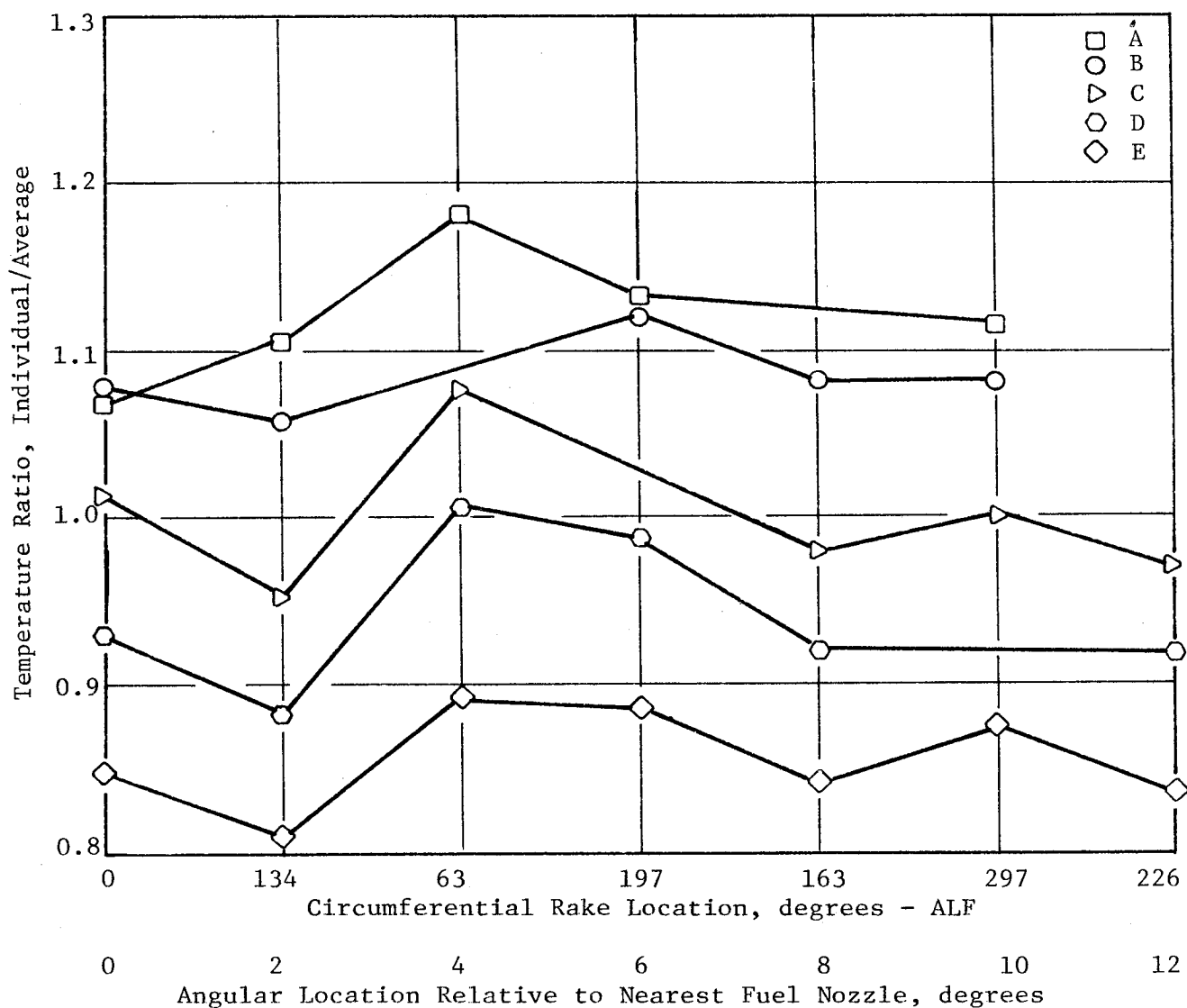
Measured Average P42			
Reading	Arc Rake kN/m ² (psia)		Radial Rake kN/m ² (psia)
246	138.9	(20.14)	141.8 (20.56)
250	225.4	(32.69)	231.2 (33.53)
258	445.8	(64.66)	451.4 (65.47)

Figure 46. Plane 42 Radial Pressure Profile Based on Radial Rakes.



<u>Measured Average P42</u>					
<u>Reading</u>	<u>Arc Rake</u>		<u>Radial Rake</u>		
	<u>kN/m²</u>	<u>(psia)</u>	<u>kN/m²</u>	<u>(psia)</u>	
246	138.9	(20.14)	141.8	(20.56)	
250	225.4	(32.69)	231.2	(33.53)	
258	445.8	(64.66)	451.4	(65.47)	

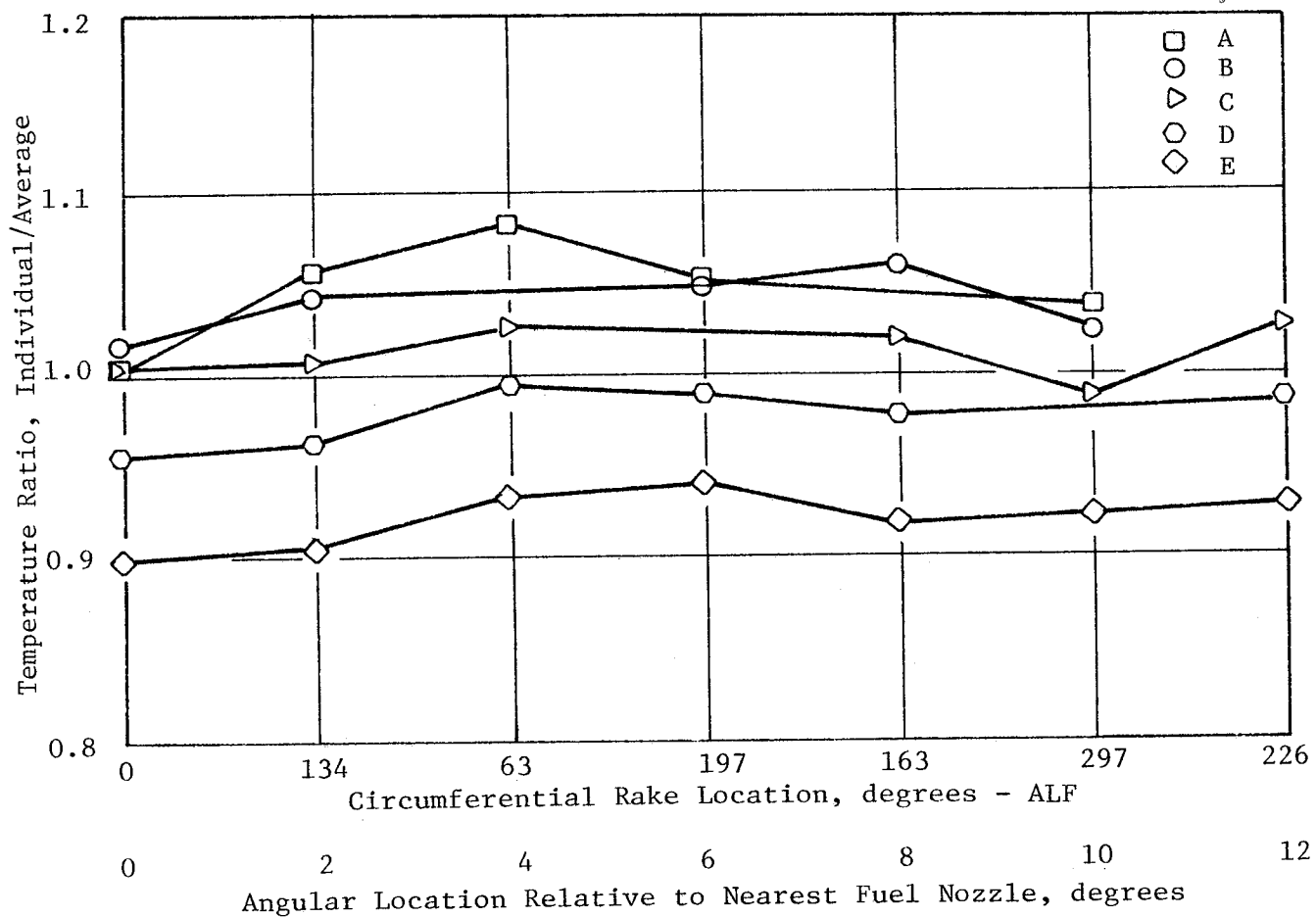
Figure 47. Plane 42 Radial Pressure Profile Based on Arc Rakes.



Measured Average Circumferential Temperatures
Average T42 - 673.3 K (1212° R)

<u>Immersion</u>	<u>K</u>	<u>(° R)</u>
A	754.4	(1358)
B	730.0	(1314)
C	673.3	(1212)
D	633.9	(1141)
E	576.1	(1037)

Figure 48. Circumferential T42 Profiles for Reading 246.

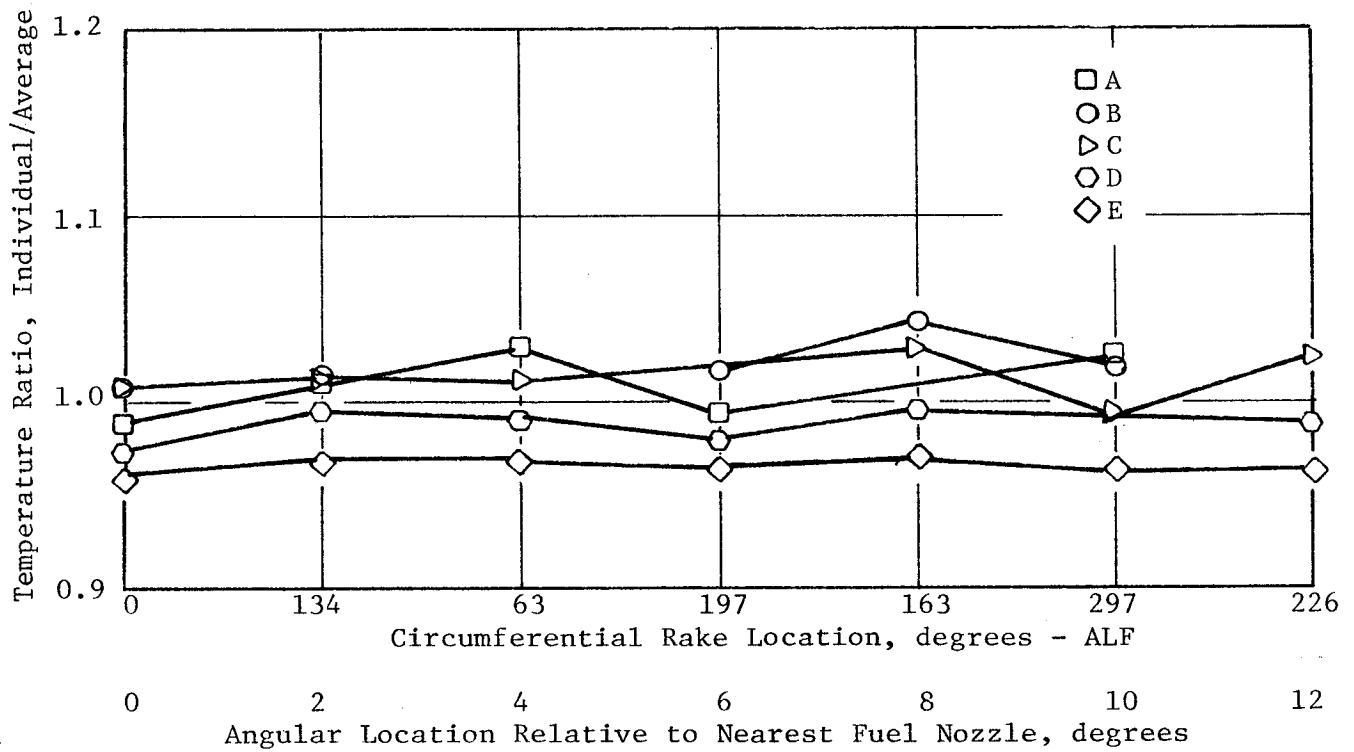


Measured Average Circumferential Temperatures

Average T42 - 822.8 K (1481° R)

<u>Immersion</u>	<u>K</u>	<u>(° R)</u>
A	861.7	(1551)
B	855.0	(1539)
C	833.3	(1500)
D	805.0	(1449)
E	758.3	(1365)

Figure 49. Circumferential T42 Profiles for Reading 250.

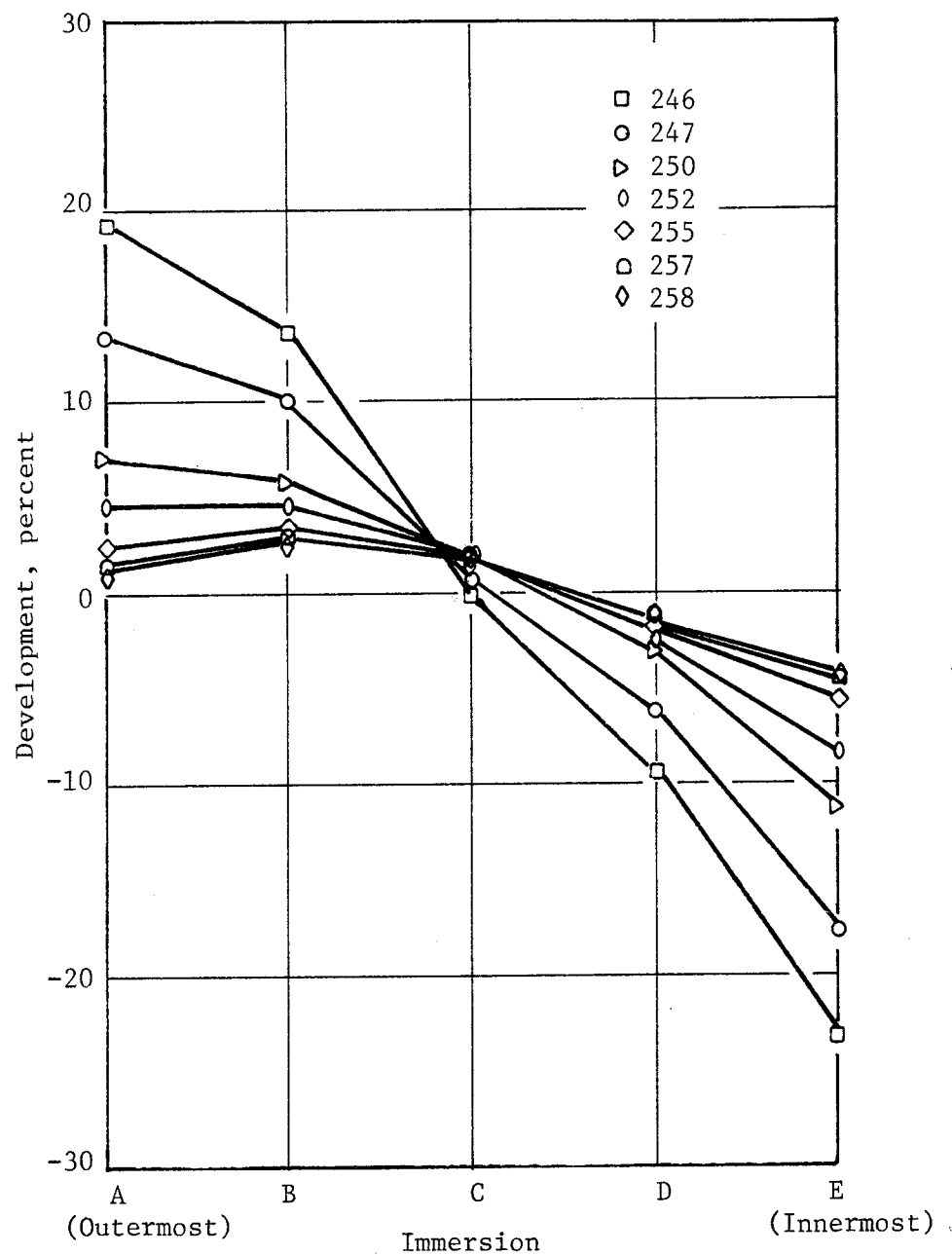


Measured Average Circumferential Temperatures

Average T42 - 1150.6 K (2071° R)

<u>Immersion</u>	<u>K</u>	<u>(° R)</u>
A	1161.7	(2091)
B	1175.0	(2115)
C	1166.7	(2100)
D	1137.2	(2047)
E	1112.2	(2002)

Figure 50. Circumferential T42 Profiles for Reading 258.



Reading	Measured Average T42	
	K	(° R)
246	673.3	(1212)
247	735.0	(1323)
250	822.8	(1481)
252	929.4	(1673)
255	1050.0	(1890)
257	1110.6	(1999)
258	1150.6	(2071)

Figure 51. Radial Profile of T42 Ring Averaged Data.

slope, with the outermost immersion indicating the peak temperature is near the wall. This indicates that at low power the actual average is close to the probe measured average calculation.

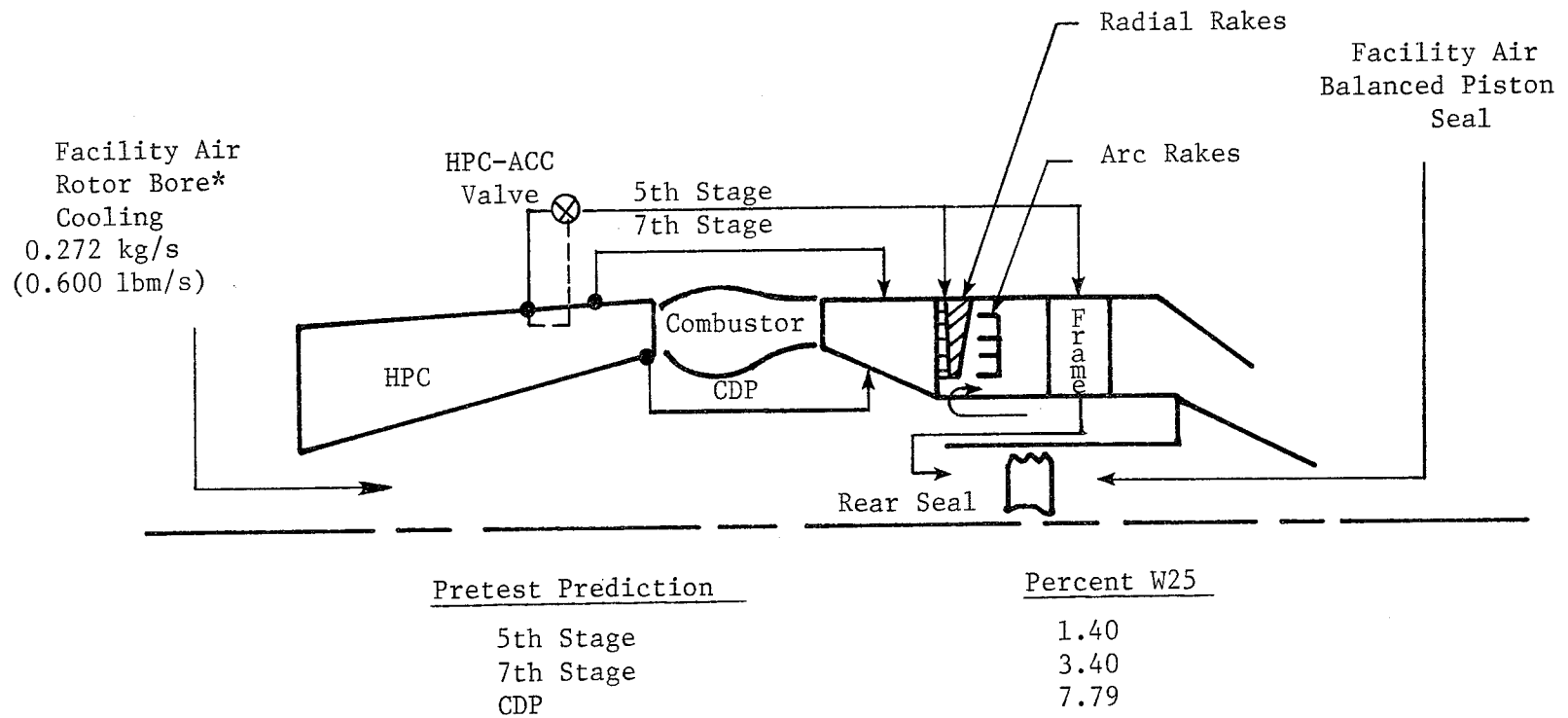
The Plane 42 temperature profiles during single-annular combustor operation were extremely severe and made it difficult to calculate an average Plane 42 temperature. Definition of the engine model with single-annular operation will be postponed until after the ICLS testing. At that time, a better definition of the core performance at ground idle power will be made based on thrust measurements and overall engine operation.

Cooling Flows

Figure 52 is a schematic illustration of the core engine showing the source and sink location of the cooling flows. Also shown are the pretest prediction levels and the facility balance piston seal air applied during the test. The Phase I calculations for the compressor fifth- and seventh-stage flows were based on piping system calibrations made prior to engine assembly. The compressor discharge cooling flow calculation was based on an orifice calibration for that system.

The compressor fifth-stage bleed flow was set at the expected ICLS level and discharged to the turbine frame area. All of this flow entered downstream of the HP turbine; at high power some of the air flowed through the rear seal. At low power, the pressure of facility air used to control rotor axial thrust balance was greater than the fifth-stage pressure, allowing facility air to flow through the rear seal into the gas stream just aft of the HP turbine. The flow levels through this seal were small and had a negligible effect on the analysis. Note that the fifth-stage air was also used for compressor active clearance control (ACC).

The compressor seventh-stage air was used for cooling the HP turbine second-stage shroud cavity and vane and affected the HP turbine efficiency calculation. Compressor discharge air was used primarily for cooling the HP turbine rotor and blades and also the HP turbine efficiency calculation.



* Rotor Bore Cooling Held Constant Except When Reduced for a Specific Test to Evaluate HPC Clearance Changes.

Figure 52. Core Engine Cooling Flow Schematic Diagram.

The measured cooling flows are shown in Figures 53 through 55 along with the curves used in the Phase II analysis. Note that the compressor fifth-stage bleed measurements appear to have more scatter than those of the seventh-stage and compressor discharge bleeds. This was caused in part by the compressor ACC valve setting. At high power, the total flow level shifted from about 1.3% of compressor physical airflow with the ACC off to about 1.8% with the ACC on. With the ACC valve closed, the flow was restricted to the design intent level by the piping system and valve flow limit. However, when the valve was opened, the flow increased because of a missing "W" seal at the outer wall interface between the flowpath and the HP turbine exit. The level of flow varied with the valve setting. During the final calibration run the valve was fully opened, allowing more flow than in earlier runs. Figure 53 shows distinct groupings of data with the ACC on and off. The ACC-on data clearly shows two levels of flow between the final calibration run data and earlier data readings.

The slope of the compressor seventh-stage bleed flow curve, shown in Figure 54, deviates from the expected constant flow level. The measurements at low power were probably incorrect because at lower power the piping check valves partially closed, increasing the piping system pressure drop. The piping system had been calibrated with the check valves wired open, giving an erroneous calibration at low flow rates. The high-power measurement was therefore considered to be the best indication of bleed flow, and a constant value of 4% was used in the final Phase II analysis.

The compressor discharge cooling flows are slightly less than the pretest prediction level of 7.79% of compressor flow. A heat transfer evaluation of the temperatures in the HP turbine correlates with the slightly lower flow level, and also substantiates the curve shape with the engine power level.

High Pressure Compressor

The compressor performance is summarized in Figures 56 through 58. The first figure shows the compressor operating line data for the final calibration run, as well as for the large and small nozzle areas. The data measurements fall below the predicted operating line because of two factors: the

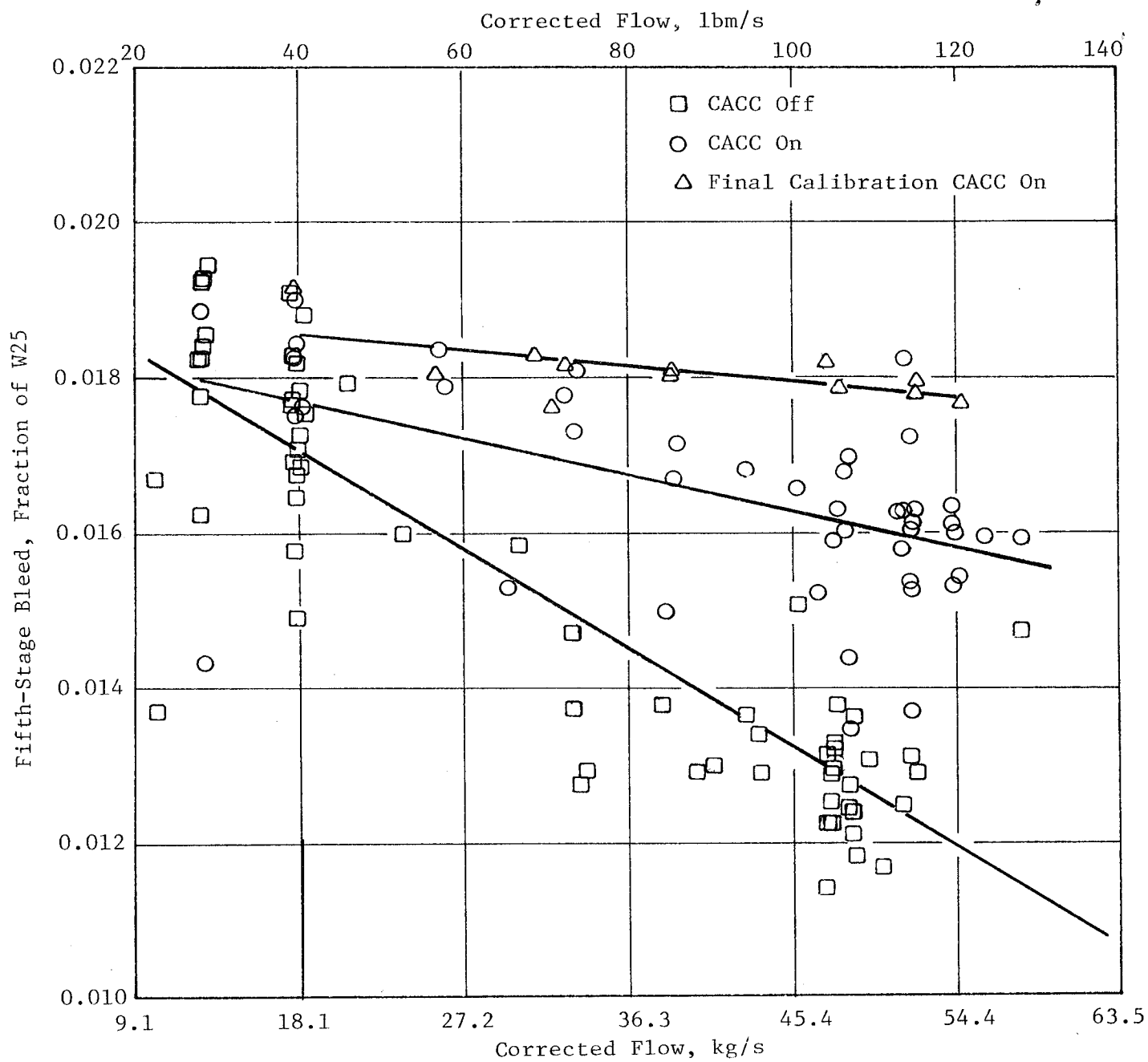


Figure 53. Total Fifth-Stage Parasitic Cooling Bleed Measured Flows - Compressor ACC Off Versus Compressor ACC On.

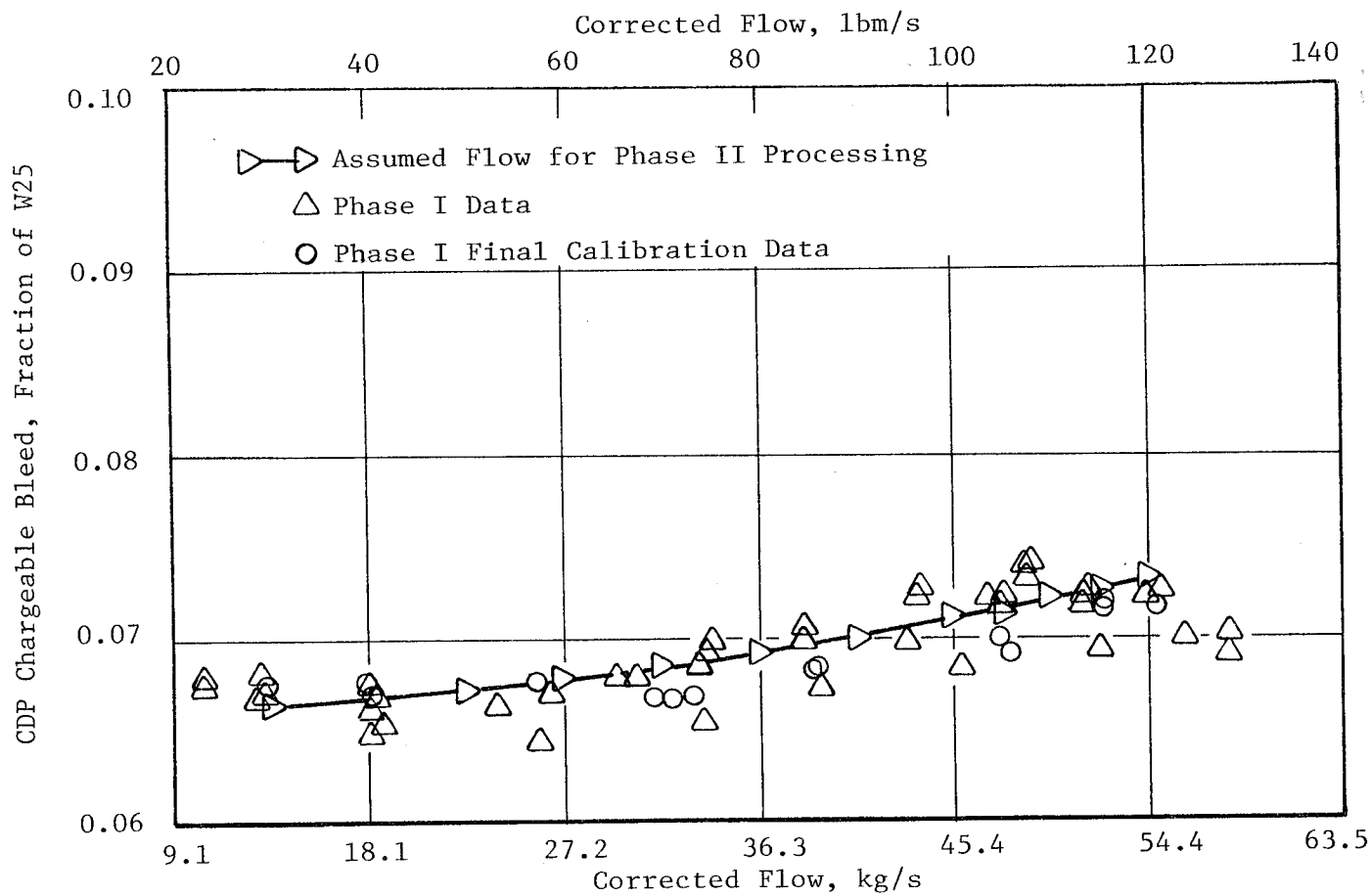


Figure 55. Total CDP Chargeable Cooling Bleed Measured Flows Versus Assumed Flows.

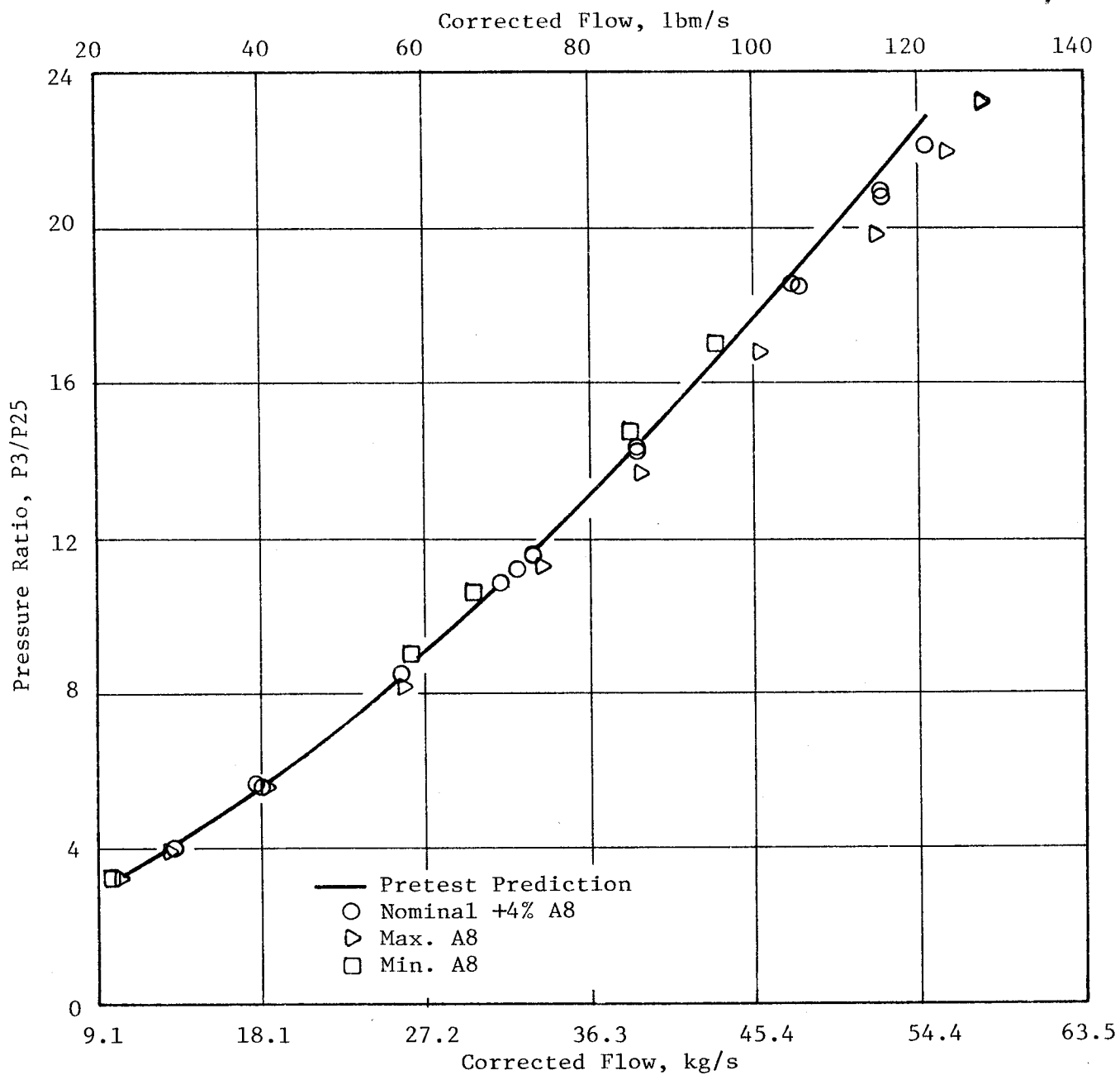


Figure 56. Phase II Results - Compressor Operating Lines.

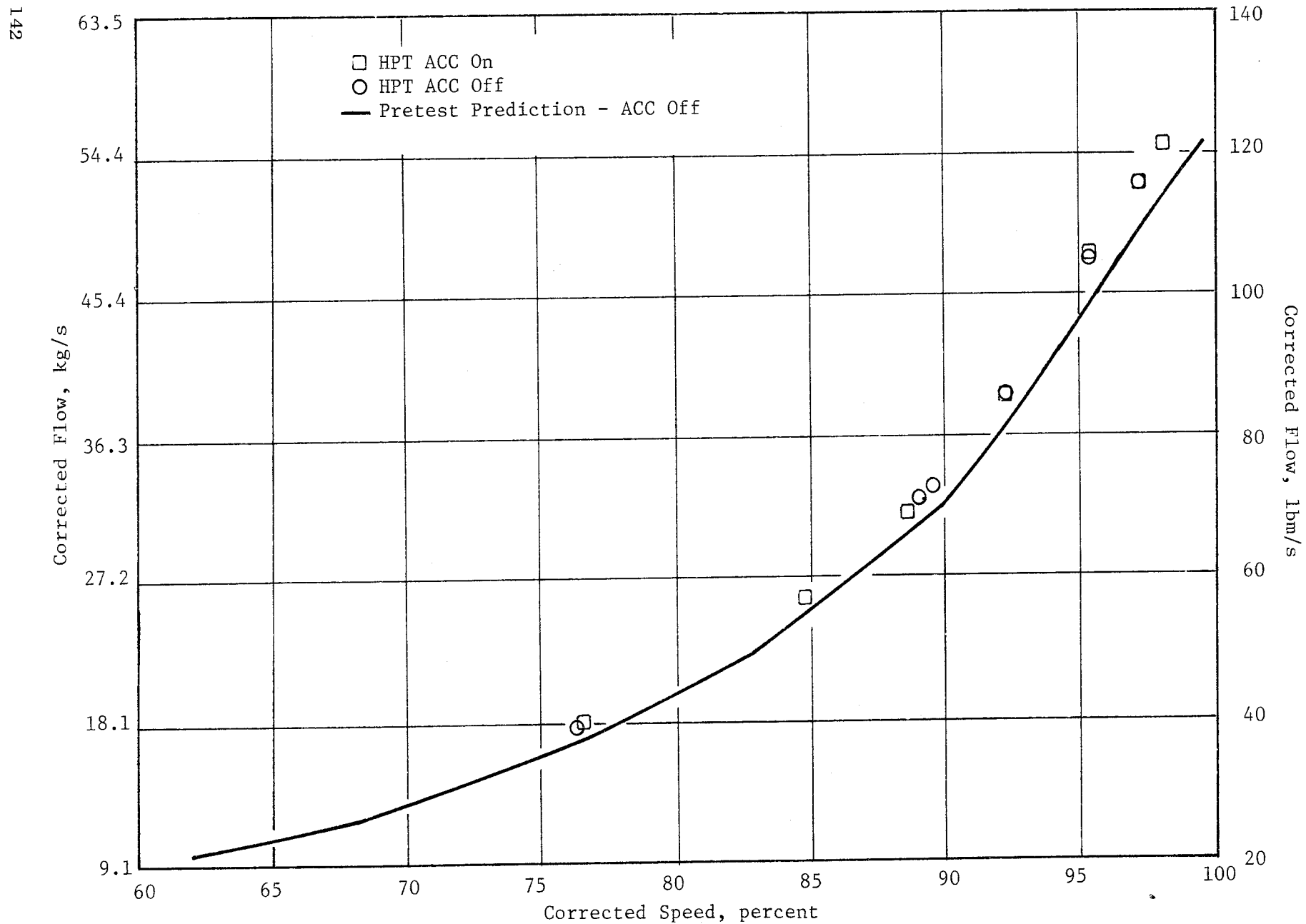


Figure 57. Phase II Results - Corrected Flow Versus Corrected Speed.

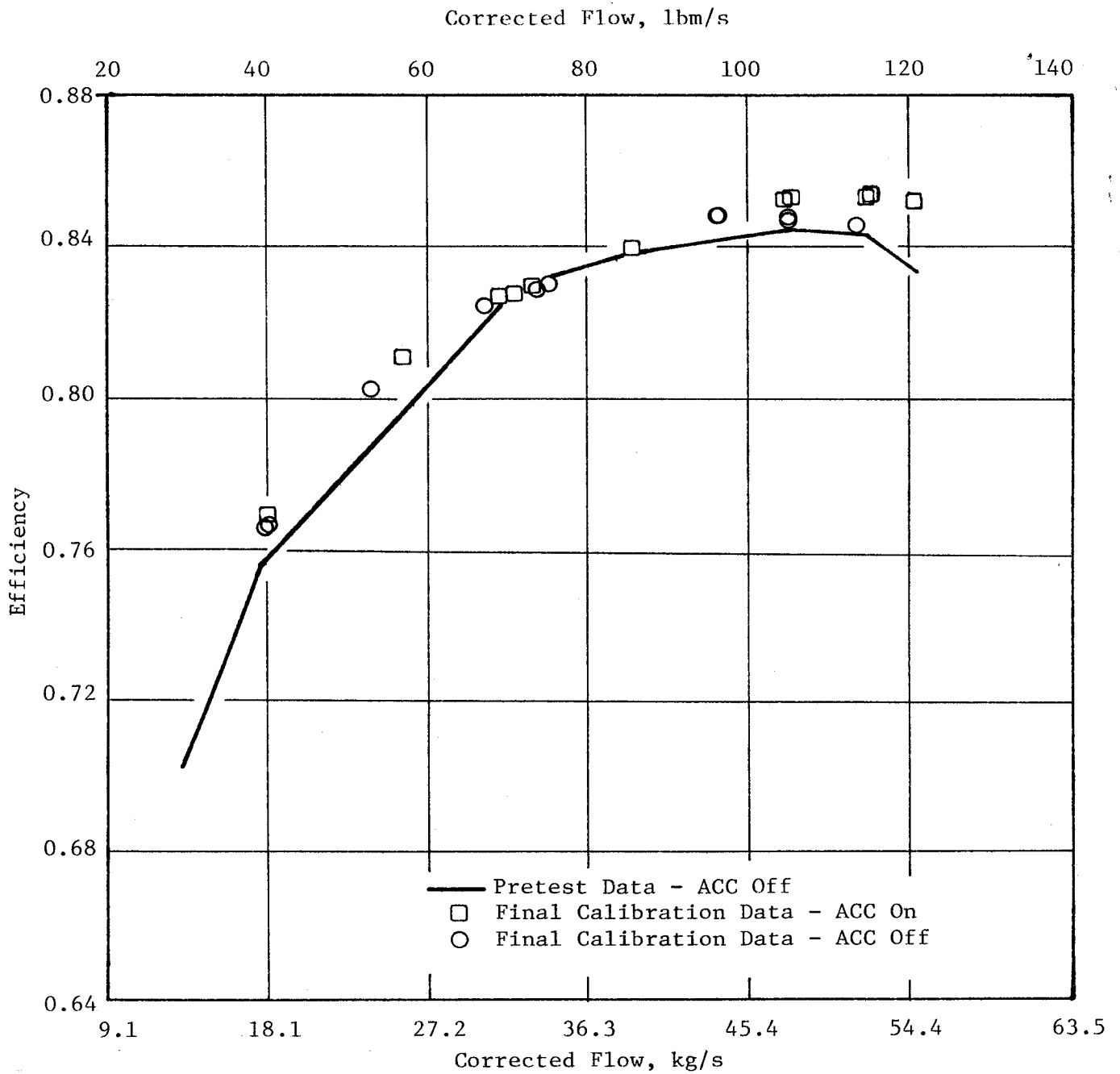


Figure 58. Phase II Analysis - Compressor Efficiency Versus Flow.

final exhaust nozzle area was larger than the nominal area, and the HP turbine flow function ($W\sqrt{T}/P$) was approximately 1% larger than expected.

The flow/speed data presented in Figure 57 show the compressor pumping more flow than predicted from prior rig tests. This was expected since the engine compressor had blading changes that gave much tighter (near design) clearances in the forward stages and new airfoils in Stator 7 through Rotor 10, which improved the pumping match between the front and rear blocks. These changes, plus a new stator schedule, resulted in a new flow/speed characteristic. With the new characteristic, the core runs slower at thrust and thus provides more core speed margin relative to the design limit.

The compressor efficiency/flow characteristic, shown in Figure 58, is the most important relationship from a performance standpoint. These data are shown for both the final calibration run, which had the compressor ACC system on for all readings, and for selected readings from previous runs which had the ACC system off. The prediction line shown is with the ACC off and must be compared with the appropriate test data. With the ACC on, the compressor efficiency was better than predicted and about 0.5% below the FPS (Flight Propulsion System) design goal.

Combustor

The combustor performance map in the cycle deck model is defined by two parameters: (1) the ratio of pressure at the turbine Stage 1 nozzle leading edge (P_4) to the pressure at the compressor discharge plane (P_3); (2) the combustor adiabatic efficiency. Figure 59 shows the pressure ratio (P_4/P_3) over the engine operating range. The data trend shows good agreement with the predicted curve. The pressure loss decreased with increasing power and correlated well with the component evaluation in Section 6.5. In that section, the pressure loss is shown as a function of compressor discharge flow function ($W_3\sqrt{T_3}/P_3$). Note that the flow function decreases with increasing engine power.

The initial Phase II analysis was conducted using the combustor efficiency as determined by the emissions testing. When using this efficiency characteristic, it was found that large differences between the measured T42 and the

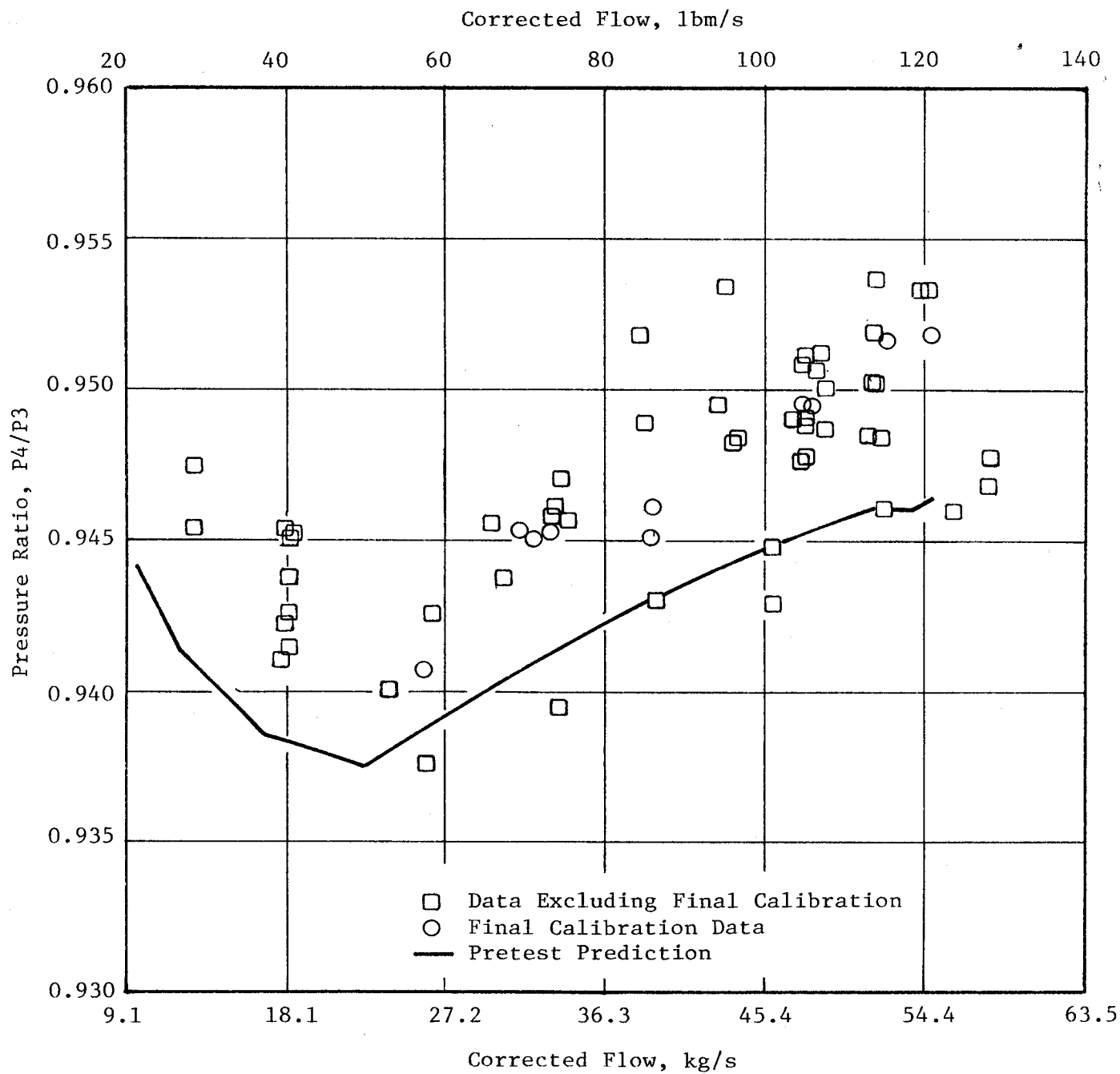


Figure 59. Phase II Results - Double-Annular Combustor Pressure Ratio Versus Flow.

Phase II calculated T42 occurred at low power, as shown in Figure 60. An acceptable tolerance band for a measured T42 deviation from an average cycle calculation would be approximately ± 7 K ($\pm 12^\circ$ F). The larger deviations at low power indicated that combustor efficiency was poorer than calculated from the emissions test.

At lower power the T42 radial profile was relatively linear, so the measured T42 was an accurate representation of the flow-averaged T42. Therefore, the Phase II analysis was revised to base combustor efficiency on measured T42. The efficiency determined by this method is shown in Figure 61 as a function of T3. The efficiency determined from emissions data is shown for comparison.

At high power, the combustor efficiency based on measured T42 exceeded 100%. This occurred because the Plane 42 temperature measurement was higher than a real flow-averaged temperature. Referring to Figure 51, at higher power the temperature decreased toward the walls. At the outer wall especially, leaking fifth-stage bleed air would contribute to the temperature fall-off at high power. For this reason, the measured T42 was higher than the real flow-averaged value, thereby giving an erroneously high combustor efficiency. Thus, combustor efficiency was limited to a maximum of 99.9% at higher power levels. This limit is incorporated into Figure 61. The efficiency at high power matches the data from emissions testing.

After final adjustments were made to the parasitic flows, the efficiency was evaluated as a function of P3 (consistent with cycle deck modeling) to determine the level to be used for the ICLS engine model. Figure 62 shows the final Phase II results and the selected model for the ICLS. Efficiencies determined from the emissions data are also shown for comparison.

Another evaluation of combustor efficiency can be made by using the HP turbine flow function. Based on combustor efficiency as determined from emissions data, the turbine flow function was more than 1.0% higher at low power than at high power. This is contrary to well-established turbine flow characteristics and therefore indicates erroneous data. The turbine section below discusses the need for combustor efficiency levels set to match the measured T42 levels at low power.

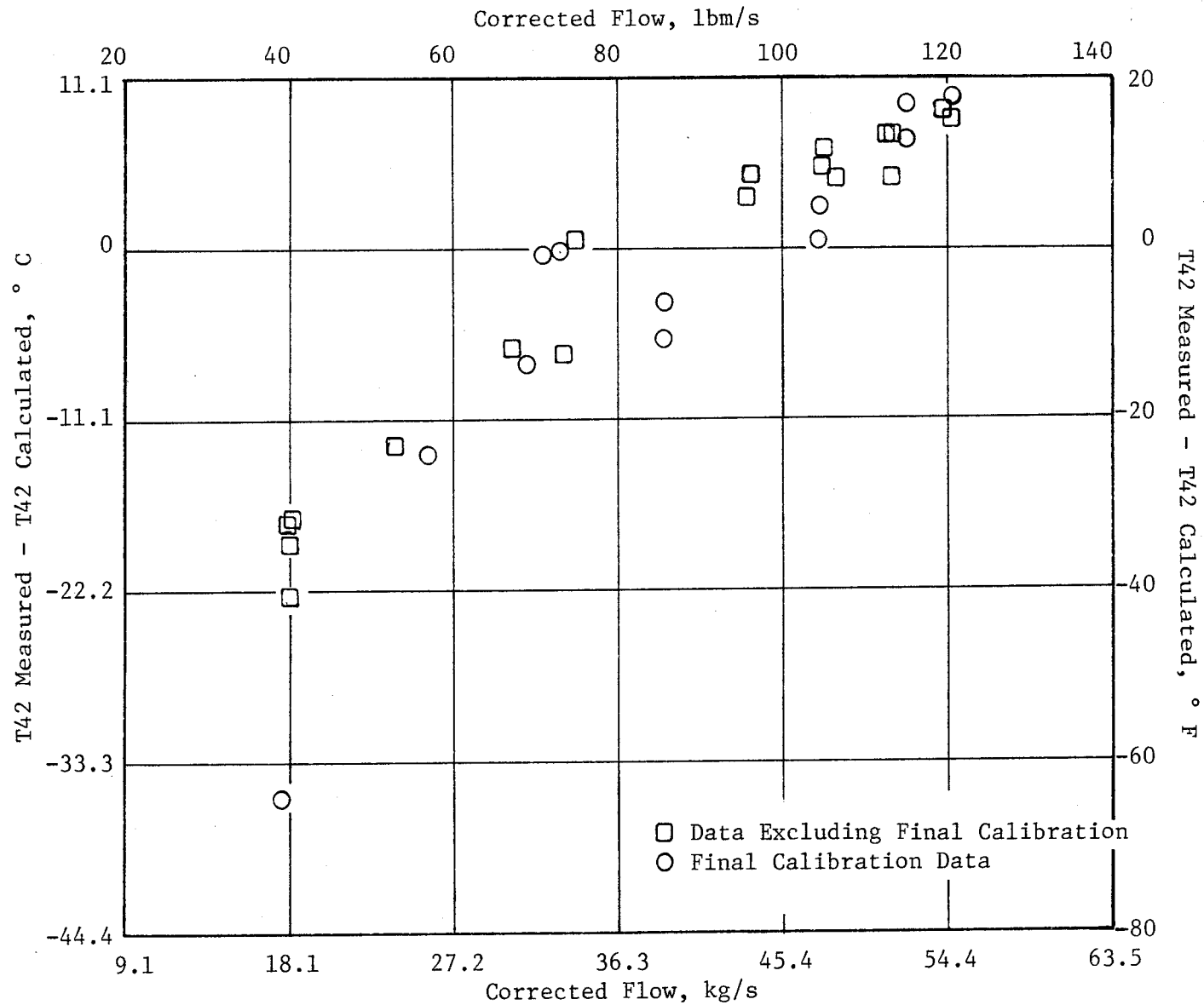


Figure 60. Phase II Results - Difference Between Measured T42 and T42 Calculated From Emissions Efficiency Data.

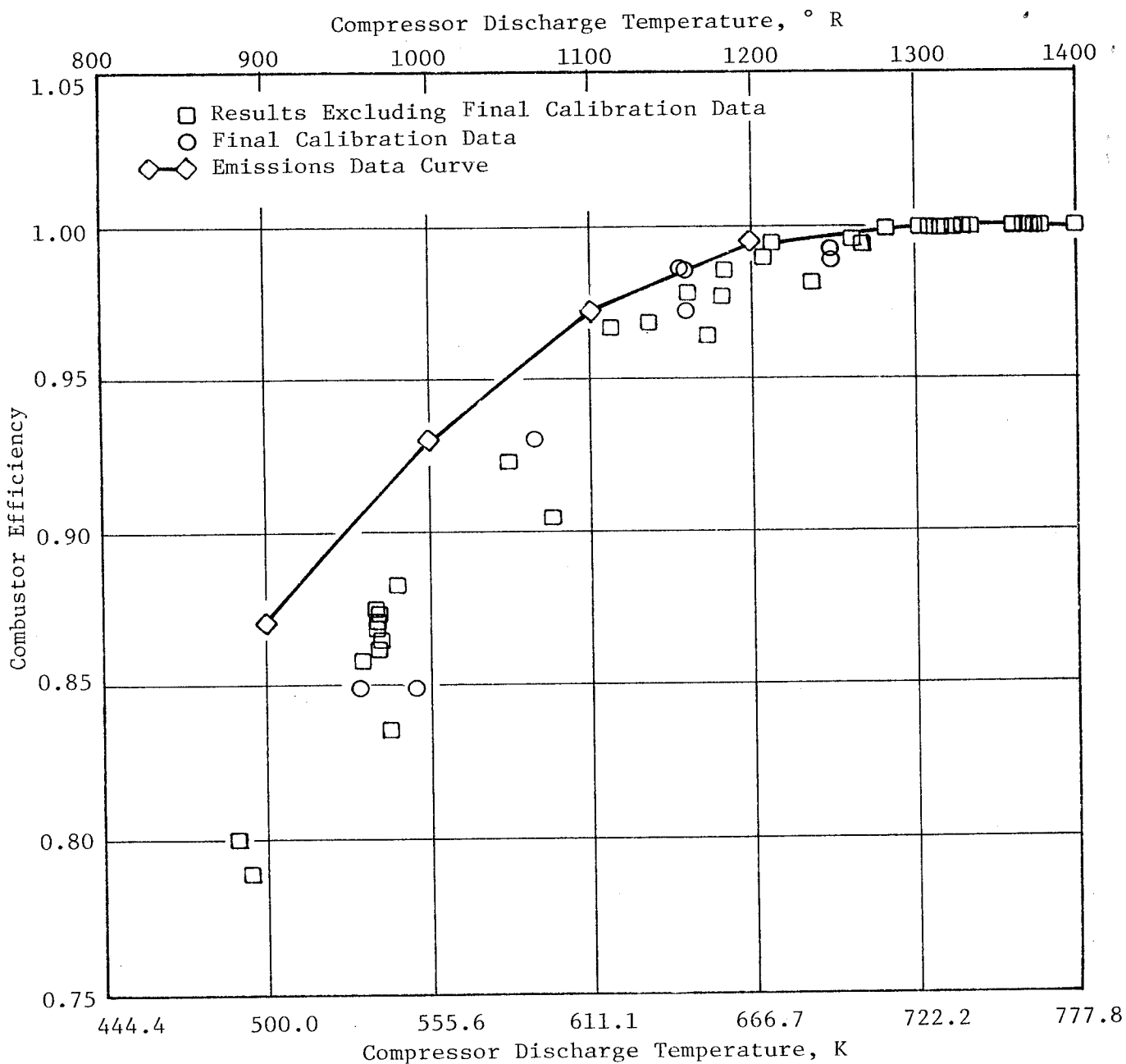


Figure 61. Phase II Results - Double-Annular Combustor Efficiency Versus Compressor Discharge Temperature.

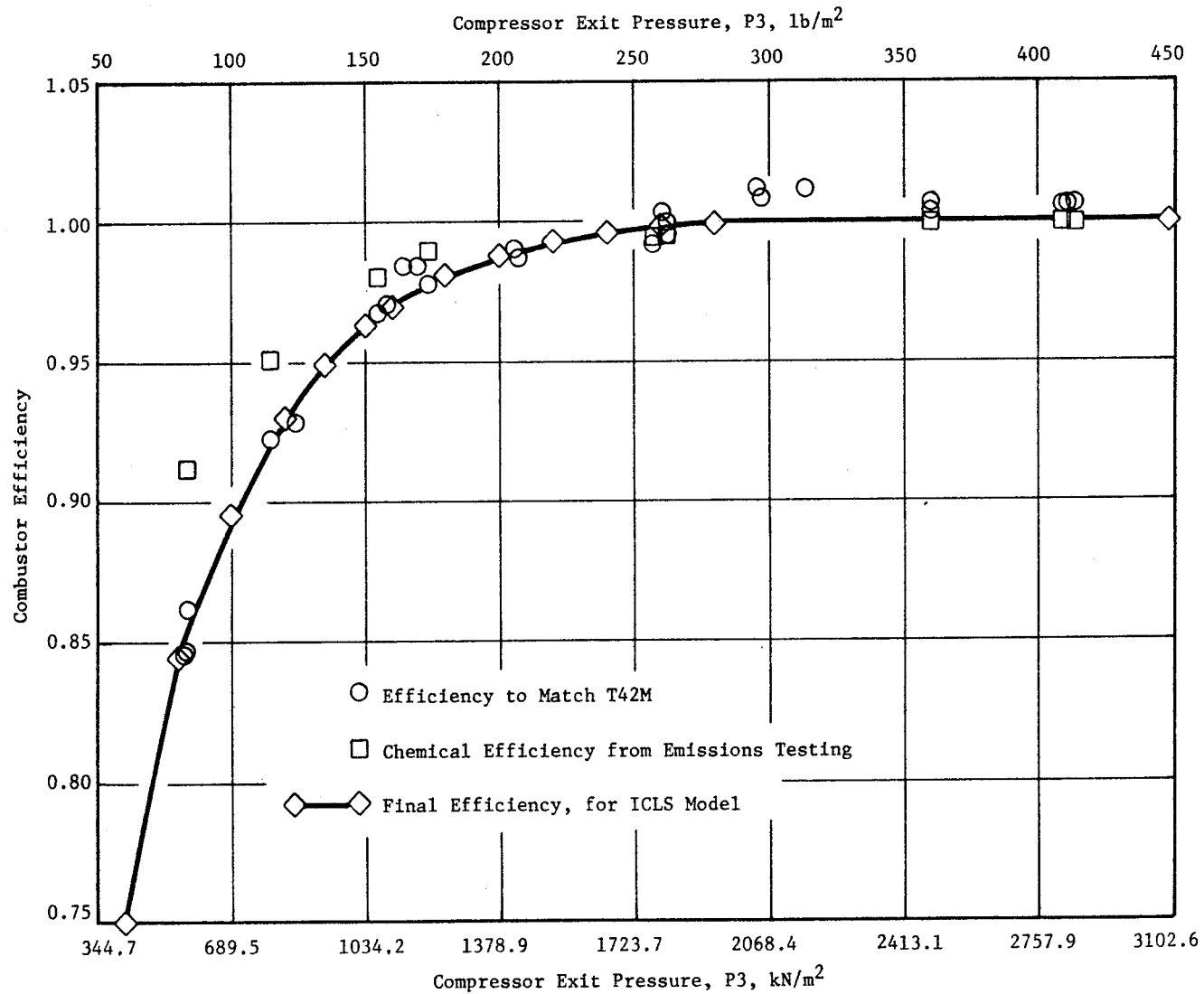


Figure 62. Phase II Results - Combustor Efficiency Emissions Data Delta Between Measured and Calculated T42.

High Pressure Turbine Performance

Figure 63 shows the HP turbine efficiency calculations for all the test data points where clearances were measured. These data are for conditions where ACC is full on or off. These efficiency levels are for measured clearances that are larger than the reference 0.406 mm (0.016 inch) used to define the HP turbine map performance.

An evaluation of the clearance effects on efficiency was made by adjusting the measured efficiency for clearance relative to the reference clearance of the map. Figure 64 shows the ratio of measured efficiency to the map efficiency (map efficiency scalar) after adjusting for clearance. The data indicates that adjusted turbine performance at the reference clearance matches the rig map level quite well except at the flight idle power level of 18.1 kg/s (40.0 lbm/s).

The concern in this evaluation is in the uncertainty in average clearance levels and the efficiency sensitivity to change. In theory, if these two factors were known exactly, the efficiency scalar for two successive points with turbine ACC off and on should be the same. It can be seen from Figure 64 that they are not and that they can differ by as much as 0.5 percent.

Because of these uncertainties, it was difficult to assess the basic aerodynamic performance relative to the predicted (rig test) map. The assumptions of basic map efficiency level, actual clearances, and efficiency sensitivity to clearance change were evaluated. It was determined that an acceptable match of measured efficiency was achieved by using the clearances as measured, then increasing the efficiency sensitivity to changes in the second-stage clearance to about 0.6 of the level for the first stage. Previously, the sensitivity was 0.4 times the level of the first stage. The model results are compared to the measured data in Figure 64, which shows the ratio of measured efficiency to that predicted by the cycle deck.

The final core cycle deck model was modified to retain the basic map characteristic at high power with a decrease of one point at idle. This characteristic will be used in the ICLS pretest prediction cycle.

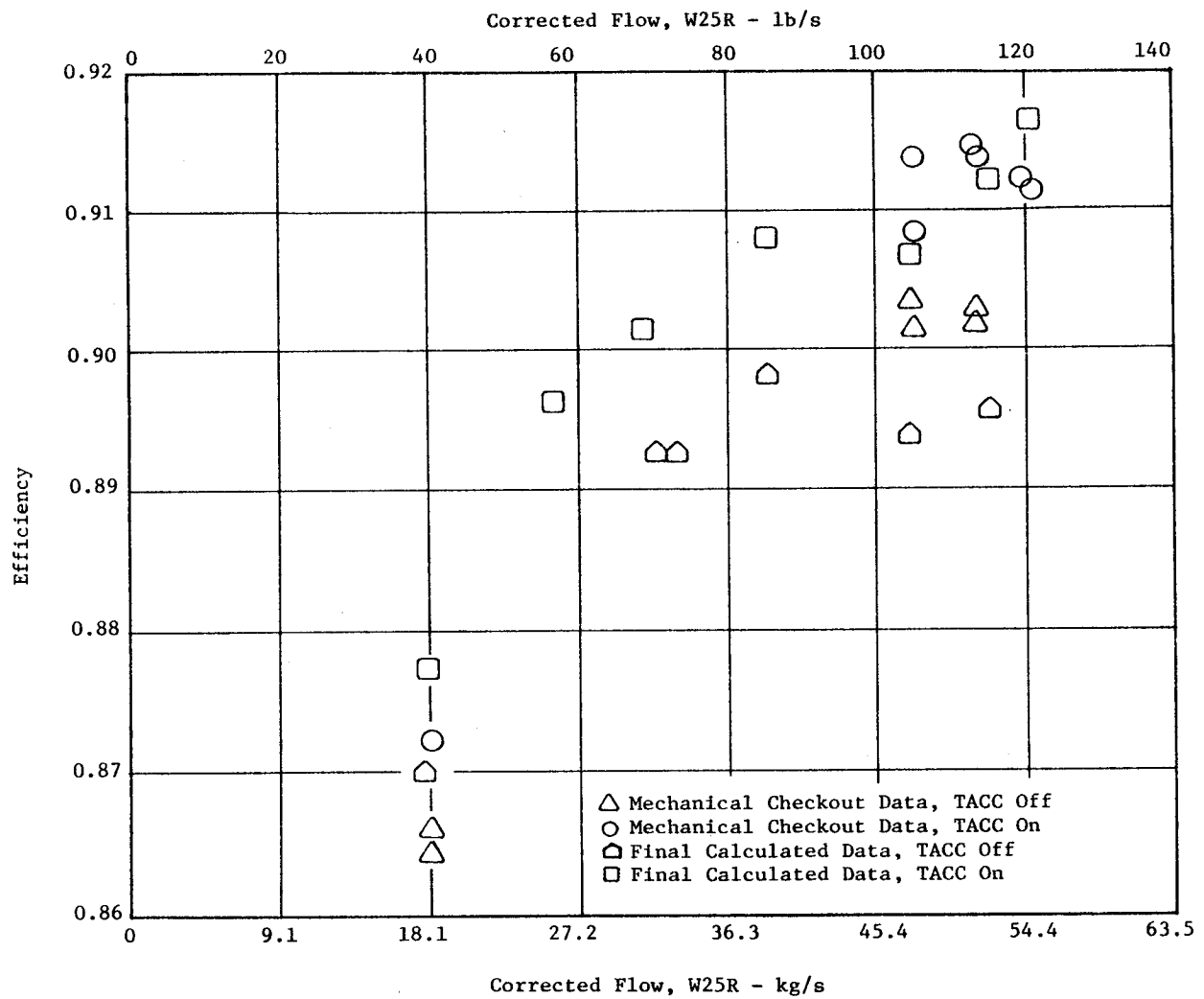


Figure 63. Phase II Results - Double-Annular HP Turbine Efficiency.

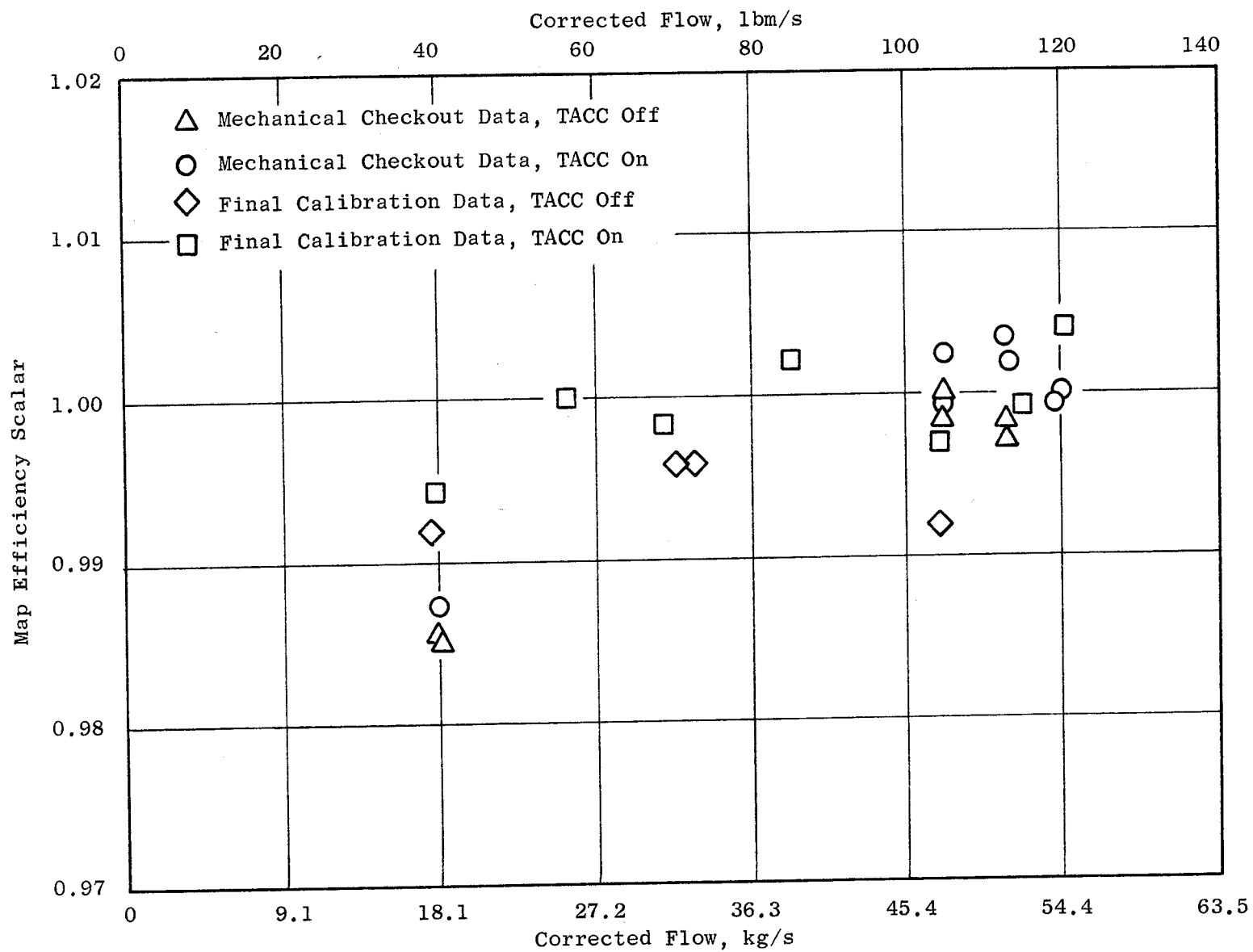


Figure 64. High Pressure Turbine Efficiency Scalar.

An evaluation of the HP turbine first-stage nozzle flow function ($W_{41} \sqrt{T_{41}}/P_{41}$) was made by using the final calibration data along with data readings for the large and small A8 runs. A ratio of the calculated flow function and the map value (map scalar) is shown in Figure 65. The trend indicates that the turbine flow function is about 0.8% larger than the predicted 1.032 modifier for the 4% opened A4 nozzle. The trend is fairly constant over the entire power range of the core when combustor efficiency is based on measured T42. When combustor efficiency based on missions data is used, and the measured T42 is not matched, the resultant flow function modifier increases more than 1.0% at low power and is inconsistent with the expected characteristic of a constant value.

Exhaust System

Core engine tests were run with four different nozzle areas. Initial tests were conducted with a nominal nozzle area which was sized to set the compressor operating line to match the expected ICLS operating line. Both a 16% larger and a 10% smaller nozzle were scheduled to provide a range of compressor operating line migration, and a shift in HP turbine pressure ratio, in order to compare the performance shift with the performance maps of these components.

After the initial nominal nozzle tests, the decision was made to modify the nominal nozzle to provide a 4% area increase. The purpose was to increase the HP turbine pressure ratio to a value nearer the design point ratio for the final calibration runs. However, only a 1% effective area increase was achieved.

In Phase II analyses, the nozzle areas were evaluated as part of the flow continuity balance of the cycle. Pressure losses for the radial rakes, arc rakes, and turbine frame were used in conjunction with nozzle flow coefficients to model the performance of the exhaust system of the engine. The results show that the effective areas calculated in Phase II analyses were close to the predicted values, except as previously noted with the +4% effective area nozzle.

Table X shows the pressure losses that were used and compares the predicted and calculated effective areas. The three original effective areas were close to predicted, although the nominal was expected to be closer than the -1.8% shown.

Figure 65. High Pressure Turbine Flow Function Scalar.

Table X. Exhaust System Characteristics.

<u>Assumed Pressure Losses</u>	<u>% $\Delta P/P$</u>
Radial Rakes	1.22
Arc Rakes	0.74
Turbine Frame	<u>1.00</u>
Total	2.96

Nozzle Area Comparison

<u>Nozzle</u>	<u>Predicted</u>		<u>Phase II Calculation</u>		<u>%Δ</u>
	<u>m²</u>	<u>in²</u>	<u>m²</u>	<u>in²</u>	
Nominal	0.1052	(163.0)	0.1032	160.0	-1.8
Large	0.1219	(189.0)	0.1208	187.2	-0.9
Small	0.0946	(146.7)	0.0945	146.4	-0.2
Nominal +4%	0.1094	(169.5)	0.1043	161.6	-4.7

The pressure losses are not actually constant; they vary depending on the turbine swirl. For areas near nominal the swirl effects are minimal, but for the large and small areas the swirl could be greater than 10° , thus increasing the rake pressure losses significantly. Losses were probably greater than assumed. Greater loss levels would then make all the calculated nozzle effective areas larger by the same percentage.

The results for the three original nozzles are considered good, particularly when considering that a radial deviation on a nozzle of 0.51 mm (20 mils) represents a 1% change in nozzle area. The major concern was the +4% nozzle which performed as though it were only about 1% larger than the nominal area. Measurements were made on this nozzle in order to ascertain why there was only a small increase in area. This investigation revealed that the nominal nozzle had been distorted after the initial runs, and even though it was cut back the prescribed distance, it was sufficiently distorted (out-of-round) that reinstallation was difficult. It is concluded that this distortion caused the apparent 3% area reduction indicated.

Overall Performance

The overall performance of the core engine as a gas generator is generally evaluated by the core pumping and the HP turbine discharge gas power available for the amount of fuel burned. Pumping is the relationship of the temperature ratio of the core to the overall pressure ratio. This relationship is a measure of the cycle and rotating component efficiencies, along with the parasitic flows. It is independent of the combustion process efficiency and FHV. The gas power is a measure of the energy available for propulsion at the LP turbine entrance. It includes all the individual component performance items, including combustor efficiency and FHV.

Figure 66 shows the pumping characteristics for the final calibration runs compared with the pretest prediction. The core engine is better at high power but poorer at low power than the prediction cycle. Resolution of the differences in components previously described is consistent with the overall pumping comparison. At high power the compressor (ACC on) is better than predicted while the HP turbine (ACC off) is slightly lower than the prediction. The larger HP turbine flow function and higher parasitics of the engine detract from the performance gains resulting from the compressor but still result in better than predicted overall performance for the engine. Proper matching of the components and use of design cooling flows would further improve the engine pumping characteristic.

The low power pumping shows the prediction data being better than measured. This is due primarily to the HP turbine clearances having been assumed substantially tighter for the prediction than what occurred in test.

Figure 67 shows the corrected gas power versus corrected fuel flow relationship of the engine for the final calibration readings compared with pretest prediction. This parameter includes the effects of all performance elements. The trend is similar to the pumping comparison except that the reduced combustion efficiency at low power is seen in the poorer than predicted engine performance.

The conclusion from evaluating contributions of the individual performance items to the differences between the two curves is that the core performance at ICLS high power will be as good or slightly better than expected. If the low

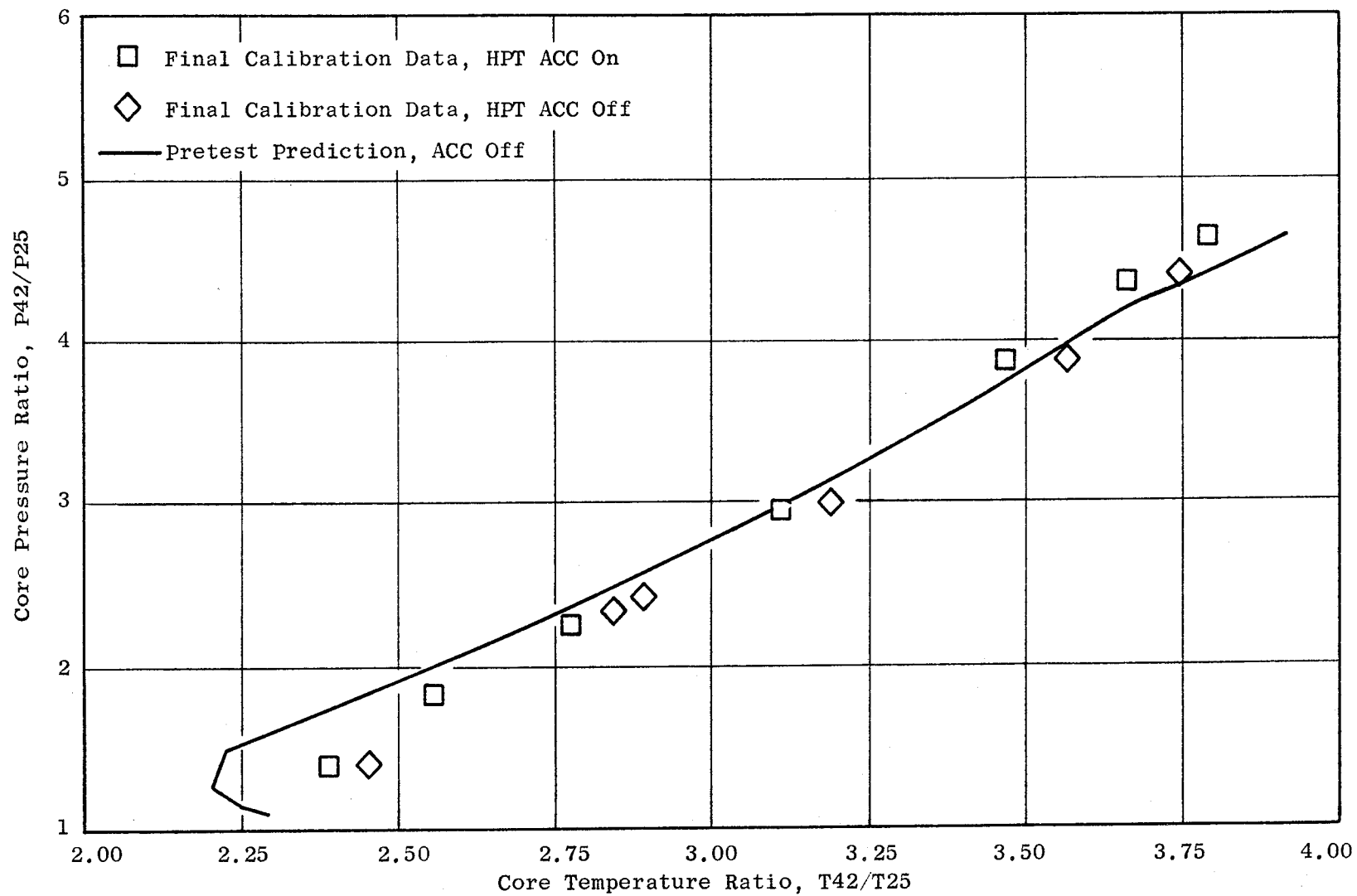


Figure 66. Core Pumping Characteristics.

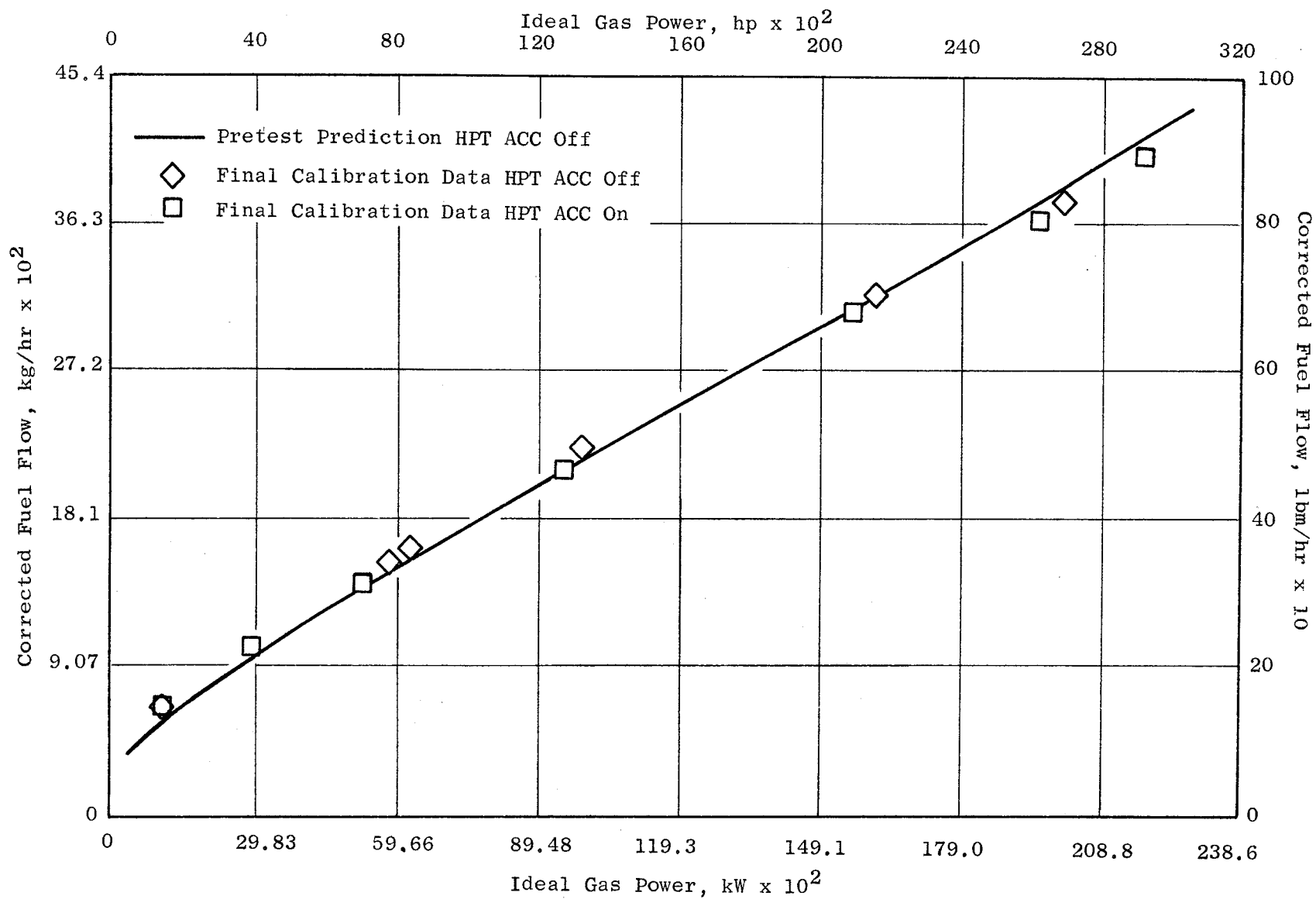


Figure 67. Corrected Fuel Flow Versus Ideal Gas Power.

pressure components perform as expected, the ICLS performance should exceed the initial forecast goal.

6.2 COMPRESSOR MECHANICAL PERFORMANCE

6.2.1 Clearances

Compressor operating clearances were monitored and measured by two clearanceometers and one touch probe for each stage on Stages 3, 5, and 10. A portion of the test was devoted to evaluating the effects of the ACC air on Stage 10 clearances. This was accomplished by taking baseline clearance readings with the ACC off and then opening the ACC to maximum cooling airflow. Readings were taken until the clearance stabilized. The results, plus predicted values, are presented in Table XI, along with clearances for Stages 3 and 5. The thermal response rate of the aft compressor casing was much quicker than expected, with 80% of the Stage 10 closure occurring within the first minute of ACC activation. The effect on compressor tip clearances of reducing the rotor bore cooling air was also evaluated. The cooling flow was reduced in two steps from 100% to 67% to 40%. The resulting clearance changes are shown in Table XII for the three measured stages. As can be seen, varying the bore cooling flow was also an effective means of controlling clearances; however, the present FPS design does not include this capability.

6.2.2 Temperatures

Signals from thermocouples mounted on the rotor and stator structures were recorded during the test. In Figure 68 the rotor temperatures are compared with predicted values at design point conditions. Discrepancies in the bore temperatures can be explained by differences in bore cooling flow rates. Differences in the Stage 3 and 5 dovetail-post temperatures are believed to be caused by increased heating of interstage seal leakage air due to tight clearances and by local windage effects.

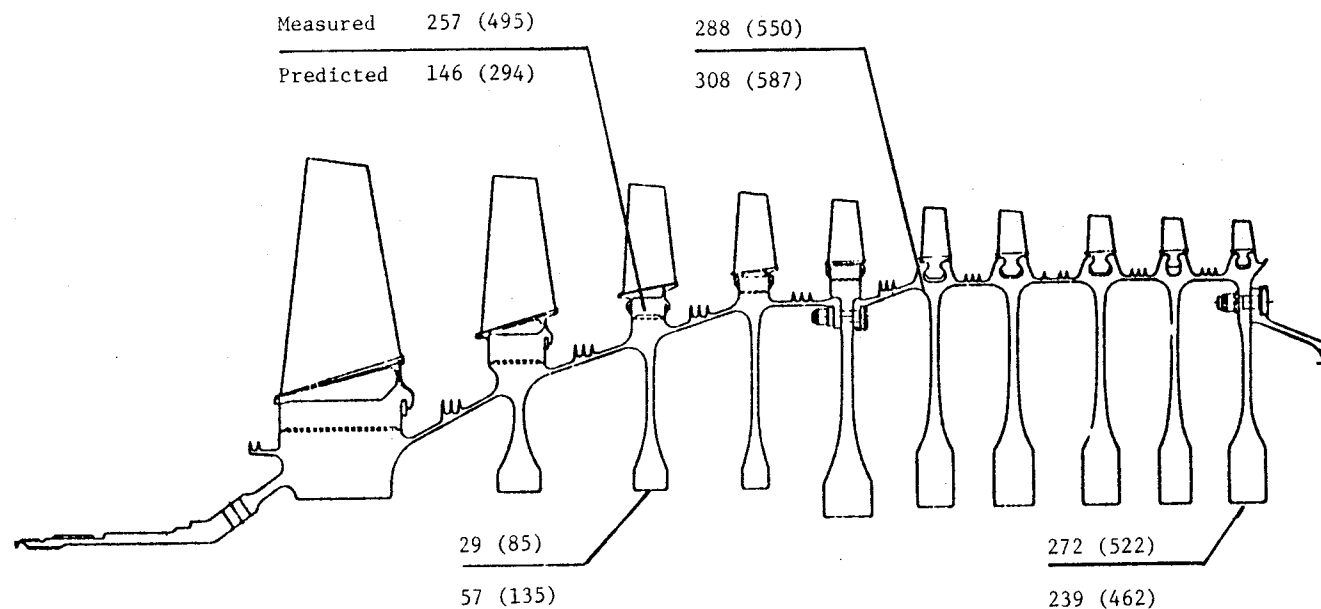
Casing temperatures, presented in Figure 69 with the ACC on and in Figure 70 with the ACC off, compare favorably with the predicted values.

Table XI. Core HP Compressor Active Clearance Control.

Stage		Engine Parameter				Average Clearance			
		T25 ° C (° F)	P25 kPa (psia)	N _{Corr} , rpm	ACC Off mm (in.)	ACC On mm (in.)	ΔClosure mm (in.)		
10	Test Point	23 (73)	101.0 (14.7)	12,210	0.73 (0.029)	0.25 (0.010)	0.48 (0.019)		
	Prediction	15 (59)	99.0 (14.4)	12,254	0.71 (0.028)	0.30 (0.012)	0.41 (0.016)		
5	Test Point	23 (73)	101.0 (14.7)	12,210	0.30 (0.012)	0.30 (0.012)	N/A		
	Prediction	15 (59)	99.0 (14.4)	12,254	0.61 (0.024)	0.61 (0.024)	N/A		
3	Test Point	23 (73)	101.0 (14.7)	12,210	0.05 (0.002)	0.05 (0.002)	N/A		
	Prediction	15 (59)	99.0 (14.4)	12,254	0.38 (0.013)	0.33 (0.013)	N/A		

Table XII. HP Compressor Clearance Change With Rotor Bore Cooling at 96% Corrected Speed.

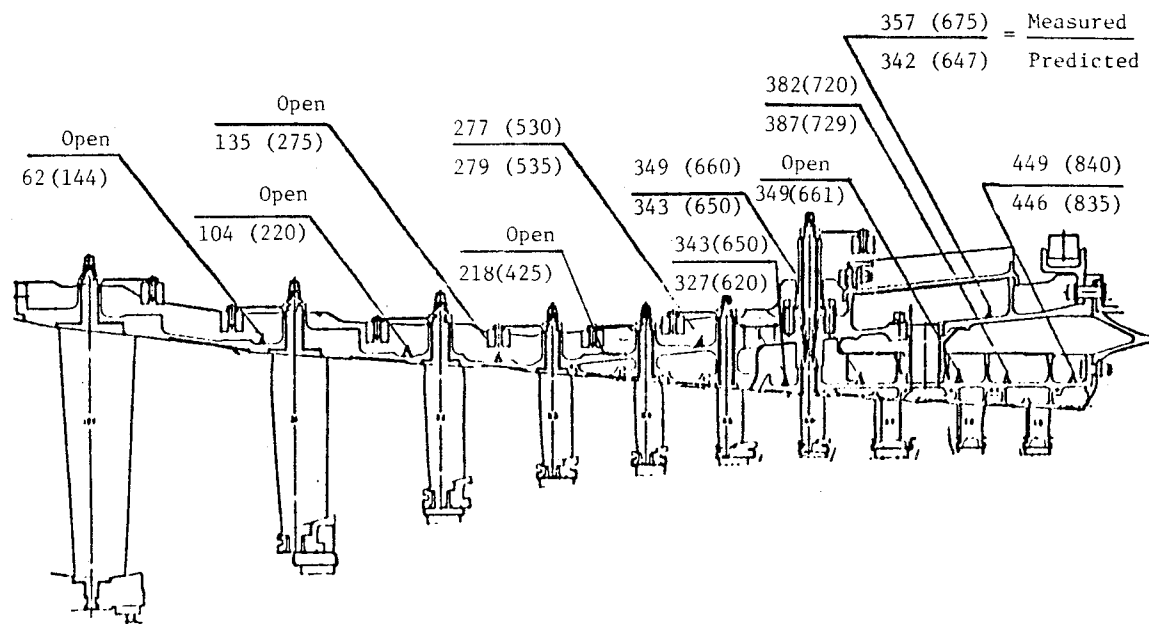
Percent Bore Cooling	Average Clearance Change		
	Stage 3 mm (in.)	Stage 5 mm (in.)	Stage 10 mm (in.)
100	Base	Base	Base
67	0.0300 (0.0010)	0.1000 (0.0040)	0.100 (0.004)
40	0.0600 (0.0025)	0.1700 (0.0065)	0.280 (0.011)



Note: All Temperatures are ° C (° F)

	T25 ° C (° F)	P25 kPa (psia)	T3 ° C (° F)	N _{Phys} rpm	%N _{Corr}	T _{Bore Cooling} ° C (° F)	W _{Bore Cooling} kg/s (lbm/s)
Test Point Conditions	29 (84)	96.6 (14.01)	535 (995)	12,602	100.43	29 (84)	0.25 (0.55)
Prediction Point Conditions	15 (59)	101.3 (14.7)	483 (902)	12,254	100.00	38 (100)	0.18 (0.40)

Figure 68. Compressor Rotor Temperature Comparison.

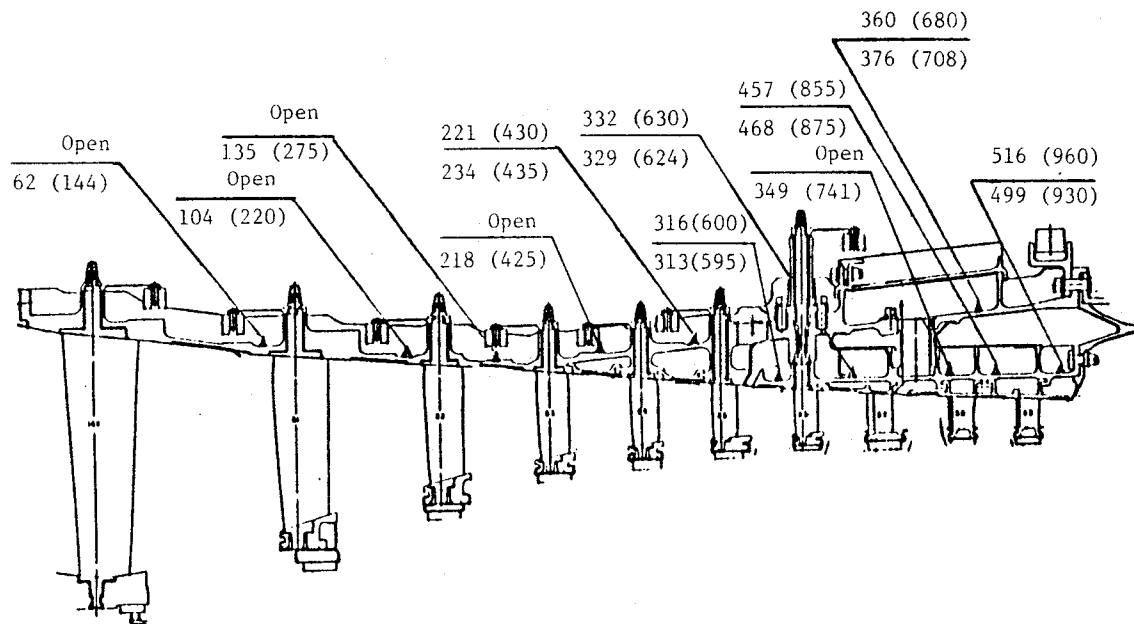


Note: All Temperatures are ° C (° F)

	T25 ° C (° F)	P25 kPa (psia)	T3 ° C (° F)	N _{Phys} rpm	%N _{Corr}	W _{Bleed Air Cooling} kg/s (lbm/s)
Test Point Conditions	29 (84)	96.6 (14.01)	535 (995)	12,602	100.43	0.41 (0.900)
Prediction Point Conditions	15 (59)	101.3 (14.7)	483 (902)	12,254	100.00	0.41 (0.907)

Figure 69. Compressor Stator Temperature Comparison With ACC On.

ORIGINAL PAGE IS
OF POOR QUALITY



Note: All Temperatures are ° C (° F)

	T25 ° C (° F)	P25 kPa (psia)	T3 ° C (° F)	N _{Phys} rpm	%N _{Corr}	W _{Bleed Air Cooling} kg/s (lbm/s)
Test Point Conditions	39 (103)	101.6 (14.73)	520 (968)	12,766	99.95	0
Prediction Point Conditions	15 (59)	99.3 (14.40)	483 (902)	12,254	100.00	0

Figure 70. Compressor Stator Temperature Comparison With ACC Off.

6.2.3 Frequencies

Rotor and stator airfoil frequencies recorded during the test compare closely to the predicted frequencies and are presented on the following Campbell diagrams, Figures 71 through 90. These Campbell diagrams show the predicted natural frequencies of the hardware in different vibratory modes such as the first flexural mode. Vibratory excitation is largely due to stimulation from nearby blade rows, with the number of airfoils determining the excitation frequency. These excitation frequencies and their more important harmonics are also shown on the Campbell diagrams. For instance, the 28 Stage 1 rotor blades (R1) cause 28 excitations each revolution (28/rev) on the stators. At the speeds where the natural frequencies match the excitation frequencies, higher resonant responses may be expected. The actual resonant responses observed during testing are spotted on the diagrams.

Maximum vibratory stresses observed on the rotor blades (R) and stator vanes (S) are presented in the tabulation below as percentages of maximum allowable vibratory limits.

<u>Stage</u>	<u>Percent Limits</u>	<u>Mode</u>	<u>Stage</u>	<u>Percent Limits</u>	<u>Mode</u>
IGV	5	1 Flex	R6	19	3 Stripe
R1	9	1 Flex	S6	5	1 Flex
S1	Bad Gage Signals		R7	37	3 Stripe
R2	23	4 Stripe	S7	44	1 Torsion
S2	5	2 Torsion	R8	76	3 Stripe
R3	35	Tip	S8	41	1 Flex
S3	12	1 Torsion	R9	37	3 Stripe
R4	20	1 Flex	S9	65	1 Flex
			R10	21	1 Flex
S4	5	1 Flex 2 Torsion	S10	Not Strain Gaged	
R5	38	3 Stripe			
S5	2	1 Torsion 2 Flex			

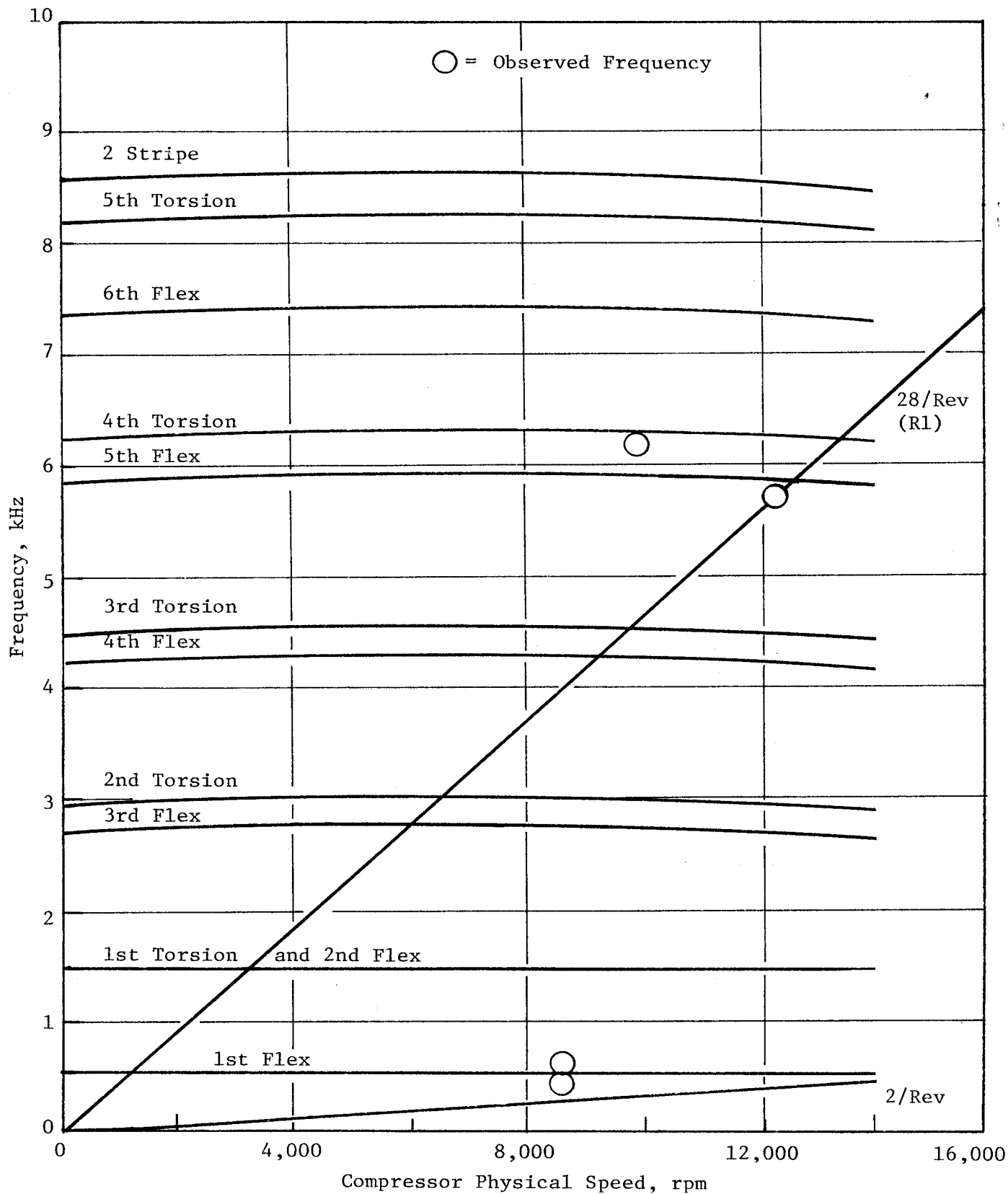


Figure 71. Inlet Guide Vane Campbell Diagram.

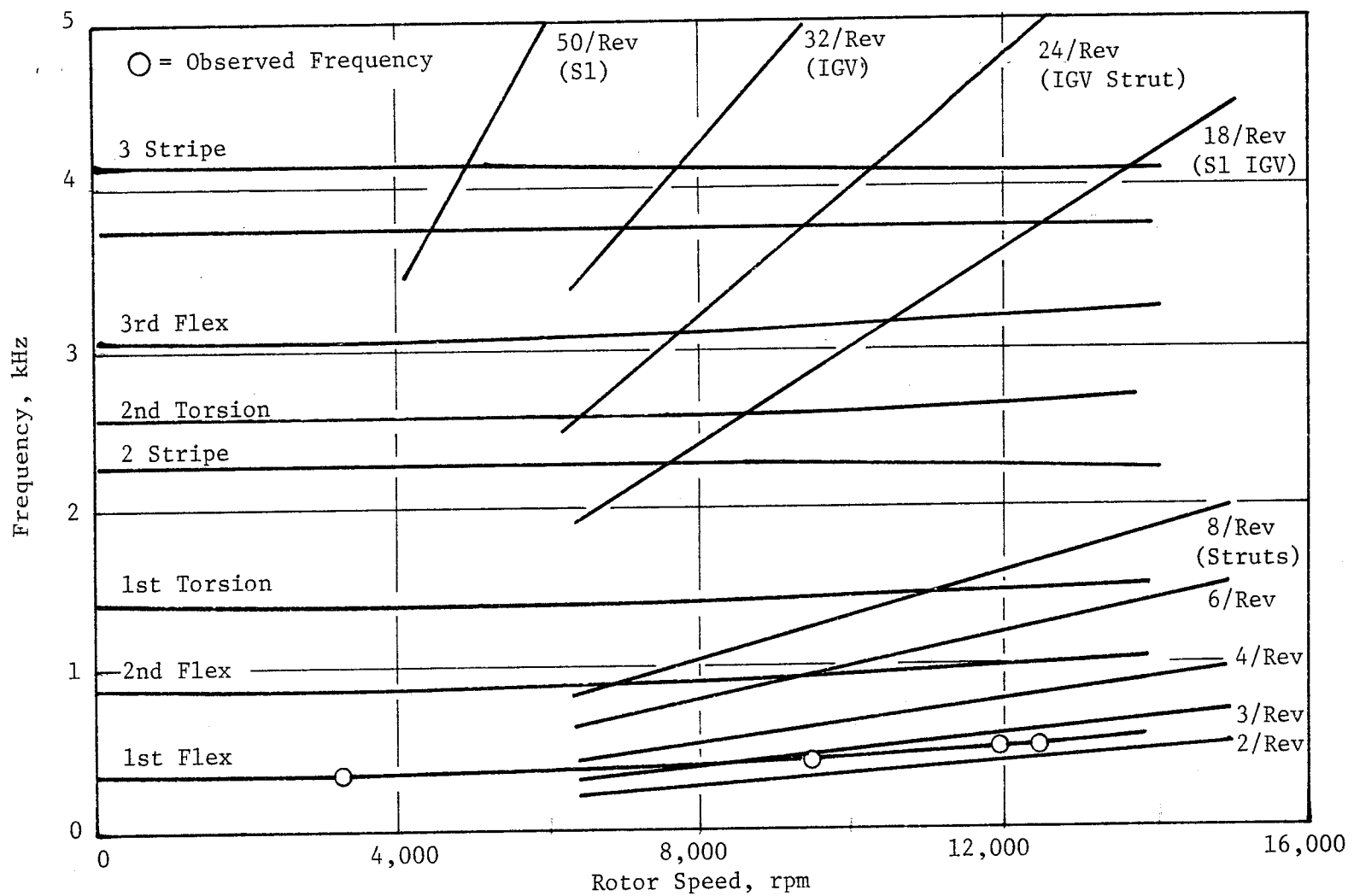


Figure 72. Compressor Stage 1 Blade Campbell Diagram.

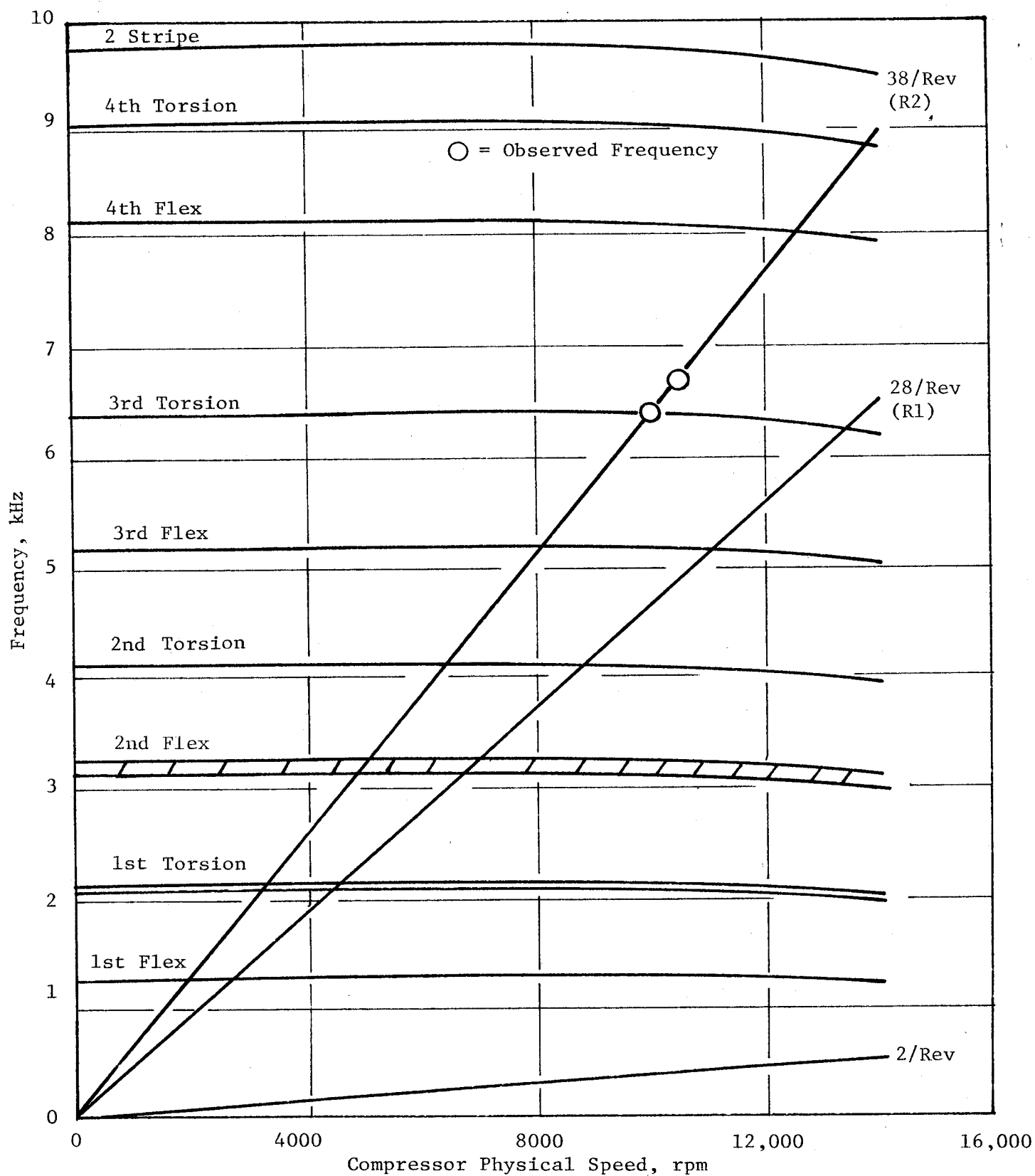


Figure 73. Compressor Stage 1 Vane Campbell Diagram.

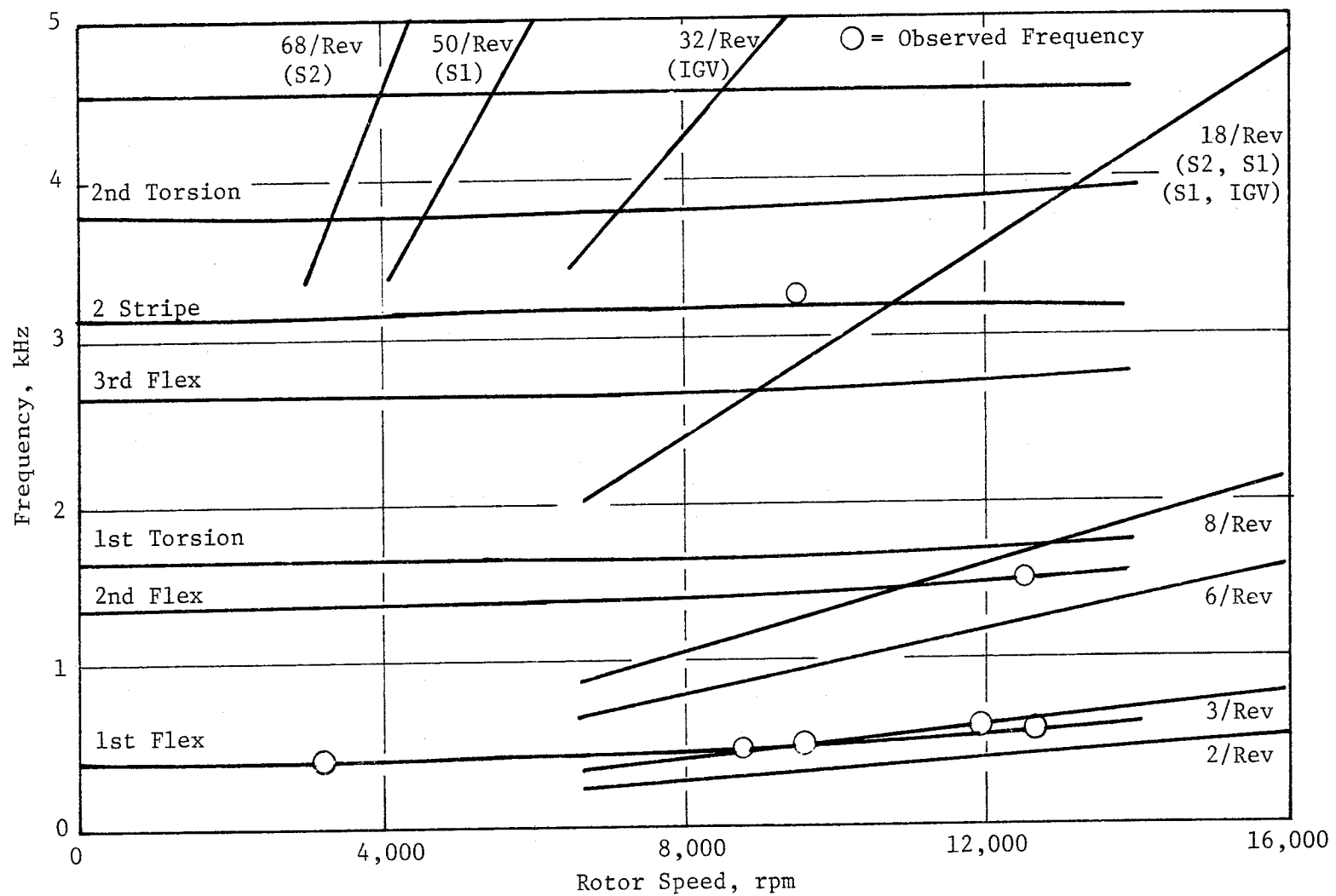


Figure 74. Compressor Stage 2 Blade Campbell Diagram.

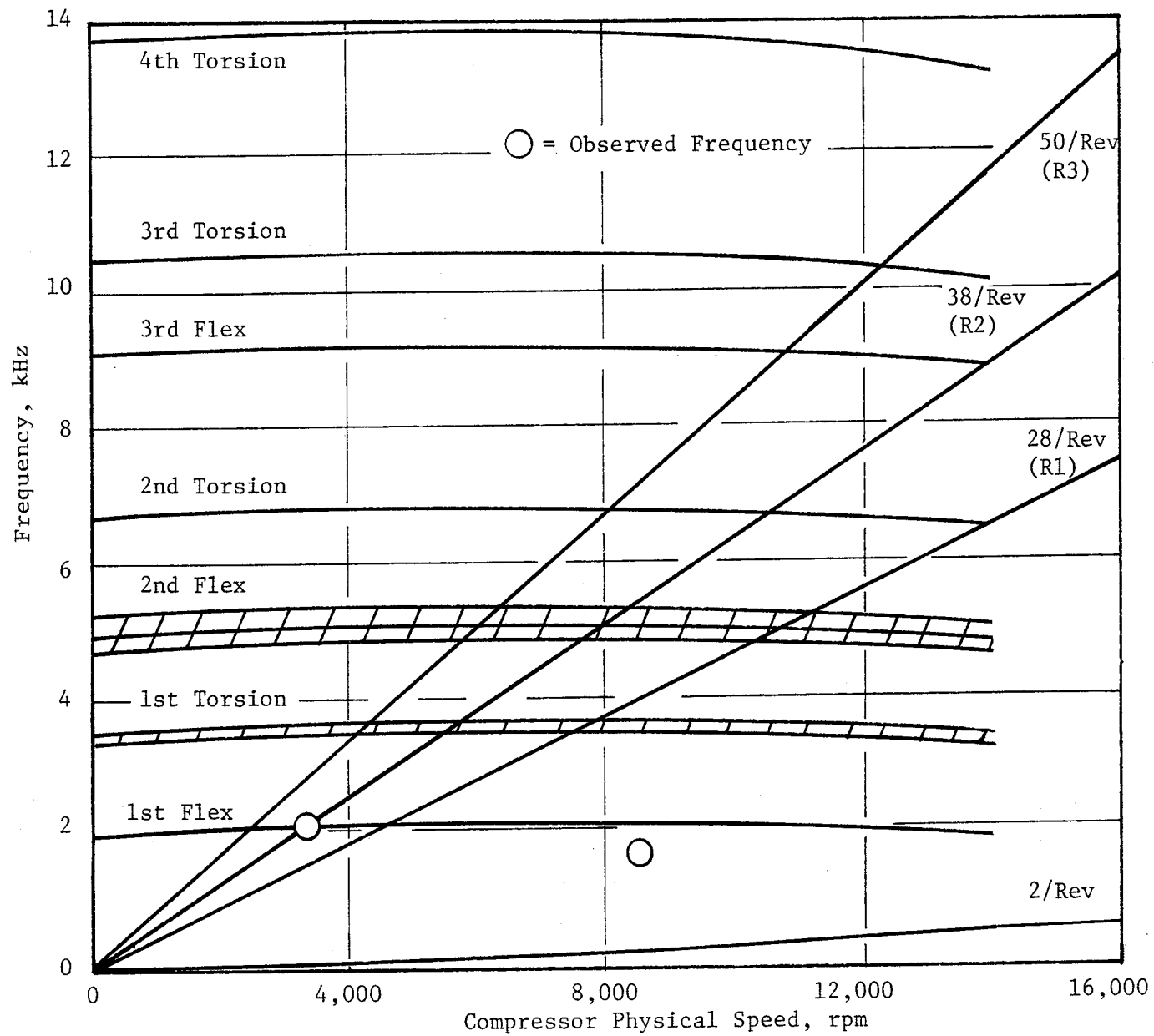


Figure 75. Compressor Stage 2 Vane Campbell Diagram.

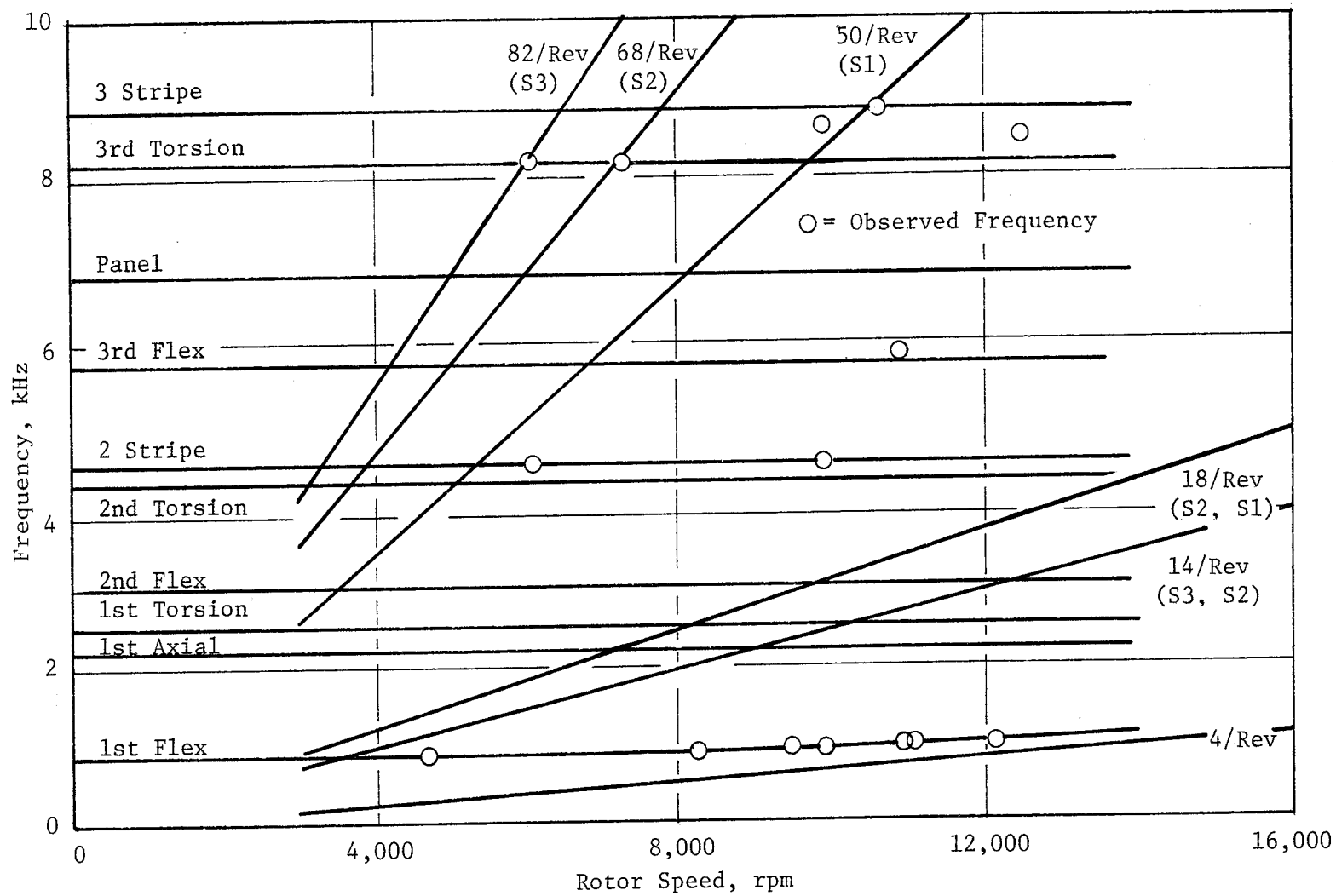


Figure 76. Compressor Stage 3 Blade Campbell Diagram.

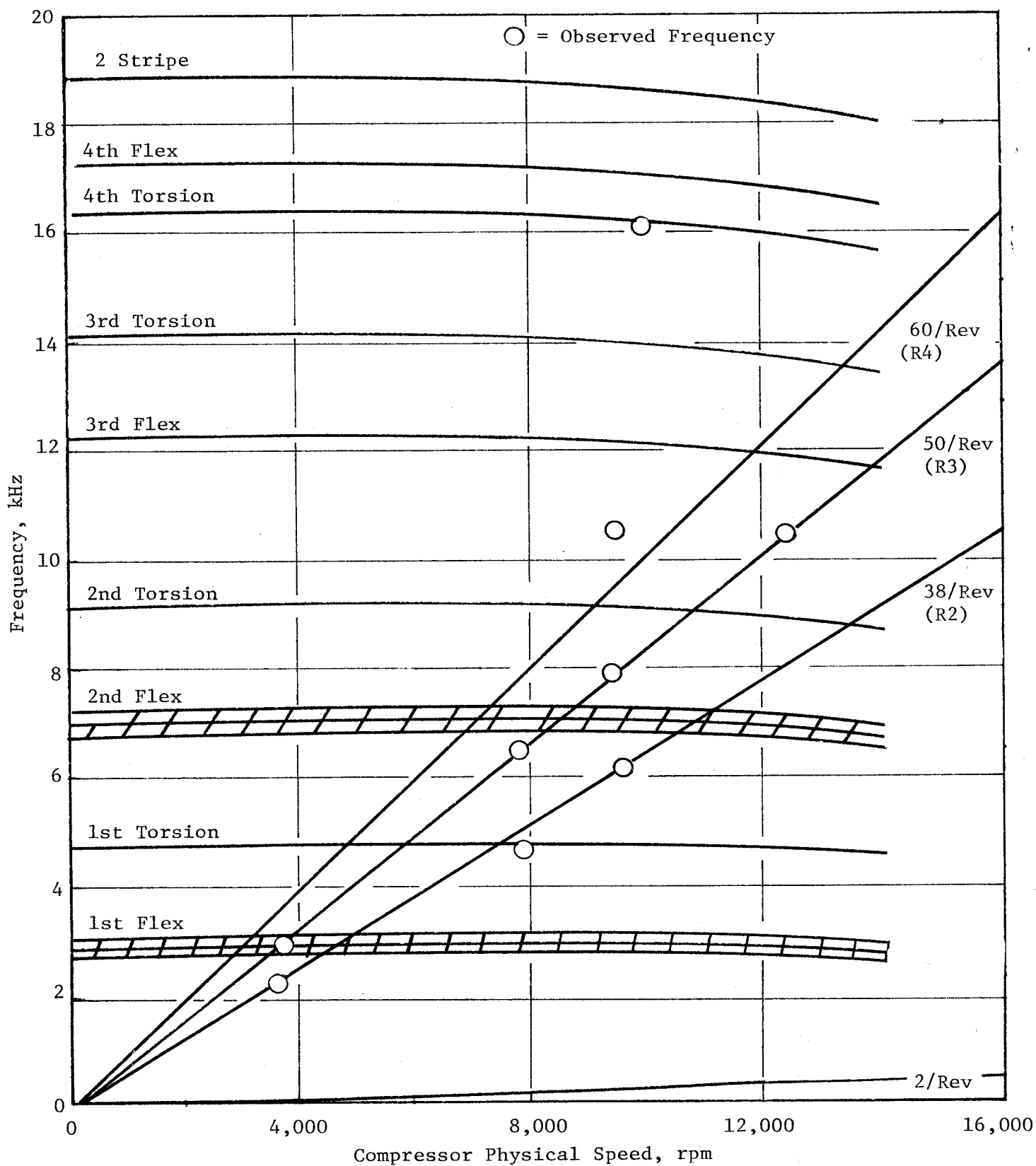


Figure 77. Compressor Stage 3 Vane Campbell Diagram.

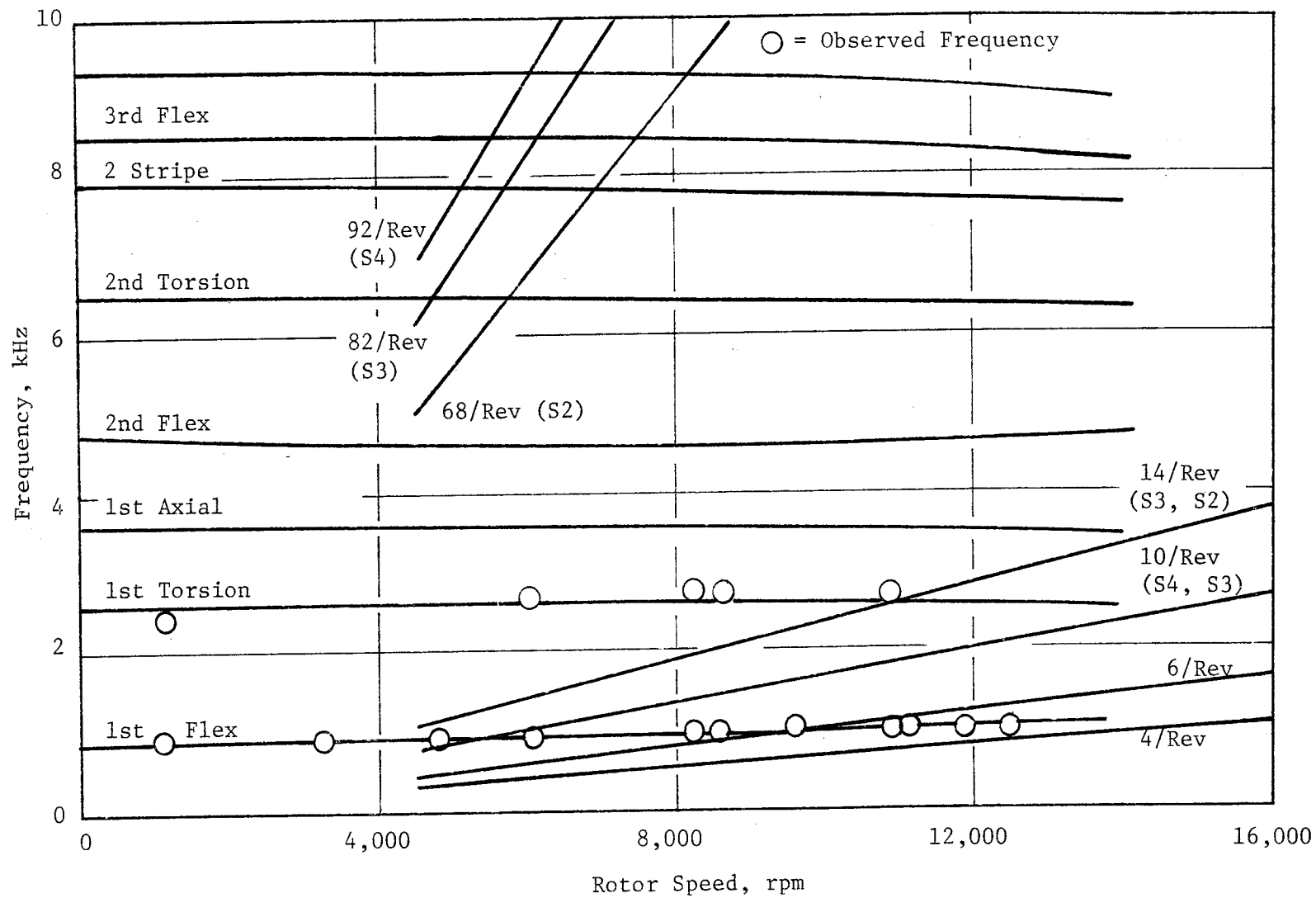


Figure 78. Compressor Stage 4 Blade Campbell Diagram.

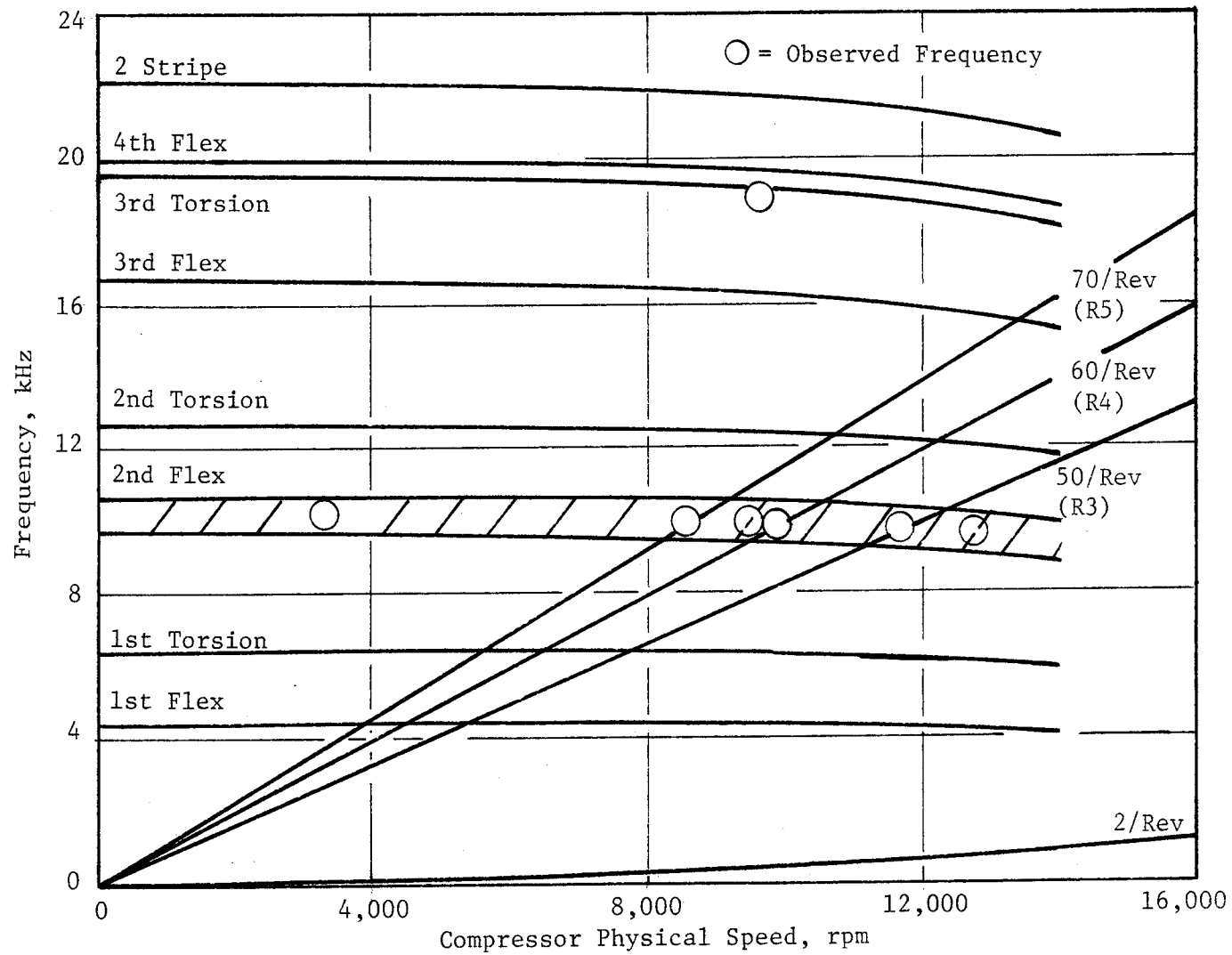


Figure 79. Compressor Stage 4 Vane Campbell Diagram.

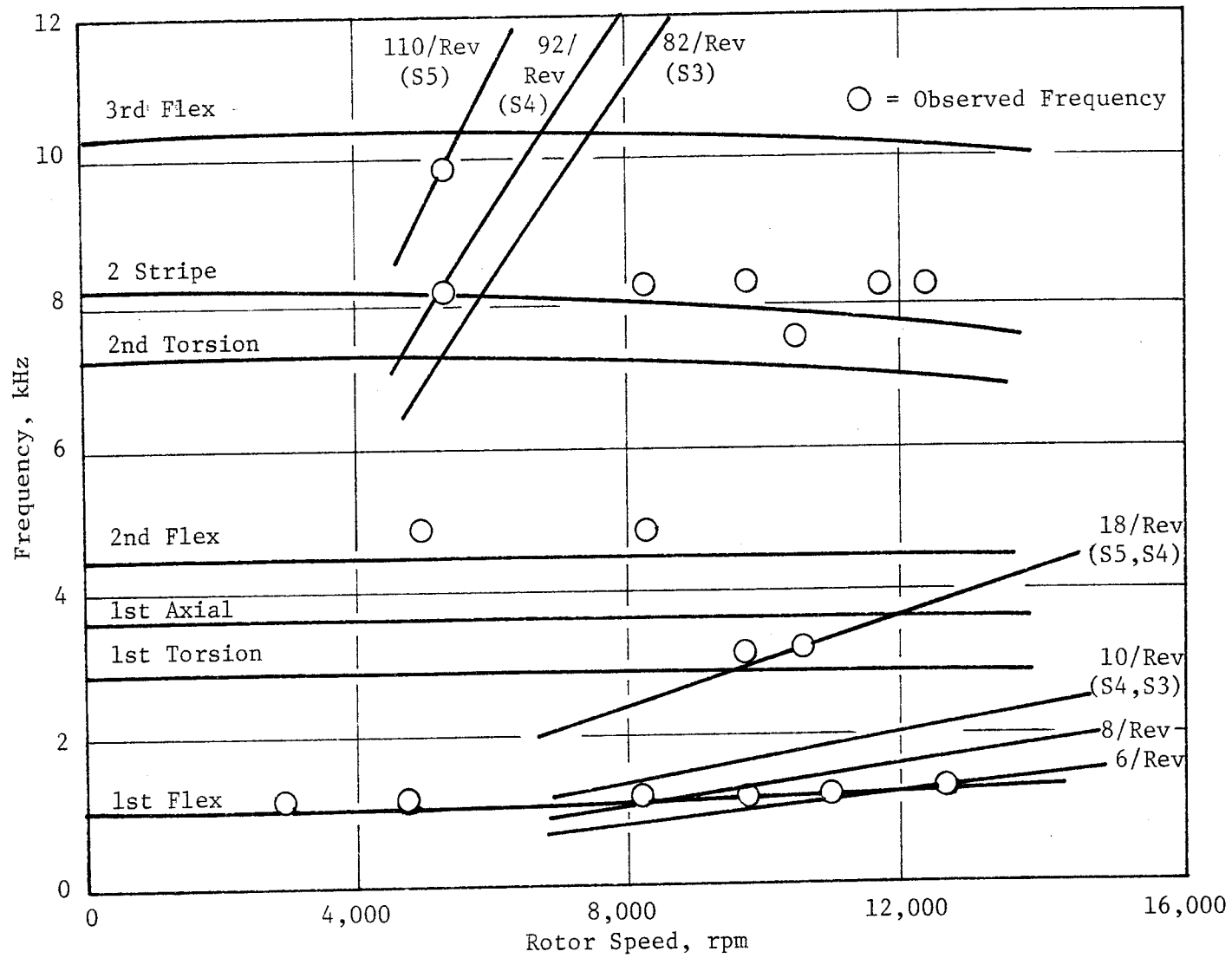


Figure 80. Compressor Stage 5 Blade Campbell Diagram.

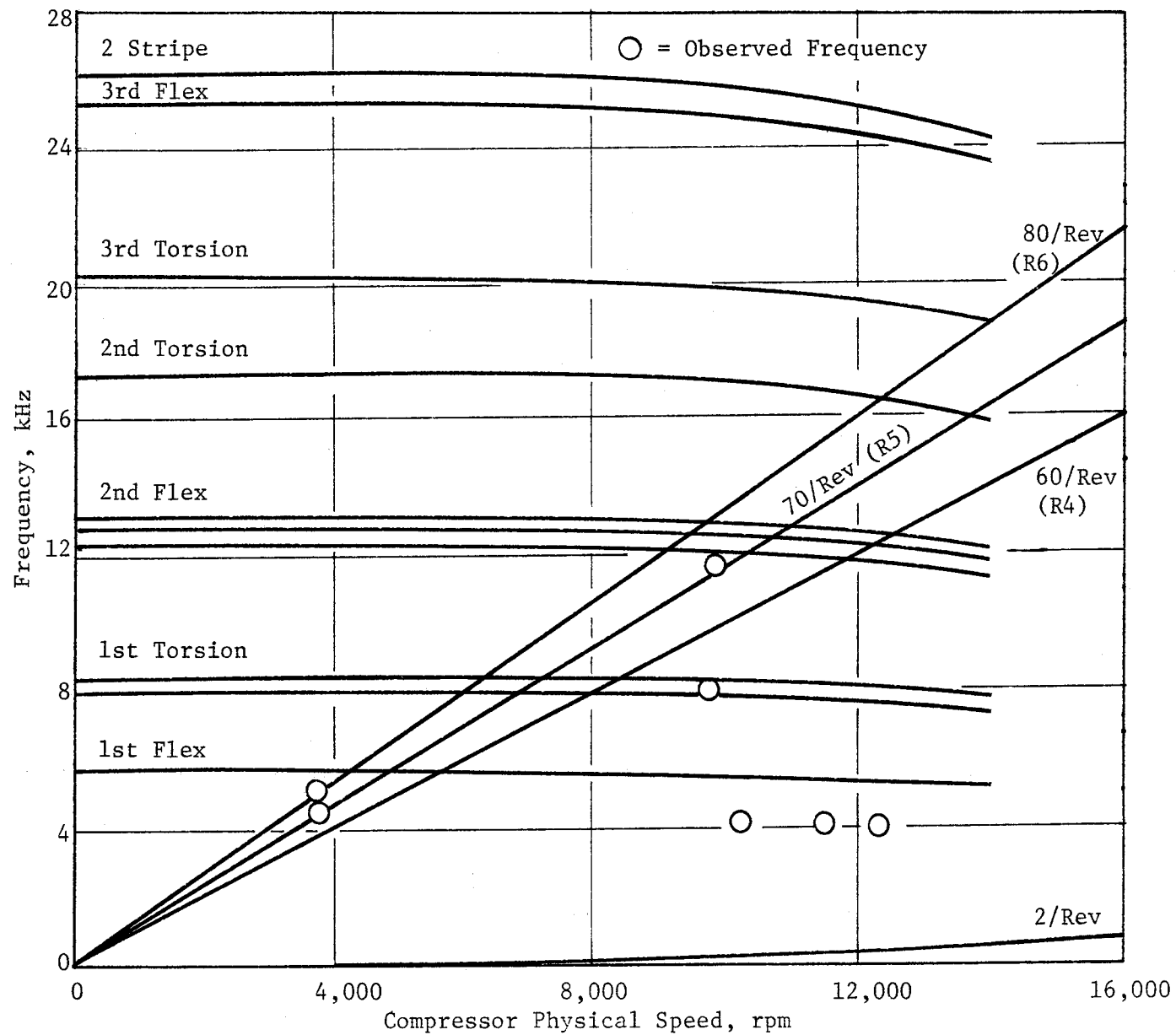


Figure 81. Compressor Stage 5 Vane Campbell Diagram.

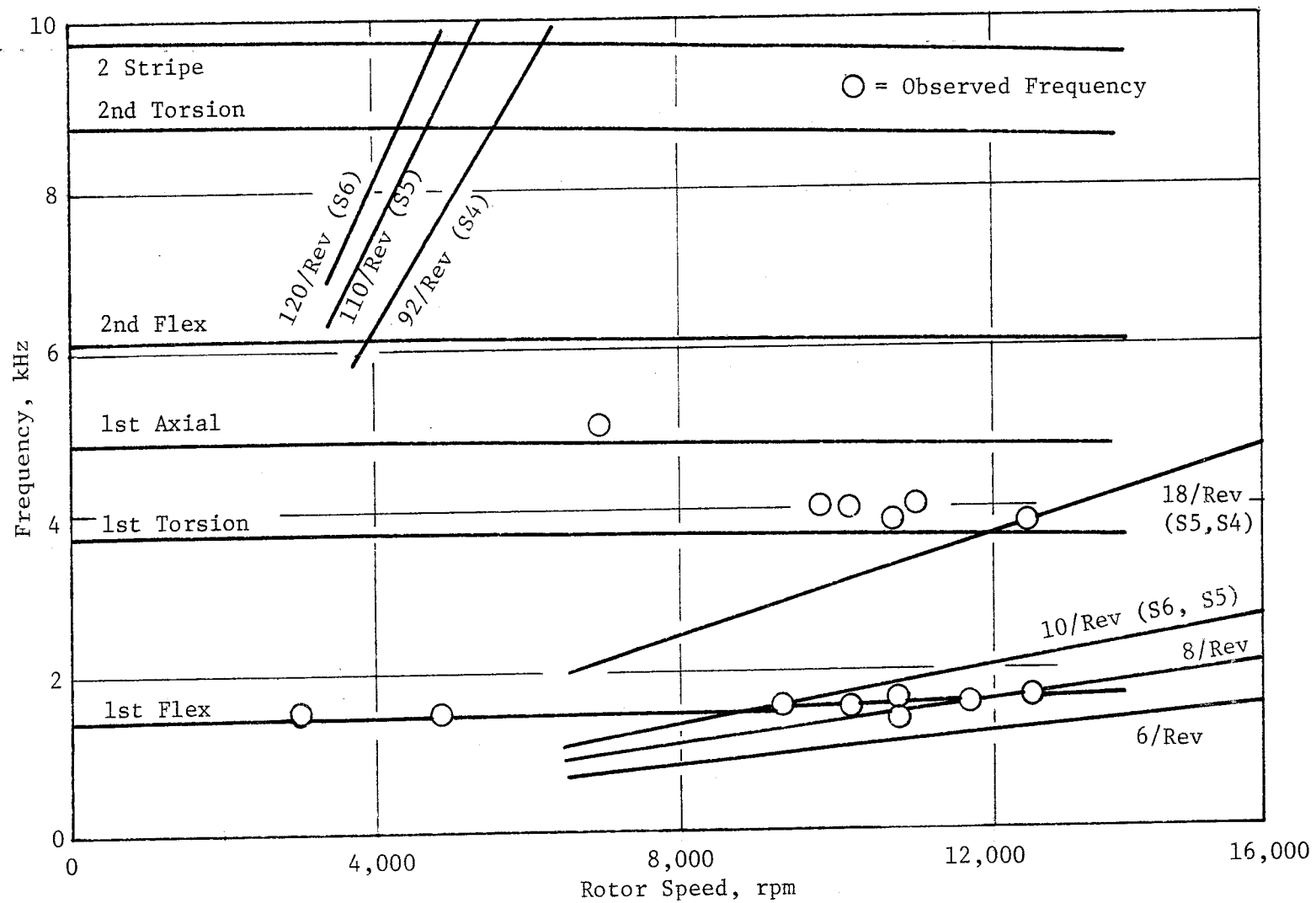


Figure 82. Compressor Stage 6 Blade Campbell Diagram.

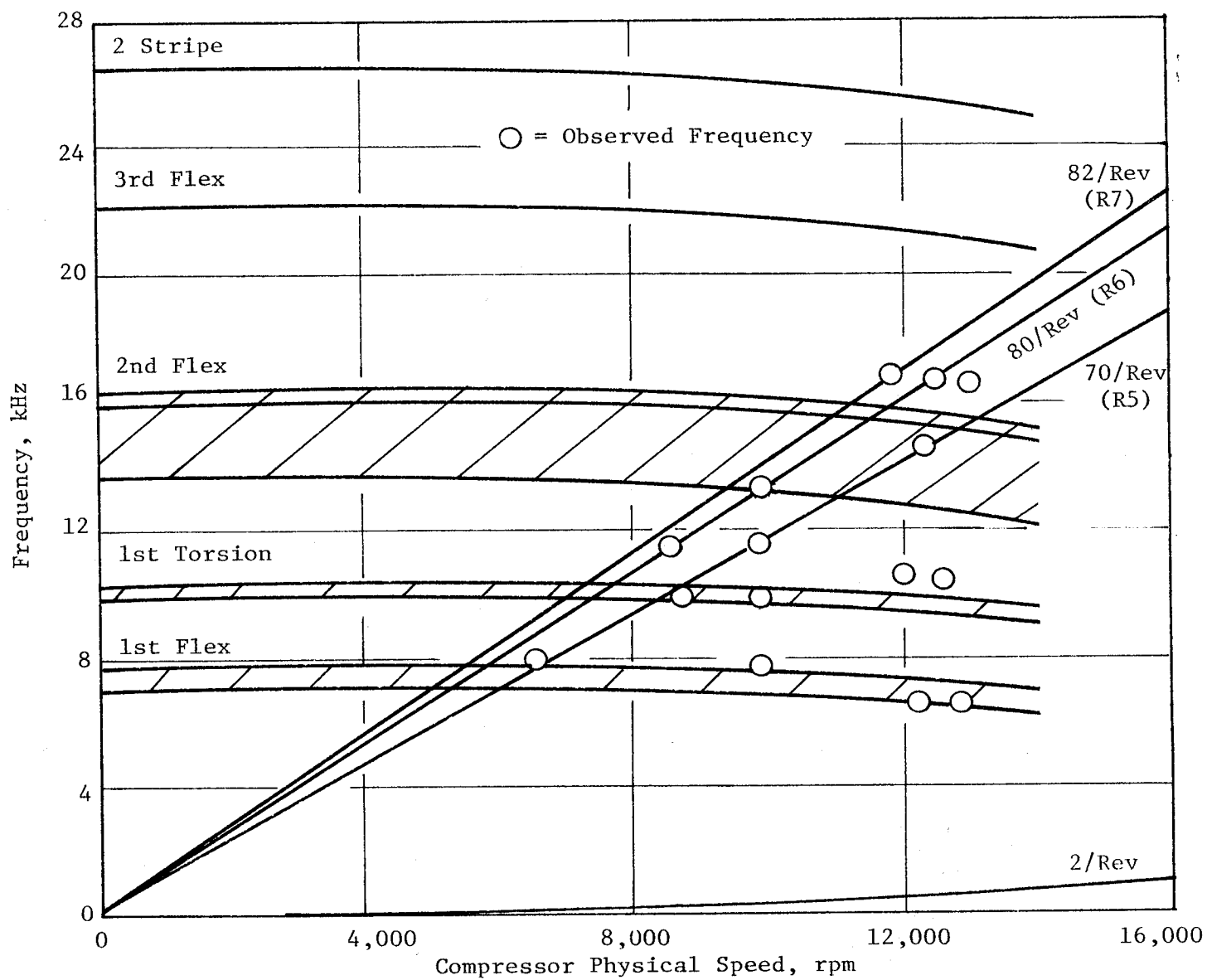


Figure 83. Compressor Stage 6 Vane Campbell Diagram.

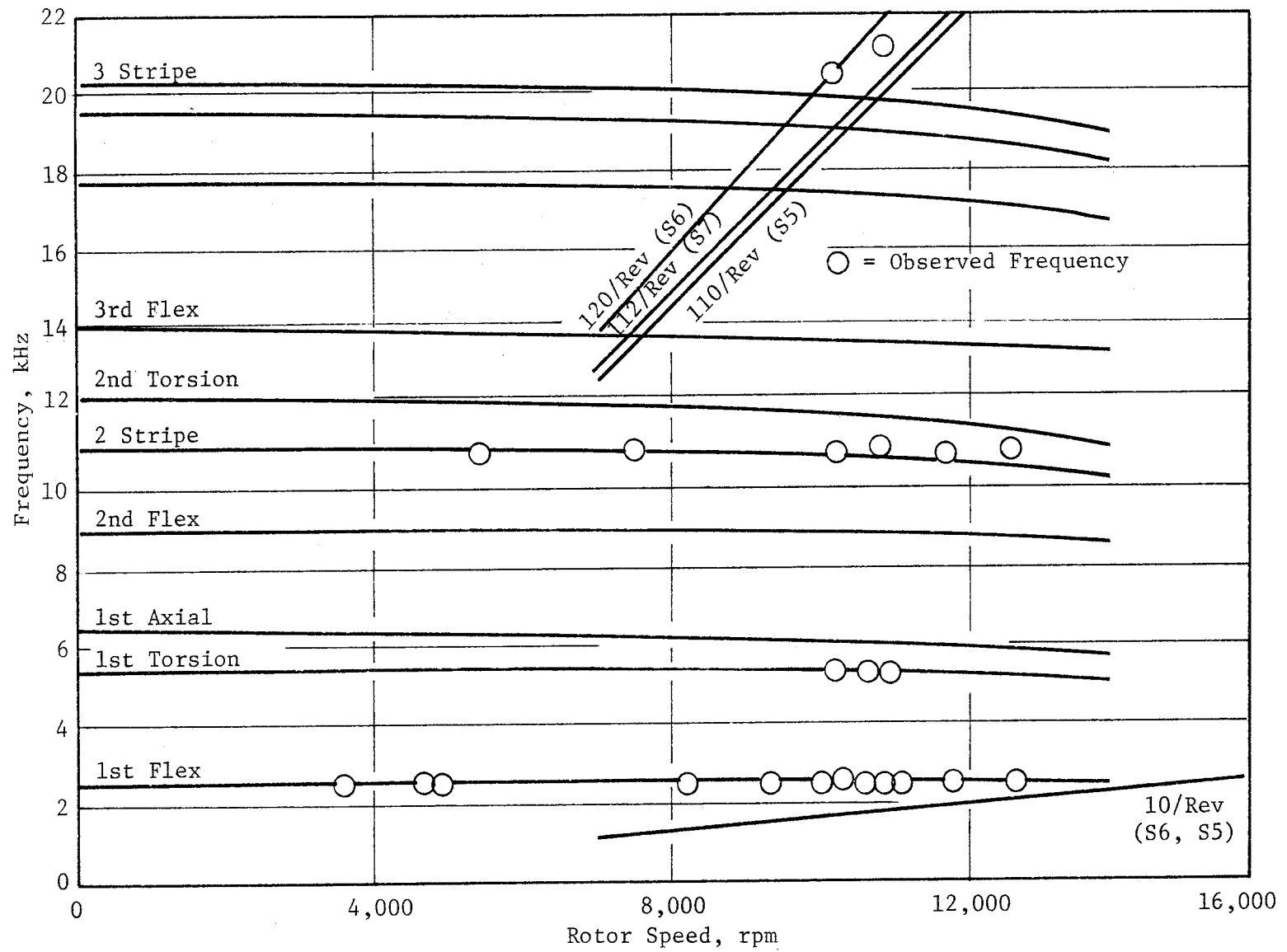


Figure 84. Compressor Stage 7 Blade Campbell Diagram.

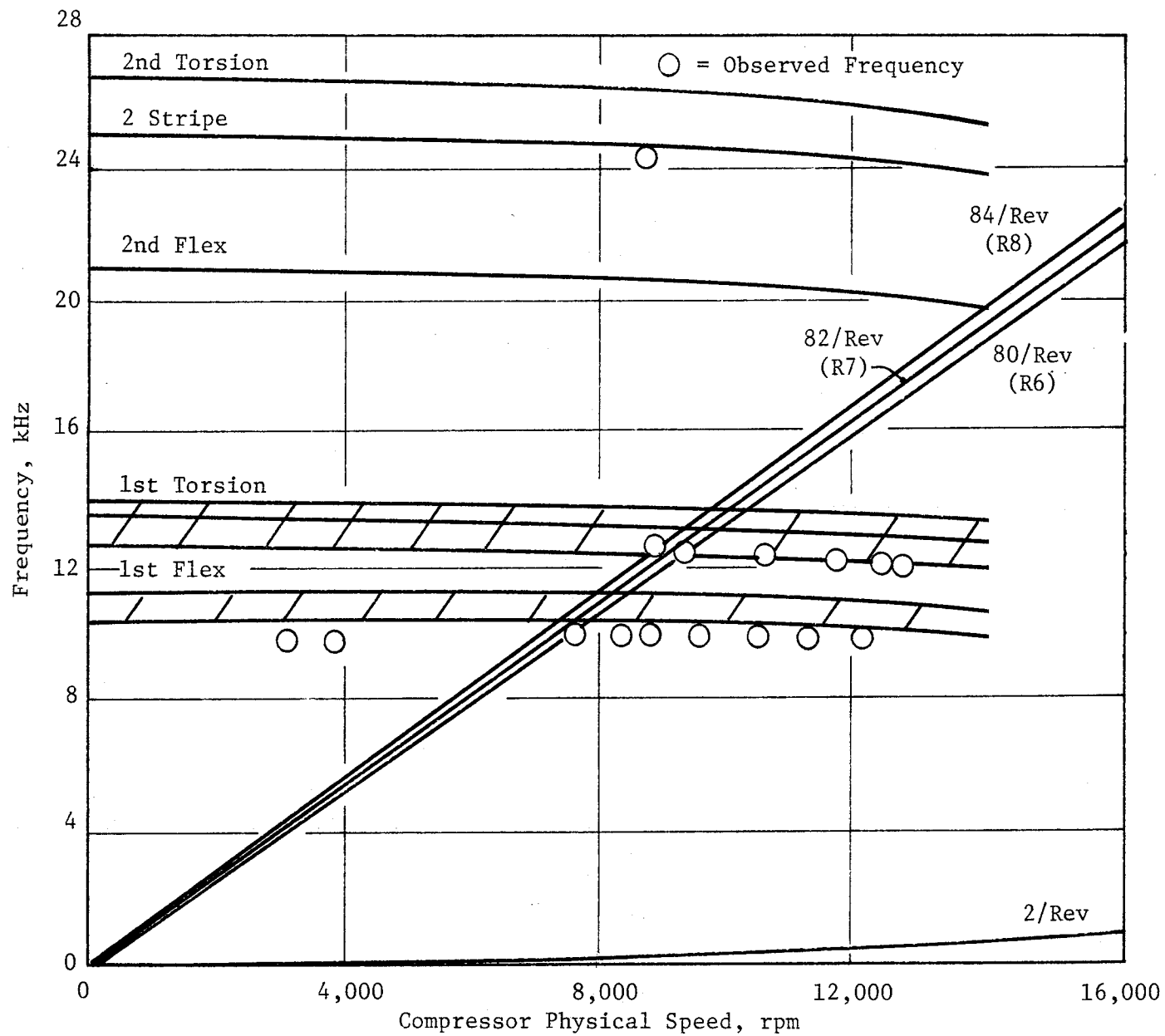


Figure 85. Compressor Stage 7 Vane Campbell Diagram.

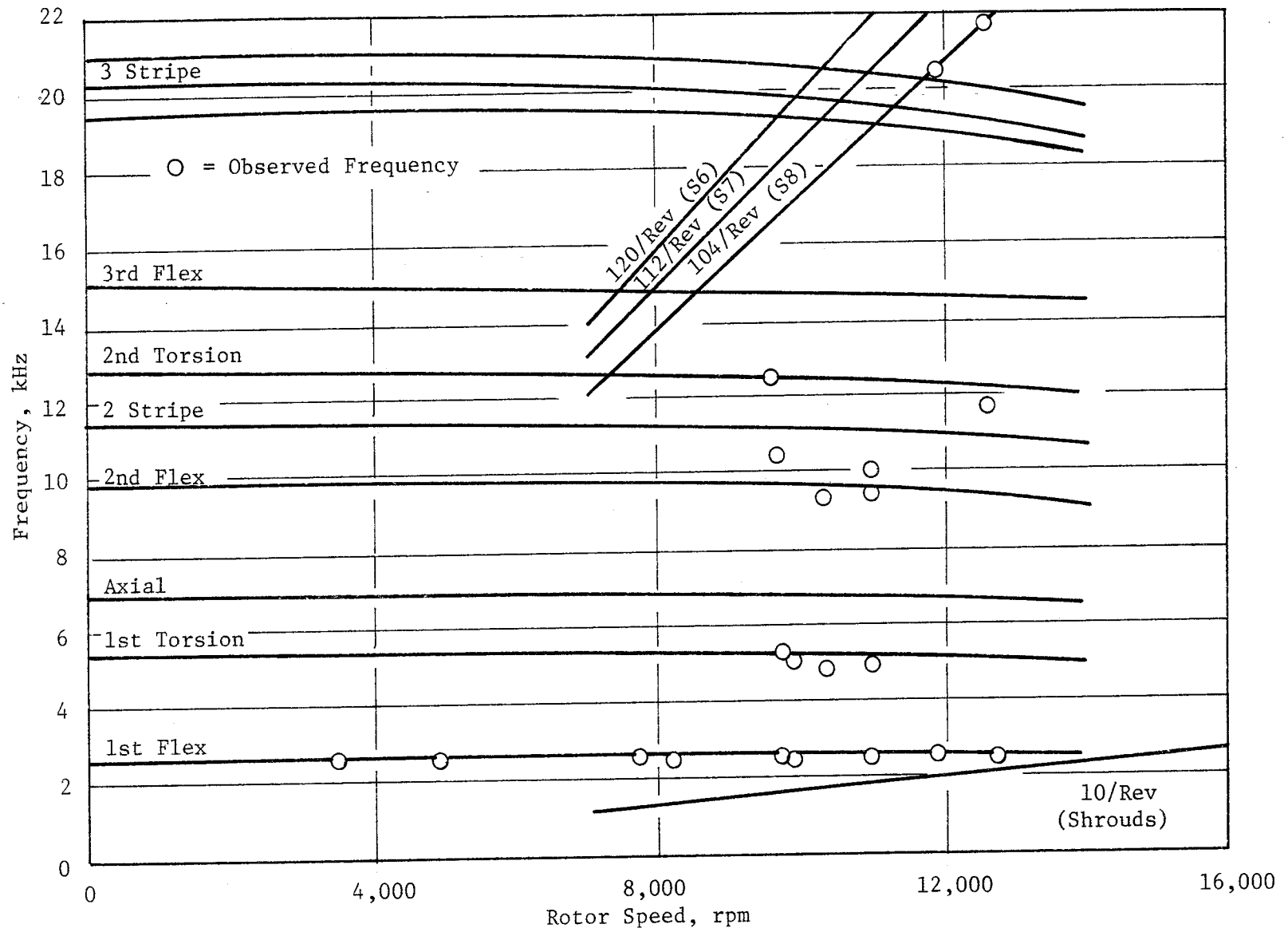


Figure 86. Compressor Stage 8 Blade Campbell Diagram.

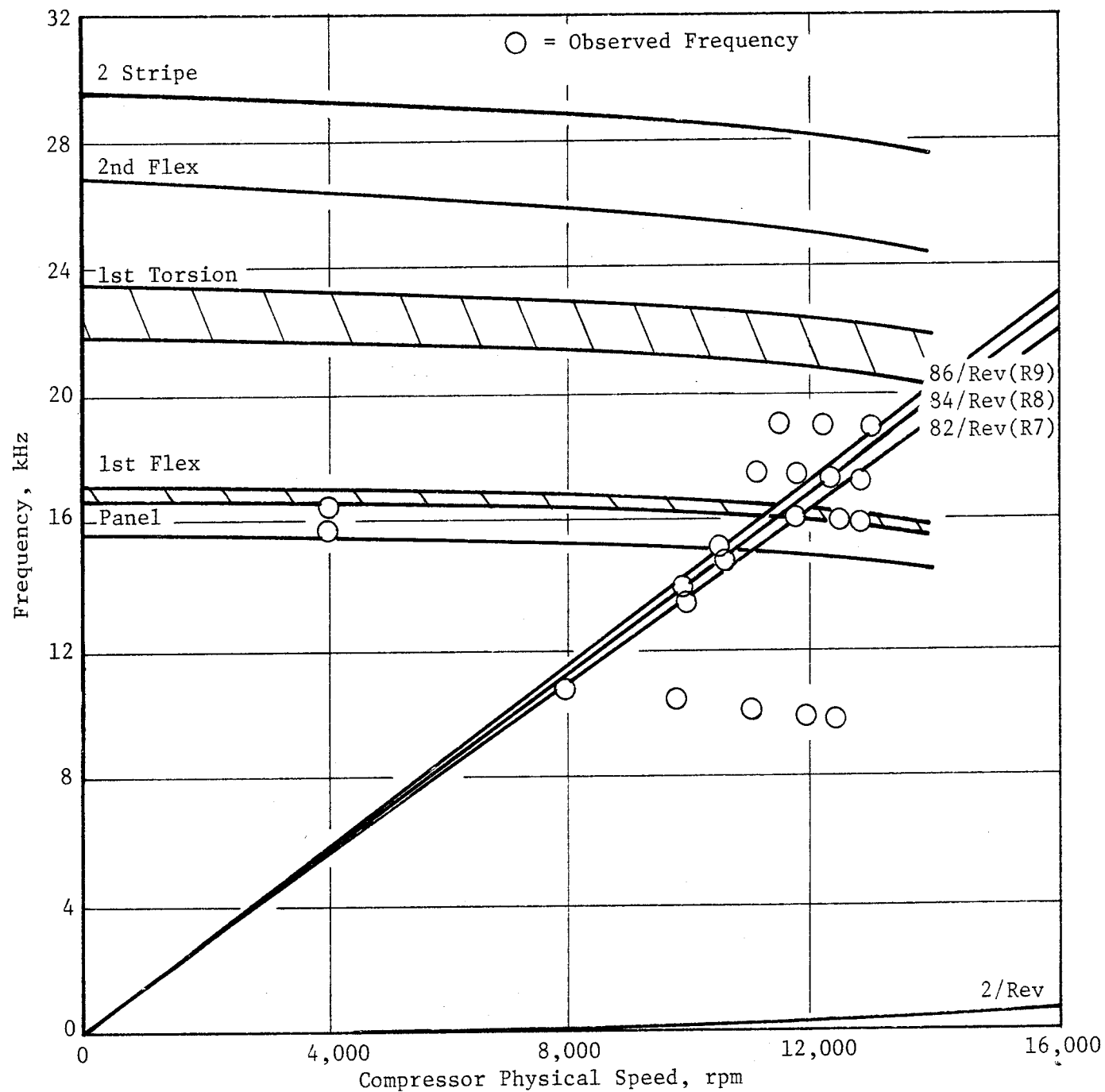


Figure 87. Compressor Stage 8 Vane Campbell Diagram.

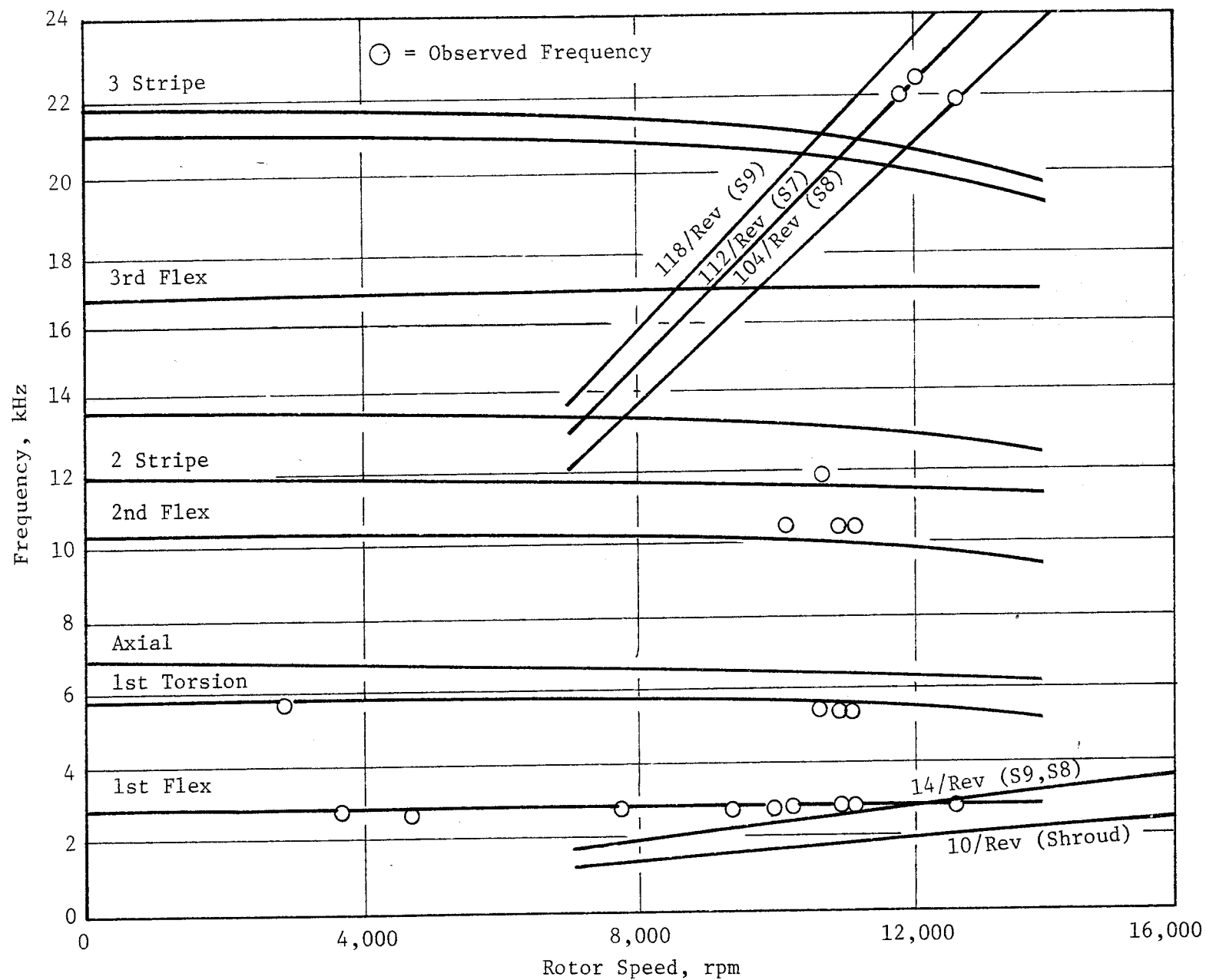


Figure 88. Compressor Stage 9 Blade Campbell Diagram.

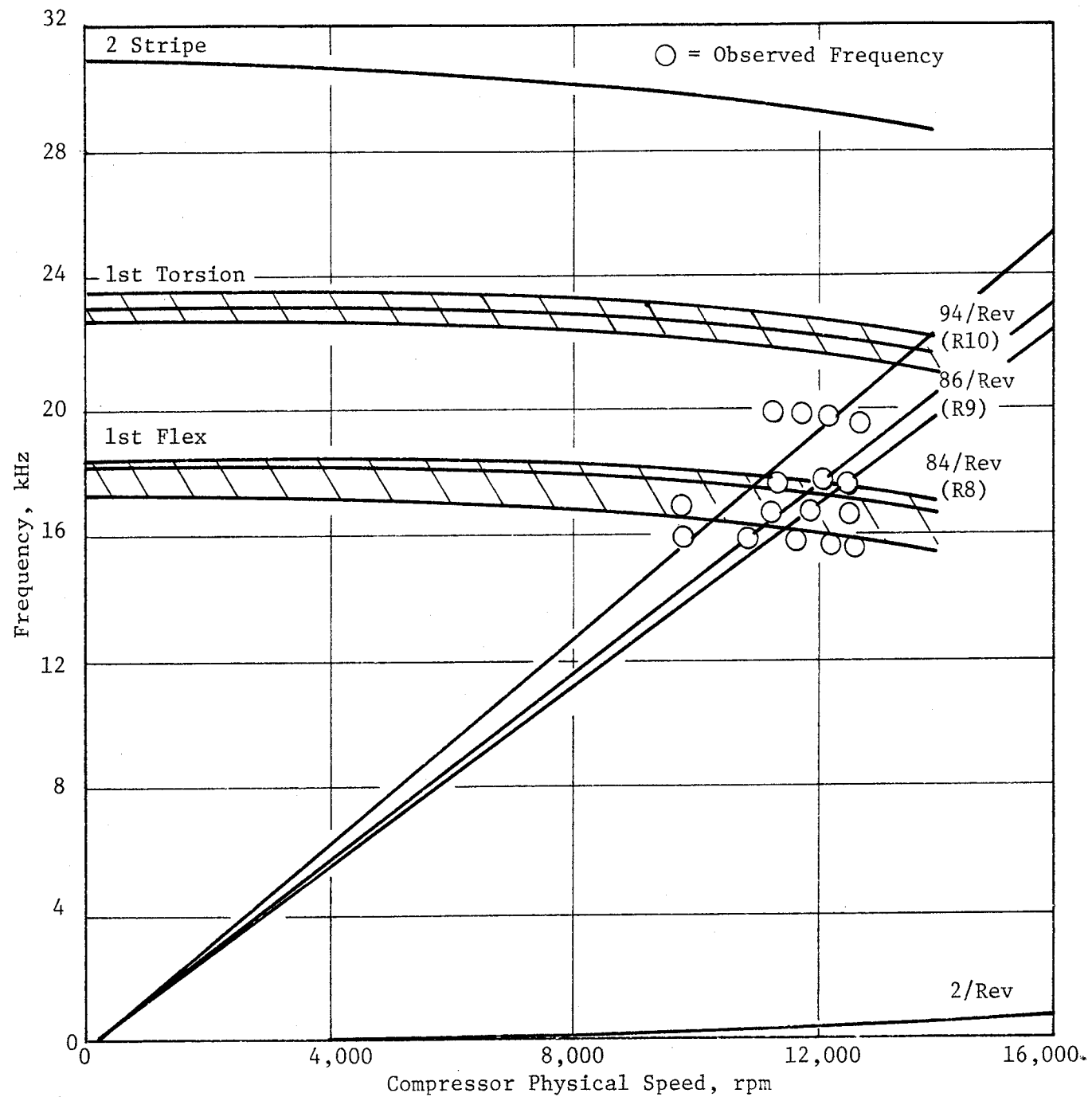


Figure 89. Compressor Stage 9 Vane Campbell Diagram.

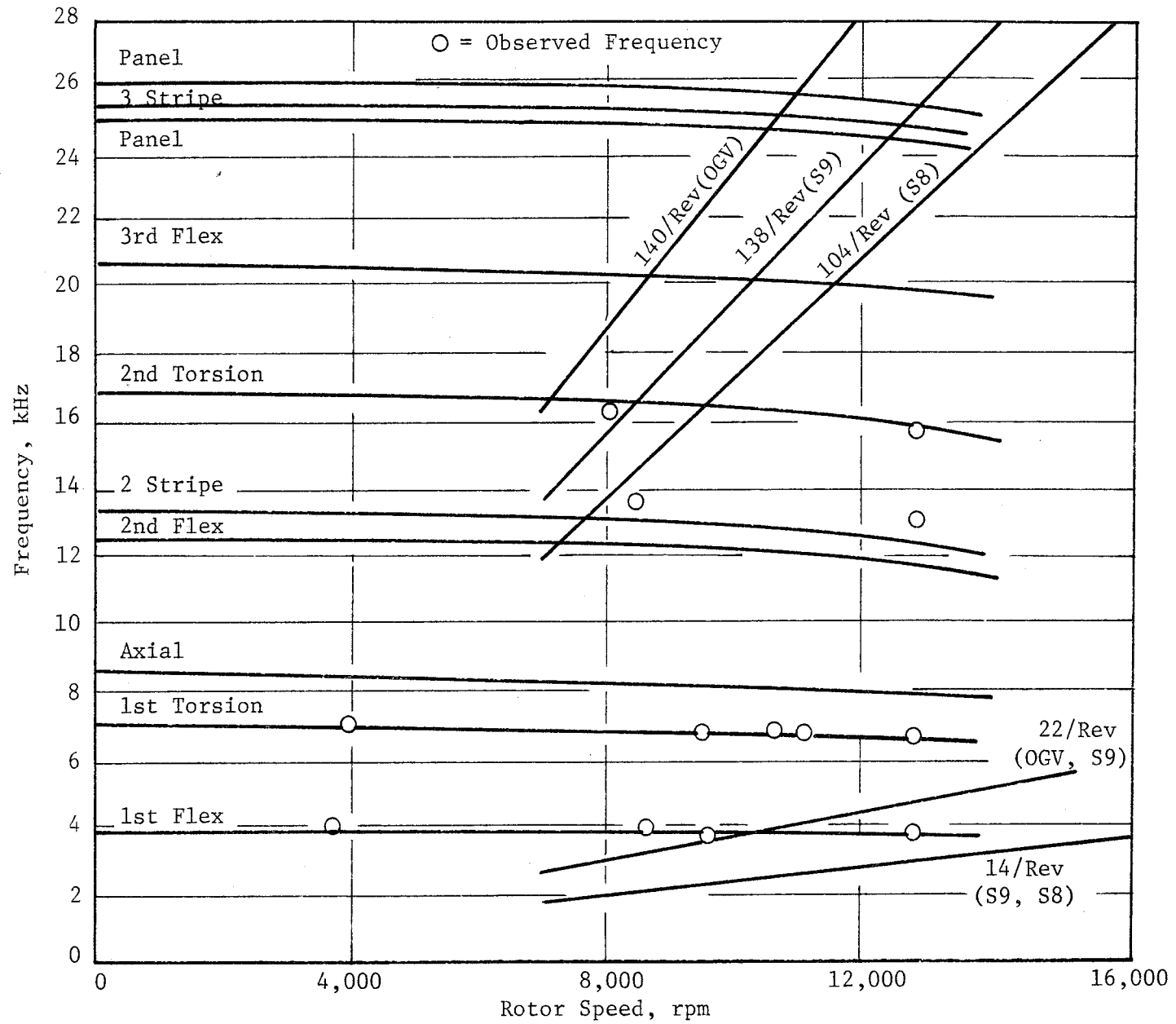


Figure 90. Compressor Stage 10 Blade Campbell Diagram.

A per-rev stimulus experienced by the aft rotor stages during the previous 10-stage rig tests was not present during the core test. As a result, more representative strain responses were observed.

The high three-stripe response observed on Rotor 8 occurred at 12,600 rpm (100.4% Nc), a speed not previously reached during rig testing. The engine gage was located in a low-response region, a factor that contributes heavily to inaccuracies in determining the actual response. This mode will not restrict ICLS testing since the core speed will not be high enough to excite it. However, further investigations are recommended if future builds of the core engine are considered. During the test, one Stator 9 gage exhibited a first torsional response of 1814.4 kPa (4 ksi) versus a scope limit of 1360.8 kPa (3 ksi), 133% limits. Another similar gage located on another vane was inactive in the torsional mode. The hypothesis that the active gage had been mislabeled could not be verified during posttest teardown. Close attention will be paid to this gage during the ICLS test. Rotor and stator stresses were unaffected by activating Stage 5 and 7 bleeds and by locking Stator 5 at a fixed position. No operational limitations to the ICLS test are forecast by the aeromechanical results of the core test.

6.2.4 Blade Tip Rubs

Compressor rubs that occurred during the test are summarized in Table XIII. Rubs on Stages 5 through 10 were detected during postrun borescoping. In addition, rubs on Stages 9 and 10 were observed on the rotor strain gage signals. The remaining rubs were noted during engine teardown inspections. Circumferential locations of the deeper rubs are compatible with wax checks taken during engine buildup. Factors contributing to the rubs were circumferential eccentricities, tight buildup clearances, higher-than-predicted inlet temperatures, and an unexpected hot rotor restart during the test. None of the rubs were severe enough to require repair prior to the ICLS buildup. The rubbed hardware is considered representative of normal postflight hardware; therefore, no performance degradations are attributed to the rubbed condition.

Table XIII. Description of Rubs - Aft Looking Forward.

<u>Stage</u>	<u>Comments</u>
1	No rub
2	75° Kiss rub at 1 o'clock
3	90° Kiss rub at 12 o'clock
4	Kiss rubs at 12 and 7 o'clock
5	Full-chord rub over 360°, 0.30 mm (0.012 in.) deep. Rubs first detected during borescoping after the 8/11/82 mechanical checkout run.
6	Partial to full-chord rubs over 350° varying in depth from 0.10 mm (0.004 in.) to 0.30 mm (0.012 in.), first observed during posttest borescoping.
7	Partial to full-chord rubs over 360°; (0.33 mm (0.013 in.) maximum depth, first observed during posttest borescoping.
8	Full-chord rub over 360°, 0.30 mm (0.012 in.) deep, first observed during posttest borescoping.
9	Partial to full-chord rubs over 320°, 0.25 mm (0.010 in.) maximum depth, first observed on strain gages during a hot rotor reburst, 8/12/82.
10	Partial to full-chord rubs over 345°, 0.13 mm (0.005 in.) deep, observed on strain gages during Start 6 and during subsequent hot rotor reburst, 8/12/82.

6.3 COMPRESSOR AERODYNAMIC PERFORMANCE

6.3.1 Overall Performance Summary

The high pressure ratio compressor tested in the E³ core fully performed to expectations at all speeds and exceeded the efficiency goals established for the ICLS test vehicle program. Tests related to compressor performance characteristics included: stator schedule optimization, ACC system exercise, fixed Stator 5 study, Stage 5 customer bleed effects investigation, starting fuel schedule and windmill start studies, and a Reynolds number effect investigation.

Overall performance was measured by four 5-element rakes at the compressor inlet downstream of a simulated transition duct and frame, and by five

6-element rakes at the diffuser exit. The diffuser pressure drop was automatically accounted for by the data reduction program using a diffuser loss correlation deduced from rig tests. For this reason, the reported pressure, ratio and efficiency represent OGV exit (or diffuser inlet) values. The diffuser pressure loss equals 0.3 point in overall efficiency at the design point.

Final performance calibration data were recorded up to a corrected speed of 98.1% using the final stator schedule and the exhaust nozzle that approximated the ICLS operating line (about 3% to 4% below the FPS design operating line). The engine was operated at roughly atmospheric inlet conditions. Stators 5 and 6 were fixed. The ACC air that was bled off the Stage 5 exit for cooling the compressor rear case was fully on at speeds above 76.5% and was off at lower speeds. The Stage 5 and 7 turbine cooling bleeds were on for all speeds. Customer and starting bleeds were not used.

The compressor operating line overall performance data are compared with the second 10-stage component test results in Figure 91. The data shown represent the measured compressor pressure ratios and efficiencies, with the inlet pressure adjusted to the inlet guide vane (IGV) leading edge and with the exit pressure adjusted to the OGV trailing edge so that it is consistent with the definition used by the engine performance model. As shown on the map, the overall efficiency of the core engine compressor was about two percentage points higher than the results of the second 10-stage component test (10B) at all speeds. No efficiency adjustments have been made to explain the differences in hardware condition and in operating environment. The 10B rig was in a deteriorated condition after extended testing, including 140 stalls, whereas the core engine was more representative of a normal broken-in engine. Of the 2.0-point improvement, 1.2 points were due to tighter tip clearances, fewer vane-mounted sensors, and a higher inlet Reynolds number index (RNI). The remaining 0.8-point improvement resulted from the better hardware quality and improved blading design of the rear stages. These stages had higher hub camber in Stators 7 to 9 and 2° higher stagger in Rotors 8 through 10. (Reference the NASA Compressor Design Report CR-165558.)

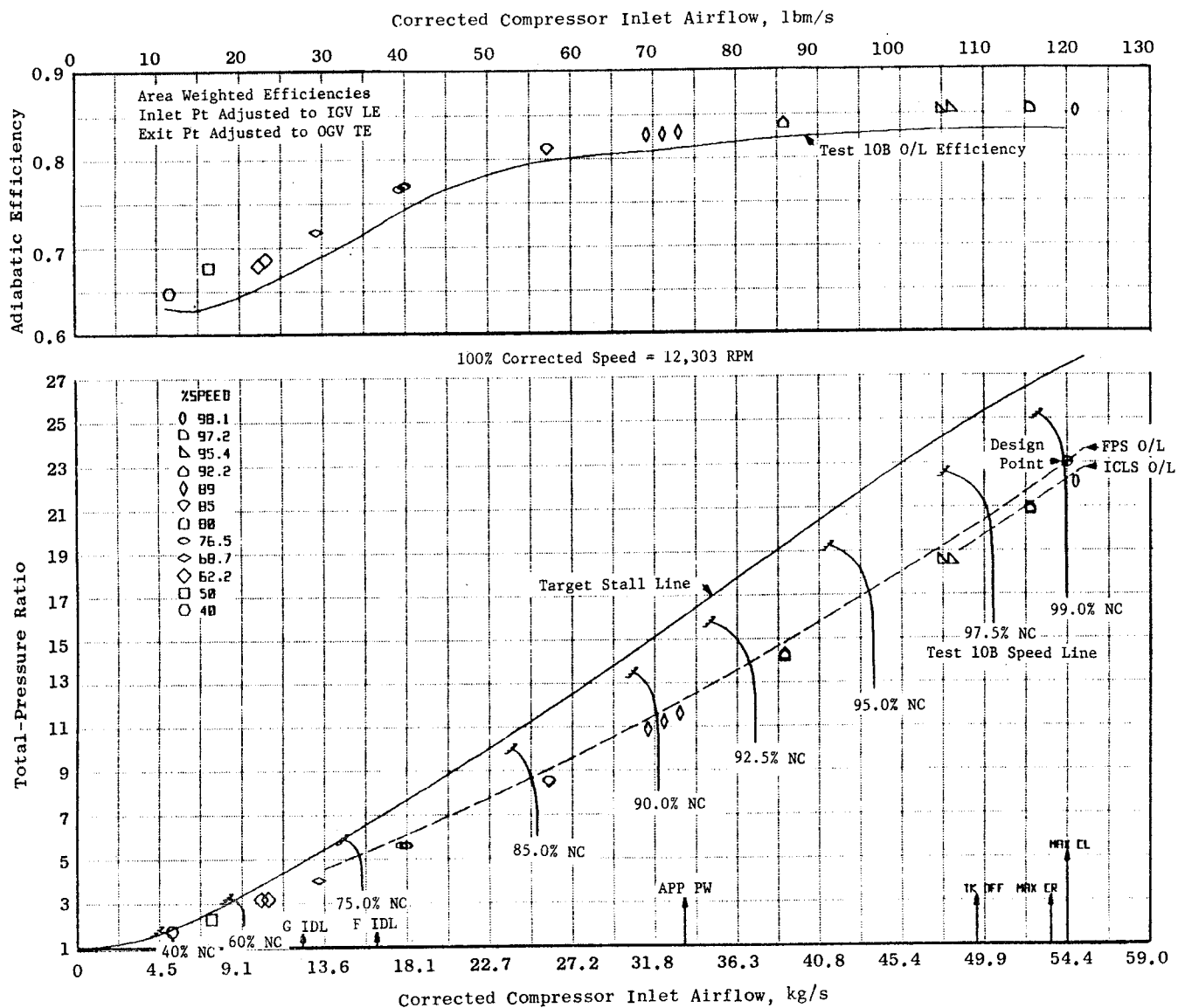


Figure 91. HP Compressor Performance Map.

ORIGINAL PAGE IS
OF POOR QUALITY

It is seen that the design flow occurred at approximately 98% speed. At speeds above takeoff (96% speed), the corrected flow of the core engine was more than 4% higher than for the second 10-stage build compressor. Two-thirds of that increase resulted from the more open IGV settings used; the remaining difference, approximately 1.5%, could be attributed to Reynolds number effects, tighter clearances, differences in blading design and hardware quality. At lower speeds, the flow difference resulted solely from hardware changes because the vane angle settings of the front variable stators were the same for both configurations below 80% speed.

A comparison of the test results at the E³ maximum cruise operating point with the ICLS and the FPS performance goals is provided in Table XIV. The first line is the as-measured data with the diffuser exit total pressure adjusted to the OGV exit. The second line gives the data with the measured inlet total pressure adjusted (for unsensed inlet duct and rake losses) to the IGV leading edge plane in order to be consistent with the E³ cycle bookkeeping. The data in this line are comparable with the data presented in Figure 91. The third line includes additional adjustments for interstage instrumentation, for losses caused by having extra variable stators, and for RNI differences between the test conditions and the maximum cruise conditions. No adjustments have been made for the difference in blade tip clearances and minor dirt accumulation on the airflow surfaces. As determined from the test data, pre- and posttest inspections, the average tip clearance in the core engine was approximately 0.046 cm (0.018 inch). In the FPS, the average tip clearance goal is 0.038 cm (0.015 inch). Minor dirt deposits on the flowpath and airfoil surfaces were noticed during teardown.

It is seen that at maximum cruise condition (RNI = 0.5) the demonstrated, fully adjusted adiabatic efficiency was 85.6% (90.2% polytropic). This was higher than the ICLS demo engine goal and was within half a point of the fully developed FPS engine maximum cruise goal of 86.1% adiabatic (90.6% polytropic). No deterioration of compressor performance was observed after the initial break-in run.

Details of adjustments to the measured data in Table XIV are as follows: An efficiency increase of 0.2 point was estimated to be possible in the FPS

engine having no vane-mounted aero sensors or airfoil strain gages, having Stators 5 and 6 fixed, and having no Stage 7 start bleed port. A loss of 0.3% in inlet pressure was predicted due to the drag of the inlet rakes; this was the equivalent of 0.1 point in efficiency and also increased the corrected airflow and pressure ratio. An efficiency penalty of 0.3 point was assessed against the data when correcting from the test RNI of 1.0 to the engine cruise RNI of 0.5. Finally, a loss in total pressure of 1.5%, undetected by the inlet rakes, was known (from component testing) to occur in the inlet and transition ducting. Adjustment of the as-measured inlet pressure for this effect increased the efficiency by approximately 0.6 point and also increased the corrected airflow and pressure ratio.

Table XIV. Maximum Cruise Operation Point.

	Corrected Compressor Airflow, $W/\sqrt{\theta/\delta}$		Pressure Ratio P3/P25	Adiabatic Efficiency $\eta_{ad}, \%$	Polytropic Efficiency $\eta_p, \%$
	kg/s	(lbm/s)			
As Measured	52.6	(116.0)	21.03	84.5	89.3
Adjusted for Unsensed Inlet Duct and Inlet Rake Losses	53.5	(118.0)	21.40	85.2	89.9
Also Adjusted for Interstage Instrumen- ation Loss, Variable Stage 5, 6, and RNI	53.5	(118.0)	21.40	85.6	90.2
ICLS Goal	53.5	(118.0)	21.70	85.1	89.9
FPS Goal	53.5	(118.0)	22.40	86.1	90.6

Engine starting tests were highly successful. It was possible to begin the light-off sequence at low core corrected speeds and to accelerate to the 4% takeoff thrust, ground idle setting (62% speed) within 29 seconds after ignition. Rapid starts were accomplished without the use of either Stage 7

demonstrated without experiencing compressor stall. A few, very mild low-speed compressor rotating stalls (not surges) were observed when Stage 5 stators were accidentally misset and when inlet pressure was accidentally reduced too far. During normal operation the compressor was completely stall-free. It is believed that this version of the compressor should have at least as much, and probably more, stall margin as the second 10-stage component test rig (10B) had. However, core engine testing was not used to demonstrate this.

6.3.2 Stator Schedules

Because of improved pumping in the middle stages relative to that in the second 10-stage test rig, the core engine compressor stator schedule was adjusted near design flow by opening the IGV 3° and closing Stator 1 by 2° . This improved the balance of aerodynamic loadings between the front and middle stages at high speeds. These adjustments were blended into the baseline schedule (established from the second 10-stage test) near 80% design speed. Stator 5 was fixed at 3° closed from its design value at all speeds, whereas it had varied between 3° open to 15° closed during the second 10-stage component test. A comparison of the final core engine stator schedule with the baseline schedule is shown in Figure 92. The new schedule is gangable through a torsion bar actuation system and will be incorporated into the stator control system of the ICLS engine. The stagewise loading distribution resulting from this schedule was close to the original design intent, with Stages 7, 8, and 9 having the highest loadings. The front and rear blocks of the stages were well matched, even though the measured flow at speed was higher than design intent.

Figure 93 shows the changes in compressor overall efficiency which resulted from adjusting the IGV and Stator 1 vane angle settings as noted above and from fixing Stator 5 at 3° . It is noticed that by using the second 10-stage test stator schedule, compressor efficiency began to drop below its peak value at an inlet airflow rate of approximately 47.2 kg/s (104 lbm/s), resulting in a +0.5-point efficiency loss at maximum cruise flow. This loss was due to the increased pumping in the middle stages, substantially unloading the first stage below its peak efficiency point. By opening the IGV and closing Stator 1, the mismatch between the front and middle stages was

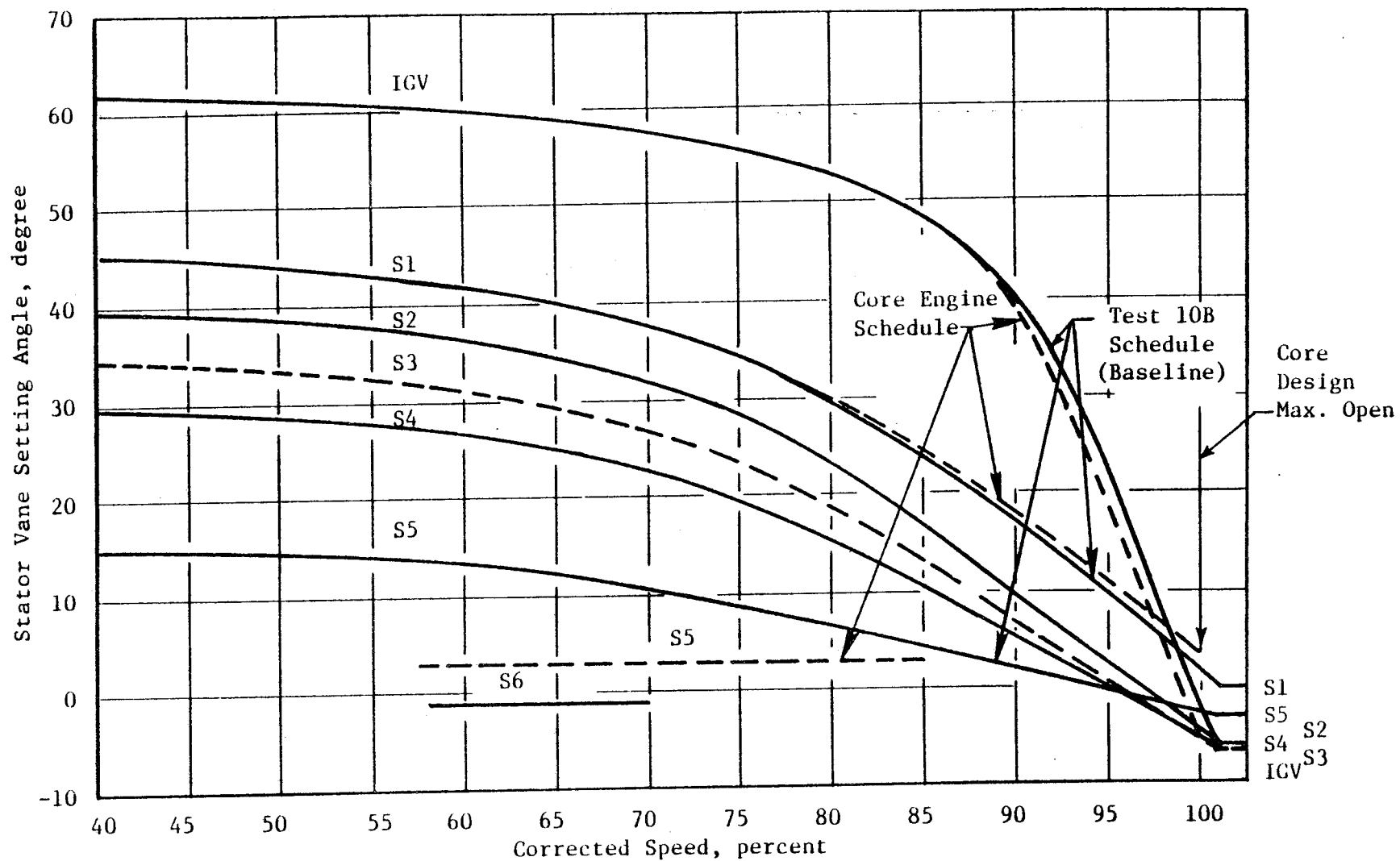


Figure 92. Comparison of Compressor Stator Schedule.

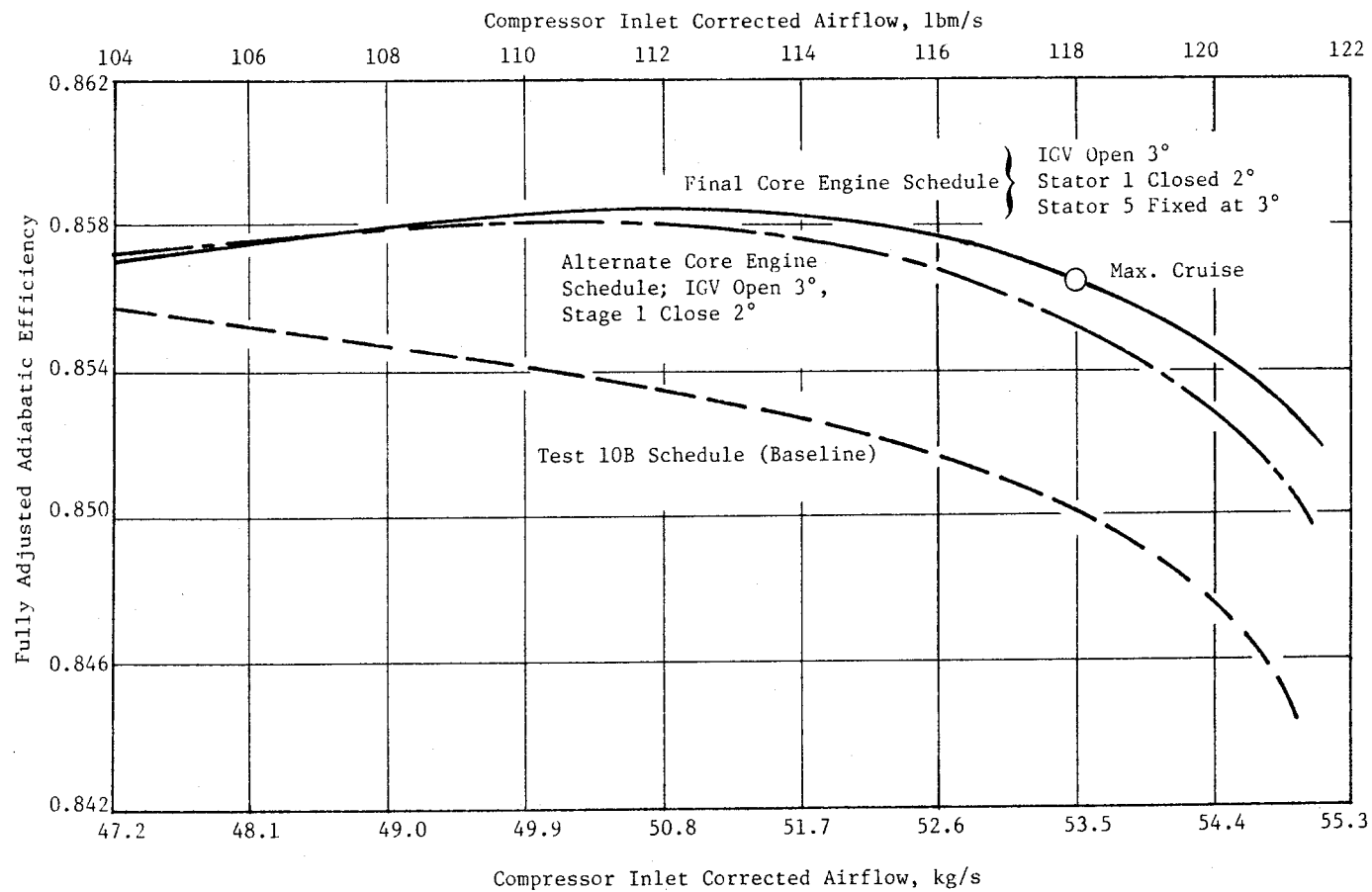


Figure 93. Core Engine Test Stator Schedule Optimization.

corrected. Fixing Stator 5 at 3° closed, rather than tracking the more open high-speed angle settings of the second 10-stage test schedule, further improved the loading distribution of the middle stages. As a result, maximum cruise operating point compressor efficiency increased more than 0.6 point with the final core engine stator schedule. Because the baseline schedule produced good performance at lower speeds, the IGV and Stator 1 angle adjustments were gradually reduced to zero near 80% speed.

Due to the fact that compressor inlet airflow at speed was mainly governed by the IGV position, core engine airflow increased when the IGV was opened 3°. A comparison of the flow-speed relationship of the final core engine schedule with the baseline schedule is shown in Figure 94. These data indicated a flow increase of about 3% at speed.

The engine start procedure was optimized first with Stator 5 tracking and then with Stator 5 fixed. Inlet pressure was set at ambient and starting bleed was not used. During optimization exercises, the engine was ignited at 25% speed and idled at 62% speed. The fuel schedule was progressively increased until a 46-second start (29 seconds from light-off to idle) was accomplished. One additional start was performed with 4% more fuel enrichment to demonstrate fuel margin. Two locked Stator 5 starts were performed, one with this same enriched fuel schedule and procedure and the other with the light-off speed reduced from 25% to 20%. Data showed little change in starting time. There was no indication of compressor stall in any of the starts, and all indications were that fully satisfactory engine starting characteristics could be achieved with a fixed Stator 5 and without interstage bleed.

6.3.3 Internal Performance

Front block (Stages 1 through 6) aerodynamic performance data were computed from the same inlet conditions used in the overall performance calculations (measured by Plane 25 rakes and adjusted to IGV leading edge) and from the Stator 6 leading edge plane data recorded by the vane-mounted instrumentation. Stator 6 inlet total pressure was measured at five immersions corresponding to centers of equal annulus area, and total temperature was measured at the first, third, and fifth immersions. Rear block (Stages 7 through 10)

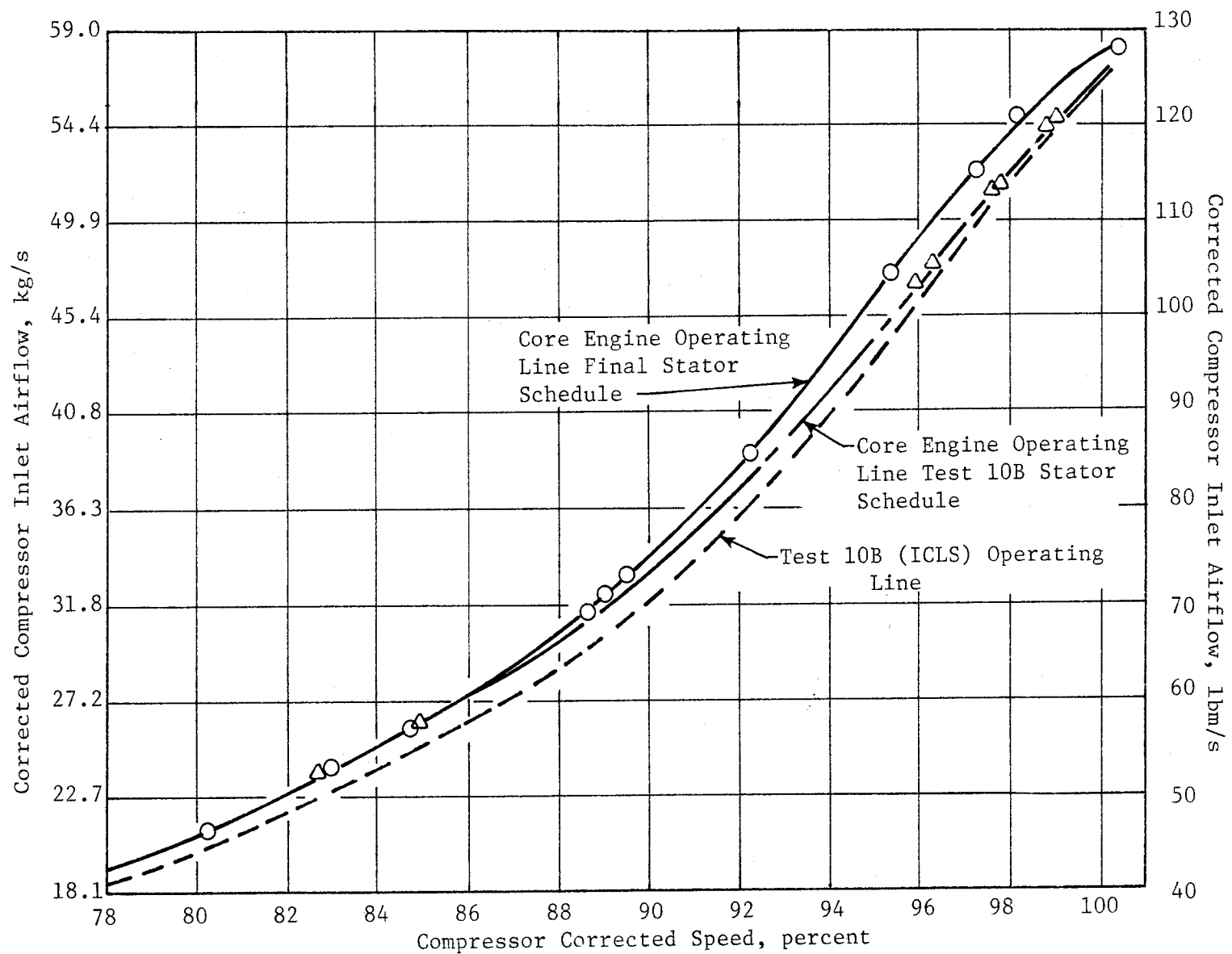
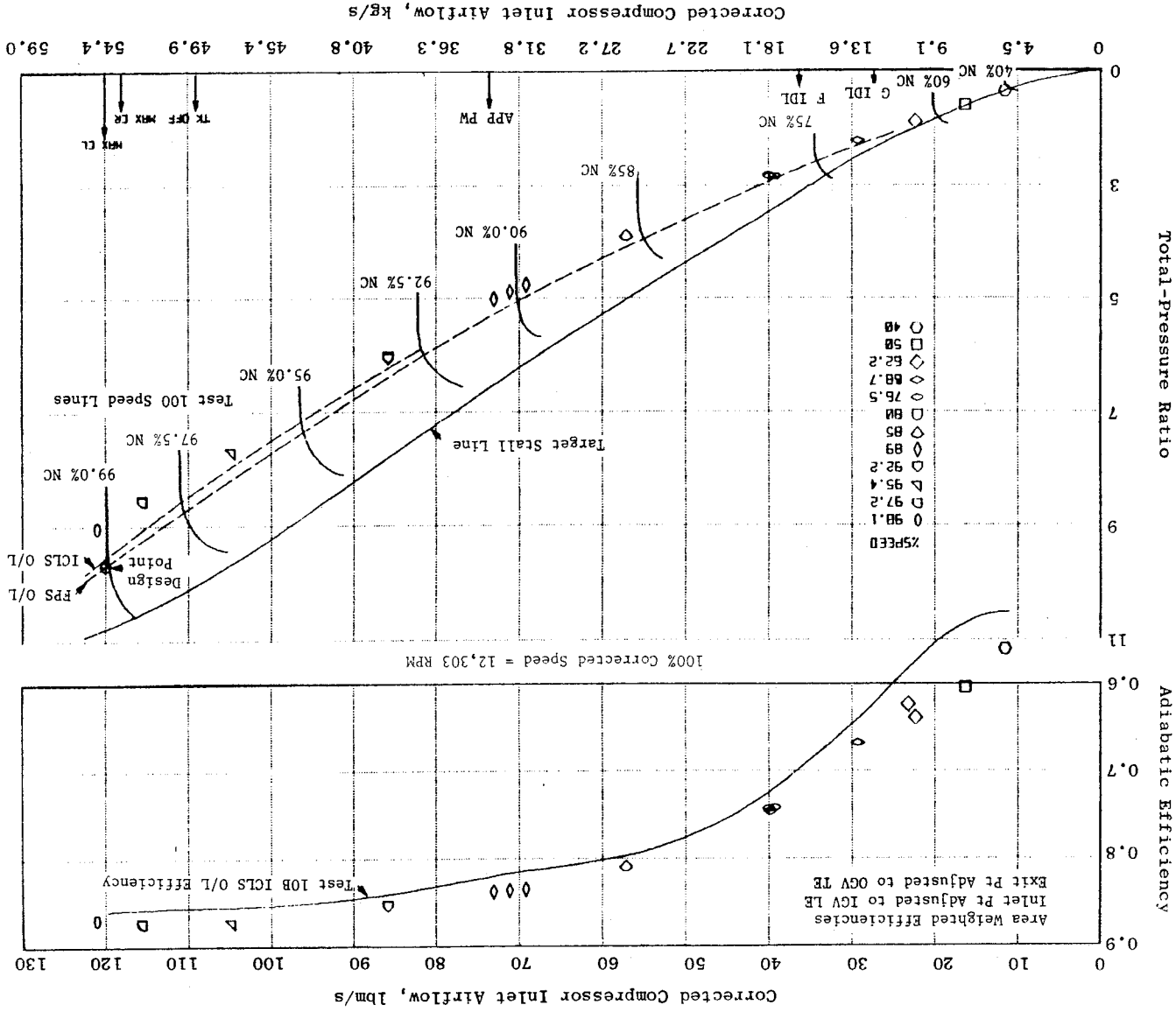


Figure 94. Core Compressor Flow Versus Speed.

performance data were calculated from the Stator 6 leading edge measurements and from the OGV exit data (computed from the diffuser exit measurements).

The performance map for the front six stages is shown in Figure 95. The speed lines and operating line efficiencies of the second 10-stage component test are also shown for comparison. The FPS and ICLS operating lines are for the front block of the second 10-stage test. As shown, the front block efficiency of the core engine compressor is about two points higher at all speeds. These two compressors had an identical aerodynamic design in the front stages, so that efficiency differences were due primarily to hardware deterioration and more open clearances of the second 10-stage build compressor. The map also shows that the front block of the core engine compressor operated at high speed with a lower pressure ratio than that of the second 10-stage build. This can be attributed partially to the slightly lower operating line of the core engine compressor, relative to that predicted for the ICLS engine, and to the higher pumping produced by the new rear stages.

The performance map for the rear stages is shown in Figure 96. The speed lines shown are for the overall compressor; that is, corrected by the compressor inlet temperature, as determined from the second 10-stage component test. The actual rear block corrected speed (speed corrected by Stator 6 inlet temperature) remained virtually constant near the design level between 90% and 100% overall compressor corrected speed; hence, only the 100% overall compressor corrected line is shown. FPS and ICLS operating lines shown in the map are from the second 10-stage compressor test. Note that at speeds above 96% (near takeoff speed) the rear block operates on a single point. A comparison of the core engine data with the ICLS operating line of the second 10-stage test indicated that at high speeds the rear block flow of the core engine compressor was about 2.7% greater than that of the second 10-stage test. For the second 10-stage component test data, a comparison of the high speed point on the FPS operating line with the design showed that the rear block flow was about 1.4% higher than the design intent. The increased rear block pumping of the core engine compressor resulted from the higher-cambered rear Stators 7 through 9 and the significantly tighter rear rotor clearances. Evidently, the 2° closure of Rotors 8, 9, and 10 designed into this build did not quite offset the effects of the higher stator camber and the reduced clearances.



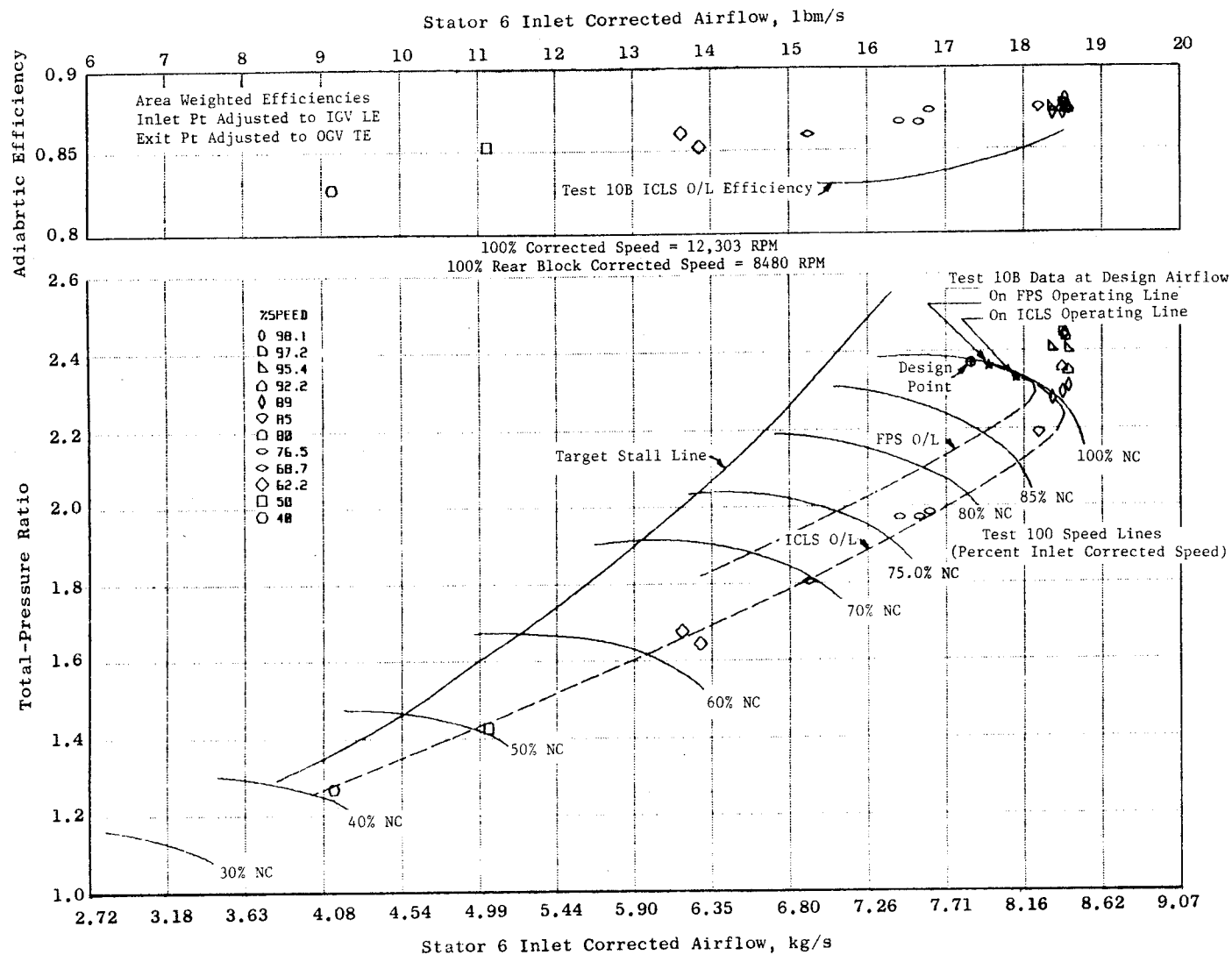


Figure 96. HP Compressor Rear Block Performance Map.

A comparison of the rear block efficiencies is shown in the upper portion of the map. The observed efficiency improvement was due primarily to the improved rear stator design and the tighter rear rotor clearances. This higher rear block efficiency is a major contributor to the substantial improvement in the overall compressor efficiency demonstrated in the core engine test.

Comparisons of the total-pressure radial profiles at the Rotor 6 and the diffuser exit planes with the second 10-stage component test data are shown in Figure 97(a) and (b), respectively. It can be seen that the distributions of total pressure ratio at Rotor 6 exit were similar, except that the core engine data displayed a more linear profile, suggesting a stronger tip flow. This improvement resulted from the undeteriorated core engine hardware and the much tighter rotor clearances, since the blading design was not changed. At the diffuser exit the core engine data showed a much more uniform profile than the component test results. Since the diffuser design of these two builds was identical, the improvement in the exit flow profile was attributed to the better rear stator design and to the tighter clearances.

6.3.4 Other Operational Effects

Compressor rear case cooling and rotor bore cooling flows of the ACC system were exercised independently during the test. The effects of rear case cooling on the overall compressor efficiency are shown in Figure 98. Data were taken with the cooling flow off, half on, and fully on at two high speeds near maximum cruise. The efficiency change was approximately linear with respect to the casing cooling flow showing a 0.5-point efficiency improvement with full rear case cooling. The effect of rotor bore cooling was to reduce the rotor thermal growth, thus increasing rotor tip clearance and reducing efficiency. Tests were conducted by progressively reducing the rotor cooling flow from a maximum (design) rate to 40% at maximum cruise condition (see Figure 99 for the results). The efficiency increase was approximately 0.3 point when rotor cooling flow was reduced to 40% of its design rate. Note that in this bore cooling exercise, the ACC casing cooling air was off. The efficiency change varied almost linearly with the rotor cooling flow reduction. However, all this efficiency gain may not be available because some rotor cooling flow would be necessary at all times and it may not be superposable

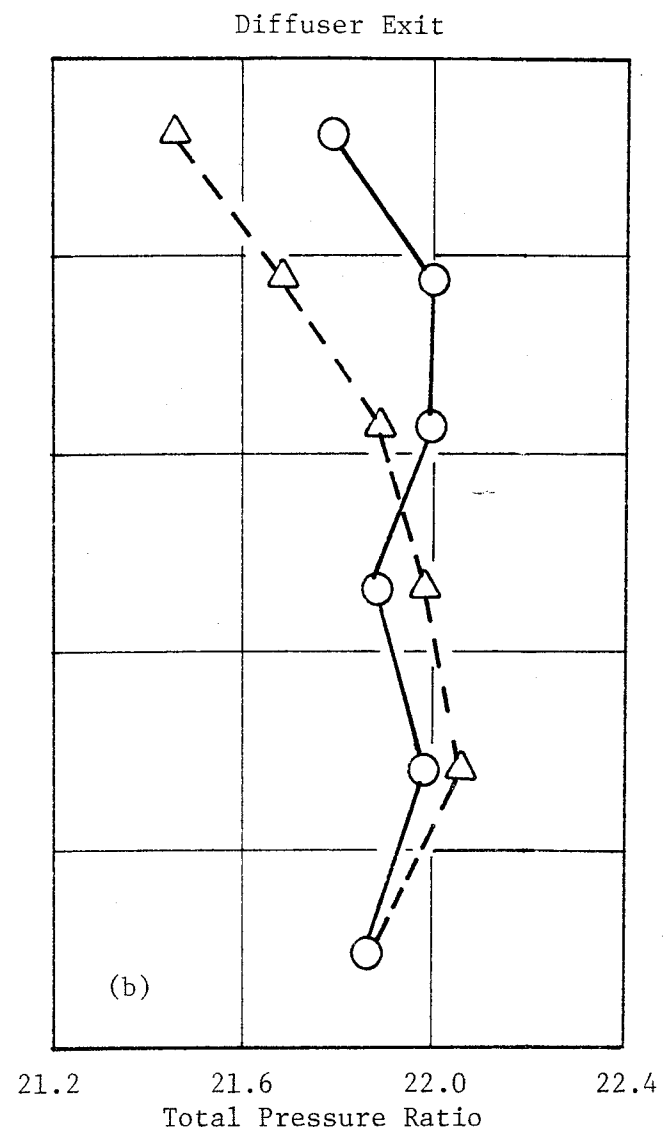
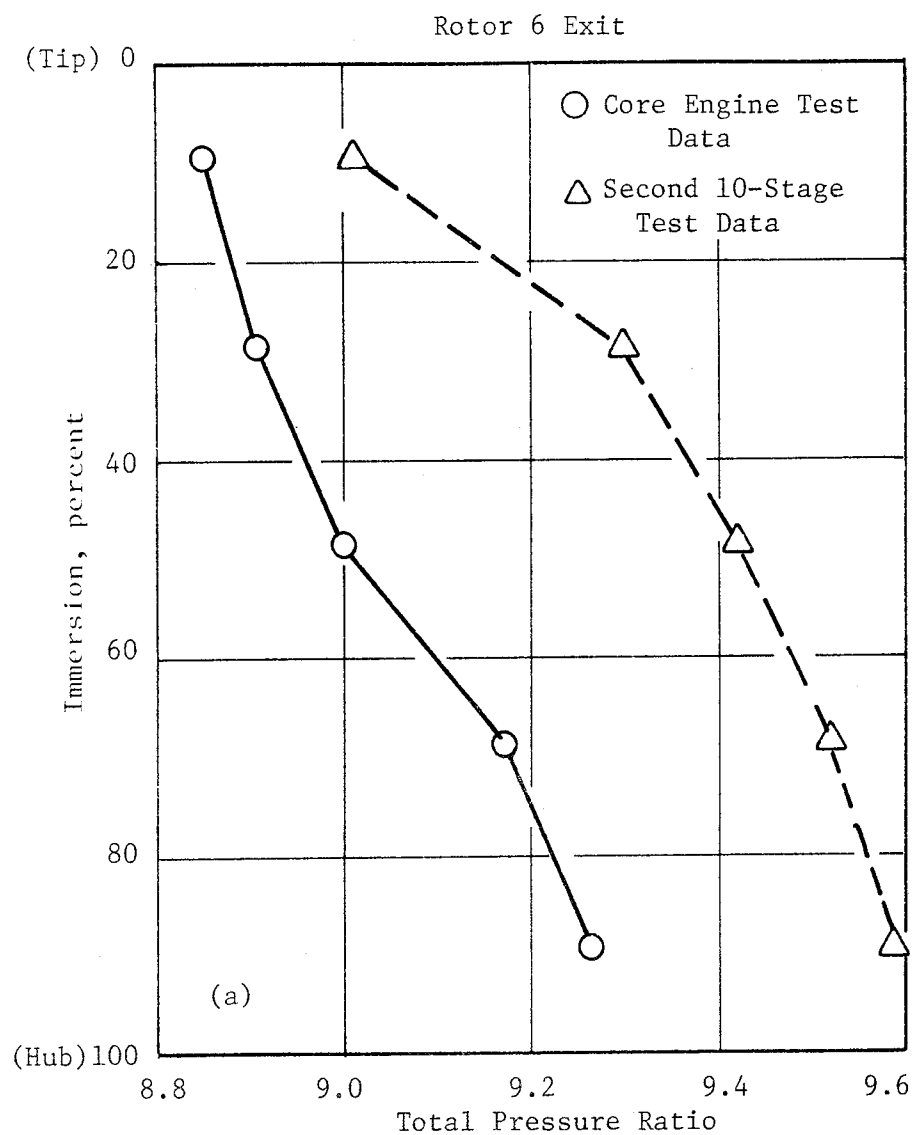


Figure 97. Core Compressor Radial Pressure Distribution.

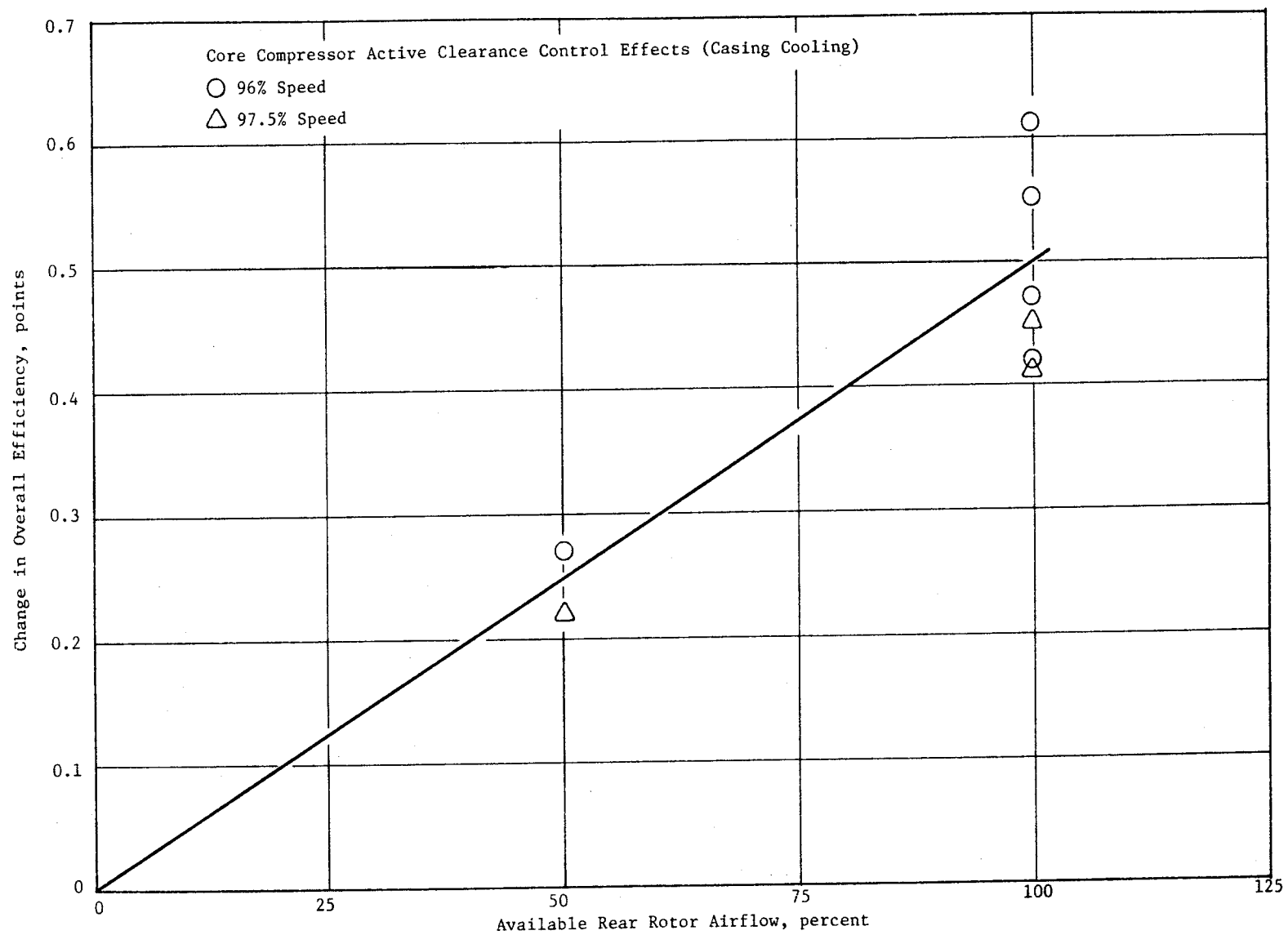


Figure 98. Core Compressor Active Clearance Control Effects (Casing Cooling).

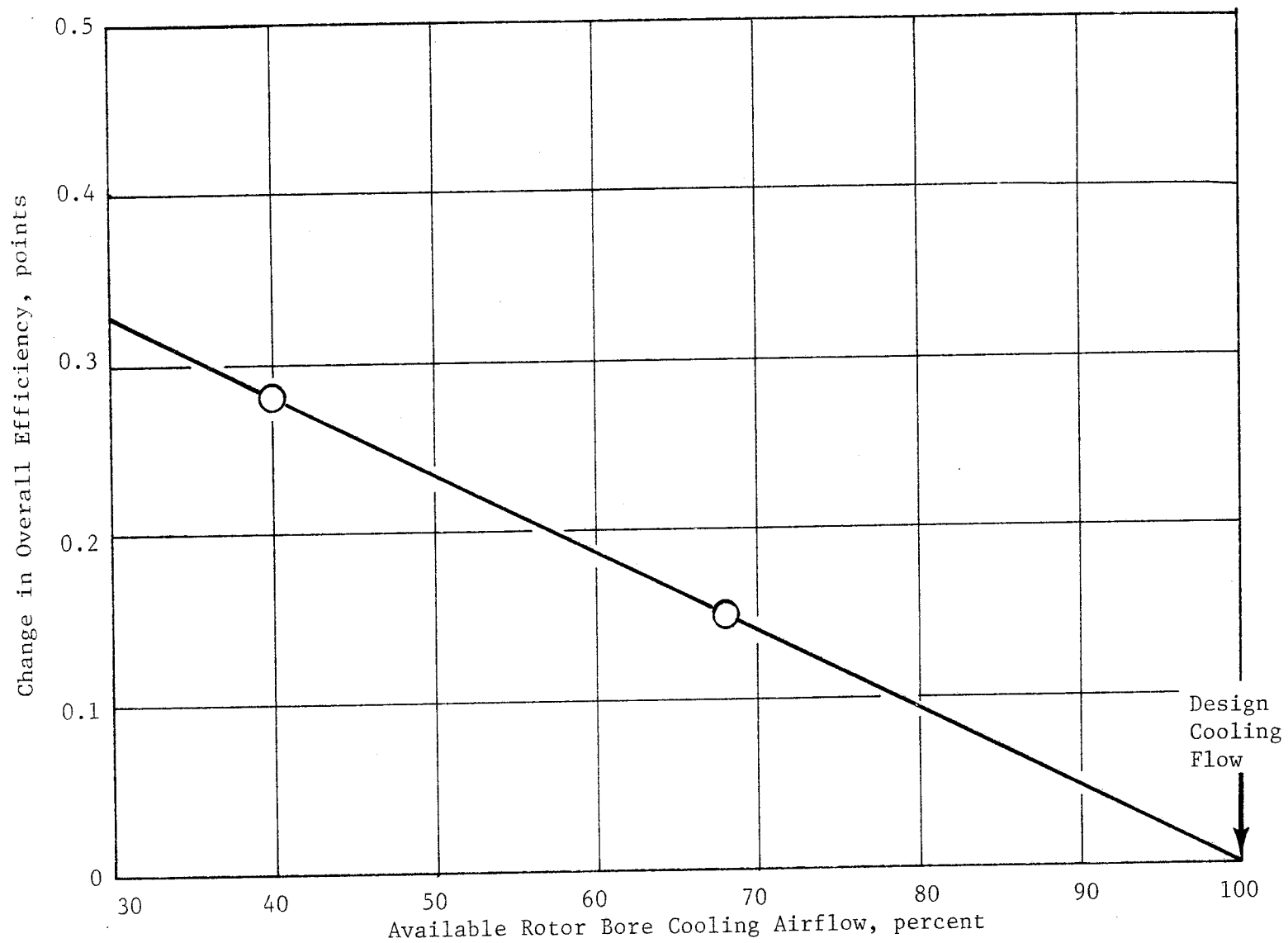


Figure 99. Core Compressor Rotor Bore Cooling Effects.

to casing cooling effects due to the minimum clearance requirements. The exact minimum amount of cooling flow that would be required will be determined by further tests and data analyses.

The effects of customer bleed extraction at the Stage 5 exit were evaluated near flight idle, takeoff, and maximum cruise speeds. The maximum bleed flow, expressed as a percent of the total inlet flow, was approximately 7.3% at all speeds. The recorded overall efficiency change showed a 0.5-point reduction at each condition. This loss in efficiency resulted from lowering the operating line and from stage rematching, since Stage 5 bleed unloaded the front stages and loaded Stages 6 through 10. Near maximum cruise speed, approximately 0.4 point of the efficiency loss was attributed to the operating line shift, and a 0.1-point loss was caused by stage rematching. Near the takeoff point, the total 0.5 efficiency loss was split equally between these two causes. The available data in the flight idle region were insufficient for making an accurate assessment of the cause of the efficiency reduction.

High RNI data (1.0 and above) at high speeds were taken for the first time on the E³ compressor during the core engine test. Previously, due to facility limitations during the component tests, high speed data were obtained only at RNI's of 0.5 or lower. Comparisons of these data trends with General Electric's performance prediction model are shown in Figure 100. Seeing that the efficiency level increased from the second 10-stage test to the core engine test, it was necessary to shift the data of each group so that the highest RNI points matched the prediction curve. It can be seen that the data trends agreed very well with the GE model in the region of interest, RNI's of 0.5 to 1.5. For an RNI below 0.4, component test data indicated a steeper efficiency penalty than did the model.

6.4 COMBUSTOR MECHANICAL PERFORMANCE

The core engine combustor was instrumented with pressure probes and thermocouples at significant locations. These included flowpath pressures and temperatures, impingement cavity pressures, and component metal temperatures. Figure 101 shows the combustor instrumentation. In addition to the

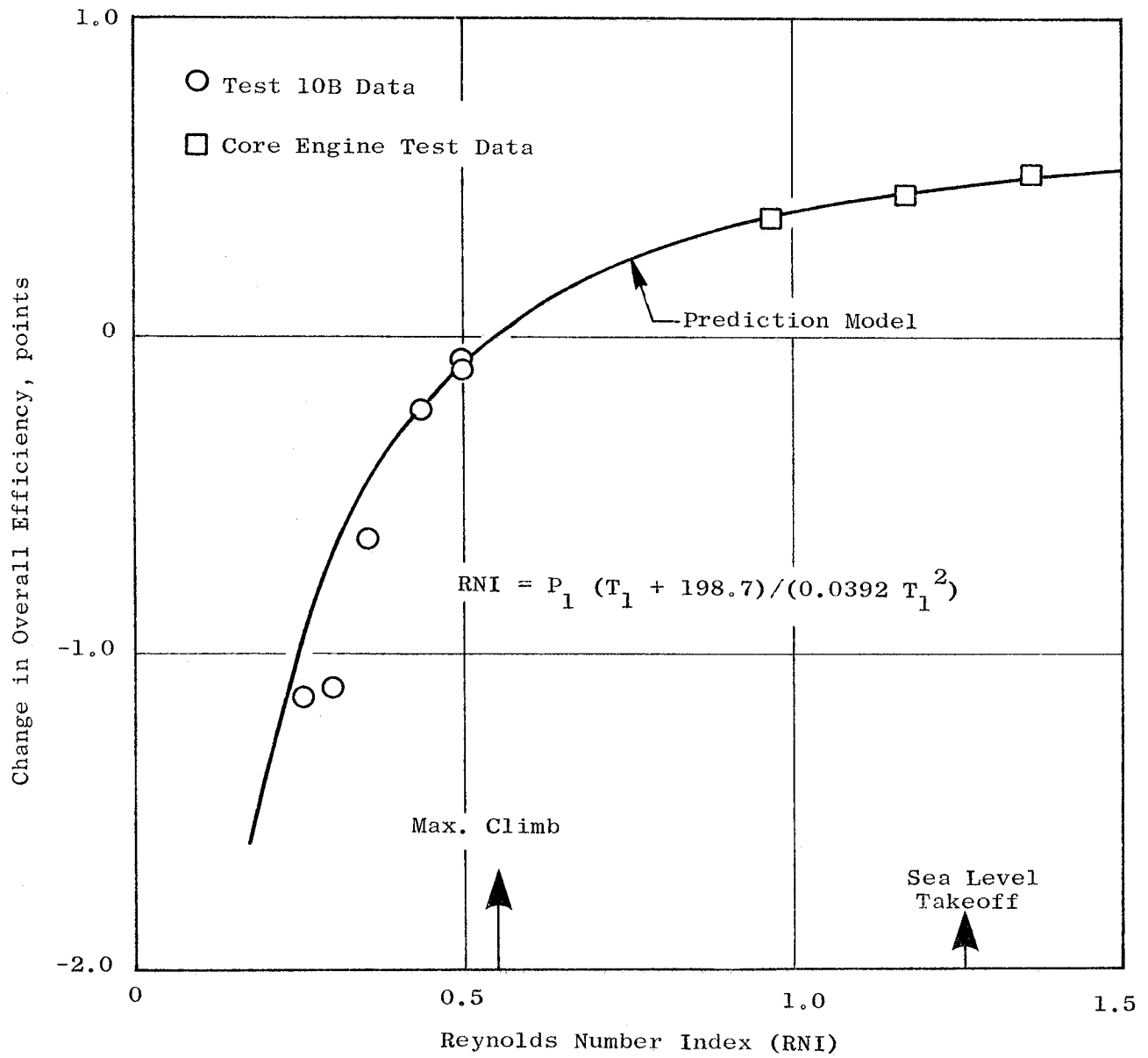


Figure 100. Core Compressor Reynolds Number Effects.

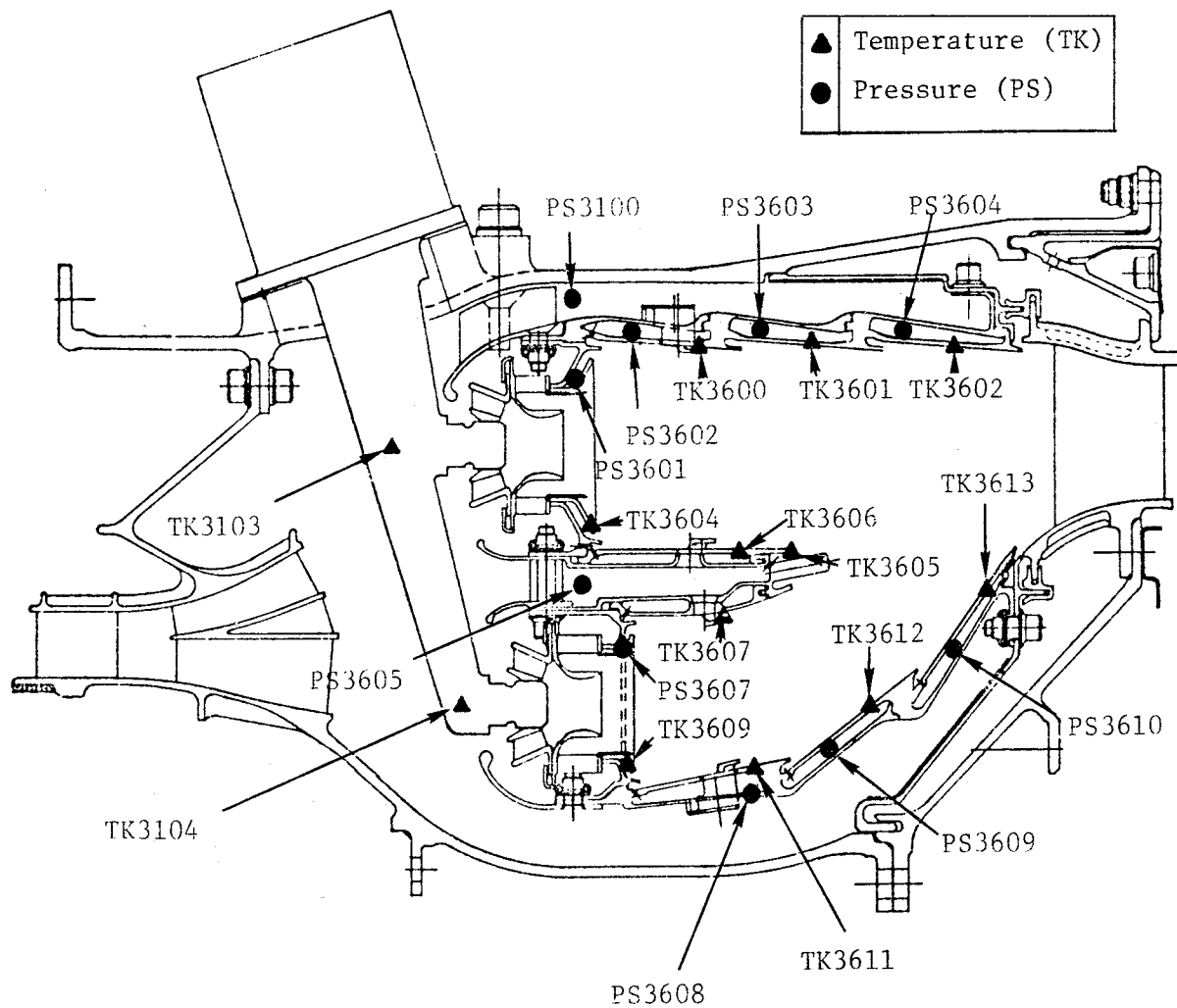


Figure 101. Combustor Instrumentation.

data recorded with this instrumentation, several key combustor parameters were computed from other recorded data in order to analyze overall combustor performance.

As indicated by the combustor instrumentation, mechanical performance has been evaluated on the basis of pressure drops in the impingement cavities and on local metal temperatures. The pressure drops present a survey of the impingement airflow. The local metal temperatures, when compared to predicted values, indicate cooling performance. Throughout testing of the core engine, the combustor operated well mechanically and within the defined maximum operating metal temperature.

6.4.1 Temperatures

The core combustor metal temperatures were predicted analytically utilizing temperature data taken during combustor rig tests. The predicted temperatures included: (1) corrections for the radiation effects of the higher pressures attained during core testing, as well as (2) the higher fuel-air ratios expected during core testing. The reasons for the higher fuel-air ratios are discussed in the emissions section that follows. The metal temperatures measured during the entire test were compared to the predicted values. For the shingles, these temperatures were measured on the backside by surface thermocouples. A typical attachment technique is shown in Figure 102.

Figures 103 through 105 show the metal temperatures of the pilot zone and main zone liner shingles and centerbody. These data were taken during the mechanical checkout early in the test program. Temperature trends of the liner shingles in Rows 2 and 3 of the pilot and main combustors closely followed the predicted trends. The temperature trend of the shingles in Row 1 of the pilot combustor uniformly exceeded the predicted trend but did not exceed the material temperature limit of 1093° C (2000° F). As the core engine exceeded 12,000 rpm, the Row 1 shingle temperature trend changed slope and approached the predicted line. The maximum metal temperature was predicted to be at the Row 1 shingles of the main combustor. Reliable data for main zone Row 1 shingles was not obtained during the test; however, a borescope inspection was performed periodically and indicated no metal distress. Centerbody temperatures correlated well with predictions.

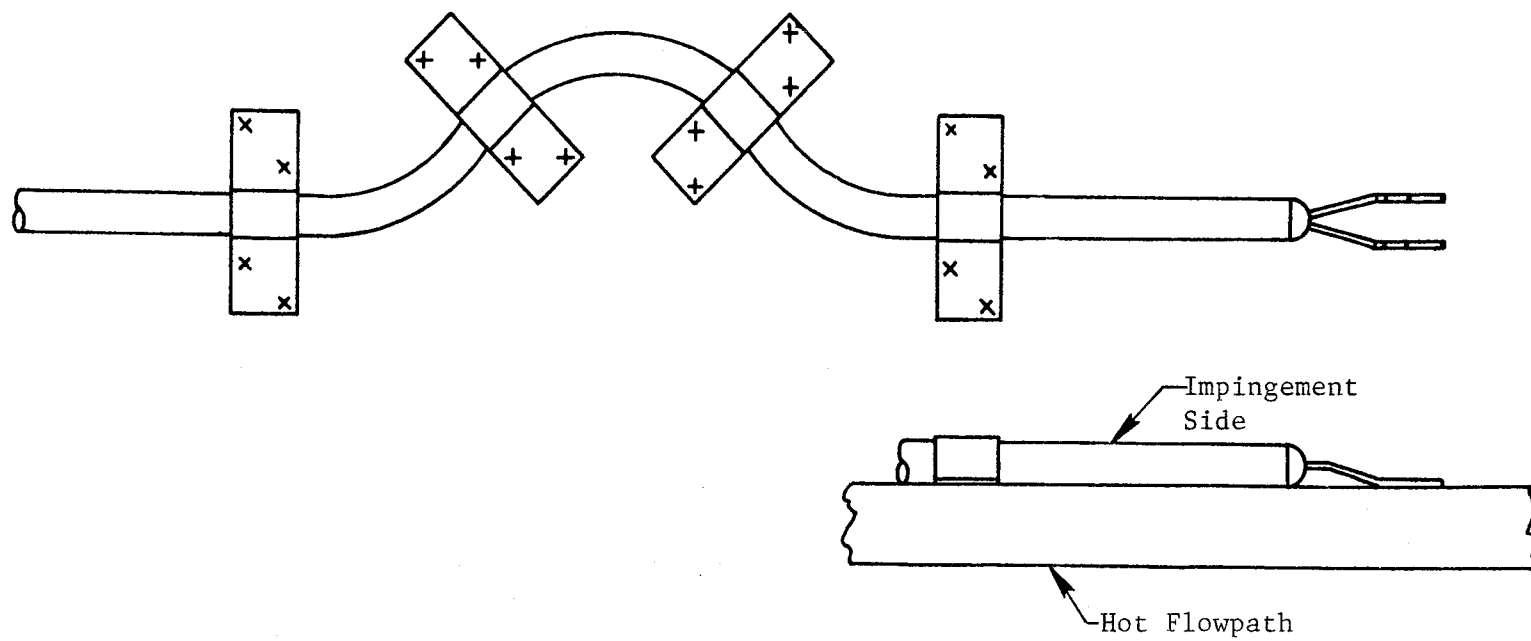


Figure 102. Typical Shingle Backside Thermocouple Attachment.

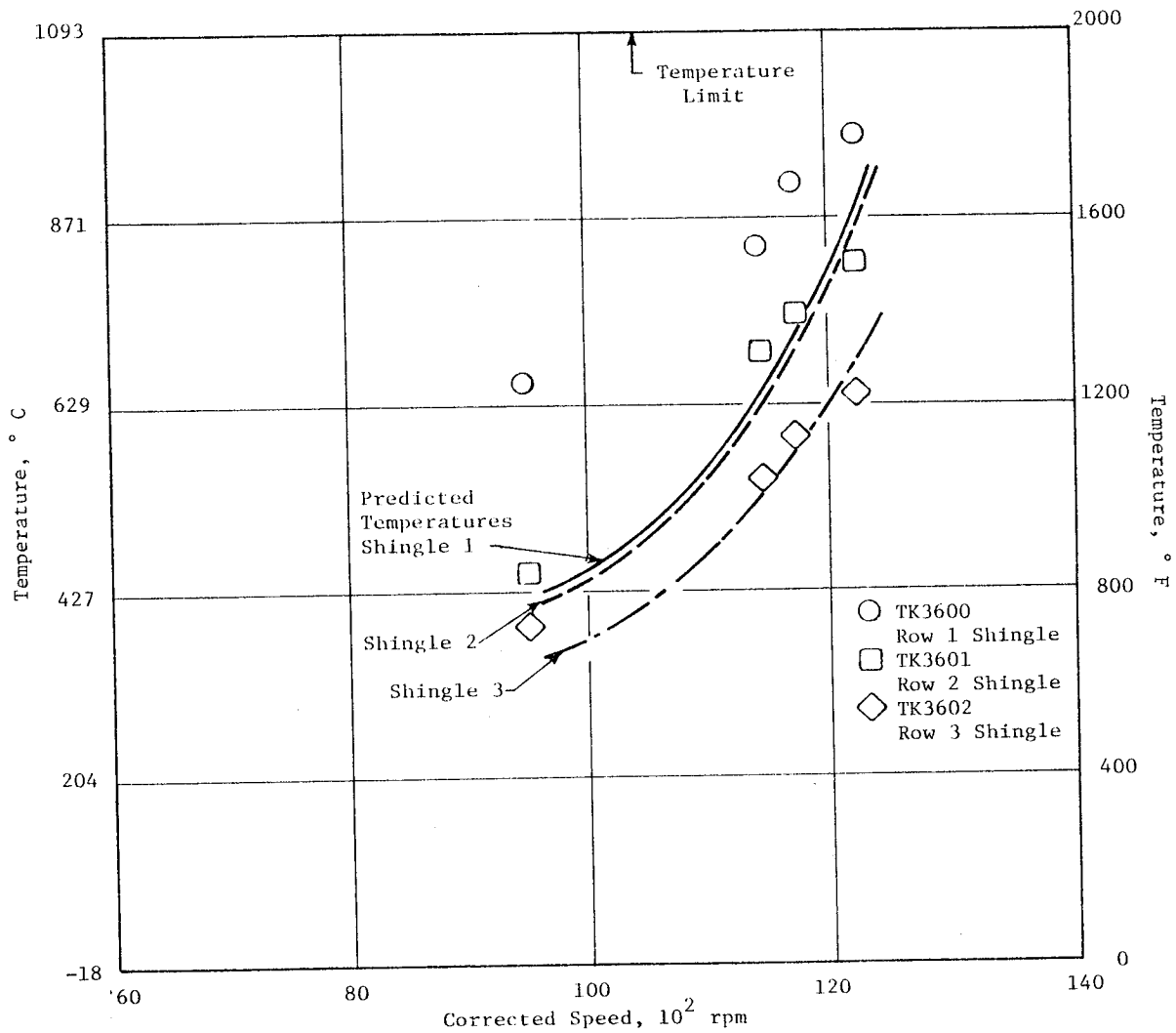


Figure 103. Pilot Zone Shingle Backside Temperatures Compared to Predicted, Mechanical Checkout With Ambient Inlet.

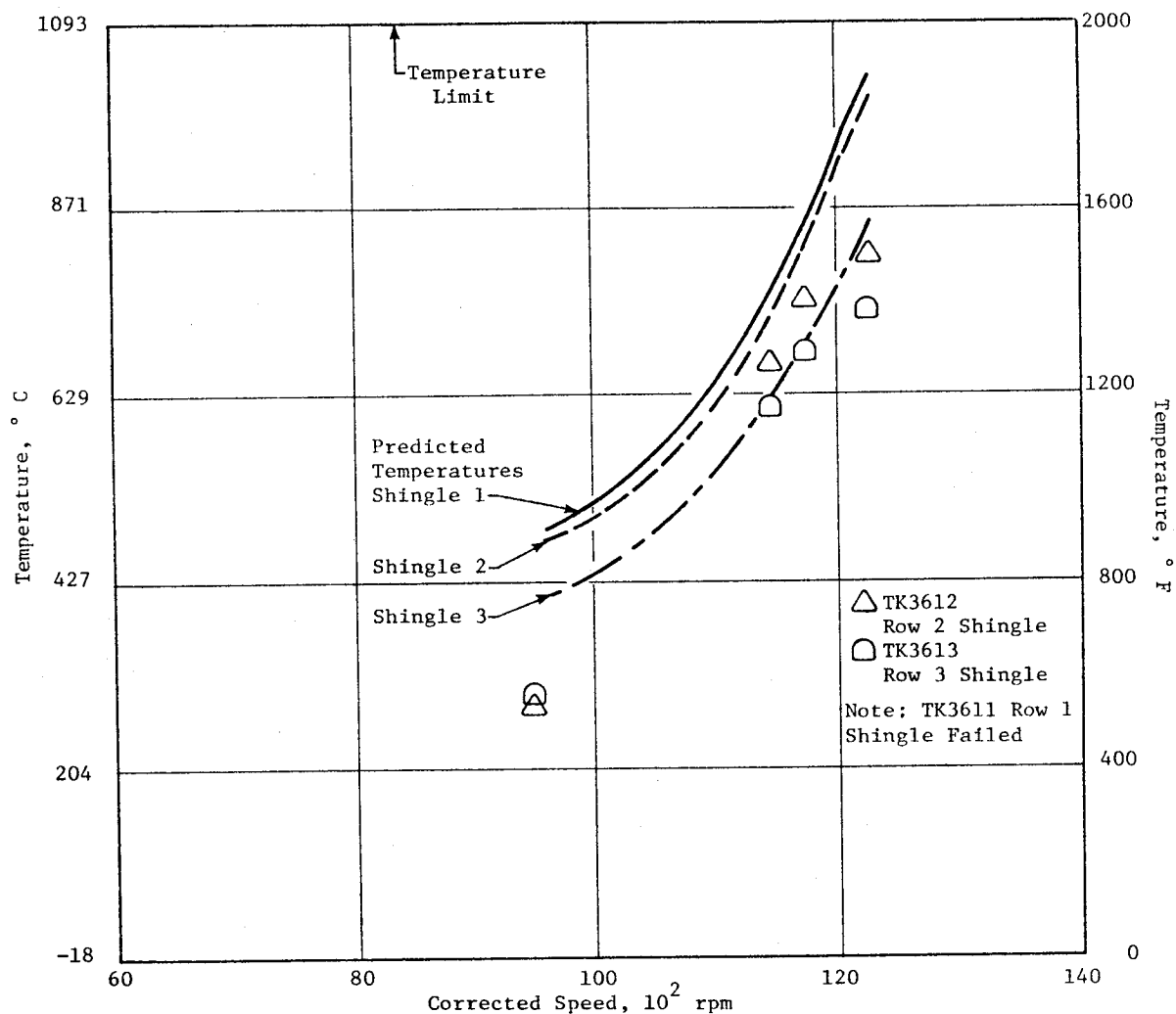


Figure 104. Main Zone Shingle Backside Temperatures Compared to Predicted, Mechanical Checkout With Ambient Inlet.

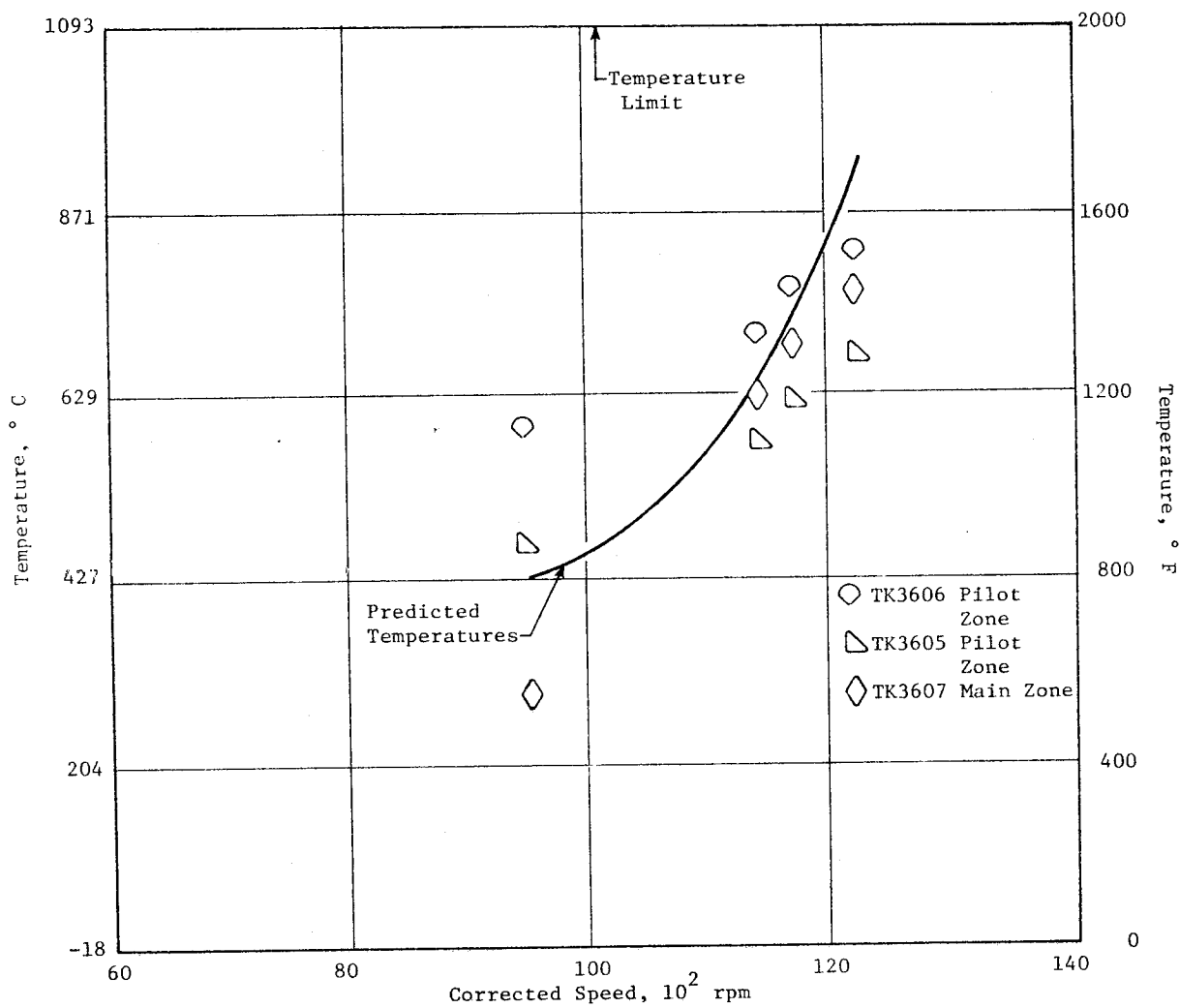


Figure 105. Centerbody Temperatures Compared to Predicted, Mechanical Checkout With Ambient Inlet.

The temperature predictions were for double-annular combustion only. Below 76% core speed (9400 rpm), only the pilot zone was burning; therefore, pilot zone temperatures were higher and main zone temperatures were lower than for the double-annular combustor mode. Staging from pilot-only to double-annular burning occurred smoothly with no excessive metal temperature excursions. The effects of pilot-only operation can be seen in the lowest speed point shown in Figures 103 through 105.

Figures 106 through 108 show the liner shingles and centerbody temperatures during core operation with ram-inlet conditions (151.7 kPa [22 psia] engine inlet pressure) simulating ICLS operation. The metal temperatures were slightly higher than during ambient inlet operation due to radiation effects at higher pressures. The temperatures were within the defined limits. It should be noted that the lowest speed point shown represents pilot-only operation, while the remaining speed points shown are for double-annular operation.

Temperatures at critical locations were continuously monitored. Other temperatures were frequently reviewed, especially at changes in power settings. Figures 109 through 111 show the temperature data taken near the conclusion of core testing. No significant changes in the temperatures of the liners and centerbody were apparent during core testing.

Splash plate temperatures were measured during the test. Figure 112 shows measured temperatures in the pilot and main zones throughout the operating range. The temperatures were within the material limits of 1093° C (2000° F) and indicated proper functioning of the splash plate cooling.

Measured fuel nozzle assembly temperatures are shown in Figure 113. The thermocouples were located internally to the heat shield. At the 9600 rpm point, the combustor was operating on pilot only. The main thermocouple reading was equal to T3 (compressor discharge air temperature), while the pilot thermocouple reading was significantly lower because of the fuel flow. Hence, measured wall temperatures were well below T3. These data indicate that the thermal shield functioned as desired to prevent high wall temperatures and subsequent fuel coking in the passages of the nozzle stem.

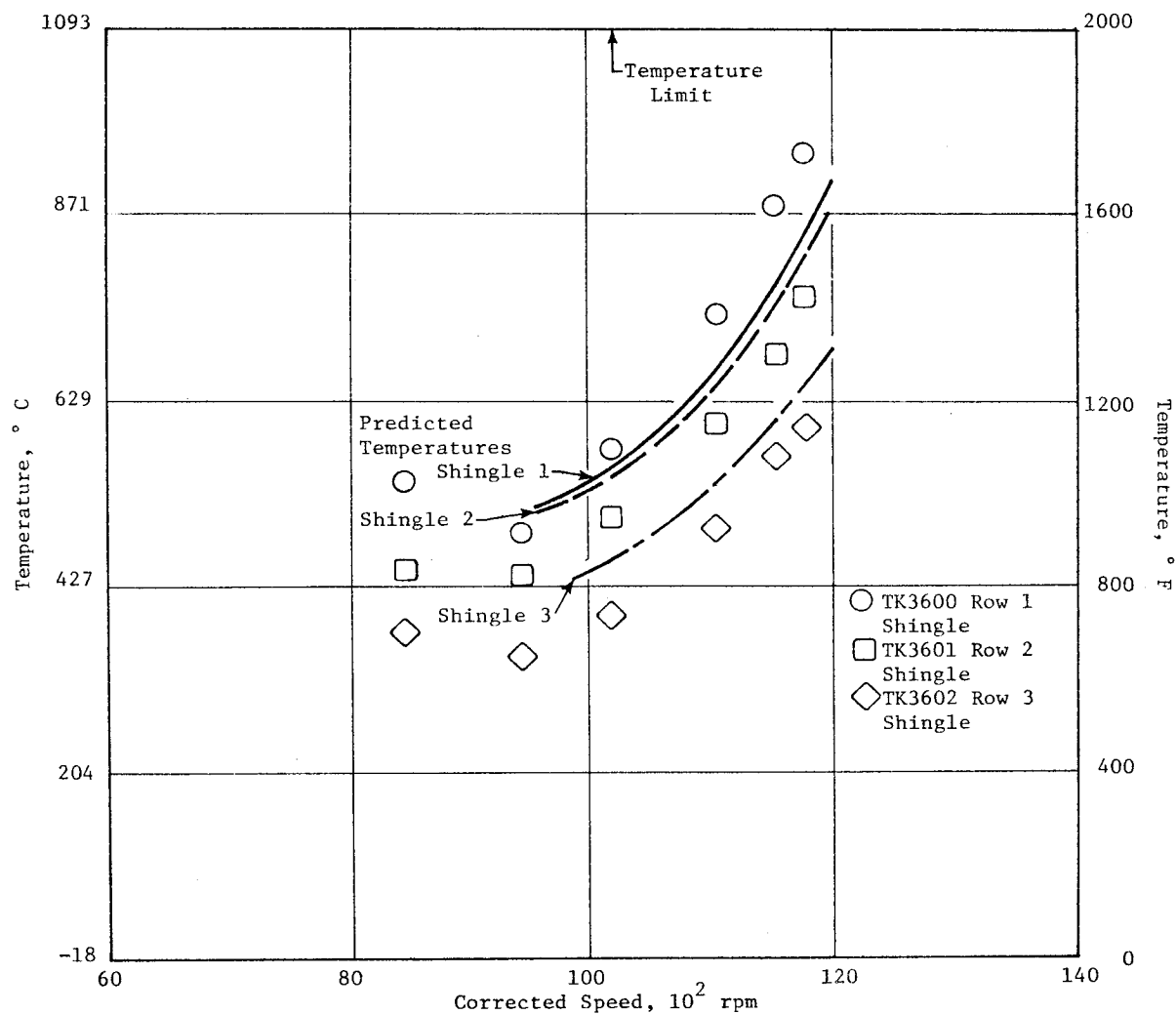


Figure 106. Pilot Zone Shingle Backside Temperatures Compared to Predicted, Ram Inlet Conditions.

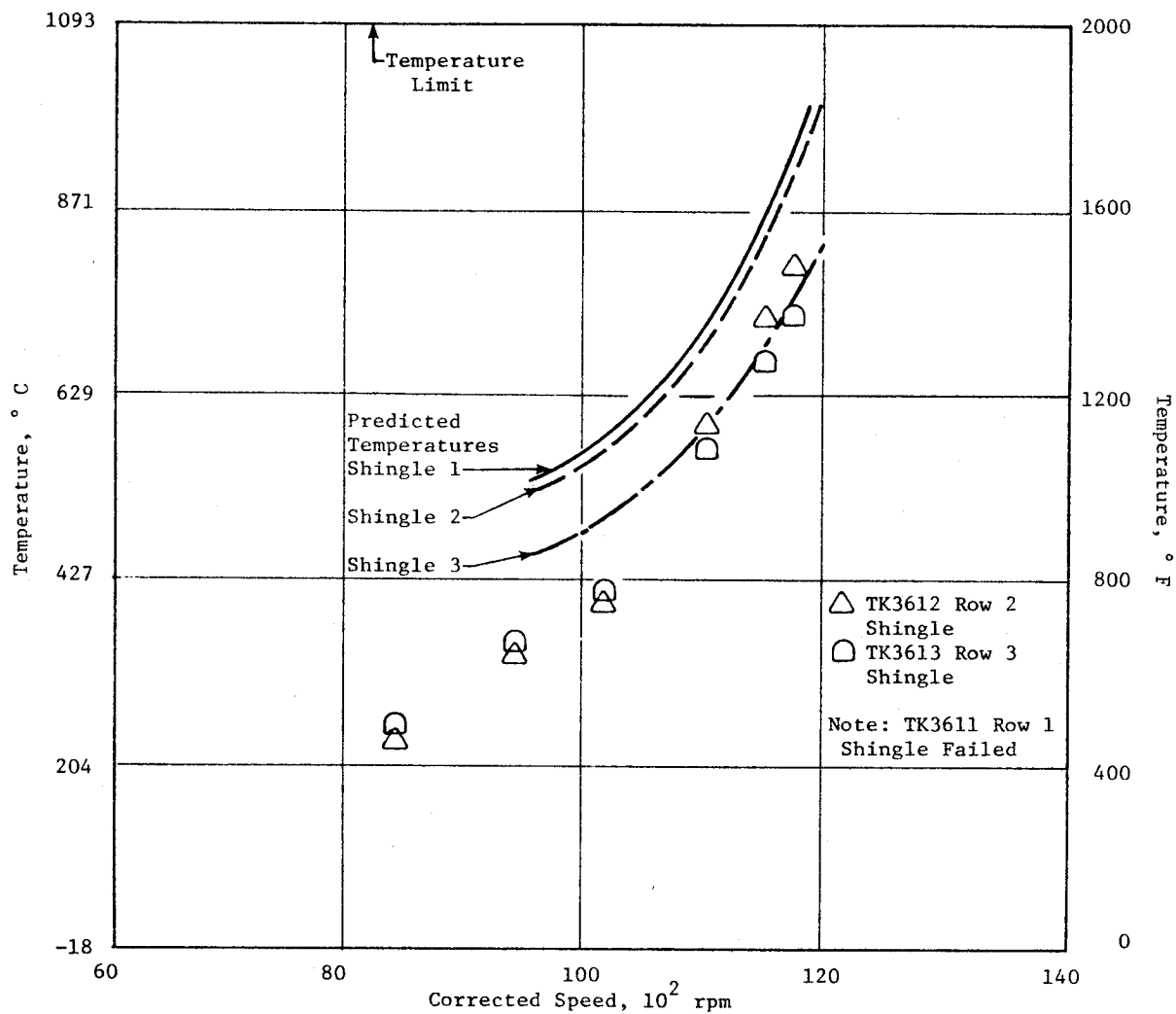


Figure 107. Main Zone Shingle Backside Temperatures Compared to Predicted, Ram Inlet Conditions.

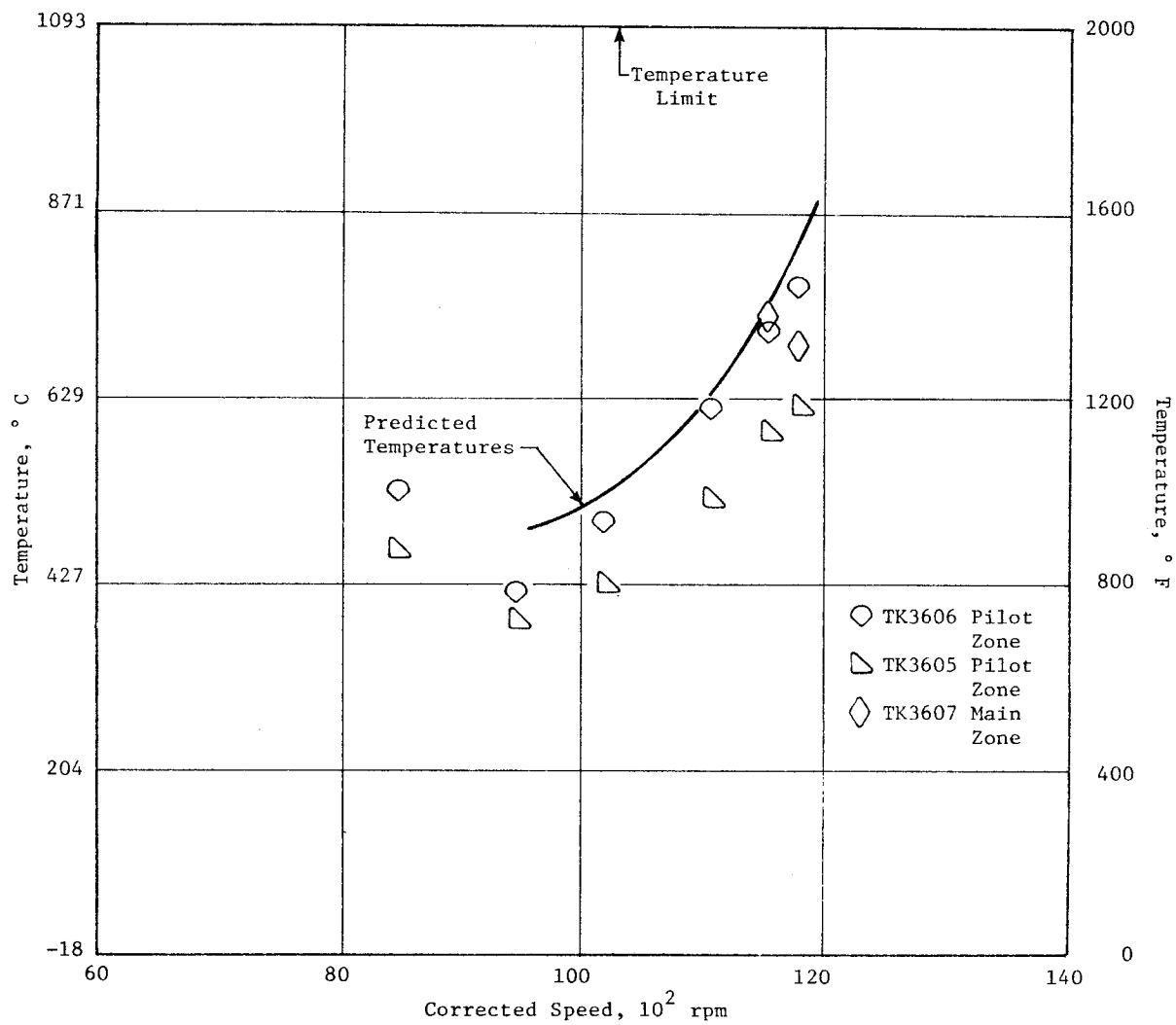


Figure 108. Centerbody Temperatures Compared to Predicted, Ram Inlet Conditions.

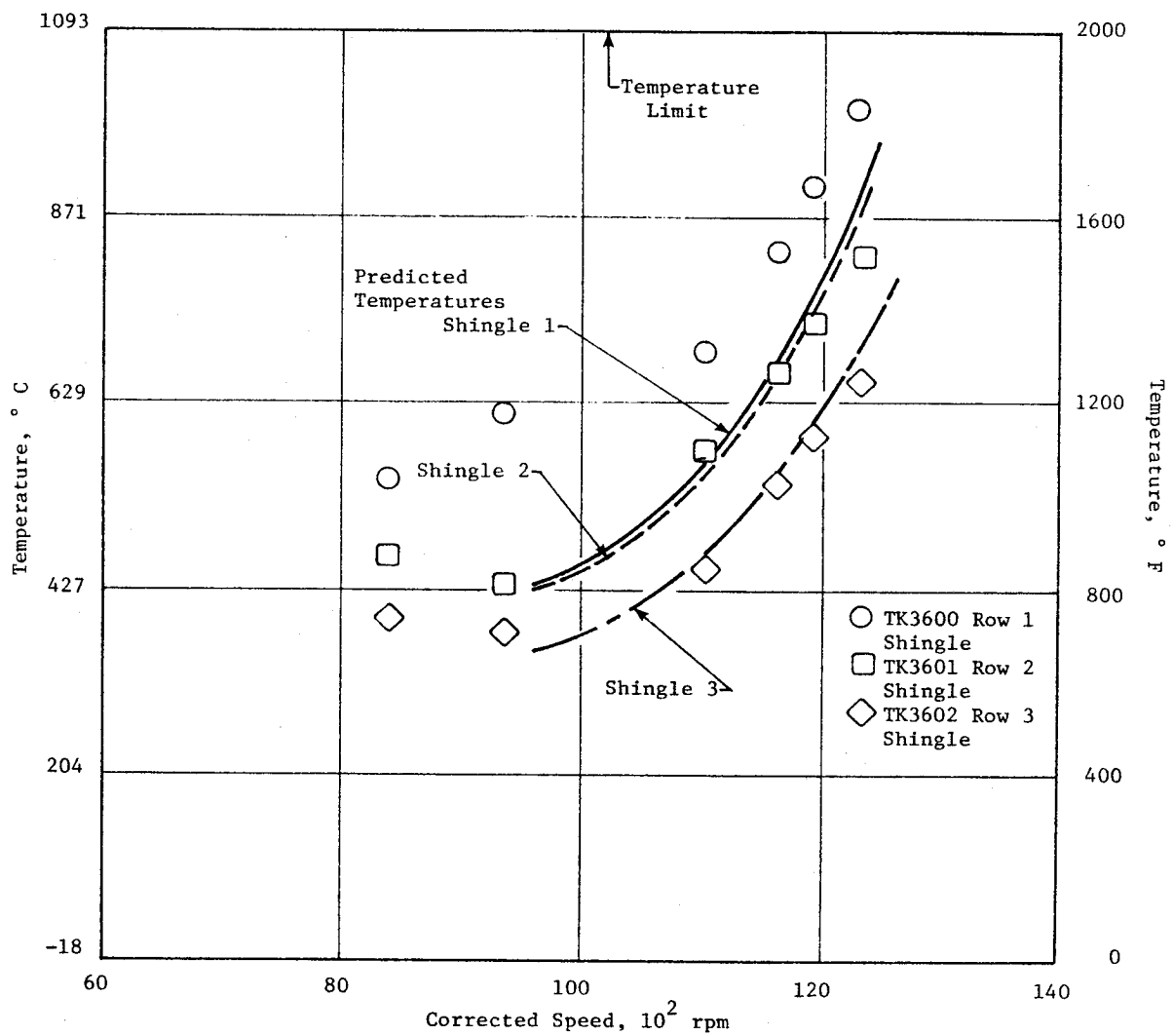


Figure 109. Pilot Zone Shingle Backside Temperatures Compared to Predicted at Test Conclusion.

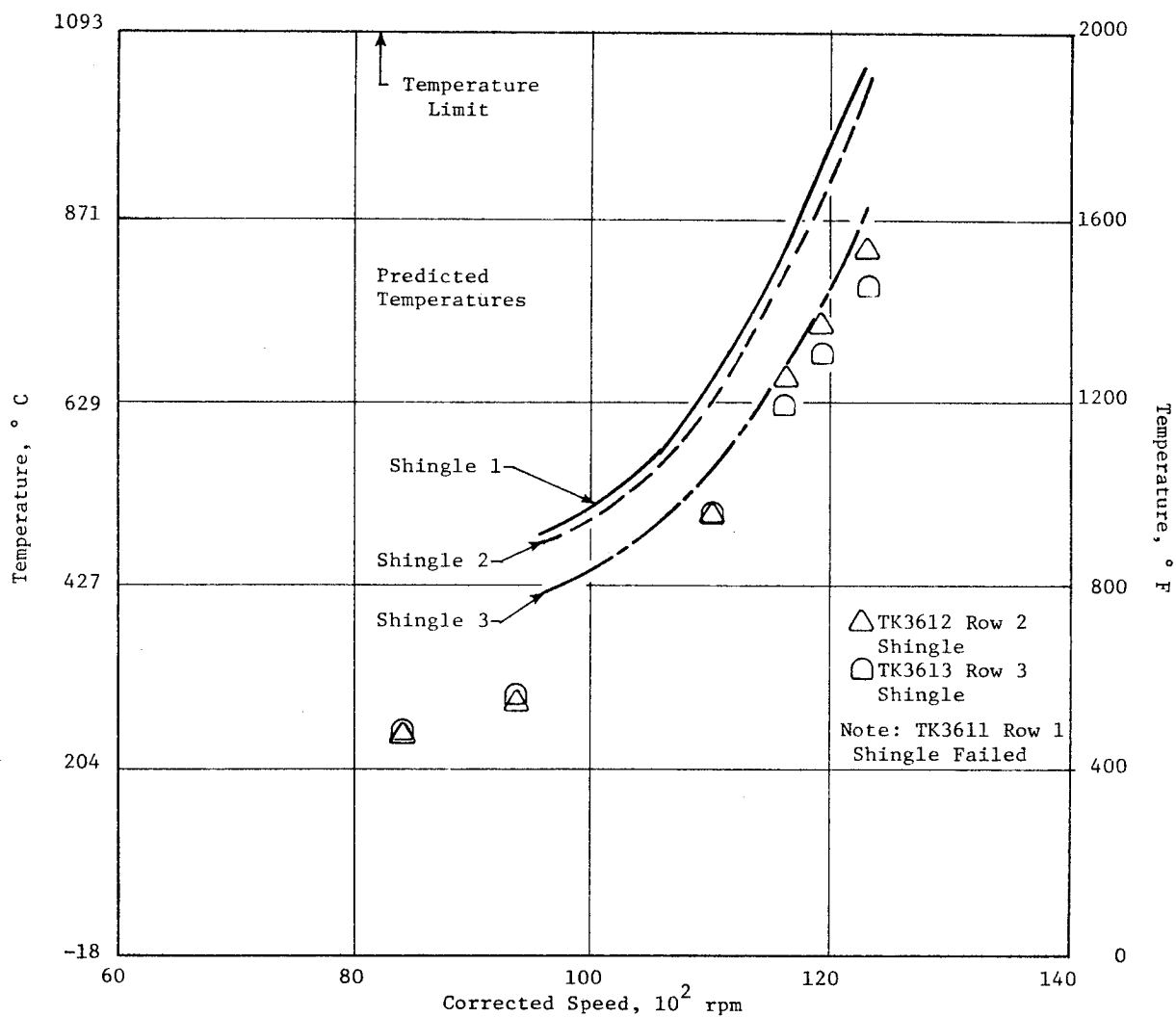


Figure 110. Main Zone Shingle Backside Temperatures Compared to Predicted at Test Conclusion.

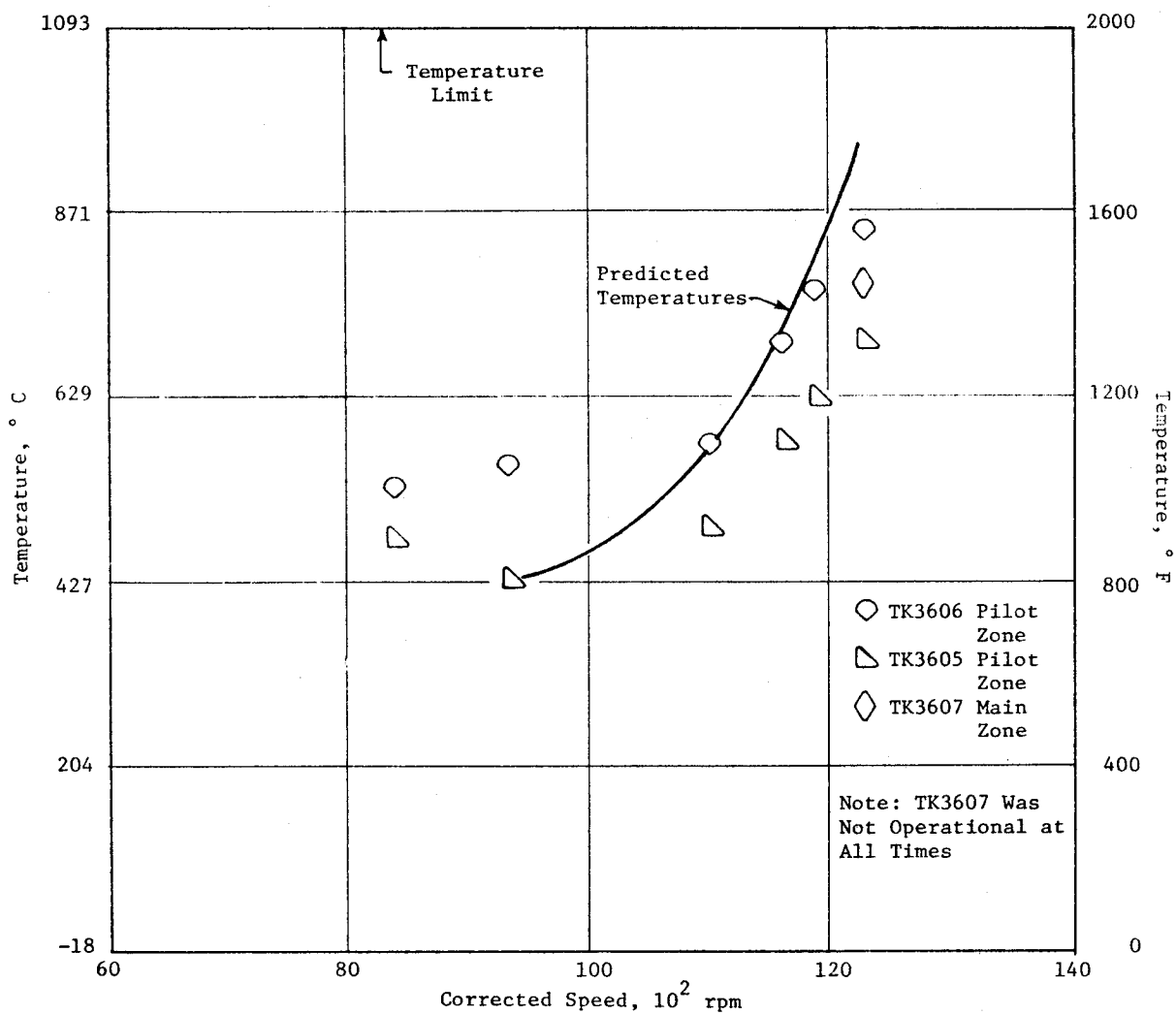


Figure 111. Centerbody Temperatures Compared to Predicted at Test Conclusion.

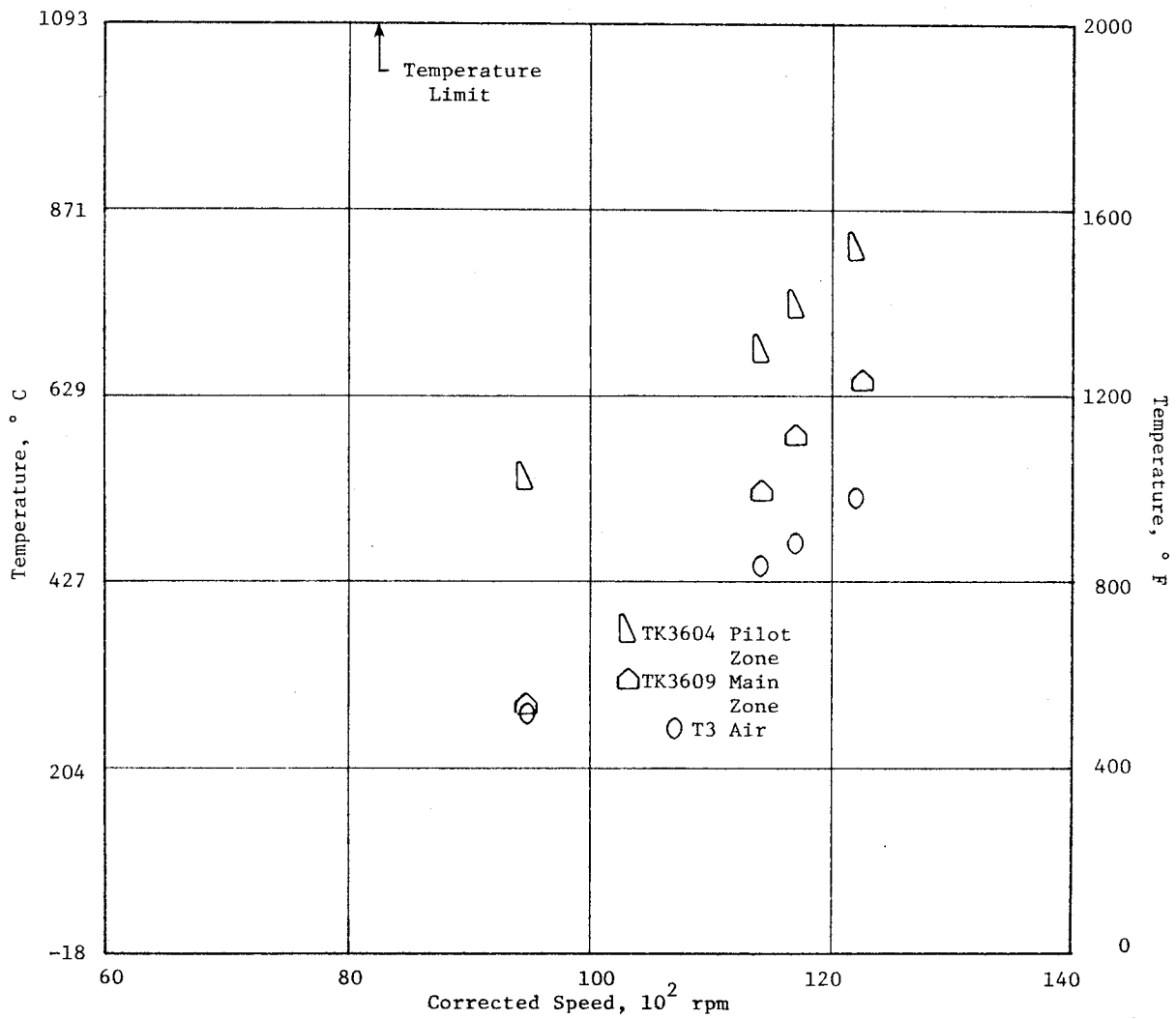


Figure 112. Measured Dome Splash Plate Temperatures.

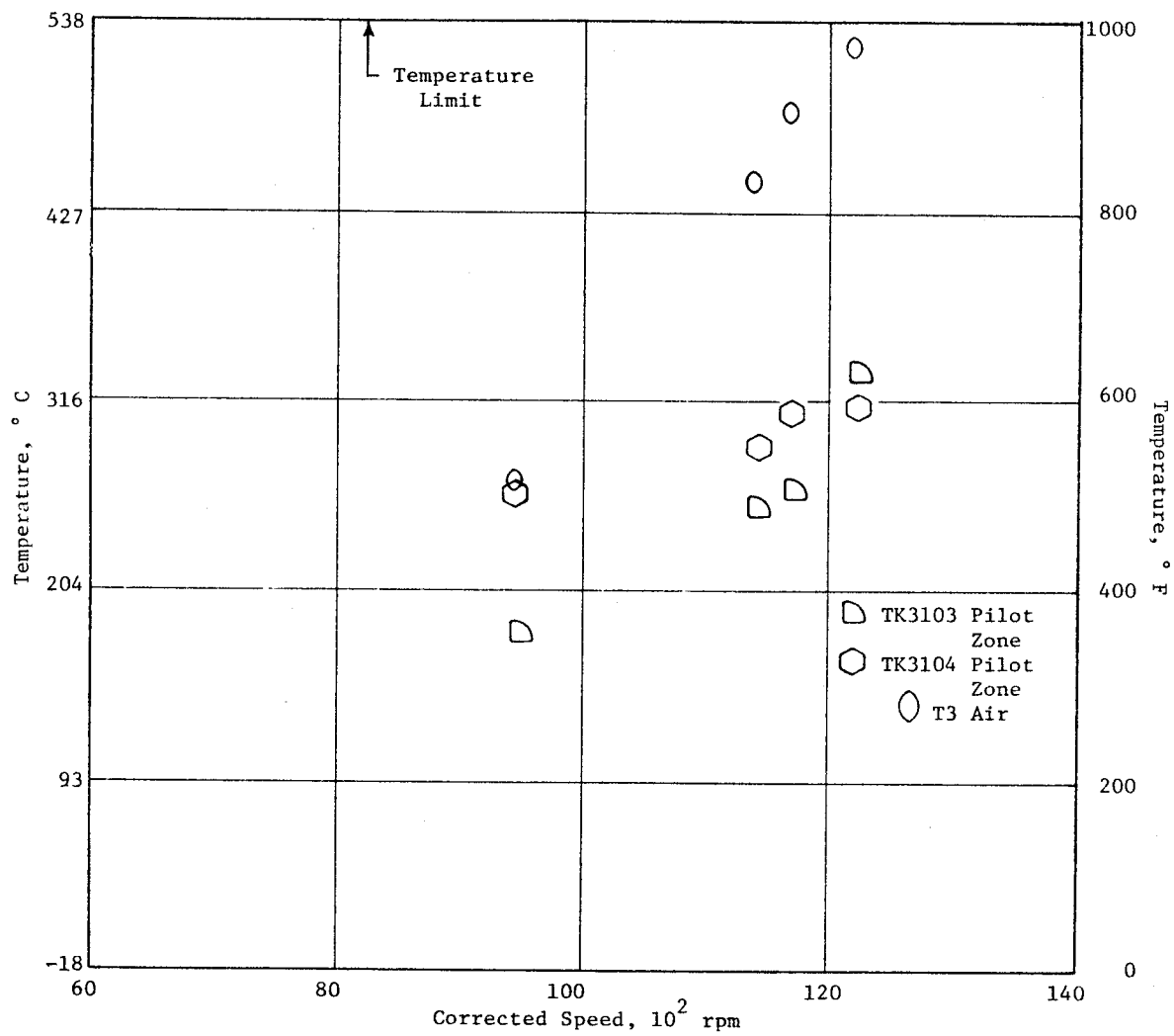


Figure 113. Measured Fuel Nozzle Assembly Temperatures.

6.4.2 Pressures

Static pressures in the liner impingement cavities were measured during the test. Significant scatter in the data was present resulting in unusable pressure data. Hence, no data have been presented. Based on liner temperature results that correlate well with predicted values, it is likely the cavity pressures were close to design values.

6.4.3 Component Evaluation

The combustor was borescoped at several intervals during the core test and at its completion. The combustor parts were found to be in excellent condition. The patterns on the shingles indicated no severe hot spots. Minor oxidation and distress were observed on some splash plate edges and sleeves.

Spallation of the thermal barrier coating on the pilot side of the centerbody was evident. A detailed inspection of these areas indicated no metal distress or oxidation.

It is concluded that the core combustor mechanical performance was acceptable, with only minor deviations from predicted metal temperatures and pressure drops, and that the mechanical design is satisfactory.

6.5 COMBUSTOR AERODYNAMIC PERFORMANCE

The E³ core engine combustor was developed from a comprehensive series of annular sector combustor development tests which ran in parallel to, but leading, a series of full-annular combustor development tests. The design was evolved over a two-year period and culminated in tests of the core engine combustor and core engine fuel nozzles to measure thermal performance, emissions, starting characteristics, staging characteristics, and liner skin temperatures.

Overall combustor performance in the core engine was excellent. The combustor demonstrated satisfactory starting and staging (to double-annular combustion) characteristics and had measured emissions levels that met goal levels for carbon monoxide and hydrocarbon emissions. However, the emission goal level for oxides of nitrogen was exceeded. The combustor did not limit engine testing and met overall pressure loss and efficiency goals.

During core engine testing, the items of particular interest to the combustor were:

- Ignition and staging from pilot-only to double-annular burning
- Combustor efficiency and pressure losses
- Emissions and smoke levels
- Stability (noise)
- Metal temperatures

Starting and staging characteristics and metal temperature trends with speed were noted throughout the test. Gaseous emissions, smoke, efficiency, and pressure loss data were obtained during Test 9. The points run in Test 9 are listed chronologically in Table XV. They constitute an operating line that includes subidle points using both double- and single-annular combustion.

Subsequent tests were done for starting optimization. During these tests the lengthy initial starting times were shortened by adjusting the acceleration fuel schedule. Eventually, a time of 29 seconds from ignition to idle was achieved.

The entire engine test was run on Jet A fuel. A fuel analysis sample is shown in Table XVI.

While taking low power emissions data, the engine was run at ambient (cell) inlet conditions since pressures at the core inlet are not much different under this condition than they would be if a fan were at the front of the engine. However, at the higher power points the inlet was rammed to 151.68 kPa (22 psia) in an effort to simulate the elevated inlet pressure levels that would be produced by the fan and booster operation. The core engine could not be run up to 100% speed at ram conditions because of flow limitations of the air supply facility.

6.5.1 Instrumentation

The combustor performance instrumentation consisted of 14 static pressure taps and 14 grounded and capped chromel-alumel thermocouples. There were nine static pressure taps on the inlet prediffuser. In addition, five rakes

Table XV. Core Emissions Testing.

(Points Presented in Order Test Was Run)

Percent Core Speed, PCN25R	Data Management System, DMS	Combustor Mode	Core Engine Inlet Pressure, P25	Emissions Data	Smoke Data
68.5	187	Single Annular	Ambient	X	X
62.0	188	Single Annular	Ambient	X	X
76.5	189	Single Annular	Ambient	X	
77.5	190	Double Annular	Ambient	X	
83.0	191	Double Annular	Ambient	X	
88.0	192	Double Annular	Ambient	X	X
90.0	193	Double Annular	Ambient	X	
	194	Double Annular	152 kPa (22 psia)	X	
94.0	195,196	Double Annular	Ambient	X	X
96.0	197,198,199	Double Annular	Ambient	X	X
90.0	200	Double Annular	Ambient	X	
76.5	201	Double Annular	Ambient	X	
76.5	202	Single Annular	Ambient	X	
68.5	203	Single Annular	Ambient	X	
62.0	204	Single Annular	Ambient	X	
58.0	205	Single Annular	Ambient	X	
46.0	206	Single Annular	Ambient	X	

Table XVI. Core Engine Test Fuel Sample Analysis.

Engine 531001/1, Postrun 11, Jet A Fuel

Specific Gravity at 15.6°/15.6° C (60°/60° F)	0.8064
Flash Point	54.4° C (130° F)
Viscosity at 38° C (100° F)	1.59 Cs
Total Water	37 ppm
Gravimetric	0.026 mg/l (0.1 mg/gal)
Aromatics	17.3%
Olefins	1.7%
Aniline Point	65.8° C (150.4° F)
Aniline Gravity Product	6613
Aniline	43,285 kJ/kg (18,609 Btu/lb)
Bomb Test	43,252 kJ/kg (18,595 Btu/lb)
Hydrogen	14.03%
Sulfur	0.019%
Smoke Point	24.5
Distillation: Initial Boiling Point	171.1° C (340° F)
10%	193.9° C (381° F)
20%	203.9° C (399° F)
50%	217.8° C (424° F)
90%	243.3° C (470° F)
End Point	264.4° C (508° F)
Percent at 204° C (400° F)	22%
Residues	0.8%
Loss	1.0%

were used to measure total pressure and temperature at the exit of each passage of the prediffuser. Each rake had three probes in each discharge passage, six probes each rake. The locations of this instrumentation on the combustor hardware are shown in Figures 114 through 120. The instrumentation is listed in Table XVII. Also indicated in Table XVII is the instrumentation still functioning at the end of the test. Note that of the four centerbody thermocouples available when core testing began, only one lasted the duration of the test. Dynamic pressure probes (PX3100, PX3101, Figure 114) were installed through available ports and flush with the combustor case outer flowpath wall. These probes were used to monitor the characteristic frequencies and pressure fluctuations of the engine airflow.

Gaseous emissions and smoke samples were obtained with seven 5-element (Plane 42.0) total pressure rakes. Each element consisted of a stainless steel tube of 0.0508 cm (0.020 inch) inside diameter. All 35 elements were manifolded together to provide a single, ganged combustion gas sample for the gas analyzers and smoke console.

The CAROL V (Contaminants Are Read On Line) gas analysis system was used to analyze the gas samples. This equipment, along with a GE smoke console, was installed in an adjacent cell. The instrumentation in this system includes:

- Beckman Model 865 carbon monoxide and Model 864 carbon monoxide analyzer (NIDR)
- Beckman Model 402 total hydrocarbon analyzer (flame ionization detector)
- Beckman Model 955 (NO_x) analyzer (heater chemiluminescence with converter)

Prior to testing, the CAROL V system was calibrated by using a set of calibration gases. Inlet air humidity measurements were obtained as part of the engine data acquisition system.

All emissions and instrumentation data acquisition were handled automatically by the DMS. Through this system, the digital signals from all sensors were converted to engineering units and processed through two data reduction

ORIGINAL PAGE IS
OF POOR QUALITY

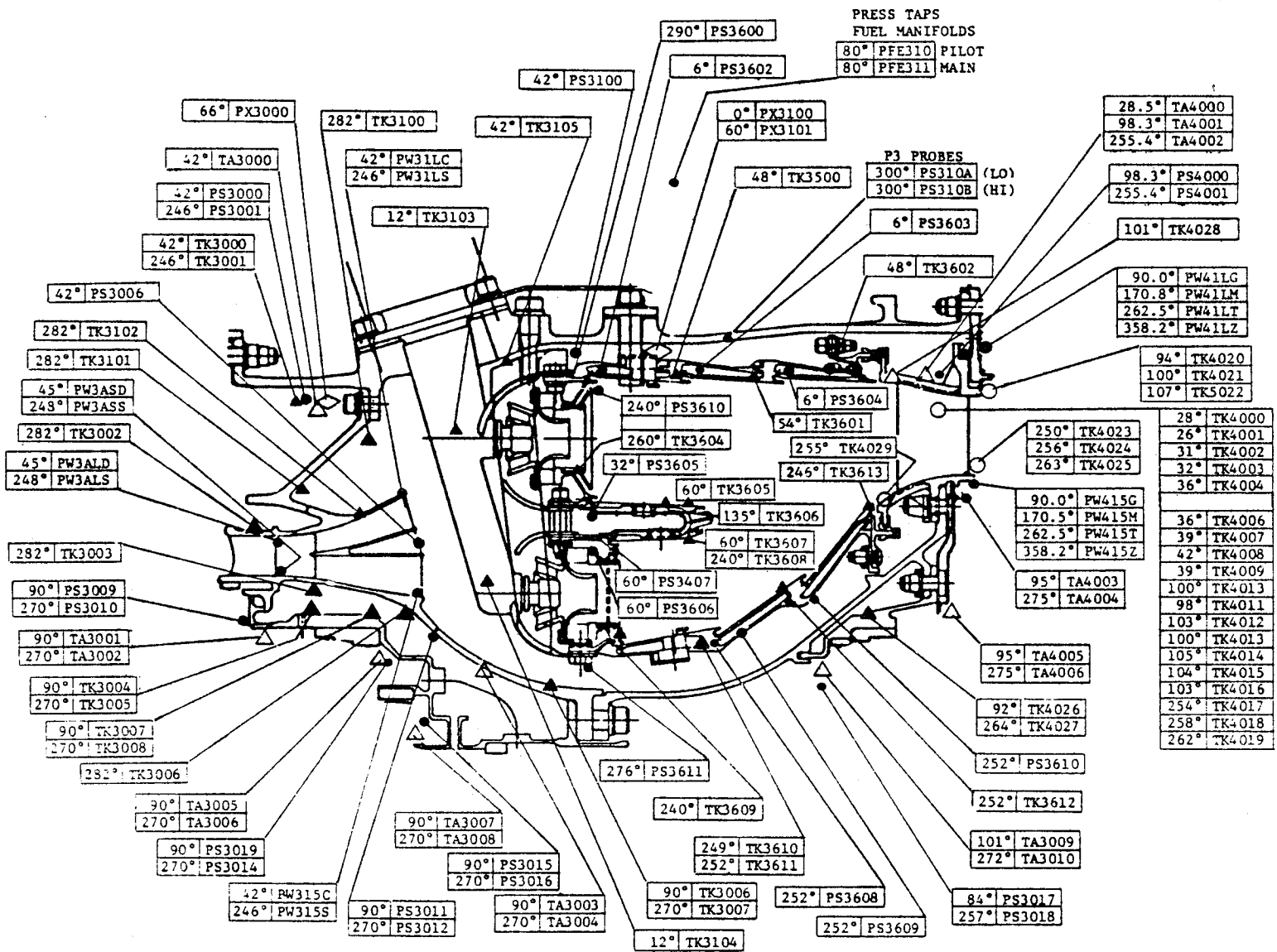


Figure 114. Combustion System Instrumentation Diagram.

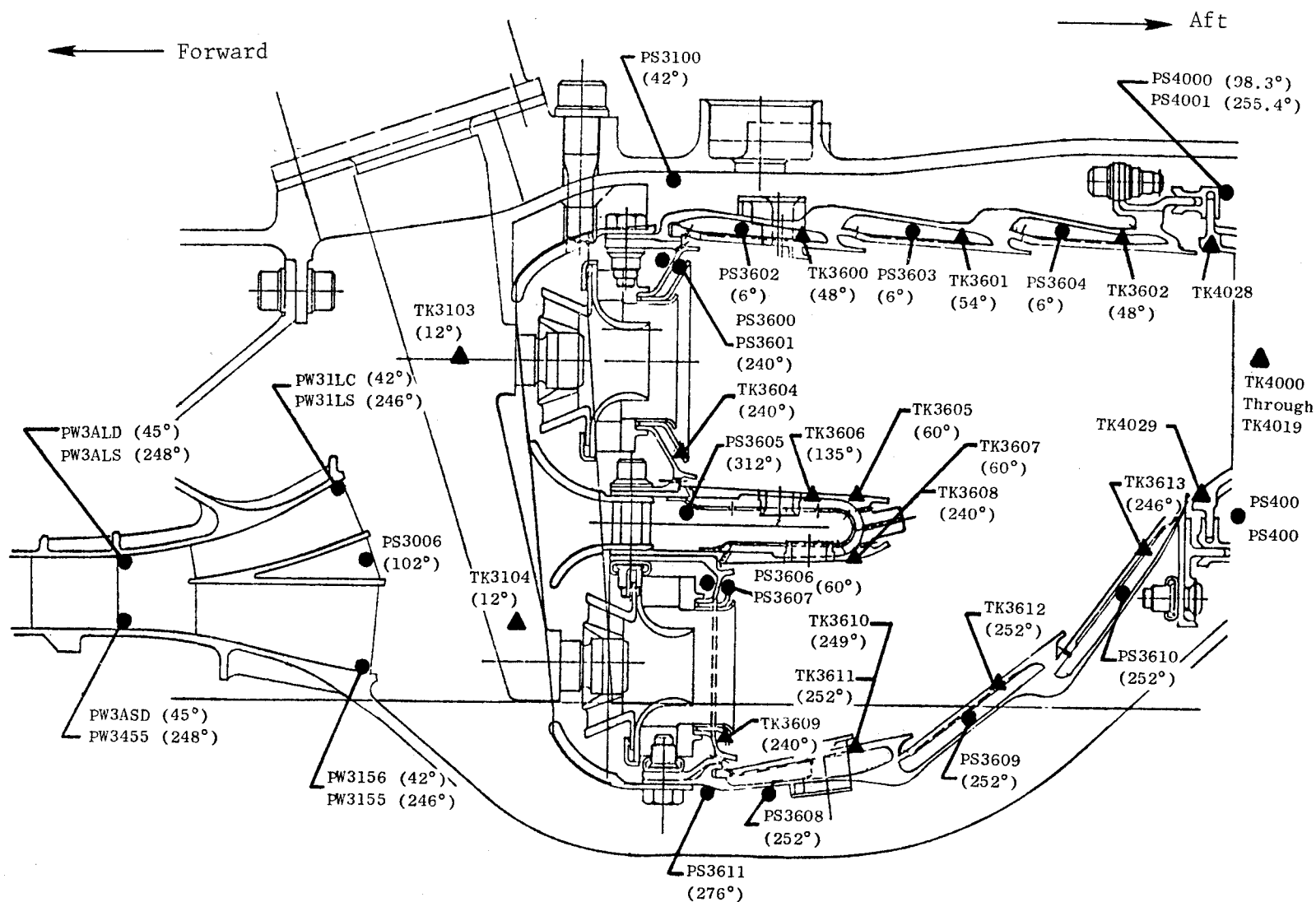


Figure 115. Combustor Instrumentation Layout.

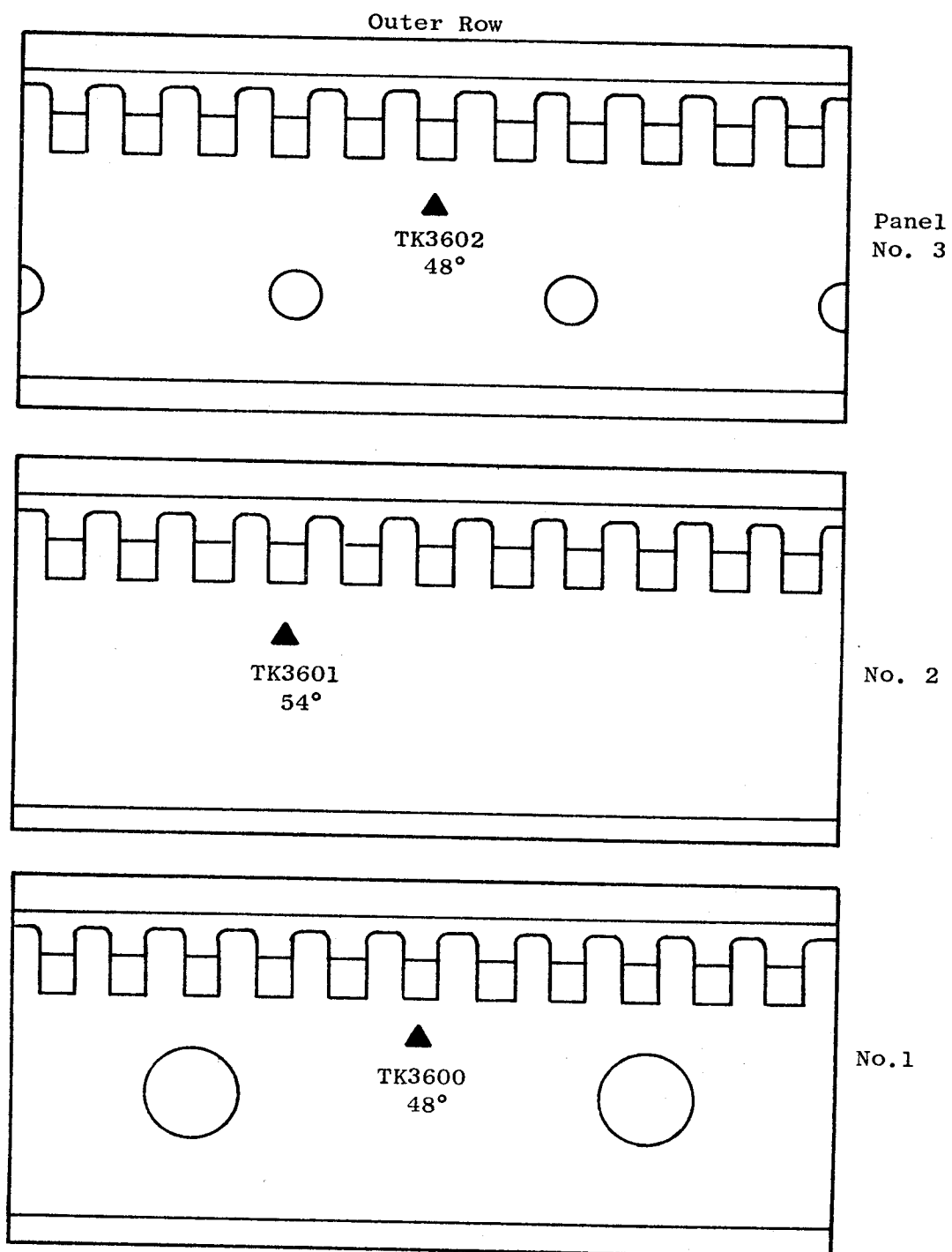


Figure 116. Combustor Liner Thermocouple Location, Outer Liner Shingles.

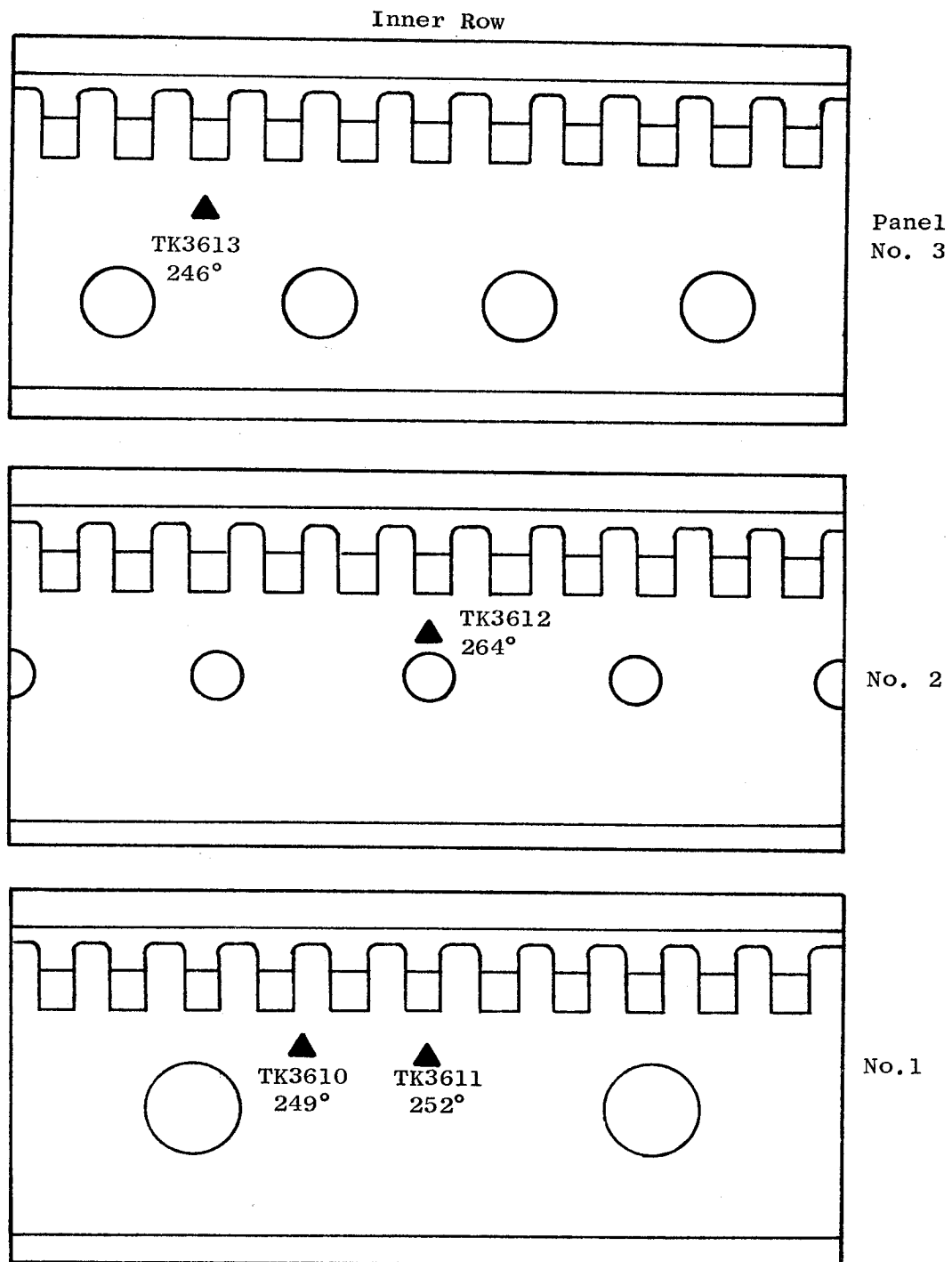


Figure 117. Combustor Liner Thermocouple Location, Inner Liner, Shingles.

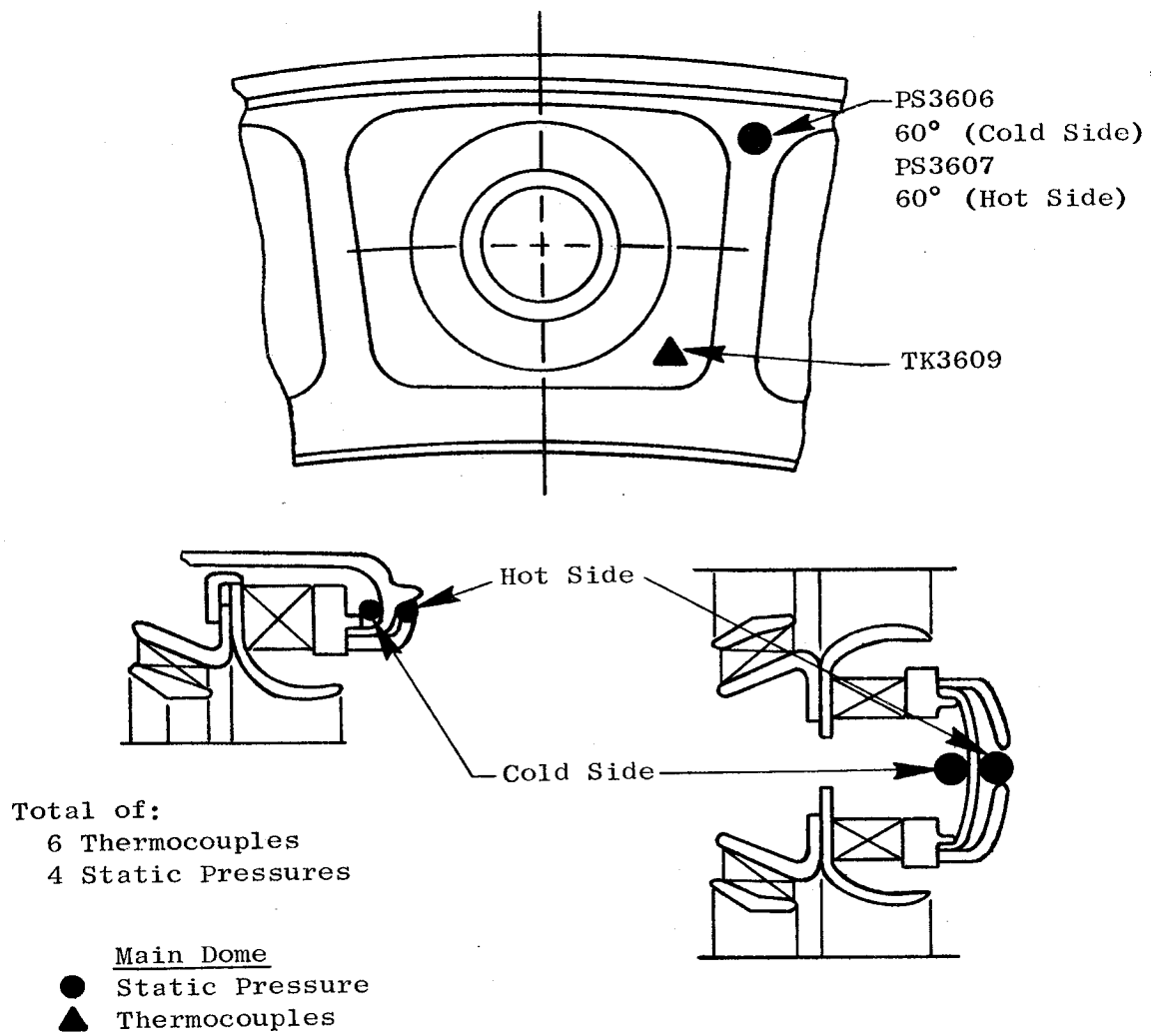


Figure 118. Main Dome Instrumentation.

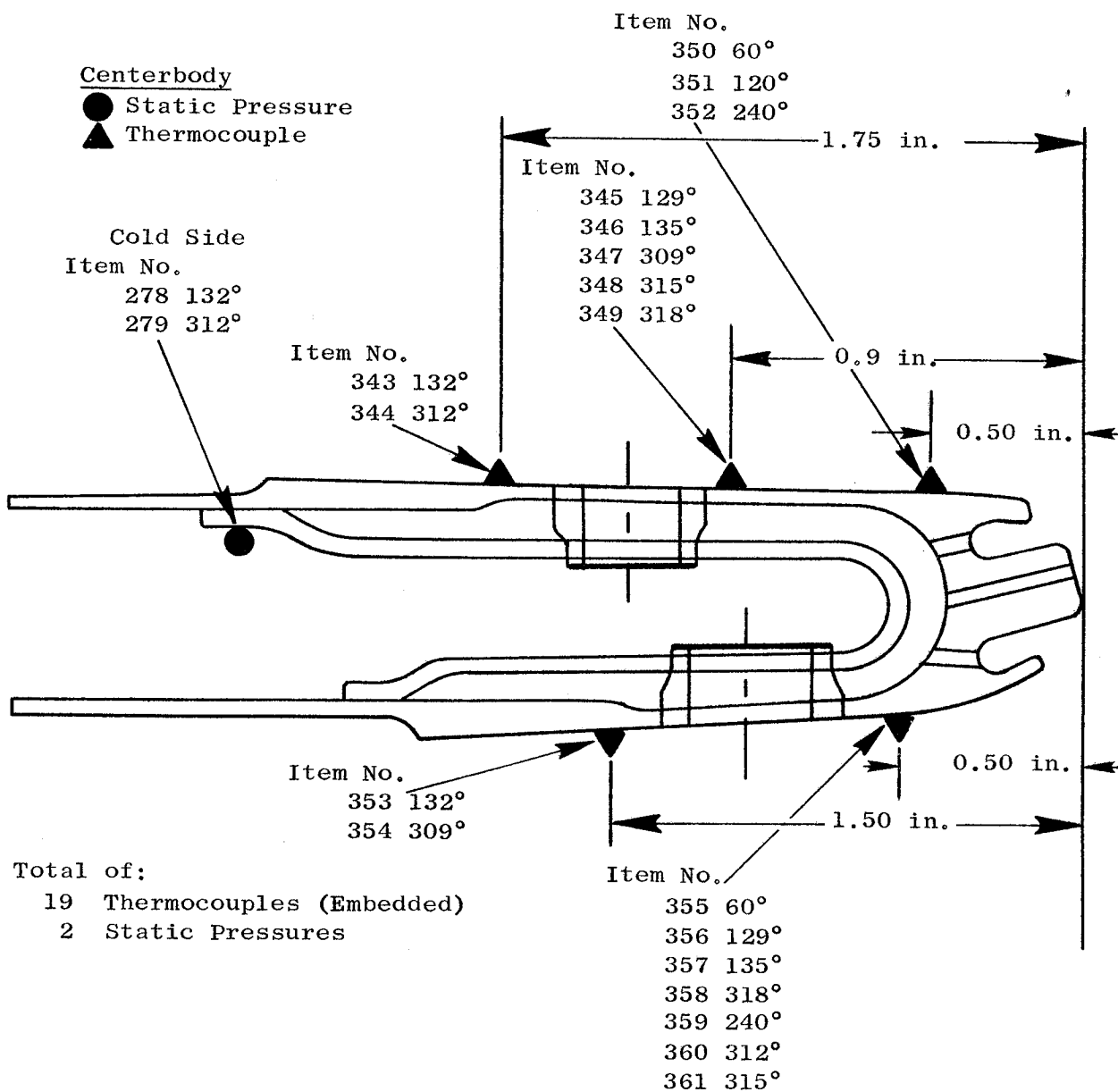


Figure 118. Main Dome Instrumentation (Concluded).

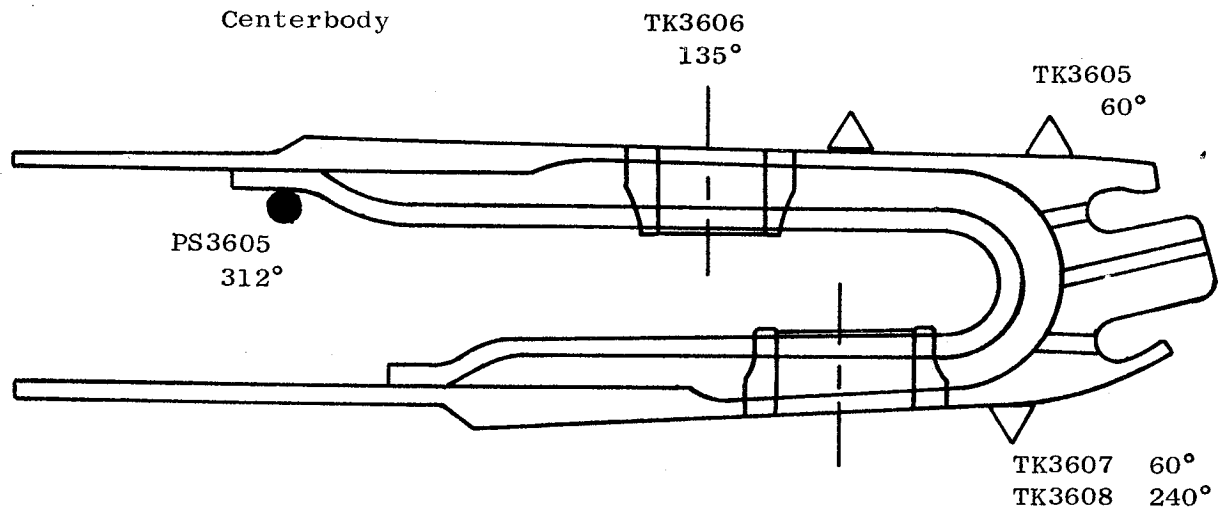


Figure 119. Centerbody Instrumentation.

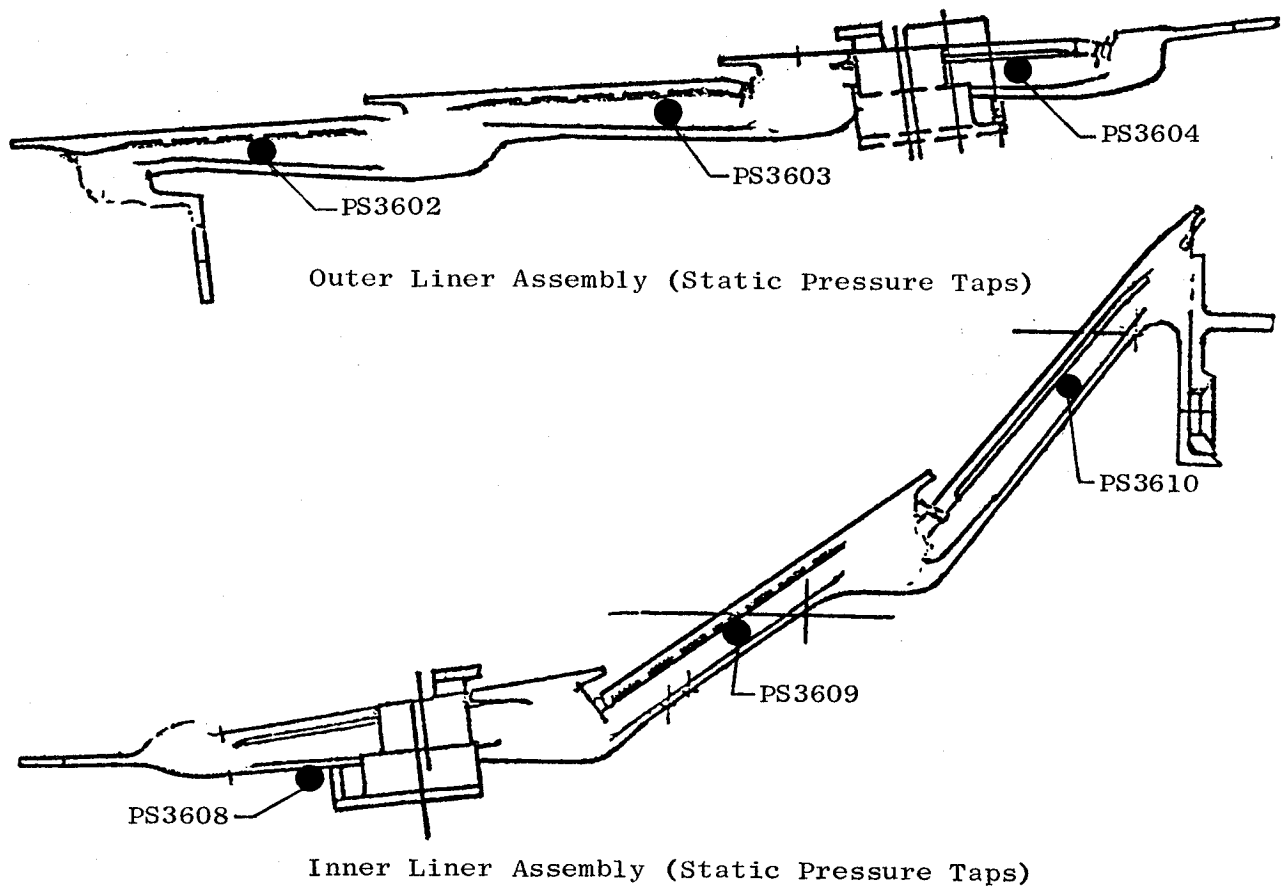


Figure 120. Combustor Liner Assemblies Pressure Instrumentation.

Table XVII. E³ Core Engine Test Combustor Instrumentation.

Temperatures, (Thermocouples)	Location	Still Functioning at End of Test
TK3103	Fuel Nozzle	X
TK3104	Fuel Nozzle	X
TK3600	Outer Liner Panel 1, Shingle	X
TK3601	Outer Liner Panel 2, Shingle	X
TK3602	Outer Liner Panel 3, Shingle	
TK3604	Pilot Splash Plate	
TK3605	Centerbody Aft (Pilot Side)	X
TK3606	Centerbody Forward (Pilot Side)	X
TK3607	Centerbody Aft (Main Side)	
TK3608	Centerbody Aft (Main Side)	
TK3609	Main Cup Diffuser	X
TK3611	Inner Liner Panel 1	
TK3612	Inner Liner Panel 2	X
TK3613	Inner Liner Panel 3	X
<u>Pressures</u>		
PW3ALD	Prediffuser Inlet	X
PW3ALS	Prediffuser Inlet	X
PW3ASD	Prediffuser Inlet	X
PW3ASS	Prediffuser Inlet	X
PW31LC	Prediffuser Exit	X
PW31LS	Prediffuser Exit	X
PW31SC	Prediffuser Exit	X
PW31SS	Prediffuser Exit	X
PS310A	Outer Flowpath	X
PS310B	Outer Flowpath	X
PS3006	Prediffuser Exit	X
PS3600	Pilot Dome ΔP	X
PS3601	Pilot Dome ΔP	X
PS3602	Outer Liner Panel 1 Cavity	X
PS3603	Outer Liner Panel 2 Cavity	X
PS3604	Outer Liner Panel 3 Cavity	X
PS3605	Centerbody (Pilot Side)	X
PS3606	Main Dome ΔP	X
PS3607	Main Dome ΔP	X
PS3608	Inner Liner Panel 1 Cavity	X
PS3609	Inner Liner Panel 2 Cavity	X
PS3610	Inner Liner Panel 3 Cavity	X
PS3611	Inner Liner Forward of Panel 1	X

programs which performed calculations to compute the various emissions indices and combustor operating parameters.

Smoke samples were taken only at key combustor operating points in Test 9. All smoke samples were obtained on Wattman No. 4 filter paper. Following completion of Test 9, the smoke samples were analyzed on a Densichron in order to determine the optical density to be used to compute the SAE Smoke Number. Due to an instrumentation failure, smoke data were obtained only up to 30% power. This is discussed in detail in the Emissions Section.

6.5.2 Testing and Data Acquisition

Steady-state data were obtained on the DMS throughout the test. Starts were made with (1) an air starter (at ambient or near-ambient engine inlet) and (2) by windmilling the engine to 20%, 25%, and 30% speed using 151.68 kPa (22 psia) or 179.26 kPa (26 psia) engine inlet. All starts were made on pilot zone only. Staging from single-to double-annular burning was initiated at stabilized 76.5% corrected core speed. Generally, full propagation after staging raised the core speed another 8% to 10%.

Several accelerations and decelerations, such as from 76.5% corrected core speed to 97% and back, were recorded on transient DMS. Also, transient data were taken on many of the automatic starts as an aid for optimizing the engine acceleration fuel schedule. Engine speed was dropped below idle while operating on single-annular and double-annular burning in order to examine subidle combustion characteristics. No problems arose during these idle to subidle decelerations and accelerations.

6.5.3 Starting

During core testing, engine starts were made successfully and without difficulty. No seventh-stage compressor bleed was necessary, and no temperature limits were approached. Concern about overtemperaturing the turbine nozzle, due to the sharply outward-peaked turbine inlet gas temperature profile associated with pilot-only operation, proved illusory.

Early in the test, starts were made by ramming the inlet to 179.26 kPa (26 psia), which windmilled the engine to (usually) 30% speed. Three start attempts were required during Initial Start Test 4 to find a sufficient level of minimum fuel flow. The first trial was made with manual fuel control and a starting fuel flow of 130.8 kg/h (300 pph). No ignition was detected after 15 seconds of ignition sparking, and the start was aborted. A second trial was made under the same conditions. There was a 40-rpm rise in core speed and a slight increase in exhaust gas temperature [up to 49° C (120° F)], indicating that ignition in only one or two cups had occurred. This start was also aborted.

During the third trial at the same inlet conditions, a starting fuel flow of 174.4 kg/hr (400 pph) was used. Ignition occurred almost immediately, and the engine smoothly accelerated to 4780 rpm with no change in starting fuel flow. All subsequent starts up to Test 8 were made in the same manner with the engine windmilling and with manual fuel control. One start (No. 13) was made with a 157.2 kPa (22.8 psia) inlet, the engine windmilling at 25% speed.

Beginning with Start Optimization, Test 8, a number of manual and automatic starts were successfully completed, many using the starter rather than ram air. A manual start from 20% windmilling speed resulted in a quick ignition due to a lower inlet airflow with 174.4 kg/h (400 pph) fuel flow. Next, two automatic ram starts were made from 20% windmilling speed, with a 20% lean, $-1 W_f/P_{S3}$ (ϕ) unit*, and a 10% lean acceleration schedule. During automatic starts, fuel flow was set by the acceleration fuel schedule which is defined in terms of W_f/P_{S3} and varies as a function of core rpm and inlet temperature. A schedule multiplier provides percentage adjustments, and a bias provides adjustment in unit increments of W_f/P_{S3} .

The first starts using the air starter were trouble-free. Start 17 was a manual start from maximum motoring speed (32% corrected speed), as determined by maximum allowable starter air pressure 379.2 kPa (55 psia), with an engine inlet pressure 3.45 kPa (0.5 psia) above ambient. Two more automatic starts from maximum motoring speed and ambient engine inlet completed Test 8. The

* $W_f/P_{S3} \equiv \phi \equiv$ Unit of fuel flow/unit compressor discharge pressure, pph/psi.

first, on an acceleration schedule of nominal +12%, was made with a time-to-idle (68.5%) of 107 seconds. The slow start time was due in part to the air starter performance, which was poorer than expected. The facility installation was another contributing factor because, with the engine inlet directly connected to the facility air supply, it was possible for the engine inlet pressure to drop slightly below cell ambient during part of the acceleration to ground idle. Thus, engine acceleration was retarded by some amount of negative torque. The second automatic start was made with an acceleration schedule of "nominal +5 W_f/P_{S3} " units. Time to idle was one minute, which met an internally set acceleration goal.

All subsequent starts were made using automatic fuel control. These starts are detailed in Table XVIII. Ignition to idle time was brought down to approximately 30 seconds by enriching the acceleration schedule to "nominal +20% +4 ϕ " with the fifth-stage stator locked at +3° from nominal schedule.

6.5.4 Staging Transition from Pilot-Only to Double-Annular Burning

The combustor was staged from pilot-only burning to double-annular burning at 76.5% speed throughout the engine test. An unexpected difficulty was encountered on the first attempt to stage: there was not enough fuel in the main manifold and nozzles for ignition. It was determined that leaky fuel nozzle check valves were allowing the entire main zone system to drain all fuel when not in use. Therefore, it was necessary to fill the entire system just prior to staging. Consequently, the procedure outlined below was adopted and followed throughout the test.

The main zone shutoff valve was cracked open for a period of 10 to 15 seconds before staging, directing a small portion of the total fuel flow to the main zone fuel manifold. The main manifold pressure was monitored until it was seen to build up and stabilize. After this fill time, the main zone shutoff valve was fully opened while the pilot zone reset valve was fully closed to initiate staging. Generally, ignition of the main zone occurred within two seconds. Engine speed would decrease 100 rpm during this lag, but would quickly recover as combustion in the main zone propagated fully. Because of the lengthy fill time, all transitions were performed by manual

Table XVIII. Automatic Starts.

Test Number and Description	Start Number	Inlet	Core Speed, PCN25R	Acceleration Schedule	Compressor Stator Stage 5	Minimum Fuel Flow kg/hr (pph)	Time Ignition to Idle, s	Exhaust Nozzle
9 Emissions	21	158.6 kPa (23 psia)	25%	Nominal - 10%	Schedule	174.4 (400)	N/A	Nominal
10 Start optim.	22	Ambient	30%	Nominal + 20%	Schedule	174.4 (400)	42	Nominal
Start optim.	23	Ambient	25%	Nominal + 20% + 1 ϕ	Schedule	174.4 (400)	42	Nominal
Start optim.	24	Ambient	25%	Nominal + 20% + 2 ϕ	Schedule	174.4 (400)	36	Nominal
Start optim.	25	Ambient	25%	Nominal + 20% + 3 ϕ	Schedule	174.4 (400)	35	Nominal
Start optim.	26	Ambient	25%	Nominal + 20% + 4 ϕ	Schedule	174.4 (400)	31	Nominal
Start optim.	27	Ambient	25%	Nominal + 20% + 5 ϕ	Schedule	174.4 (400)	31	Nominal
Start optim.	28	Ambient	25%	Nominal + 20% + 5 ϕ	+ 3°	174.4 (400)	31	Nominal
Start optim.	29	Ambient	20%	Nominal + 20% + 5 ϕ	+ 3°	174.4 (400)	32	Nominal
10A Max. A8 perf.	30	Ambient	25%	Nominal + 20% + 3 ϕ	+ 3°	174.4 (400)	36	Maximum A8
Max. A8 perf.	31	Ambient	25%	Nominal + 20% + 3 ϕ	+ 3°	174.4 (400)	N/A	Maximum A8
10B Min. A8 perf.	32	Ambient	25%	Nominal + 20% + 3 ϕ	+ 3°	174.4 (400)	N/A	Minimum A8
11 Final perf.	33	137.9 kPa (20 psia)	20%	Nominal	+ 17°*	196.2 (450)	"Sluggish"	Nominal
Final perf.	34	137.9 kPa (20 psia)	20%	Nominal	+ 17°	196.2 (450)	"Faster"	
Final perf.	35	158.6 kPa (23 psia)	25%	Nominal	+ 17°†	196.2 (450)	N/A	
Final perf.	36	158.6 kPa (23 psia)	25%	Nominal	+ 17°	196.2 (450)	N/A	
Final perf.	37	118.6 kPa (17.2 psia)	15%	Nominal	+ 3°	196.2 (450)	N/A	

* Miscalibrated Stator 5, therefore points not representative

† Misrigged S2 and S4 also

 ϕ = W_f/PS_3 units

control to maintain better control over the main manifold fill procedure. Sanborn traces of engine speed, pilot fuel flow (only pilot and total fuel flow were monitored, there was no indication of main fuel flow alone), and pilot and main fuel manifold pressures for a typical staging sequence are presented in Figure 121.

6.5.5 Emissions

Test 9 constituted the emissions tests. These tests are defined by the operating line conditions presented in Table XIX. The inlet temperature remained at 32° C (90° F) throughout the test.

Emissions testing was originally scheduled to be conducted on the ICLS vehicle, but the location of that test, Site IV-D at Peebles, Ohio, does not have close access to a sheltered area to assemble the emissions equipment. As a result, the decision was made to run the emissions testing on the core engine and correct the results to turbofan conditions. Normally, this correction involves only pressure terms. However, two things occurred which made the job more difficult: First, turbine hardware was received with larger-than-desired cooling air holes. This meant that combustor overall fuel-air ratios would be higher than expected, necessitating correction of this parameter to proper FPS levels. Component fuel-air data were available to do this correction for carbon monoxide (CO) and hydrocarbons (HC) at 4% and 6% idle. There were no fuel-air data available for other engine operating conditions, nor were any fuel-air ratio variation data available for the oxides of nitrogen (NO_x) data. An estimate of the NO_x level was obtained by using the ratio of the test fuel-air ratio divided by the FPS fuel-air ratio all raised to the 0.65 power from the NO_x severity parameter at takeoff conditions, as a weighting factor. The second thing that occurred was a contaminated pump, discovered in the gas analysis equipment, which affected HC emissions. Correction for this problem was achieved by monitoring the "pump only" contamination level throughout the test and factoring out the effect in the posttest analysis. Other problems affecting combustor airflow level are noted later in the discussion.

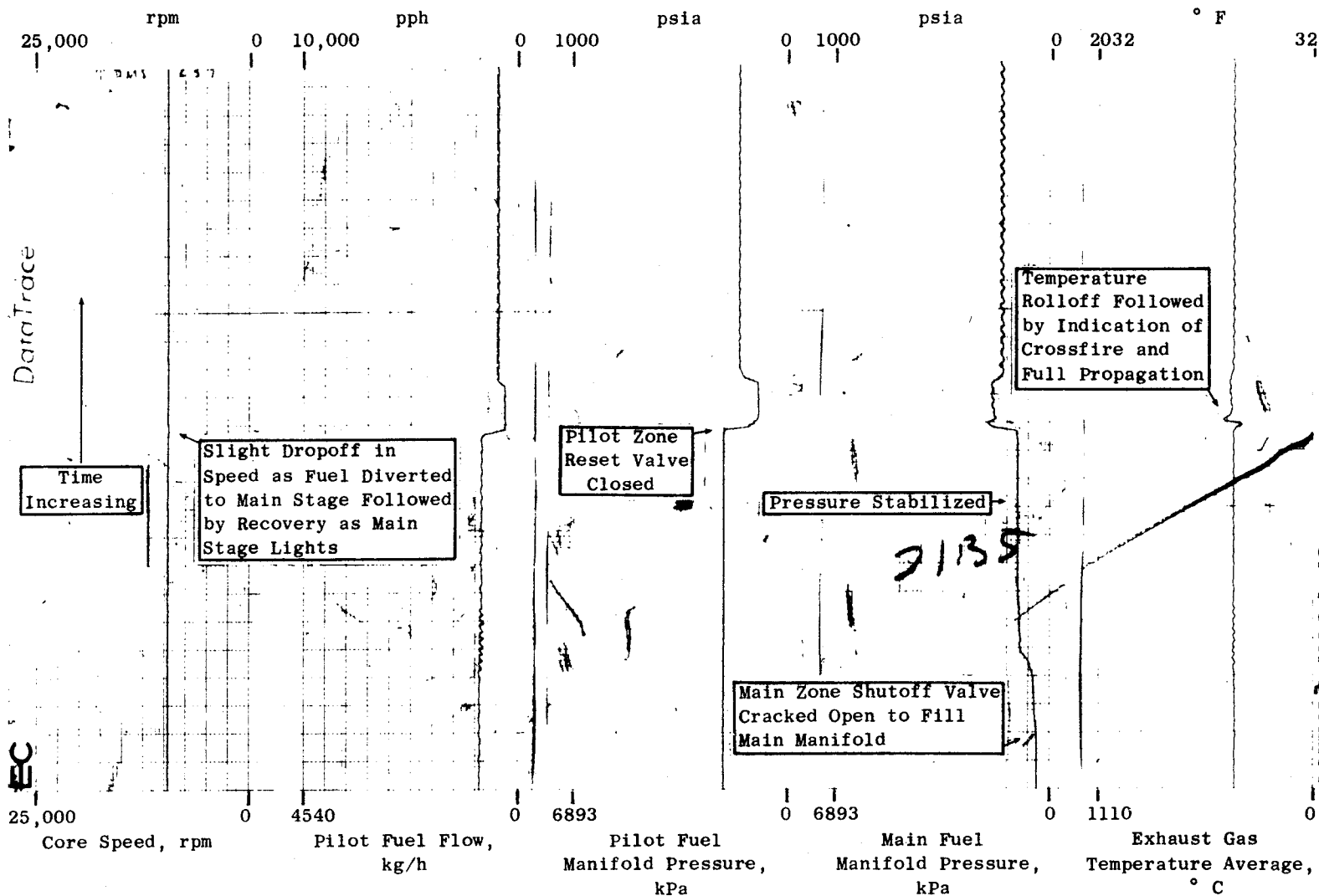


Figure 121. Staging From Pilot-Only to Double-Annular Burning.

Table XIX. Emissions Test Operating Line Parameters and Measured Emissions.

DMS Rdg	PCN25R, %	P3		T3		W36		f/a	P4		CO	HC	NO _x	Chemical nComb.
		kPa	(psia)	° C	(° F)	kg/s	(lbm/s)		kPa	(psia)	Measured, g/kg			
187	68.9	409.5	(59.4)	219	(426)	9.5	(21.9)	.0156	386.1	(56.0)	42.8	2.84	5.5	.987
188	61.8	320.6	(46.5)	187	(368)	7.1	(16.2)	.0173	304.7	(44.2)	62.1	0.86	4.6	.985
189	77.1	584.0	(84.7)	268	(514)	14.3	(32.8)	.0142	550.9	(79.9)	27.5	0.14	7.1	.993
190	76.9	577.1	(83.7)	266	(510)	14.2	(32.5)	.0139	554.7	(79.0)	91.7	52.2	3.7	.926
191	83.0	790.8	(114.7)	309	(589)	18.7	(42.9)	.0144	743.3	(107.8)	67.8	24.5	5.2	.960
192	87.8	1067.3	(154.8)	358	(677)	23.6	(54.1)	.0168	1007.3	(146.1)	30.6	3.37	7.9	.989
193	89.8	1196.9	(173.6)	383	(722)	24.5	(56.2)	.0192	1132.8	(164.3)	16.2	1.20	10.3	.995
194	90.2	1811.3	(262.7)	401	(753)	38.6	(88.6)	.0184	1712.7	(248.4)	9.6	0.23	11.7	.998
195	-	-	-	-	-	-	-	-	-	-	0.9	0.18	18.4	.999
196	94.1	2489.0	(361.0)	459	(858)	48.0	(110.2)	.0234	2360.1	(342.3)	0.7	0.09	18.4	.999
197	96.0	2826.2	(409.9)	484	(904)	53.7	(123.3)	.0252	2689.0	(390.0)	0.5	0.16	23.7	.999
198	96.0	2842.0	(412.2)	484	(903)	53.1	(121.8)	.0256	2695.9	(391.0)	-	-	-	-
199	96.0	2857.2	(414.4)	483	(902)	53.3	(122.3)	.0255	2714.5	(393.7)	-	-	-	-
200	90.0	1774.0	(257.3)	398	(748)	35.4	(81.3)	.0194	1680.3	(243.7)	11.9	0.84	10.5	.996
201	77.1	579.2	(84.0)	278	(533)	12.6	(29.0)	.0159	546.1	(79.2)	29.5	0.81	7.1	.992
202	77.4	586.7	(85.1)	276	(529)	13.0	(29.8)	.0157	553.0	(80.2)	28.8	2.41	7.2	.991
203	68.5	399.2	(57.9)	222	(432)	8.8	(20.3)	.0164	378.5	(54.9)	45.6	0.28	5.4	.989
204	62.0	320.6	(46.5)	189	(372)	7.1	(16.2)	.0174	304.7	(44.2)	62.6	0.32	4.1	.985
205	57.8	281.3	(40.8)	168	(335)	6.3	(14.4)	.0176	268.2	(38.9)	73.2	0.23	4.0	.983
206	47.1	206.8	(30.0)	122	(252)	4.3	(9.91)	.0201	198.6	(28.8)	89.1	2.96	3.13	.976
207	29.4	159.3	(23.1)	39	(102)	5.1	(11.8)	0	147.5	(21.4)	+ Posttest Zero +			

As a result of these problems, it was possible only to compare core engine results to requirements at discrete FPS operating conditions for CO, HC, and NO_x. Nevertheless, the core engine data, when corrected for all effects, agreed reasonably well with the core combustor annular component test results at FPS conditions. This bolsters the confidence level in both the data and the estimated ability of the core engine combustor to meet EPA (Environmental Protection Agency) CO and HC goals set at the start of the E³ Program.

The combustor in the core engine was not expected to meet NO_x goals because it did not incorporate all necessary main dome aerodynamic design features. However, a design has been rig tested which achieved goal NO_x levels. An FPS combustor incorporating this design would achieve all emissions goals.

Core engine emissions data were taken at 76.5%, 83%, 88%, 90%, 94%, and 96% corrected speeds with double-annular burning and at 76.5%, 68.5%, 62%, 58%, and 47% speeds with single-annular burning. Smoke data were recorded at 62%, 68.5%, 88%, and 96% speeds. However, at the higher engine speeds, a failure of the sample line heat tape at the smoke console caused the sample line temperature to drop, allowing water in the system to condense and spoil the smoke spots on the Wattman paper tapes by water spotting, especially at 96% corrected speed.

The compressor discharge pressure (CDP), temperature, and airflow levels were measured during the emissions test and are presented as a function of percent corrected core speed and compressor discharge temperature in Figures 122 through 128. Also, combustor zone fuel flows and fuel-air ratios are presented as functions of the same parameters in Figures 129 through 132.

Prior to starting the engine, gas samples were taken to obtain a measure of residual hydrocarbons in the sampling system. The data obtained indicated the presence of significant levels of trapped hydrocarbons within the sampling system. Attempts to purge the system of the residual hydrocarbons succeeded in reducing levels to 200 ppm just before start-up. These residual hydrocarbon levels were measured at several points prior to fire-up and after engine shutdown so that it was possible to construct a curve showing the

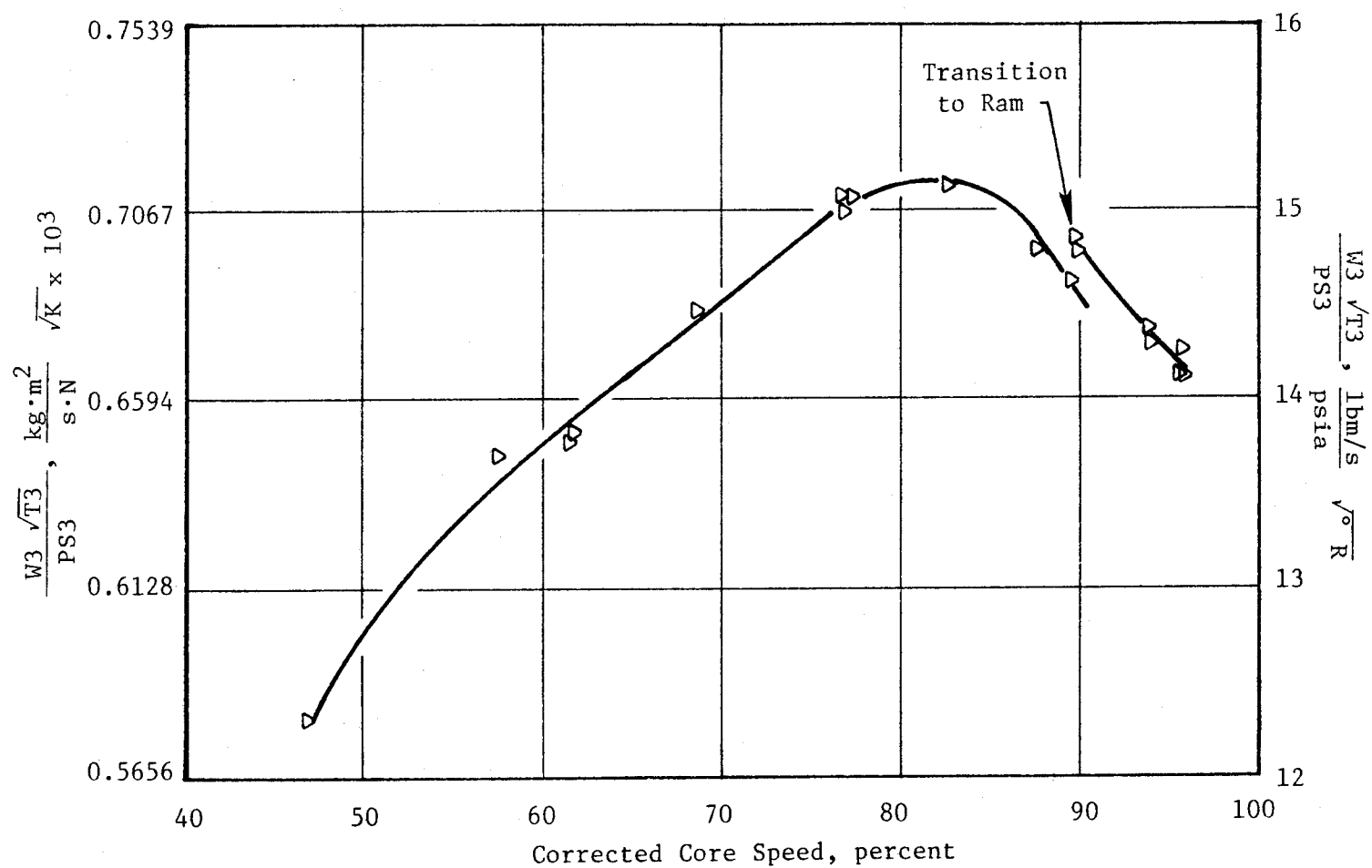


Figure 122. Combustor Flow Function Versus Corrected Core Speed.

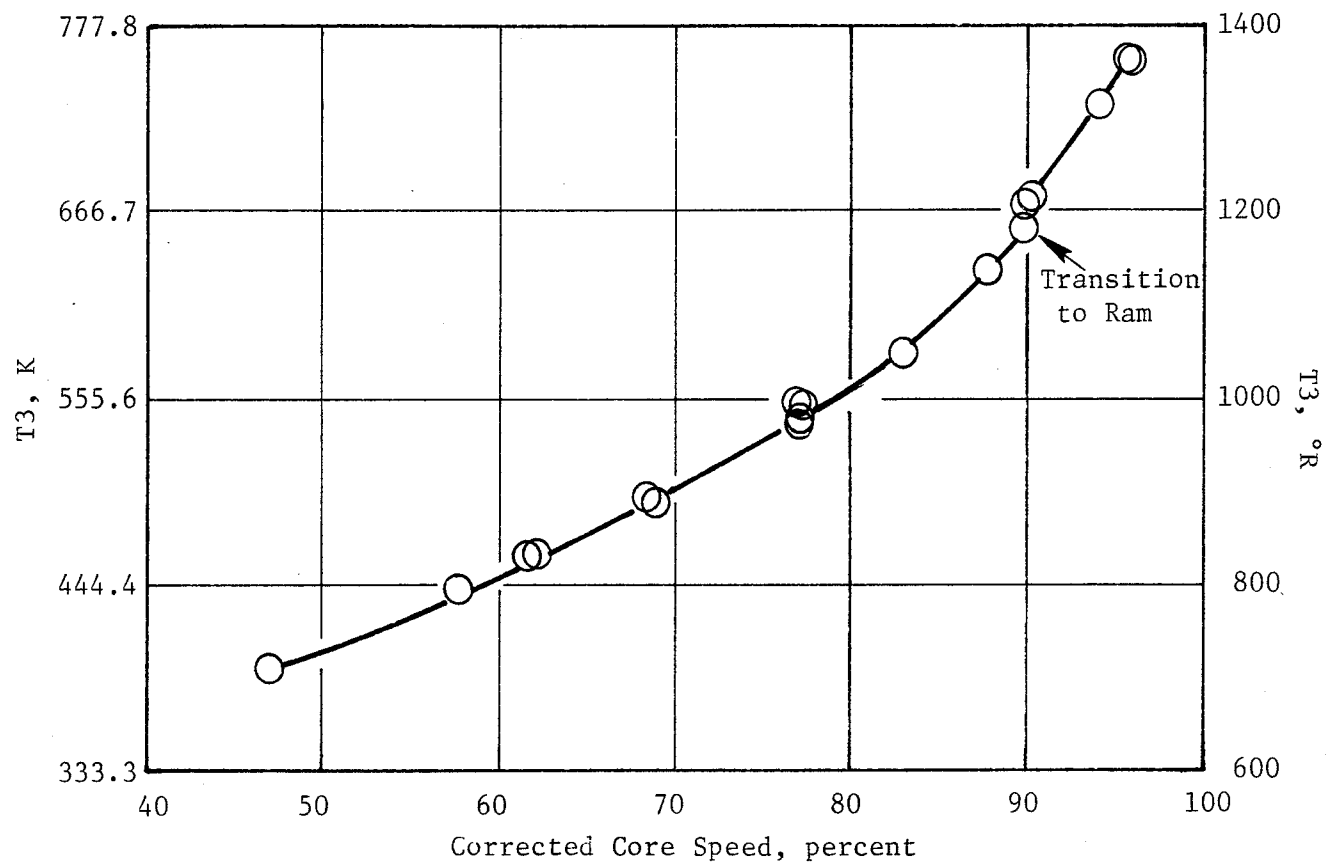


Figure 123. Combustor Inlet Temperature Versus Corrected Core Speed.

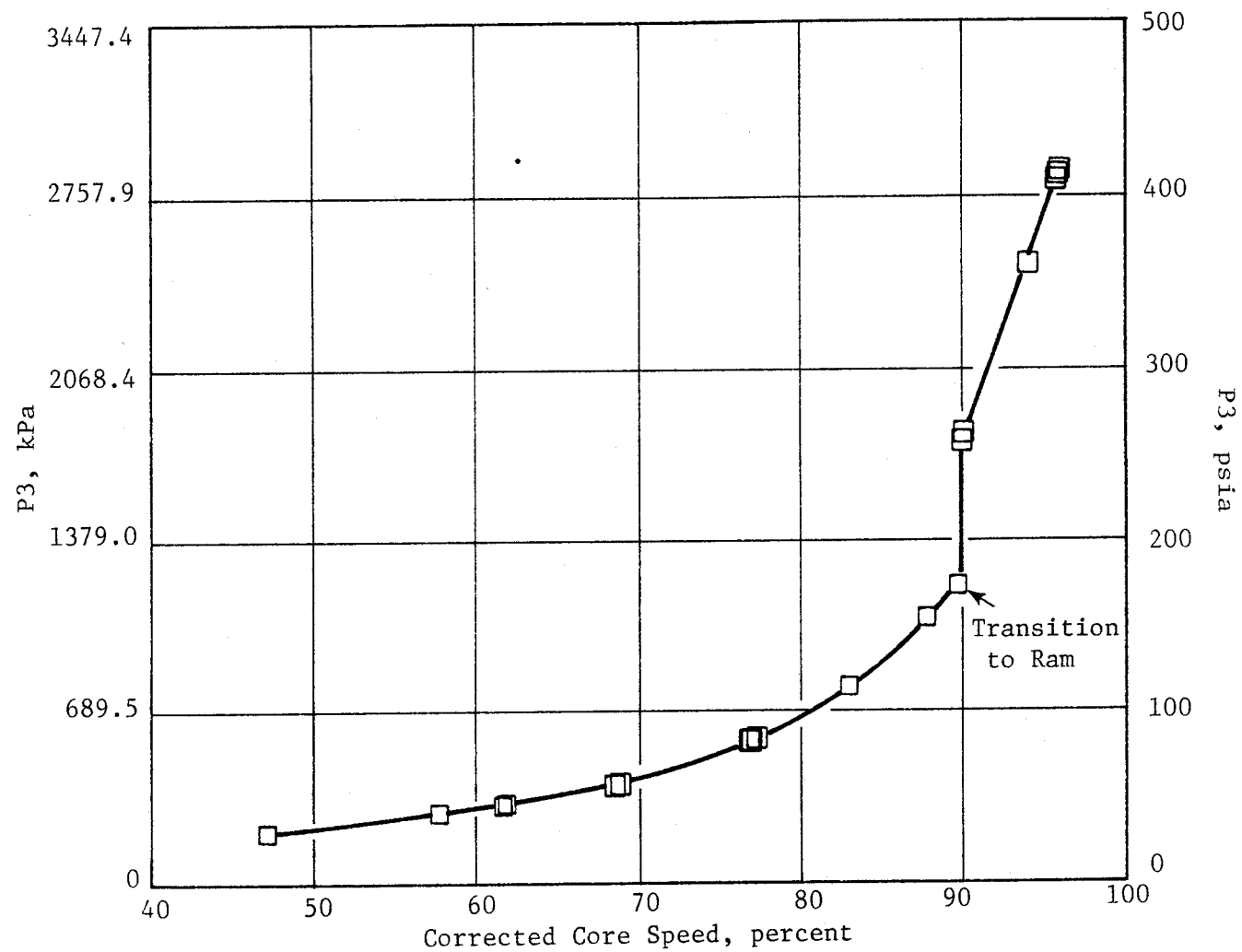


Figure 124. Combustor Inlet Pressure Versus Corrected Core Speed.

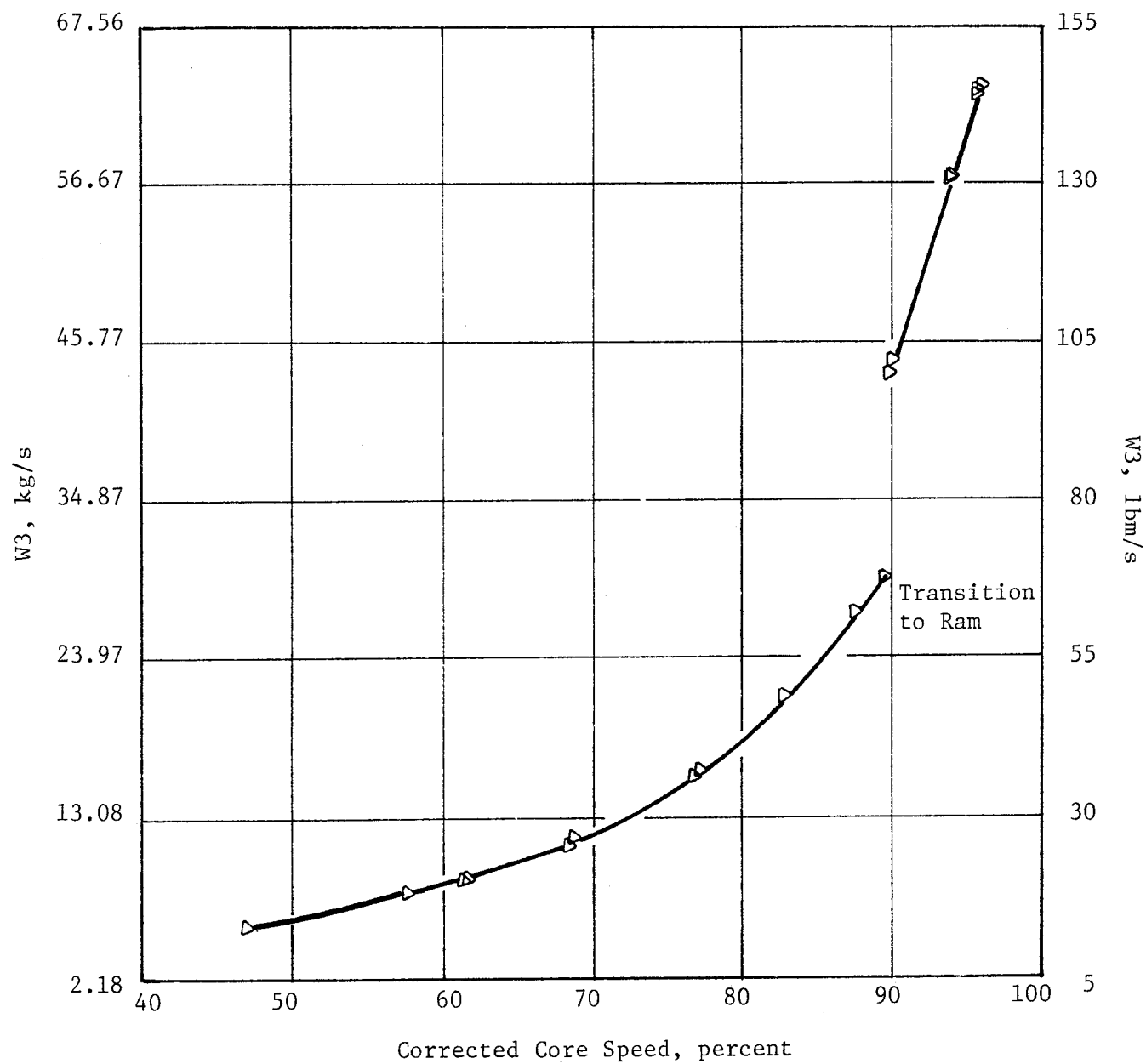


Figure 125. Combustor Airflow Versus Corrected Speed.

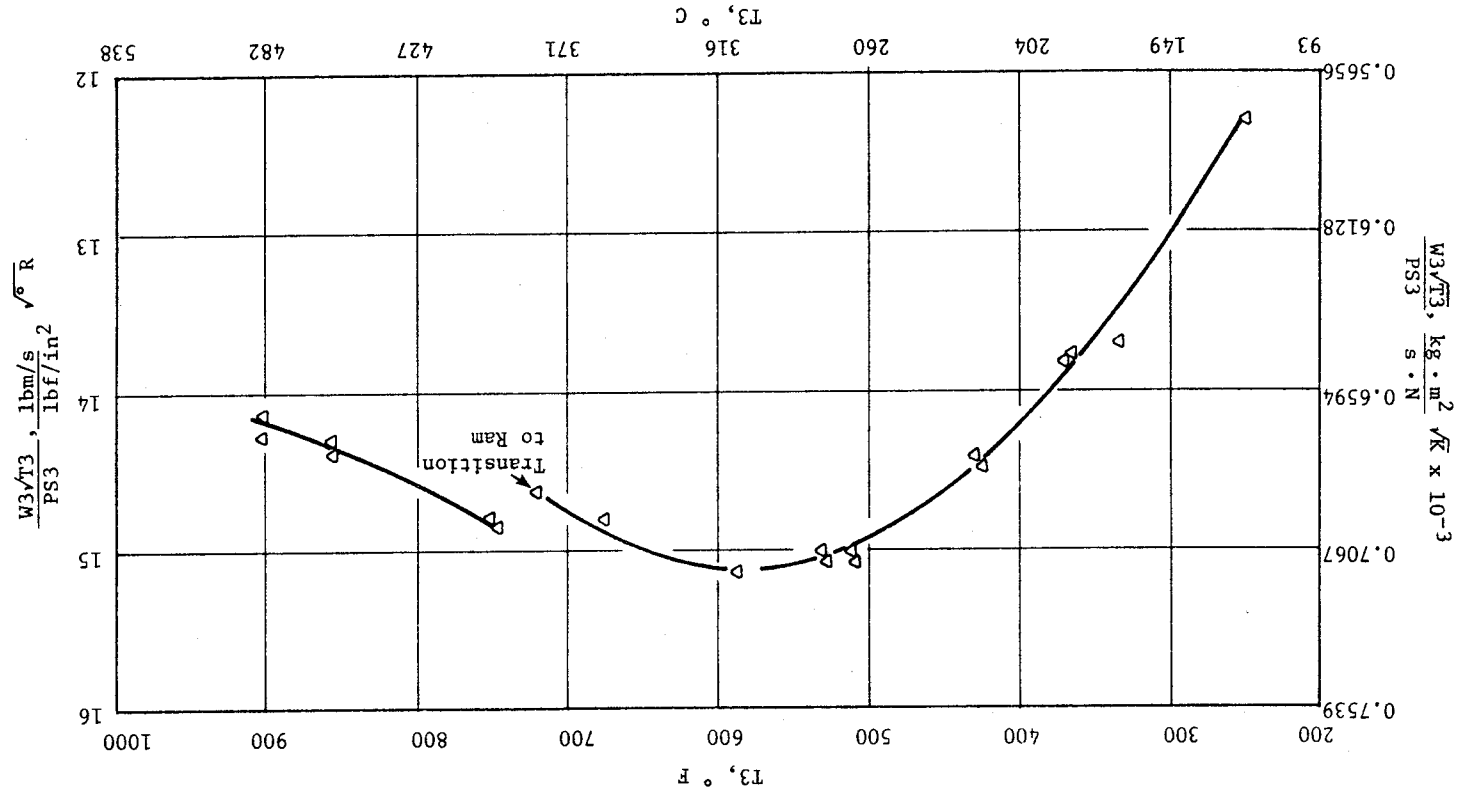


Figure 126. Combustor Flow Function Versus Combustor Inlet Temperature.

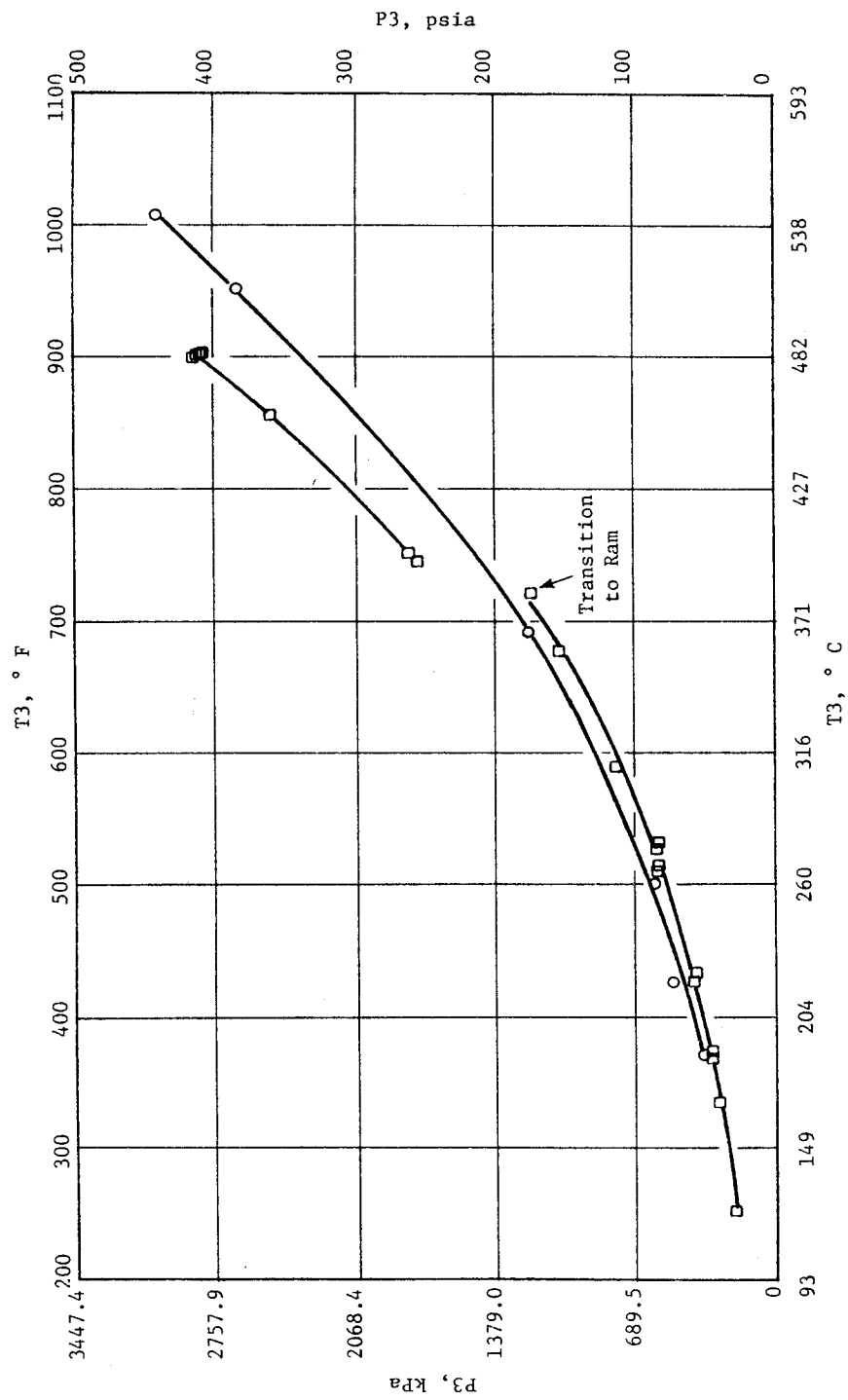


Figure 127. Combustor Inlet Pressure Versus Combustor Inlet Temperature.

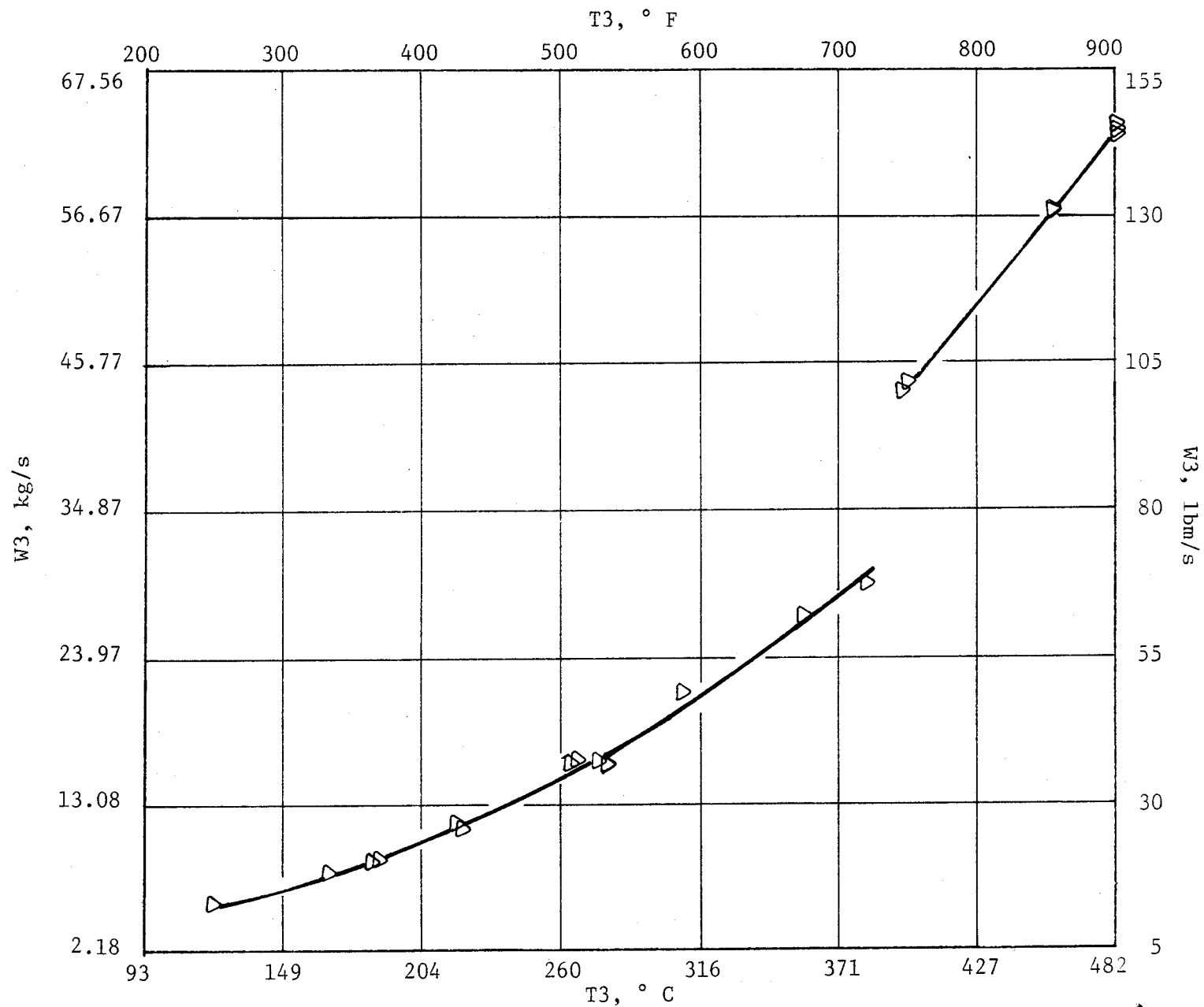


Figure 128. Combustor Airflow Versus Combustor Inlet Temperature.

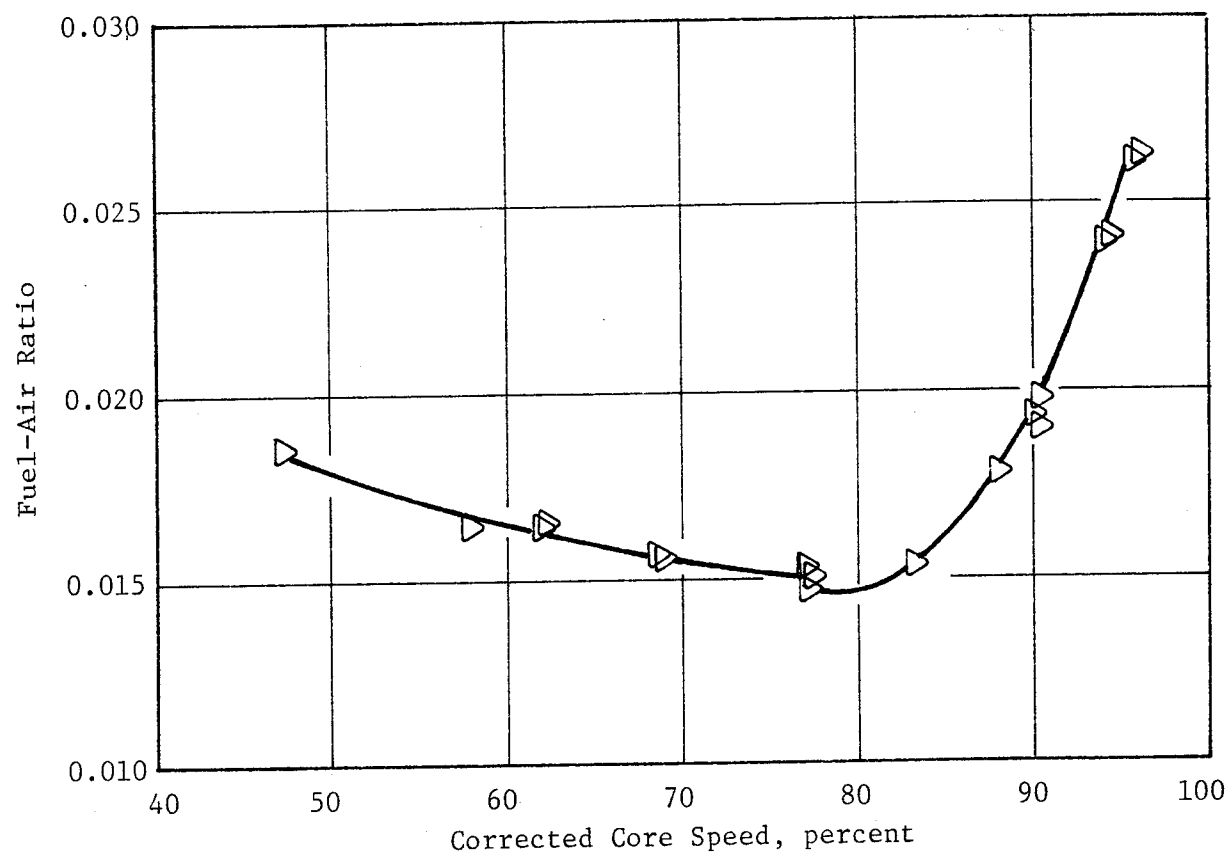


Figure 129. Combustor Fuel-Air Ratio Versus Corrected Core Speed.

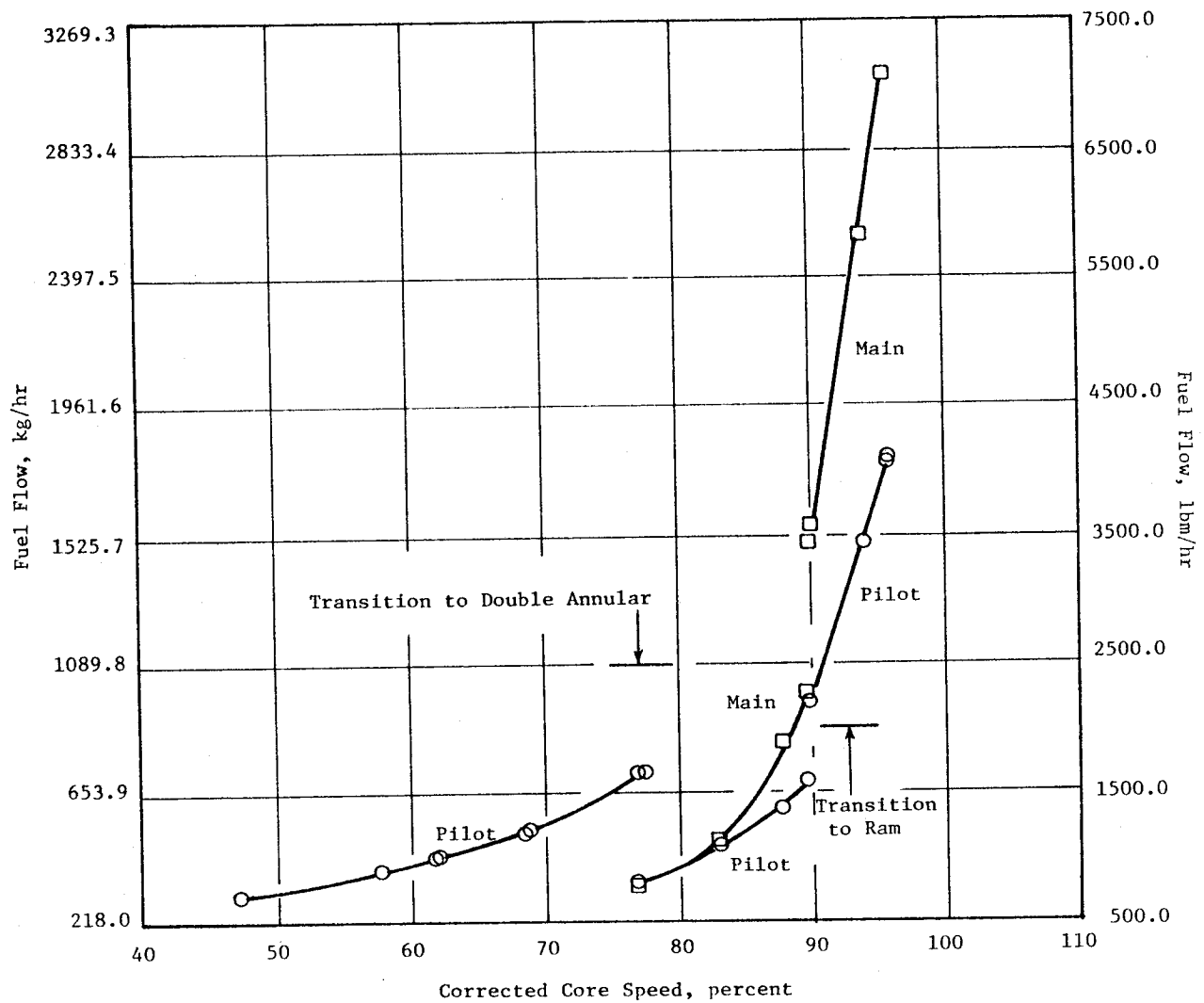


Figure 130. Combustor Pilot and Main Fuel Flow Versus Corrected Core Speed.

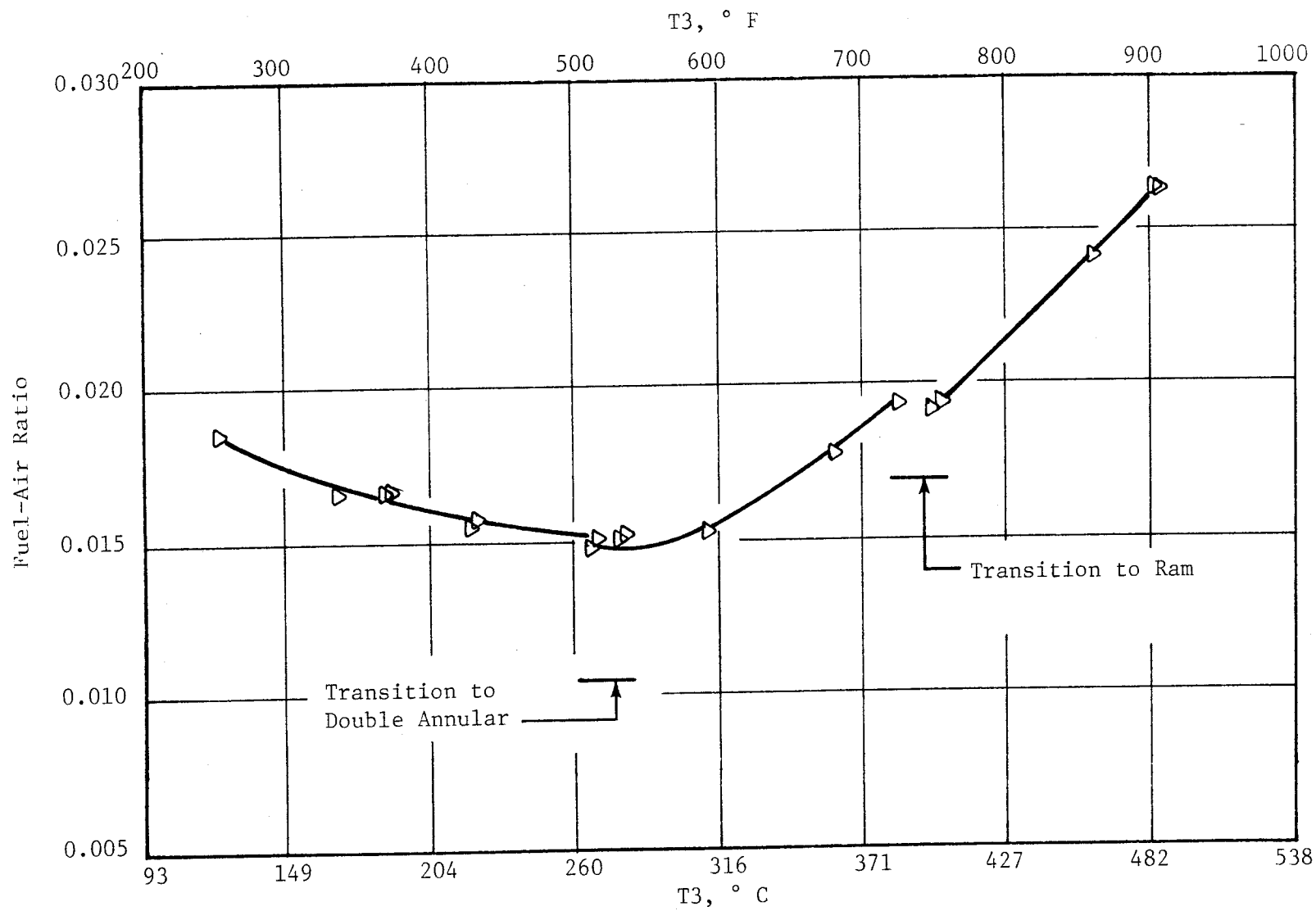


Figure 131. Combustor Fuel-Air Ratio Versus Combustor Inlet Temperature.

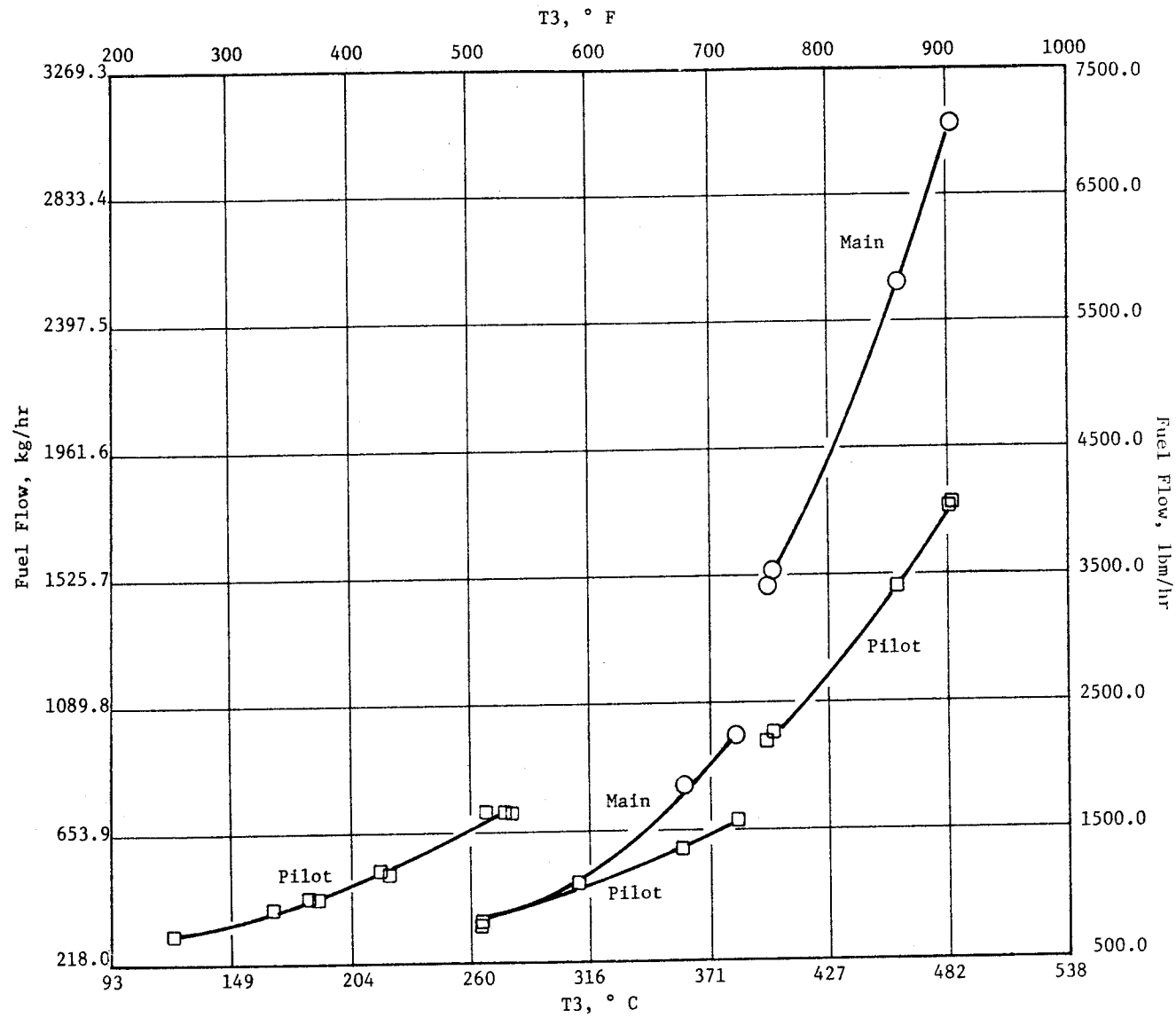


Figure 132. Combustor Pilot and Main Fuel Flow Versus Combustor Inlet Temperature..

decrease in contaminant level with time. This distribution was then used to eliminate the effect of hydrocarbon contamination from the engine emissions measurements. Carbon monoxide and oxides of nitrogen samples were not affected. It was later determined that the sampling pump was dirty; it had not been cleaned after being used in a previous emissions test and had accumulated high levels of hydrocarbons which were freed by the heating of the sample line during the E³ test. The measured core engine data are shown in Table XIX. The efficiencies shown are based on chemical analyses rather than engine thermodynamic performance.

The emissions data, adjusted to FPS cycle conditions, are presented in Table XX and Figures 133 through 135. These adjustments are made using the following relations:

$$EI_{CO} \text{ (Adj.)} = EI_{CO} \text{ (Meas.)} \left[\frac{P_3 \text{ Engine}}{P_3 \text{ Cycle}} \right]^{1.5}, \text{ g/kg Fuel}$$

$$EI_{HC} \text{ (Adj.)} = EI_{HC} \text{ (Meas.)} \left[\frac{P_3 \text{ Engine}}{P_3 \text{ Cycle}} \right]^{2.5}, \text{ g/kg Fuel}$$

$$EI_{NO_x} \text{ (Adj.)} = EI_{NO_x} \text{ (Meas.)} \left[\frac{P_3 \text{ Cycle}}{P_3 \text{ Engine}} \right]^{0.37}, \text{ g/kg Fuel}$$

These relations were derived as part of the data reduction effort for the NASA/GE Experimental Clean Combustor Program and the EPA/GE CFM56 Program. They have been used throughout the E³ combustor development program. The reference cycle pressure represents that predicted by the FPS cycle at the same compressor discharge temperature that the measurement was made. No adjustment for core engine fuel-air ratios was made for the data presented in these figures.

The figures represent plots of the emissions indices for carbon monoxide, (EI_{CO}) hydrocarbons (EI_{HC}), and oxides of nitrogen (EI_{NO_x}) versus compressor discharge temperature (T3). The hydrocarbon data shown have been adjusted for air pump contamination. The fuel split in the double-annular burning mode was about 40/60. The impact of staging on the emissions is clearly evident.

Table XX. Emissions Data Corrected to the FPS Cycle.

DMS	P3				Emissions Indices, g/kg						Burning Mode
	Core Engine		FPS		CO	HC	NO _x	CO	HC	NO _x	
	kPa	(psia)	kPa	(psia)	Measured			Adjusted			
187	409.5	(59.4)	468.8	(68)	42.8	2.84	5.5	34.9	2.03	5.8	Pilot only ↓ Staged 35/65 ↓ Pilot only ↓
188	320.6	(46.5)	372.3	(54)	62.1	0.86	4.6	49.5	0.59	4.9	
189	584.0	(84.7)	634.3	(92)	27.5	0.14	7.1	24.3	0.11	7.3	
190	577.1	(83.7)	620.5	(90)	91.7	52.2	3.7	82.2	43.5	3.8	
191	790.8	(114.7)	827.4	(120)	67.8	24.5	5.2	63.4	21.9	5.3	
192	1067.3	(154.8)	1144.5	(166)	30.6	3.37	7.9	27.6	2.88	8.1	
193	1196.9	(173.6)	1337.6	(194)	16.2	1.20	10.3	13.7	0.91	10.7	
194	1811.3	(262.7)	1489.3	(216)	9.6	0.23	11.7	12.9	0.38	10.9	
195	2489.0	(361.3)	2068.4	(300)	0.9	0.18	18.4	1.19	0.29	17.2	
196	2489.0	(361.0)	2068.4	(300)	0.7	0.09	18.4	0.92	0.14	17.2	
197	2826.2	(409.9)	2337.3	(339)	0.5	0.16	23.7	0.66	0.26	22.1	
198	2842.0	(412.2)	2337.3	(339)	← No Emissions →						
199	2857.2	(414.4)	2337.3	(339)	← No Emissions →						
200	1774.0	(257.3)	1468.6	(213)	11.9	0.84	10.5	15.8	1.35	9.8	
201	579.2	(84.0)	675.7	(98)	29.5	0.81	7.1	23.4	0.55	7.5	
202	586.7	(85.1)	596.4	(86.5)	28.8	2.41	7.2	28.1	2.31	7.2	
203	399.2	(57.9)	468.8	(68)	45.6	0.28	5.4	35.8	0.19	5.7	
204	320.6	(46.5)	379.2	(55)	62.6	0.32	4.1	48.7	0.21	4.4	
205	281.3	(40.8)	337.8	(49)	73.2	0.23	4.0	55.6	0.15	4.3	
206	206.8	(30.0)	234.4	(34)*	89.1	2.96	3.13	73.8	2.16	3.3	
207	159.3	(23.1)			← Posttest Zero →						

*Extrapolated

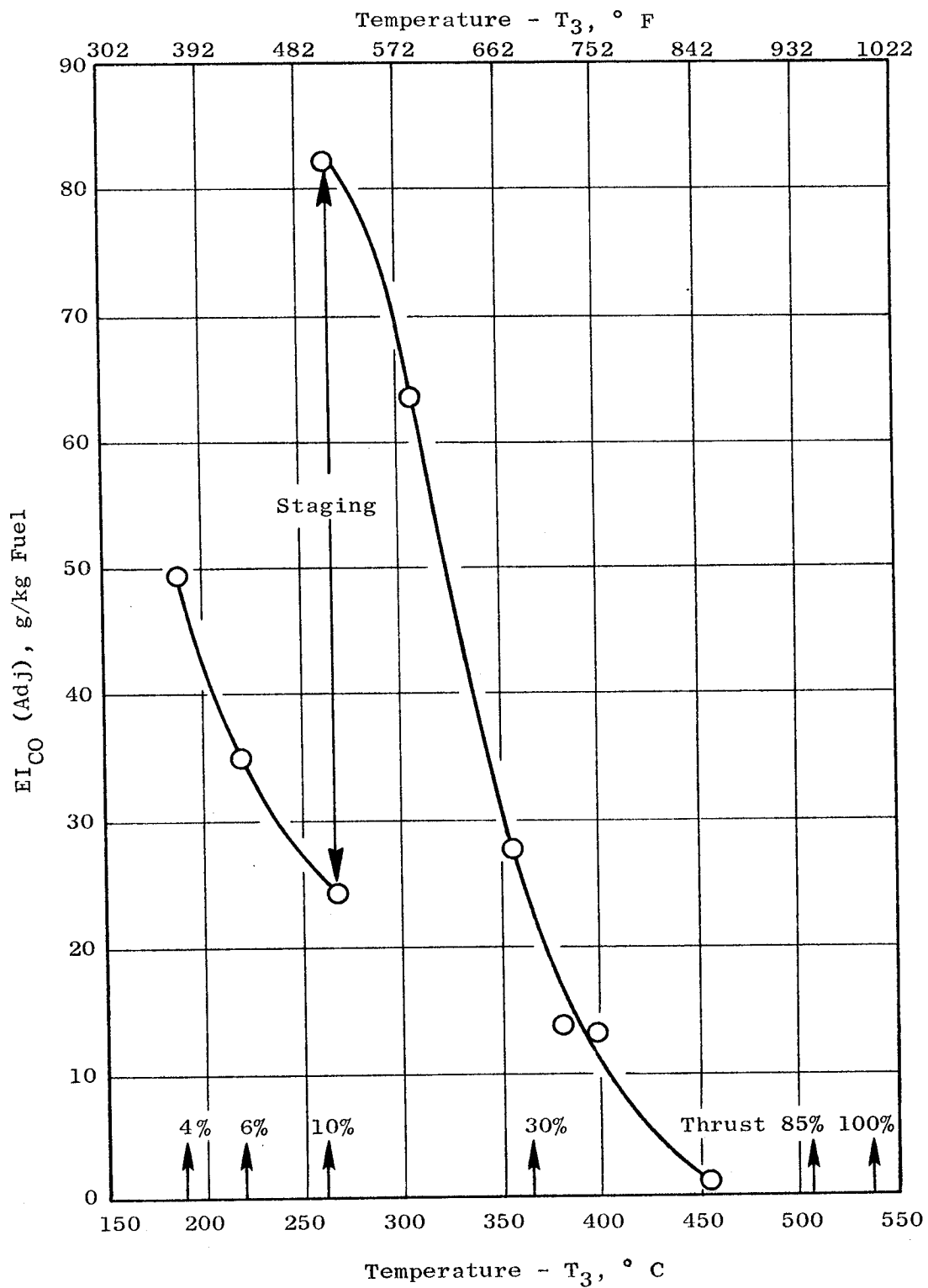


Figure 133. FPS Adjusted Carbon Monoxide Emissions Versus Compressor Discharge Temperature.

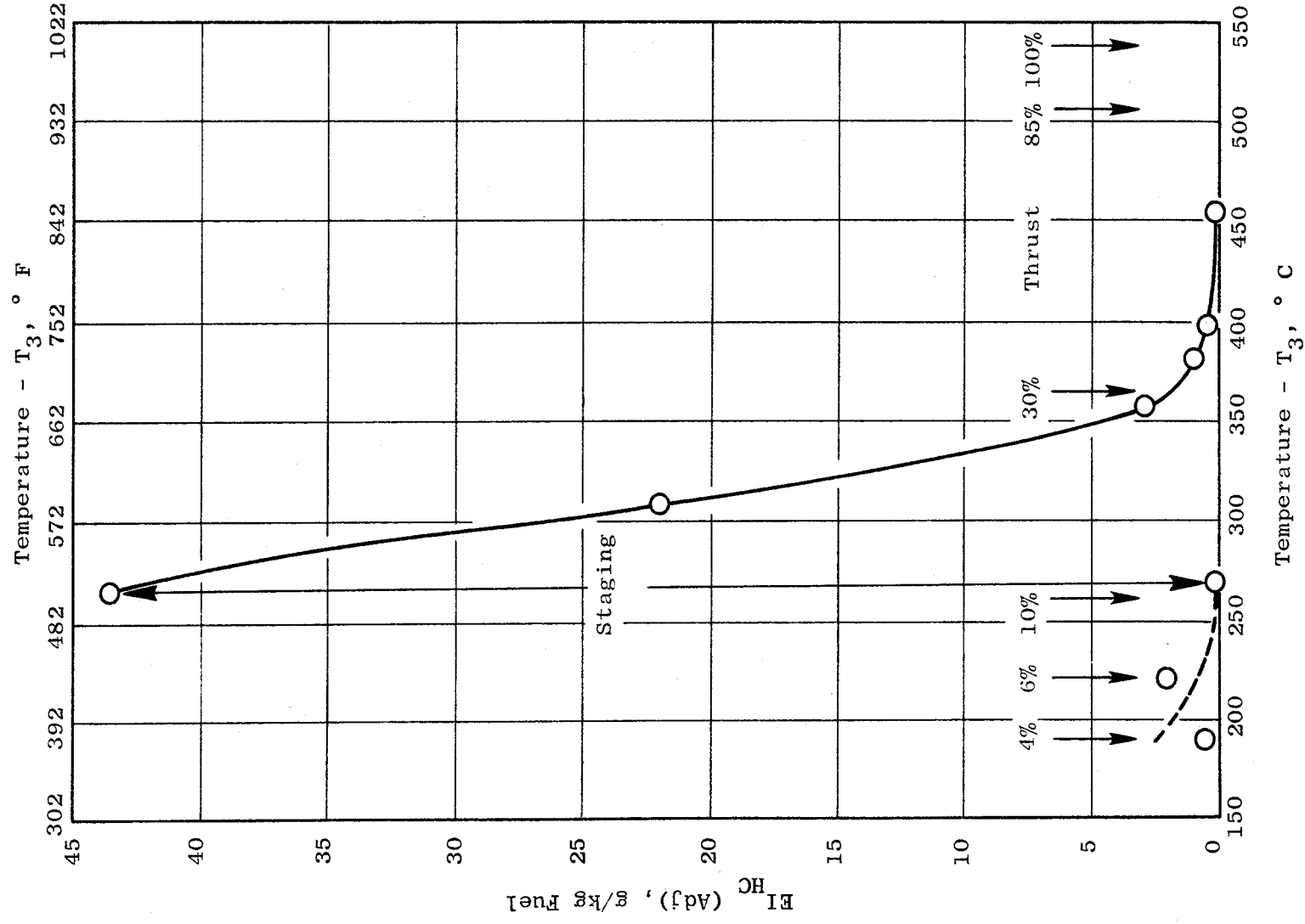


Figure 134. FPS Adjusted Hydrocarbon Emissions Versus Compressor Discharge Temperature.

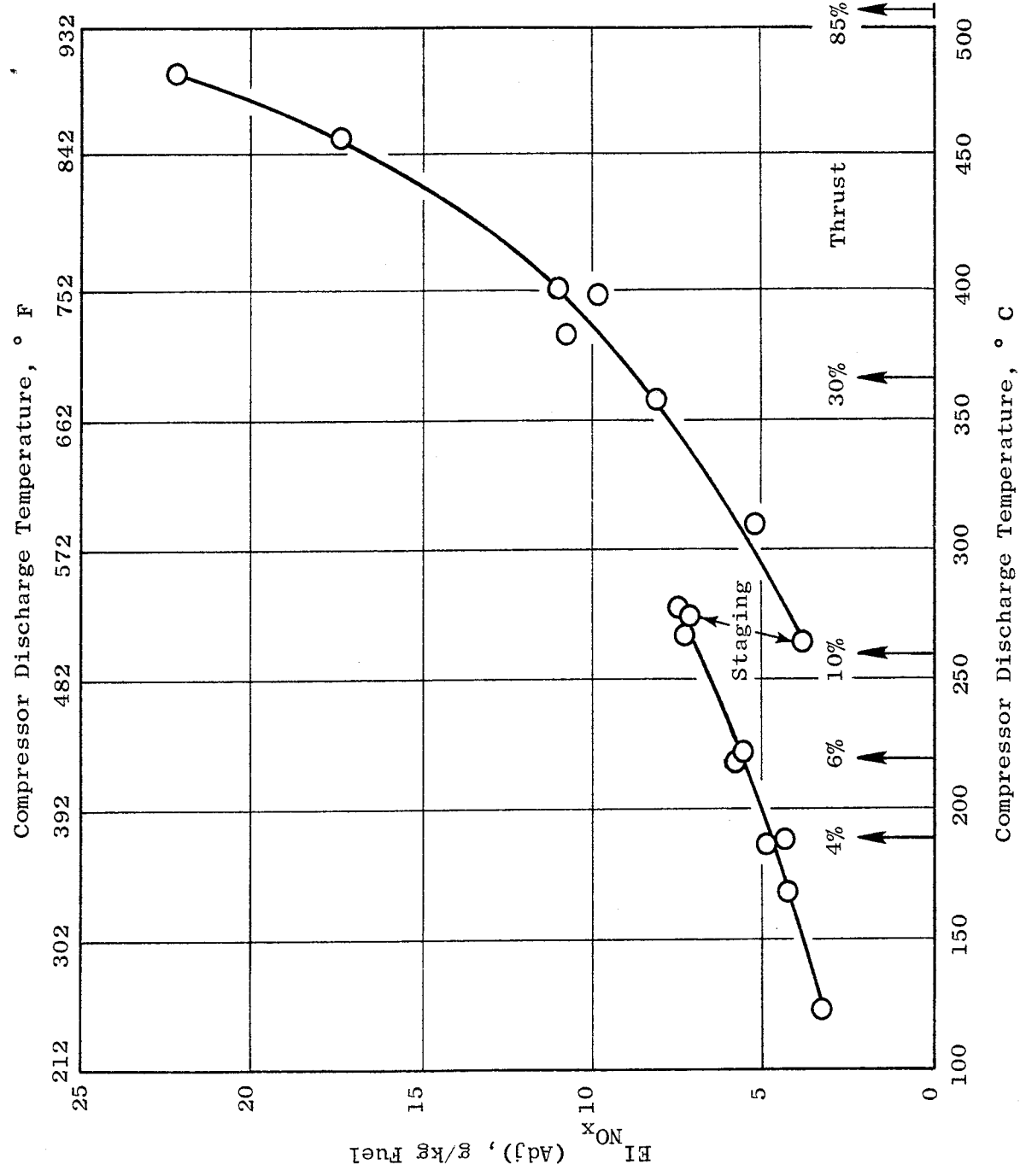


Figure 135. FPS Adjusted NO_x Emissions Versus Compressor Discharge Temperature.

Figure 136 compares the fuel-air ratios above idle at which the engine ran to the predicted FPS cycle fuel-air ratios as a function of physical core speed. It can be seen that the core engine ran at considerably higher fuel-air ratios than predicted at all points in the test. Several factors contributed to this: all turbine hardware was on the high side of machining tolerances so the cooling circuits drew higher flow levels; additional parasitic bleed flows were required for instrumentation (laser probe) cooling, and the active clearance controls were not used during the emissions test which lowered turbomachinery efficiency and, in turn, requiring greater fuel flows at given speeds.

The difference between the actual and predicted fuel-air ratio curves is a key to understanding the level of core engine measured emissions. These high fuel-air ratios cause an apparent lack of agreement between the core engine test and full-annular component test data. Figure 137 shows the variation of CO and HC with fuel-air ratio change at the FPS 4% and 6% idle thrust operating conditions obtained from annular rig testing. Using this data, the core engine data can be corrected for fuel-air ratio effect as shown in Table XXI.

The correction of NO_x data was generated from the extrapolation of core engine data, adjusted to FPS pressure, to the FPS T3, and then ratioed by the FPS to core engine fuel-air ratios to the 0.65 power, in the same manner as the NO_x severity parameter. This provided an estimate of the FPS engine NO_x level expected, also shown in Table XXI. The last two columns of Table XXI show a comparison of totally adjusted core engine emissions to rig measured emissions at FPS operating conditions. The comparison indicates that both tests agreed well at 4% idle for CO and HC, but that at 6% idle, the core engine levels were higher for these two gaseous emissions. Oxides of nitrogen were in reasonable agreement at the ICLS SLTO condition.

In general then, the core engine measured emissions levels, adjusted to FPS cycle pressure levels, were higher than those indicated by annular component rig results of the same combustor because of the higher than FPS cycle fuel-air ratios in the core engine. At specific test conditions where fuel-air ratio variation data existed from full annular core engine combustor

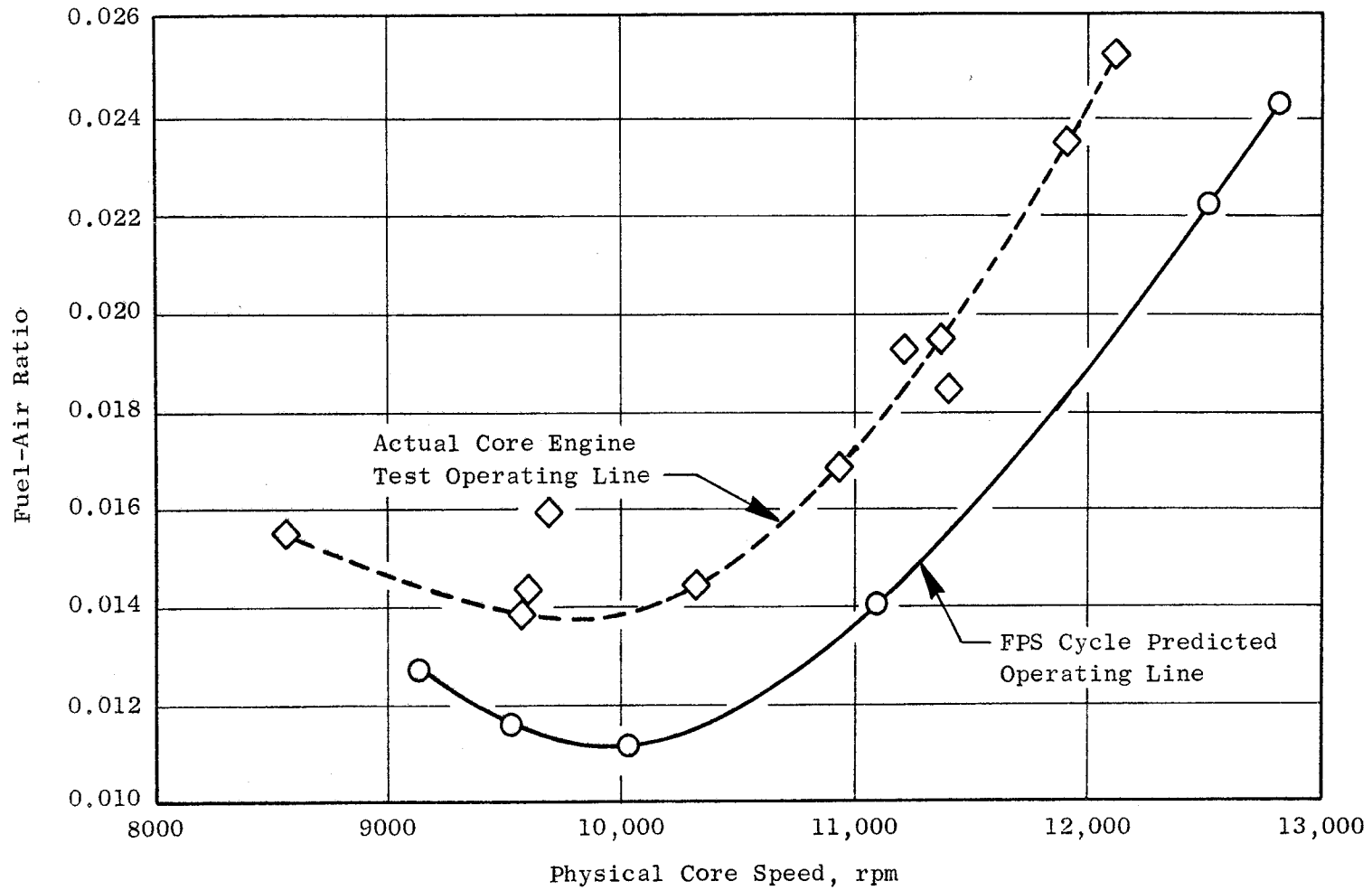


Figure 136. Core Engine Test and FPS Predicted Fuel-Air Ratios Versus Physical Core Speed.

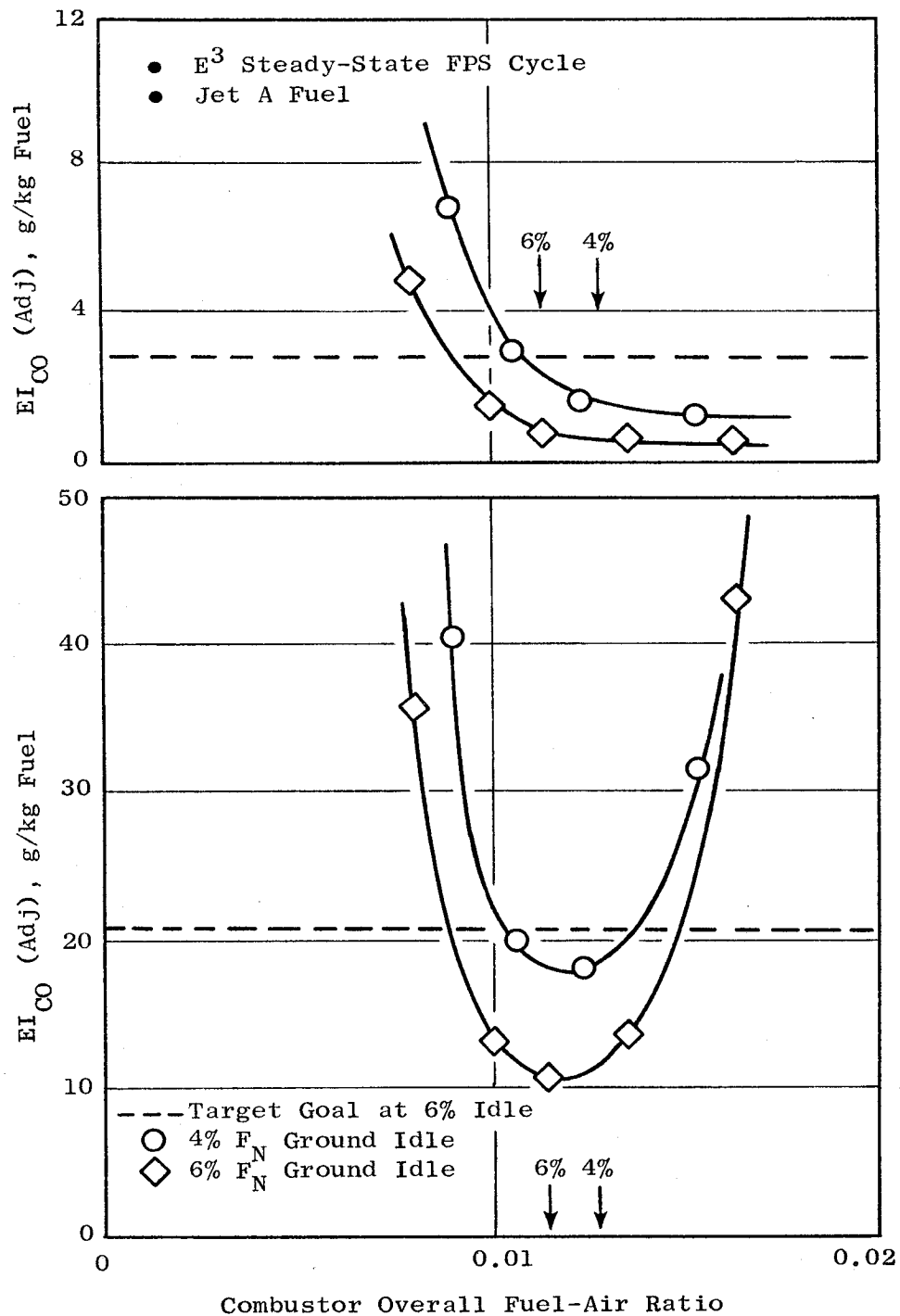


Figure 137. Combustor Component Test Idle Emission Results.

Table XXI. Core Engine Emissions Levels Corrected for Fuel-Air Ratio Effect.

Emission	Core Engine Data		FPS Fuel-Air Ratio	Emissions % Change as f_{cn} of F/A	Core Engine Data Corrected for P3 and F/A lb/1000 lb W_f	Rig Measured at FPS Condition lb/1000 lb W_f
	Emissions lb/1000 lb W_f	Fuel-Air Ratio				
Hydrocarbons, 4% Idle	1.20	0.0175	0.0128	+21.0%	1.45	1.60
6% Idle	0.65	0.0155	0.0111	+50.0%	1.30	0.80
Carbon Monoxide, 4% Idle	60.50	0.0175	0.0128	-68.4%	19.13	18.75
6% Idle	45.50	0.0155	0.0111	-63.1%	16.80	10.75
Oxides of Nitrogen, SLTO	29.70	0.0314	0.0244	-15.1%*	25.2	27.0

* Reduction based on $\left(\frac{F/A_{fps}}{F/A_{core}}\right)^{0.65}$ at FPS T3

component testing, the core engine emissions data were corrected for this effect and were in close agreement with annular component test data.

The FPS goal, in terms of an operating cycle (takeoff-landing), are expressed as EPA parameter values in Table XXII. Listed also are the demonstrated core engine levels adjusted to FPS operating conditions. The measured values indicated that when using pilot-dome-only operation at approach:

- The core engine combustor at ICLS operating conditions will meet the gaseous emissions goals for CO and HC at 4% SLTO thrust at idle. The combustor would also meet these goals at 6% SLTO thrust at idle with increased margin.
- The core engine combustor at ICLS operating conditions will exceed the gaseous emissions goals for NO_x.

If pilot-only operation were not used by commercial operators at the approach power setting, then the ICLS engine would be expected to exceed the gaseous emissions goals for CO and NO_x by the margins shown in Table XXII.

Smoke

No high-power smoke data were obtained during core engine testing. Only the three points shown in Figure 138 were obtained, due to water spotting of the high-speed samples (discussed earlier). The smoke data represent points taken at up to 88% core speed and show very low SAE levels: 2.5 SAE Smoke Number.

Efficiency

The efficiency levels determined by chemical reaction measurements are presented in Figure 139 and compare the operation of the core engine with FPS prediction based on component test. At the 4% and 6% thrust idle points, the efficiency level was lower than predicted, reflecting the higher CO emissions produced at the higher engine fuel-air ratio. However, combustion efficiency during subidle operation was better than predicted. This is attributed to richer, more efficient pilot stage burning at the higher engine fuel-air ratio. At staging, the efficiency drops below prediction, but responds rapidly to throttle advance and is higher than predicted from 30% power and up.

Table XXII. Core Emissions Adjusted to FPS Operating Conditions.

(lb/1000 lbf. hr. cycle)

Emission	Program Goal	4% FN G-Idle				6% FN G-Idle			
		Pilot Only at Approach	Percent Margin	40/60 Split at Approach	Percent Margin	Pilot Only at Approach	Percent Margin	40/60 Split at Approach	Percent Margin
CO	3.00	2.82	6	3.45	None	2.58	14	3.14	None
HC	0.40	0.202	50	0.26	35	0.19	53	0.24	20
NO _x	3.00	4.23	None	4.10	None	3.95	None	3.83	None

- E³ FPS sea level static standard day operating cycle.

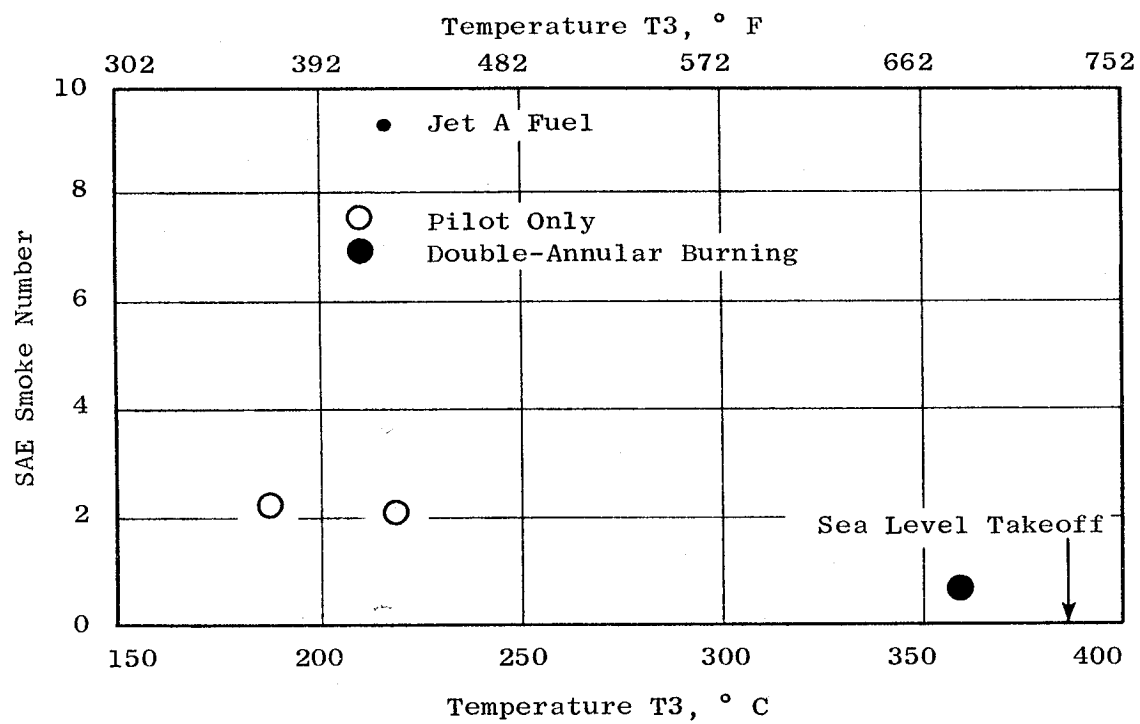


Figure 138. Measured Smoke Number Versus Compressor Discharge Temperature.

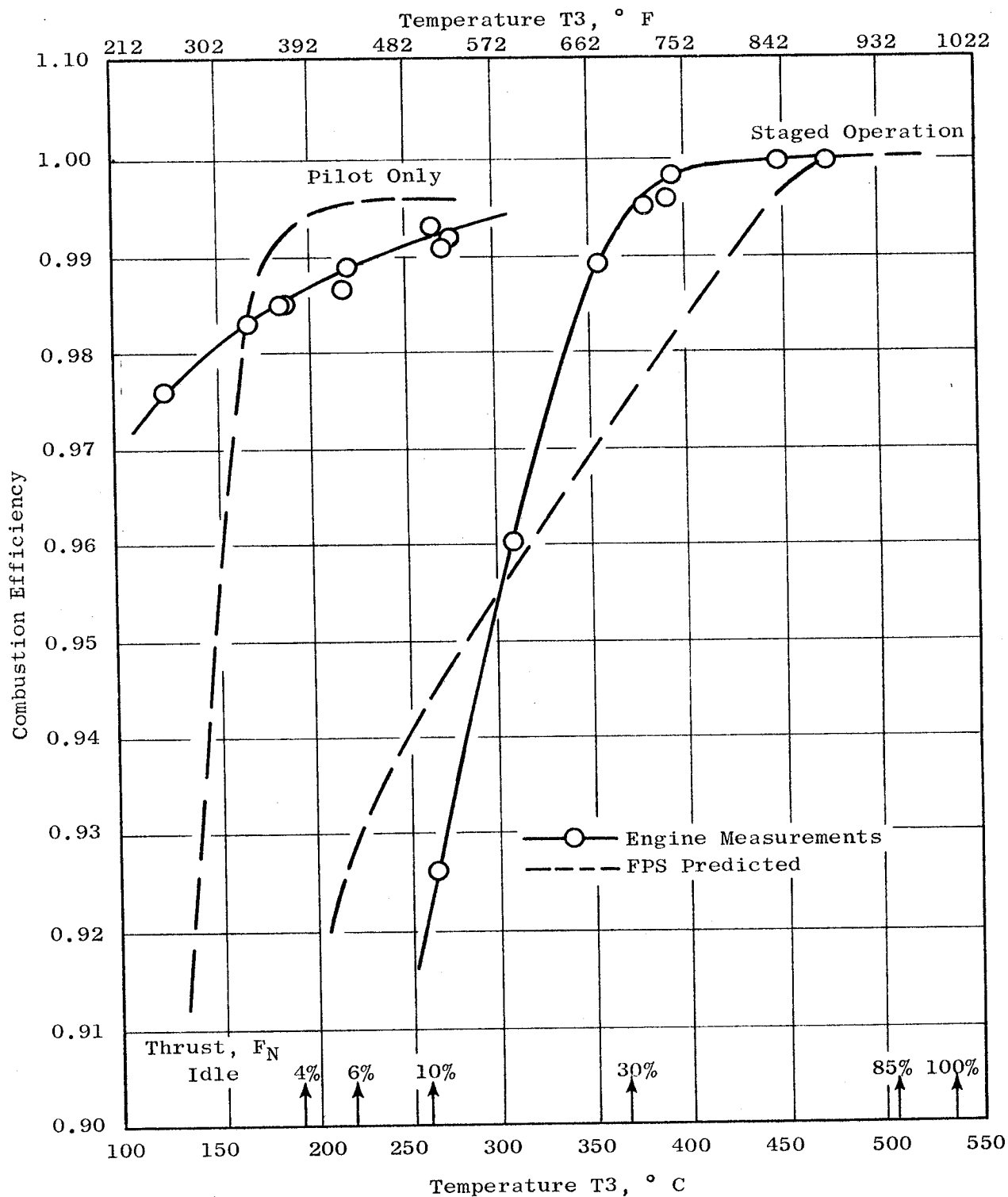


Figure 139. Combustion Chemical Efficiency Versus Compressor Discharge Temperature.

Efficiency levels were independently calculated from engine thermodynamic measurements. Measurements of engine airflow, fuel flow, compressor inlet air temperature, and turbine discharge gas temperature allow for the calculation of combustor efficiency. The calculated thermodynamic combustor efficiency was slightly lower than chemical efficiency at medium power levels and significantly lower at very low power levels when using double-annular burning. The differences are presented in Section 6.1. At high power rating condition, the demonstrated combustor efficiency was taken to be 99.9%, matching the chemical efficiency. This exceeded the goal by 0.3%.

Combustor Pressure Loss

Core engine combustor overall pressure loss is shown in Figure 140. The goal level was 5.0% at the FPS compressor flow function value and the engine demonstrated this value. The core engine operated at a slightly higher flow function at sea level rated conditions and, consequently, had a higher measured pressure loss of 5.4%.

Figure 141 shows the compressor exit radial profiles of pressure and temperature at 97.4% corrected speed and compares them with the profiles measured in a compressor component test at similar exit conditions. The core engine combustor inlet temperature profile was identical to that predicted by component test results.

The combustor prediffuser exit pressure profile has slightly higher pressures, than those measured in the component test, at the outside wall of the outer prediffuser passage and at the inside wall of the inner prediffuser passage. The opposite was true around the splitter walls of the two prediffuser passages. However, the discrepancy was small enough that its contribution was not discernible in the overall pressure combustor loss.

Dynamic Stability

Three dynamic pressure sensors (Kulites) were mounted on the core engine to measure dynamic stability during transients and at steady-state conditions. One Kulite was mounted at the 10th stage bleed manifold. Two Kulites were

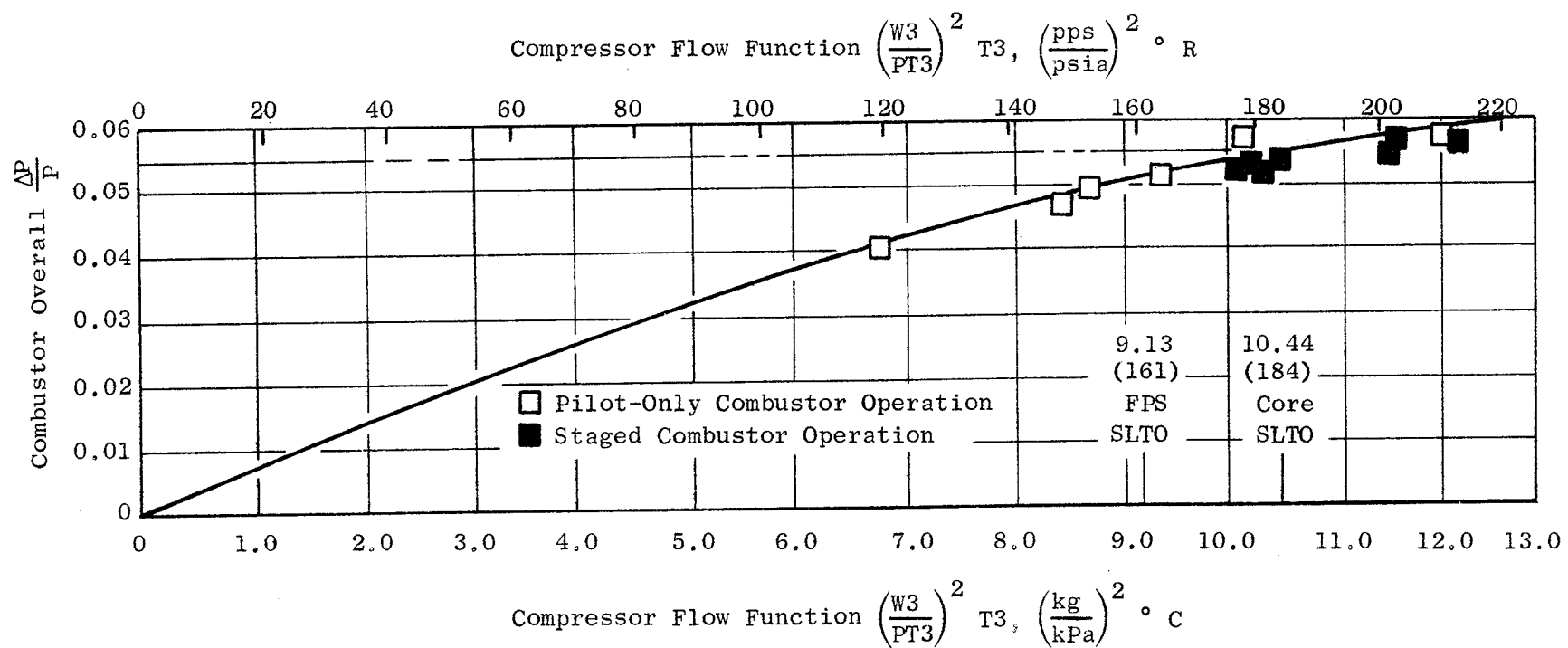


Figure 140. Combustor System Overall Pressure Losses.

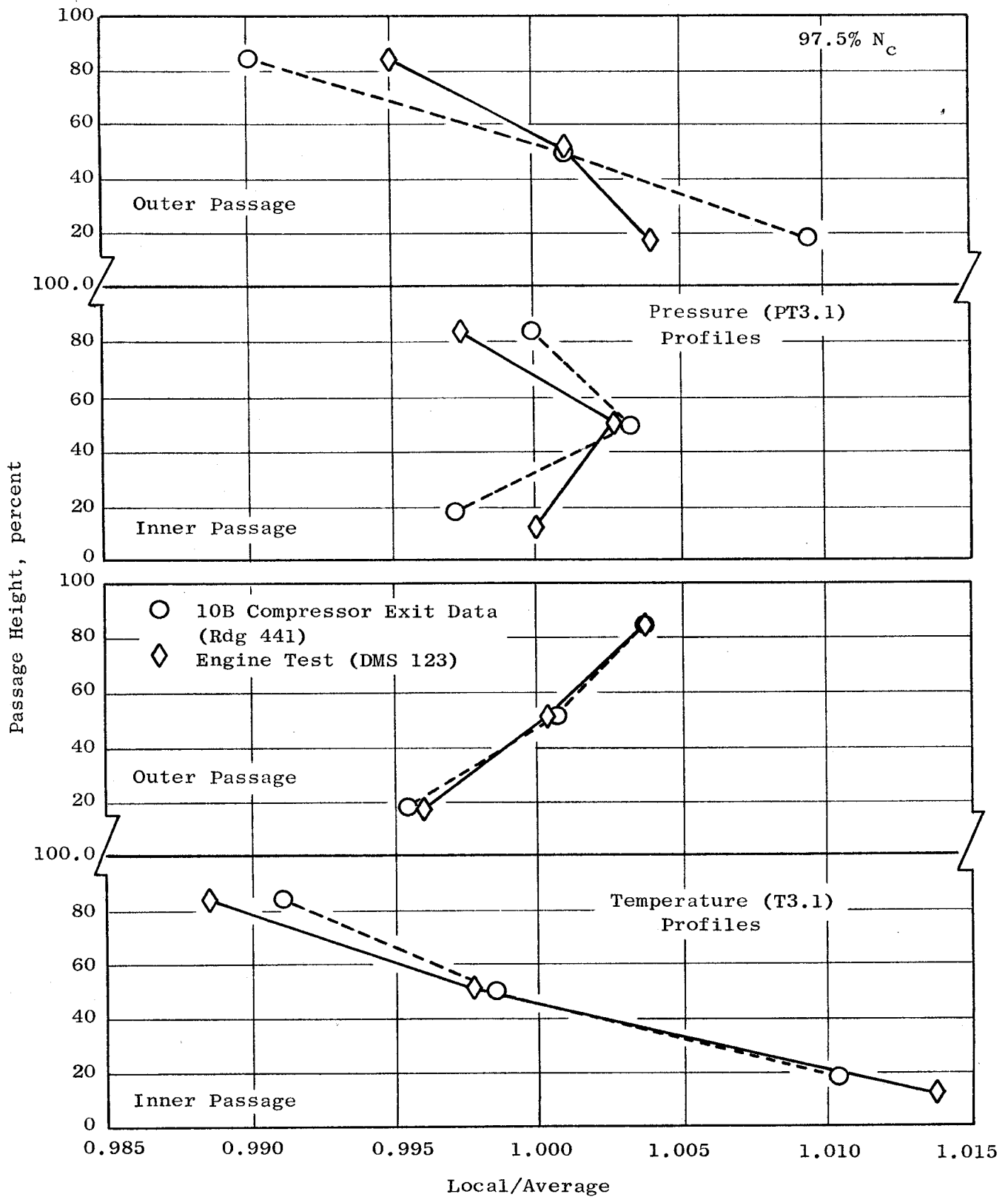


Figure 141. Compressor Discharge Total Pressure and Temperature Profiles.

C4

mounted in the combustor case and sensed the pressure in the outer diffuser passage of the combustor. One of these two instruments failed during the test, yielding no meaningful data. Transient data is shown in Figures 142 through 149.

Figures 142 and 143 show Start 2. There was no audible noise, as was true for most of the starts. This start was a windmilling start with manually controlled fuel flow.

Figures 144 and 145 show no noise during a switch from pilot-only to double annular combustion.

Figures 146 and 147 show Start 18, an automatic start using the air starter motor. Some combustor activity is noted from just after ignition and up to idle. Pressure amplitude of the signal is less than 0.5 psia (very low), and is at a frequency level of greater than two per core rotor revolution for most of the acceleration. It was not audible.

Figures 148 and 149 show a subidle deceleration with an audible level of activity. In Figure 148, 10th-stage bleed manifold pressure has about 6.9 kPa (1.0 psi) peak-to-peak of activity at two frequency levels: One at 500-600 Hz (or greater than 4/rev) and the other at about 300 Hz (or about 3/rev). This activity is stronger (higher pressure amplitude) in the 10th-stage manifold than at the combustor (Figure 149). It was determined that this noise was the result of blanking off the 10th stage bleed, creating a quarter wave resonator in that pipe. The steady-state noise data from the Kulites was recorded on spectral analysis charts for the speed points of interest. Early in core engine testing, nothing unusual was noted. It was observed in later testing that the engine exhibited low speed audible combustor noise.

Subsequent investigation revealed that when the turbine clearance measurement probes were in operation, the combustor operated quietly throughout the engine speed range. When the turbine laser probes were disconnected, cooling air for these probes was shut off by capping a 0.28-m (11-inch) long pipe at the 10th stage bleed manifold. This capped-off pipe became a quarter wave resonator for the 10th stage bleed cavity, which has swirling flow in it caused by the feed air from the rotor (Figure 150). The core speed range over which audible noise occurred during these tests was from 3200 rpm to 9600 rpm.

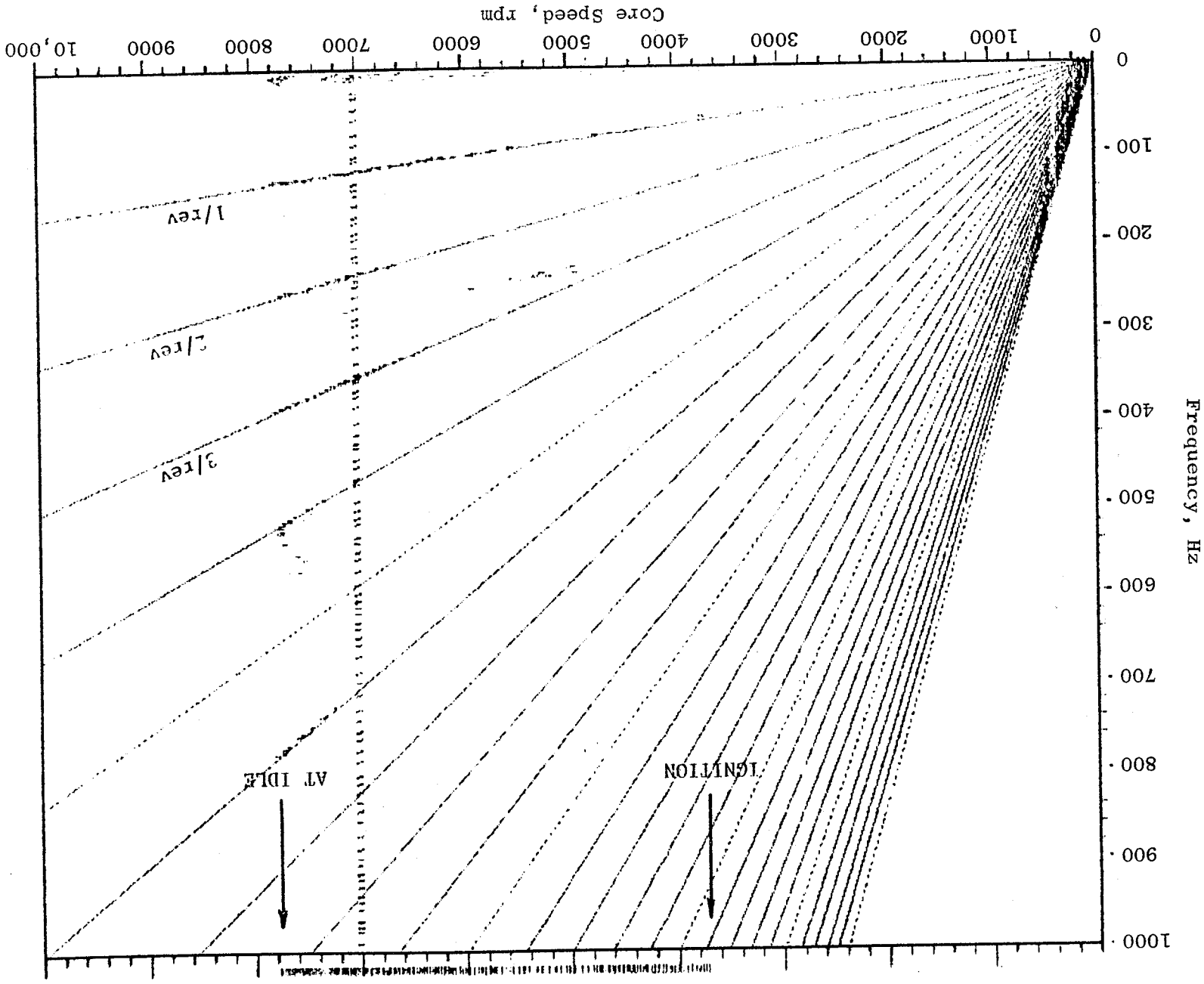
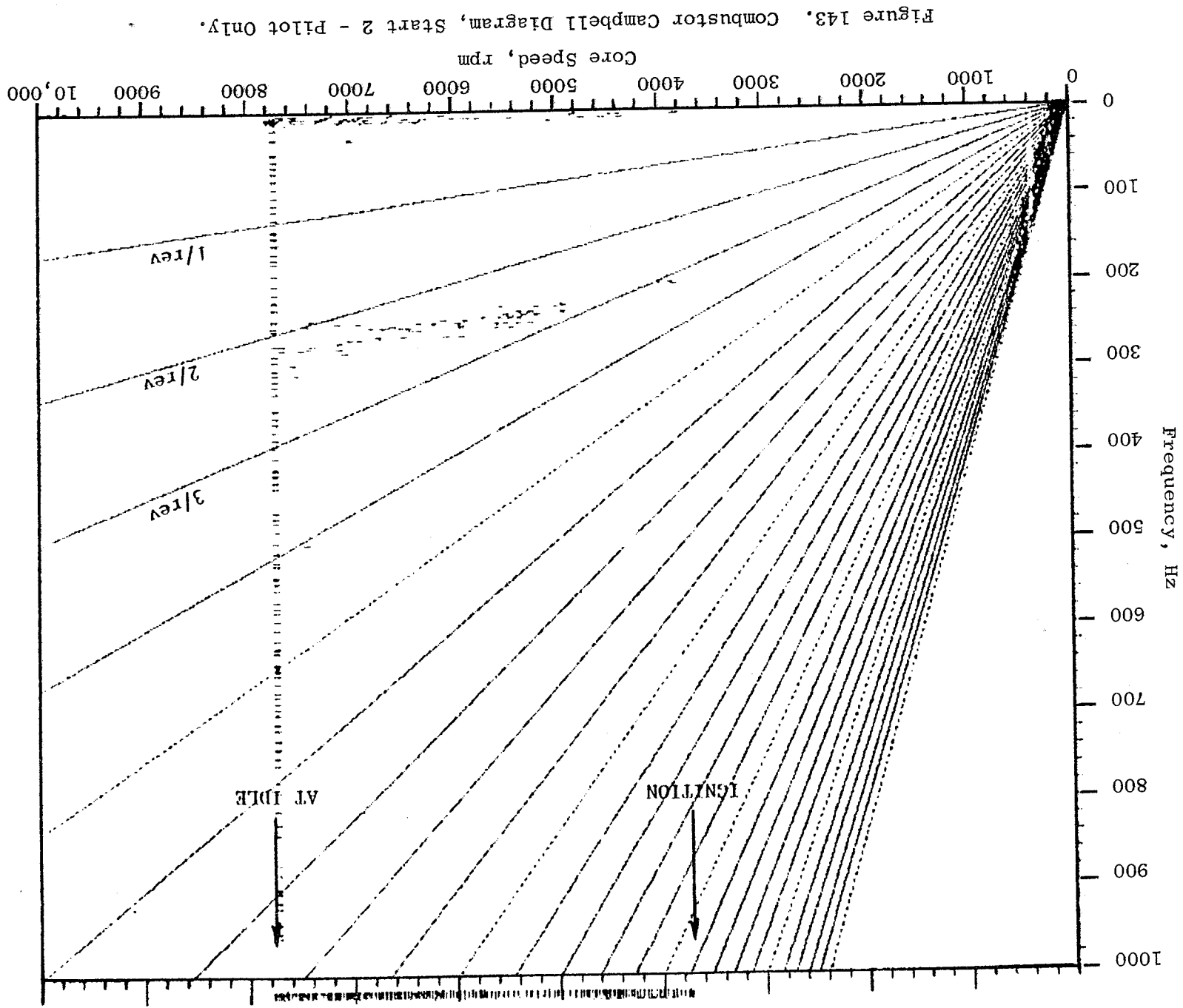
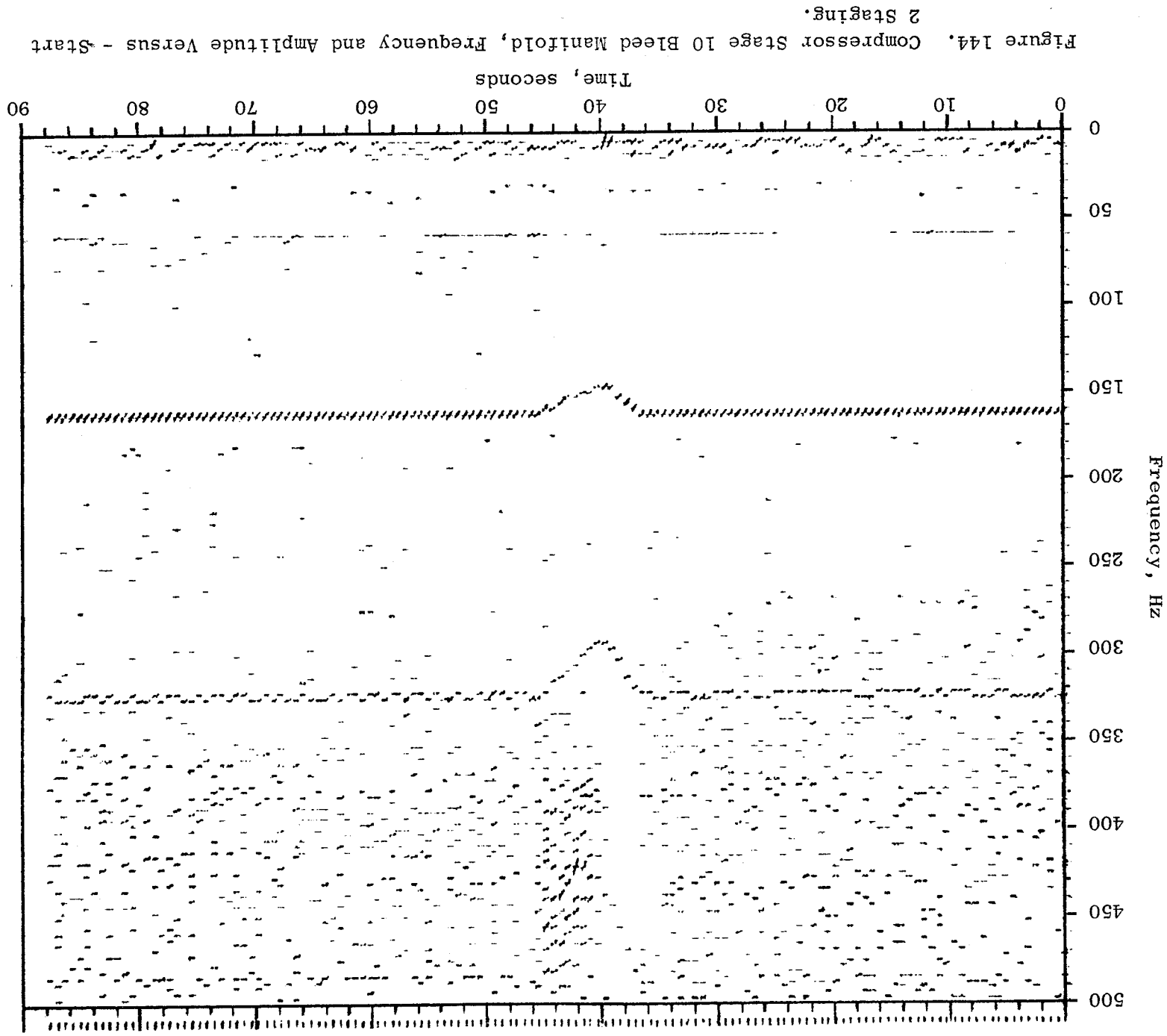


Figure 142. Compressor Stage 10 Bleed Manifold Campbell Diagram, Start 2 - Pilot Only.

ORIGINAL PAGE IS

ORIGINAL PAGE IS
OF POOR QUALITY





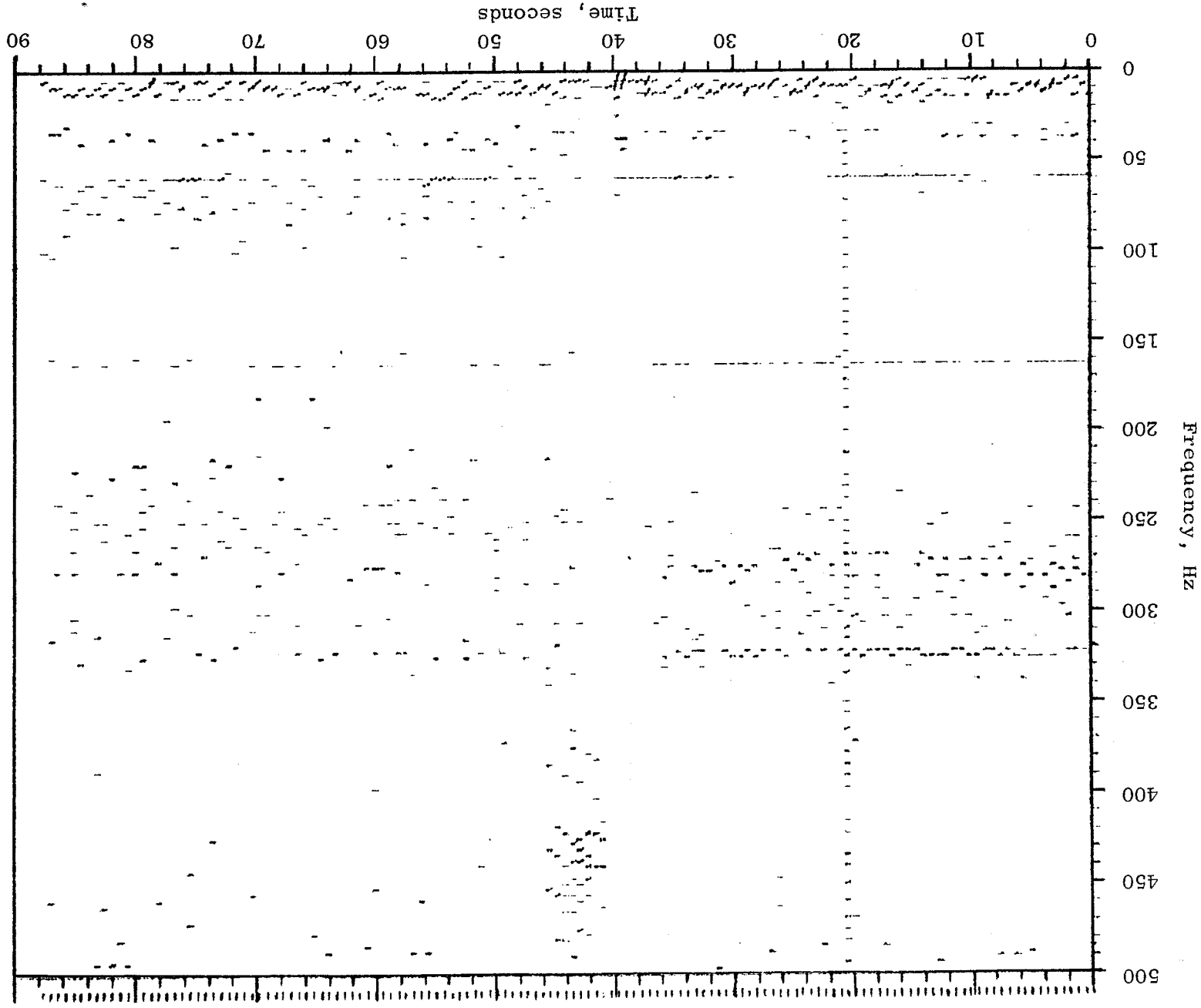


Figure 145. Combustor Frequency and Amplitude Versus Time, Start 2 Staging.

ORIGINAL PAGE IS
OF POOR QUALITY

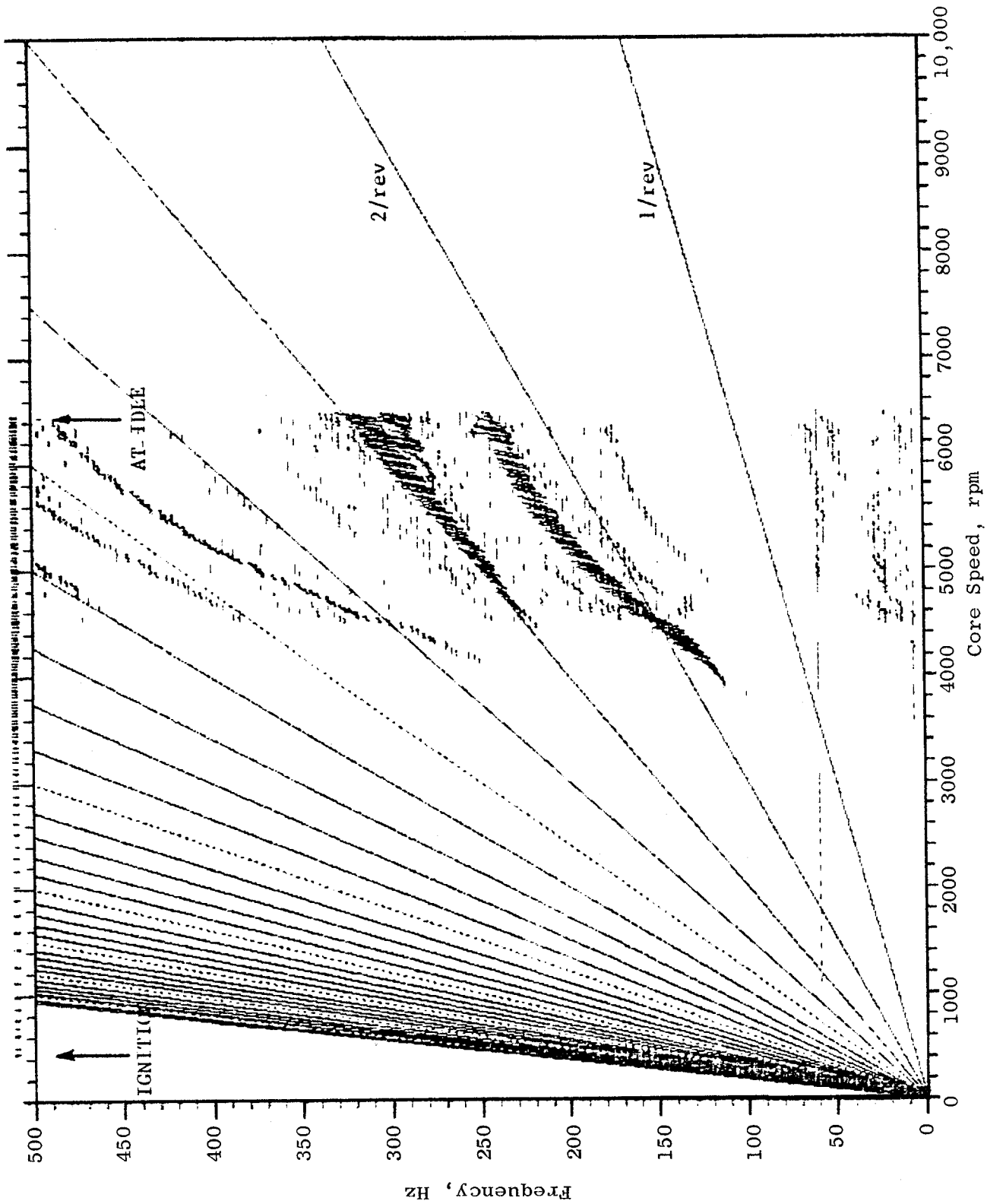
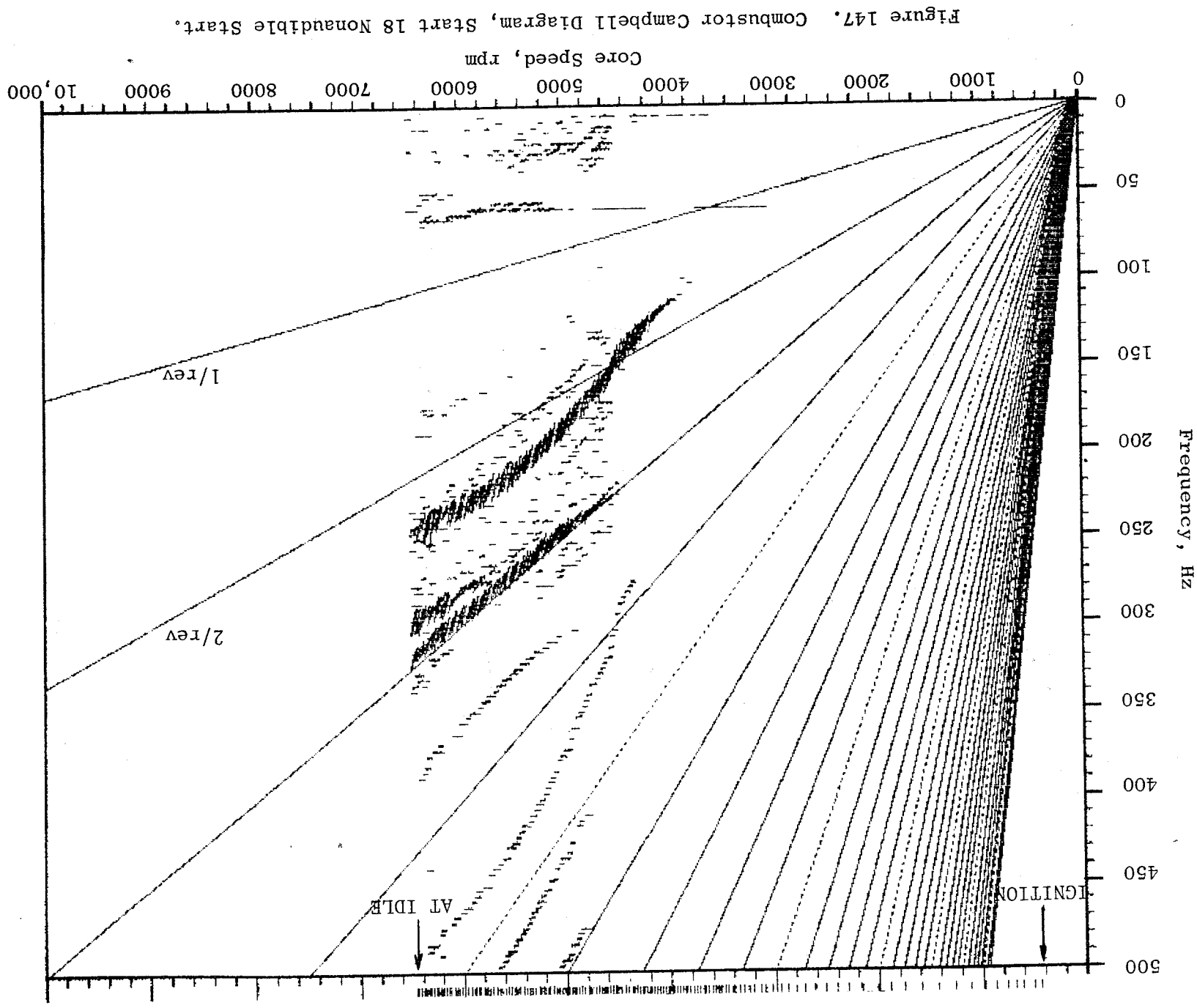
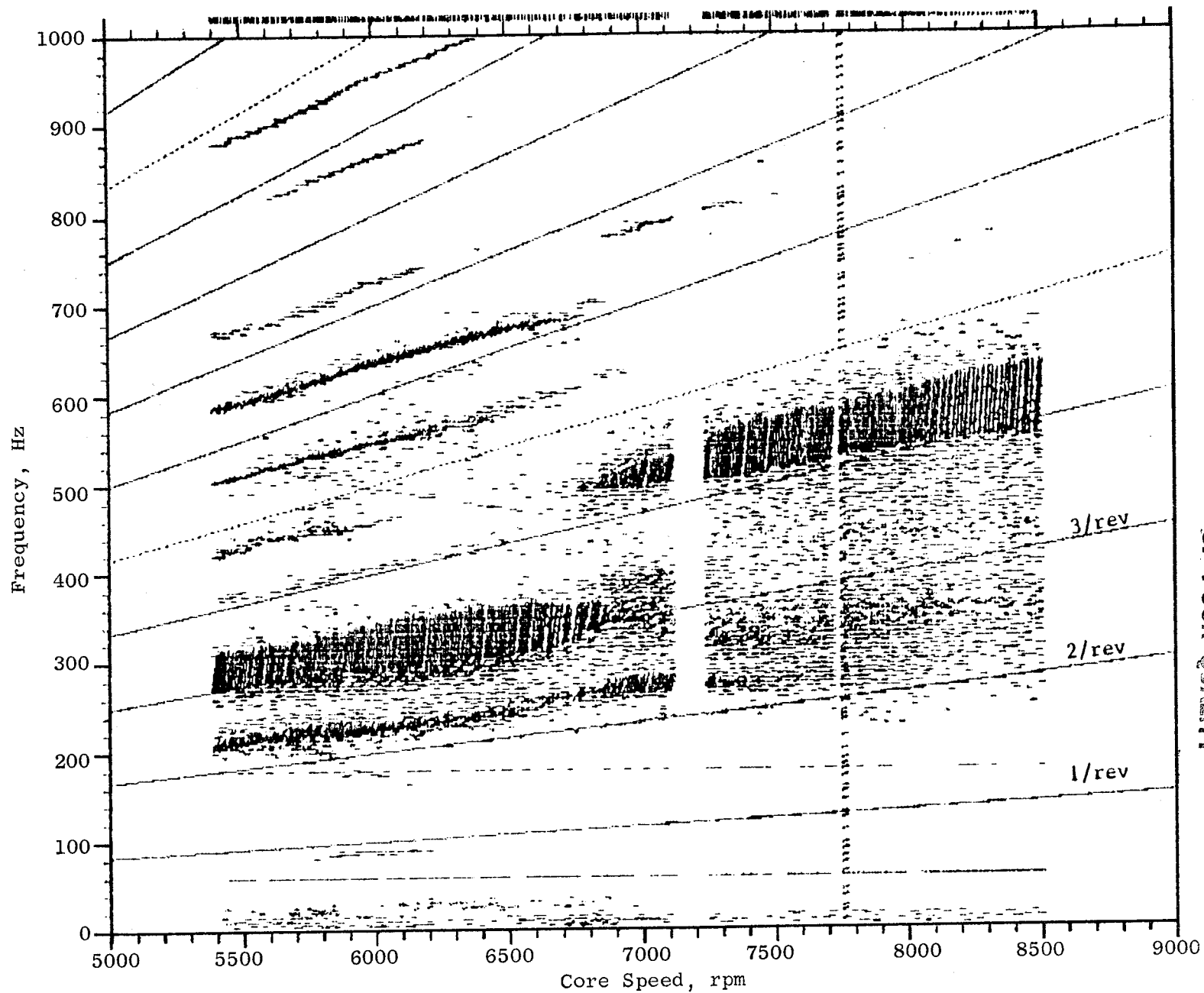


Figure 146. Compressor Stage 10 Bleed Manifold Campbell Diagram, Start 18
Nonaudible Start.

ORIGINAL PAGE IS
OF POOR QUALITY





ORIGINAL PAGE IS
OF POOR QUALITY

Figure 148. Compressor Stage 10 Bleed Manifold Campbell Diagram, Subidle Deceleration Audible Noise.

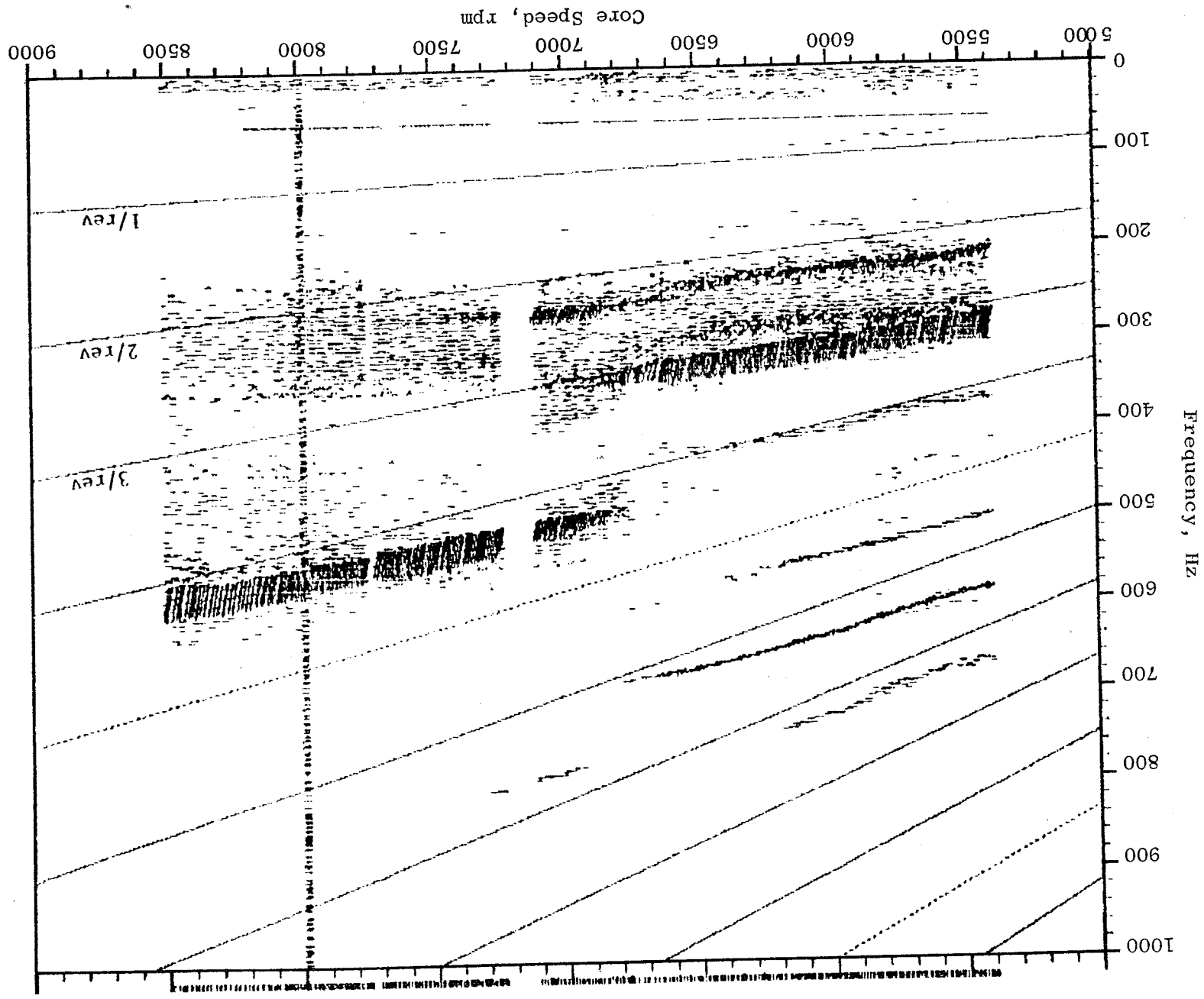


Figure 149. Combustor Campbell Diagram, Subidle Deceleration Audible Noise.

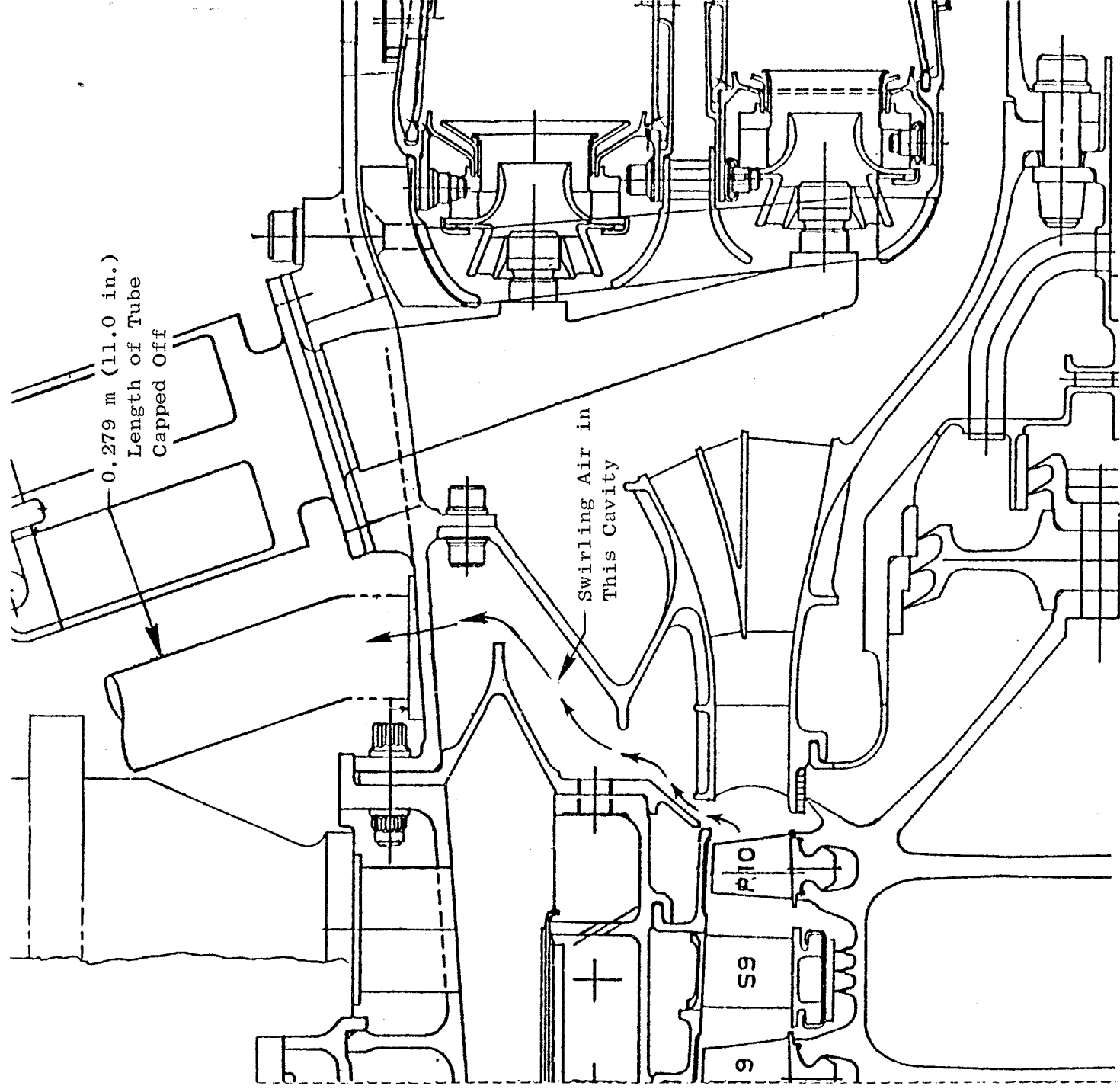


Figure 150. Cutaway Showing Passage of Swirl Air to Capped Tube.

Pressure amplitudes in the 10th stage bleed cavity ranged from 5.5 kPa (0.8 psi) peak-to-peak at 310 Hz up to 8.3 kPa (1.2 psi) at 590 Hz. Background noise level was generally less than 3.5 kPa (0.5 psi) peak-to-peak at all other frequencies up to 1000 Hz. Figures 151-153 show the steady-state spectrum of core speeds of 7200, 7690, and 8550 rpm when resonance occurs. The noise conditions shown are of some concern because of the strong pressure signal, relatively low frequency level, and steady-state existence. A pressure signal of 13.8 kPa (2 psi) peak-to-peak or higher could have caused mechanical damage. Figure 154 shows the spectrum from earlier testing when the 10th stage bleed was operational.

During ICLS engine testing, a long 18-m (~60-feet) hose section will be attached to this standpipe, effectively cancelling the resonant tendencies of the system.

SUMMARY

The performance of the E³ combustor is summarized in Table XXIII. Six performance parameters are examined in the summary. Pressure loss and efficiency relate to engine specific fuel consumption and thrust level. The combustor meets the goal levels for both of these parameters when the core data is extrapolated to FPS engine levels. Note that the combustor pressure loss will be slightly higher than the goal level in the ICLS vehicle due to high compressor discharge loading values ($W/P\sqrt{T}$), which may not be altered by the addition of the low pressure system to the core.

During core engine testing, combustor ignition and staging characteristics were acceptable and should remain so in the ICLS vehicle. Engine minimum fuel flow for ignition was higher than the goal value, but this did not present any operational problems.

The combustor was dynamically stable and was not excited by the quarter-wave tube oscillations which occurred in the 10th-stage bleed manifold.

The gaseous emissions levels of the core engine combustor appeared to be close to those predicted from component tests, after corrections for both cycle and operating fuel-air ratio had been made to the core engine data.

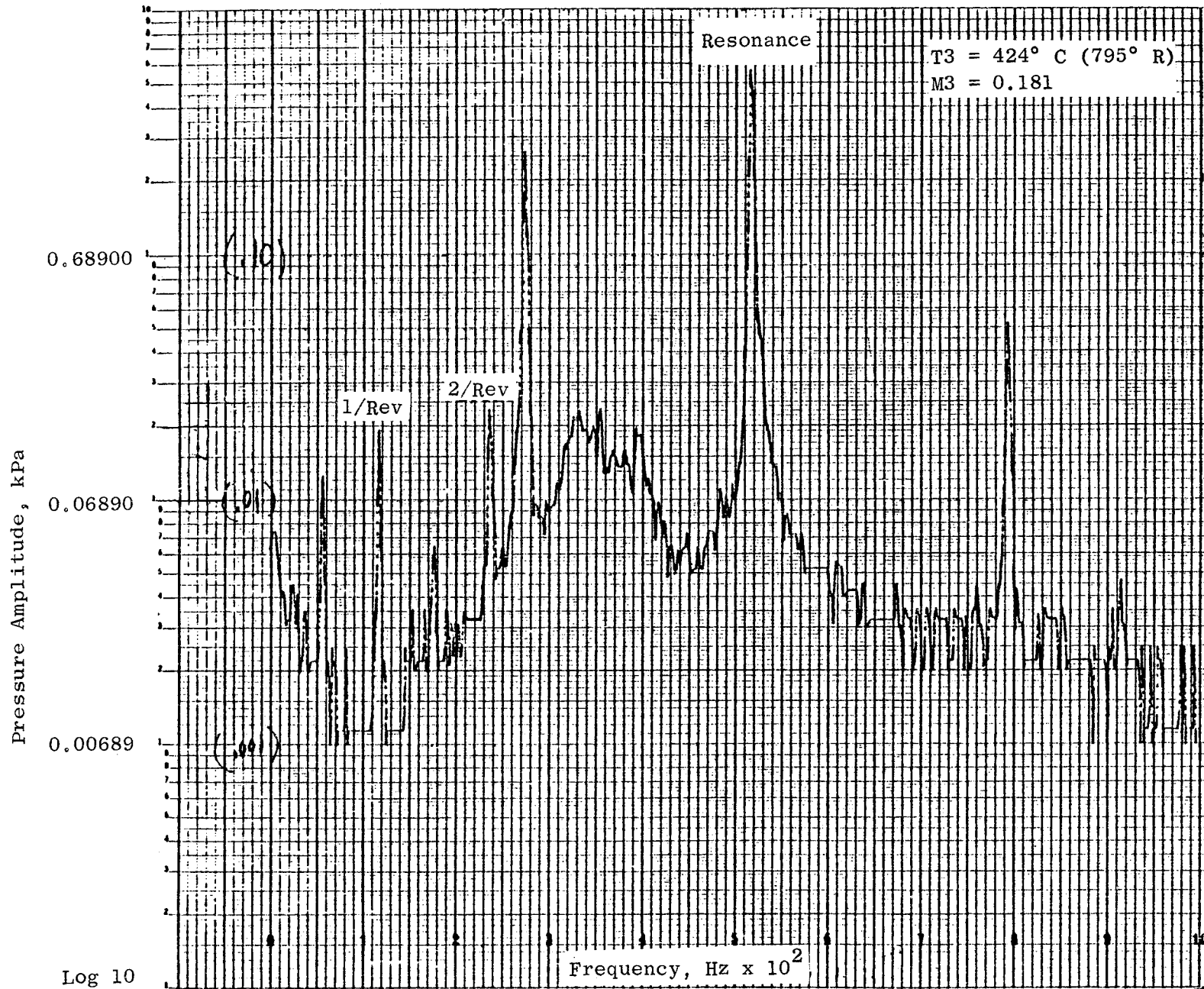
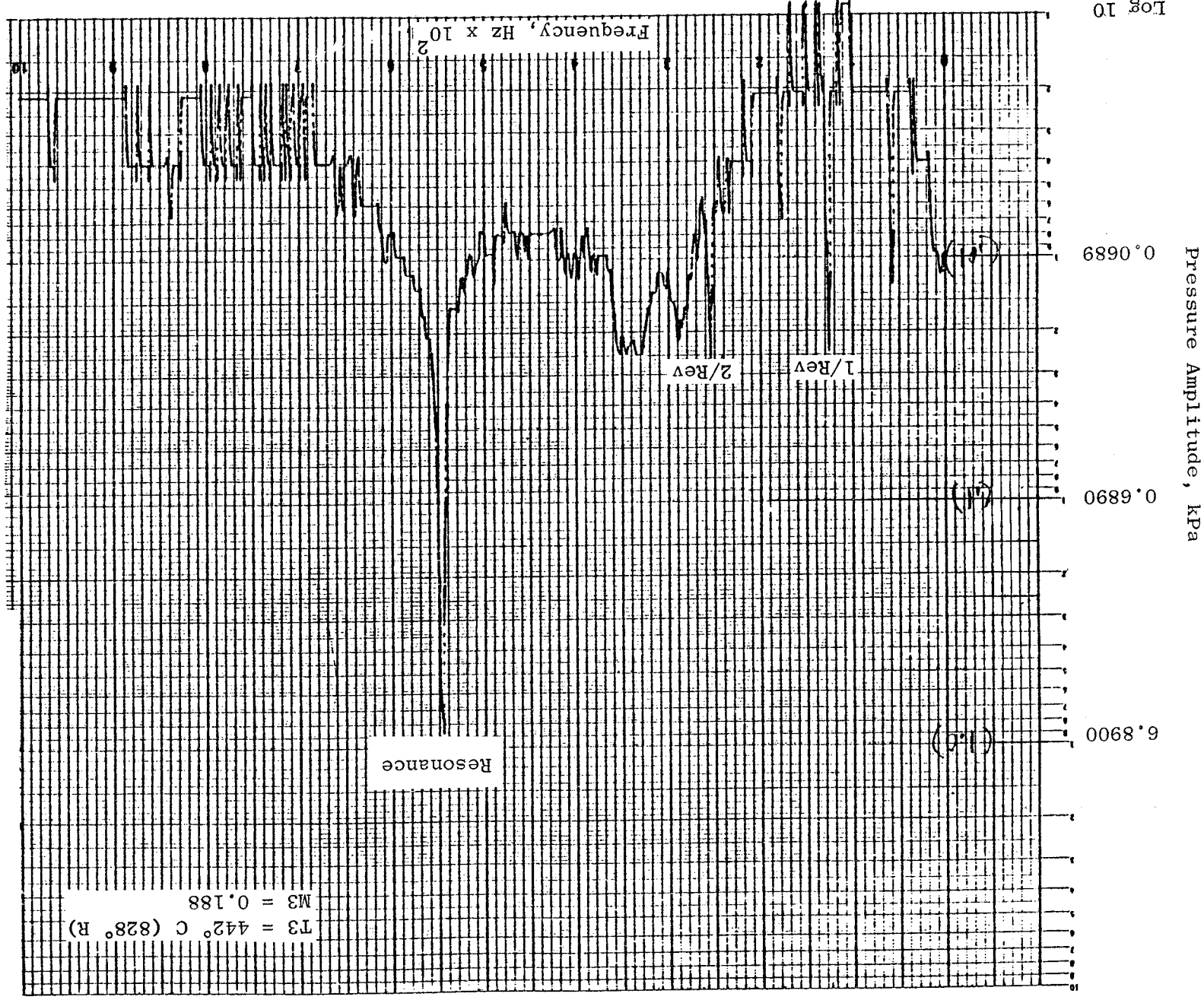


Figure 151. Compressor Stage 10 Bleed Manifold Spectral Analysis at 7200 rpm.

ORIGINAL PAGE IS
OF POOR QUALITY

ORIGINAL PAGE IS
OF POOR QUALITY



Pressure Amplitude, kPa

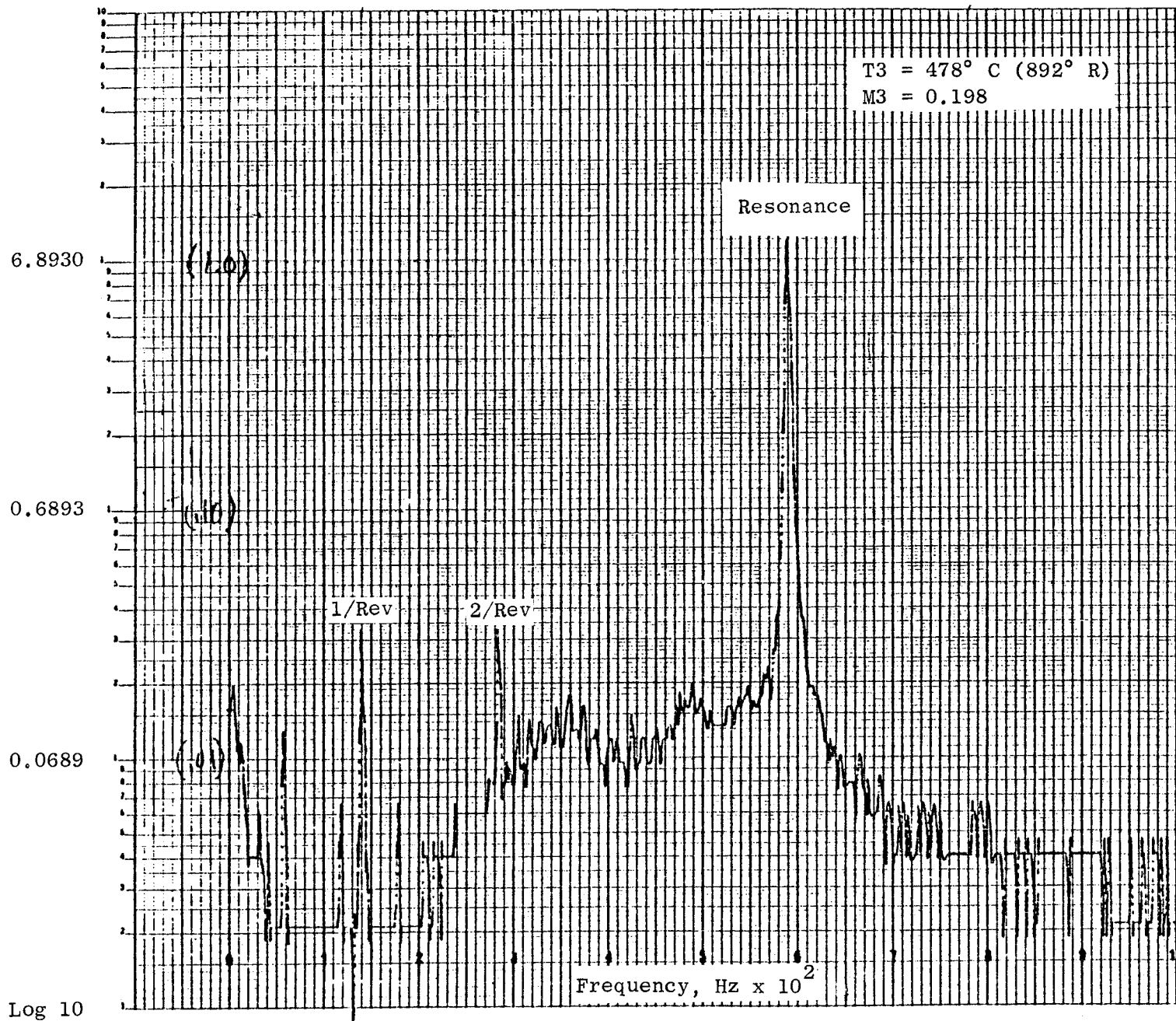


Figure 153. Compressor Stage 10 Bleed Manifold Spectral Analysis at 8550 rpm.*

ORIGINAL PAGE IS
OF POOR QUALITY

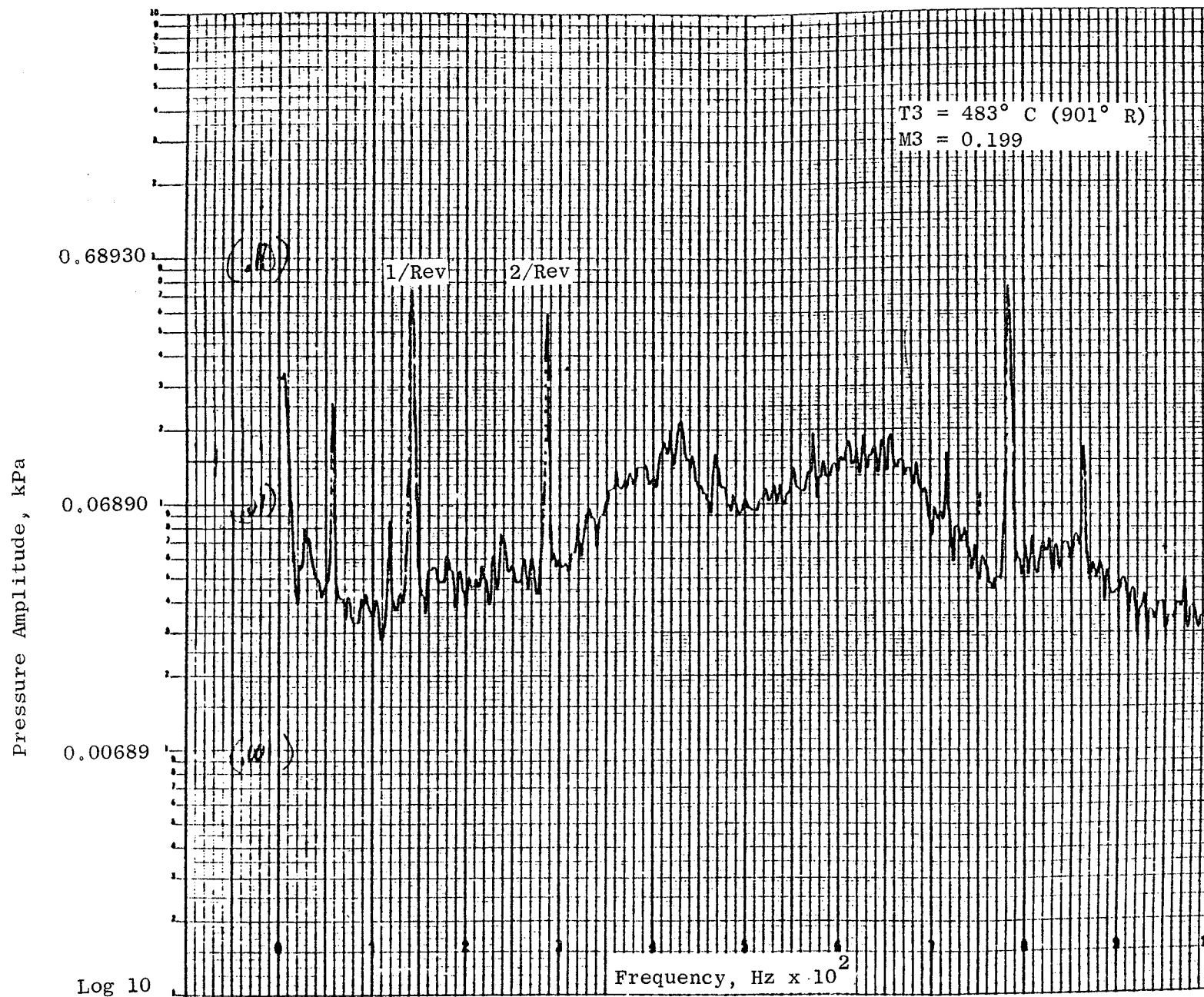


Figure 154. Compressor Stage 10 Bleed Manifold Spectral Analysis at 8650 rpm,
No Pipe Blank-Off.

Table XXIII. Combustor Aerodynamic Performance Summary.

<u>Parameter</u>	<u>Requirement/Goal</u>	<u>Core Engine Result</u>	<u>Extrapolated to FPS Engine</u>
<u>Pressure Loss</u>	5.0% at Maximum Power	5.4% at Maximum Power	5.0% at Maximum Power
<u>Efficiency</u>	99.6% at Maximum Power	99.9% at Maximum Power	99.9% at Maximum Power
<u>Starting</u>	Achieve Ignition at 300 pph Fuel Flow	400 pph Fuel Flow Required	400 pph Fuel Flow Will Be Required
<u>Staging</u>	Successful at 10% Power	Successful at 10% Power	No Problems Anticipated
<u>Stability</u>	No Starting Noise, No Resonance at High Power	Combustor Ran Without Audible Noise or Resonance	Combustor Expected to be Dynamically Stable, ICLS Measurement Required
<u>Emissions</u>			
• Smoke	≤ 20 SAE at High Power	Measurement Not Completed Low Levels (≤ 10 SAE) Where Measured	< 20 SAE at High Power ICLS Plume Observation Required
• Carbon Monoxide	3.0 lb/1000 lb F_N ·Hr·Cycle	Specific Levels Not Calculated for Core Engine	2.82 with Pilot Only at Approach 3.45 with Pilot and Main Dome Operation at Approach
• Hydrocarbons	0.4 lb/1000 lb F_N ·Hr·Cycle	Specific Levels not Calculated for Core Engine	0.20 with Pilot Only at Approach 0.26 with Pilot and Main Dome Operation at Approach
• Oxides of Nitrogen	3.0 lb/1000 lb F_N ·Hr·Cycle	Specific Levels not Calculated for Core Engine	3.0 with Pilot Only at Approach 3.83 with Pilot and Main Dome Operation at Approach for ICLS 4.23 with Pilot Only at Approach for ICLS

The combustor will meet the FPS goals for CO and HC with pilot-only operation at approach power and will meet the HC goal with staged operation at approach power. The combustor slightly exceeds the NO_x goals in either case. However, design changes could be made in a production design to achieve the NO_x goals.

While smoke levels were measured over only part of the operating range of the core engine, measured levels were low enough to allow prediction that the ICLS vehicle will produce no visible smoke.

Overall, combustor performance was good. The combustor operating characteristics did not limit the performance evaluation of the core engine and are not expected to limit ICLS engine performance evaluation. The combustor met the requirements for efficiency and pressure loss, was dynamically stable, and exhibited low emissions levels.

6.6 HIGH PRESSURE TURBINE MECHANICAL PERFORMANCE

High pressure turbine mechanical and thermal results are presented here and compared with analytical predictions. The discussion covers vibrations, stresses, temperatures, cooling system performance, seal system performance, and ACC system performance.

The following engine parameters summarize the levels achieved during core engine testing:

<u>Parameter</u>	<u>Level Obtained</u>	<u>FPS Design</u>
Speed, rpm	12,811	13,414
P3, MPa (psia)	2.857 (414)	3.08 (447)
T41 Avg., ° C (° F)	1365.5 (2490)	1421 (2590)
T3, ° C (° F)	538 (1001)	597 (1107)

Figure 155 indicates all of the flow values calculated for the test DMS Reading 258 compared to predicted FPS cruise data. Figure 155 gives all the temperature and pressure values (in SI units) for three conditions, which are actual engine data for the high operating efficiency point (DMS Reading 258), with the data scaled to FPS cruise conditions and the predicted FPS cruise data [Mach 0.8, 10.67 km (35,000 ft)]. Figure 156 contains the same information in English units. Other more detailed test information is covered for the specific components and systems in Figures 157 and 158.

6.6.1 Instrumentation Status

Figure 159 shows the total planned turbine instrumentation. No high-speed engine run was made following DMS Reading 258; therefore, the functioning sensors at that point are assumed to be the final total instrumentation count.

Of the 258 sensors (strain gages, thermocouples, and pressure sensors) originally installed and operative, 194 were operational at the end of the core test. This represents a loss of 25% of the planned instrumentation. Rotor and stator instrumentation losses are tabulated below and show that the rotor instrumentation was, as expected, much more susceptible to damage.

	<u>Installed</u>	<u>Lost</u>	<u>Percent</u>
Rotor	86	34	40
Stator	<u>172</u>	<u>30</u>	<u>17.5</u>
Total	258	64	25

Rotor instrumentation will not be available during the ICLS test because all leadouts have been terminated and the HP rotor slipring removed. However, the remaining stator instrumentation will be available and will be monitored.

ORIGINAL PAGE IS
OF POOR QUALITY

E³ HPT COOLING FLOWS, TEMPERATURES AND PRESSURES

(ALL TEMPERATURES ARE IN °C)
(ALL PRESSURES ARE IN KPa)
(ALL FLOWS = % W25)

ENGINE OPERATING PARAMETERS		
PARAMETER	READING 258	PREDICTED FPS-SS CRUISE MACH .8 - 10668 M
P25	.087 MPa	.055 MPa
P3	2.17 MPa	1.13 MPa
T3	508°C	502.7°C
T4	1348°F	1248°C
T42	858°C	800°C
% CORR SPEED	98.1 %	98.6%
PHYL SPEED	12348.2 RPM	12529.4 RPM

T= 619.5

.12(.1) %

.56(1.38) %

DATA BLOCK	DATA FROM DMS 258	258 DATA SCALED TO FPS-SS CRUISE	PREDICTED FPS-SS CRUISE, MACH .8 - 10668 M DATA
------------	-------------------	----------------------------------	---

DATA BLOCK FLOWS	DATA FROM DMS 258	(PREDICTED FPS-SS CRUISE, MACH .8 - 10668 M DATA)
------------------	-------------------	---

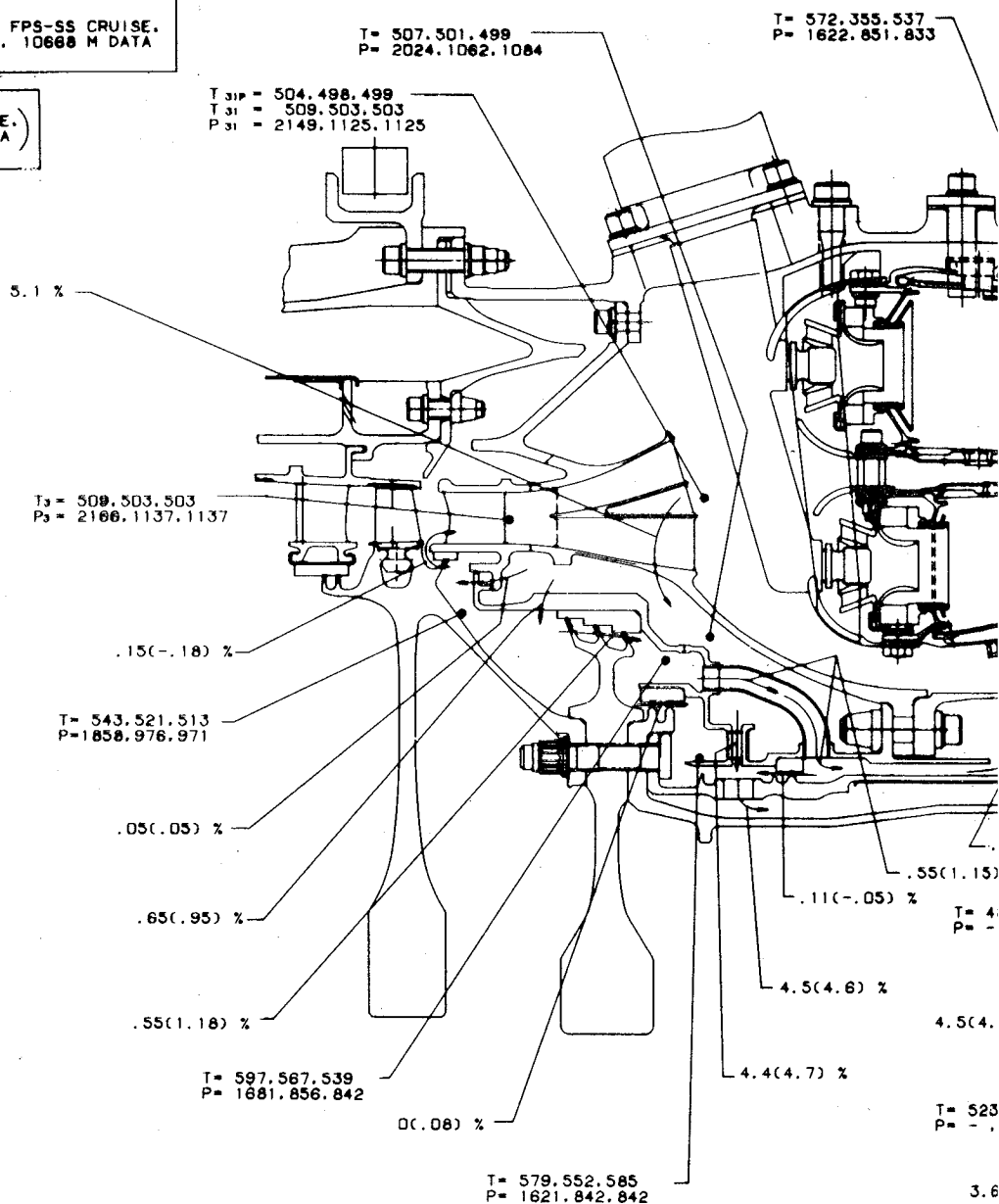
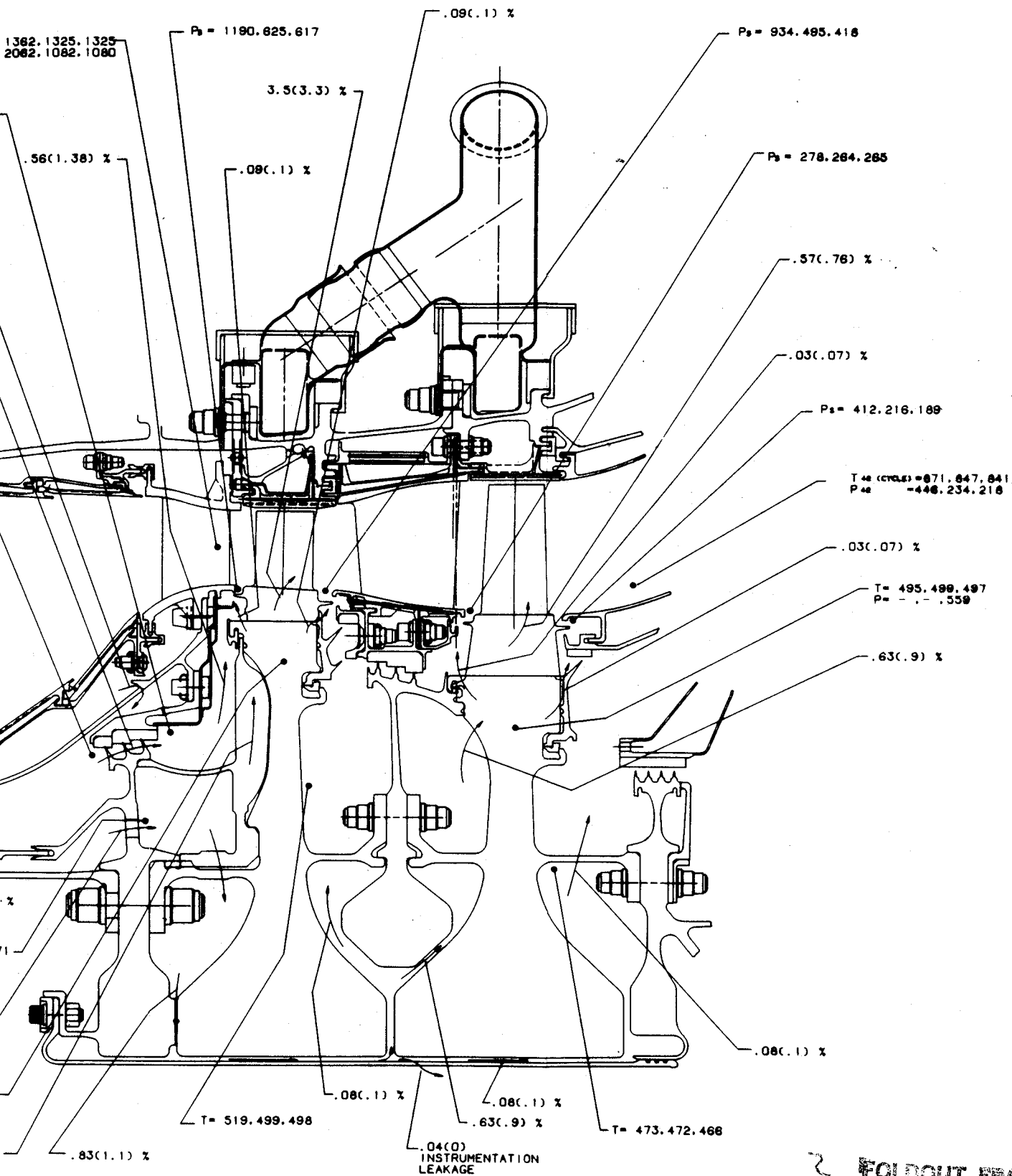


Figure 155. HP Turbine Cooling Flows, T

FOLDOUT FRAME

ORIGINAL PAGE IS
OF POOR QUALITY



FOLDOUT FRAME

tures, and Pressures in SI Units.

ORIGINAL PAGE IS
OF POOR QUALITY

E' HPT COOLING FLOWS, TEMPERATURES AND PRESSURES

(ALL TEMPERATURES ARE IN °F)
(ALL PRESSURES ARE IN PSIA)
(ALL FLOWS = % W25)

ENGINE OPERATING PARAMETERS		
PARAMETER	READING 258	PREDICTED FPS-SS CRUISE MACH .8 - 35000 FT
P25	14.1 PSIA	8.01 PSIA
P3	314 PSIA	164.9 PSIA
T3	948°F	938°F
T4	2480.8°F	2278.4°F
T42	1578°F	1473°F
% CORR SPEED	98.1 %	98.8%
PHYL SPEED	12348.2 RPM	12528.4 RPM

DATA BLOCK	DATA FROM DMS 258	258 DATA SCALED TO FPS-SS CRUISE	PREDICTED FPS-SS CRUISE, MACH .8 . 35000 FT DATA
---------------	----------------------	-------------------------------------	---

DATA BLOCK FLOWS	DATA FROM DMS 258	(PREDICTED FPS-SS CRUISE, MACH .8 . 35000 FT DATA)
------------------------	----------------------	---

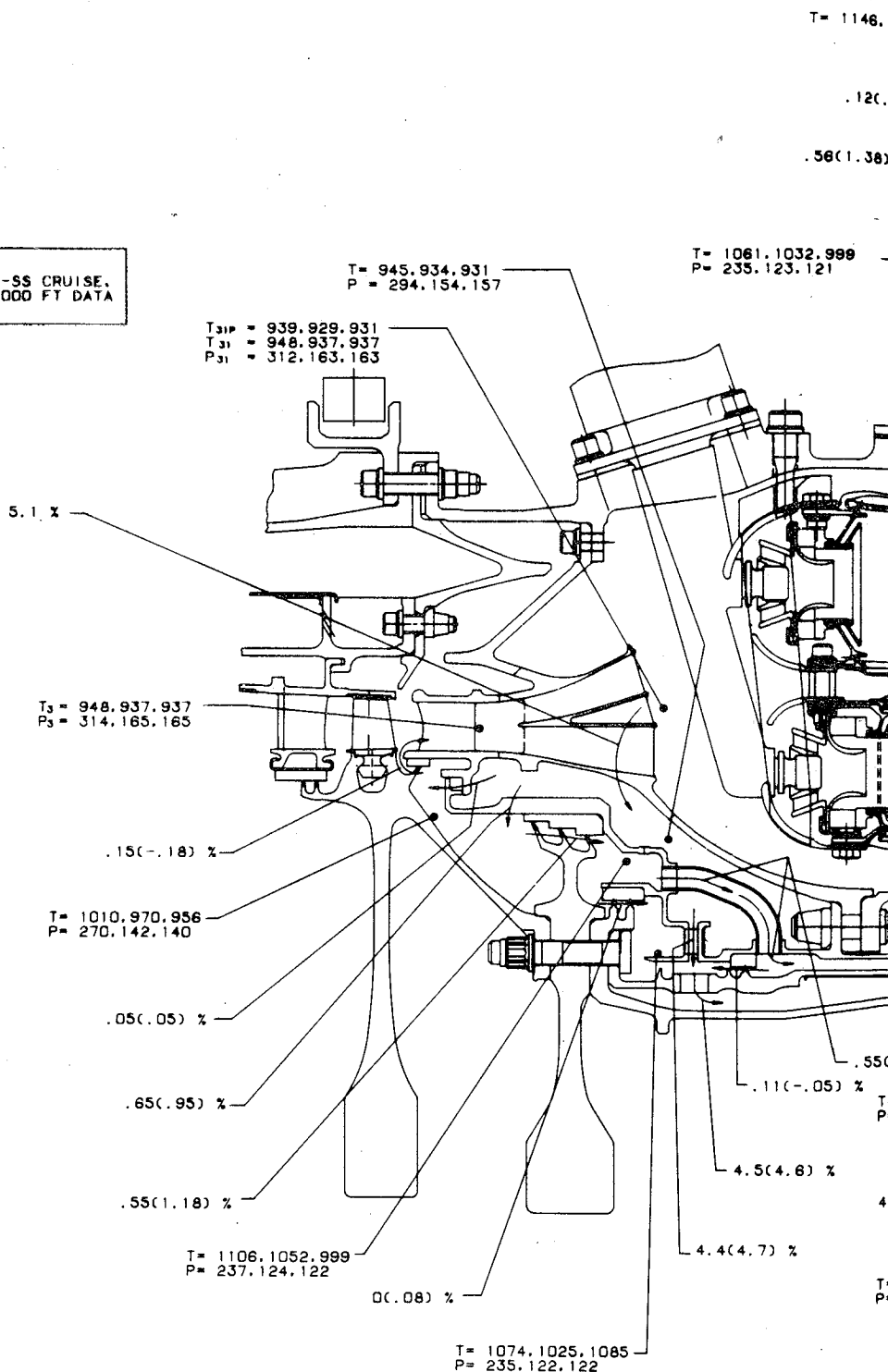
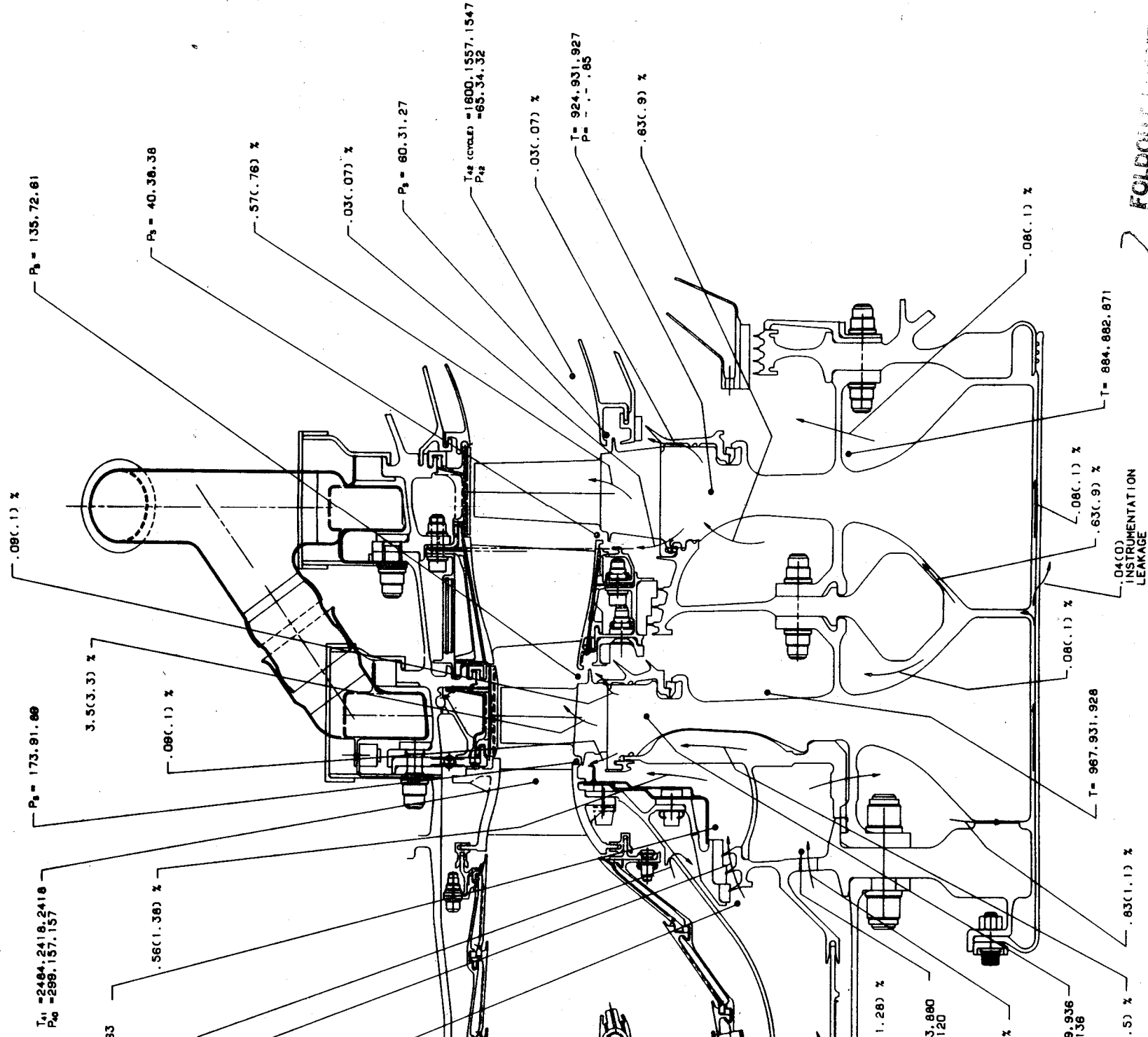


Figure 156. HP Turbine Cooling Flows, Tempe

FOLDOUT FRAME

ORIGINAL PAGE IS
OF POOR QUALITY



2 FOLDOUT DRAWING

es, and Pressures in English Units.

ORIGINAL PAGE IS
OF POOR QUALITY

E³ H P TURBINE-ENGINE CORE TEST MEASUREMENT SUMMARY AT MAXIMUM PHYSICA

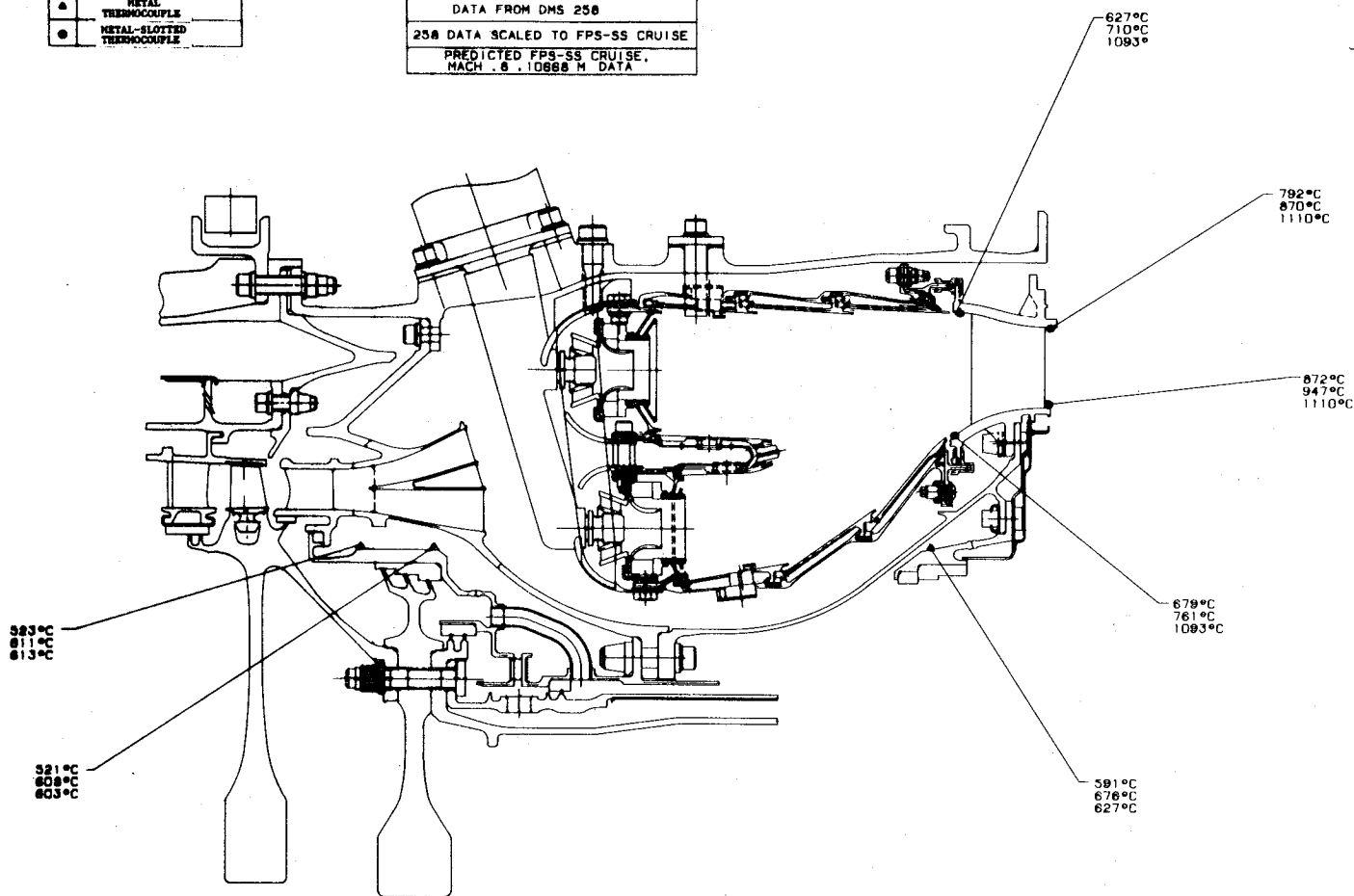
(ALL TEMPERATURES ARE IN DEGREES CENTIGRADE "°C")

ENGINE OPERATING PARAMETERS		
PARAMETER	READING 250	PREDICTED FPS-SS CRUISE MACH .8 - 10000 M
P25	.097 MPa	.055 MPa
P3	2.17 MPa	1.13 MPa
T3	508°C	502.7°C
T4	1348°C	1248°C
T42	889°C	800°C
% CORN SPEED	98.1 %	98.6 %
PHYL SPEED	12348.2 RPM	12329.4 RPM

* SCALE TO FPS CRUISE CONDITION WITH THE EFFECT OF TEST CELL AIR ENTRAINMENT ALONG CASIN

INSTRUMENTATION SYMBOLS	
▲	METAL THERMOCOUPLE
●	METAL-SLOTTED THERMOCOUPLE

DATA BLOCK	
DATA FROM DMS 250	
250 DATA SCALED TO FPS-SS CRUISE	
PREDICTED FPS-SS CRUISE, MACH .8, 10000 M DATA	



NOTE : ALL TEMPERATURES ARE AVERAGED FROM AVAILABLE DATA

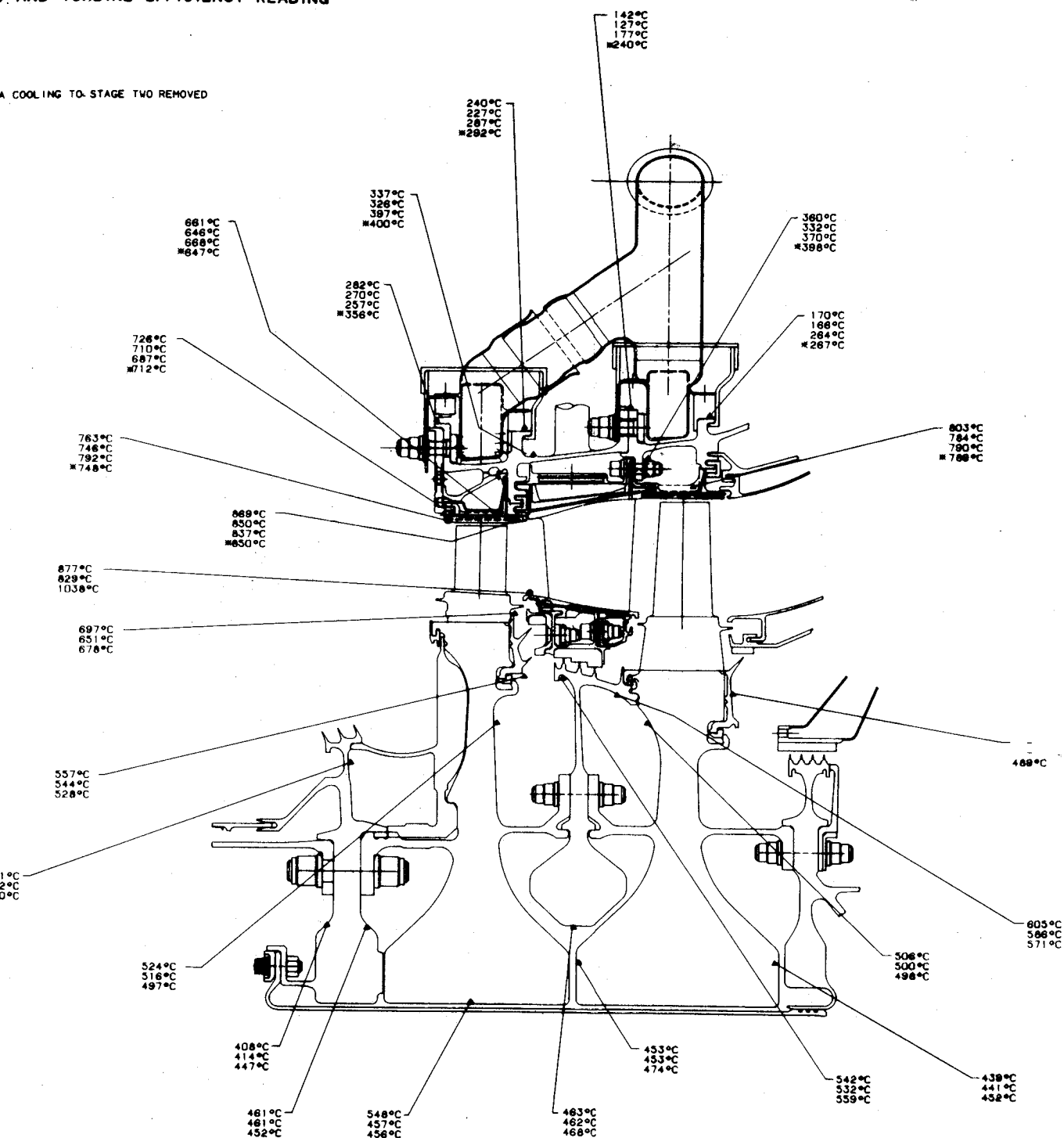
Figure 157. HP Turbine Engine Test Measure and Turbine Efficiency Reading

FOLDOUT FRAME

AND TURBINE EFFICIENCY READING

ORIGINAL PAGE IS
OF POOR QUALITY

A COOLING TO STAGE TWO REMOVED



Summary at Maximum Physical Speed
(units).

PRECEDING PAGE BLANK NOT FILMED

2 FOLDOUT FRAME

ORIGINAL PAGE IS
OF POOR QUALITY

E³ H P TURBINE-ENGINE CORE TEST MEASUREMENT SUMMARY AT MAXIMUM PHYSI

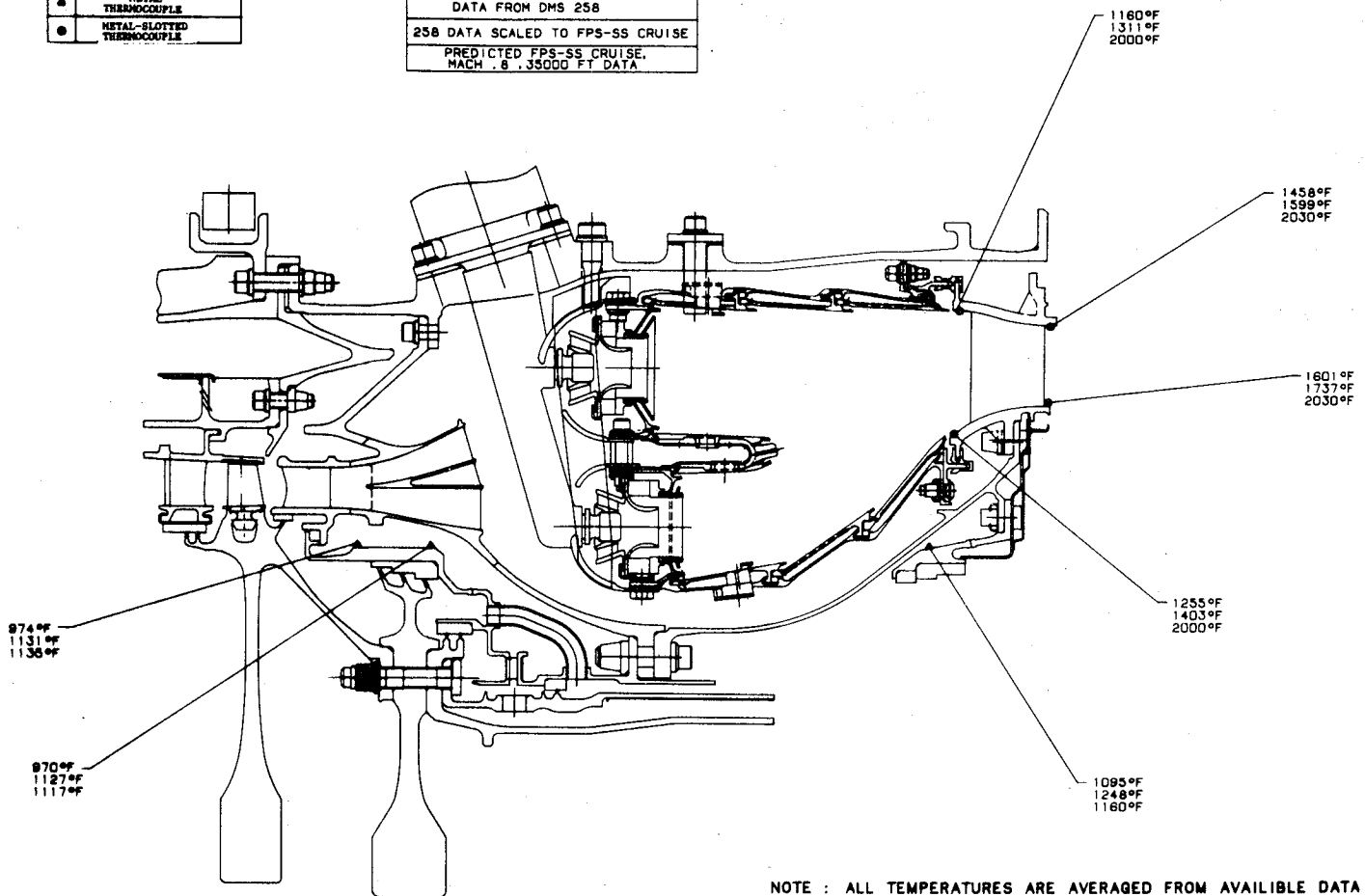
(ALL TEMPERATURES ARE IN DEGREES FAHRENHEIT "°F")

* SCALE TO FPS CRUISE CONDITION WITH THE EFFECT OF TEST CELL AIR ENTRAINMENT ALONG CA

ENGINE OPERATING PARAMETERS		
PARAMETER	READING 258	PREDICTED FPS-SS CRUISE MACH .8 - 35000 FT
P28	14.1 PSIA	8.01 PSIA
P3	314 PSIA	164.9 PSIA
T3	948°F	938°F
T4	2480.8°F	2278.4°F
T42	1578°F	1473°F
A CORR SPEED	98.1 %	98.8%
PHYL SPEED	12548.2 RPM	12528.4 RPM

INSTRUMENTATION SYMBOLS	
▲	METAL THERMOCOUPLE
●	METAL-SLOTTED THERMOCOUPLE

DATA BLOCK	
DATA FROM DMS 258	
258 DATA SCALED TO FPS-SS CRUISE	
PREDICTED FPS-SS CRUISE MACH .8 - 35000 FT DATA	



NOTE : ALL TEMPERATURES ARE AVERAGED FROM AVAILABLE DATA

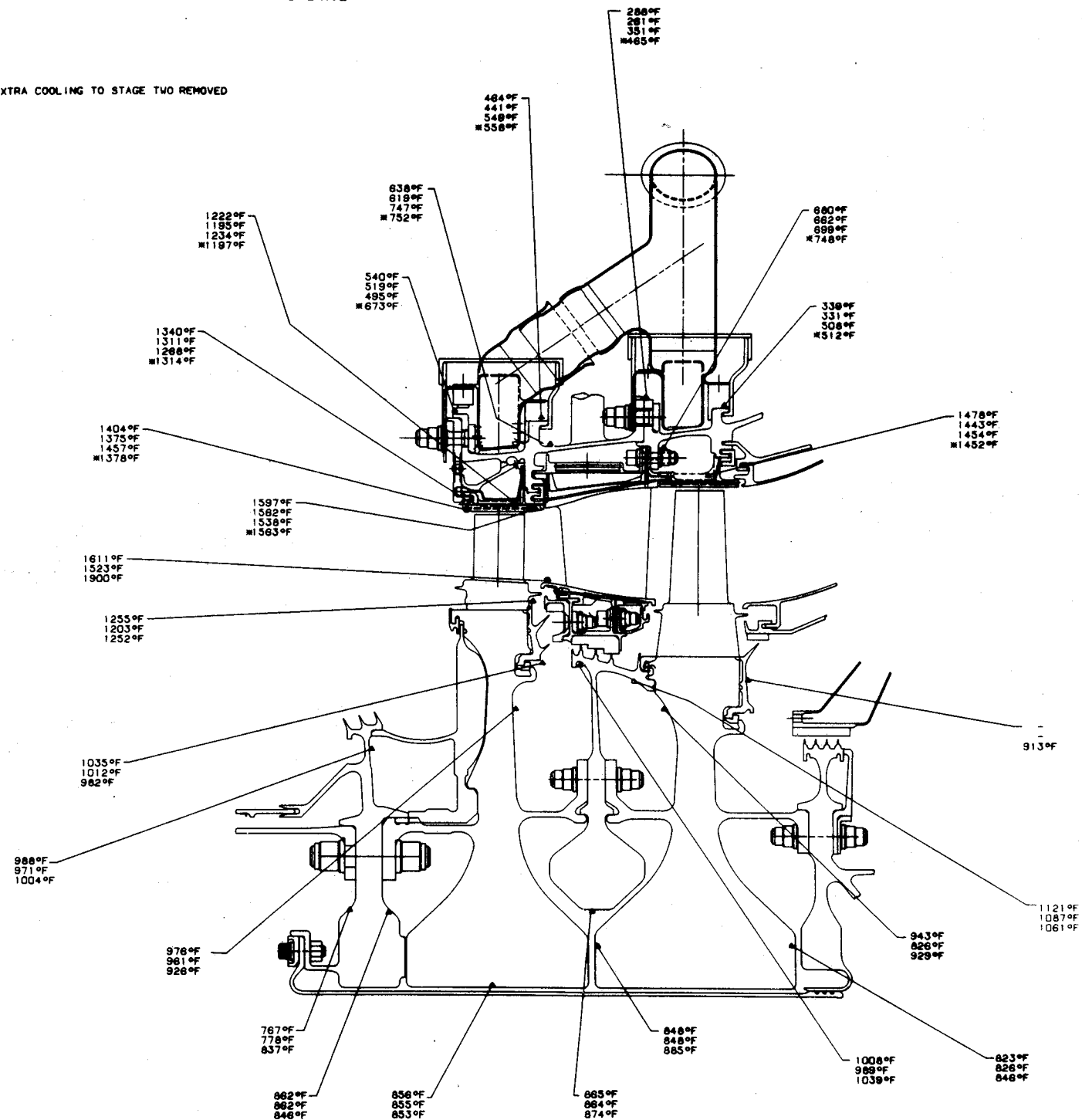
Figure 158. HP Turbine Engine Test Measurement and Turbine Efficiency Readings

FOLDOUT FRAME

ORIGINAL PAGE IS
OF POOR QUALITY

ED AND TURBINE EFFICIENCY READING

EXTRA COOLING TO STAGE TWO REMOVED



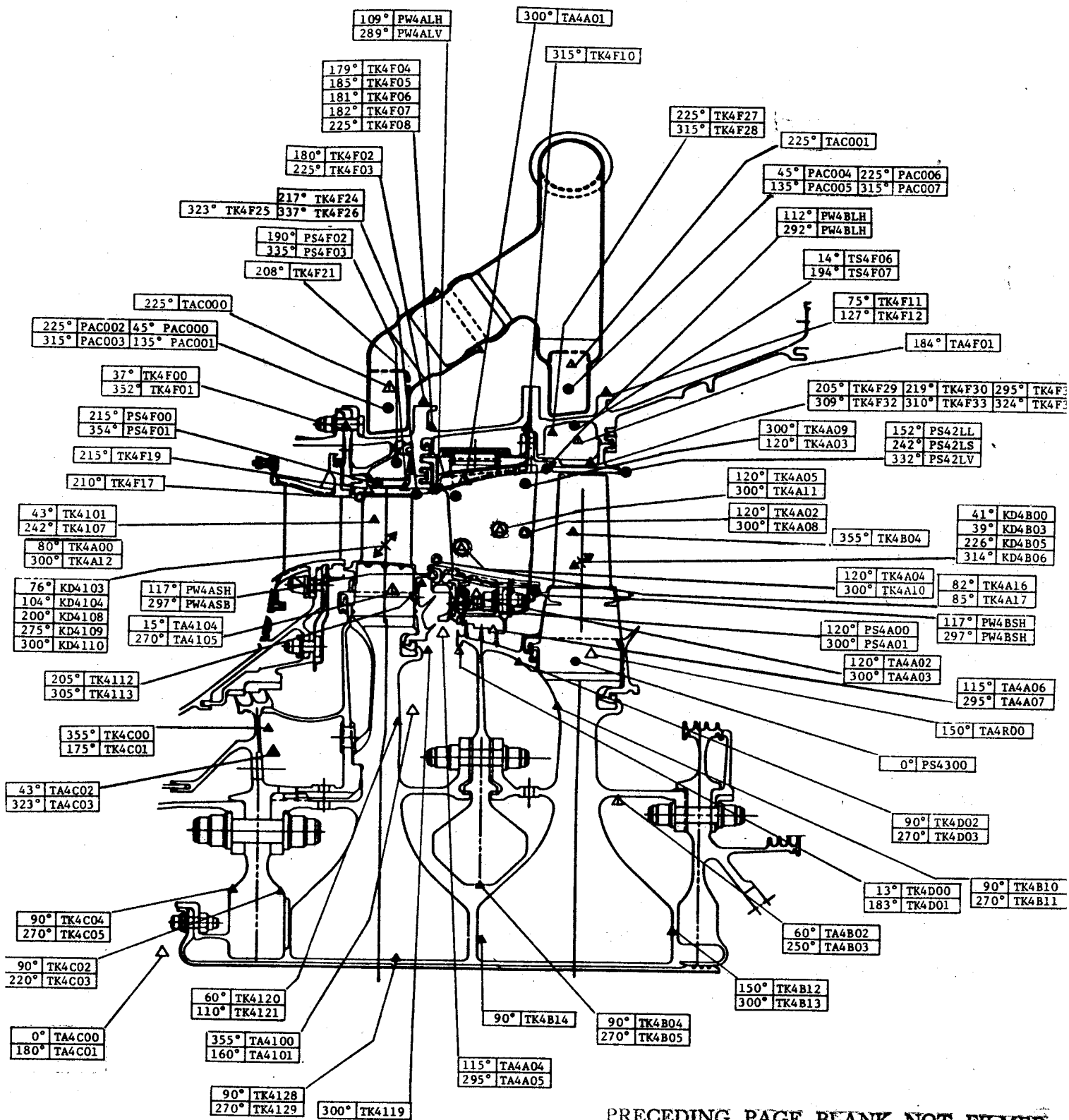
Summary at Maximum Physical Speed
(English Units).

PRECEDING PAGE BLANK NOT FILMED

293

2 FOLDOUT FRAME

ORIGINAL PAGE IS
OF POOR QUALITY



PRECEDING PAGE BLANK NOT FILMED

Figure 159. HP Turbine Instrumentation and Losses.

6.6.2 Blade Instrumentation

Stage 1 and 2 HP turbine blade instrumentation consisted of thermocouples for temperature measurements and strain gages for vibratory stress and frequency measurements. The following tabulation summarizes the type and quantity of blade instrumentation:

<u>Type of Instrumentation</u>	<u>Quantity Applied</u>		<u>Quantity at Start of Test</u>	
	<u>Stage 1</u>	<u>Stage 2</u>	<u>Stage 1</u>	<u>Stage 2</u>
Strain Gage (S/G)	11	8	11	8
Thermocouple (T/C)	11	8	9	8

Figure 160 shows the locations for Stage 1 and 2 surface-mounted strain gages on the airfoils. For better statistical data analysis, all strain gages for each stage were applied at the identical location on the airfoils. The selected location was based on the following considerations:

- Minimum sensitivity to expected location variations
- Adequately active stress measurement (relative to maximum stress) in all primary modes
- Location compatible with long durability (cool airfoil surface)

All blade serial numbers were identified with a corresponding strain gage identification number used throughout the test. Also, the locations of these blades in the disk post slots were defined relative to disk slot No. 1. Figures 161 and 162 show the location of these blades in specified disk post slot numbers for Stages 1 and 2, respectively.

The thermocouples were embedded in 0.050 cm (0.023 inch) wide by 0.050 cm (0.023 inch) deep slots which were formed in the airfoil wall by the EDM (electrical discharge machining) process. Each groove ran radially from the platform to the 25% or 50% airfoil span, depending on the location defined for a particular thermocouple. Holes varying in size from 0.076 cm (0.030 inch) to 0.16 cm (0.063 inch) diameter were also EDM drilled into the platform. These holes were used to route the thermocouple wiring to the blade shank and through the aft blade retainer.

Figures 163 and 164 show the thermocouple locations and identifications with the corresponding blade serial numbers for both stages. Two airfoil

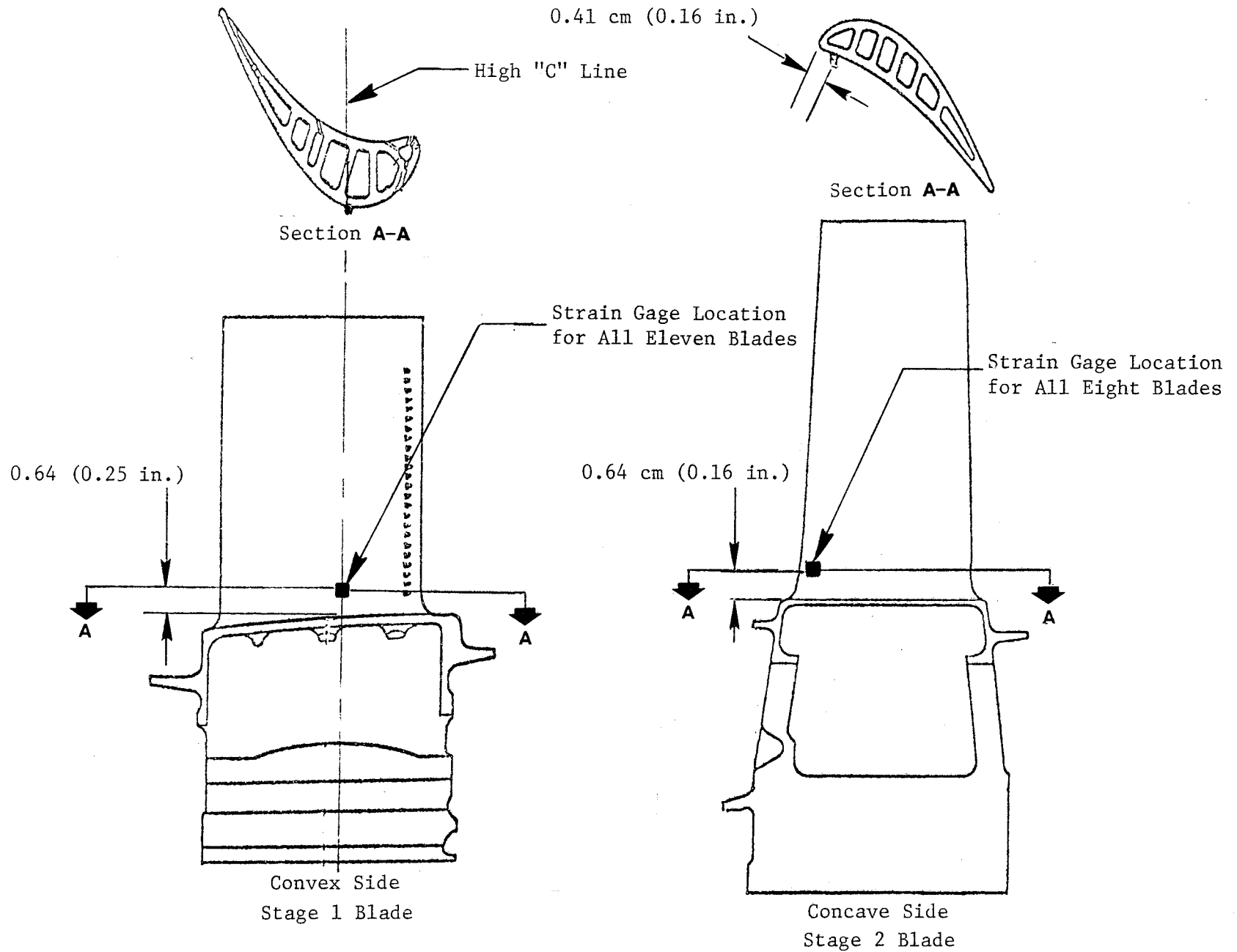


Figure 160. HP Turbine Strain Gage Location for Stage 1 and 2 Blades.

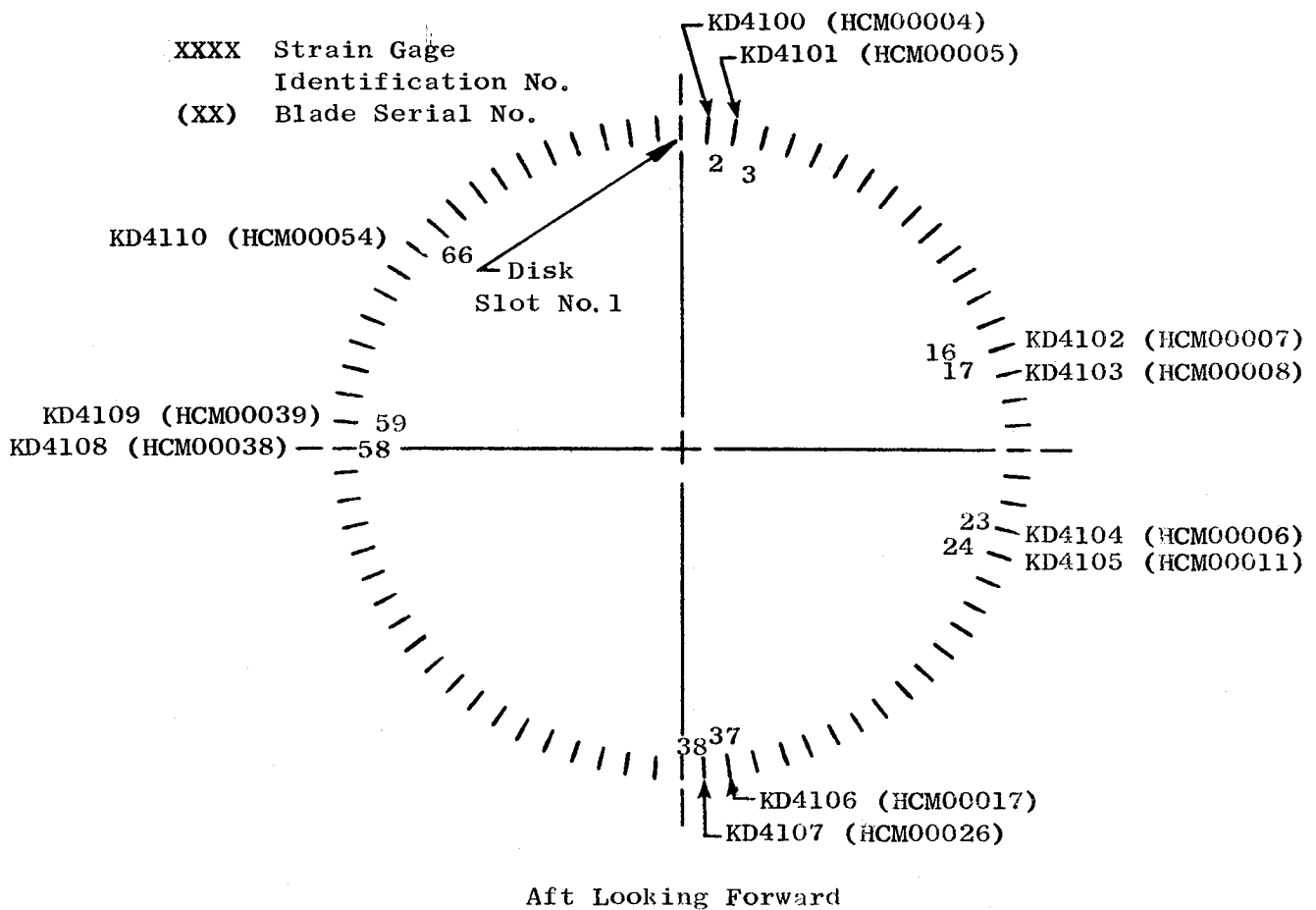
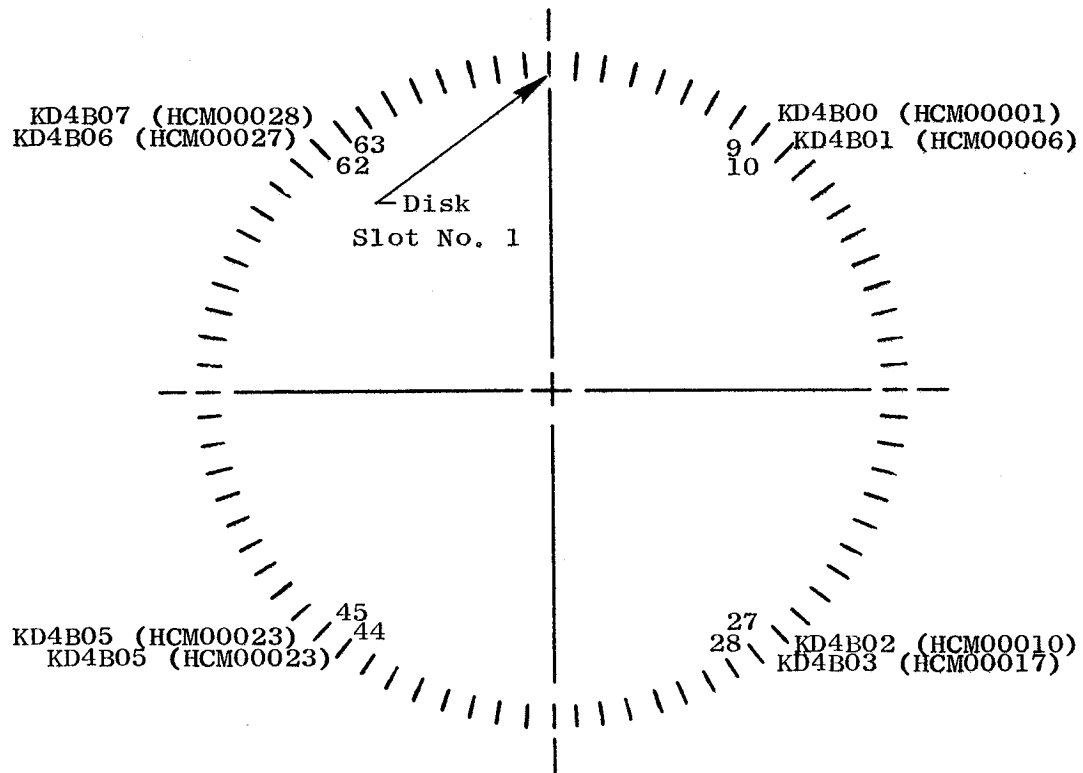


Figure 161. HP Turbine Stage 1 Blade Strain Gage Identification and Blade Serial Number.

XXXX Strain Gage Identification No.
 (XX) Blade Serial No.



Aft Looking Forward

Figure 162. HP Turbine Stage 2 Blade Strain Gage Identification and Blade Serial Number.

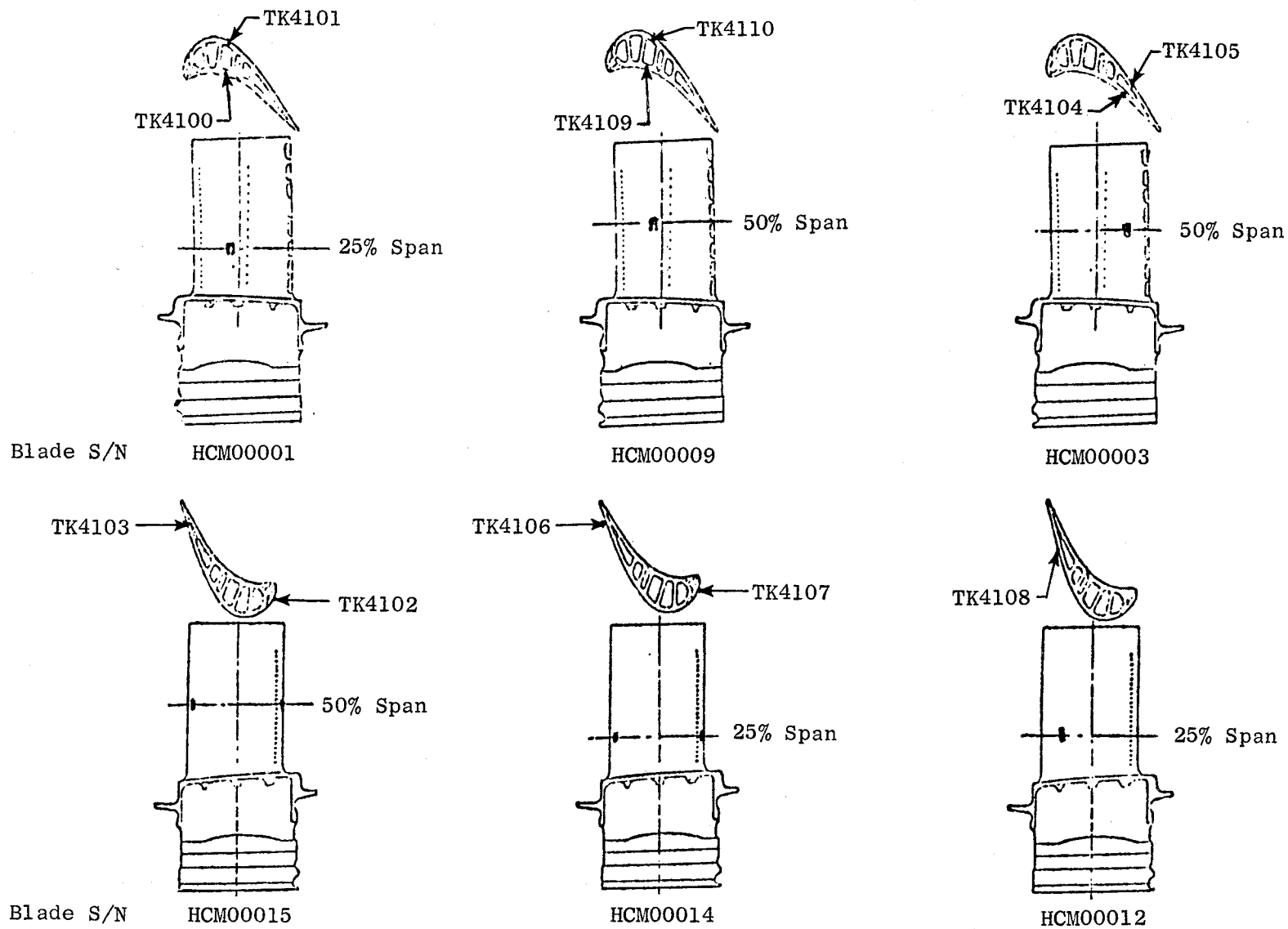


Figure 163. HP Turbine Stage 1 Blade Thermocouple Locations and Identification.

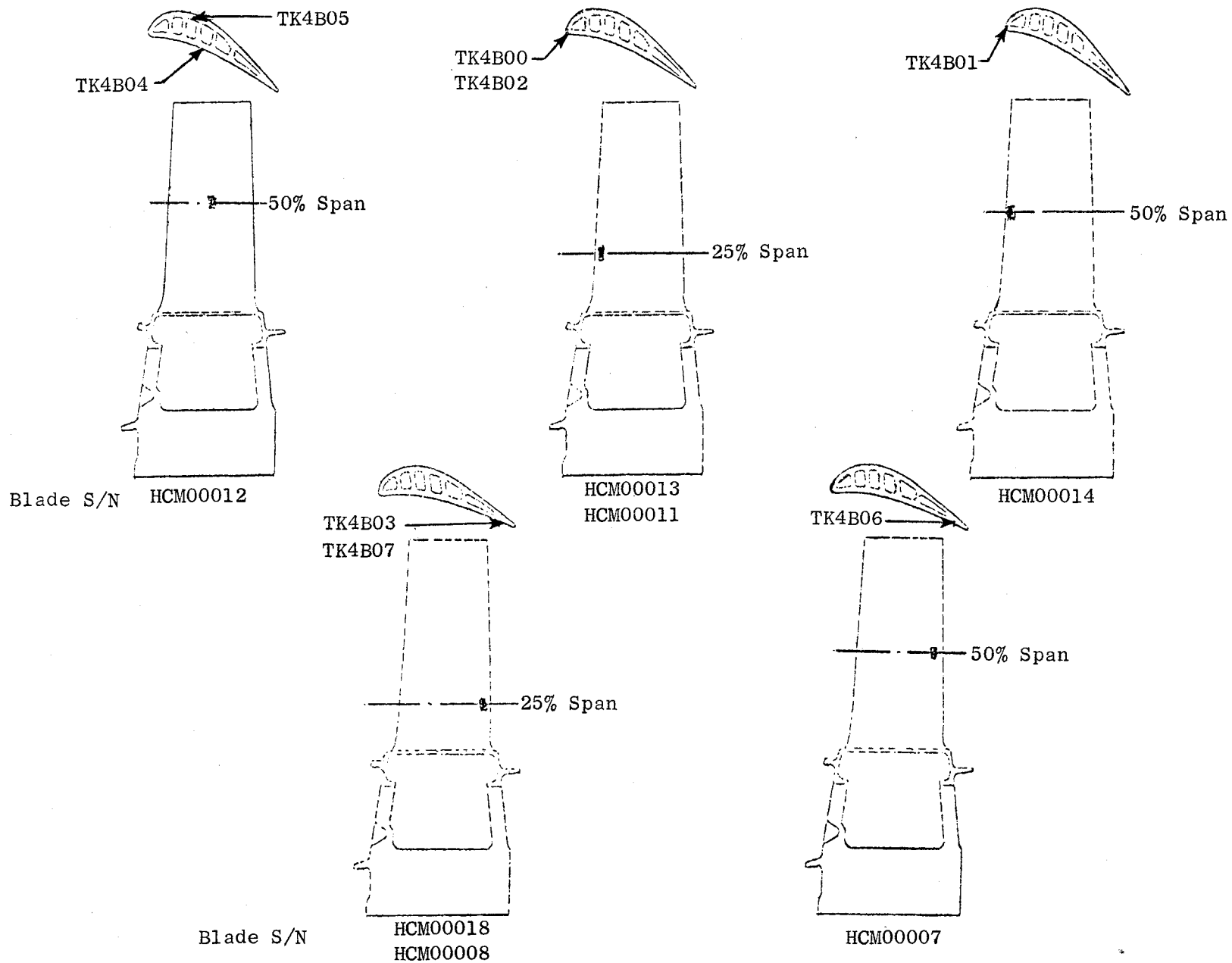


Figure 164. HP Turbine Stage 2 Blade Thermocouple Locations and Identification.

spans were used to record the blade temperatures at 25% and 50% span, as stated above. These sections were compatible with the design and life predictions used in the analyses for both stages of blades.

The locations of these blades in the disk post slots were used for identification purposes. Figures 165 and 166 show Stage 1 and 2 blade serial numbers in specified disk post slots, respectively.

One blade from each stage contained local tip notches on the suction side (Figures 167 and 168). Each of these blades carried two pairs of three different depth notches which served a two-fold purpose: First, they provided a means for estimating the blade tip rub depth by comparing the photographs of the notch depth taken at assembly, during test borescope inspections, and after engine tests. Second, they provided a means for locating and identifying any blade in the turbine relative to these blades.

Blade Vibration

Vibratory strains were measured on Stage 1 and 2 blade rows. The measurements were adjusted to reflect stresses at the life limiting locations on each blade row. These stress levels determined the severity of blade vibration levels. The method of analysis and results are described below for the Stage 1 blade, and then the results are given for the Stage 2 blade.

In order to determine the most life limiting location on a blade, a mechanical and thermal stress analysis was performed. The results yielded steady-state local stresses (mechanical plus thermal) at temperature. This analysis was based on the most life limiting condition; the FPS engine at hot day takeoff.

The blade area having the most severe combination of steady-state stress, vibratory stress, and metal temperature was considered to be the life limiting point. The limiting location for the Stage 1 blade was determined to be at the 12% span leading edge near the pressure side row of shower-head holes.

Since the strain gages were not located at the life limiting point, the strain at the limiting point had to be related to gage strain. The analysis utilized results from prior blade component vibratory strain distribution tests.

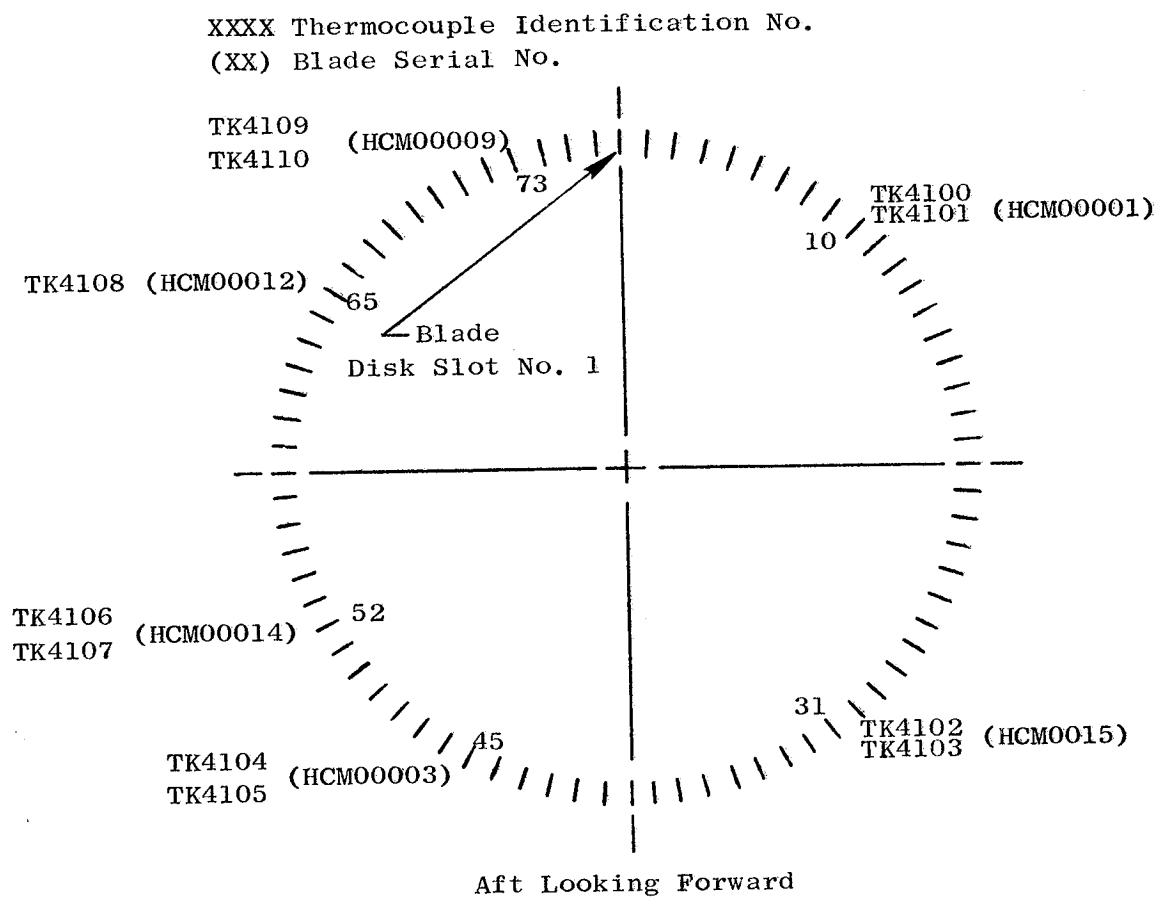


Figure 165. HP Turbine Stage 1 Blade Thermocouple Identification and Blade Serial Number.

XXXX Thermocouple Identification No.
 (XX) Blade Serial No.

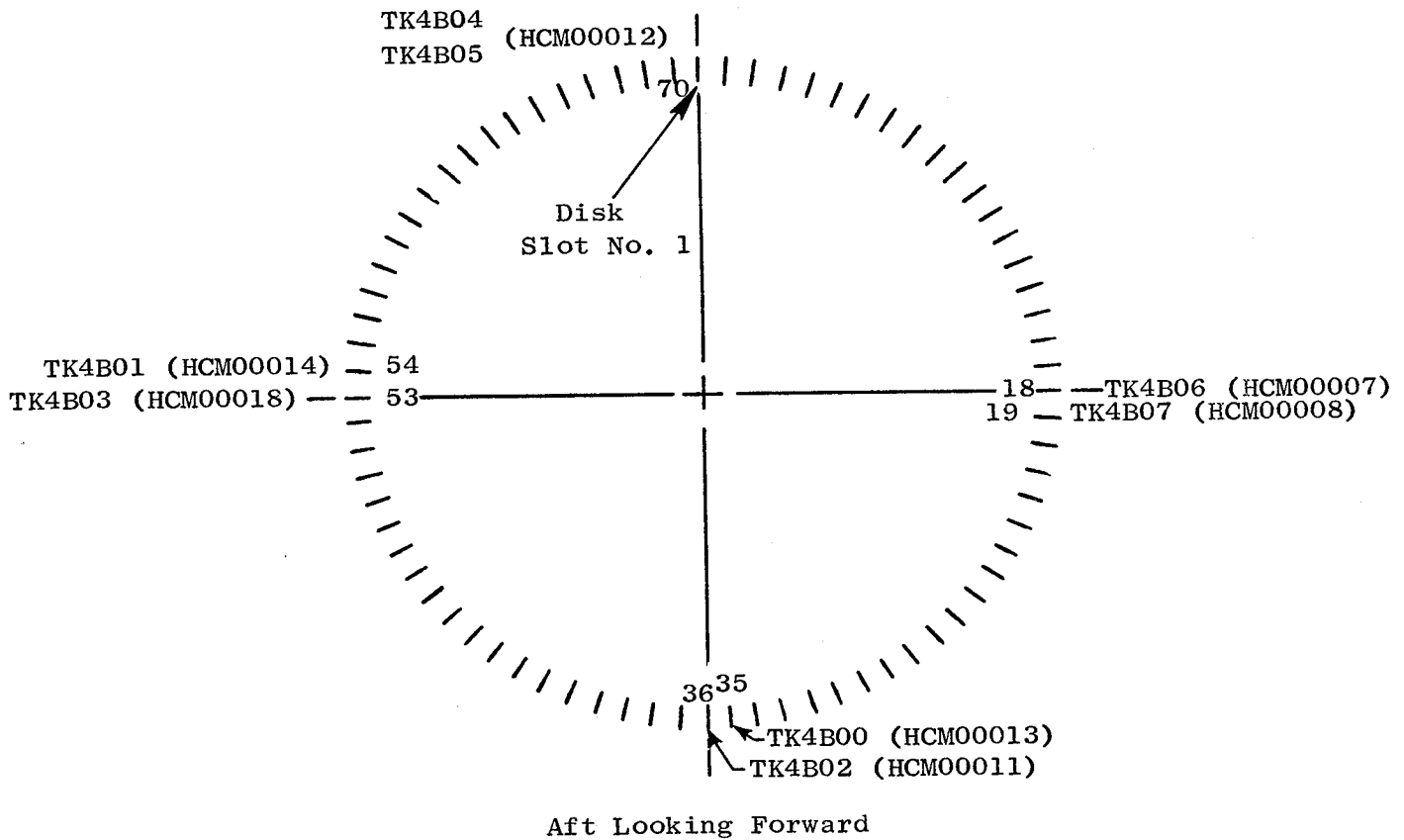


Figure 166. HP Turbine Stage 2 Blade Thermocouple Identification and Blade Serial Number.

• Measurements = mm (inch)

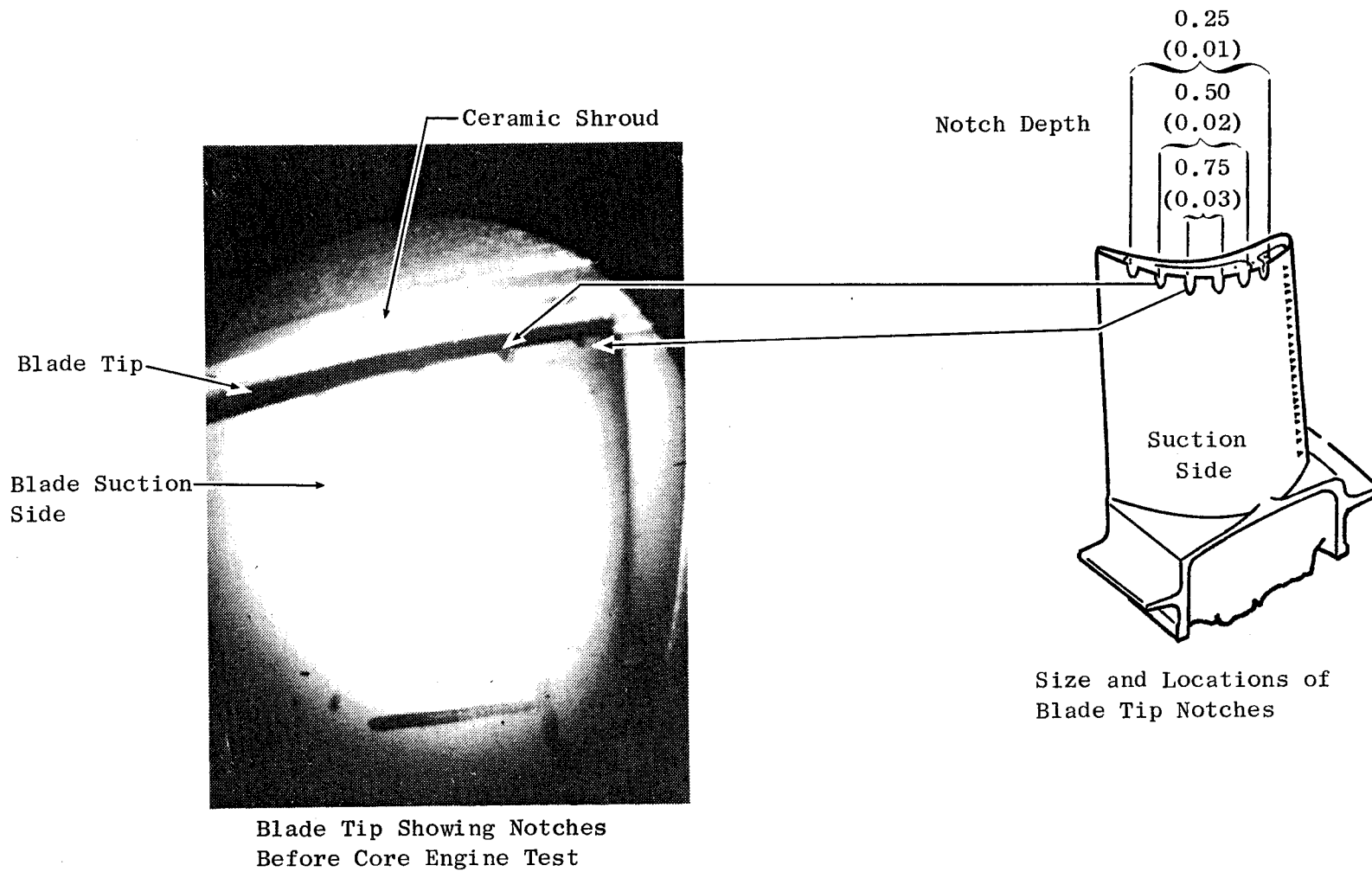
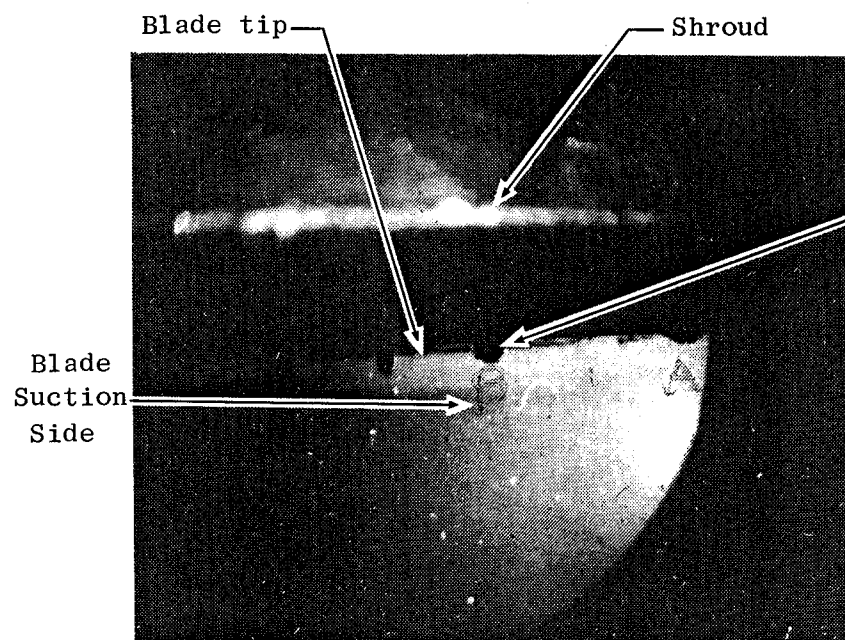


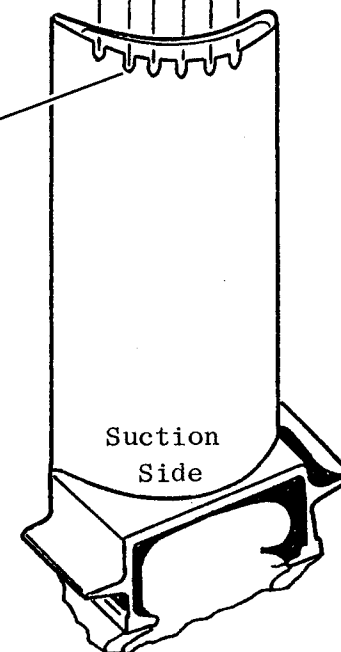
Figure 167. HP Turbine Stage 1 Blade.

• Measurements = mm (inch)



Blade Tip Showing Notches
Before Core Engine Test

0.25
(0.01)
0.50
(0.02)
0.75
(0.03)
Notch Depth



Size and Locations of
Blade Tip Notches

Figure 168. HP Turbine Stage 2 Blade.

In the blade component vibratory strain distribution tests, strain gages were mounted in the same locations as the gages mounted on the engine blades, thereby establishing a reference datum between the two systems. The component test results yielded strain distribution levels, relative to the engine gage location, when the blade was excited at its natural frequencies. Each blade frequency resulted in a different relative strain distribution throughout the blade.

The total vibratory stress at a point in the blade is the summation caused by the blade natural frequencies matching some form of per rev excitation. The level of stress varies according to the type of stimulus and the blade frequency level.

In general, the first three primary modes of vibration contributed most of the vibratory stresses; these were the first flexural, first axial, and first torsional modes. The core engine blade vibrational activity in each of these modes was determined by spectral analysis. The vibration levels of each mode could then be treated separately.

The ratios of strain at the life limiting point to strain at the gage location were determined from the blade vibratory strain distribution tests for each of the primary modes. These "strain ratios due to primary modes" provide the first step in relating measured strain to strain at the limiting point.

The next step accounted for the remaining vibratory contributions. A "strain ratio due to higher modes" was applied to the ratios for the primary modes. This ratio varied for each blade design and was based on a spectral vibrational data analysis. The analysis was performed using engine data recorded at the speed considered the most life limiting. The spectral characteristics are shown in Figure 169 for Stage 1. Note that the sum of the stress contributions from the first three primary modes represents a fraction of the total stress, and that the total stress is the sum of all stresses shown when the blade is excited at all its frequencies (through 20 kHz). For the Stage 1 blade, the ratio was: $\text{Strain due to all modes} / \text{strain due to first three primary modes} = 1.5$.

ORIGINAL PAGE IS
OF POOR QUALITY

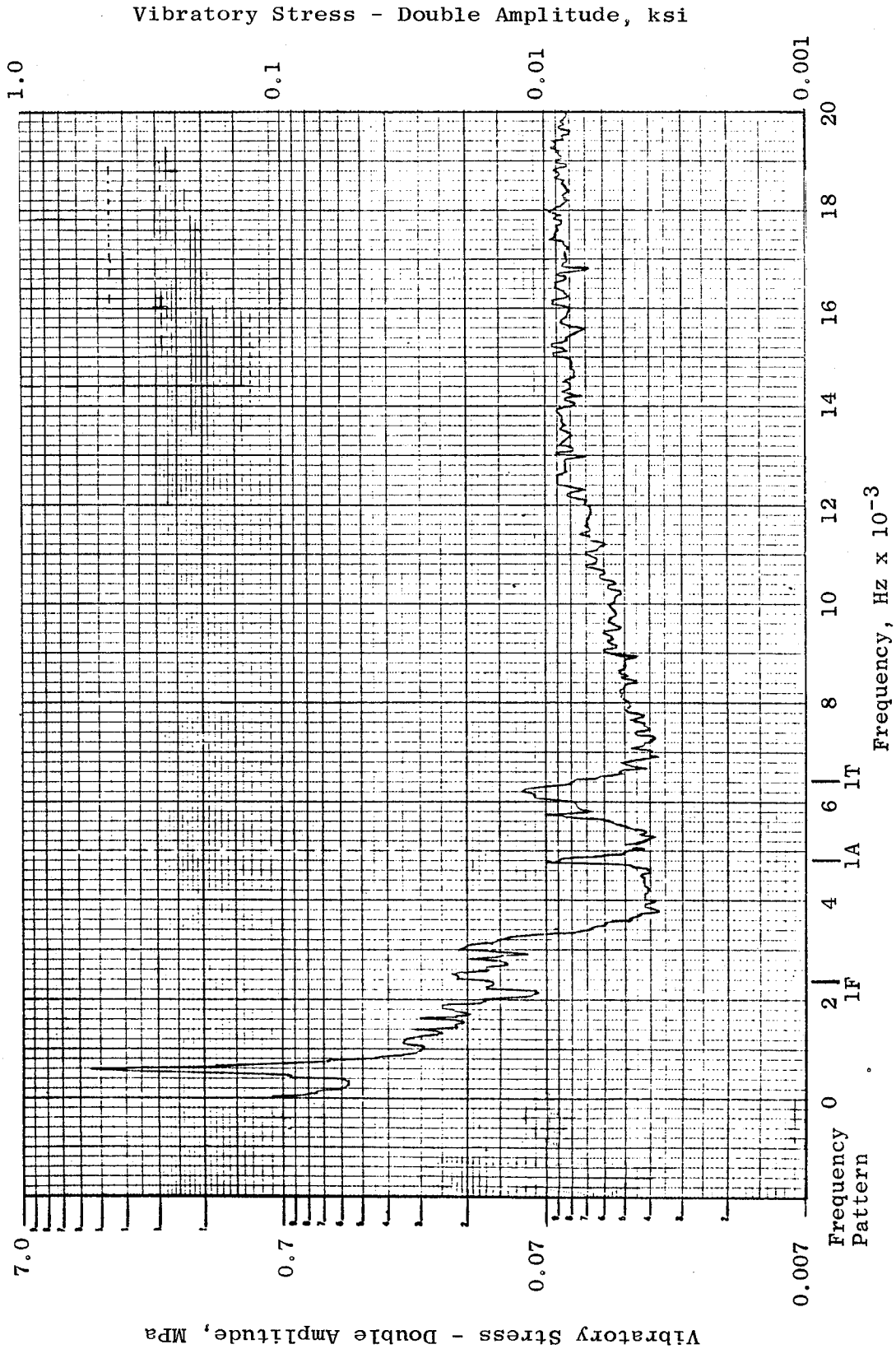


Figure 169. HP Turbine Stage 1 Blade Spectrum Frequency Analyzer and
Vibration Stress Levels.

Measured strains were automatically converted to stress by the data recording equipment. This conversion used Young's modulus for a standard temperature of 954° C (1750° F). Since the airfoil metal temperature was different, the recorded stress was subsequently adjusted to reflect Young's modulus for the airfoil temperature. Displayed stress was ratioed by a "modulus ratio" which was Young's modulus at the design metal temperature at the life limit location over Young's modulus at 954° C (1750° F).

The recorded stresses could then be related to stress at the life limiting location by the following equation:

$$\begin{aligned} \sigma \text{ Limit} &= \sigma \text{ Recorded} \\ \text{Point} &\quad X \text{ (Strain Ratio Due to Primary Modes)} \\ &\quad X \text{ (Strain Ratio Due to Higher Modes)} \\ &\quad X \text{ (Modulus Ratio)} \end{aligned}$$

Due to the number of strain gages being limited to a small quantity in each blade row, a statistical analysis was employed to project a maximum probable vibratory stress based on the measured stresses. The maximum probable stress was taken to be higher than the average measured stress by a three-sigma (σ) deviation.

The recorded blade vibratory stress results obtained at 12,000 rpm were used to establish the statistical deviations. A ratio of the maximum probable vibratory stress to the maximum observed vibratory stress was calculated for each blade row. This ratio was subsequently used to determine maximum probable vibratory stress in the blade row. The results of the statistical analysis and the ratio of maximum probable to maximum observed stresses are shown in Table XXIV.

In all discussions that follow in this section, the recorded vibratory stress levels shown are for the single most active blade with the highest recorded stress levels.

Prior to engine testing, individual blades had been subjected to hot high cycle fatigue tests. These blades were tested to failure in the first flexural mode. Next, the average stress at the failure location for all failed blades was compared to round, smooth bar test data. The average failure

stress for the Stage 1 test blades lower by a 2.38 factor from the smooth bar data. This derate factor accounts for the cooling air hole stress concentration, material derate for surface coating, thin wall, grain orientation, and biaxial stress field effects, all of which are not present in smooth bar testing. Projected stresses were increased by this factor so that they could be related to the material strength data.

Table XXIV. Turbine Blade Vibratory Stress Statistical Analysis.

Stage	Average Observed Stress	3σ	Stress in MPa (ksi)		<u>Maximum Probable Stress</u> <u>Maximum Observed Stress</u>
			Maximum Probable Stress	Maximum Observed Stress	
1	12.4 (1.8)	4.8 (0.7)	17.2 (2.5)	15.9 (2.3)	1.08
2	50.3 (7.3)	45.5 (6.6)	95.8 (13.9)	76.0 (11.0)	1.26

The stress factors from the preceding discussion are presented for the Stage 1 blade in Table XXV. Vibratory stress at the life limiting location is determined by establishing the recorded stresses for the primary modes from spectrum analysis and applying the factors as follows:

$$\begin{array}{lcl} \sigma & \text{Total at} & = \\ & \text{Limiting Point} & 3.48 \text{ Recorded, 1st flexural} \\ & \text{for Blade 1} & +4.87 \text{ Recorded, 1st axial} \\ & & +10.18 \text{ Recorded, 1st torsional} \end{array}$$

The stress values for the recorded deviation were determined from the spectrum analyzer plots shown typically in Figures 170 through 172. These plots were arranged to show stress for the overall level and primary modes as a function of speed. The first torsional mode is not displayed in the figures because values were lower in magnitude. The stress levels from all modes were used in the above equation which then yielded the total blade stress at the limiting point.

ORIGINAL PAGE IS
OF POOR QUALITY

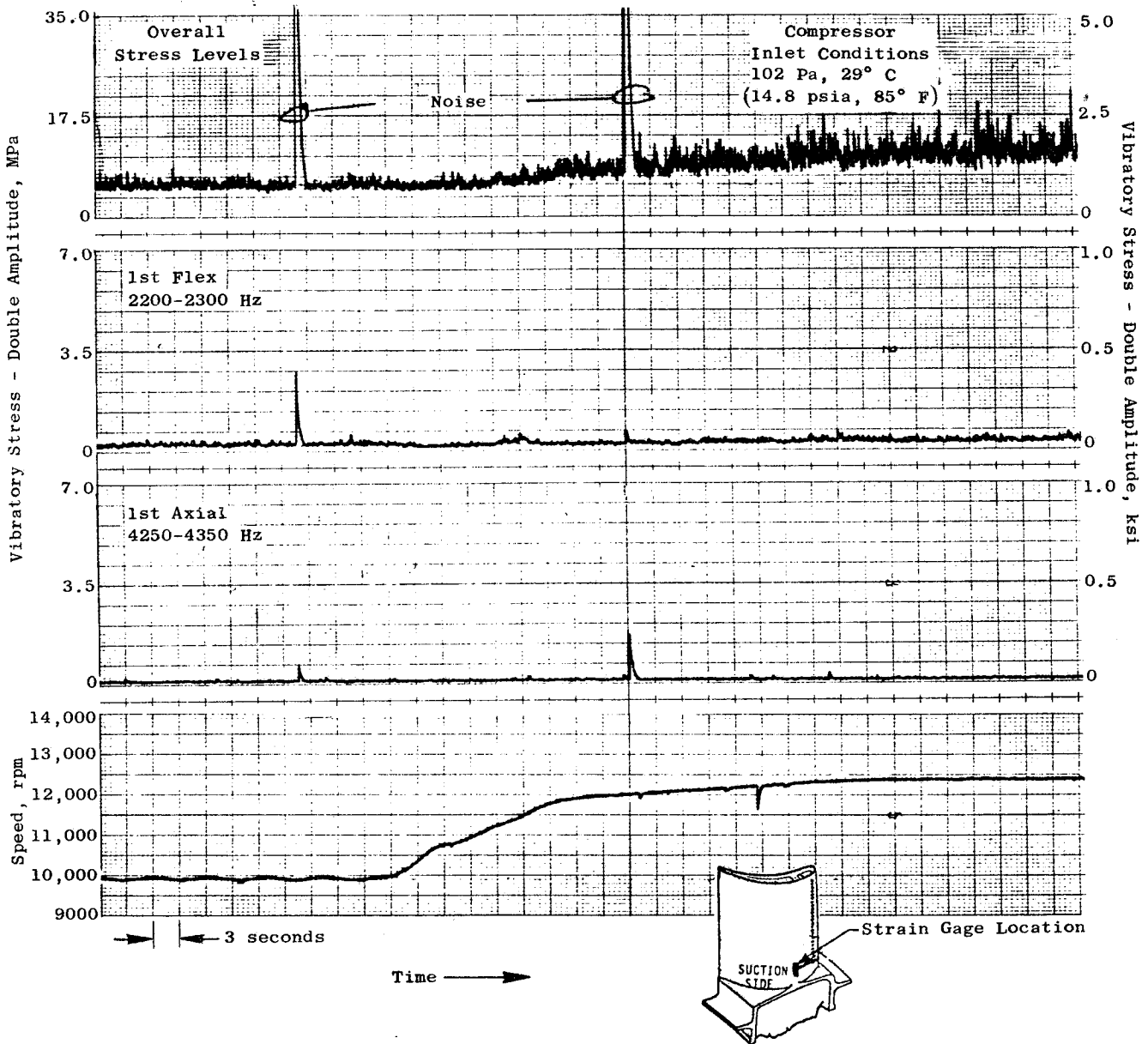


Figure 170. HP Turbine Stage 1 Blade Vibratory Stress Characteristics (Accel from Idle to 12,800 rpm).

ORIGINAL PAGE IS
OF POOR QUALITY

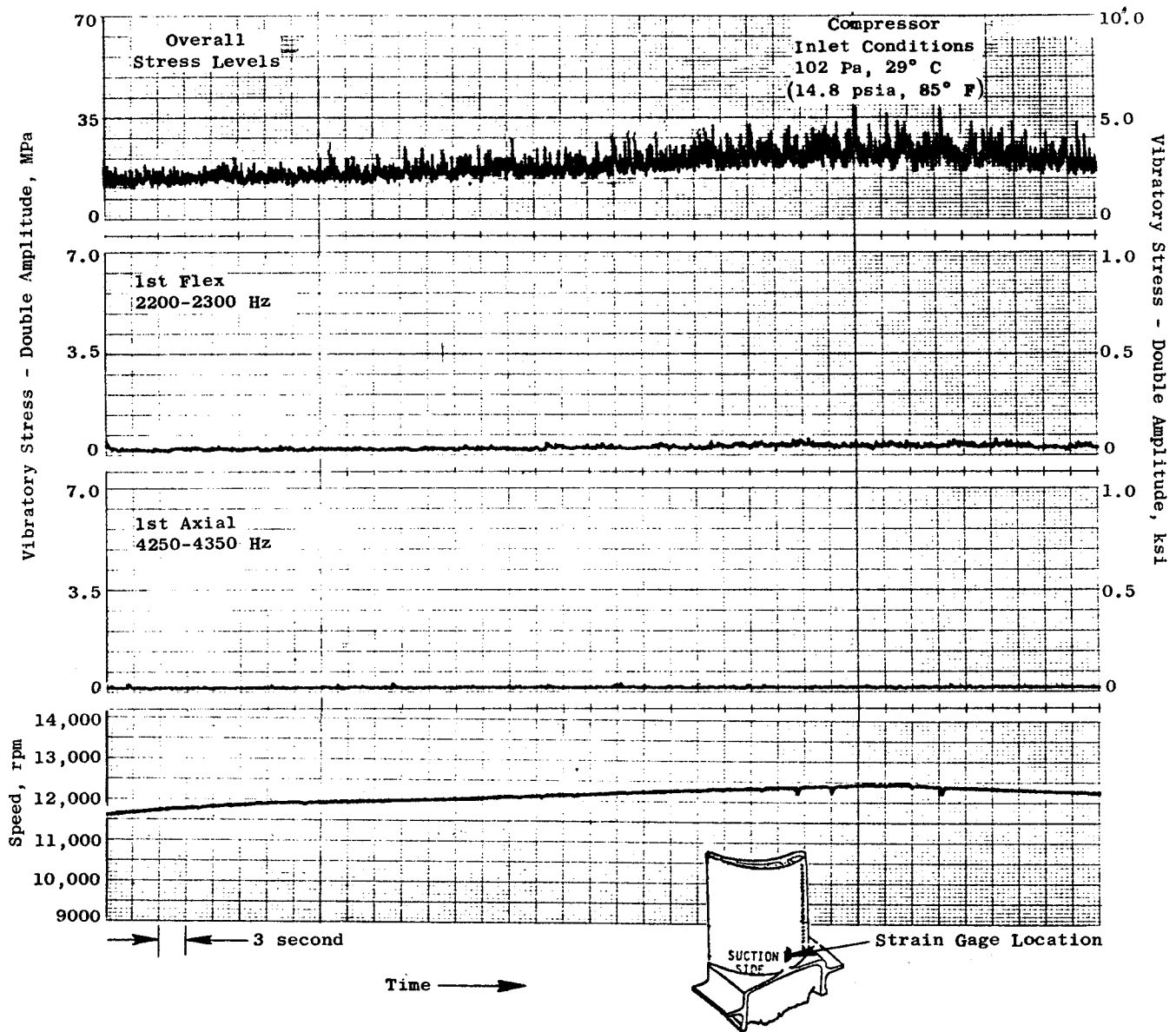


Figure 171. HP Turbine Stage 1 Blade Vibratory Stress Characteristics
(Accel from 11,550 to 12,450 rpm).

ORIGINAL PAGE IS
OF POOR QUALITY

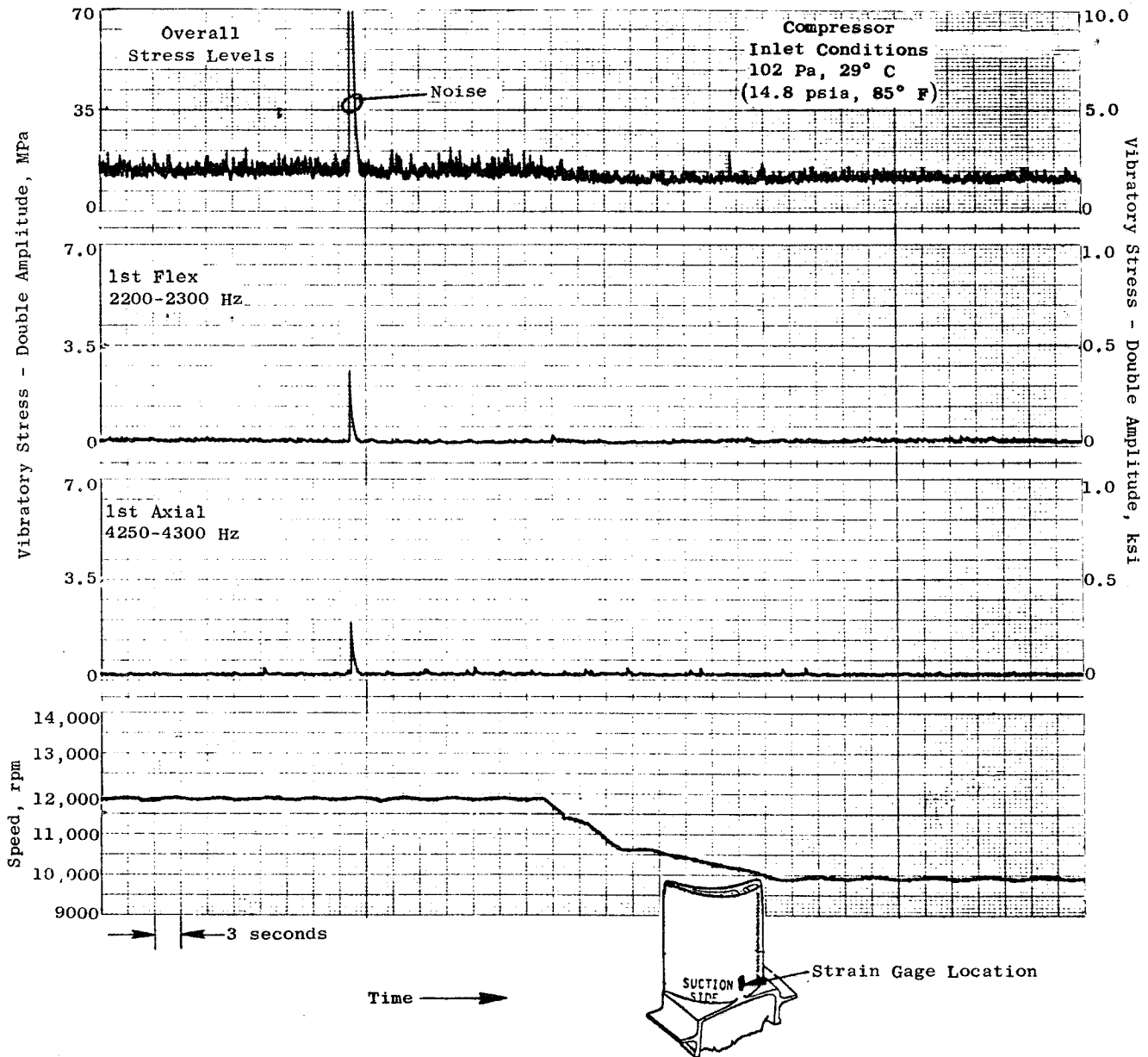


Figure 172. HP Turbine Stage 1 Blade Vibratory Stress Characteristics (Decel from 11,850 rpm to Idle).

Table XXV. Stage 1 Blade Factors for Projecting Maximum Stress at Life Limiting Location.

	<u>1st Flex</u>	<u>1st Axial</u>	<u>1st Torsional</u>
Strain Ratio Due to Primary Modes	0.95	1.33	2.78
Strain Ratio Due to Higher Modes	1.50	1.50	1.50
Modulus Ratio	0.95	0.95	0.95
<u>Max Probable Stress</u> <u>Max Observed Stress</u>	1.08	1.08	1.08
Stress Derate Factor	2.38	2.38	2.38
	-----	-----	-----
Total Multiplying Factor Applied to Measured Stress (Product of the Values in Table)	3.48	4.87	10.18

The measured Stage 1 blade stresses for the three primary modes are given in Table XXVI. The maximum probable vibratory stress at the life limiting location is calculated to be 7.6 MPa (1.1 ksi), single amplitude.

Table XXVI. HP Turbine Stage 1 Blade.

Maximum Projected Stress Based on Maximum Recorded Stress

<u>Blade Frequency Characteristic</u>	<u>Most Active Stress Measurement</u> MPa (ksi) <u>Single Amplitude</u>	<u>Stress Factor</u> (Reference Table XXII)	<u>Projected Maximum Probable Stress at Blade Limiting Location</u> MPa (ksi) <u>Single Amplitude</u>	
			MPa	(ksi)
1st Flexural	0.69 (0.10)	3.48	2.4	(0.35)
1st Axial	0.34 (0.05)	4.87	1.7	(0.24)
1st Torsional	0.34 (0.05)	10.18	3.5	(0.51)
		Total	7.6	(1.10)

The maximum allowable vibratory stress in the ICLS or FPS engine at the Stage 1 blade limit location is 256 MPa (37.2 ksi), single amplitude. In the ICLS and FPS, pressure is higher. Using a 1.04 multiplier to adjust to turbofan pressure, the blade stress, expressed as a percent of allowable stress in a turbofan engine, was:

$$\text{Percent Allowable Stress} = \frac{7.6 \text{ MPa} \times 1.04}{256 \text{ MPa}} \times 100\% = 3\%$$

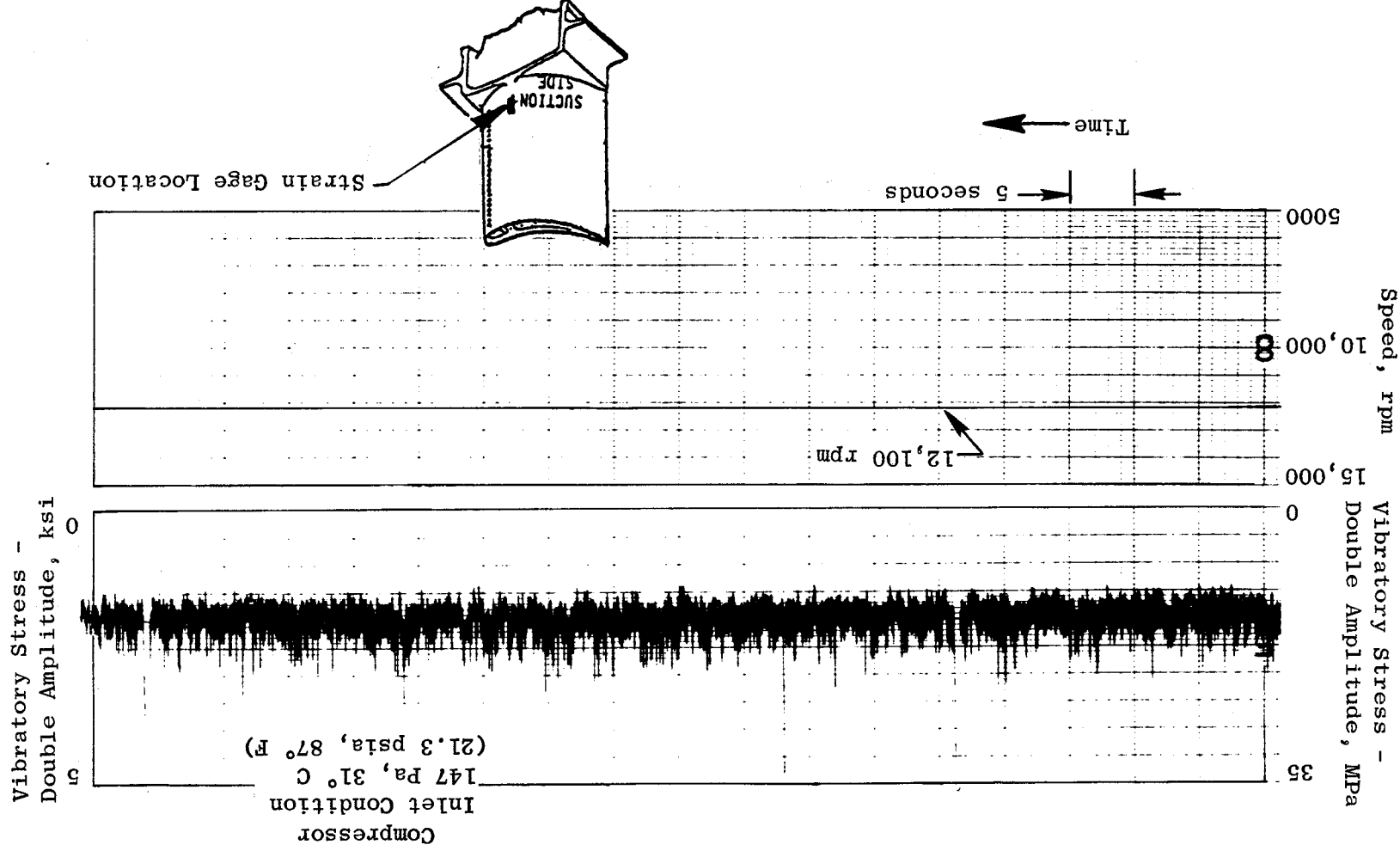
In the core engine the blade temperatures were less severe than for the FPS design values. Therefore, the percent allowable stress was less than the 3% calculated above. Because the level was so low, the exact value was not calculated.

ICLS engine compressor discharge pressures (CDP) were obtained during the core engine test by pressurizing the compressor inlet to 147 kPa (21.3 psia). Blade vibrational stresses at this maximum pressure are shown in Figure 173. The stresses did not reach the levels recorded at ambient conditions because maximum resonance speeds were not reached.

The combined result of the steady-state stresses with the vibration stresses is represented in the Goodman diagram in Figure 174 which shows that the ratio of the vibrational stresses (A) to the allowable vibrational stress (B) is 3% for the leading edge. This value is also expressed as the blade reaching 3% of scope limits. Note that this percentage is based on the FPS engine with the leading edge (12.5% span) temperature at 1004° C (1840° F).

Figure 175 represents the Stage 1 HP turbine blade Campbell diagram and shows the recorded vibratory stresses occurring at the various blade frequencies and at different speed conditions. The figure also shows very low excitation stimuli for all sources of per rev excitations. The very small changes in stress levels, caused by any form of excitation, are due to the existence of excellent damping characteristics. Figure 176 shows the predicted blade Campbell diagram with the corresponding measured frequencies plotted for the various engine core speeds. Overall, the measured frequencies for the blade primary modes closely follow the predicted frequencies.

ORIGINAL PAGE IS
OF POOR QUALITY



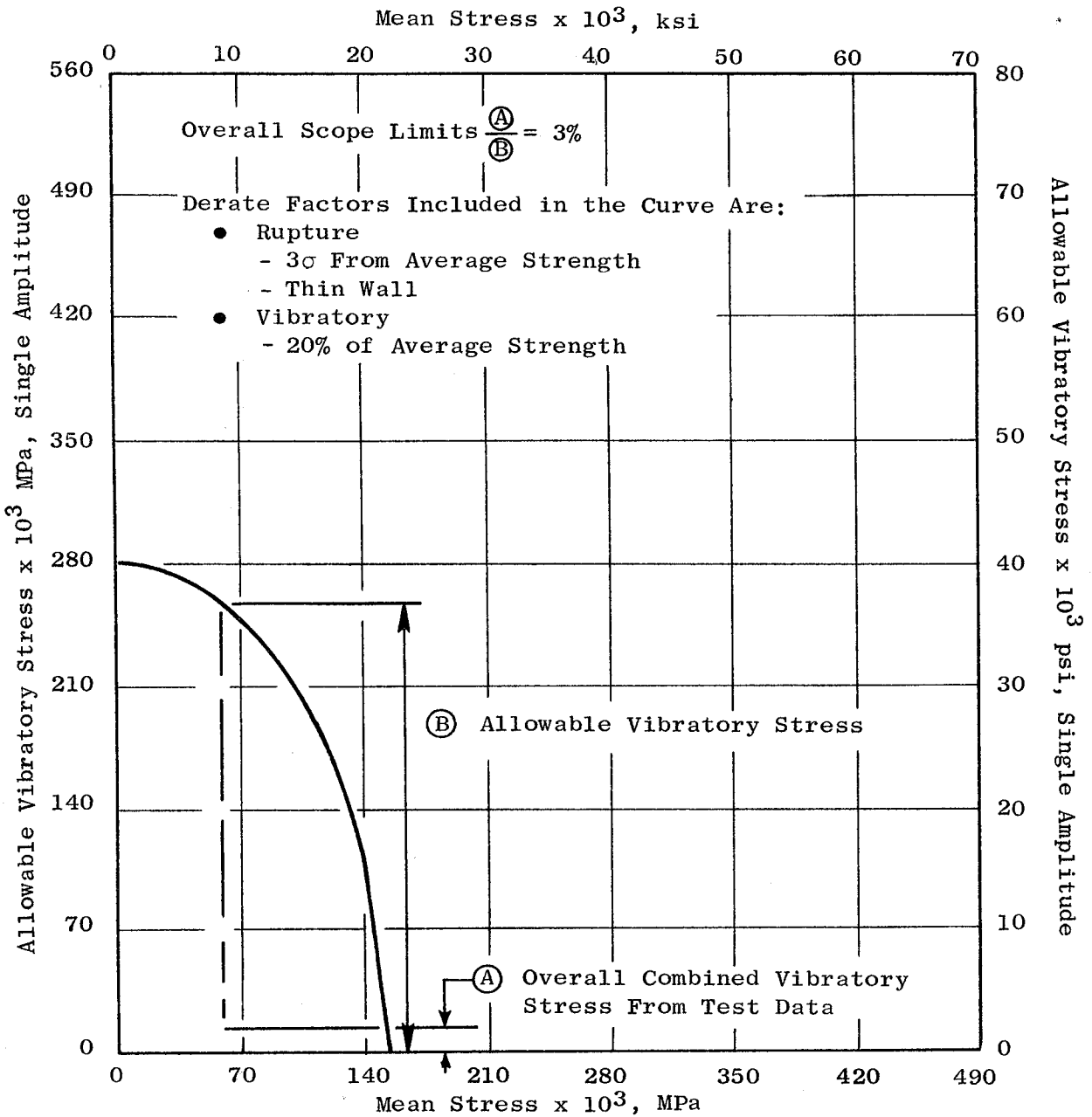
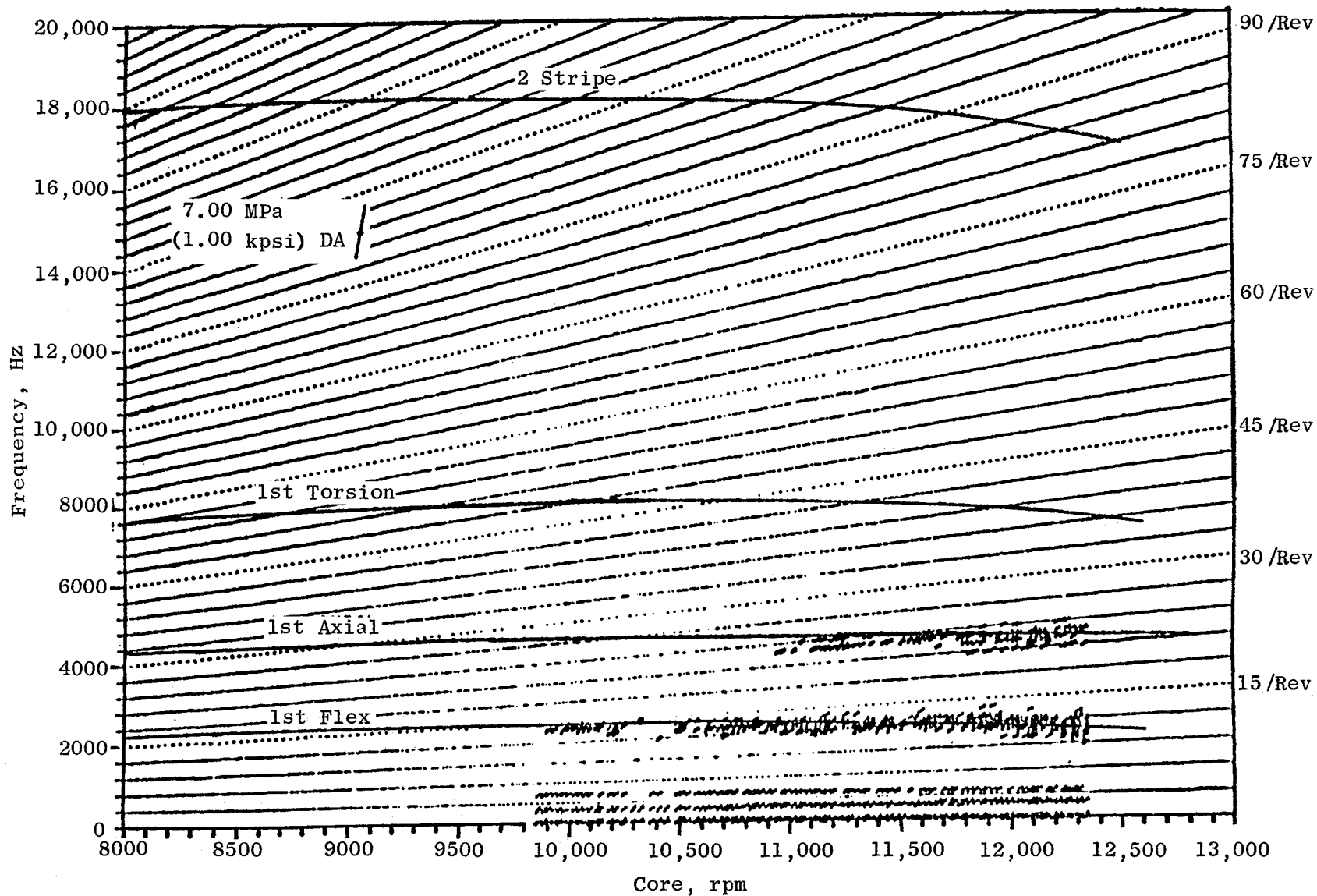


Figure 174. HP Turbine Stage 1 Blade 100-Hour Goodman Diagram at 1000°C (1840°F).



ORIGINAL PAGE IS
OF POOR QUALITY

Figure 175. HP Turbine Stage 1 Blade Campbell Diagram Showing Measured Vibratory Stresses.

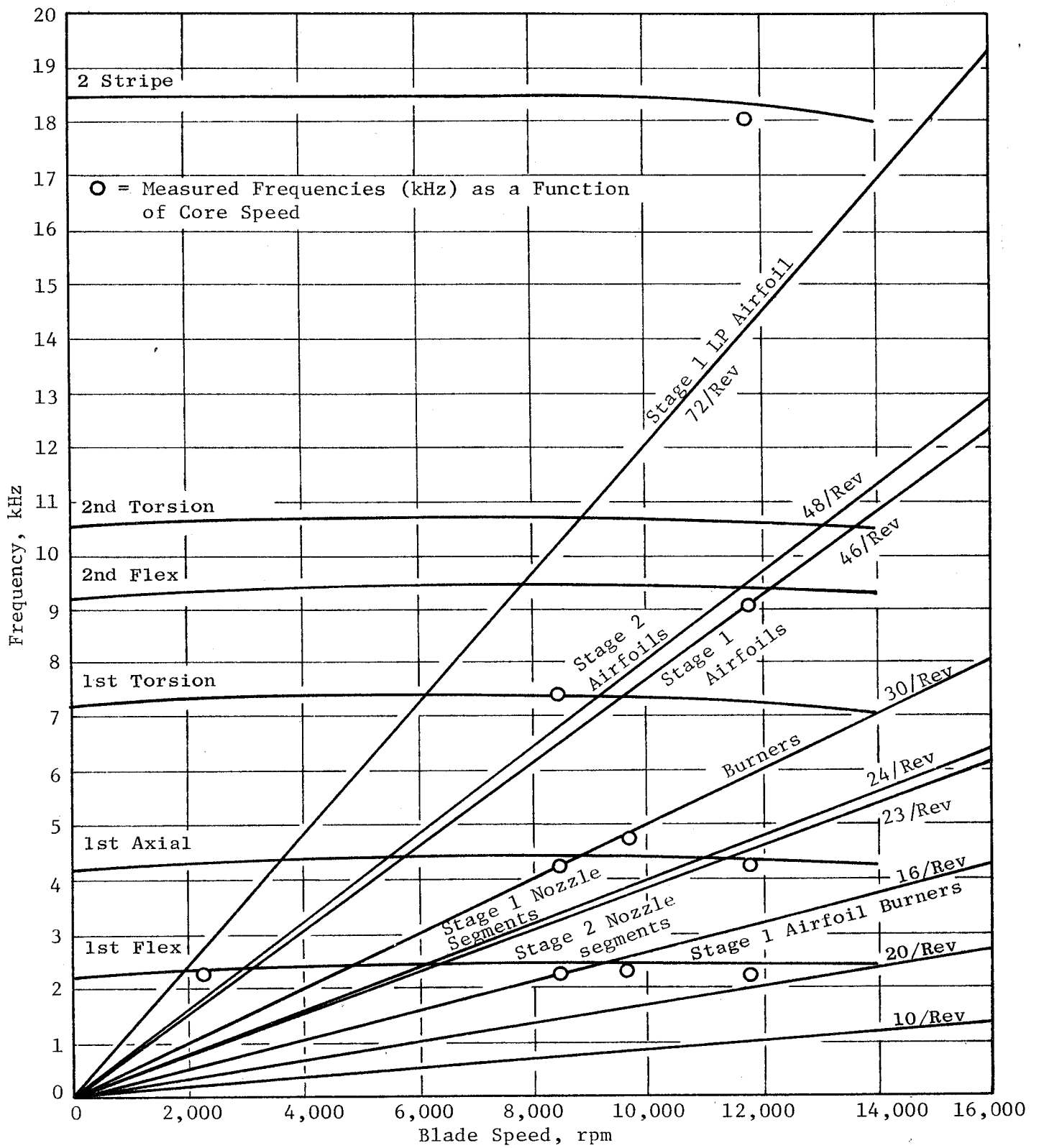


Figure 176. HP Turbine Stage 1 Blade Campbell Diagram.

The vibratory stress evaluation for the Stage 2 blade in the core engine followed the procedures described for the Stage 1 blade. The results are given below.

The life limiting location on the Stage 2 blade was at the 10% span, convex side, just aft of the high "C" point (maximum distance from chord line).

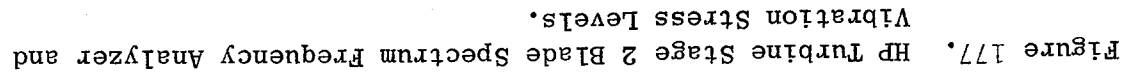
The ratio of strain at the life limiting point to strain at the gage location was determined by tests for the three primary modes. The values are given in Table XXVII.

Table XXVII. HP Turbine Stage 2 Blade Factors for Projecting Maximum Stress at Life Limiting Location.

	<u>1st Flex</u>	<u>1st Axial</u>	<u>1st Torsion</u>
Strain Ratio Due to Primary Modes	1.32	0.644	0.514
Strain Ratio Due to Higher Modes	1.05	1.050	1.050
Modulus Ratio	1.03	1.030	1.030
<u>Max Probable Stress</u> <u>Max Observed Stress</u>	1.26	1.260	1.260
Stress Derate Factor	<u>1.20</u>	<u>1.200</u>	<u>1.200</u>
Total Multiplying Factor Applied to Measured Stress	2.16	1.050	0.840

The strain ratio for the higher modes was also determined. The spectral characteristics are shown in Figure 177. Note that the stress at the first flex frequency accounted for approximately 90% to 95% of the total stress. For the Stage 2 blade, the strain ratio due to higher modes was 1.05.

Hot high cycle fatigue tests of blades produced failures at the leading edge root region. The ratio of stress for test blades at the root to that for a smooth bar was lower by a factor of 1.4. For all other locations, or where



**ORIGINAL PAGE IS
OF POOR QUALITY**

no failures occurred, a 1.2 factor was used. The 1.2 factor applies to the life limiting location and was used as the stress derate factor.

The stress factors for the Stage 2 blade are presented in Table XXVII. Vibratory stress at the life limiting location is determined by establishing recorded stresses for the primary modes from spectrum analysis and then applying the factors from Table XXVII as follows:

$$\begin{array}{lll} \sigma & \text{Total at} & = 2.16 \sigma \text{ Recorded, 1st flexural} \\ & \text{Limiting} & +1.05 \sigma \text{ Recorded, 1st flexural} \\ & \text{Point for} & +0.84 \sigma \text{ Recorded, 1st torsional} \\ & \text{Blade 2} & \end{array}$$

Determination of the recorded stress values was based on the spectograph plots in Figures 178 through 182. These plots show the level of stress for the first three primary vibrational modes plotted as a function of speed. The maximum total stress occurred when engine speed was approximately 12,120 rpm. Note that peak stresses occurring at each blade natural frequency did not necessarily occur at the same speed. Especially noteworthy was the considerable amount of change occurring between 12,000 and 12,300 rpm. The maximum contributing factor to the total stress was the stress of the first flexural mode being excited by a 6/rev stimulus.

The measured Stage 2 blade stresses for the three primary modes are given in Table XXVIII. The maximum probable vibratory stress at the life limiting location was calculated in the table to be 72 MPa (10.4 ksi), single amplitude.

The maximum allowable vibratory stress for the Stage 2 blade in the FPS engine is 162.0 MPa (23.5 ksi), single amplitude, at the life limiting location. Using a 1.04 multiplier to account for higher turbofan pressure, blade stress expressed as a percent of allowable stress in a turbofan engine was:

$$\text{Percent Allowable Stress}_{\text{FPS}} = \frac{72 \text{ MPa} \times 1.04}{162 \text{ MPa}} \times 100\% = 46.0\%$$

This level is acceptable.

The allowable stress in the core engine was higher. The operating stress as a percent of allowable stress for core operation was 23%.

ORIGINAL PAGE IS
OF POOR QUALITY

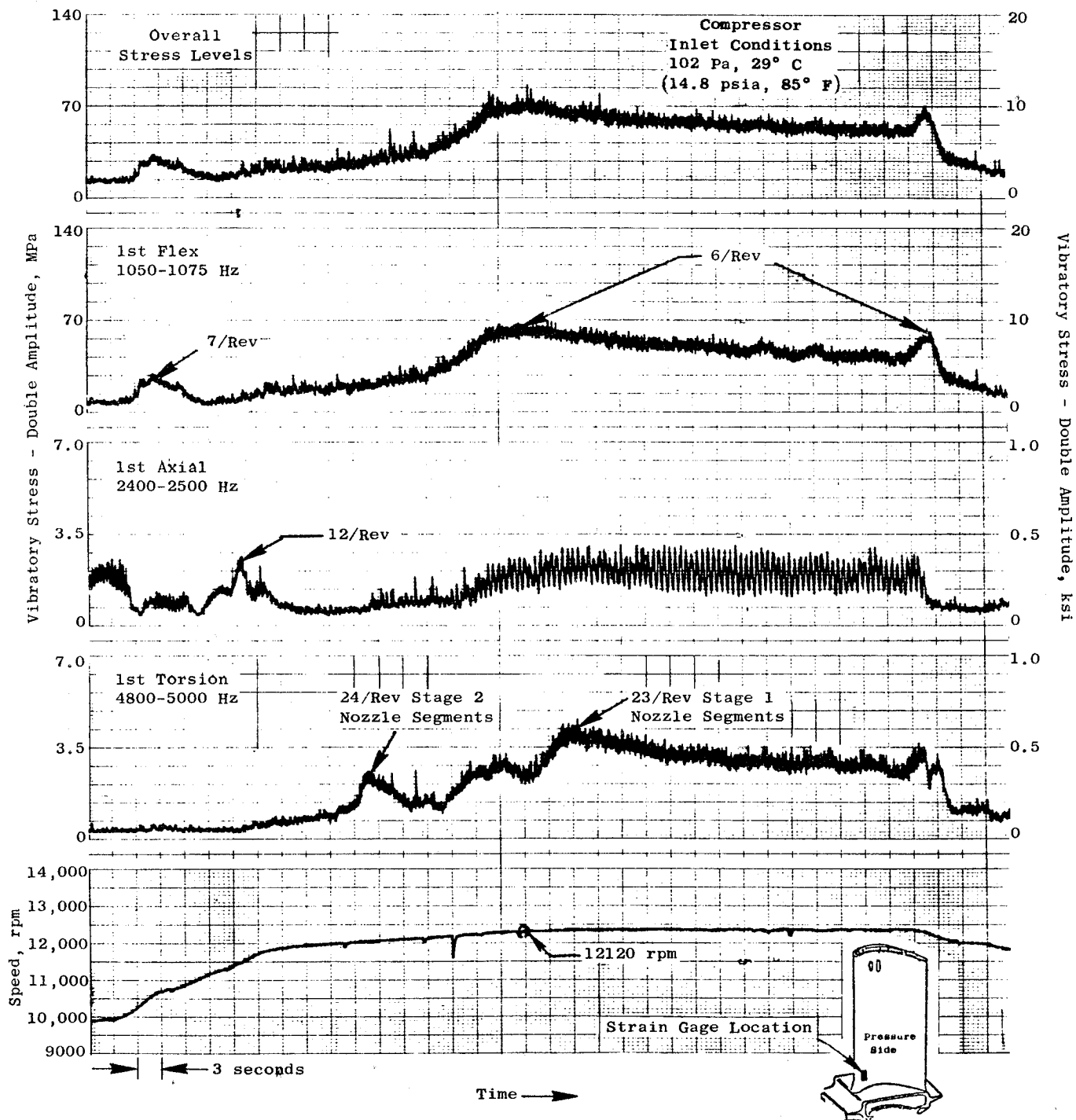


Figure 178. HP Turbine Stage 2 Blade Vibratory Stress Characteristics (Accel from Idle to 12,350 rpm).

ORIGINAL PAGE IS
OF POOR QUALITY

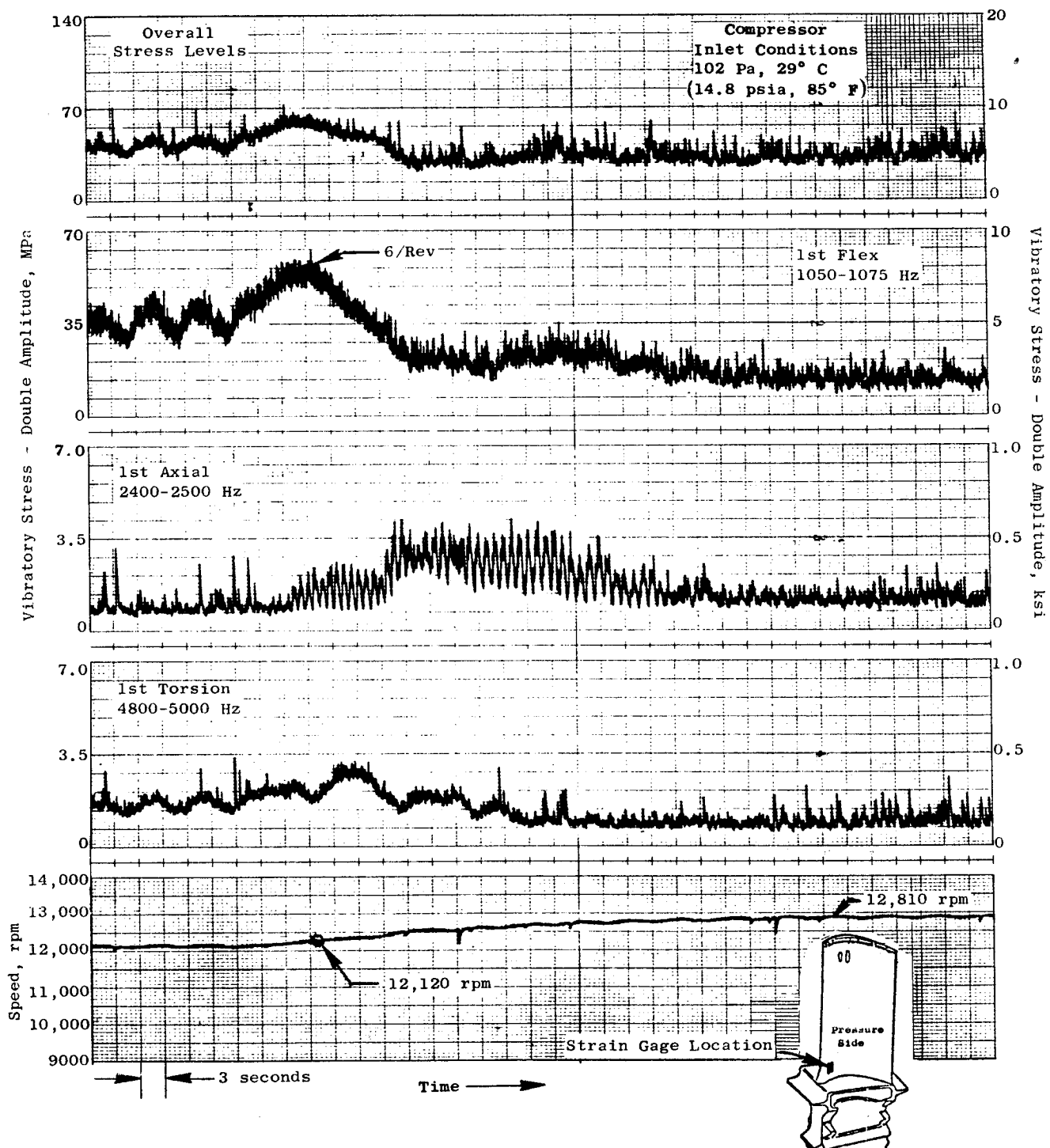


Figure 179. HP Turbine Stage 2 Blade Vibratory Stress Characteristics (Accel from 12,050 to 12,810 rpm).

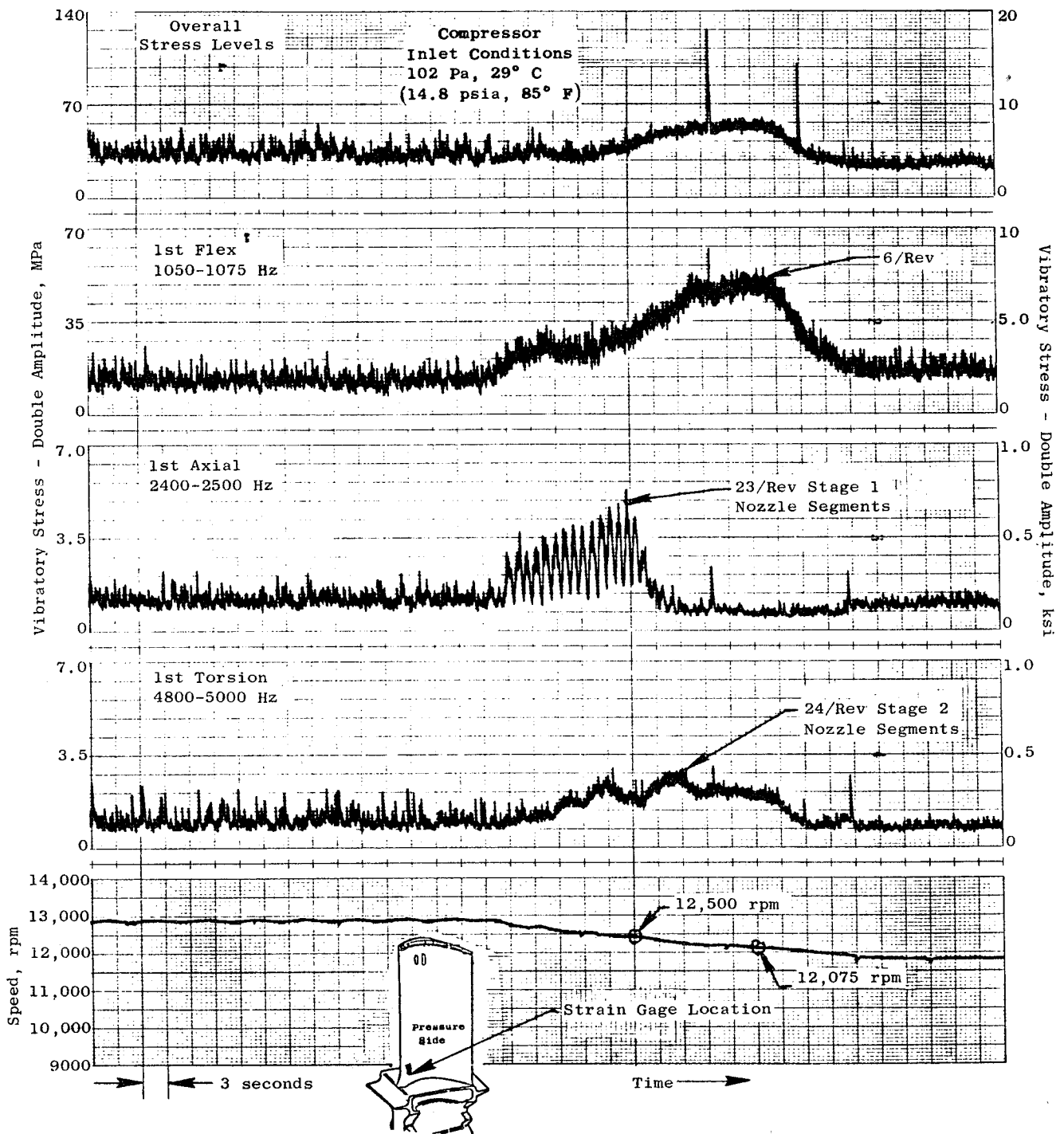


Figure 180. HP Turbine Stage 2 Blade Vibratory Stress Characteristics (Decel from 12,810 to 11,800 rpm).

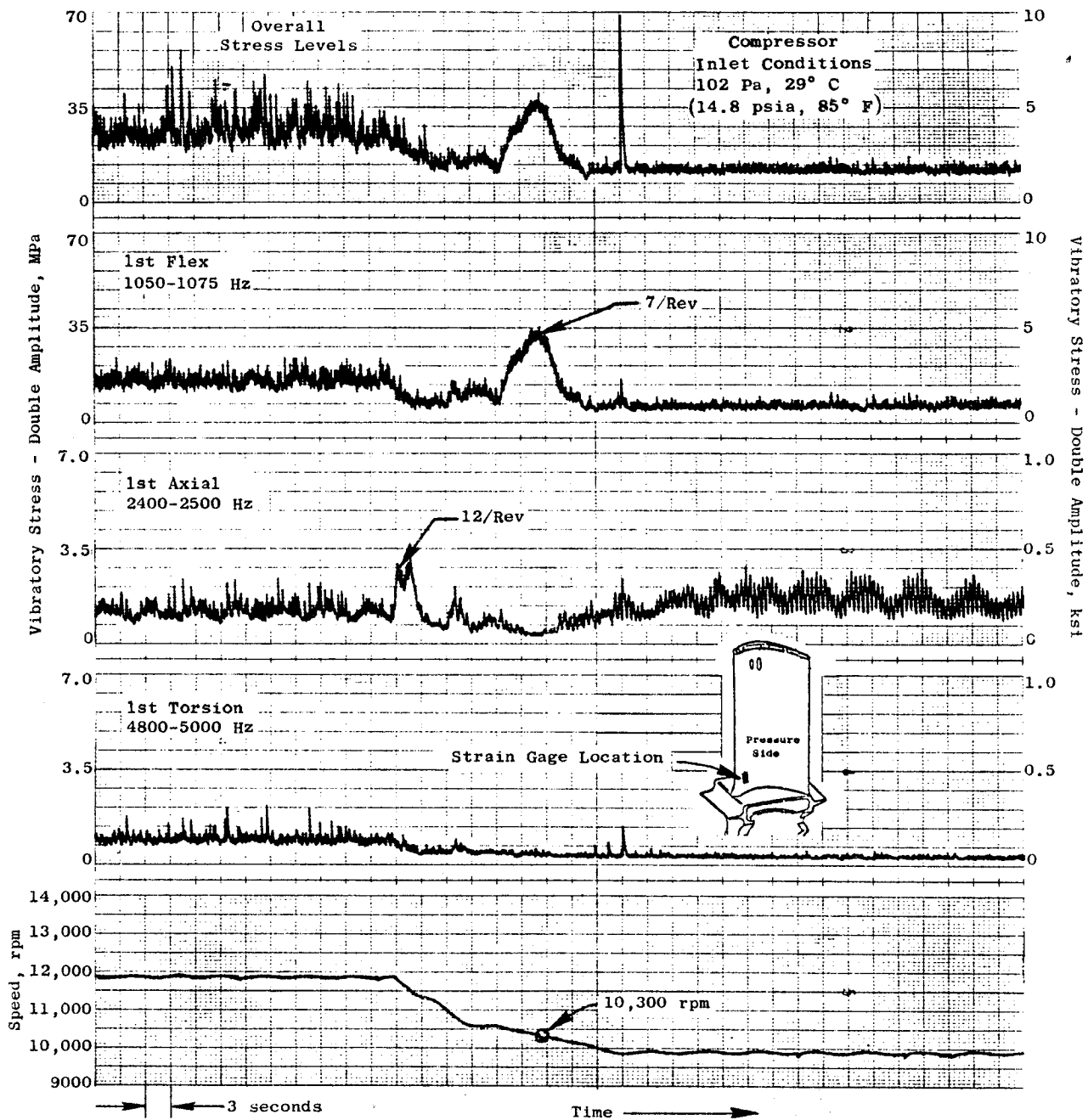


Figure 181. HP Turbine Stage 2 Blade Vibratory Stress Characteristics (Decel from 11,800 to 9850 rpm).

ORIGINAL PAGE IS
OF POOR QUALITY

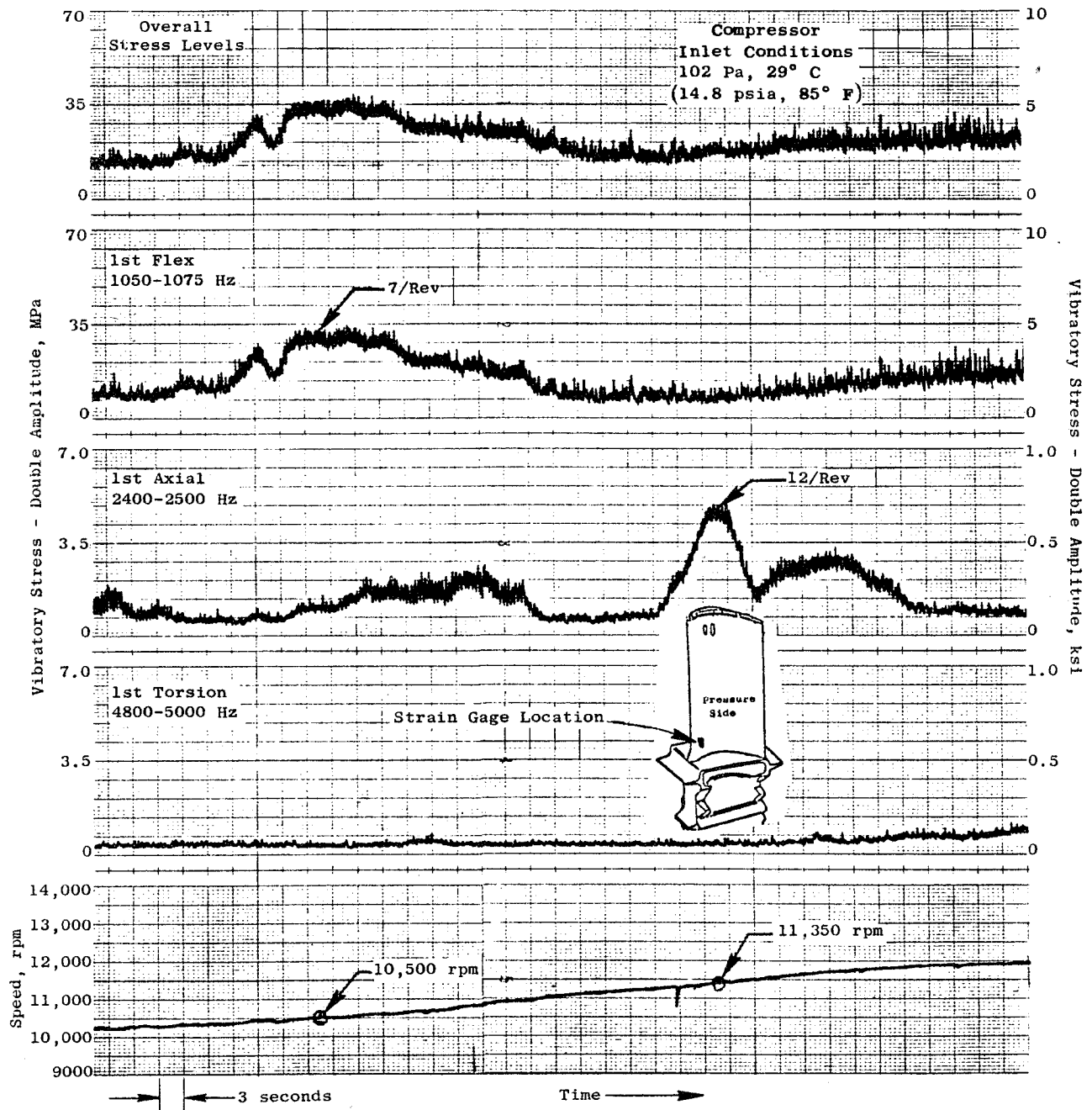


Figure 182. HP Turbine Stage 2 Blade Vibratory Stress Characteristics (Accel from 10,300 to 12,000 rpm).

Table XXVIII. HP Turbine Stage 2 Blade.

Maximum Projected Stress Based on Maximum Recorded Stress

<u>Blade Frequency Characteristic</u>	<u>Most Active Stress Measurement MPa (ksi) Single Amplitude</u>	<u>Stress Factor (Reference Table XXIV)</u>	<u>Projected Maximum Probable Stress at Bladed Limiting Location MPa (ksi) Single Amplitude</u>
1st Flexural	32.10 (4.65)	2.16	69.30 (10.00)
1st Axial	1.38 (0.20)	1.05	1.45 (0.21)
1st Torsional	1.38 (0.20)	0.84	<u>1.16 (0.17)</u>
		Total	72.00 (10.40)

In a manner similar to Stage 1, the higher pressure level was demonstrated in the core engine by using a pressurized compressor inlet of 147.0 kPa (21.3 psia) versus the normal test pressure, 102.0 kPa (14.8 psia). Figure 183 shows the blade stress characteristics versus 12,100 rpm speed for this higher inlet pressure which, like Stage 1, did not reach the levels attained for ambient conditions at higher speed.

The Goodman diagram of Figure 184 determines the percent of allowable stress level for an FPS engine. Also shown is the percent of allowable stress for the core engine environment.

Figure 185 shows the Stage 2 blade Campbell diagram with the stress amplitudes at the various blade frequencies and at different speed conditions. Note that the first flex frequency mode was excited by a 6/rev at approximately 12,250 rpm. Figure 186 shows the predicted Campbell diagram with the corresponding measured frequencies plotted for the various engine core speeds. Overall, the measured frequencies for all primary modes closely follow the predicted frequencies.

Blade Temperature

Temperature measurements recorded for Stage 1 and 2 blades were obtained by using thermocouples embedded at the 25% and 50% airfoil spans.

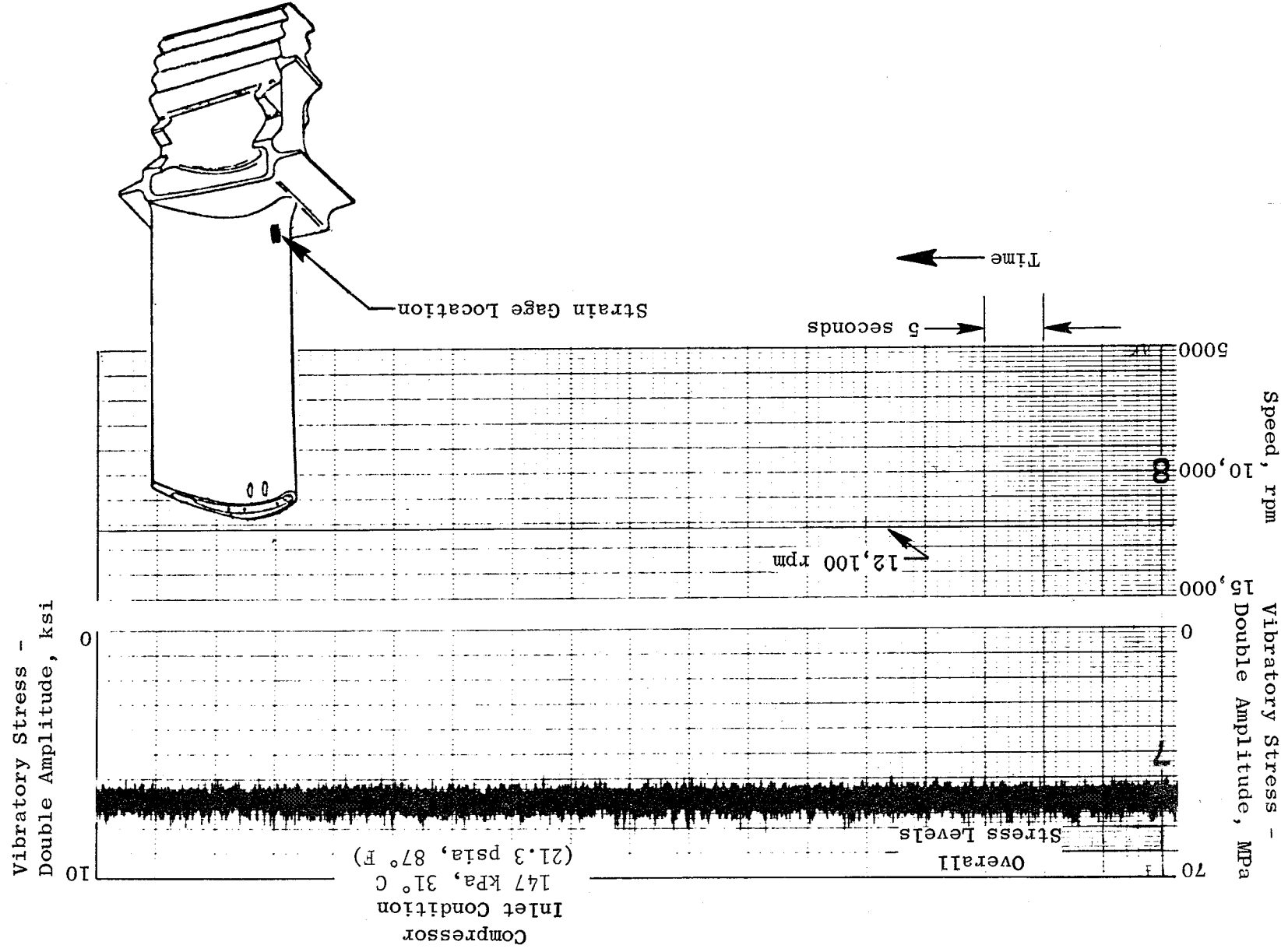


Figure 183. HP Turbine Stage 2 Blade Vibratory Characteristics at Maximum Compressor Discharge Pressure.

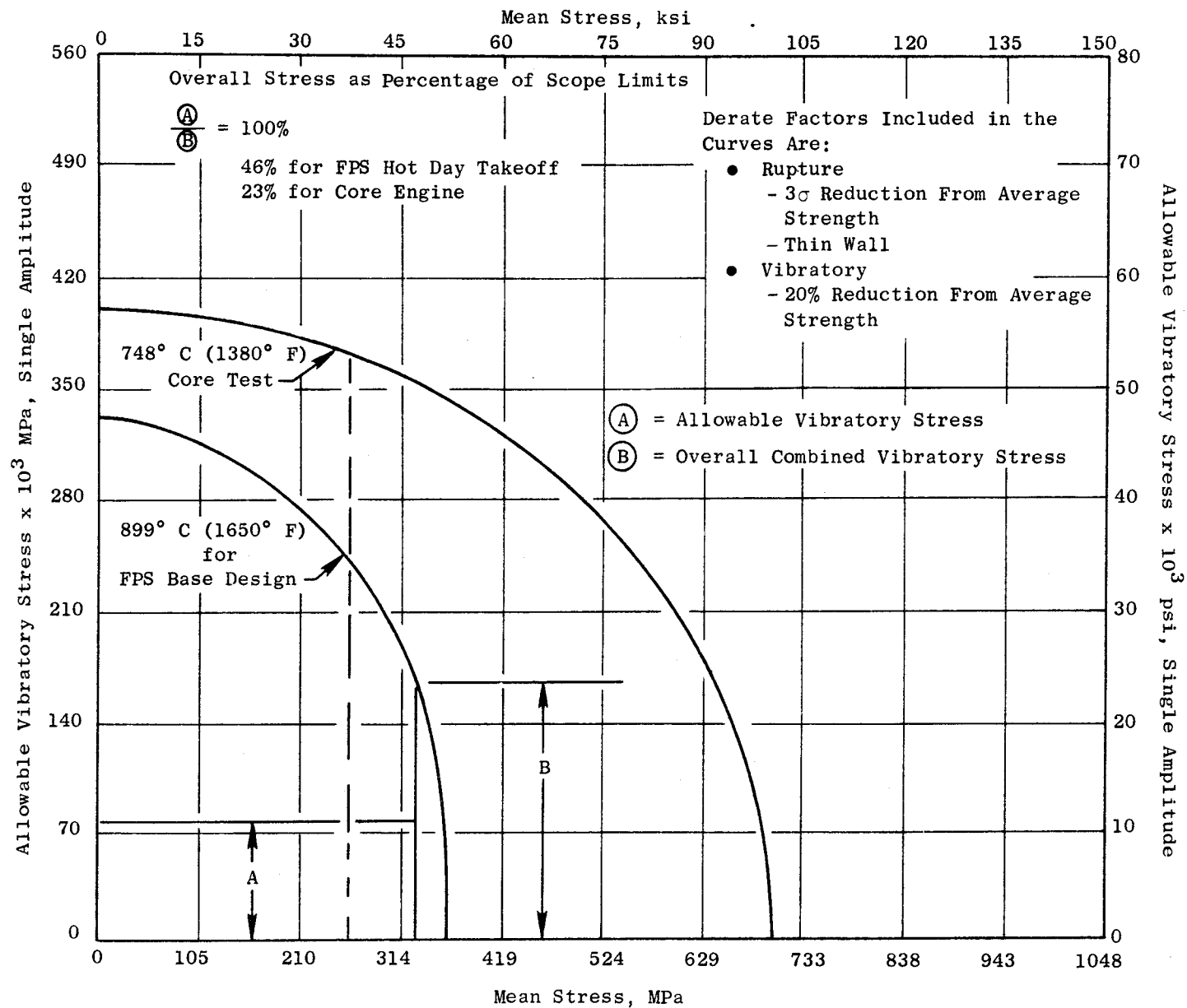


Figure 184. HP Turbine Stage 2 Blade 100-Hour Goodman Diagram.

ORIGINAL PAGE IS
OF POOR QUALITY

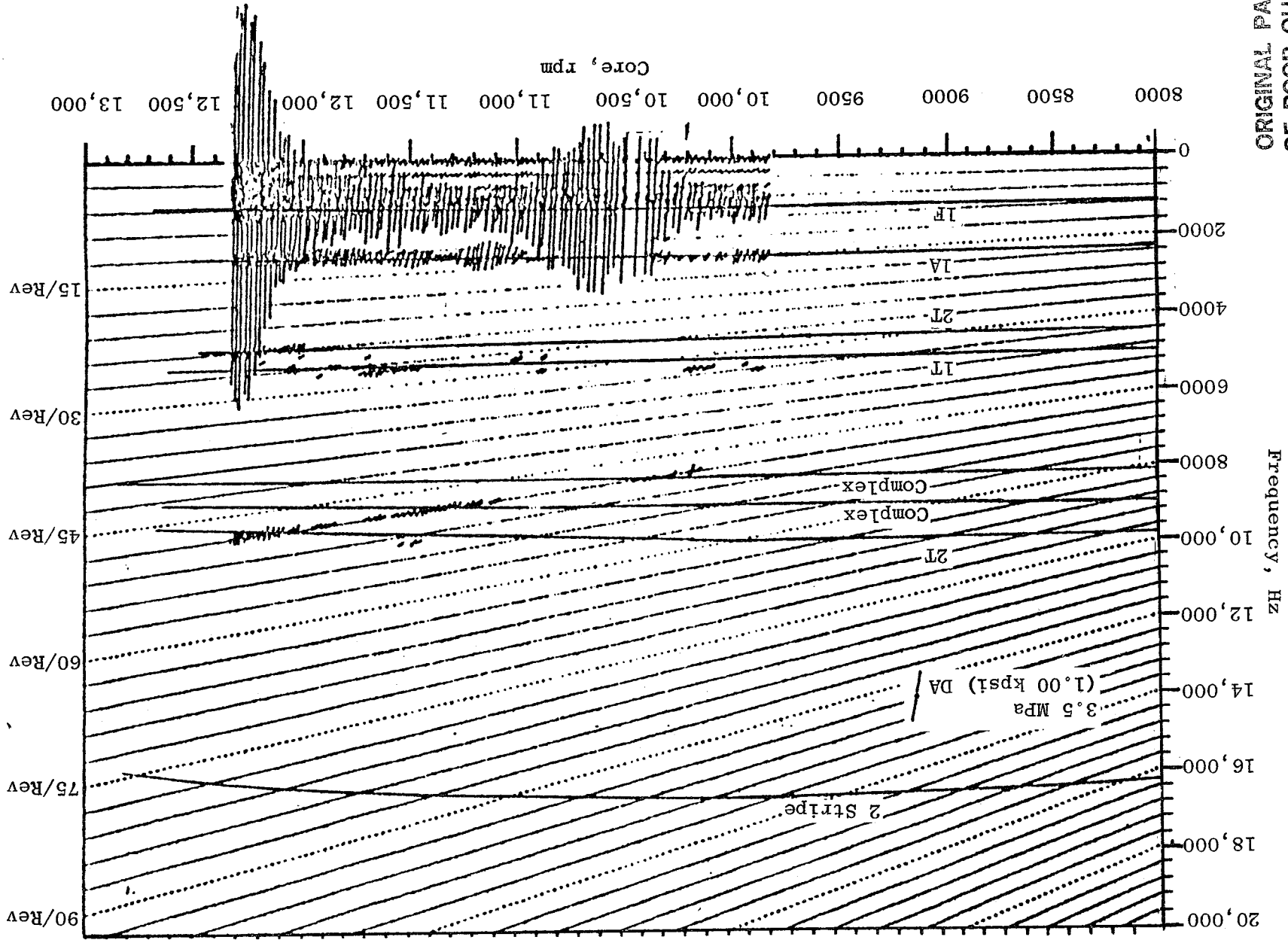


Figure 185. HP Turbine Stage 2 Blade Campbell Diagram Showing Measured Vibratory Stresses.

ORIGINAL PAGE IS
OF POOR QUALITY

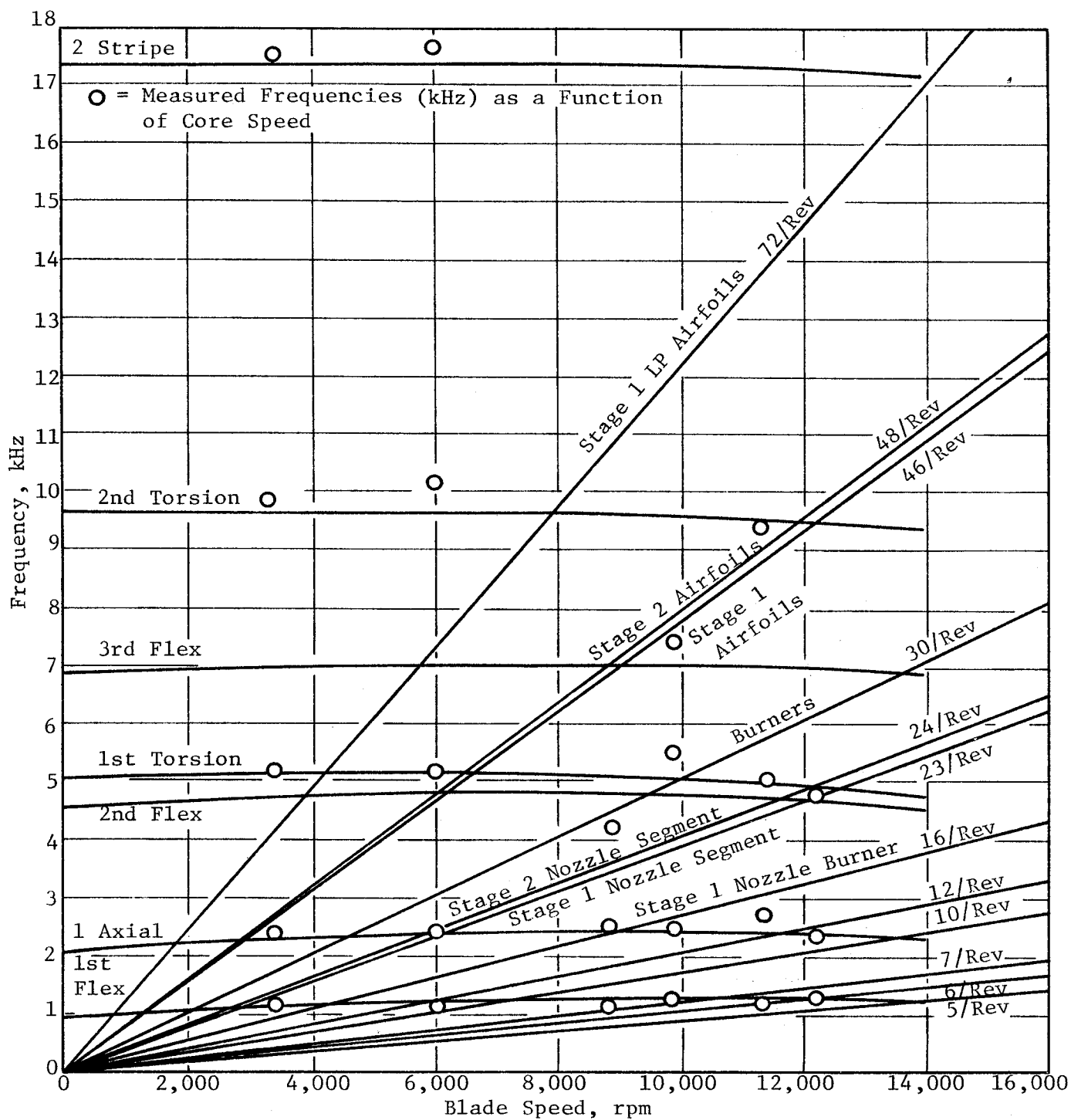


Figure 186. HP Turbine Stage 2 Blade Campbell Diagram.

Thermocouple losses during the first quarter of the test were extremely high with only three of the nine sensors remaining in operation for the Stage 1 blade and only four of the eight on Stage 2. The high percentage losses therefore limited the available information, which would have been useful in correlating test data with the predicted temperatures for engine high speed conditions. Some useful information was gained for blade locations where the thermocouples were still operable.

Figures 187 through 190 show Stage 1 and 2 blades measured temperatures plotted against T4.1 at 25% and 50% span. Figures 191 and 192 summarize the measured blade temperature data extrapolated to the FPS engine, heat transfer design cycle point (hot day takeoff). The scaling procedure assumed that the local blade cooling effectiveness remains constant, based on compressor and combustor discharge cycle temperatures.

For the most part, the scaled-up temperatures were significantly lower than the predicted levels. The leading edge temperature for the Stage 1 blade was 32° C (58° F) lower, primarily due to a 33° C (60° F) lower pitch-line gas temperature relative to design value. This lower gas temperature would result in an approximate 17° C (30° F) reduction in metal temperature.

The primary reason for the significantly lower temperatures on the pressure side for both blade stages is due to the improved pressure-side velocity distribution. At the time that E³ blades were being designed, heat transfer factors were based on the experience of GE commercial engines. However, recent analyses performed on new aero designs, similar to the E³ aero, indicate that significant reductions in gas-side heat transfer coefficients can be obtained for the pressure side.

Cascade tests and air turbine tests would be needed to confirm the level of improvements associated with the reduced gas-side heat transfer coefficients. This type of test would include the effects of film injection for downstream cooling.

The only suction-side temperature to yield any meaningful data was recorded on the Stage 1 blade. This temperature showed significantly lower value when compared to design predictions. Part of the difference was a

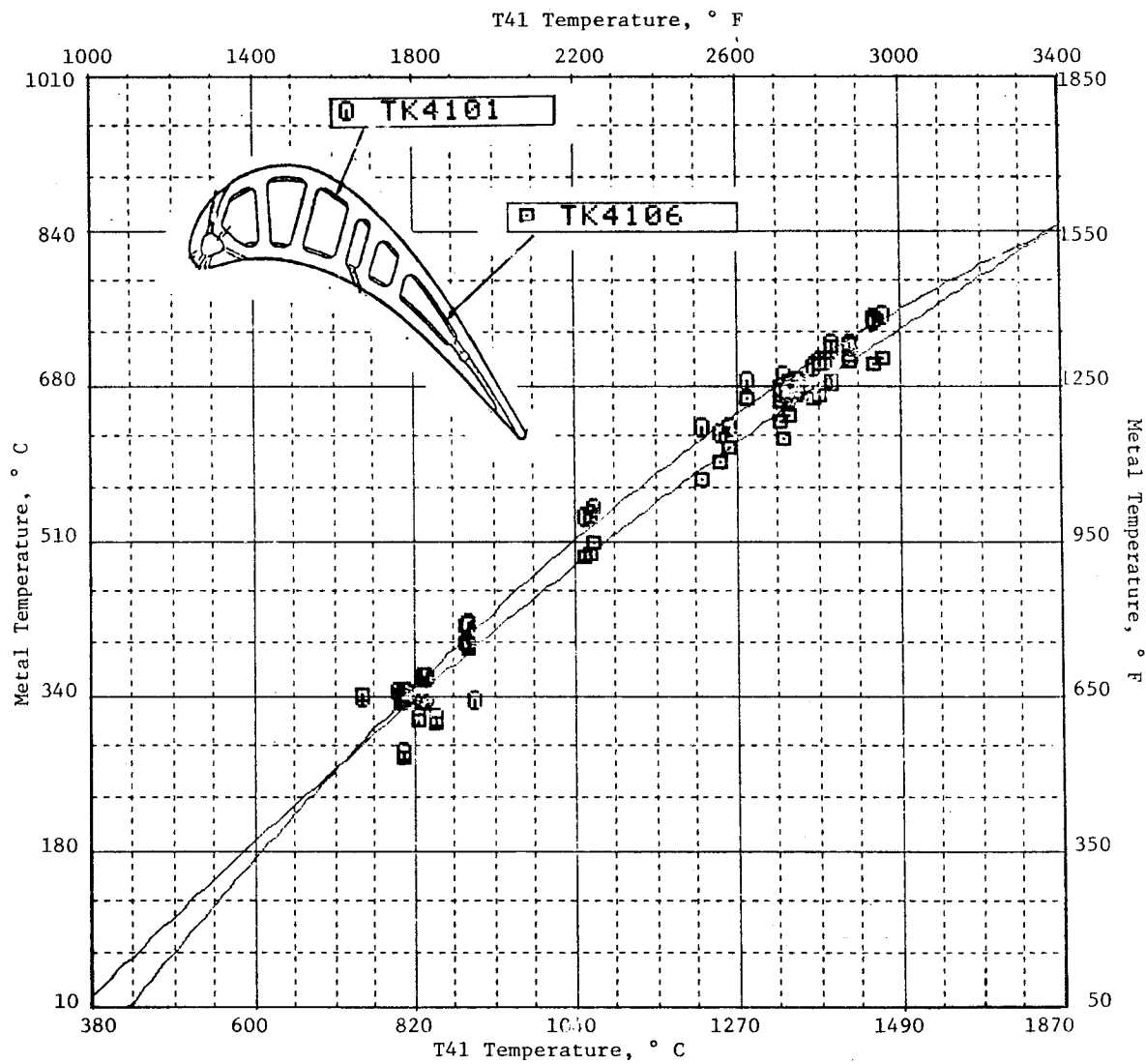


Figure 187. HP Turbine Stage 1 Blade Airfoil Temperatures - 25% Span.

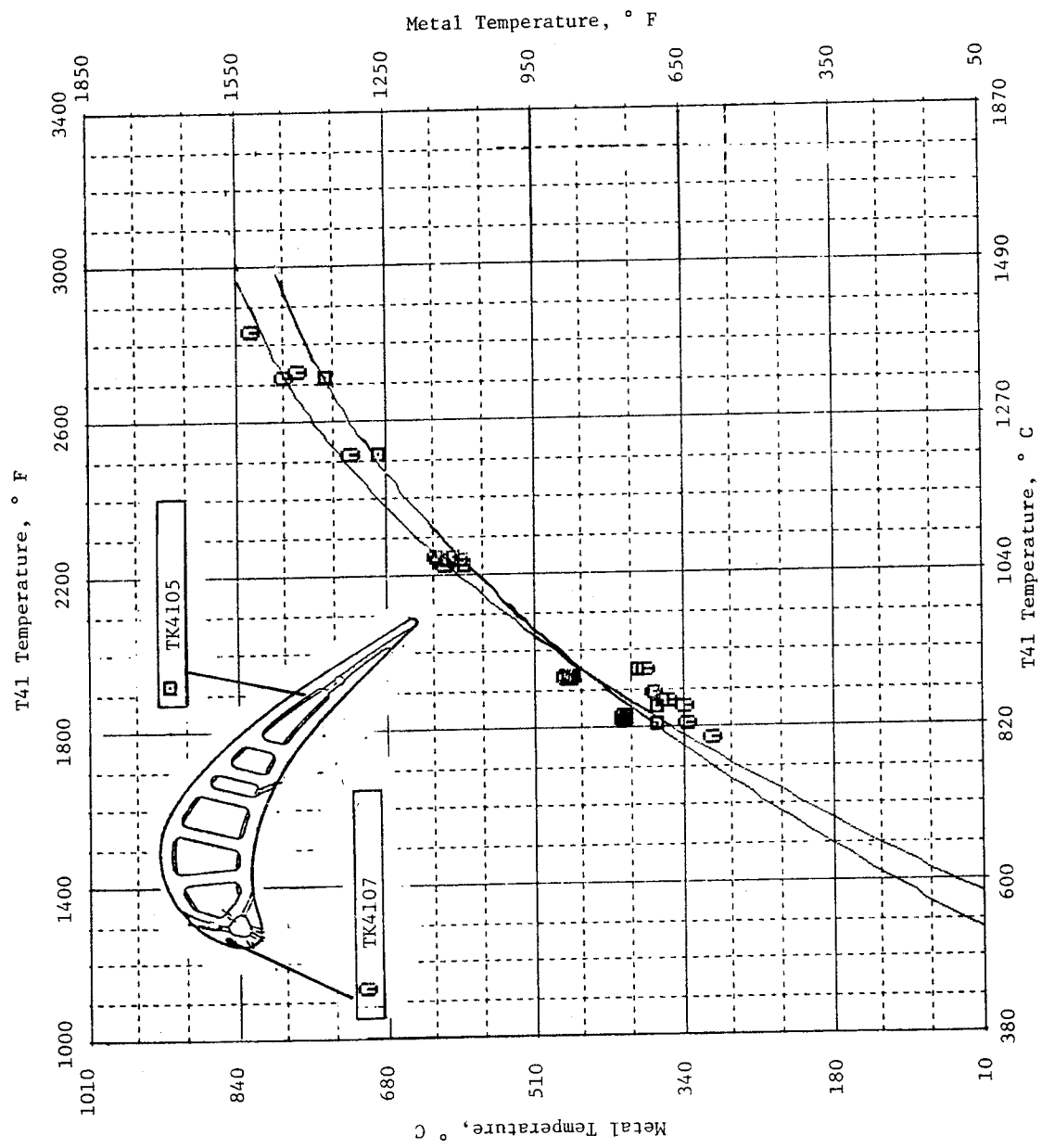


Figure 188. HP Turbine Stage 1 Blade Airfoil Temperatures - 50% Span.

ORIGINAL PAGE IS
OF POOR QUALITY

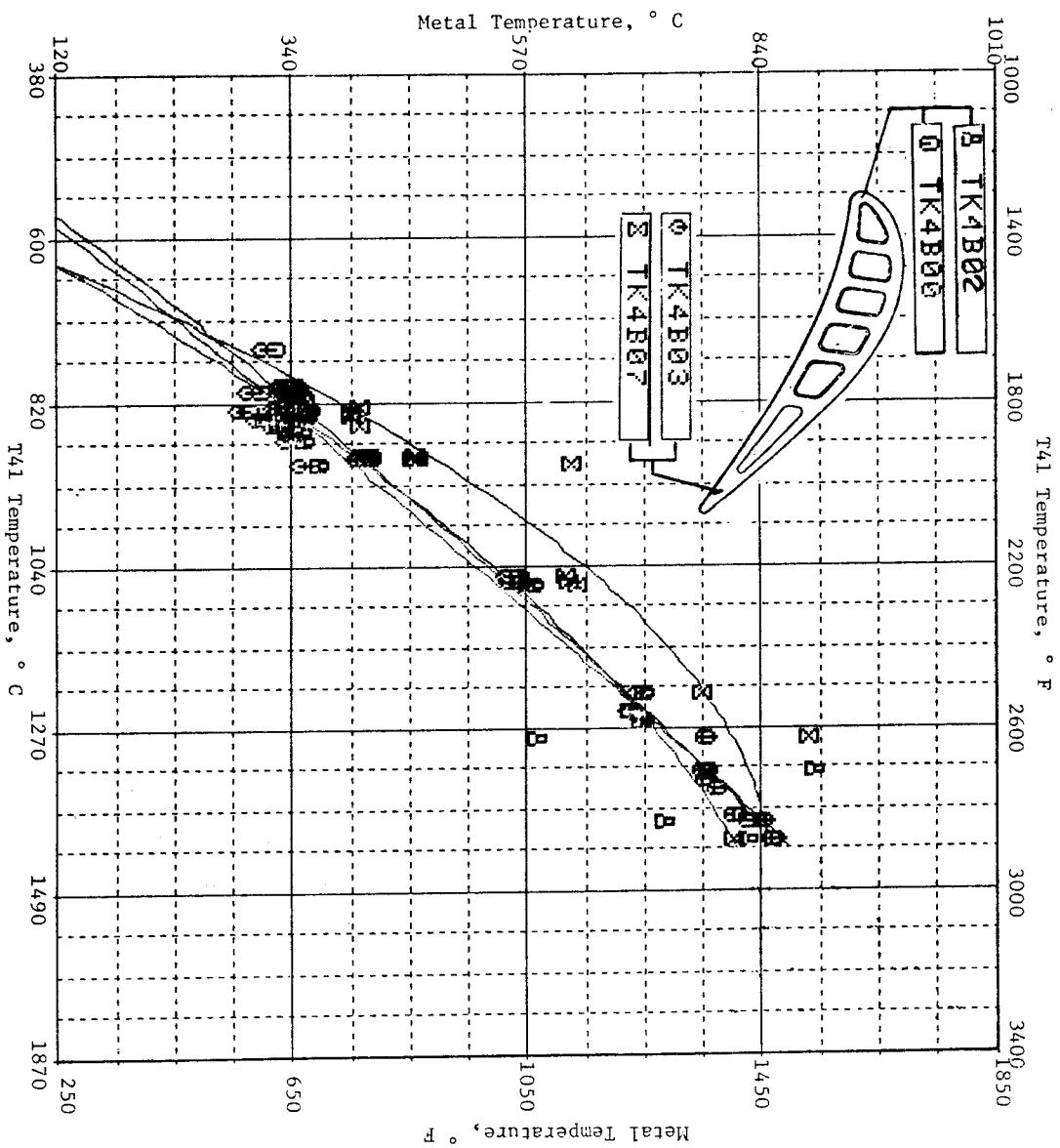


Figure 189. HP Turbine Stage 2 Blade Airfoil Temperatures - 25% Span.

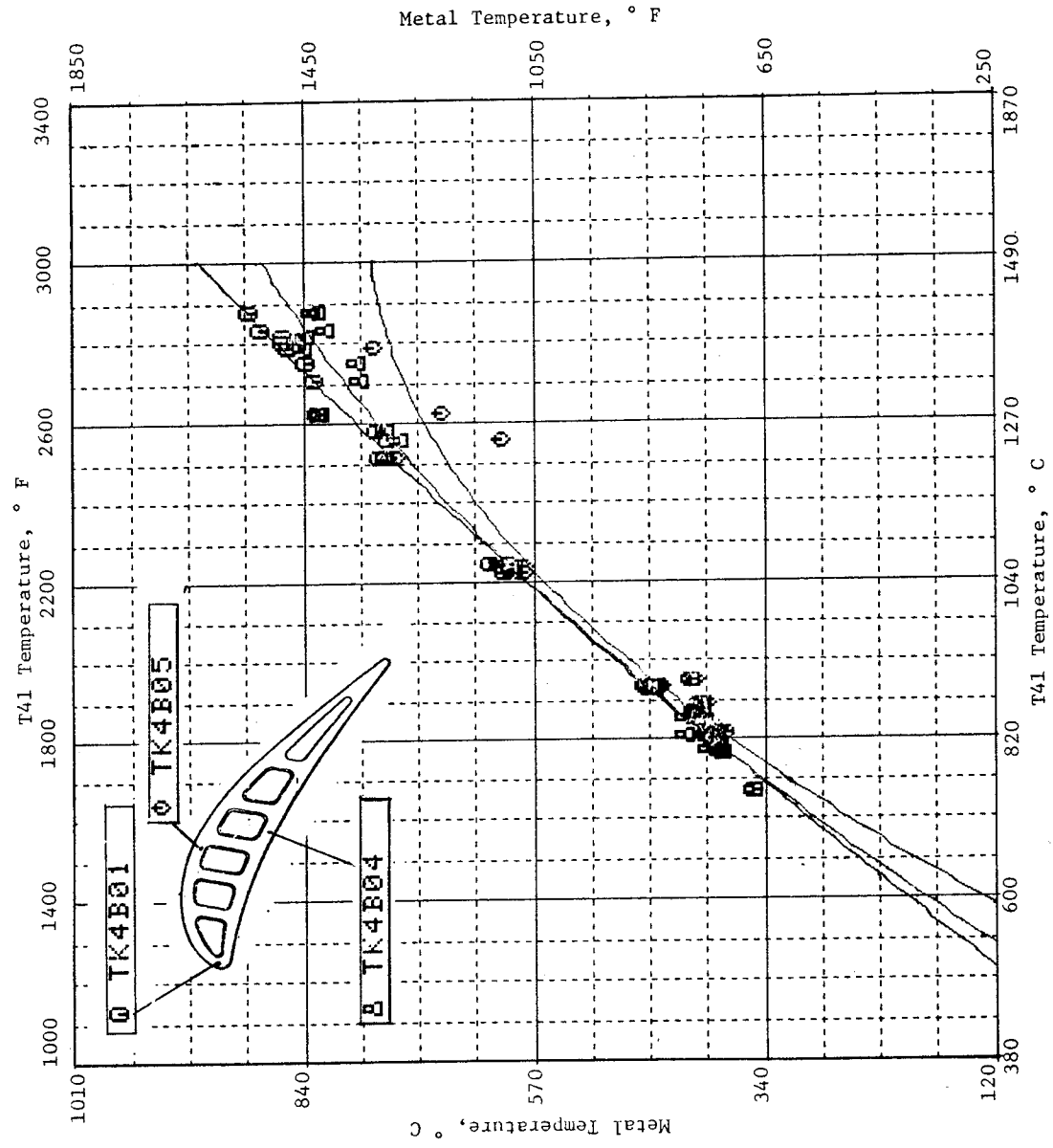
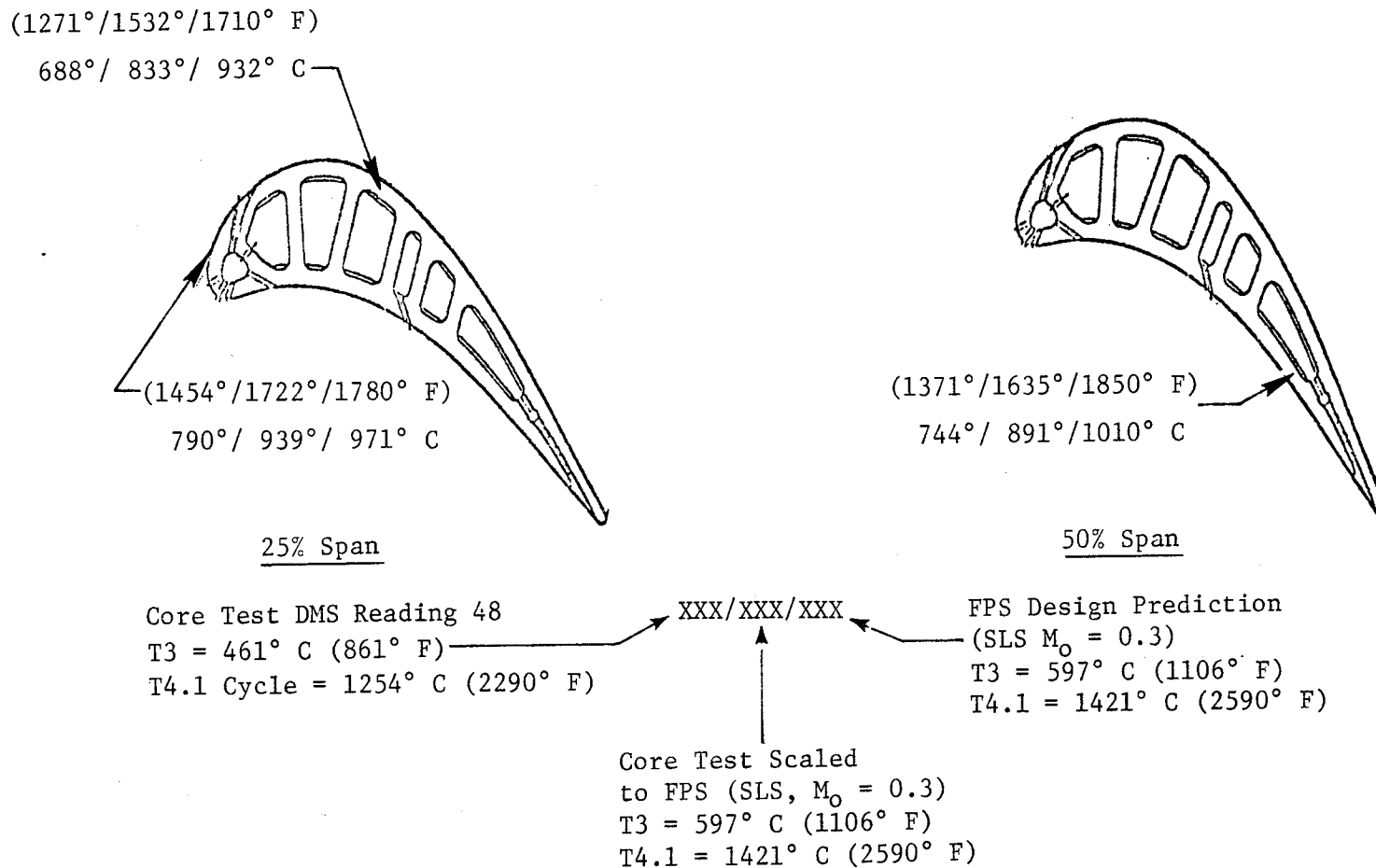


Figure 190. HP Turbine Stage 2 Blade Airfoil Temperatures - 50% Span.



The extrapolated values reflect the aero design of a $54\frac{1}{2}\%$ / $47\frac{1}{2}\%$ work split for Stage 1 and 2 blades and Stage 1 Nozzle throat area of 4% (to air turbine test nozzle throat area).

Figure 191. HP Turbine Stage 1 Blade Temperature Summary.

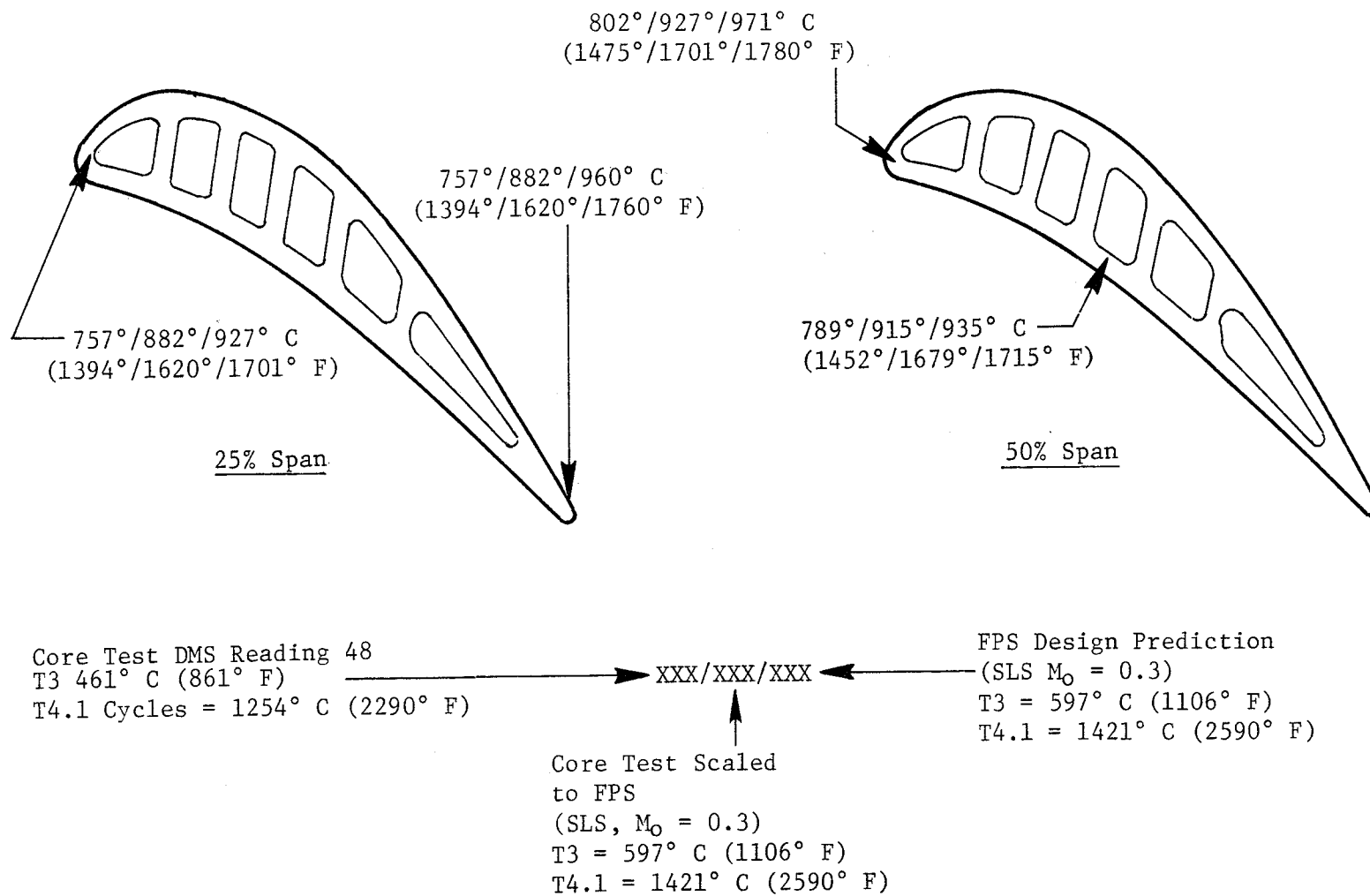


Figure 192. HP Turbine Stage 2 Blade Temperature Summary.

result of the reduced gas temperature. The reason for the balance of the larger difference is presently unknown. Some indications from cut-ups show that the dimensions of turbulence promoters are cast to the maximum or possibly slightly greater height dimensions. This would effectively increase the internal cooling heat transfer coefficients.

6.6.3 Rotor Metal Temperatures

Metal temperatures on Stage 1 and 2 disks were within design limits throughout the test. See Figures 157 and 158 for a comparison with expected design values. More detailed temperature measurements are presented in the following discussion. Figure 193 shows the metal temperatures of the Stage 1 seal disk. The temperature of the web closely tracked T3 (cooling air supply) as expected. The indicated temperature on the aft side of the bore was approximately 55° to 65° C (99° to 117° F) cooler than the web due to expansion and radial inflow of the cooling air. The axial thermal gradient across the bore of the disk was about 40° C (72° F) and was due to the cooler temperature of the facility air on the forward side, which was used to purge the rotor bores on the core engine compressor. The ICLS engine uses fan air which is expected to slightly reduce the temperature gradient.

Figures 194 and 195 plot actual test data for bore and web temperatures of the Stage 1 and 2 disks as a function of the percent corrected core speed. Data for DMS Reading 258 is highlighted. This is shown extrapolated to FPS conditions together with FPS predictions for comparison in Figures 139 and 140.

The main influence on the disk metal temperatures was CDP supplied cooling air (T3 at the source). T3, shown for reference in Figures 194 and 195, was reduced approximately 58° C (104° F) by expansion and work extraction (radial inflow) as it reached the bore of the Stage 1 disk. This accounts for the temperature difference between T3 and the disk bores. As expected, the disk web temperatures for both stages tracked T3 at low speeds and increased to a level above T3 at the higher speed points as heat was conducted into the disk from the flowpath. The larger temperature increase seen on the Stage 2 disk web is thought to be due to a reduction in purge air in the aft cavity. (See discussion of Stage 2 blade retainer.)

DMS Readings 234-258

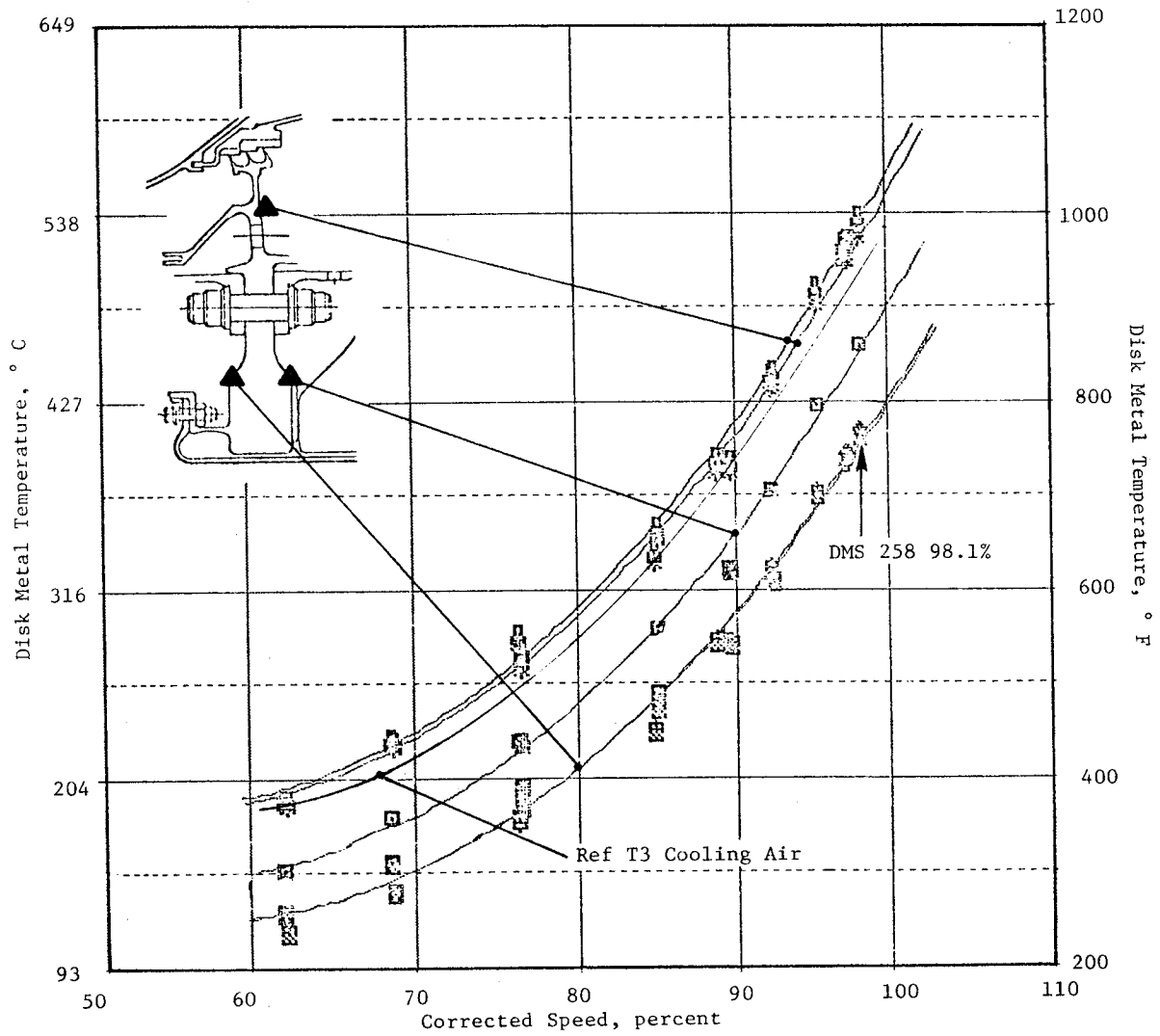


Figure 193. HP Turbine Stage 1 Seal Disk Metal Temperatures.

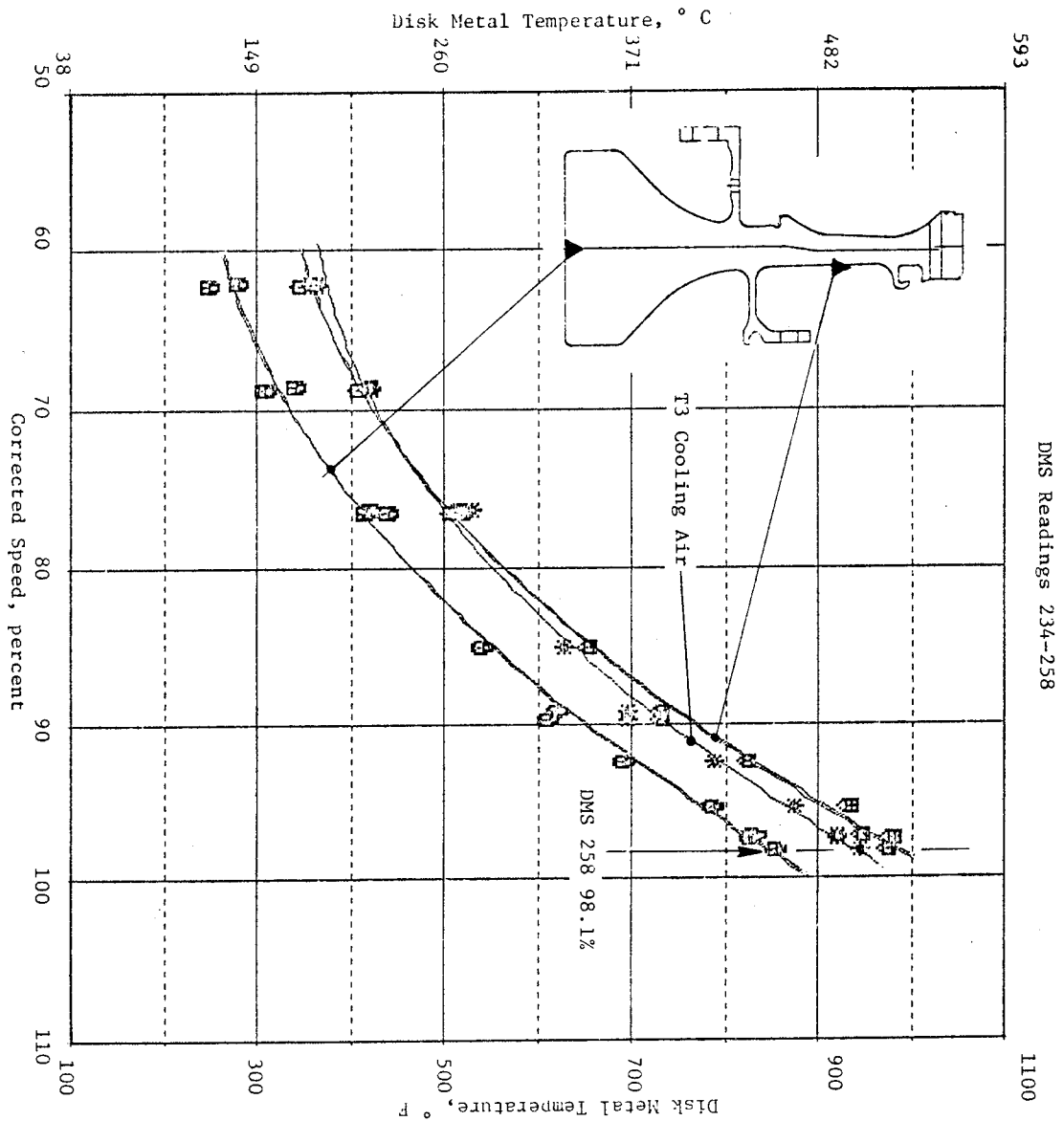


Figure 194. HP Turbine Stage 1 Disk Temperatures.

DMS Readings 210-258

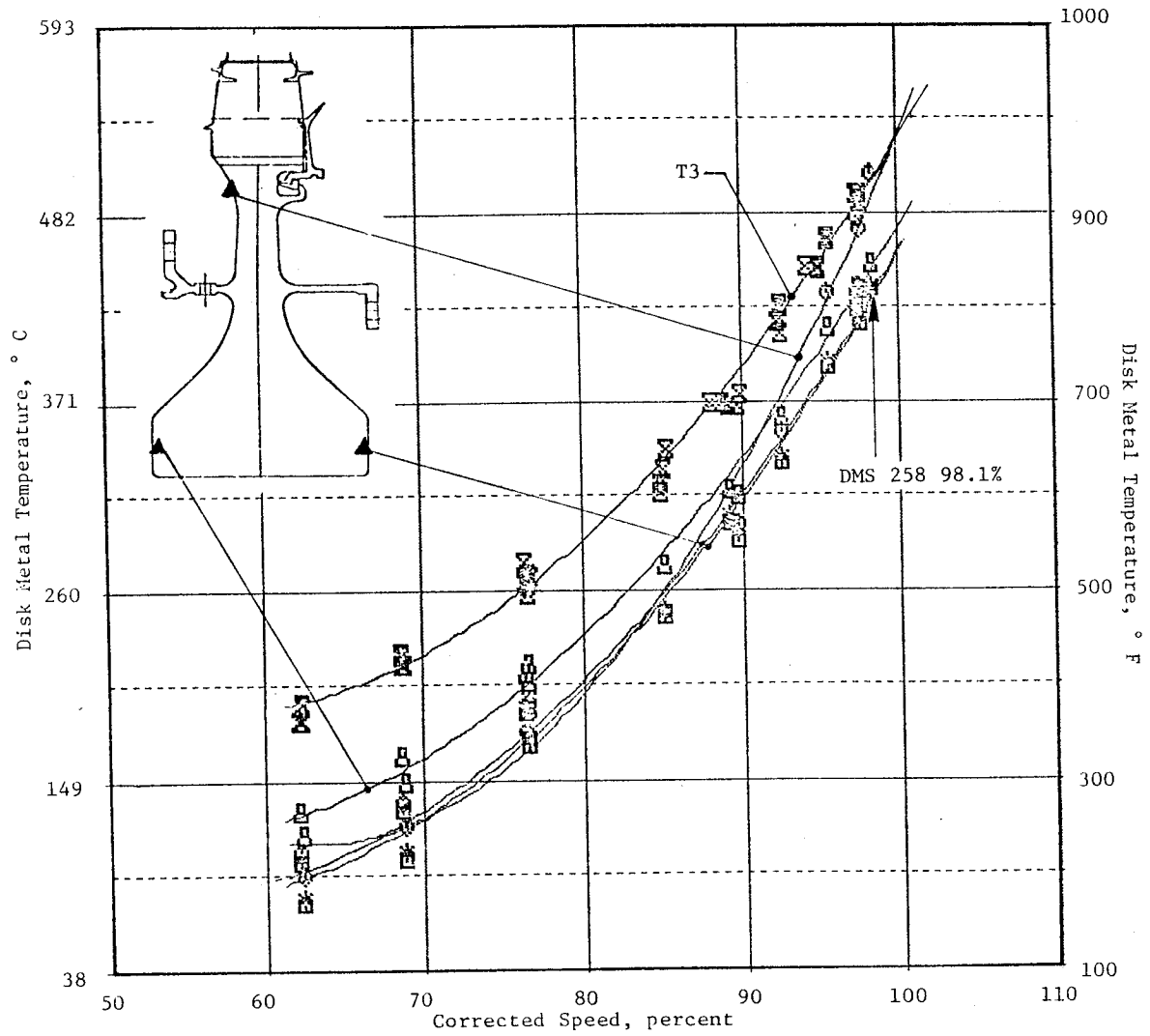


Figure 195. HP Turbine Stage 2 Disk Temperatures.

Stage 1 blade retainer metal temperatures are shown in Figure 196 together with T3 (cooling air supply) for reference. TK4112 and TK4113 increased in temperature with respect to T3 as speed increased, suggesting some limited recirculation of hot gas in the cavity at the retainer tip. However, TK4119, at the retainer root, tracked more closely to T3 temperature (that is, remained more parallel for a speed increase) suggesting that the local ingestion of heat did not progress radially inward past the retainer.

The maximum temperature on the Stage 2 blade retainer was 605° C (1122° F) recorded during DMS Reading 90 (retainer instrumentation was lost following DMS Reading 232 and was not available for the final calibration cycles). Comparison with predicted steady-state temperatures indicates the Stage 2 retainer was running approximately 100° C (180° F) hotter than expected (see Figure 197).

The temperature increase was attributed to two factors: First, the smaller than optimum A8 exhaust nozzle area used during final calibration increased the static gas path pressure downstream of the Stage 2 blade, thereby reducing the cooling airflow out past the retainer. Second, the inadvertent omission of a "W" seal between the Stage 2 shroud and the slave turbine frame outer liner structure (see Figure 198) permitted excessive leakage of the Stage 5 cooling air supply at the outer flowpath, reducing the pressure available to purge the Stage 2 disk aft cavity and cool the disk and retainer. Proper seal installation will result in adequate purge flow for ICLS testing and should result in lower retainer temperatures.

An analysis was performed for the elevated temperature condition which showed that adequate life exists for the planned ICLS testing. The retainer should be replaced following ICLS testing if additional testing is to occur.

6.6.4 Rotor Cooling Air Delivery System

Rotor cooling air delivery is accomplished by an optimized system which provides reduced dovetail cooling air temperatures, reduced seal leakage, desired rotor thrust balance, and maximum performance payoff. The major features of the system include a split diffuser extraction port, an expander,

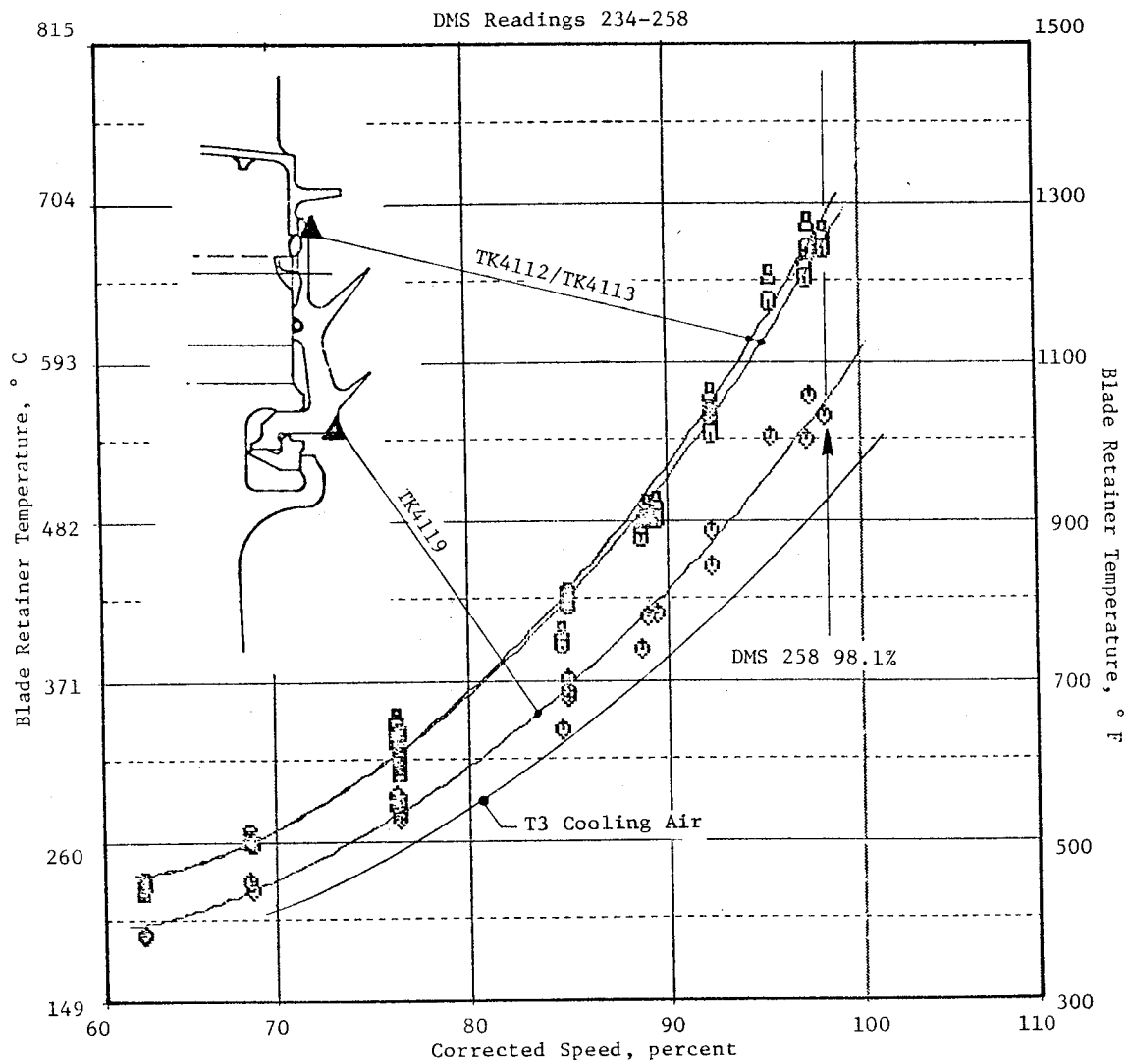


Figure 196. HP Turbine Stage 1 Blade Retainer Temperatures.

DMS Readings 77-115

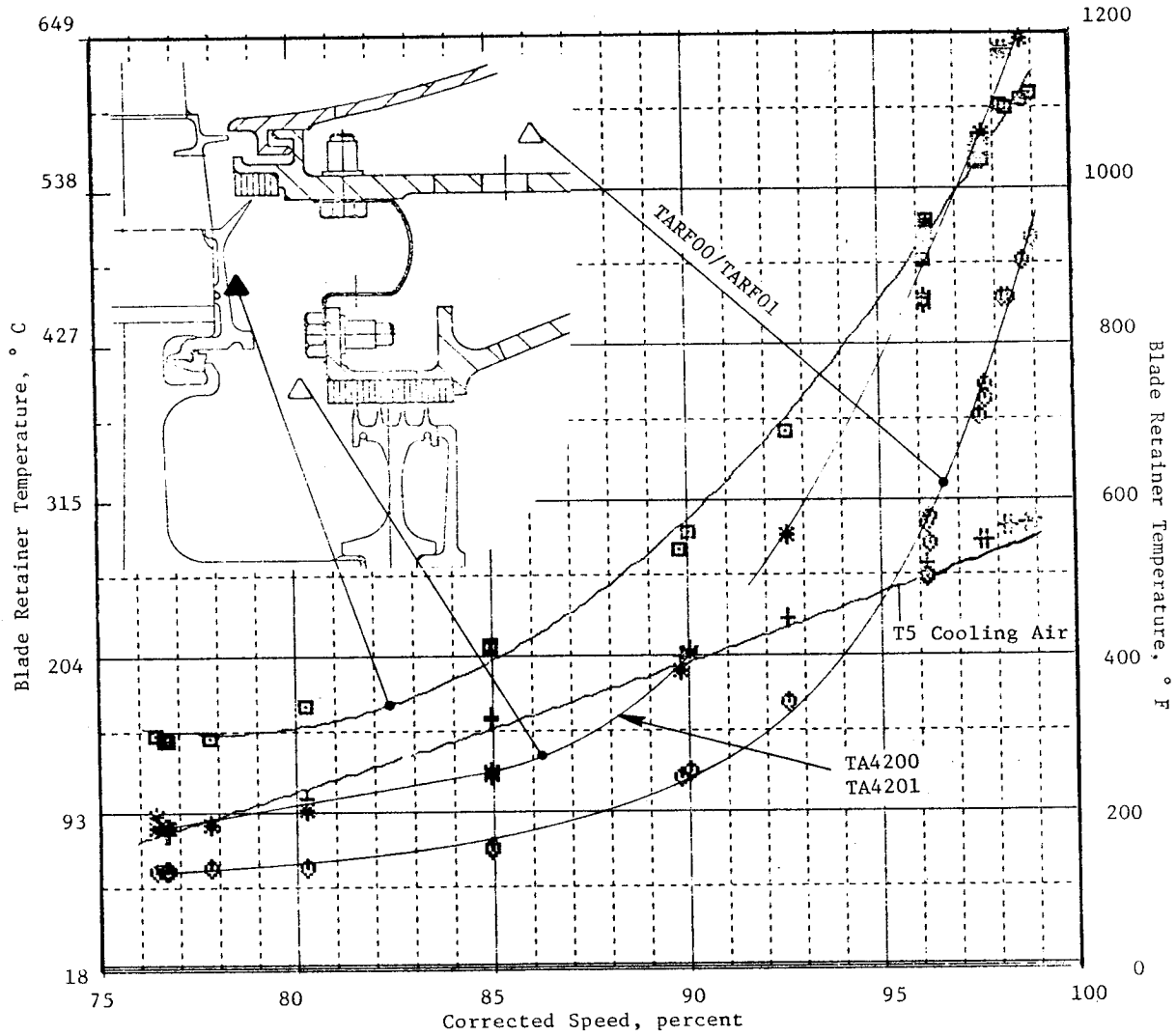


Figure 197. HP Turbine Stage 2 Blade Retainer Temperatures.

ORIGINAL PAGE IS
OF POOR QUALITY

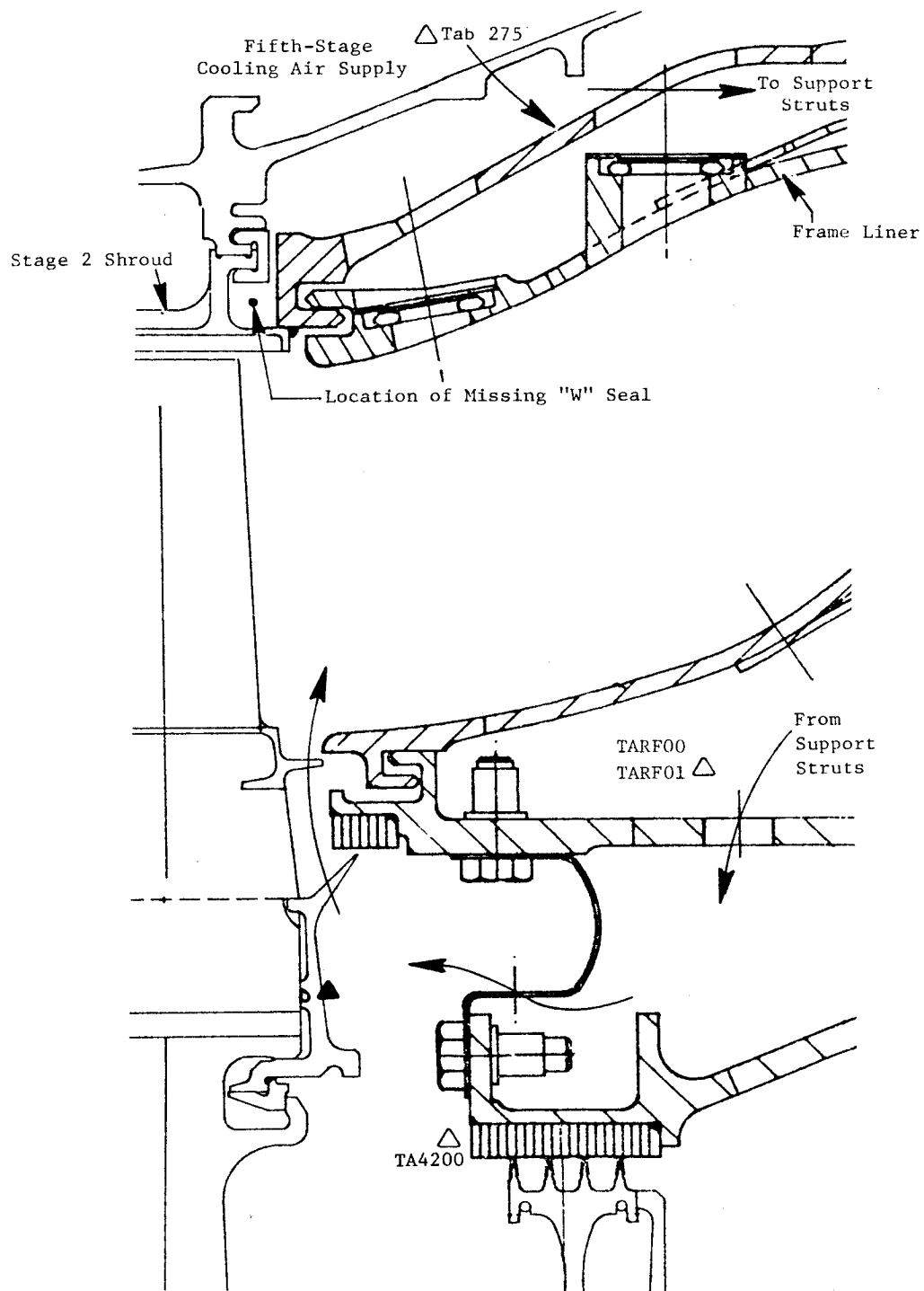


Figure 198. Stage 2 Aft Blade Retainer/Disk Cavity.

and a centrifugal impeller mounted on the forward side of the Stage 1 disk. Figures 155 and 156 show the flows and pressures of the system.

The split diffuser, incorporating pitch-line recovery of rotor cooling air, was expected to reduce the cooling source temperature by about 21° C (38° F) [T3 - 5.5° C (10° F)] for the Mach 0.3 takeoff condition. Compressor discharge is normally extracted from the inner band region which on the E³ would be about 15.5° C (28° F) higher than T3 (average) due to profile temperature variations. Thermocouples in the expander feed cavity indicated an air temperature of 514° C (958° F), or approximately 5.5° C (10° F) higher than T3, while the pitch-line compressor exit thermocouples indicated an average air temperature of 504° C (939° F). It is unlikely that this level of temperature rise would occur in the diffuser struts. Consequently, it is believed that the cavity thermocouples (TA3003 and TA3004), positioned in a region of relatively low convective heat transfer, were affected either by being in physical contact with the structure metal temperature or by conduction in the thermocouple leads. The best indications of rotor air supply temperature were the compressor rake thermocouples which indicated 504° C (939° F), about 5° C (9° F) below T3. This coincides with the expected overall temperature reduction of about 21° C (38° F).

The test data indicated the pressure drop in the diffuser was close to 0.07 P3, which was 40 % larger than the design intent of 0.05 P3. Some of this was anticipated, based on pretest flow checks; the additional amount was due to instrumentation blockage losses.

The expander/inducer was opened toward the high end of its tolerance range during the calibration flow check; this was done to account for the higher than nominal blade flows and in anticipation of some losses due to instrumentation blockage. Test results indicated that the expander supply temperature and exit static pressures were at the expected design level. The inlet pressure was slightly low resulting in a lower pressure ratio across the expander and greater exit temperature relative to the rotor. Percentage flows across the expander are shown in Figure 199 for data readings taken during final engine calibration. Design value for this flow is 4.6% W25.

DMS Readings 245-259

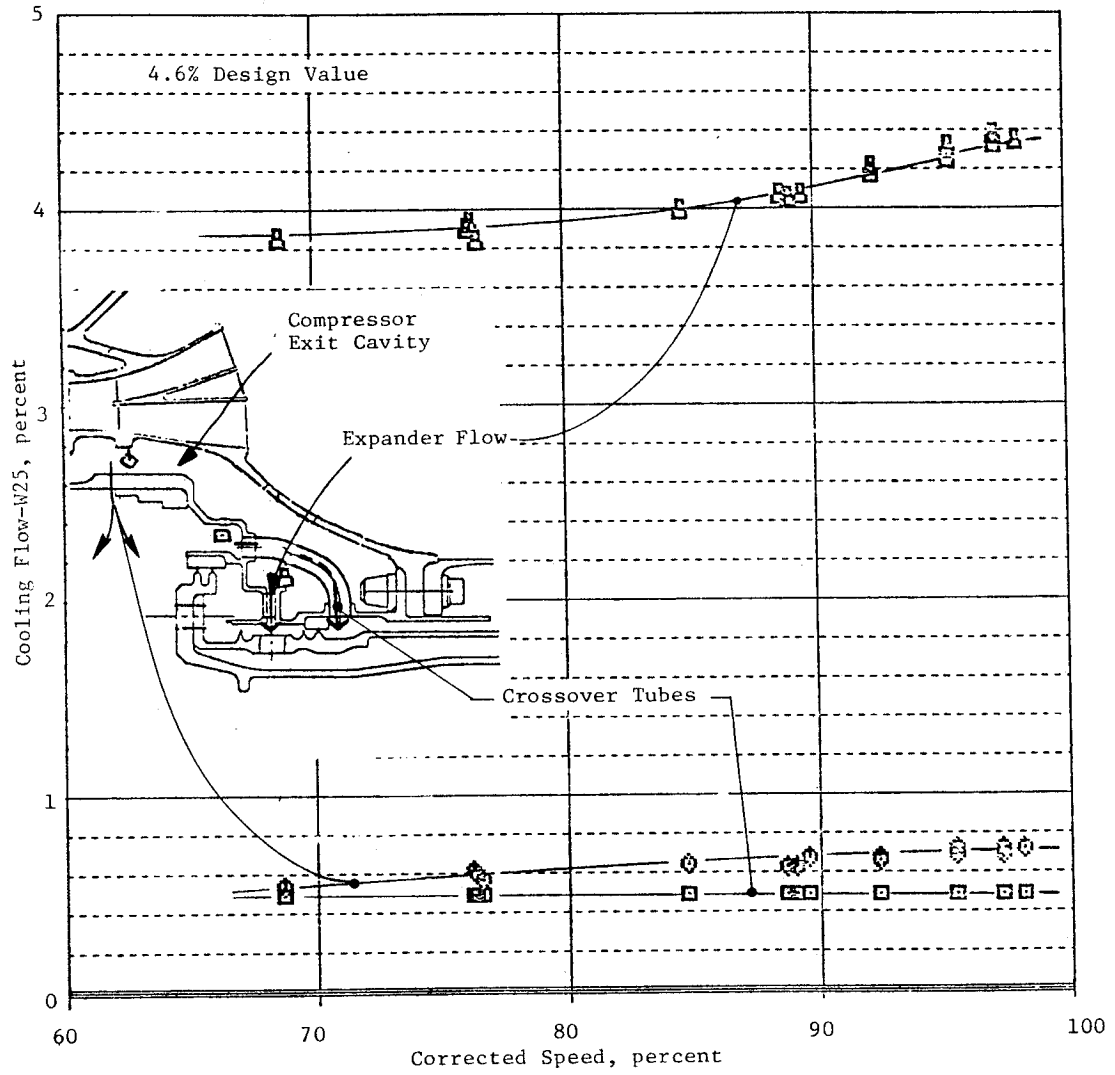


Figure 199. HP Turbine Expander Cooling Flows.

Overall, the rotor cooling air delivery system performed satisfactorily. A return of the airfoils to nominal design cooling flow and a restoration of diffuser strut pressure losses would improve the system efficiency.

An assessment of the impeller pumping system performance will be postponed until an inspection can be made of the pneumatic instrumentation tubes mounted on the rotor. Contradicting information was received from these transducers, and a post-ICLS test examination may offer a resolution. The data obtained from this instrumentation suggests these were mixed lead outs, pneumatic or electrical, and/or a leak in the tube splicing. However, current indications (Stage 1 blade temperatures and expander flows) are that the pumping performed as well or better than design intent.

No Stage 2 blade dovetail pressures were recorded due to instrumentation failure; however, the low blade temperatures and posttest blade condition are evidence that the air supply system performed well.

Expander and CDP Seal Performance and Leakage

Figure 200 shows the compressor discharge leakage flow system which is used to purge the wheel space cavity between the Stage 1 nozzle support and the Stage 1 blade. Temperatures and pressures for this system are shown in Figures 155 and 156.

Expander seal leakage can be calculated using the temperature rise across the seal as an indication of energy dissipation within the seal (see Figure 201). The expander seal leakage was estimated to be 0.56% W25 at test point No. 258 using this method. This was a reasonable value when compared to the indicated flow (0.55% W25) of spent CDP seal leakage across the expander bypass tubes (Figure 199), which were calibrated during pretest flow checks. This indicated a seal running clearance of 0.155 mm (0.006 inch) to 0.203 mm (0.008 inch) or approximately 0.03% of seal diameter, quite normal for a "green" engine that has experienced no fast transient or flight dynamic loads. The low expander seal flow resulted in a higher seal and cavity temperature rise at any given engine speed point (Figure 201). Consequently, the metal temperatures on the Stage 1 nozzle aft inner band were higher than would be seen on an engine that had experienced some rapid transients. In addition,

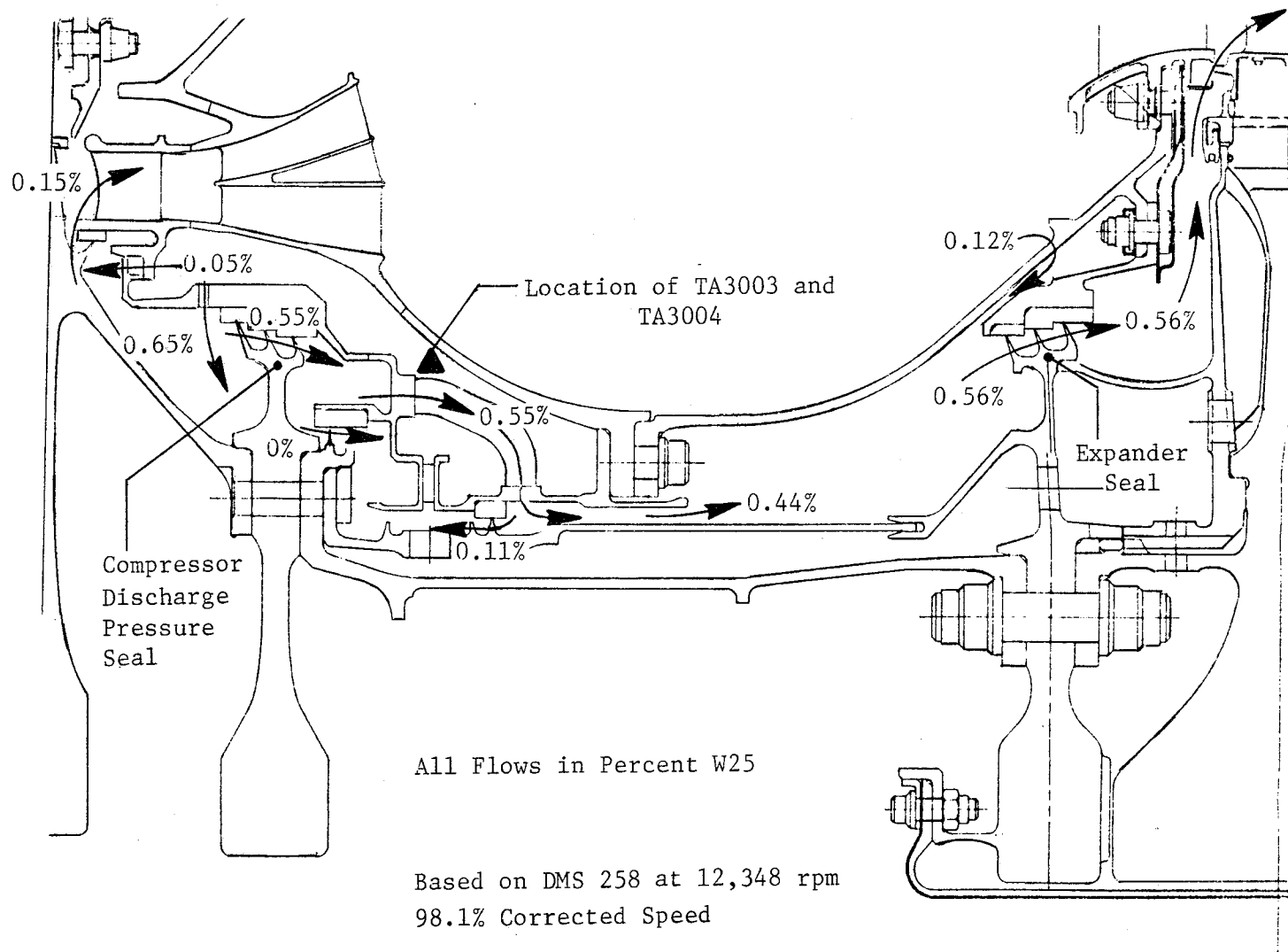


Figure 200. HP Turbine CDP Seal Leakage Flows.

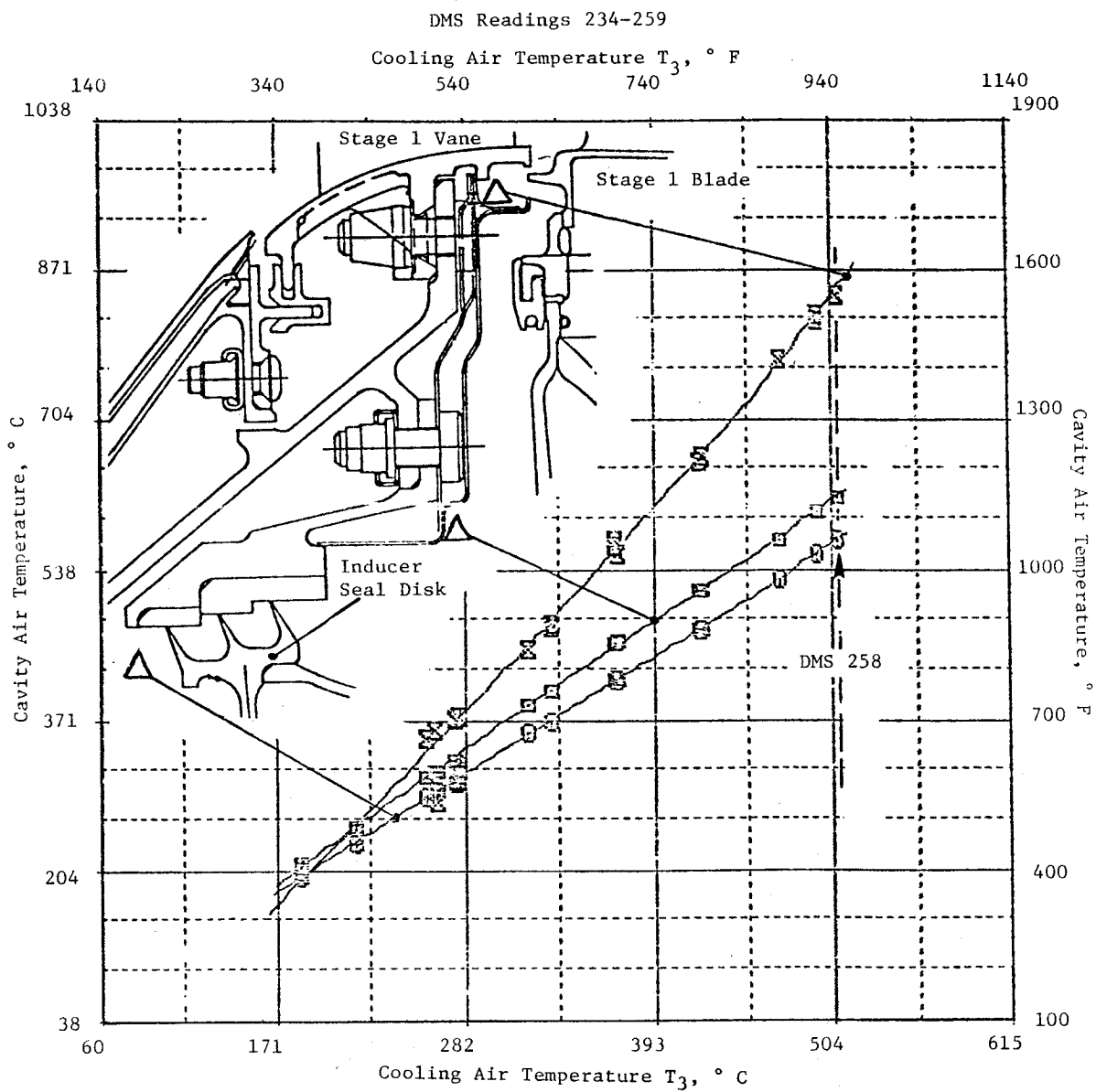


Figure 201. HP Turbine Stage 1 Cavity Air Temperatures.

this localized area was exposed to hot gas mixing as it is on most engines. The design incorporated positive protection of the Stage 1 nozzle flange support from hot gas inflow. This was provided by means of the discourager seal plates which act as a baffle. Temperatures recorded at high rotor speeds would be reduced by approximately 45° C (81° F) with increased flow.

CDP seal leakage was difficult to calculate with any certainty because of recirculation in the downstream cavity which prevented accurate measurement of the seal temperature rise. Consequently, the flow was calculated exclusively on the basis of continuity and resulted in a 0.55% W25 flow for test point No. 258. Flows through the expander crossover tubes are shown in Figure 181. The average value of this flow (0.55%) was low compared to the expected value of 1.18% W25. This was due to tighter than expected assembly seal clearances on the CDP seal disk.

As clearances open with additional engine operation and as both the aft expander seal and the CDP seal flows increase, it is expected that the Stage 1 disk forward wheel space temperature will decrease. Also, the one-tooth discourager seal flow at the expander will decrease and possibly reverse. At the same time, the positive wheel space purge flow at the compressor exit will decrease and reverse, ingesting a small amount of flowpath air (0.20%) between the Stage 10 rotor and the compressor exit guide vanes. It is expected that the test values obtained for an average broken-in engine would closely match the design values of 1.38% W25 leakage flow for the expander seal and 1.18% W25 leakage flow for the CDP seal.

6.6.5 Airfoil Radial Temperature Profiles

Figure 202 shows the average radial metal temperature distribution for all four HP turbine airfoils at the maximum 98.1% corrected speed condition (DMS Reading 258), approximately 1448° C (2638° F) T4. The metal temperatures are all leading edge temperature measurements represented by the solid lines. The dashed lines are extrapolations of data where no measurements were obtained mainly due to early instrumentation loss, particularly on the rotor.

Figure 203 is a similar plot of average metal temperature at 77.5% corrected core speed. This speed point was chosen because of the availability

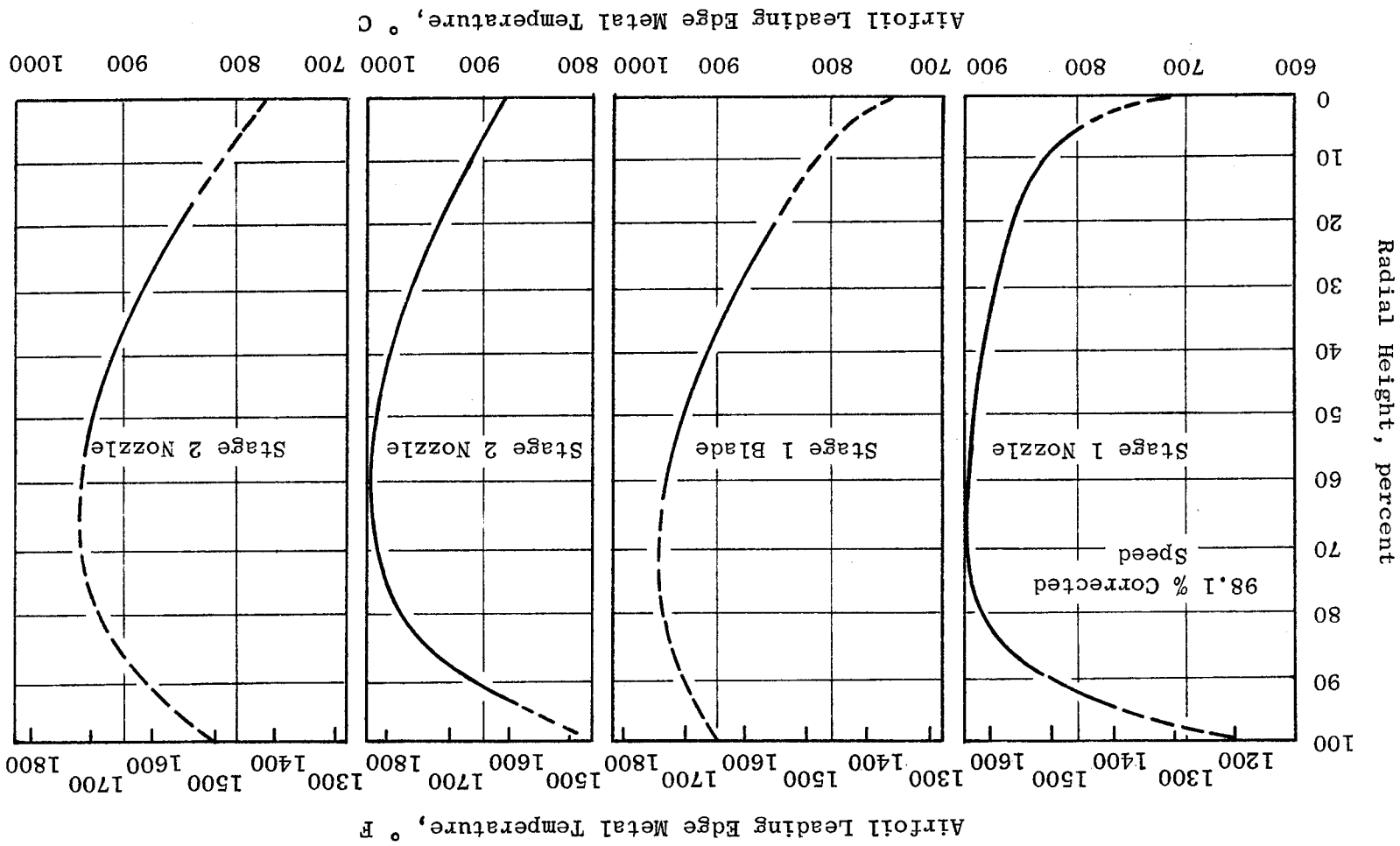


Figure 202. HP Turbine Airfoil Leading Edge Temperature Profiles.

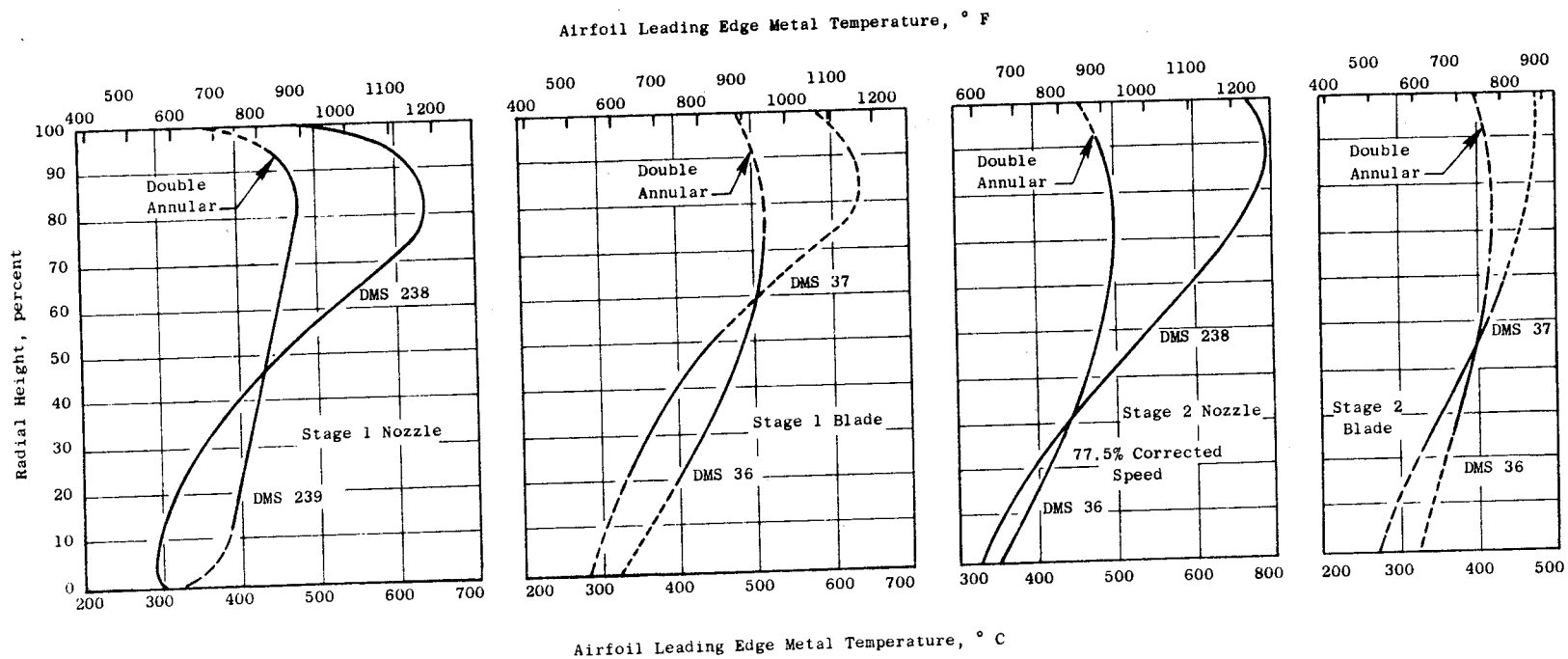


Figure 203. HP Turbine Airfoil Leading Edge Temperature Profiles.

of data for both single-and double-annular combustor burning. Data have been taken from DMS Readings 36, 37, 238, and 239 at approximately 815° C (1498° F) T4. Profile differences between single-and double-annular combustion are clear, as is the general profile dilution with axial progression through the turbine.

6.6.6 Stage 1 Nozzle Temperatures

The Stage 1 nozzle throat area, A4, was intentionally manufactured open by 4% from the flight design value. This change was provided to set a slightly lower compressor operating line to improve stall margin.

All nozzle temperatures were highly influenced by the mode of combustion. (Figure 203 shows the radial metal temperature profile change from single-to double-annular burning.) The band temperatures give an excellent indication of the profile change and are shown in Figure 204. As expected, the outer band temperatures decrease and the inner band temperatures increase during the switchover to double-annular burning. The aft ends of the bands were hotter than the forward, which is typical. The maximum indicated band temperature was 1019° C (1866° F).

Airfoil temperatures are shown in Figure 205 plotted against T4. The 60% span, suction side trailing edge thermocouple exhibited the highest temperature and reached 966° C (1771° F) during DMS Reading 258 for a corresponding T4 of 1448° C (2638° F).

Data from DMS Reading 258 was used to generate the chordwise temperature distribution shown in Figure 206. The figure shows the maximum actual recorded core engine temperatures, the temperatures scaled to FPS design conditions (Mach 0.3, SLT0) and the predicted metal temperature distribution used in the nozzle design. It serves as a basis for comparing cooling system performance. All locations with multiple thermocouples displayed consistent temperatures which, for most locations, were at or below expected levels. The comparison of the scaled results with FPS design conditions showed that the leading edge temperatures were 53° C (96° F) low and that the trailing edge temperatures were also below design values.

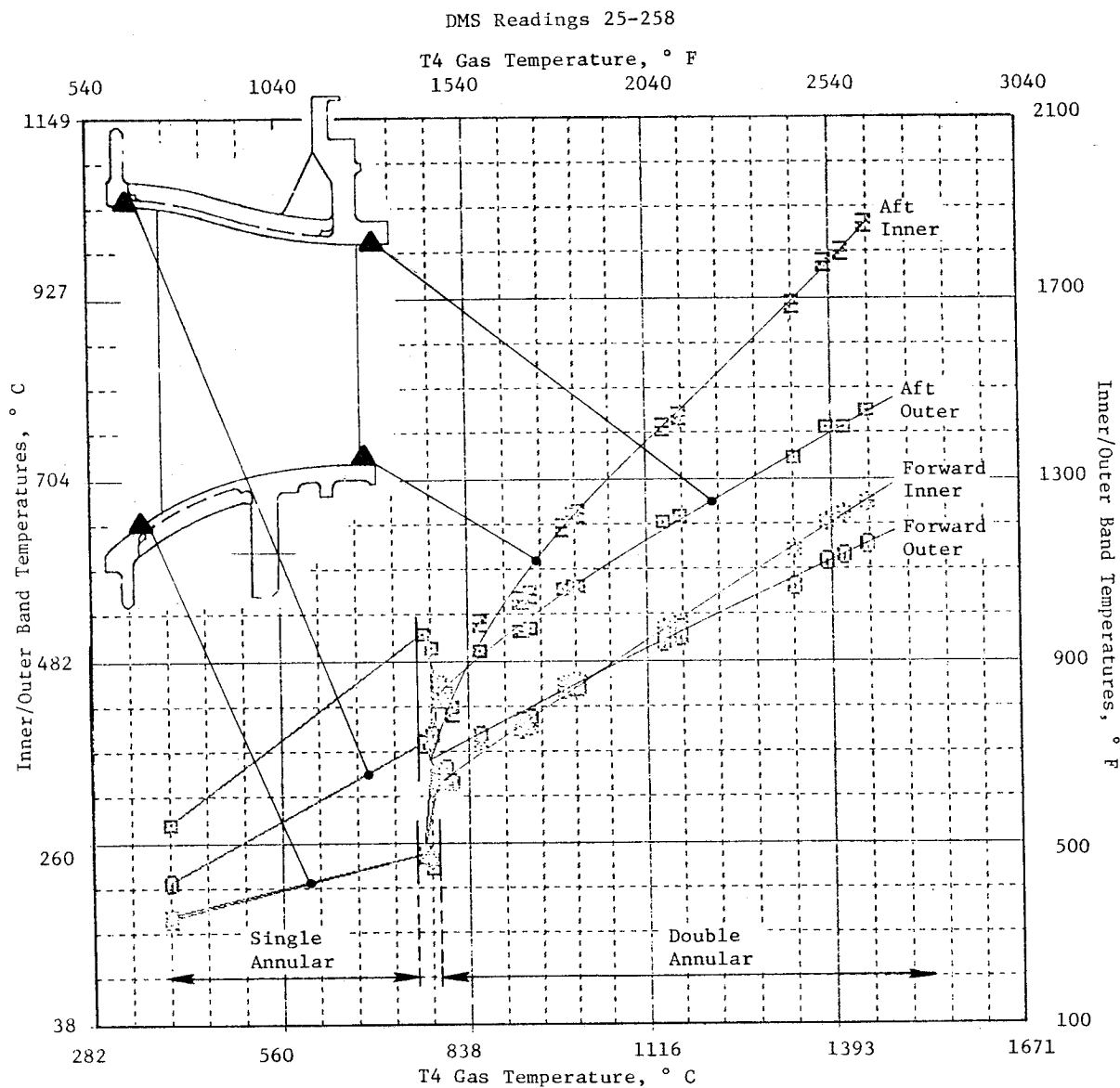
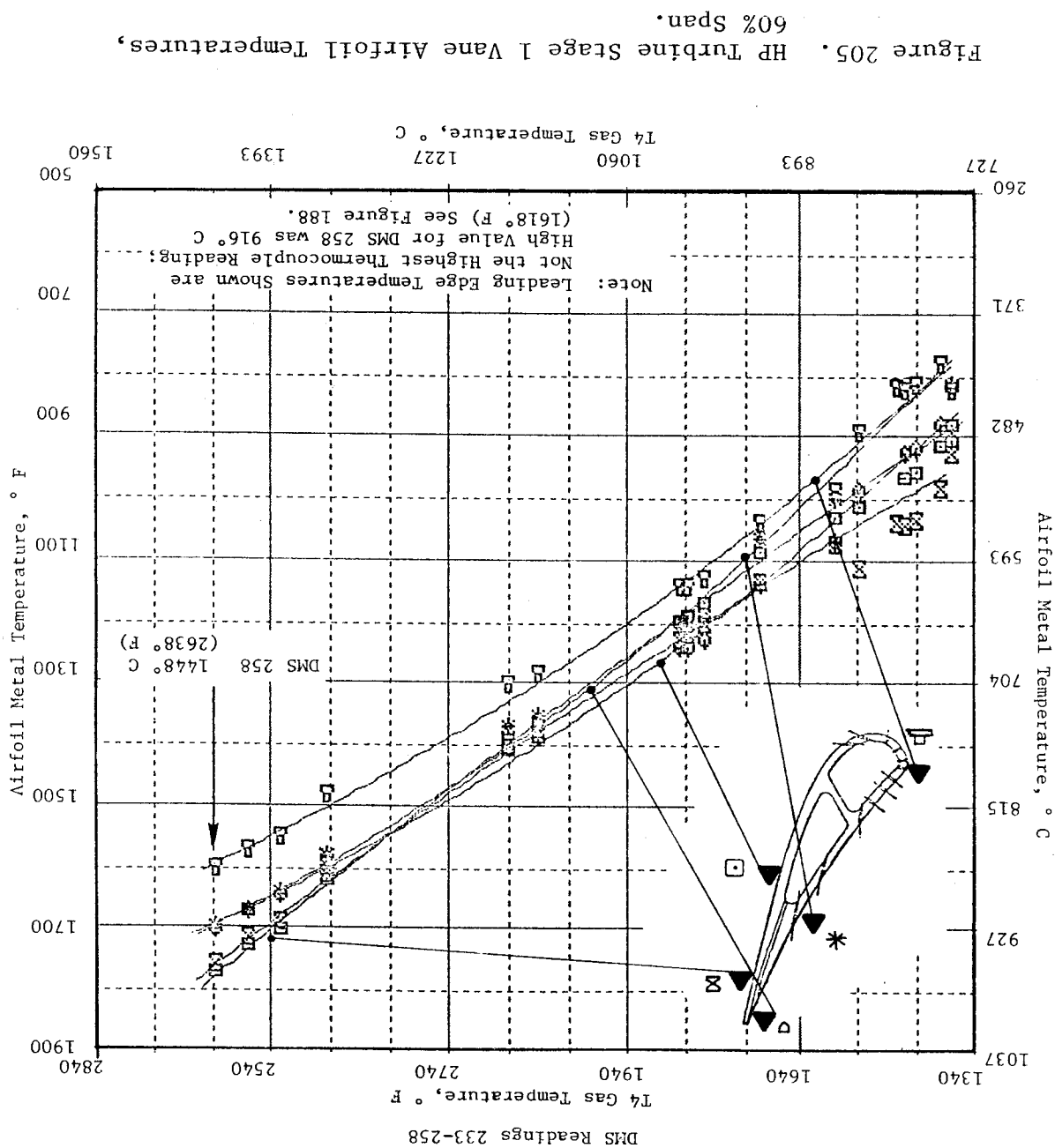


Figure 204. HP Turbine Stage 1 Nozzle Band Temperatures.

ORIGINAL PAGE IS
OF POOR QUALITY



	Core Test	Core Test	FPS*
	DMS 258, ° C (° F)	Scaled to FPS, ° C (° F)	Design, ° C (° F)
T _G Cycle	= 1362° (2484°)	1421° (2590°)	1421° (2590°)
T _G Design	= N/A	1739° (3163°)	1739° (3163°)
T3	= 509° (949°)	627° (1106°)	627° (1106°)
*Mach 0.3 Sea Level Takeoff 50° C (122° F)			

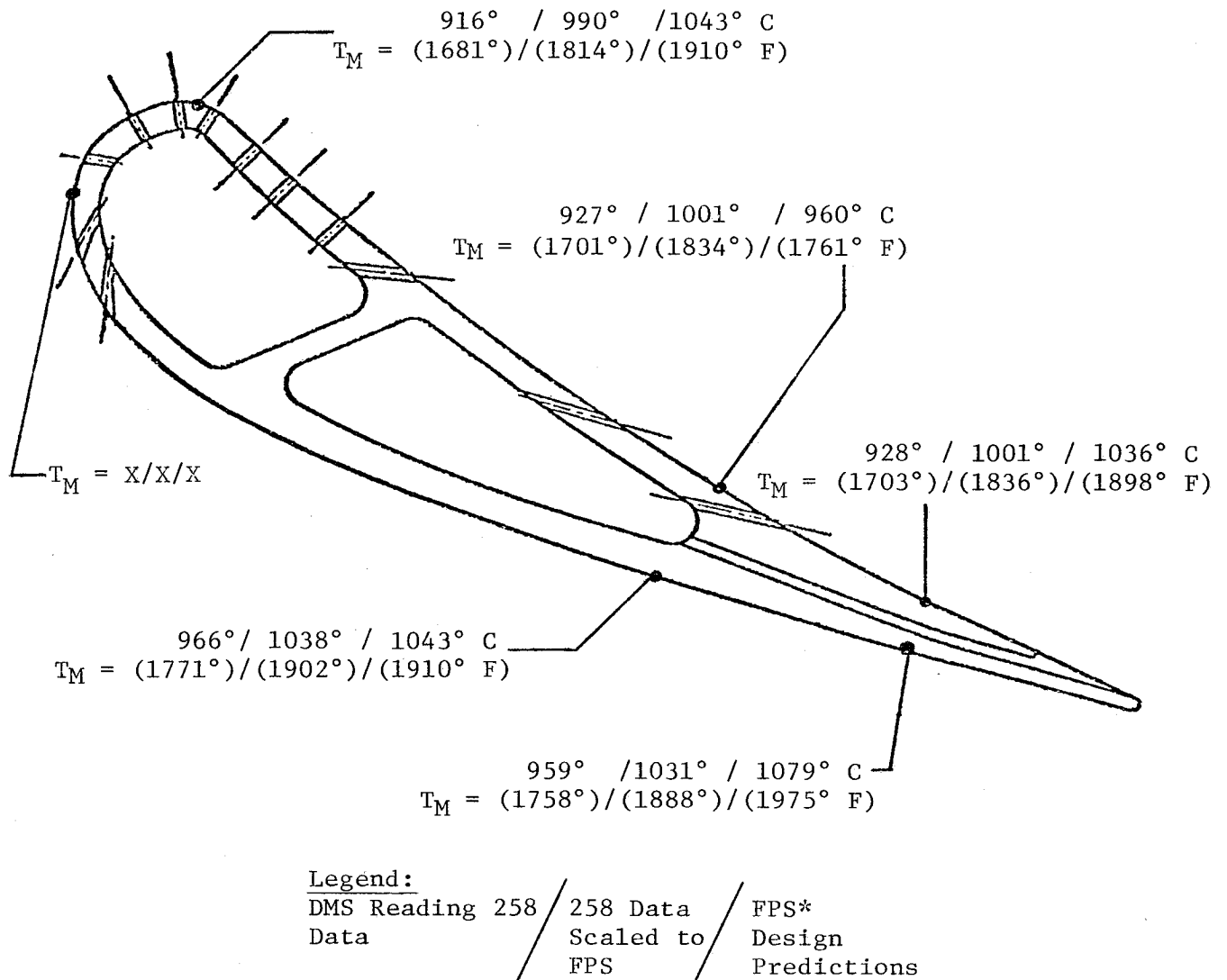


Figure 206. HP Turbine Stage 1 Vane Temperatures.

The nozzle midchord region temperatures were slightly above expected values on the pressure side. The thermocouples were located in a region where transition from impingement to slot convection cooling was taking place. Minor adjustments to the location of the aft row of impingement holes would bring the temperature down to design levels. The core testing did not exceed design temperature limits.

A posttest borescope inspection was performed. The inspected nozzles appeared in good condition, with no signs of leading edge erosion or corrosion and no indications of trailing edge distress. These parts are in excellent condition for subsequent ICLS testing.

Figure 207 shows a one-minute accel from 76% to 95% corrected core speed, and Figure 208 shows a one-minute decel between the same two speed points. No significant increases in thermal gradient were noted on either transient. Maximum ΔT was 146°C (263°F) during the accel and 136°C (245°F) for the decel. The maximum thermal overshoot noted was less than 22°C (40°F); however, high-thermal-overshoot phenomena are normally associated only with more rapid accelerations.

6.6.7 Stage 2 Nozzle Temperatures

Stage 2 vane airfoil leading edge temperatures ran sufficiently close to the design level of 1039°C (1903°F) to become the temperature limiting item at 1035°C (1896°F) at 60% span. This temperature level established maximum engine speed for nominal and small A8 areas. Alternate thermocouples located on the opposite side of the engine indicated 50°C (90°F) lower temperatures. Borescope inspections following engine running showed no signs of distress on the nozzles.

Figures 209 and 210 show the instrumentation locations and identification code numbers for the Stage 2 nozzle.

Inner band metal temperatures are plotted against T41 as shown in Figure 211 with coolant temperature (TAB284) plotted for reference. The metal temperatures (TK4A16, TK4A17) were significantly cooler than the gas temperature,

ORIGINAL PAGE IS
OF POOR QUALITY

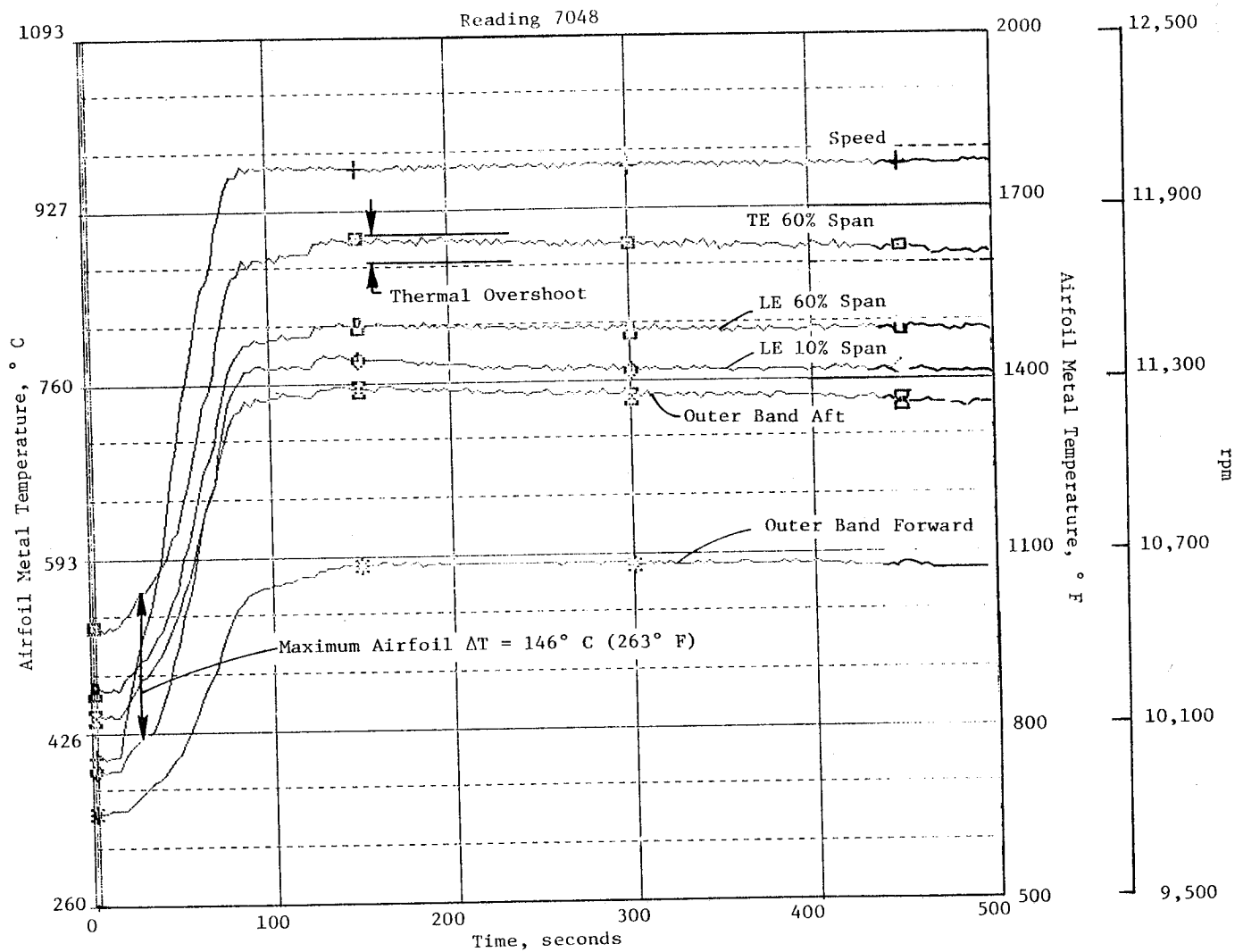


Figure 207. HP Turbine Stage 1 Nozzle Temperature Transients.

ORIGINAL PAGE IS
OF POOR QUALITY

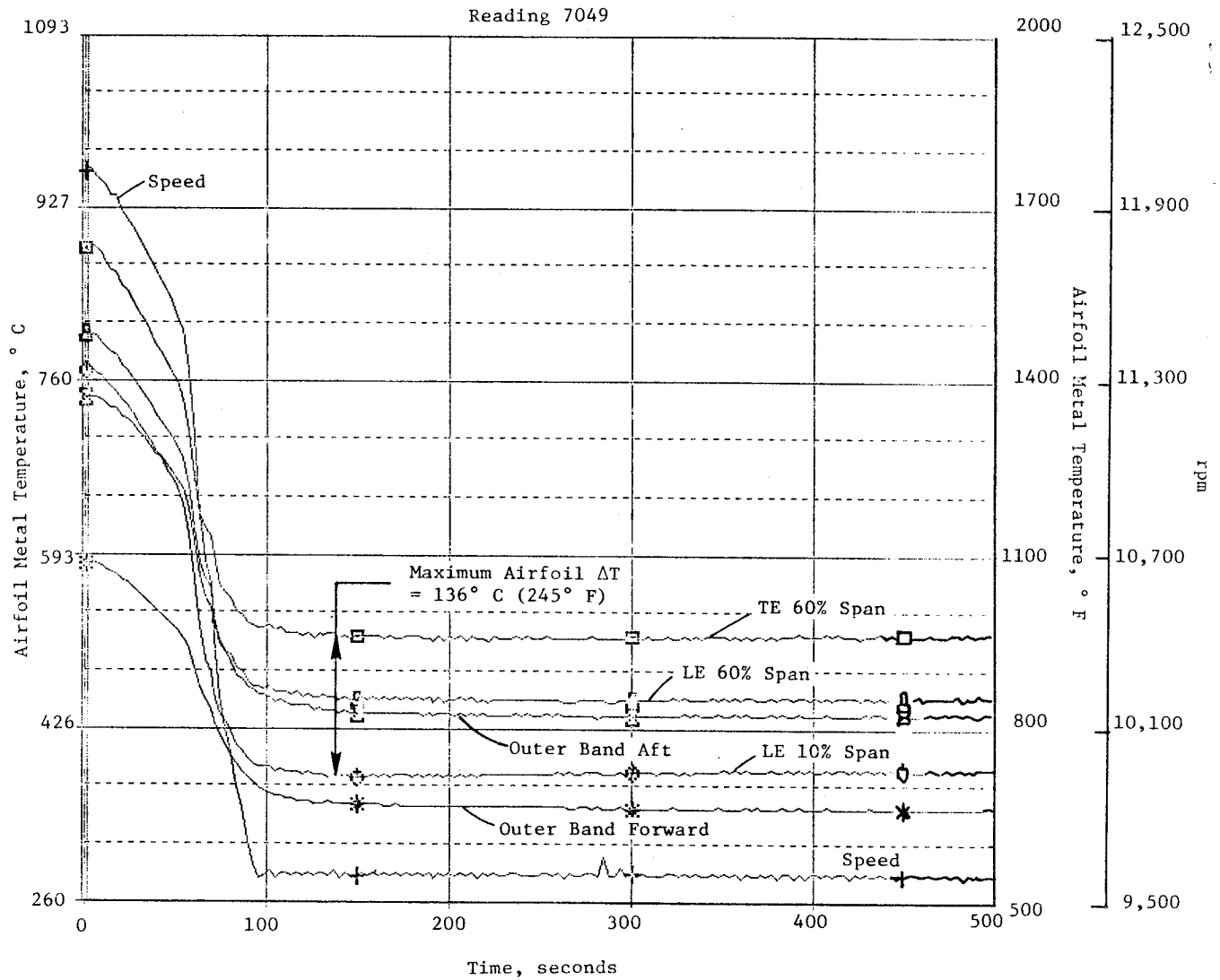


Figure 208. HP Turbine Stage 1 Nozzle Temperature Transients.

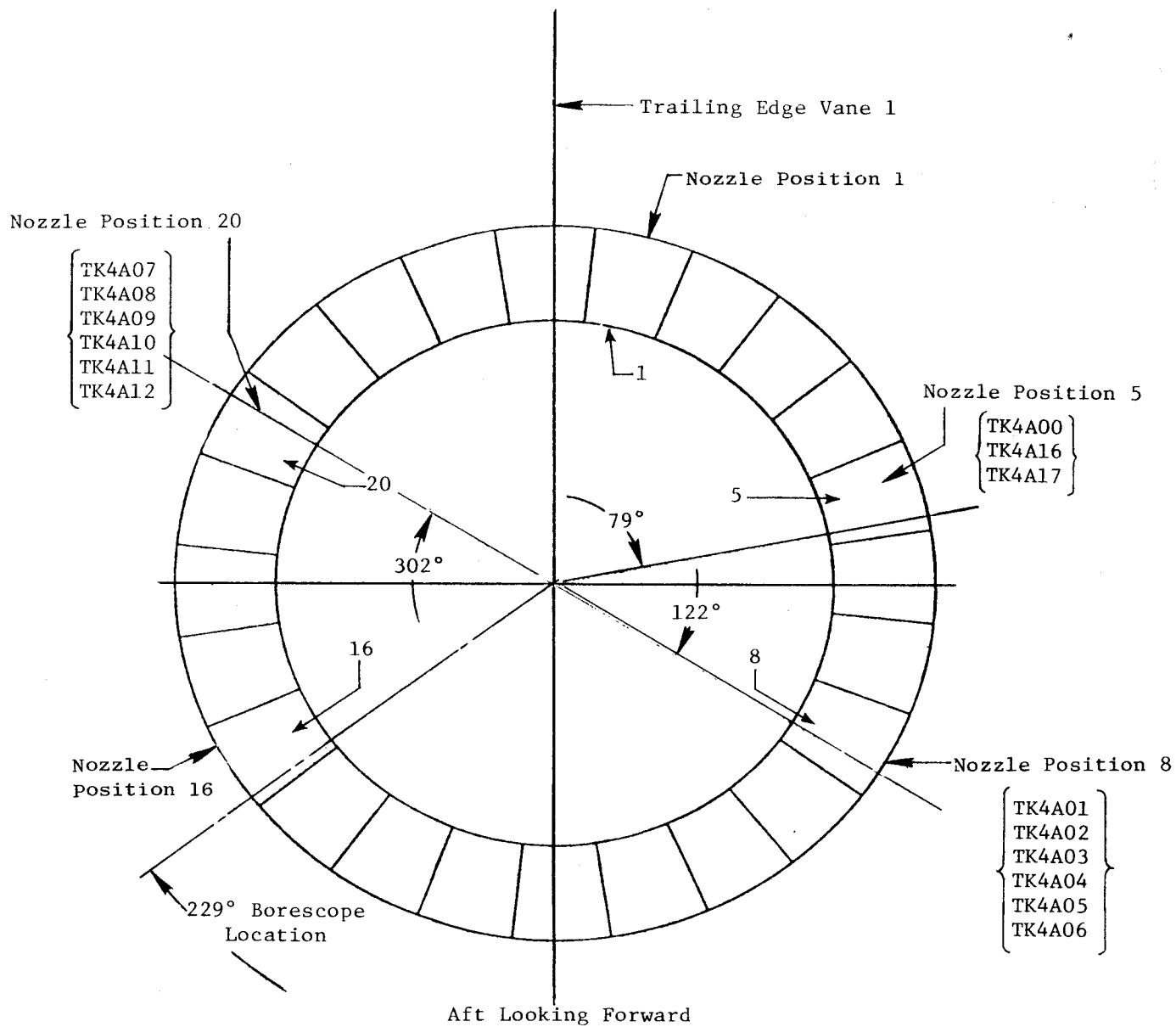


Figure 209. HP Turbine Stage 2 Nozzle Instrumentation Positions.

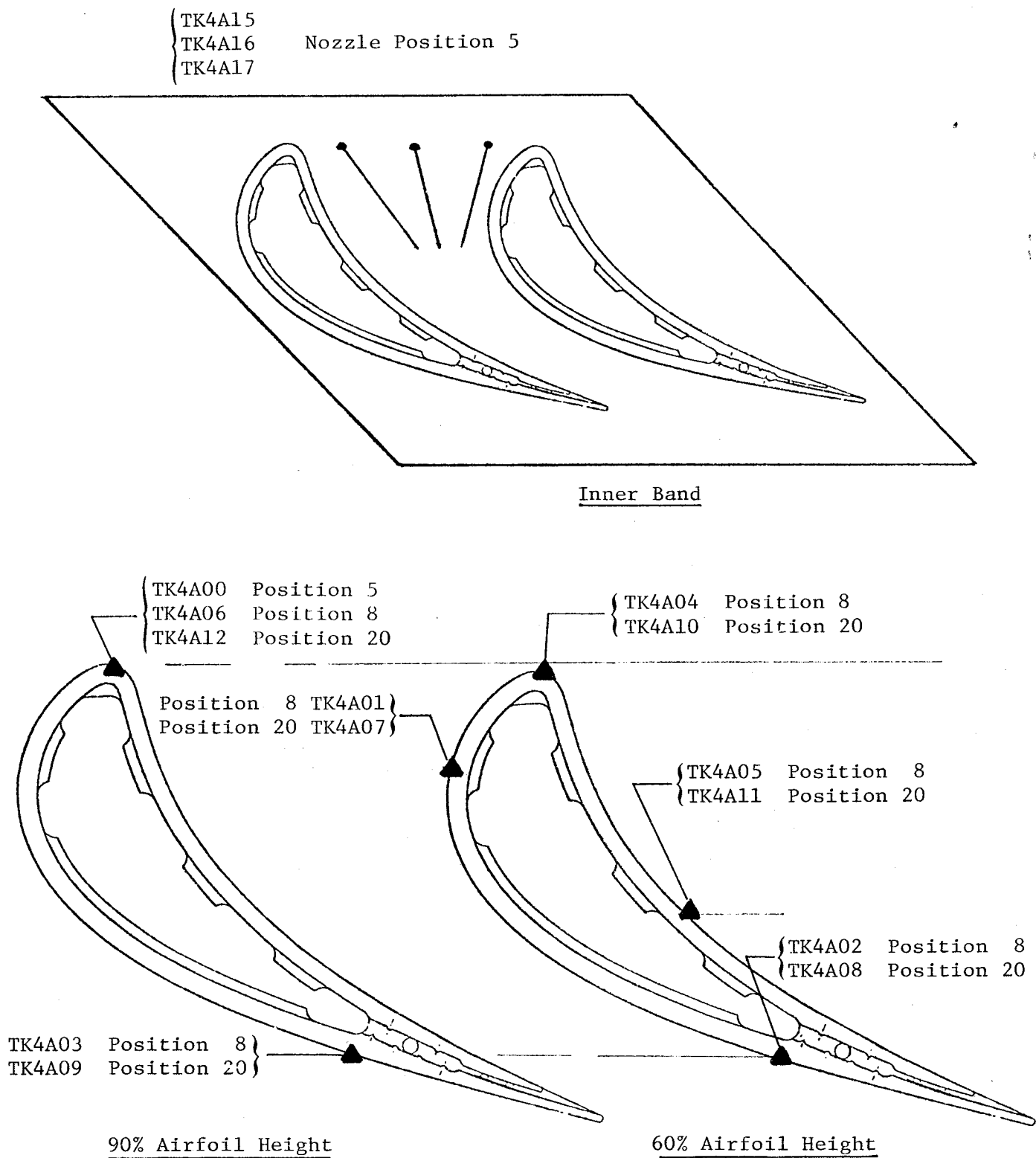


Figure 210. HP Turbine Stage 2 Nozzle Thermocouple Locations.

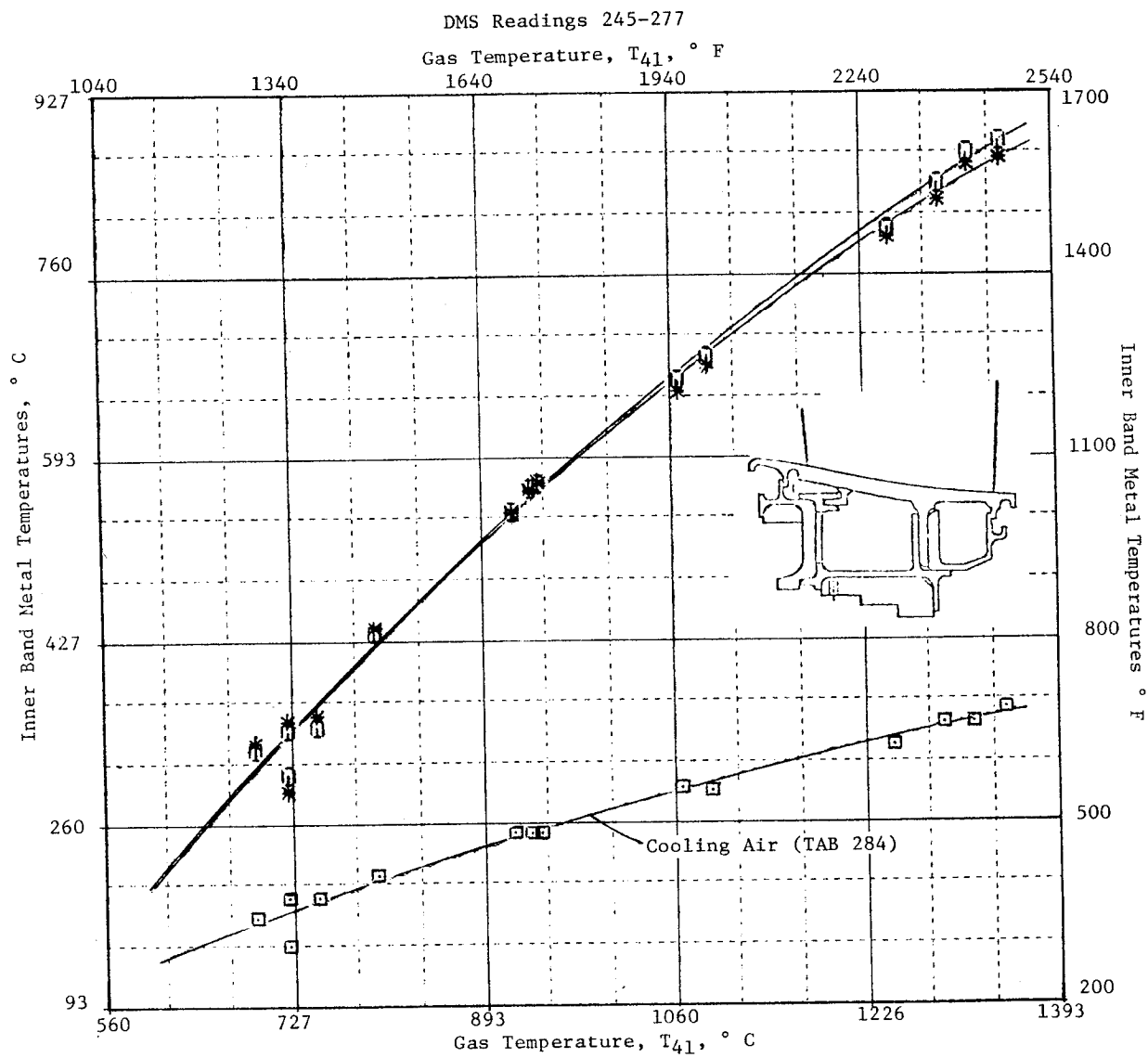


Figure 211. HP Turbine Stage 2 Nozzle Inner Band Temperatures.

demonstrating the effect of convection cooling on the underside of the forward end of the inner band.

Figure 212 shows the measured pressures and calculated airflows for the Stage 2 nozzle and interstage cavity in the core engine which takes account of performance-related deviations from blueprint such as the increased trailing edge slot area and the additional leakage around the impingement insert weld.

A comparison of the 60% span airfoil temperature distribution is made in Figure 213. The figure shows the maximum actual recorded engine data with the data scaled to FPS design conditions ($M = 0.3$ takeoff) and predicted FPS design data.

The Stage 8 vane leading edge ran 21°C (37°F) warmer than intended (above predicted peak temperatures) with the midchord region 16°C (29°F) warmer for a given local gas temperature. The other vane, similarly instrumented, ran approximately 50°C (90°F) cooler at both leading edge and midchord regions. Factors that may have caused the Location 8 vane to be warmer included the variation in circumferential gas temperature profile, up to about 80°F at the turbine outlet (T42), and changes in vane internal heat transfer due to the reported deviations in hardware.

The larger-than-intended trailing edge slots, resulting in an additional 1% W25 cooling flow, reduced the trailing edge temperatures below the original design levels by approximately 143°C (257°F). Posttest data match for the region of the airfoil surrounding the thermocouple indicated that the 143°C (257°F) temperature reduction is exactly as expected with the increased flow. Restoration of the correct flow in flight-engine hardware would result in design trailing edge temperatures.

Compressor discharge air bleed was available during initial engine testing to replace the compressor seventh-stage air supply in the Stage 2 nozzle cooling circuit under starting bleed conditions. The reason for using compressor discharge air was to ensure adequate backflow margin in the Stage 2 nozzle and the interstage seal purge. After a start, the valves close allowing seventh-stage bleed air to be supplied for nozzle cooling under normal

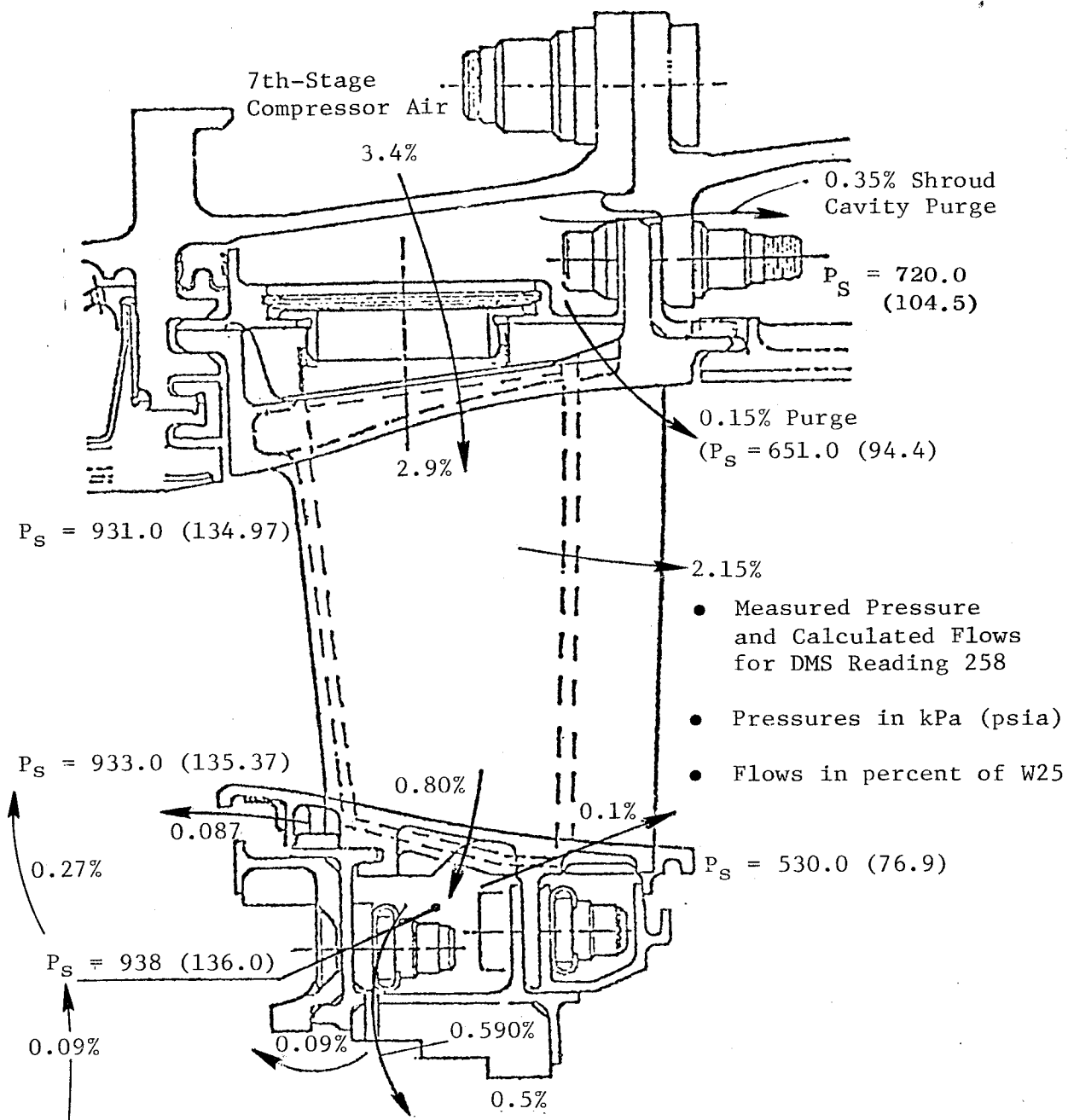
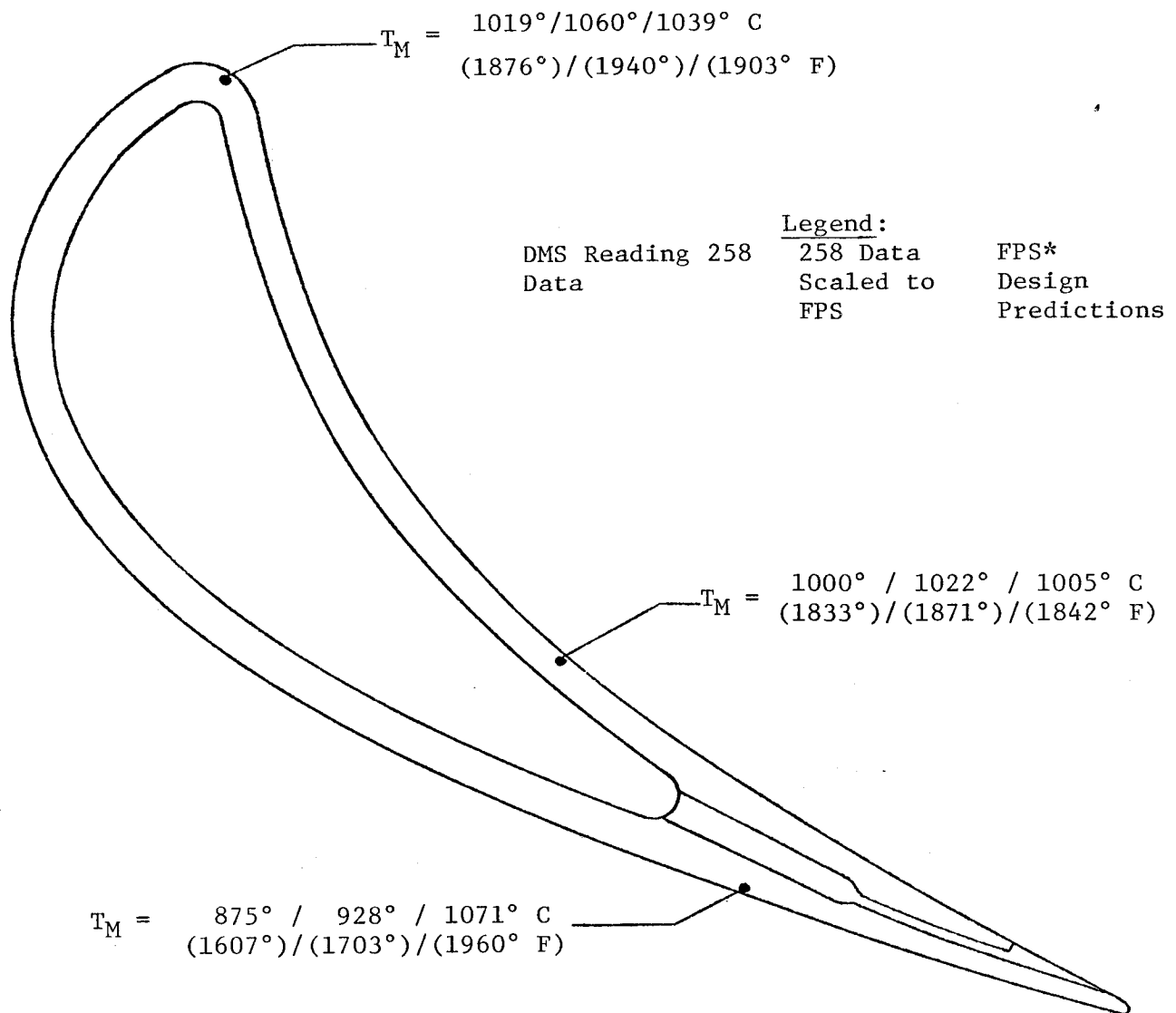


Figure 212. HP Turbine Stage 2 Nozzle and Interstage Cavity Pressures and Flows.



Core Test DMS 258 Nozzle Position 8, ° C (° F)	Core Test Scaled to FPS, ° C (° F)	FPS* Design, ° C (° F)
T_G Cycle = 1108° (2027°)	1065° (1950°)	1134° (2074°)
T_G Peak = 1308° (2516°)	1337° (2439°)	1337° (2438°)
T_C = 377° (711°)	488° (910°)	488° (910°)
T_{41} = 1362° (2484°)	1421° (2590°)	1421° (2590°)
*Mach 0.3 Sea Level Takeoff 50° C (122° F)		

Figure 213. HP Turbine Stage 2 Vane Temperatures.

conditions. Following the fourth engine start, the start range turbine cooling (SRTC) valves failed to close fully (Section 6.8, Configuration). This resulted in compressor discharge air being supplied to the nozzle cooling circuit at higher than planned power conditions prior to a supply pipe flange failure following DMS Reading 47. Thereafter, Stage 2 nozzle cooling air was a mixture of compressor seventh-stage and discharge bleed air for the remainder of the initial testing, up to and including DMS Reading 52. Figure 214 shows the resulting temperature effects on the vane. Vane temperatures with compressor discharge cooling air were approximately 28° C (50° F) warmer than with seventh-stage cooling air. Temperatures were well below the vane limit.

Figure 215 shows the changes in vane temperatures when switching from single to double annular combustion. The switch from single to double annular resulted in a temperature drop of 89° C (160° F) at 60% span for the same level of T4. The gas radial profile, which for single annular burning was peaked toward the outer region of the flowpath, shifted more toward the 60% span or pitch-line region of the flowpath during double annular burning (Figure 203). These data, combined with those obtained for the Stage 1 nozzle and blades, indicate that the double annular burning results in a more uniform radial gas profile.

The Stage 2 nozzle airfoil metal temperature was significantly affected by variations in exhaust nozzle area (A8), as expected. Figure 216 presents the effect on the Stage 2 vane leading edge metal temperature (60% span) for a range of engine operating speeds and three different exhaust nozzle areas. At the higher speeds, vane metal temperatures differed by about 222° C (400° F) between minimum and maximum nozzle areas tested. This change in metal temperature was due to changes in the turbine pressure ratio requiring changes in T4 to maintain speed. The final calibration exhaust nozzle area was used from DMS Reading 233 to completion of the core engine test; its effect is also shown.

Transient data were gathered for Stage 2 nozzle temperatures during certain parts of the testing. Figure 217 shows the transient temperature indicated by the airfoil thermocouples (nozzle Position 8 aft looking forward) during Start 27. This was the most severe start performed in terms of fuel-air ratio and temperature levels on the turbine. The maximum temperature

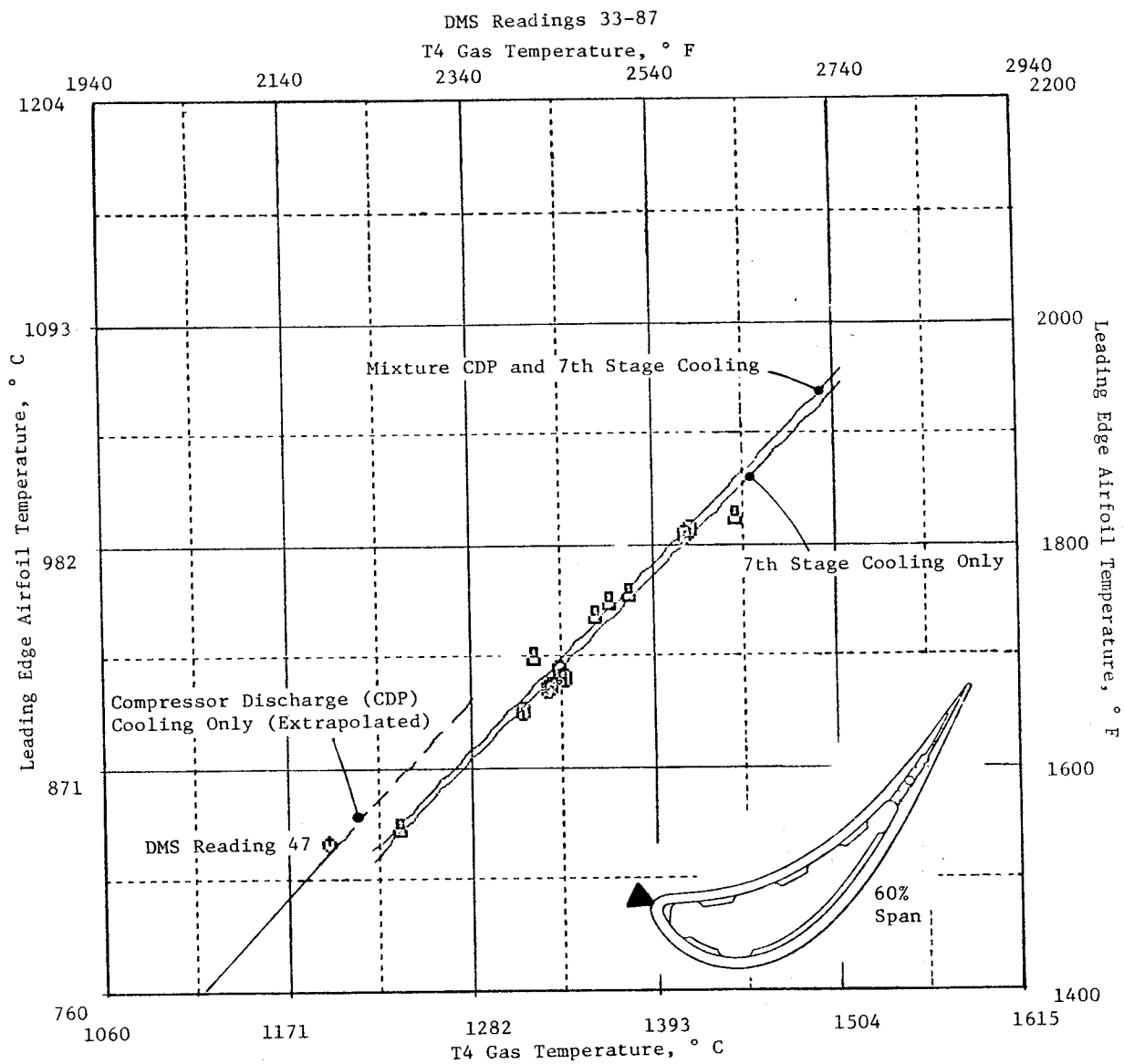


Figure 214. HP Turbine Stage 2 Nozzle Airfoil Temperatures.

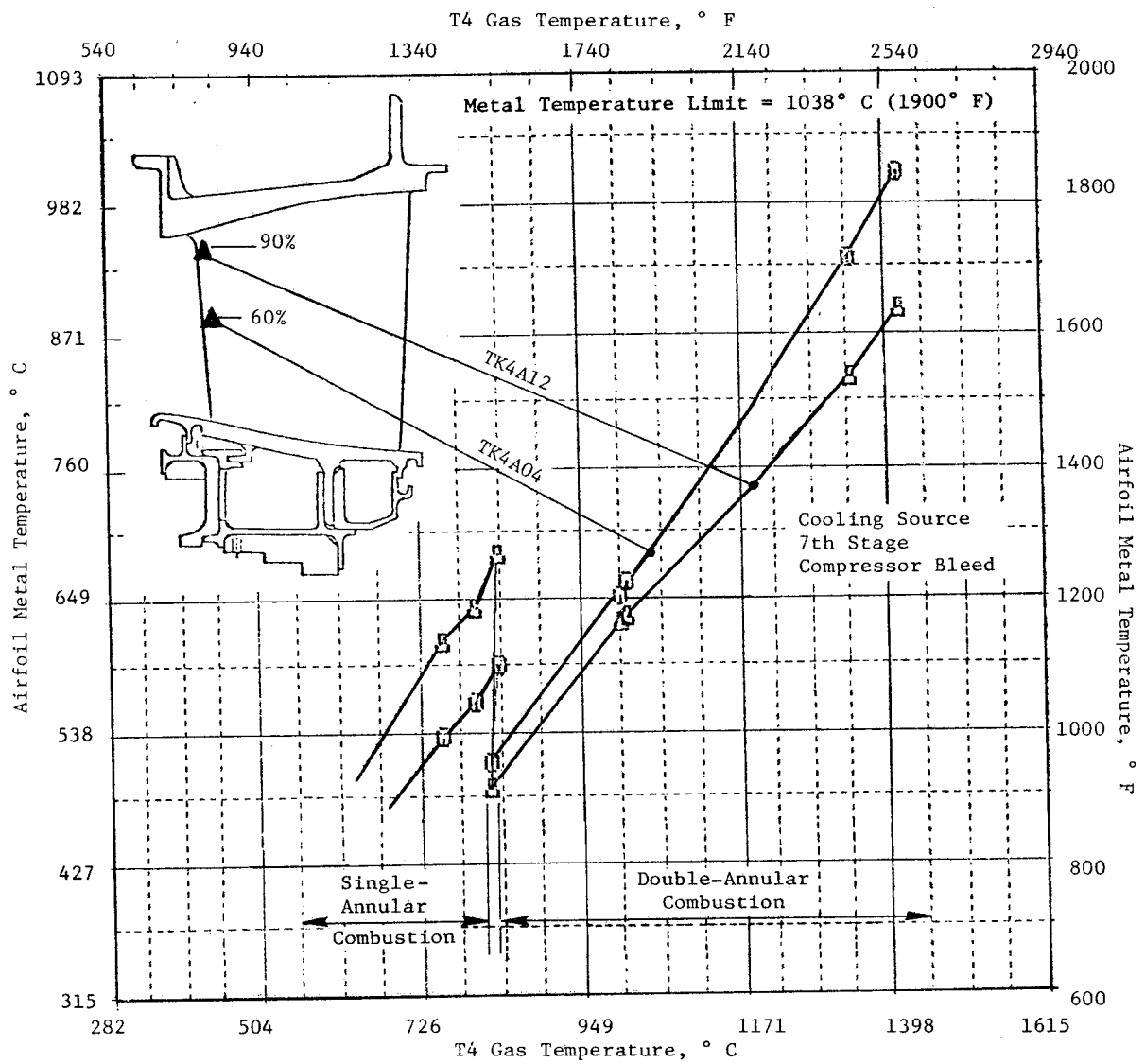


Figure 215. HP Turbine Stage 2 Nozzle Airfoil Temperatures.

ORIGINAL PAGE IS
OF POOR QUALITY

DMS Readings 213-259

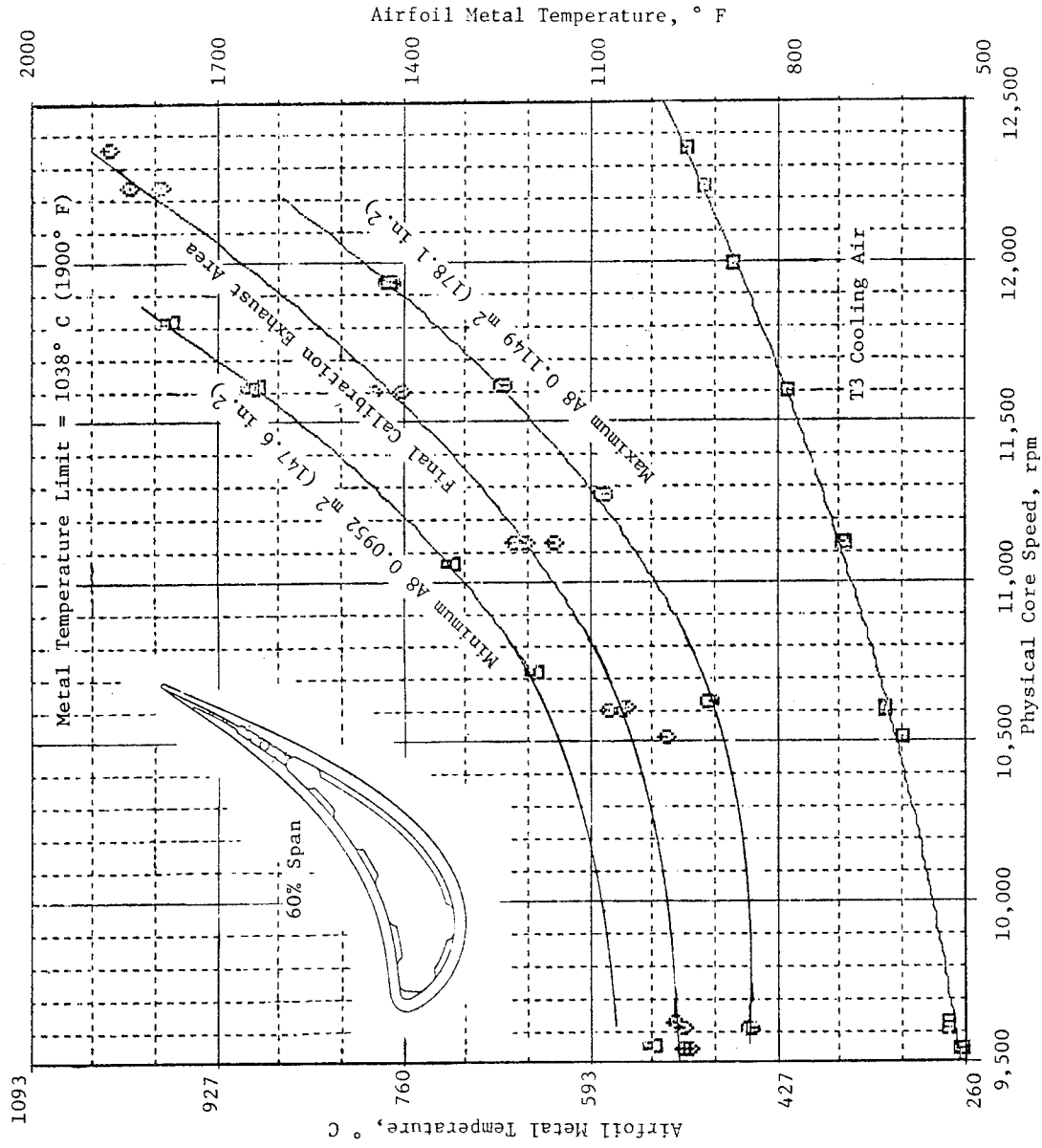


Figure 216. HP Turbine Stage 2 Airfoil Temperature Versus Exhaust Area.

Reading 7037

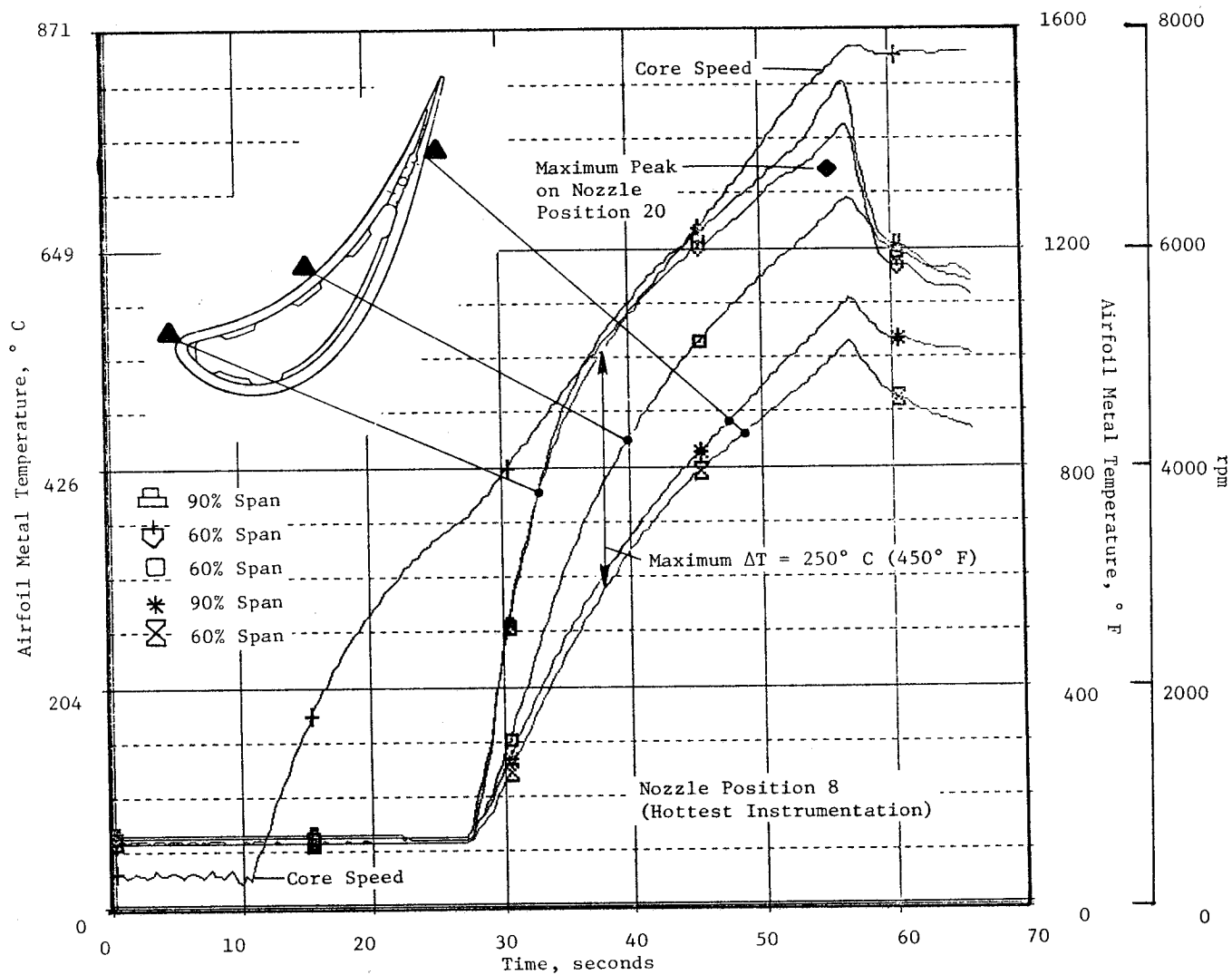


Figure 217. HP Turbine Stage 2 Nozzle Airfoil Start Transient Temperatures.

observed during starting was 818° C (1506° F) on nozzle Position 8 at 90% span leading edge. The peak temperature for the nozzle in Position 20 was 64° C (115° F) cooler for the same start and is indicated in Figure 217. The maximum temperature gradient was approximately 250° C (450° F) and occurred 37.5 seconds after start initiation. Engine speed (shown for reference) starts to increase 11 seconds after start initiation.

Stage 2 vane airfoil temperatures were approximately 56° C (100° F) higher than anticipated, and the maximum achievable engine speed was sometimes limited by leading edge temperatures approaching 1040° C (1900° F) at 60% span. Several factors contributed to the high temperatures: A decision to increase the A4 by 4% to increase compressor stall margin, opening the Stage 1 blade throat approximately 4.3% by cutting back trailing edges to remove casting defects, and a less-than-nominal Stage 2 nozzle throat area (-2.9%) - all served to increase the Stage 2 workload. The transfer of stage work resulted in higher gas temperatures [approximately 28° C (50° F)] entering the Stage 2 nozzle.

In addition, the overall turbine pressure ratio ran low at 4.62 instead of 4.95 due to the exhaust nozzle area (A8) being less than optimum during the final calibration. The resultant back pressure created a need for more fuel input to maintain the same work output and resulted in higher gas temperatures. (Discussion of the selection of the exhaust nozzle area for final calibration is made in Section 6.1, Core System Thermodynamic Performance.)

6.6.8 Interstage Seal System Performance

Figure 218 shows the interstage seal cavity under the Stage 2 nozzle, together with the feed system and instrumentation positions. The measured flows and pressures are shown in Figure 212.

Figure 219 shows the interstage region pressure measurements versus percent corrected core speed. Both the cavity and forward side of the interstage seal showed a 69 kPa (10 psia) to 400 kPa (58 psia) higher pressure than the downstream side of the seal. However, no discernible pressure differences existed between the forward side and the cavity. An analysis of the data

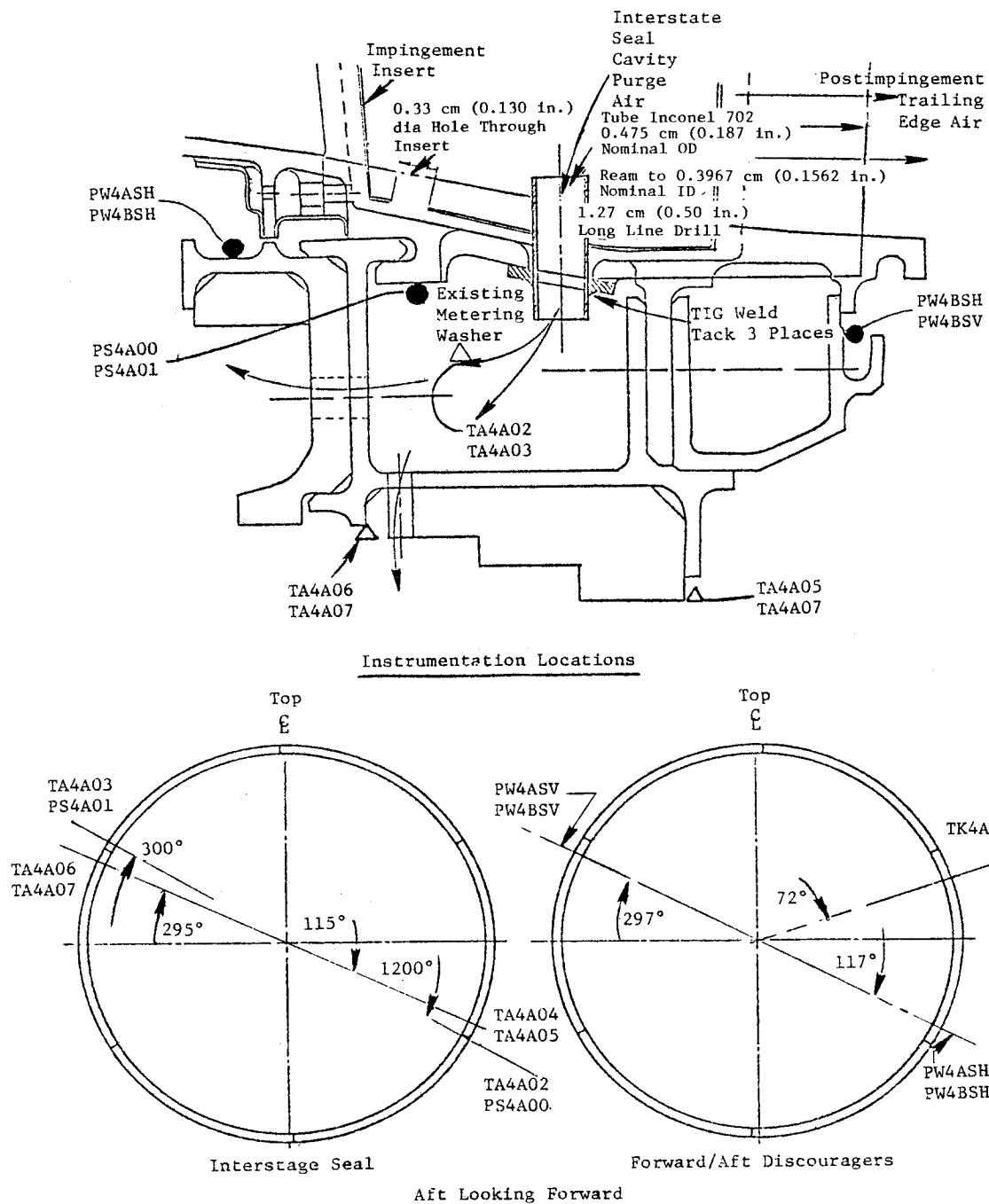


Figure 218. HP Turbine Interstage Cavity Purge System.

ORIGINAL PAGE IS
OF POOR QUALITY

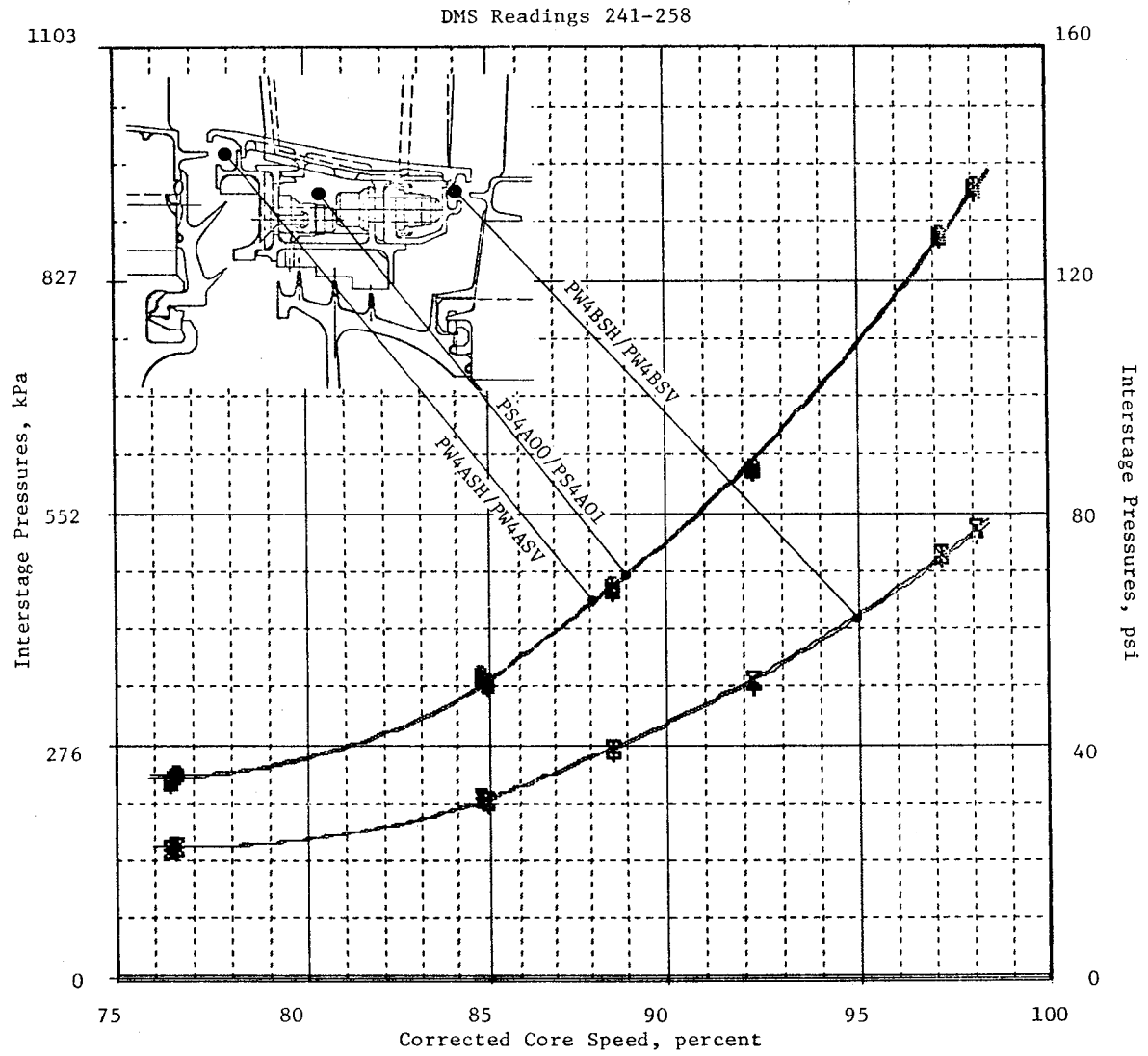


Figure 219. HP Turbine Interstage Pressures.

confirmed that the anticipated 2.8% backflow margin (0.28% W25 outward flow) did not exist and ingestion may have taken place under some conditions. This situation became apparent early in the core engine test and required continuous temperature monitoring of the area, particularly within the cavity.

Measurements of the cooling air temperature after it discharged from the nozzle insert and entered the cavity is represented by Figure 220 for the final calibration. A maximum temperature of 703° C (1297° F) for DMS Reading 258 was indicated. This temperature, while not expected in the cavity, was below the limit of 760° C (1400° F) and is acceptable for safe engine operation. The alternate thermocouple, in a similar location, indicated a temperature 122° C (220° F) cooler for the same engine condition. The temperature of the cooling air entering the nozzle insert (thermocouple TAB284) is also presented for reference purposes. It was not expected that the temperature rise across the insert would exceed 11° C (20° F). Thermocouple TA4A03 (and to a lesser extent TA4A02) exhibited a more rapid temperature rise and reached a higher final temperature than the majority of the other thermocouples in the interstage region (Figure 221). While a major influence on this temperature reading would appear to be gas ingesting into the cavity, a greater possibility exists that the thermocouple(s) may have been incorrectly installed and thus picked up radiation from the nozzle inner band or may have been in partial contact with the metal. Figure 222 shows TA4A03 tracking a parallel line to the inner band metal temperatures which support this theory. TA4A02 was affected somewhat less, but still appears to have between 38° C (100° F) and 132° C (270° F) temperature pickup relative to TAB284 cooling air supply. Postcore engine test instrumentation checks for electrical resistance and grounding have not shown that these thermocouples are in contact with the surrounding hardware.

It may be noted from the temperatures shown in Figure 221 that while some small amount of gas recirculation may be present behind the Stage 1 blade aft angle wing (blade retainer outer thermocouple), it is not likely that it progressed past the retainer seals and down into the forward interstage cavity, as indicated by the relatively cool retainer inner thermocouple measurements and the air thermocouple on the Stage 1 disk aft face.

ORIGINAL PAGE IS
OF POOR QUALITY

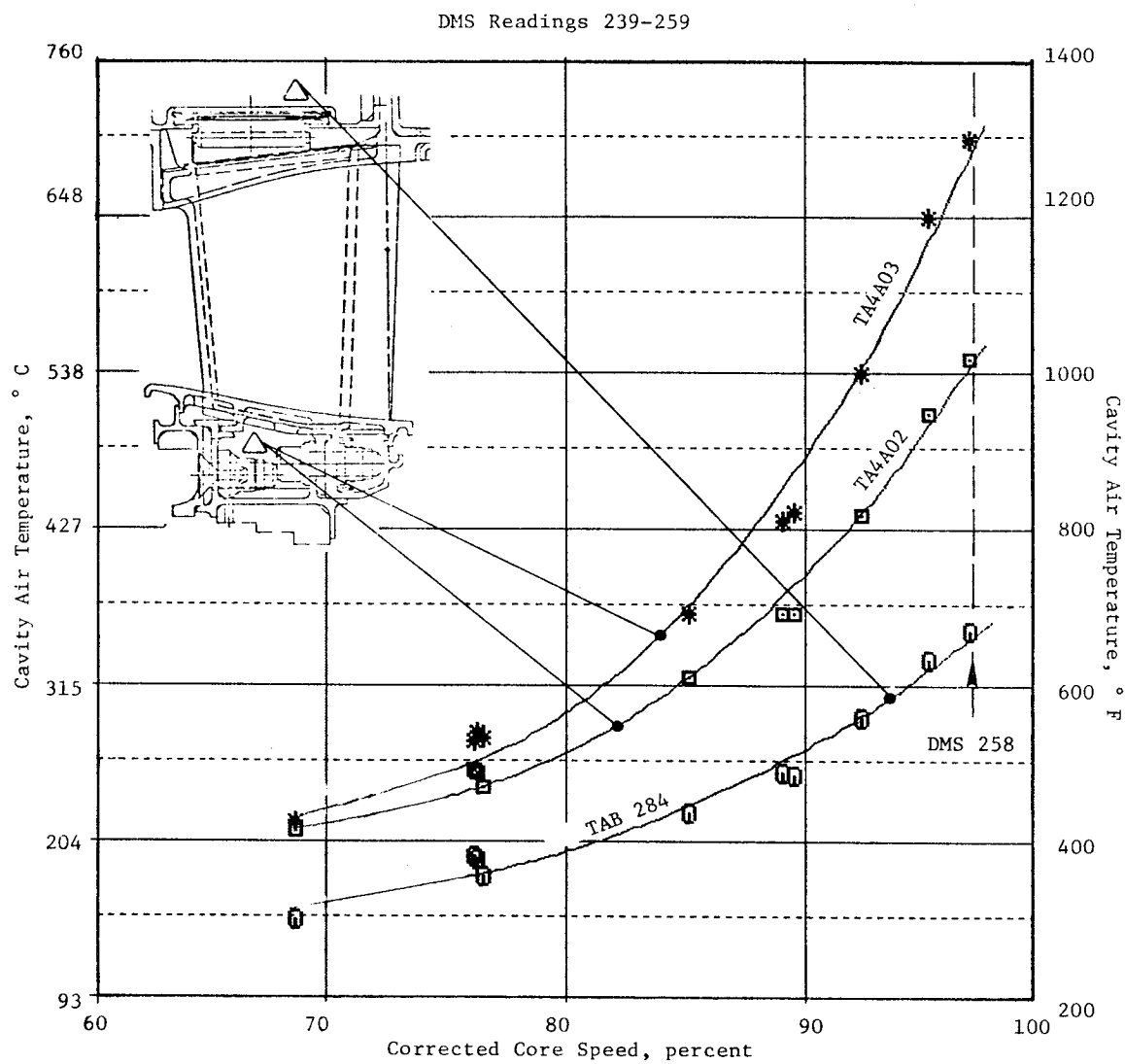


Figure 220. HP Turbine Interstage Cavity Temperatures.

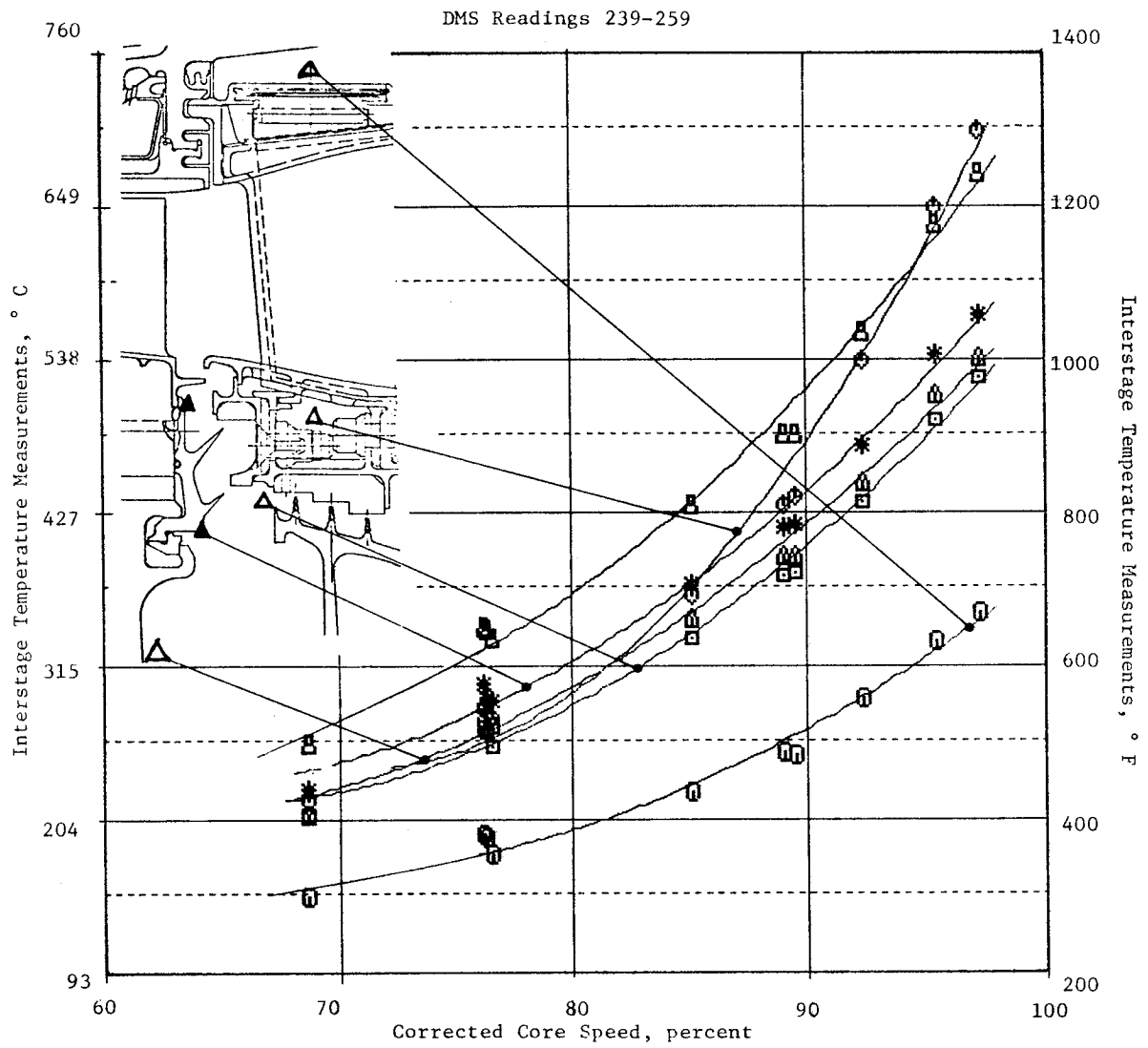


Figure 221. HP Turbine Interstage Forward Cavity Temperatures.

ORIGINAL PAGE IS
OF POOR QUALITY

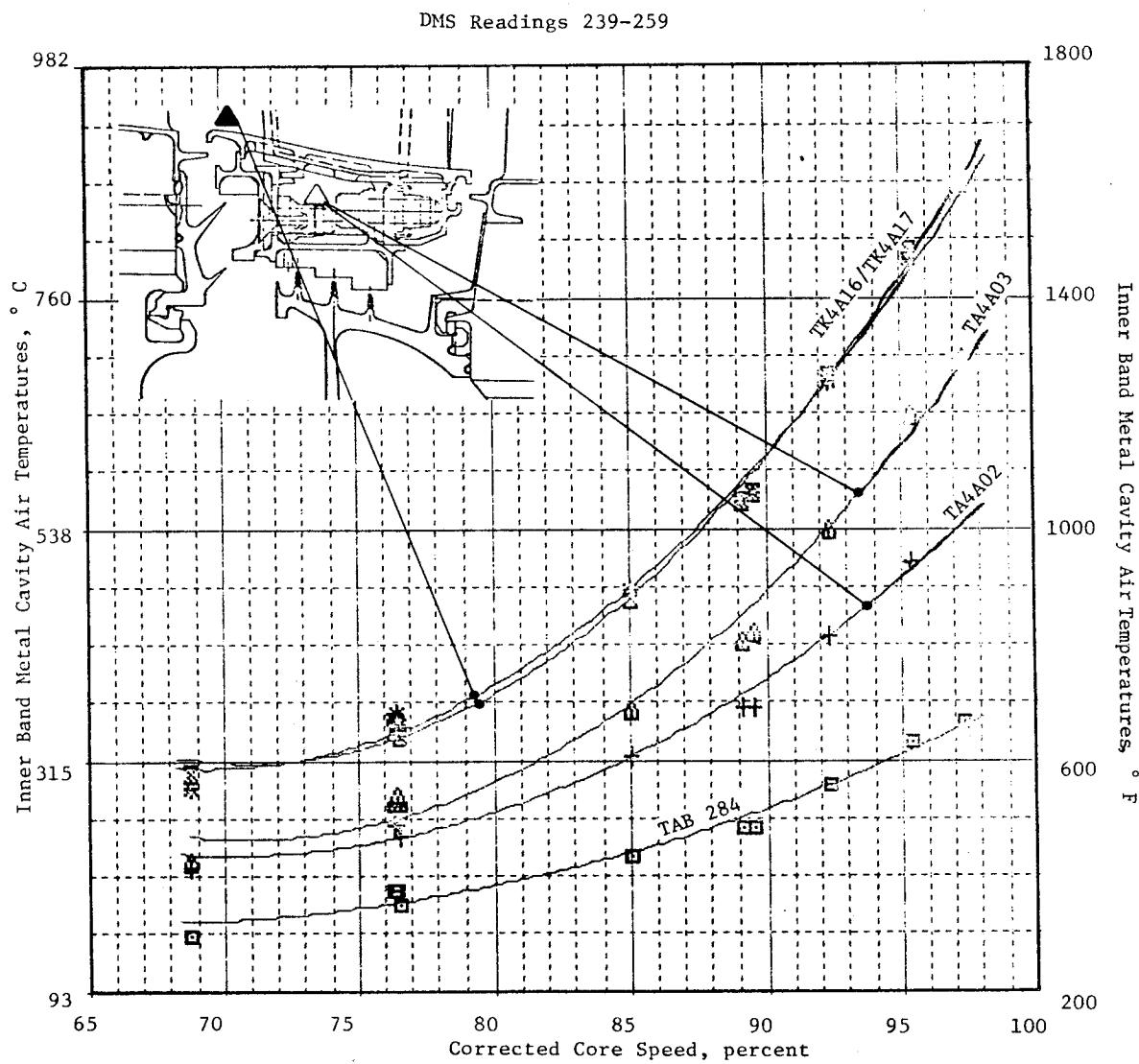


Figure 222. HP Turbine Stage 2 Nozzle Band and Interstage Cavity Air Temperatures.

Postcore test investigation has revealed that thermocouples TA4A05 and TA4A06 may have been reversed during the engine test. This would mean that the two air thermocouples forward of the interstage seal were TA4A04 and TA4A06, and those behind the seal were TA4A05 and TA4A07. The results presented in Figure 223 assume this to be the case. Confirmation of the correct installation and operation of any of the three pairs of interstage air thermocouples cannot be confirmed without a complete engine teardown.

Figure 224 shows the metal temperature distribution in the interstage disk. The temperature gradient from the front to the rear of the disk seal is as expected and provides a more realistic indication than that provided by the air thermocouples. The metal temperatures indicate a rise across the seal of approximately 11°C (20°F) at idle to 67°C (120°F) at maximum conditions. Figure 224 also indicates that there is a radial temperature gradient in the disk ranging from 50°C (90°F) at idle to 111°C (200°F) at maximum speed. The predicted cooling air temperature rise due to the increase in radius was approximately 90°C (125°F). When this temperature rise is combined with the heat input to the disk rim from the seal teeth, it appears that the interstage seal disk and surrounding cooling circuit are performing as expected.

Figure 225 shows the effect of the application of turbine ACC on the interstage cavity temperatures. Thermocouple TA4A03 at the 300° aft looking forward location showed a temperature reduction of 22°C (40°F) when ACC was applied. TA4A02 showed some response [11°C (20°F)] at lower speeds, but almost no effect at speeds above 94%. There was a reduction in local gas temperature when the ACC was applied [26°C (47°F) effect on average T41] which was reflected by a lowering of metal temperatures surrounding the interstage cavity. Figure 222 has already shown the interrelationship between the cavity air and inner band temperatures. In addition, the lower interstage seal flow, due to tighter seal clearances when ACC air was applied, made extra cooling air available to purge the forward cavity (behind the Stage 1 blade retainer) and reduced the recirculation of hot gases. A temperature reduction of 22°C (40°F) at the thermocouples would seem reasonable.

ORIGINAL PAGE IS
OF POOR QUALITY

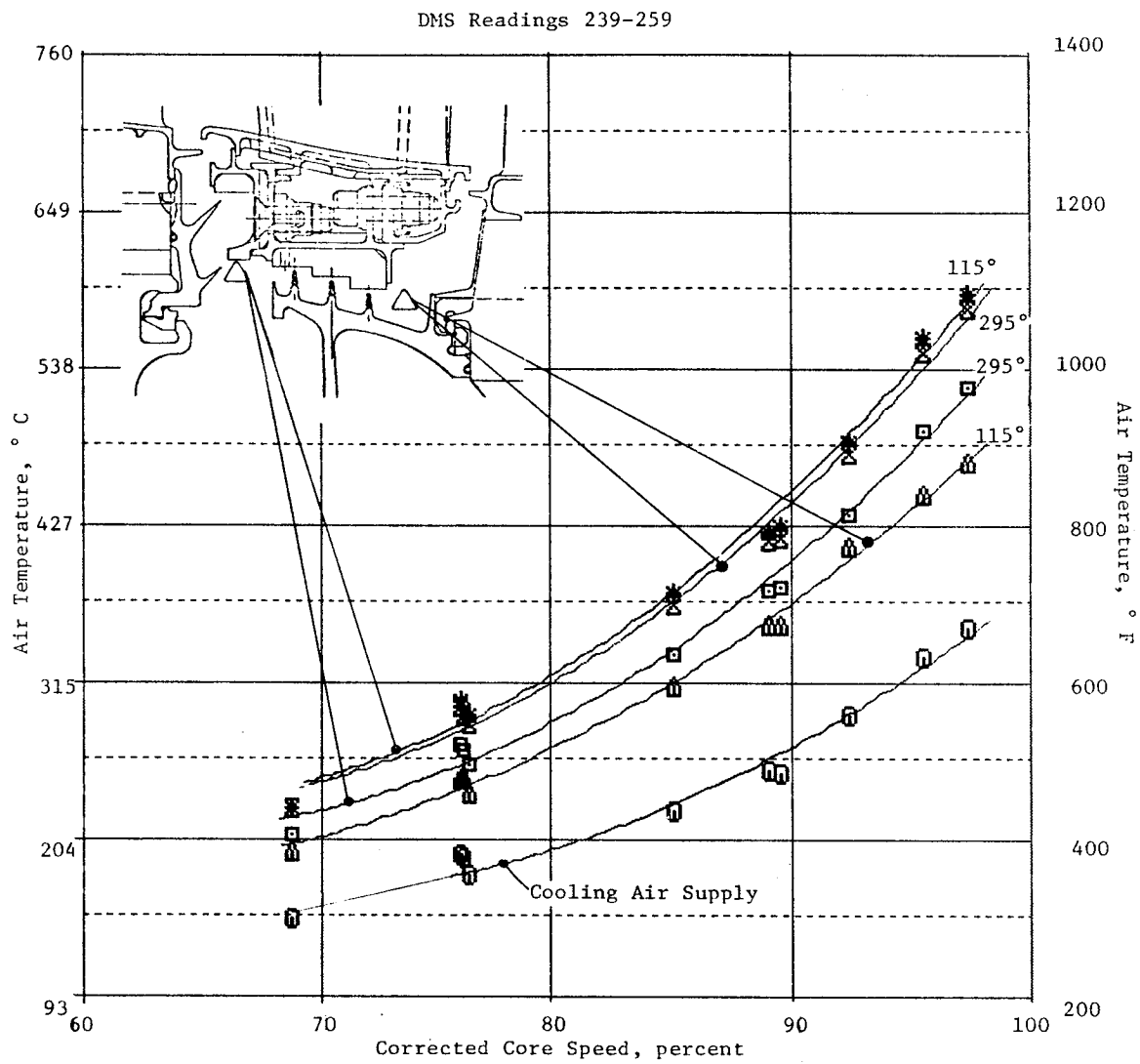


Figure 223. HP Turbine Interstage Seal Air Temperatures.

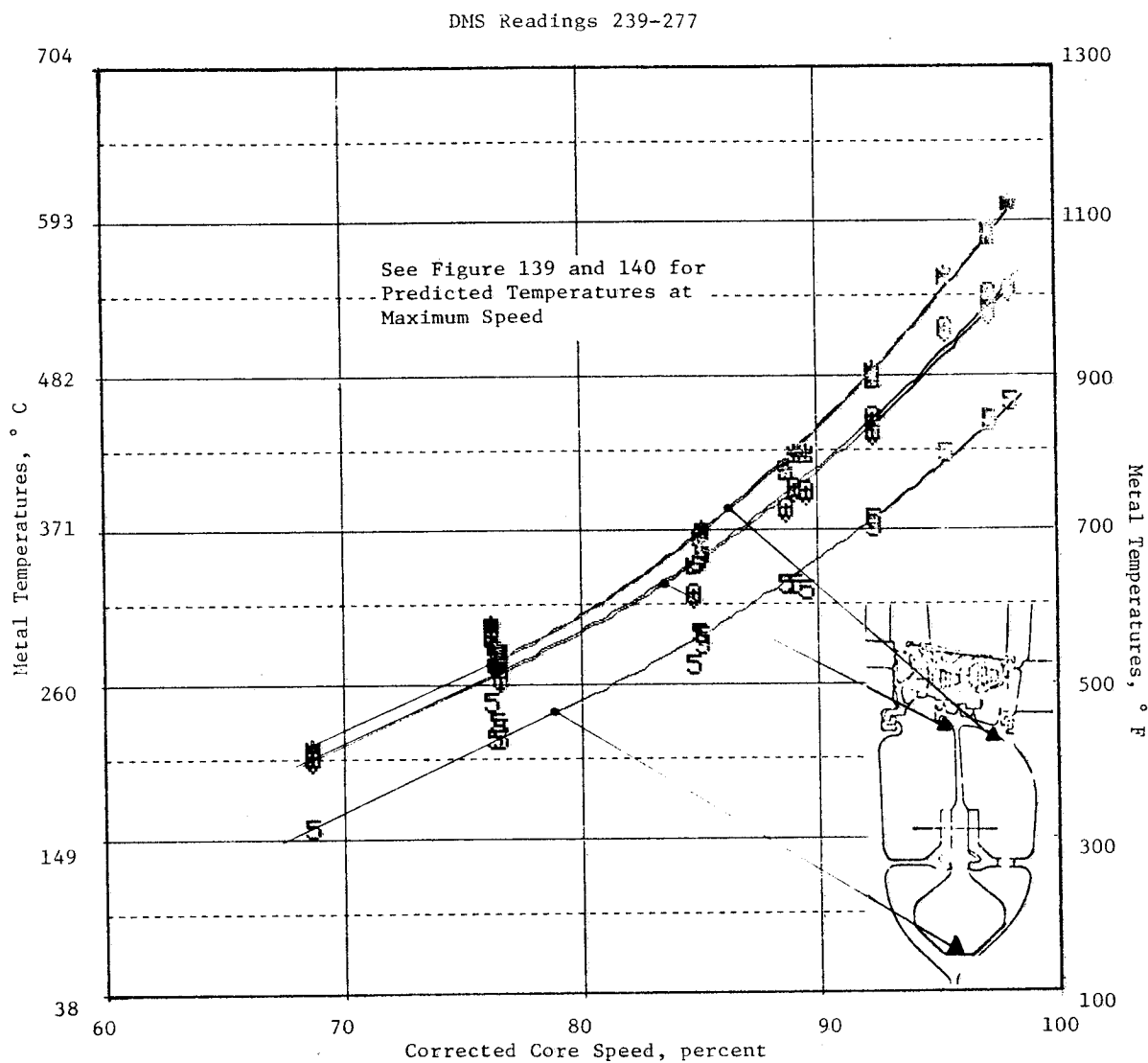


Figure 224. HP Turbine Interstage Disk Metal Temperatures.

ORIGINAL PAGE IS
OF POOR QUALITY

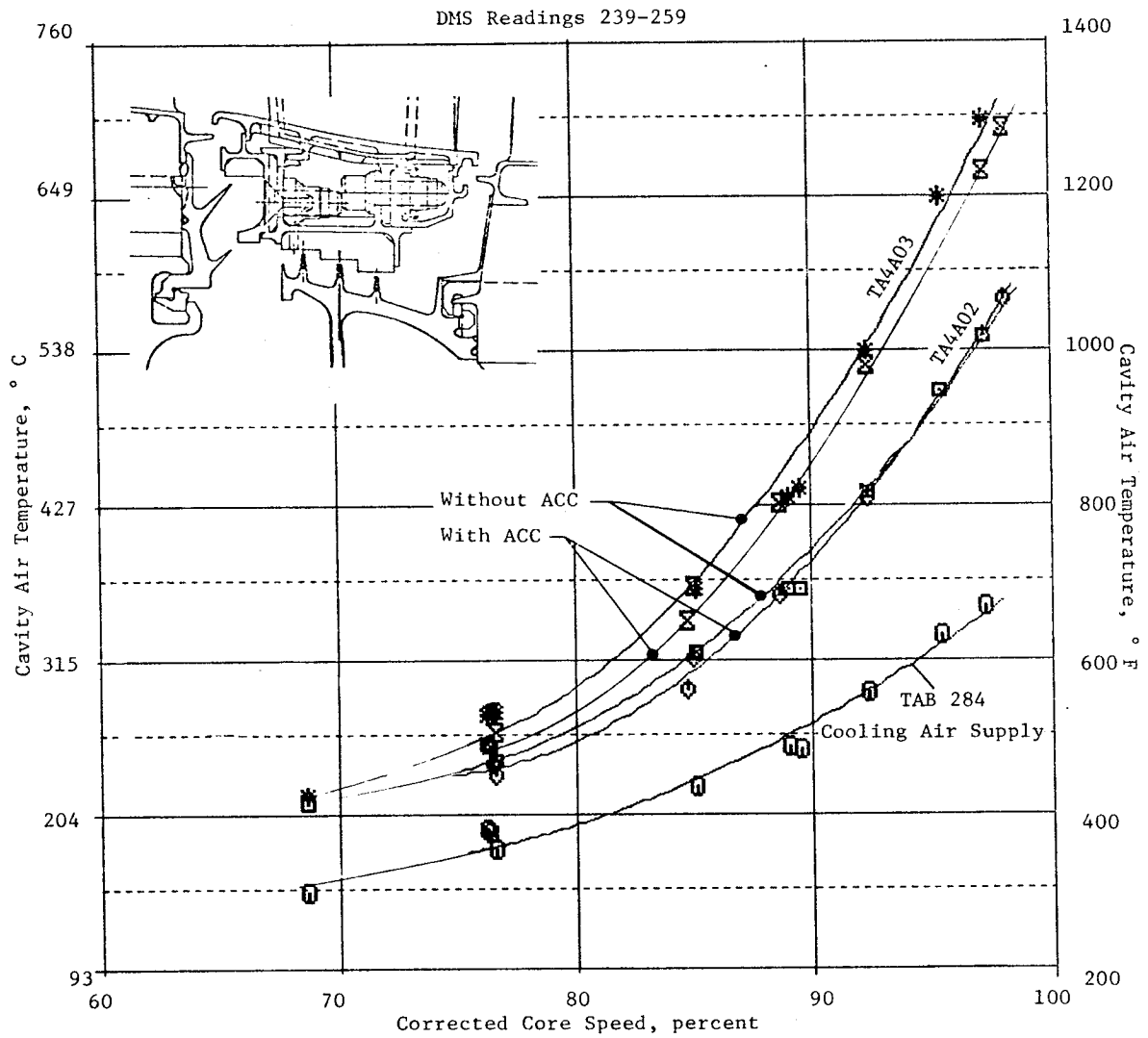


Figure 225. HP Turbine Interstage Cavity Air Temperatures.

Figure 226 shows the effect of ACC on the air temperature upstream of the interstage seal. Turbine ACC was operated above approximately 77.5% corrected speed and showed a marked effect on TA4A04 at 115° aft looking forward. Above 84% speed the ACC reduced the temperature by about 33° C (60° F). However, for the 295° aft looking forward location, a maximum temperature reduction of only 17° C (30° F) was achieved at approximately 85% when ACC was applied, and almost no change was indicated at speeds above 94%. As in Figure 225, the fall in gas temperature associated with ACC and the additional purge air in the forward cavity resulted in lower temperatures. A constant temperature reduction of approximately 33° C (60° F) was expected when the ACC was applied.

Figure 227 displays similar characteristics to Figure 226 and shows the effects of ACC on the air temperature downstream of the interstage seal. TA4A07 at the 295° (aft looking forward) location indicated a temperature reduction of about 33° C (60° F) consistently above 83% speed, similar to TA4A04. However, TA4A05 (located 115° aft looking forward) indicated a temperature drop of less than 11° C (20° F) at 85% speed and almost zero effect at maximum conditions. Under normal operation, it was expected that the aft cavity temperatures would increase when ACC was applied due to the reduction in cavity purge, caused by lower interstage seal flow and the increased seal heat input each unit flow.

The results of thermocouple TA4A07 do not substantiate this theory. However, if the overall reduction in heat input (due to lower gas temperatures) overcame the above effects, some small temperature reduction could be expected.

6.6.9 Outer Casing Temperatures

The HP turbine casing consists of a forward section and an aft section. The forward casing houses the Stage 1 shrouds and the aft member supports the Stage 2 shrouds, with both supporting the Stage 2 nozzle assembly. Thermocouples were located on the casing as shown in Figure 228. This instrumentation was used to monitor the temperature distribution around and along the casing during the core test.

ORIGINAL PAGE IS
OF POOR QUALITY

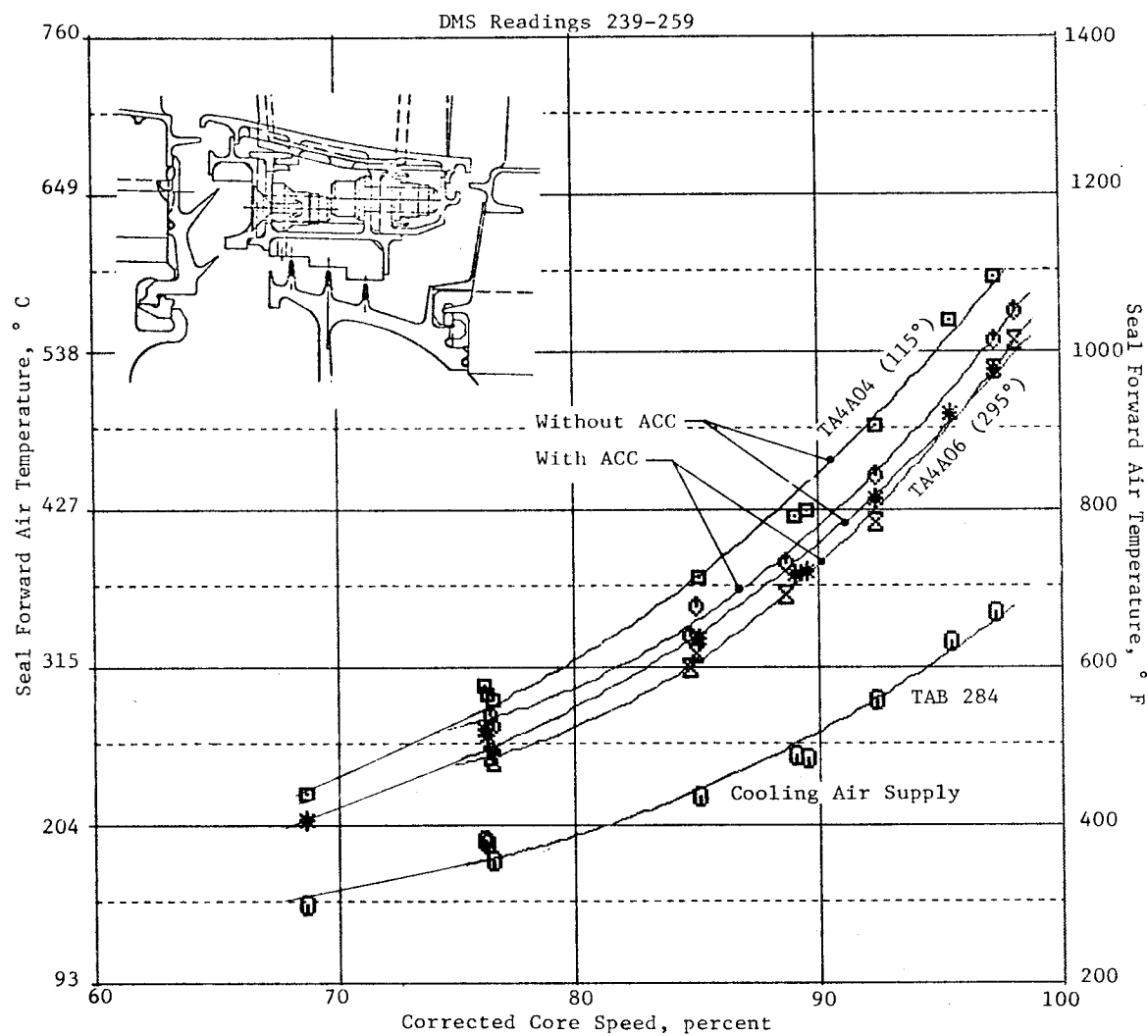


Figure 226. HP Turbine Interstage Seal Forward Air Temperatures.

ORIGINAL PAGE IS
OF POOR QUALITY

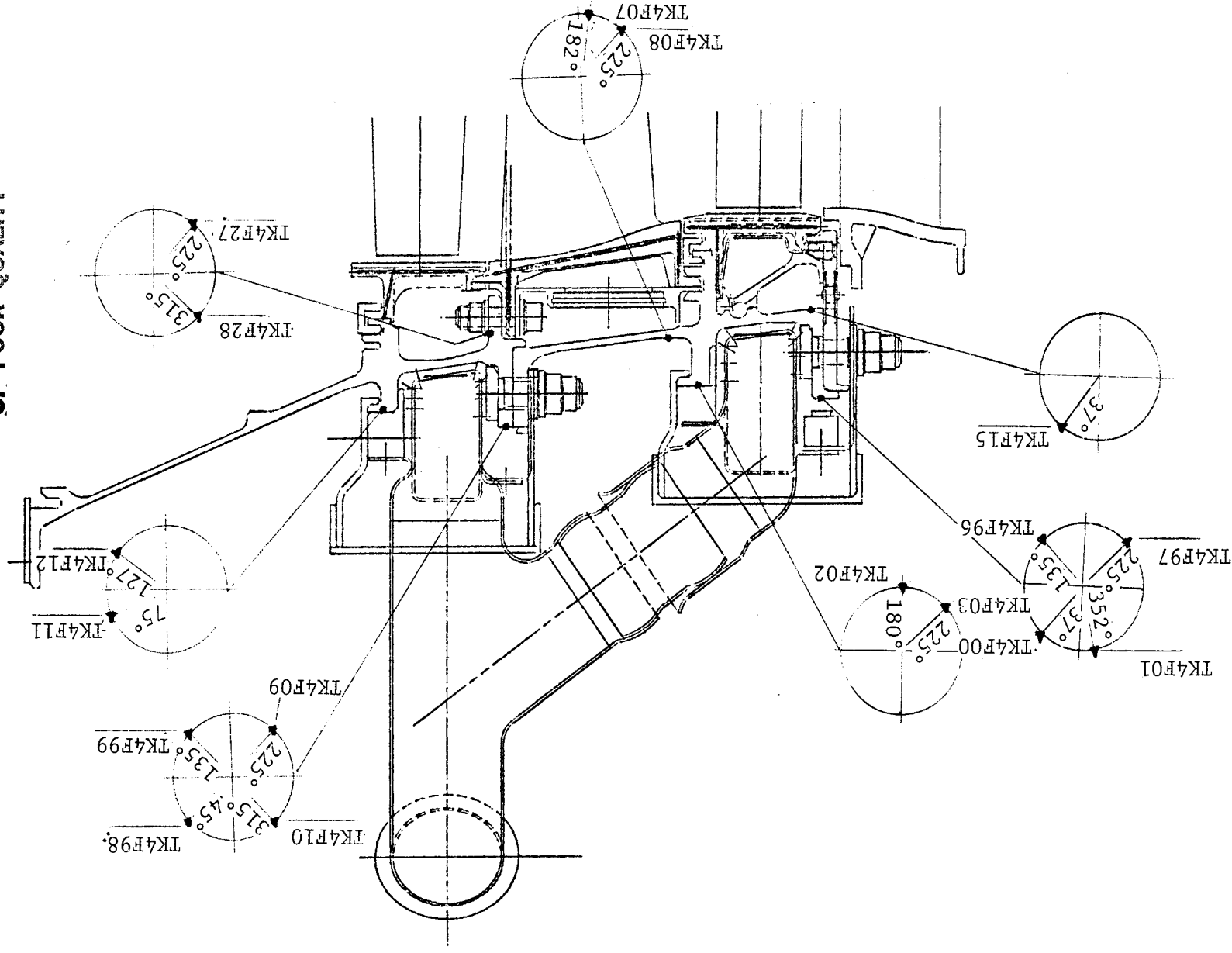


Figure 228. HP Turbine Casing Thermocouple Locations.

In general, the recorded test temperatures were far lower than the predicted values for all test runs. A typical comparison between predicted and recorded temperatures for the casing, as presented in Figures 229 and 230, indicated that circumferential temperatures at each axial location of the casing were reasonably uniform. Thermocouple TK4F15 depicted in Figure 228 did not function properly during the test and so no valid data was available at this location.

Investigation into the discrepancies between predicted and recorded temperatures revealed two contributing factors: One, the predicted temperatures were calculated based on boundary conditions for the FPS at 50° C (122° F) steady-state takeoff, whereas the test cell condition was 29° C (85° F). This difference, though small, did contribute to certain deviations. Two, and the more dominant factor, is that during the core test the casing was totally exposed to and in direct contact with the test cell environment. Test cell air, entrained by the exhaust, flowed past the outer casing external surfaces at such a significant high speed that the casing was substantially surface cooled during engine running. The magnitude of this cooling increased in relationship to the proximity with the exhaust; this explains why the Stage 2 casing temperature discrepancies between predicted and recorded values were much larger than those of Stage 1 (Figures 229 and 230). The lower than expected casing temperature had a direct impact on the ACC system; it reduced the performance of the system, a topic that will be discussed in the ACC section.

A cowling will surround and isolate the HP turbine casing in the upcoming ICLS engine test. The configuration is expected to keep the casing temperatures more in line with the predicted values, which in turn will give greater response to the ACC system.

HPT Shrouds

The shroud instrumentation consisted of embedded and surface-mounted thermocouples as depicted in Figure 231 for Stages 1 and Stage 2. Out of 24 shrouds for each stage, two Stage 1 and three Stage 2 shrouds were instrumented. Some thermocouples in Stage 1 were lost during engine assembly.



Predicted Bulk Average Temperature at 50° C/122° F Day SLS Takeoff (FPS)



Actual Test Temperature at 29° C/85° F

P = 101.4 kPa (14.7 psi) Cell Condition

All T/C Locations Are Aft Looking Forward, Clockwise

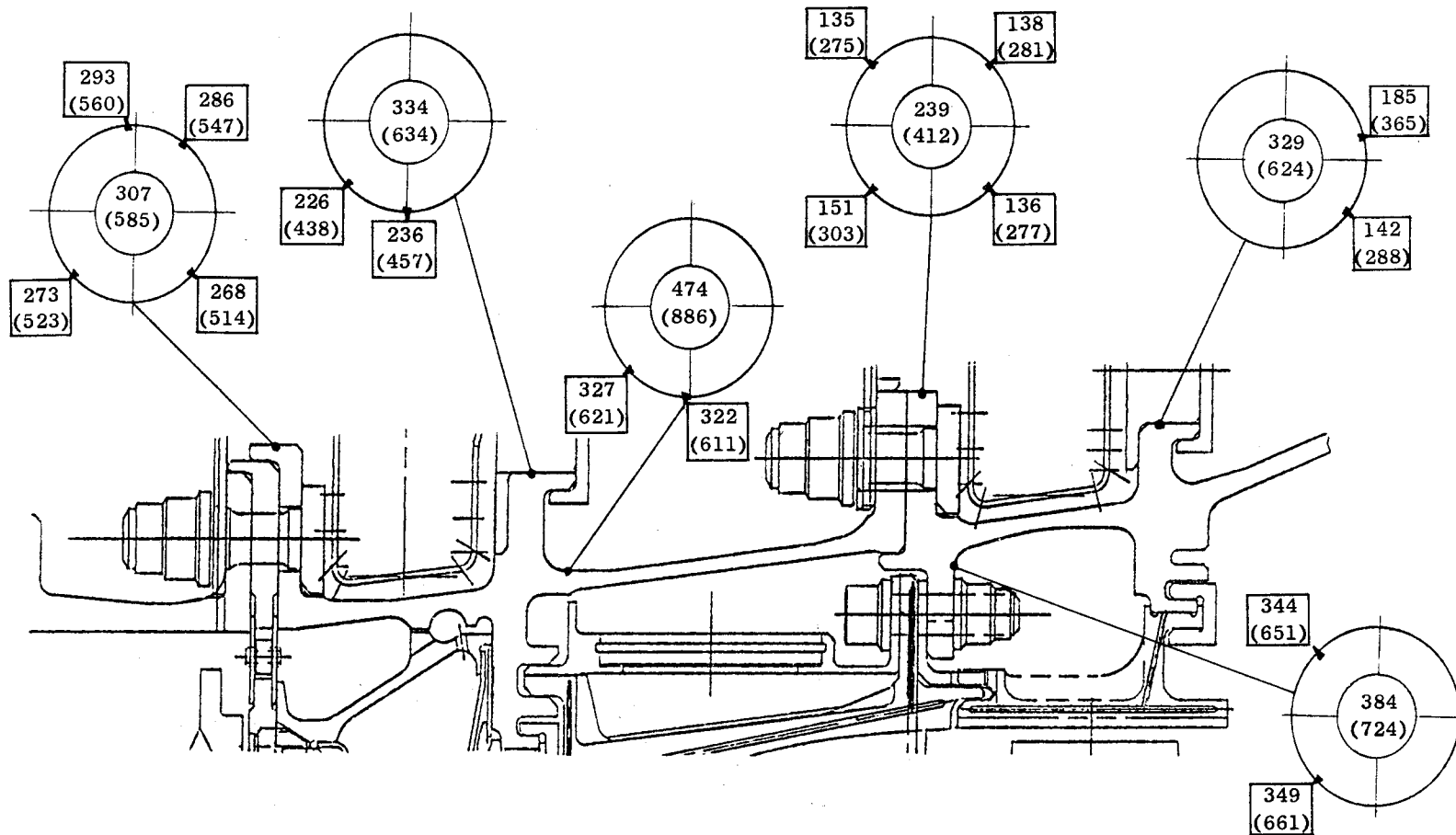

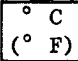


Figure 229. HP Turbine Casing Temperature Distribution (With ACC Cooling, DMS No. 258).

 Predicted Bulk Average Temperature at 50° C/122° F Day SLS Takeoff (FPS)
 Actual Test Temperature at 29° C/85° F, P = 101.4 kPa (14.7 psi) Cell Condition

All T/C Locations Are Aft Looking Forward, Clockwise

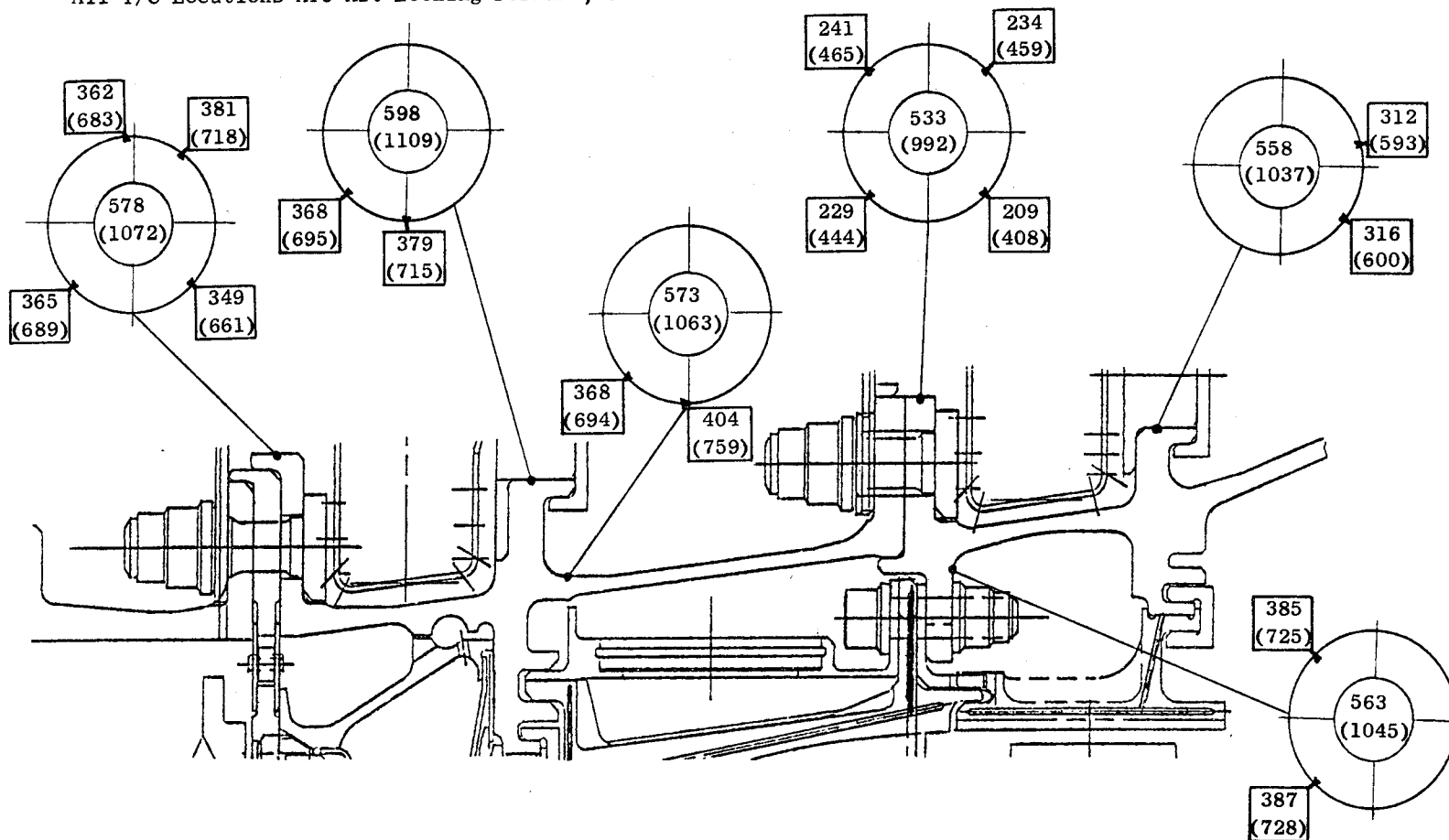


Figure 230. HP Turbine Casing Temperature Distribution (No ACC Cooling, DMS No. 256).

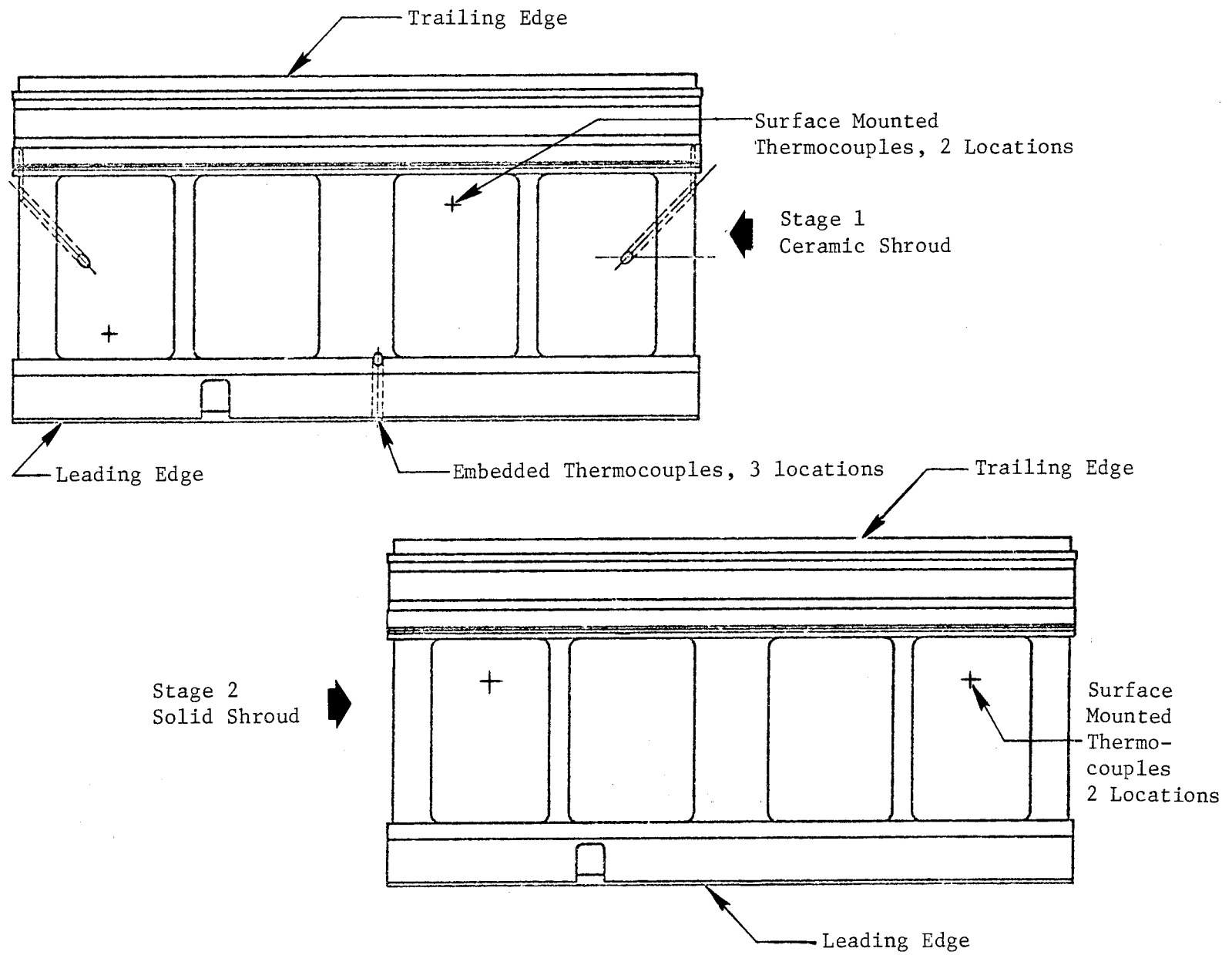


Figure 231. HP Turbine Shroud Thermocouple Locations.

The recorded data showed that for Stage 1 (Figure 232), the backside temperatures (TK4F19, TK4F21) and the aft temperatures near the flowpath (TK4F24, TK4F25, TK4F26) were near the predicted value. However, the temperatures at the front and near the flowpath (TK4F17) indicated a cooler level than expected. A check of the amount of impingement cooling flow to the back of the shroud revealed that it was less than predicted and, consequently, could possibly have produced hotter temperatures at the leading edge, which contradicts the recorded cooler measurement. It is strongly suspected that thermocouple TK4F17 registered a temperature somewhere other than the location intended.

All backside temperatures at the aft end of the Stage 2 shrouds were near the predicted value (Figure 233), except for thermocouple TK4F31 which did not respond properly during the test.

6.6.10 HP Turbine Clearances and Active Clearance Control

Initial Clearances

The blade tip running clearances on both Stage 1 and 2 during early testing with ACC off were less than predicted. Figures 234 and 235 show the predicted clearance along with the average actual clearance as indicated by the four laser probe readings at each stage.

The difference between actual and predicted clearances was approximately 0.56 mm (0.022 inch) and 0.51 mm (0.020 inch) for Stage 1 and 2, respectively. Review of the measured casing temperatures revealed that they were lower than predicted as shown in Figures 236 and 237. The casing temperatures were 83° C (182° F) or more below those that were expected.

An extensive effort was made to understand why the casing was significantly cooler than anticipated, and DMS Reading 258 was chosen for the condition at which the analysis was primarily done. The expected casing temperatures at that T3 and T41 condition without any ACC cooling is presented in Figure 238. The actual indicated metal temperatures at the same T3 and T41 condition are presented in Figure 239. Since DMS Reading 258 was taken with ACC on, the data was obtained using DMS Reading 256 which was at a slightly

ORIGINAL PAGE IS
OF POOR QUALITY

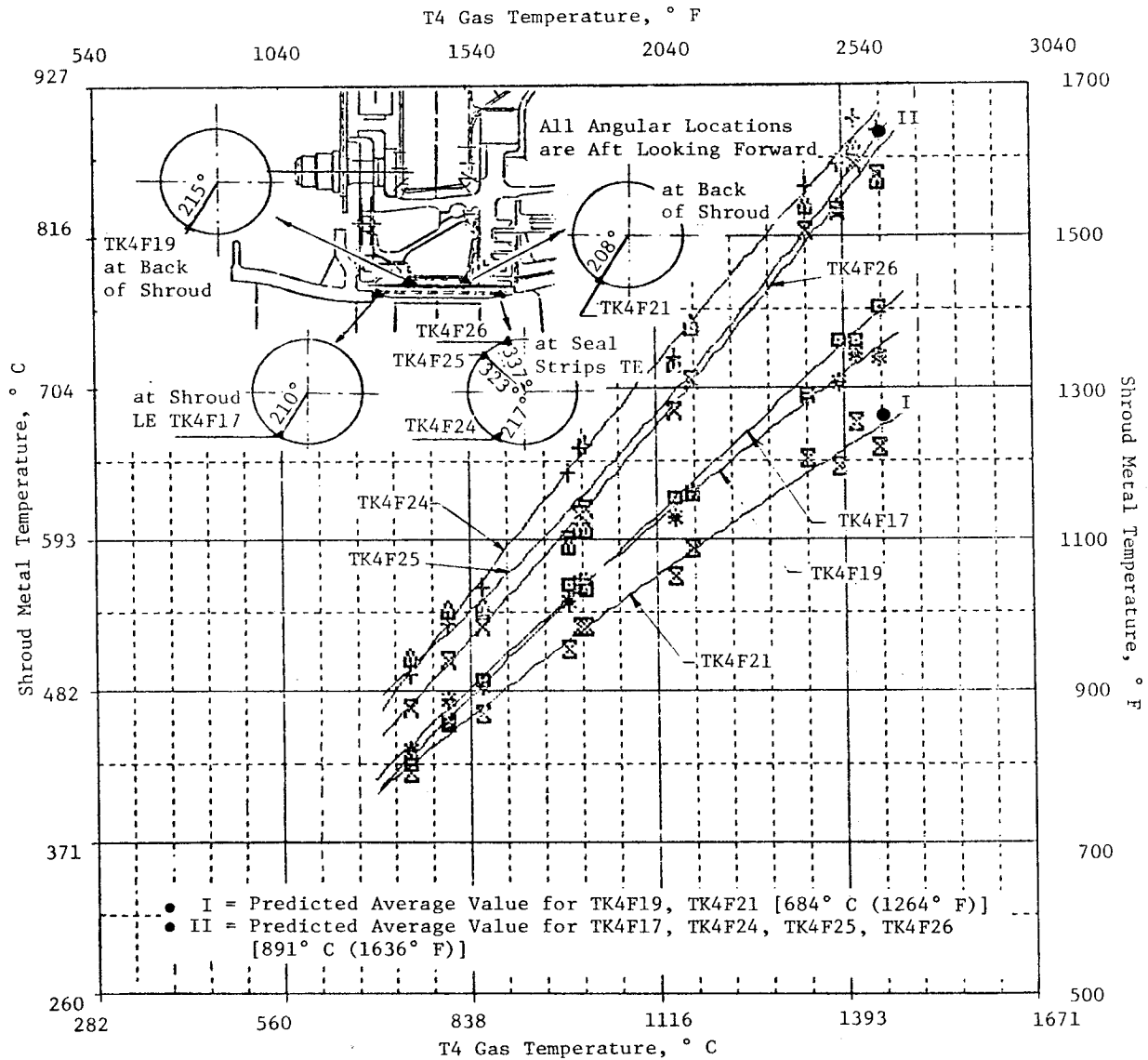


Figure 232. HP Turbine Stage 1 Shroud Temperatures.

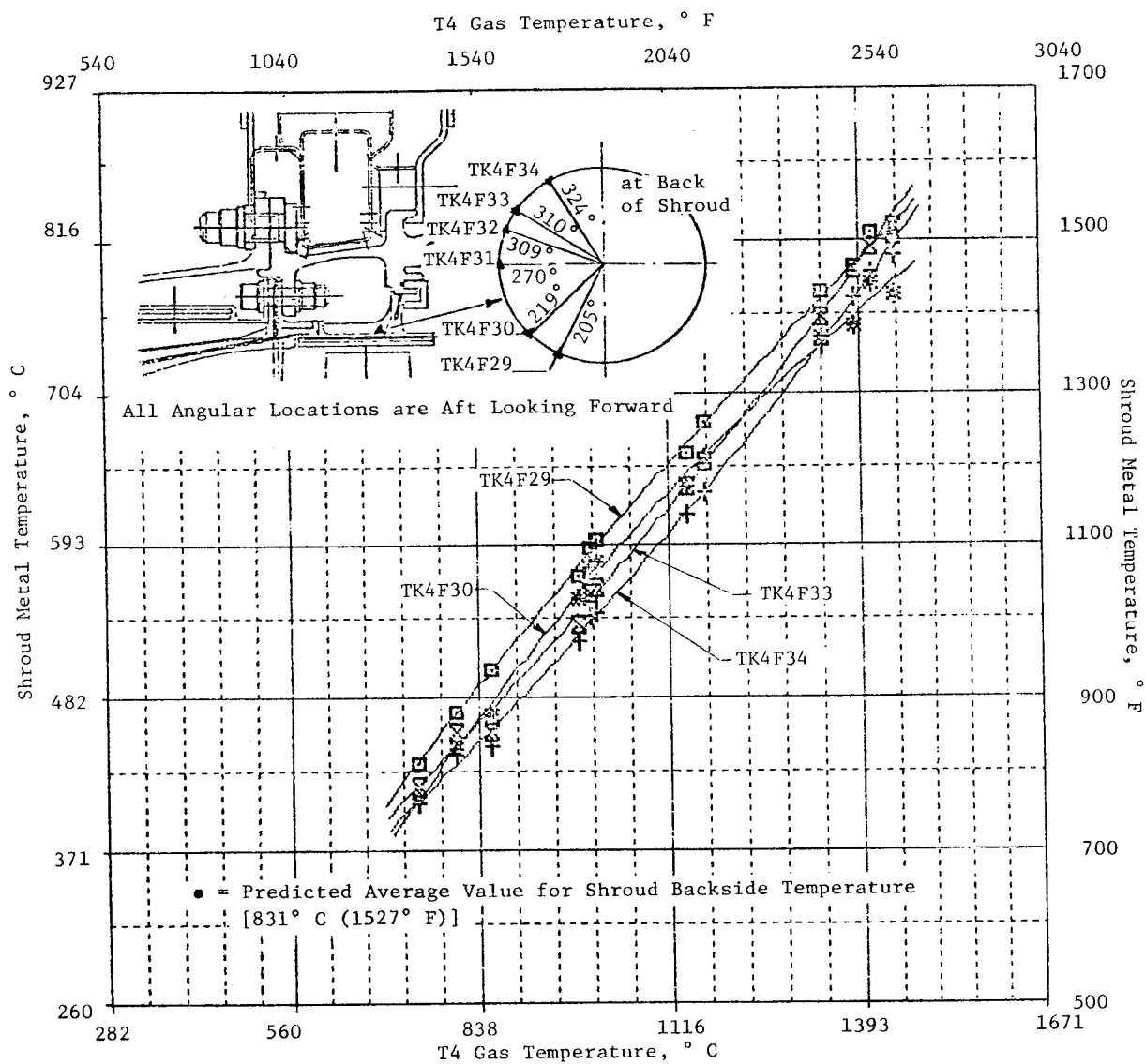


Figure 233. HP Turbine Stage 2 Shroud Temperatures.

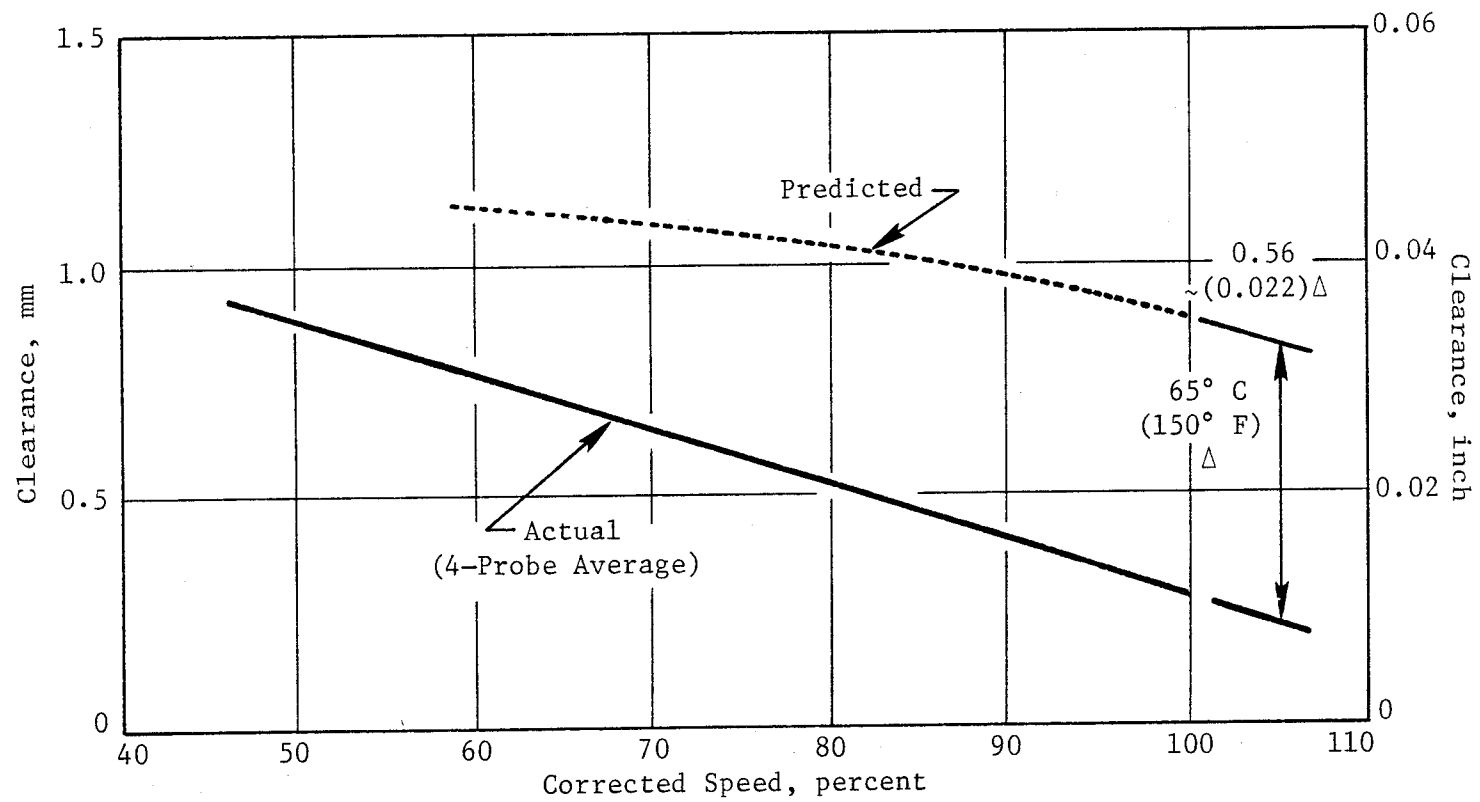


Figure 234. HP Turbine Stage 1 Blade Tip Clearance Versus Speed (Prior to Rub), ACC Off.

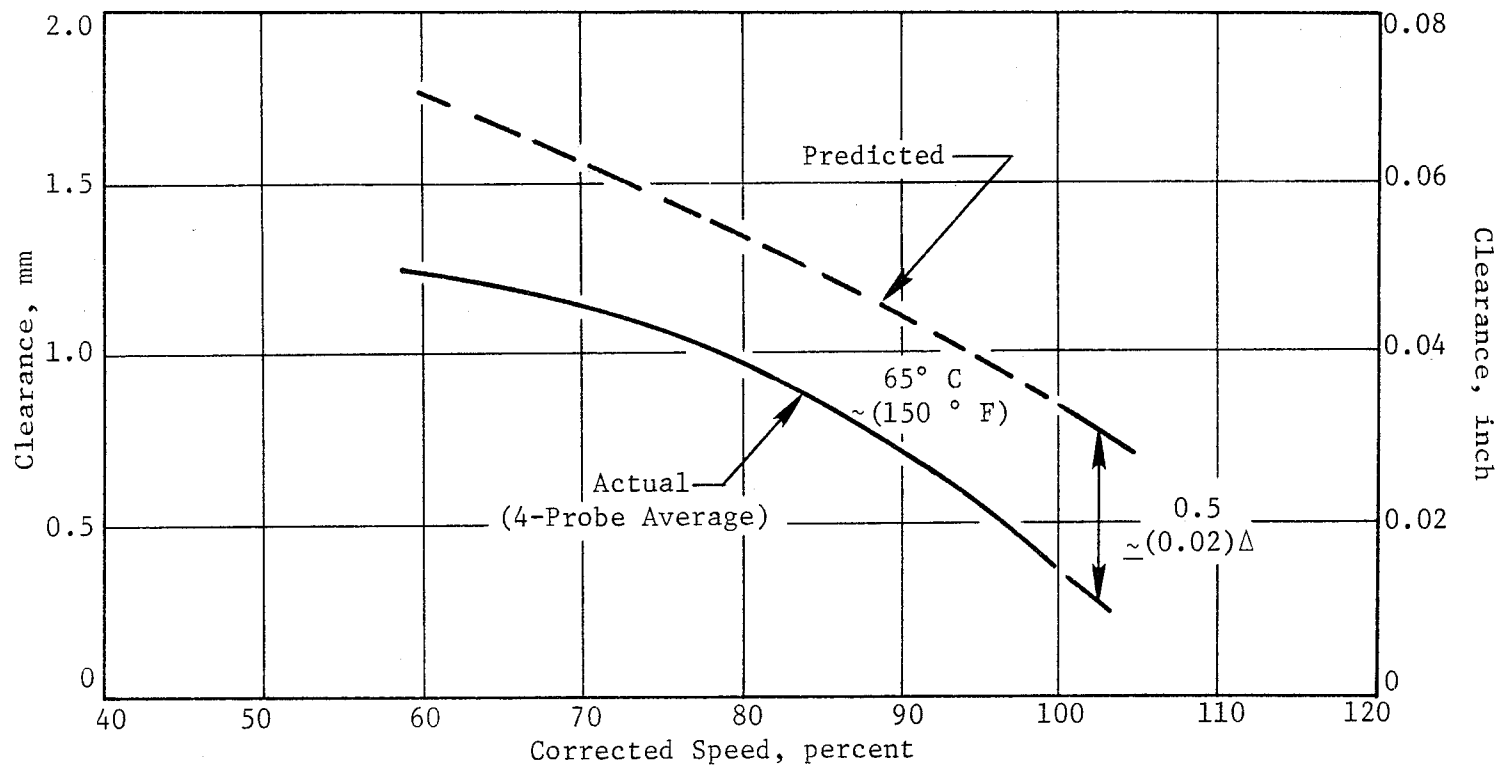


Figure 235. HP Turbine Stage 2 Blade Tip Clearance Versus Speed (Prior to Rub), ACC Off.

ORIGINAL PRINTED
OF POOR QUALITY

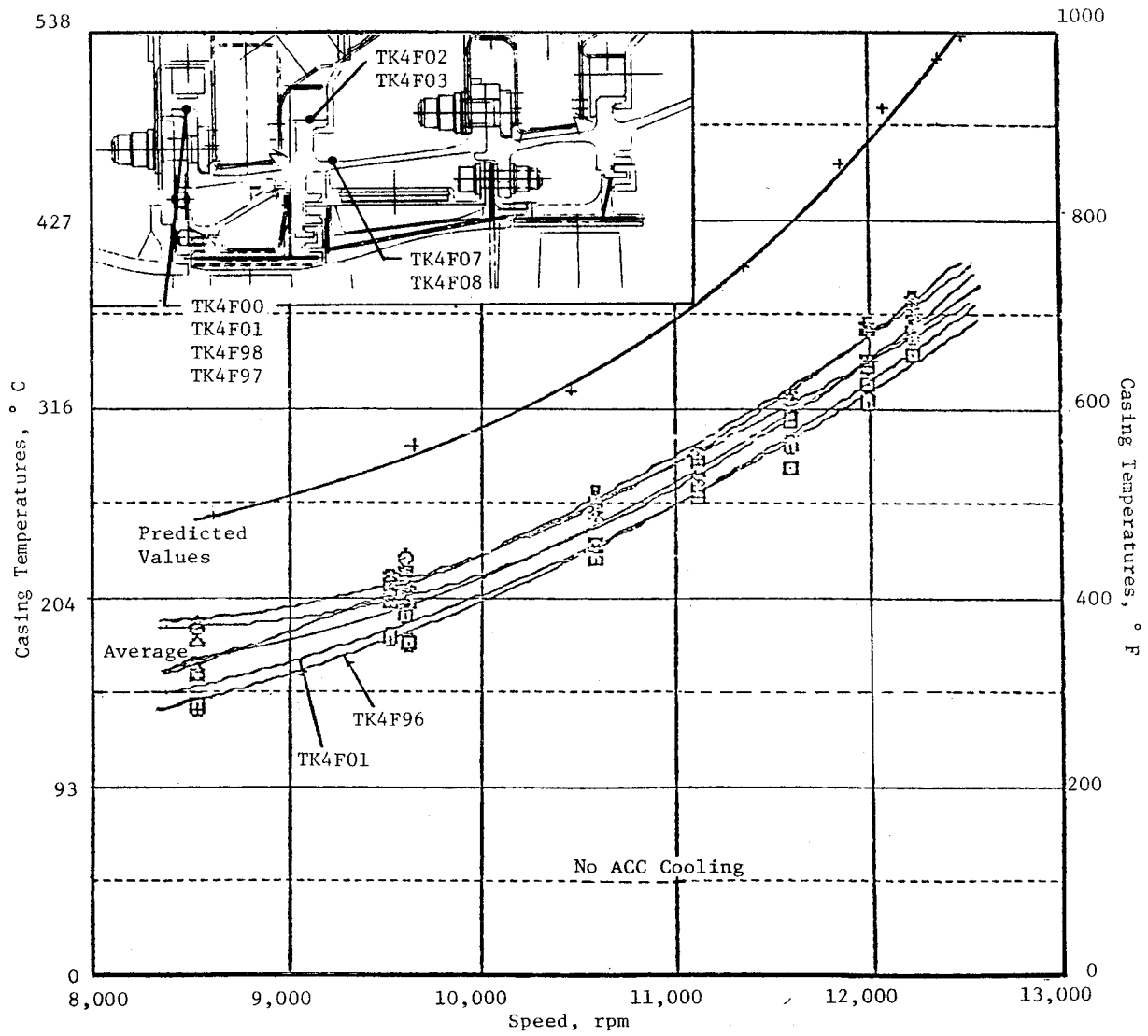


Figure 236. HP Turbine Stage 1 Casing Temperatures Versus RPM.

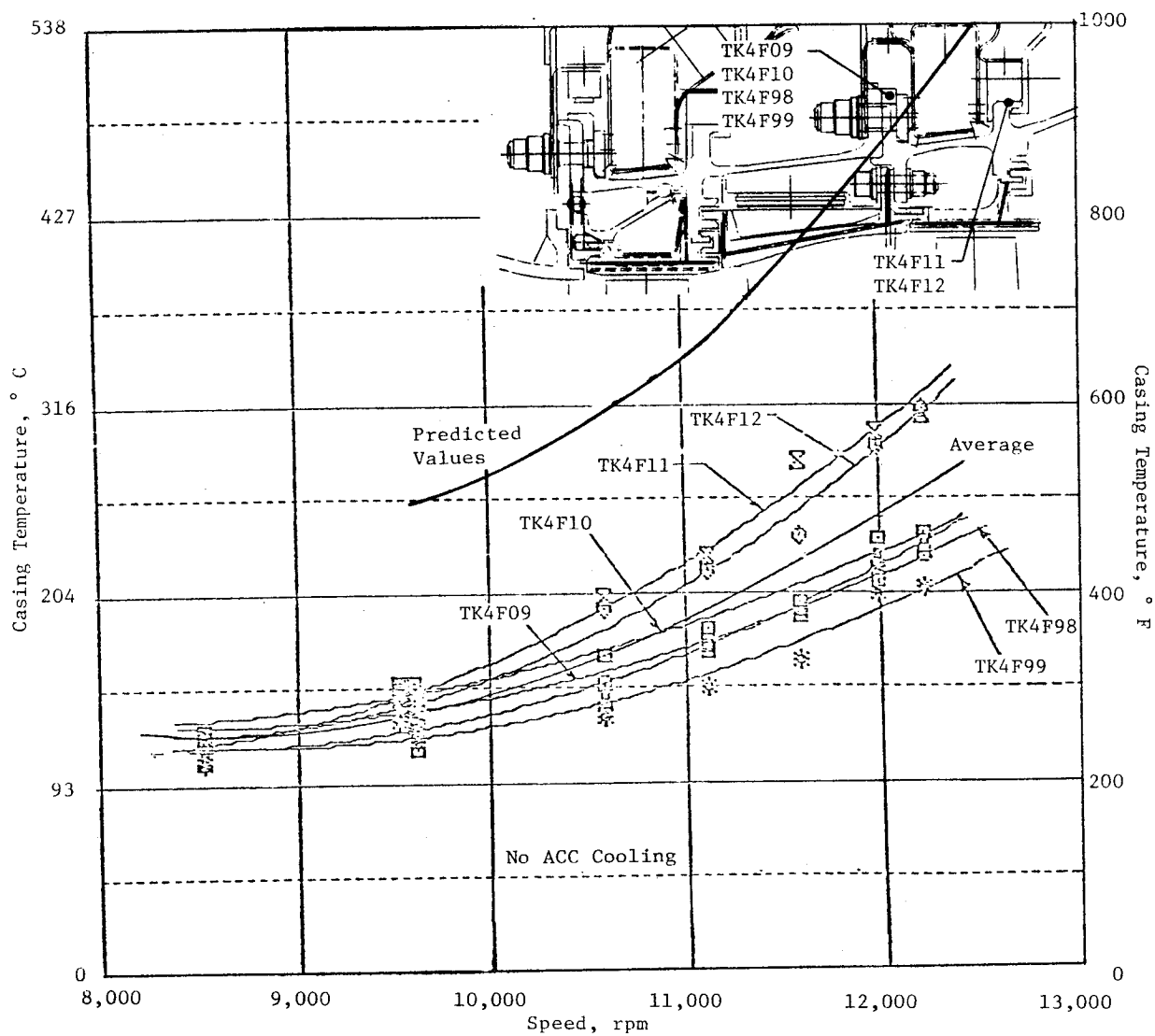


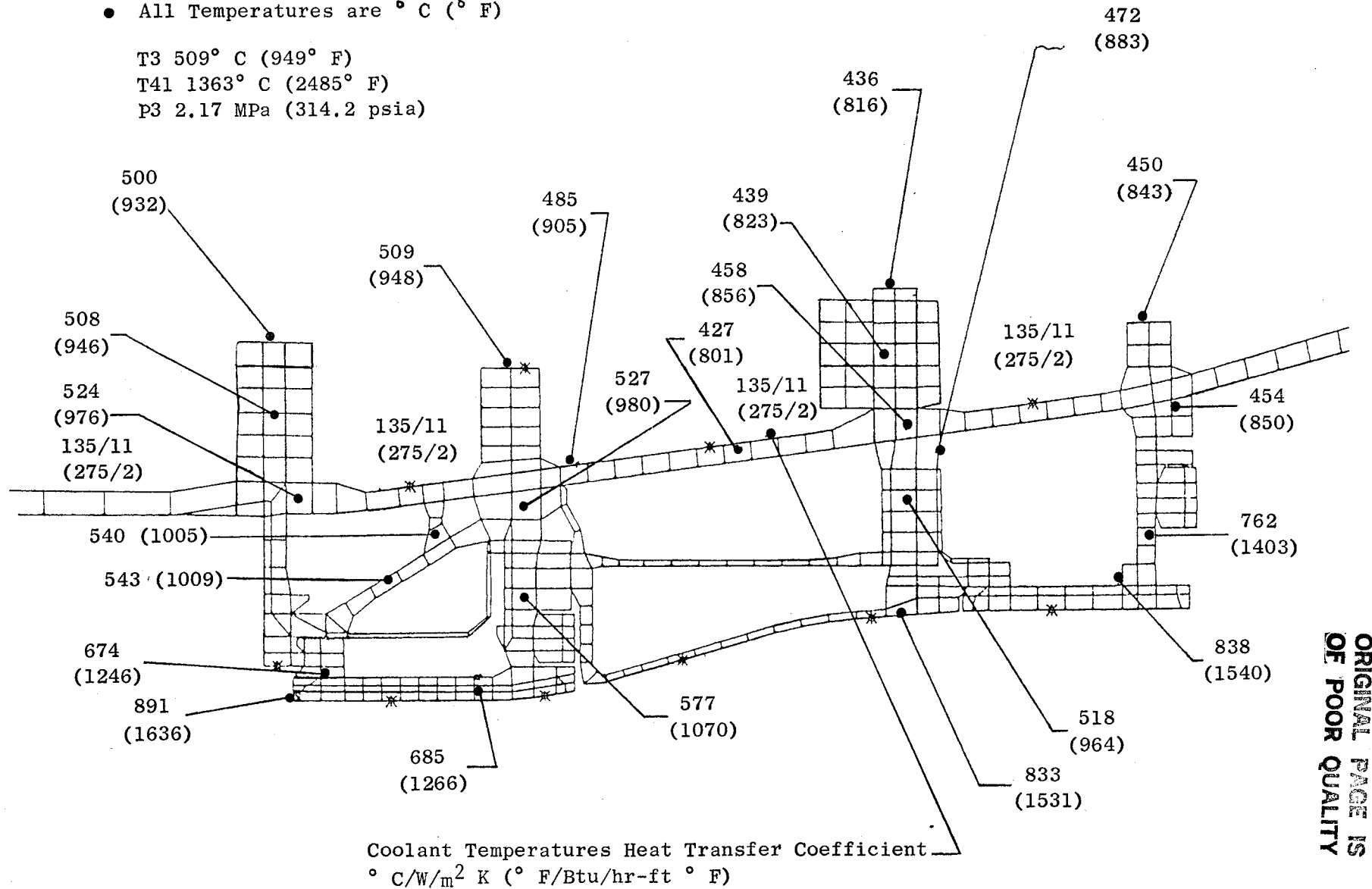
Figure 237. HP Turbine Stage 2 Casing Temperatures Versus RPM.

• All Temperatures are ° C (° F)

T3 509° C (949° F)

T41 1363° C (2485° F)

P3 2.17 MPa (314.2 psia)



ORIGINAL PAGE IS
OF POOR QUALITY

Figure 238. HP Turbine Anticipated Casing Temperatures Without ACC Cooling or Test Cell Entrainment.

- All Temperatures are ° C (° F)

T41 1363° C (2485° F)

T3 509° C (949° F)

T_{Meas} Indicated Metal Temperatures After
Extrapolating from 256 to 258 Cycle
Conditions

T_{Avg} Average of T_{Meas} Temperatures

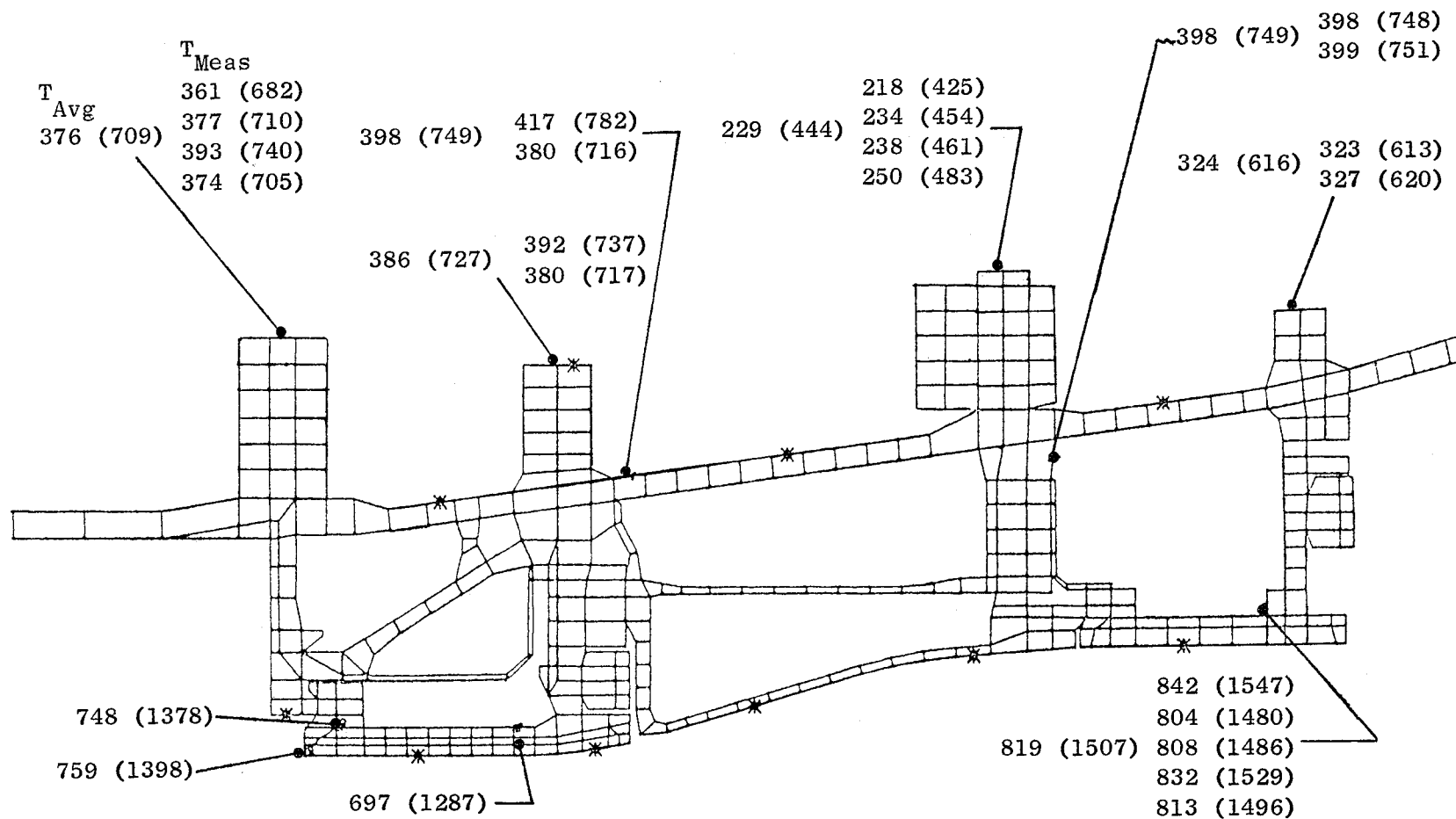


Figure 239. HP Turbine Measured Casing Temperatures Without ACC Cooling (DMS No. 256).

lower T3 and T41 (that is, measured casing temperatures from DMS Reading 256, no ACC air, were extrapolated up to the T3 and T41 levels consistent with DMS Reading 258). The data showed substantial variation in the outer ring surface temperature from predicted values, as tabulated below.

Ring No.	Stage 1		Stage 2	
	1	2	3	4
Average Anticipated Outer Ring Surface Temperature, ° C (° F)	500 (932)	509 (948)	436 (816)	451 (843)
Average Measured Outer Ring Surface Temperature, ° C (° F)	376 (709)	386 (727)	229 (444)	324 (616)
Average Temperature Variation, ° C (° F)	-124 (-223)	-123 (-221)	-206 (-372)	-126 (-227)

Analysis was then directed toward explaining temperature variations of the above magnitude. Using the detailed thermal analysis model, the external boundary conditions (heat transfer coefficients and air temperatures) were adjusted in an effort to match the indicated metal temperatures of Figure 239. It was found that the heat transfer coefficient had to be increased significantly over what might be expected for a quiescent environment surrounding the core turbine casing in an actual engine. Investigation of test cell history revealed that during other engine tests the casings were generally cooler than anticipated.

The measured test cell pressure during the test indicated a drop below the ambient barometric pressure as the engine was brought up to maximum power, an indication that ambient air was being entrained with the hot exhaust gases and pumped out the exhaust stack. The reduction in the test cell pressure indicated there was an effective air velocity of 64 km/h (40 mi/h) entering the cell to replace the air that was entrained with the engine exhaust. The most significant source of ambient air was a standard size 0.9 x 2.4 m (3 x 8 ft) test cell door that was kept open during the test. This information lead to the conclusion that a substantial quantity of ambient air was being entrained with the exhaust gases and was cooling the casing as it approached the engine exhaust nozzle. A fan that had been placed in the test cell to

make the casing temperatures more uniform enhanced the circulation of the ambient air from the front of the engine and increased the local velocity of the air over the casing as it flowed to the engine exhaust nozzle.

A detailed analytical data match was accomplished for DMS Reading 258 as adjusted for no ACC (Figure 240). In order to match the analytical temperatures with the measured values, the external heat transfer coefficient had to be increased from $11 \text{ W/m}^2 \text{ K}$ ($2 \text{ Btu/hr-ft}^2 \text{ }^\circ \text{ F}$) to $57 \text{ W/m}^2 \text{ K}$ ($10 \text{ Btu/hr-ft}^2 \text{ }^\circ \text{ F}$) over the aft section of the combustor casing and from $11 \text{ W/m}^2 \text{ K}$ ($2 \text{ Btu/hr-ft}^2 \text{ }^\circ \text{ F}$) to $130.23 \text{ W/m}^2 \text{ K}$ ($23 \text{ Btu/hr-ft}^2 \text{ }^\circ \text{ F}$) over the HP/LP transition casing. This reinforced the conclusion that the test cell air was being entrained with the exhaust gases and was accelerating as it approached the exhaust nozzle. In the casing area covered by the ACC impingement baffle, the analytical heat transfer coefficients had to be increased from $11 \text{ W/m}^2 \text{ K}$ ($2 \text{ Btu/hr-ft}^2 \text{ }^\circ \text{ F}$) to $19 \text{ W/m}^2 \text{ K}$ ($3.3 \text{ Btu/hr-ft}^2 \text{ }^\circ \text{ F}$) for Stage 1 and to $40 \text{ W/m}^2 \text{ K}$ ($7 \text{ Btu/hr-ft}^2 \text{ }^\circ \text{ F}$) for Stage 2. Using the data match temperature distribution of DMS Reading 258, the bulk average ring temperature variation and resulting clearance difference were calculated.

	<u>Stage 1</u>	<u>Stage 2</u>
Anticipated Bulk Average Ring Temperature, $^\circ \text{ C}$ ($^\circ \text{ F}$)	516 (961)	464 (868)
Data Match Indicated Bulk Average Ring Temperature, $^\circ \text{ C}$ ($^\circ \text{ F}$)	449 (841)	359 (679)
Temperature Difference (Due to Test Cell Air Entrainment), $^\circ \text{ C}$ ($^\circ \text{ F}$)	66 (120)	105 (189)
Calculated Clearance Difference, mm (inch)	0.43 (0.017)	0.69 (0.027)

Stage 2 showed a greater temperature difference due to closer proximity of the exhaust nozzle and therefore higher local velocity of cell air.

The clearance difference indicated above agrees essentially with the measured differences of 0.56 mm (0.022 inch) and 0.5 mm (0.020 inch) for Stage 1 and 2, respectively, as indicated in Figures 234 and 235. The variation of 0.08 to 0.13 mm (0.003 to 0.005 inch) can be the result of a 11° to 19° C (20° to 25° F) error in establishing the bulk average temperatures.

- All Temperatures are ° C (° F)

T3 509° C (949° F)

T41 1363° C (2485° F)

P3 2.17 MPa (314.2 psia)

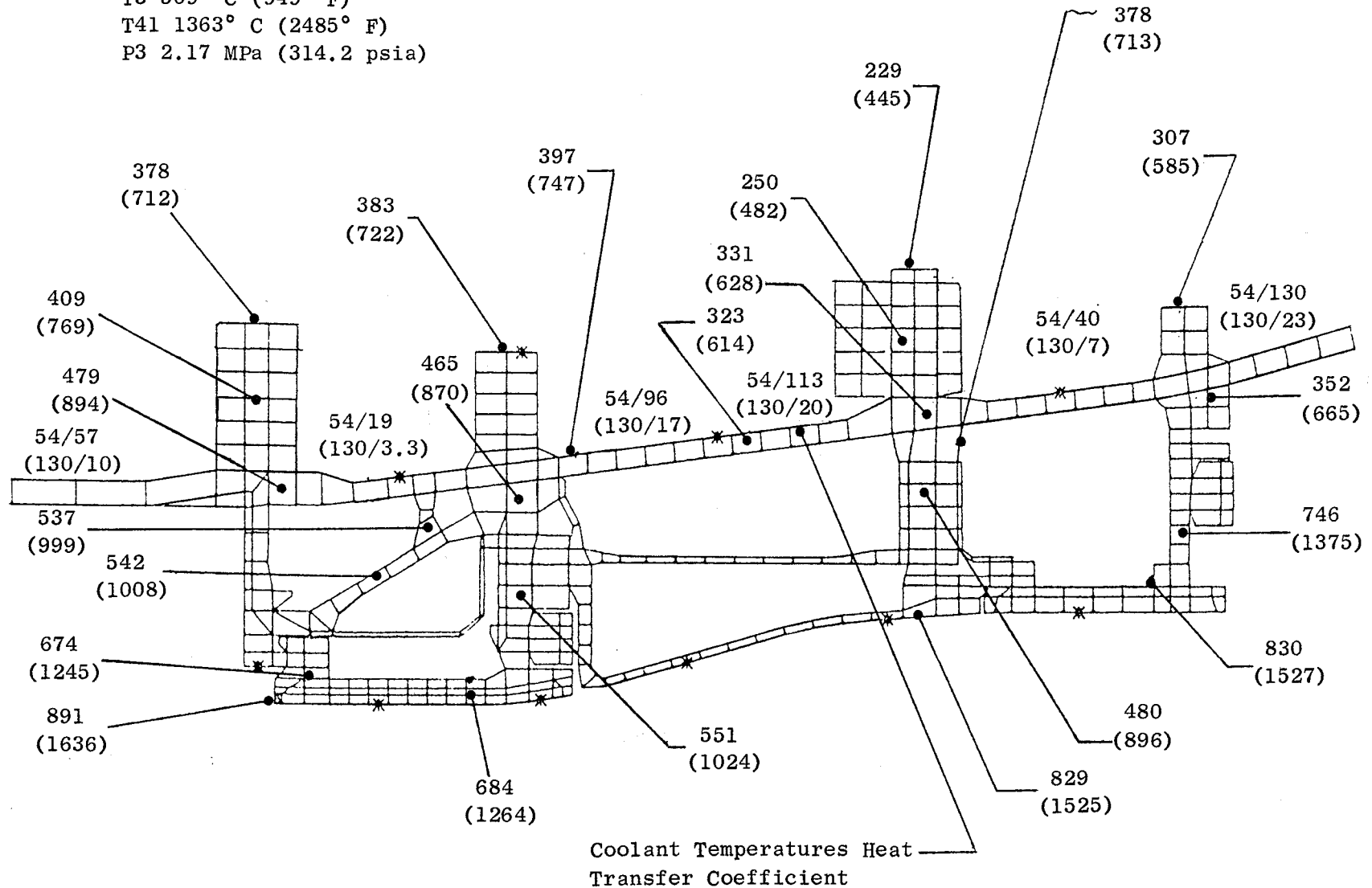


Figure 240. HP Turbine Best Data Match of Extrapolated Data to Cycle Conditions .
(No ACC Cooling).

Rub Occurrence

A significant rub occurred during the first approach to high speed when the HP turbine casing was suddenly and locally overcooled by the air pipe flanges failure reported previously.

Figure 241 shows a schematic of the piping with the failure location. Figure 242 shows the casing temperatures as maximum speed was approached. Cooling system instrumentation indicated the pipe failed after a reading at 93% speed and prior to the reading at 94.6%; Figure 242 also shows the dramatic drop in casing temperatures between these speed points. Both the most forward and the most aft rings indicated no drop in temperature because the thermocouples were located in a circumferential position away from the failure.

Average clearance readings from the four laser probes at each stage, before and after the pipe failure, are shown in Figures 243 and 244. It is apparent that approximately 0.38 mm (0.015 inch) and 0.76 mm (0.030 inch) of material was removed from the Stage 1 and 2 blade tips, respectively.

Out-Of-Roundness

The laser clearance probe readings indicated a variation in clearance around the circumference of the engine during the initial test run. This variation from average is shown in Figures 245 and 246. Subsequent to the first run, a fan was placed in the front of the test cell to improve circulation and minimize circumferential temperature gradients in the casings. Some improvement was noted, and the fan remained on for the rest of the test. The variation from average at the conclusion of the test is shown in Figures 247 and 248. The exact cause of the apparent out-of-roundness is not known. Extra thermocouples that were placed on the casing flanges to detect a circumferential temperature variation during the last test series did not show the external gradients that would result in the indicated out-of-roundness.

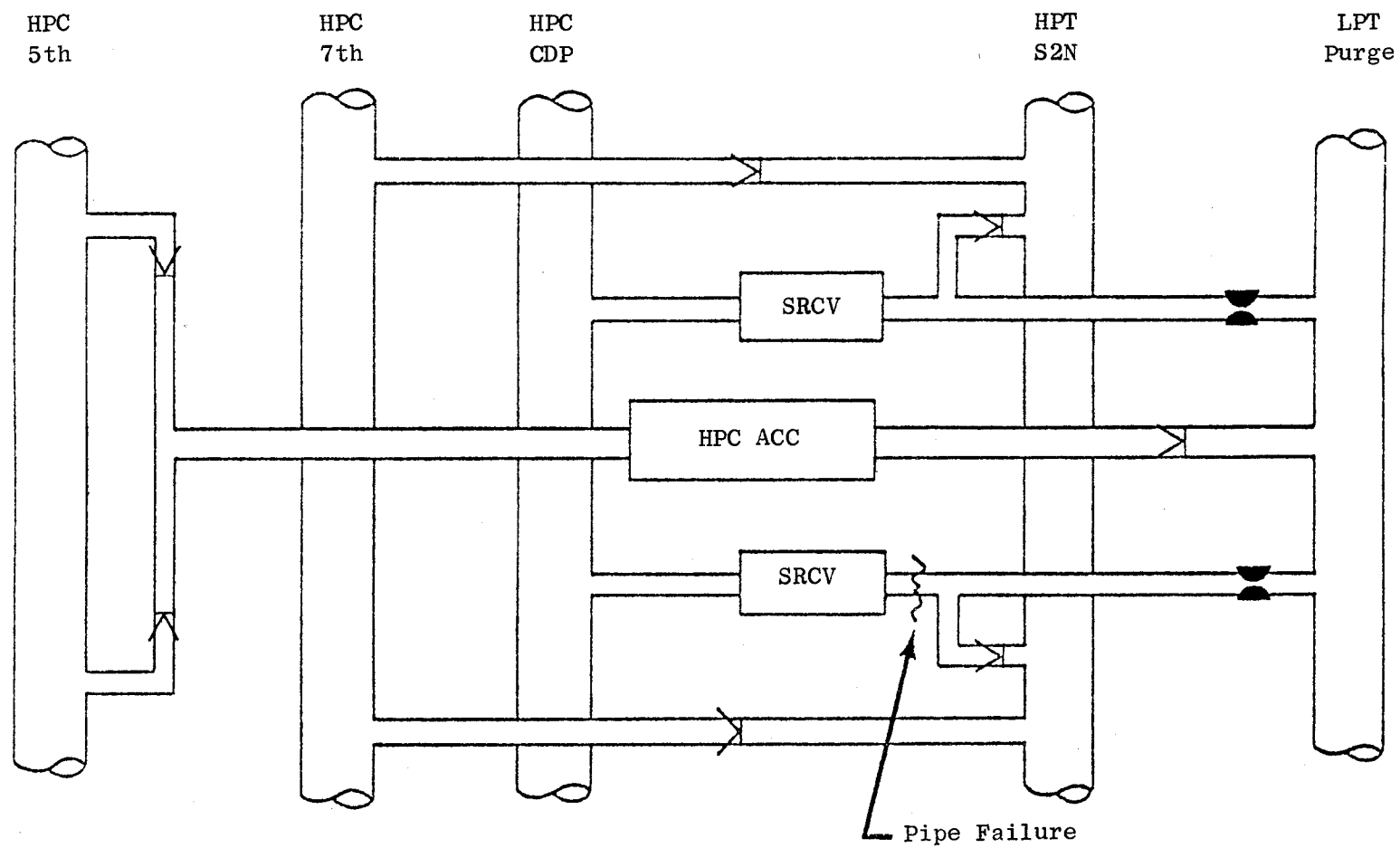


Figure 241. HP Turbine Core Cooling Air Piping.

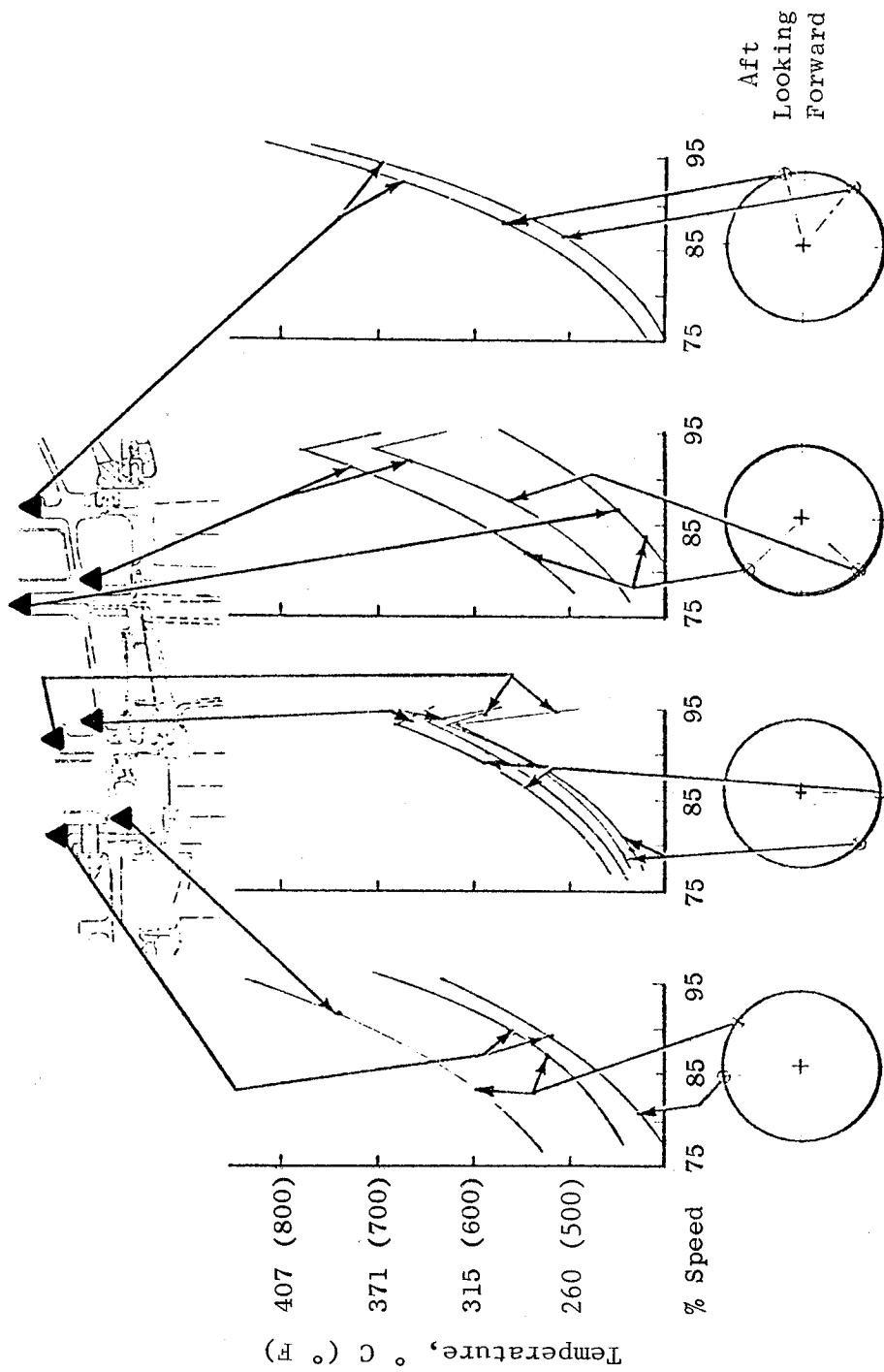


Figure 242. HP Turbine Casing Temperatures Versus CDP Supply Pipe Failure Between 93% and 94%.

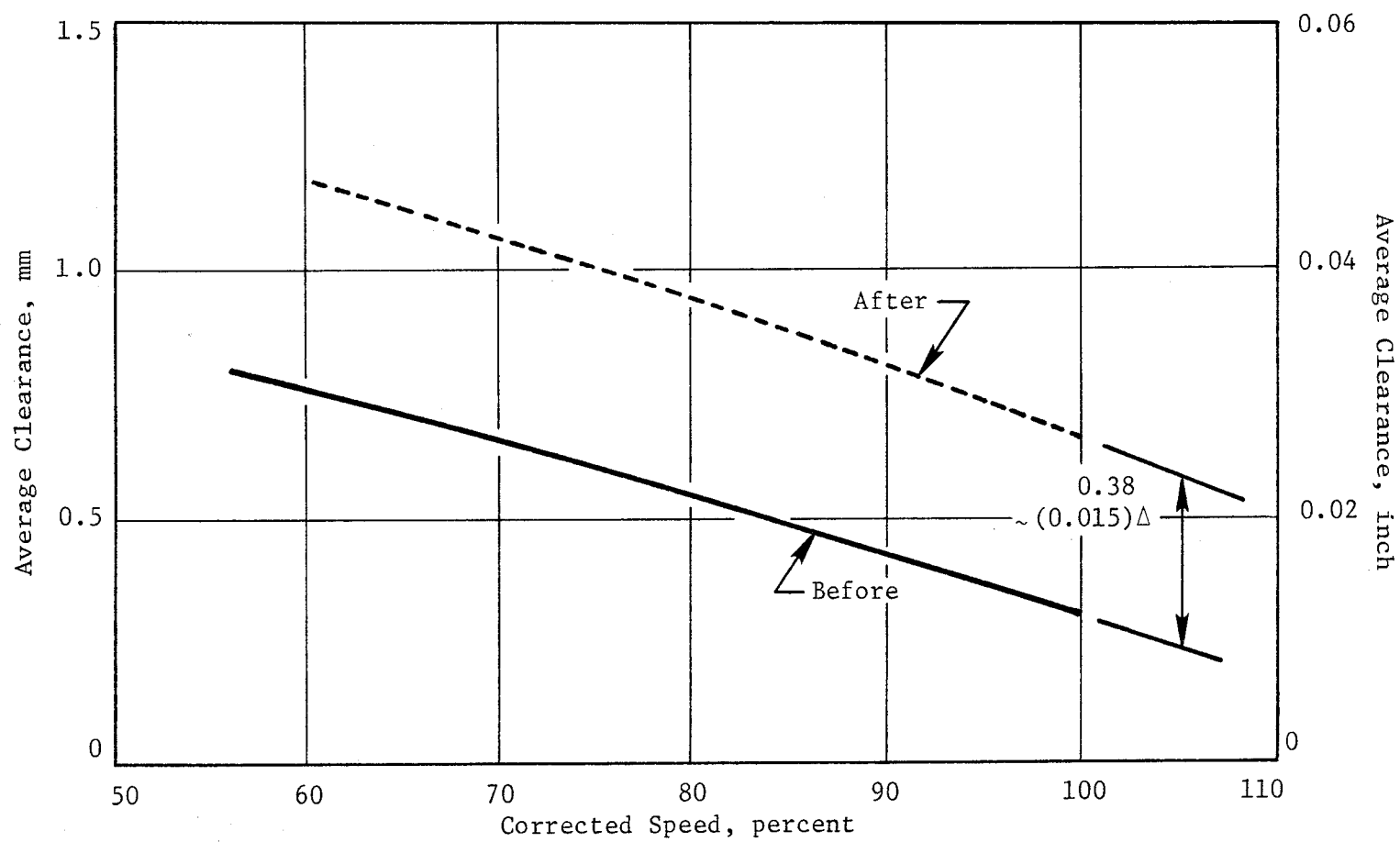


Figure 243. HP Turbine Stage 1 Blade Tip Clearance Versus Speed Before and After Rub, ACC Off.

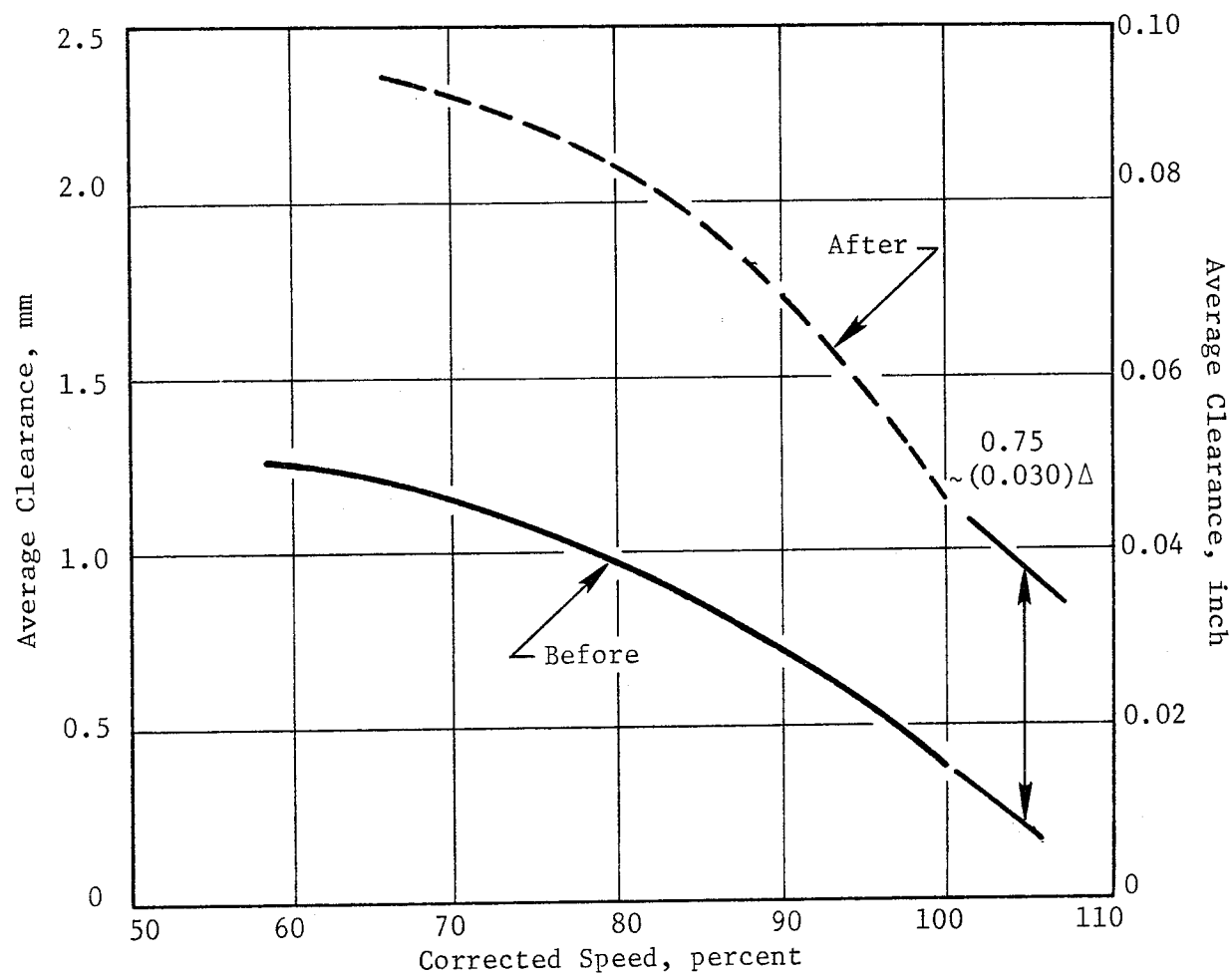


Figure 244. HP Turbine Stage 2 Blade Tip Clearance Versus Speed Before and After Rub, ACC Off.

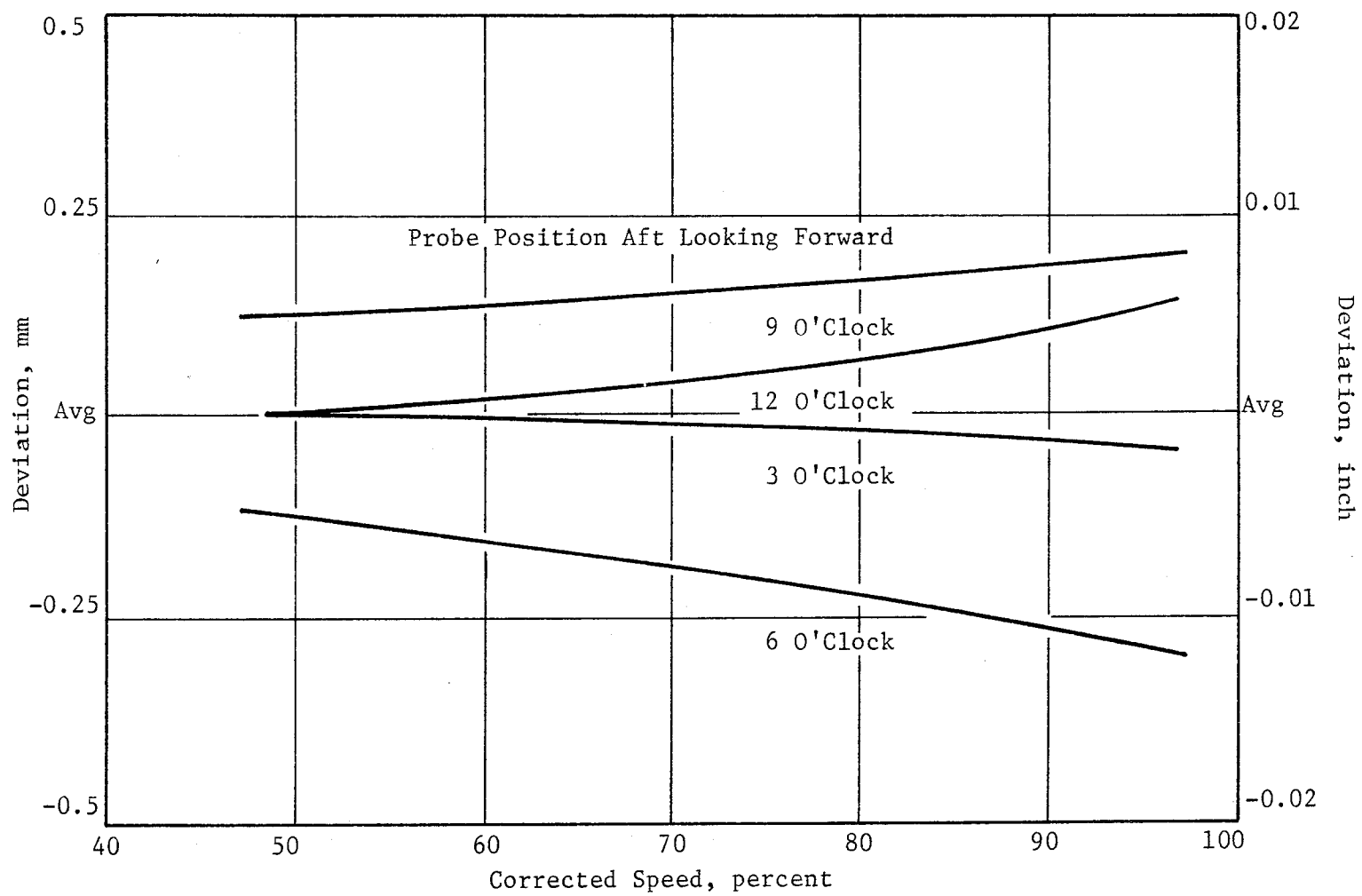


Figure 245. HP Turbine Stage 1 Blade Tip Clearance Circumferential Deviation From Average (Initial Test).

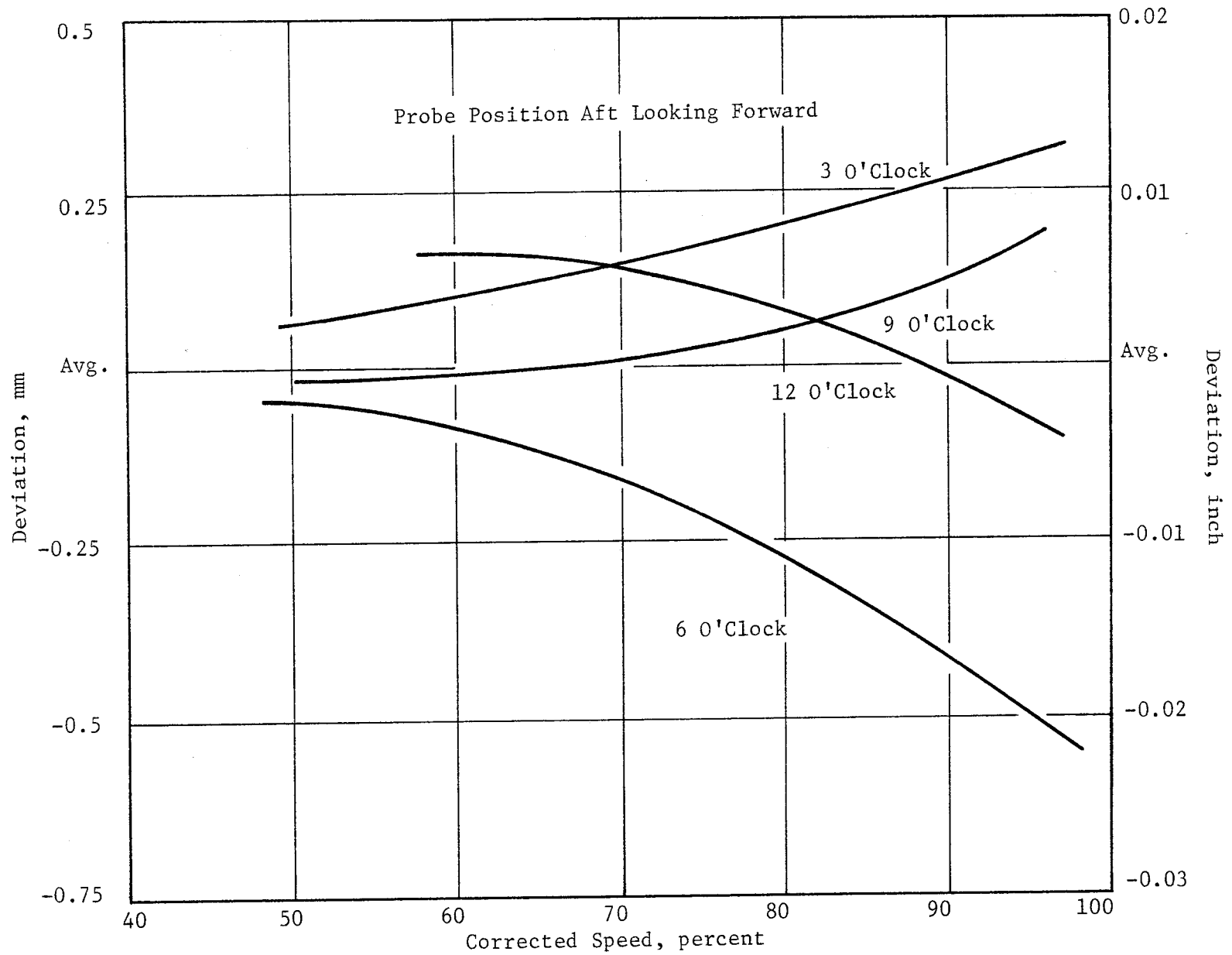


Figure 246. HP Turbine Stage 2 Blade Tip Clearance Circumferential Deviation From Average (Initial Test).

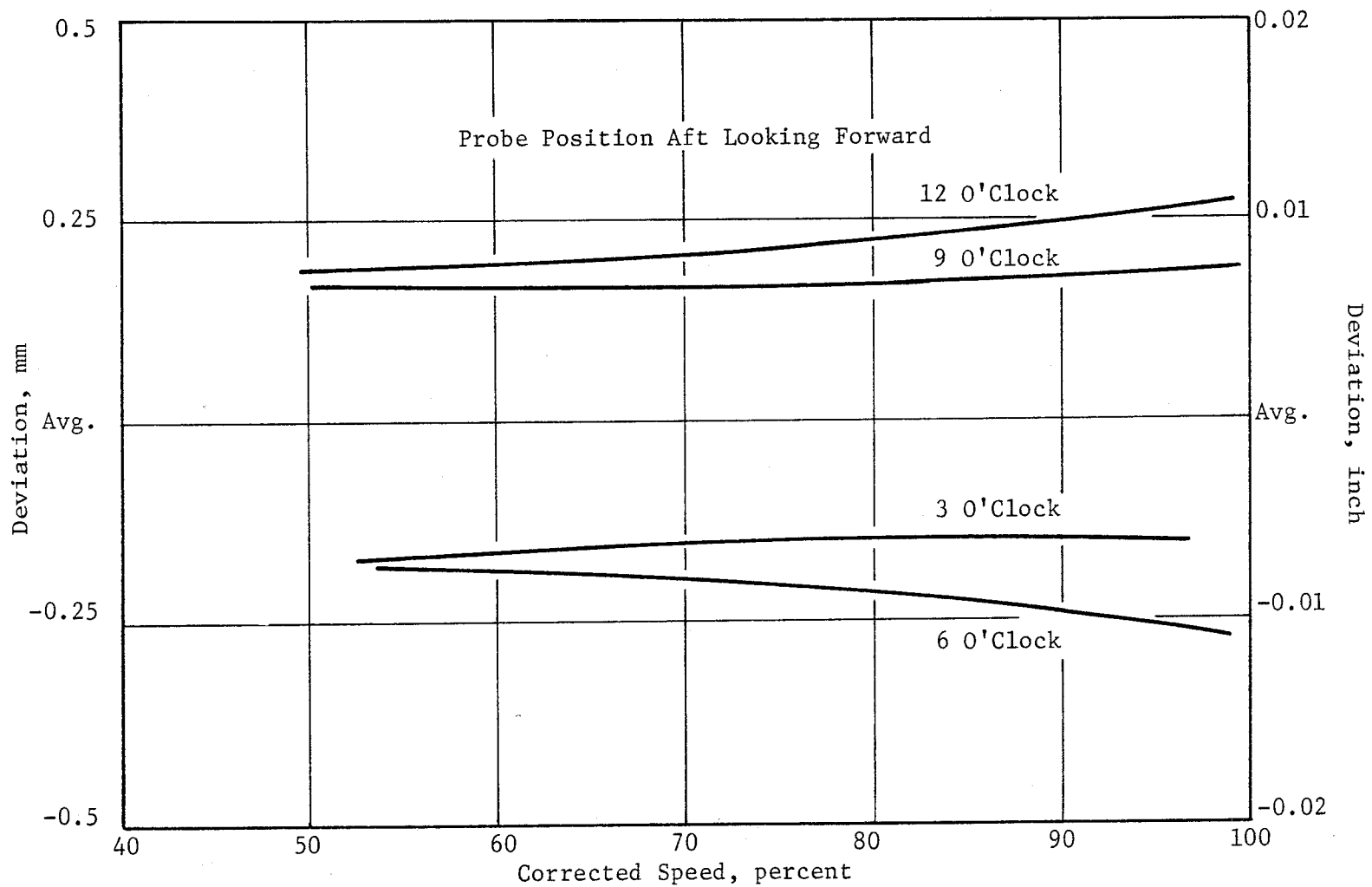


Figure 247. HP Turbine Stage 1 Blade Tip Clearance Circumferential Deviation From Average (Final Test).

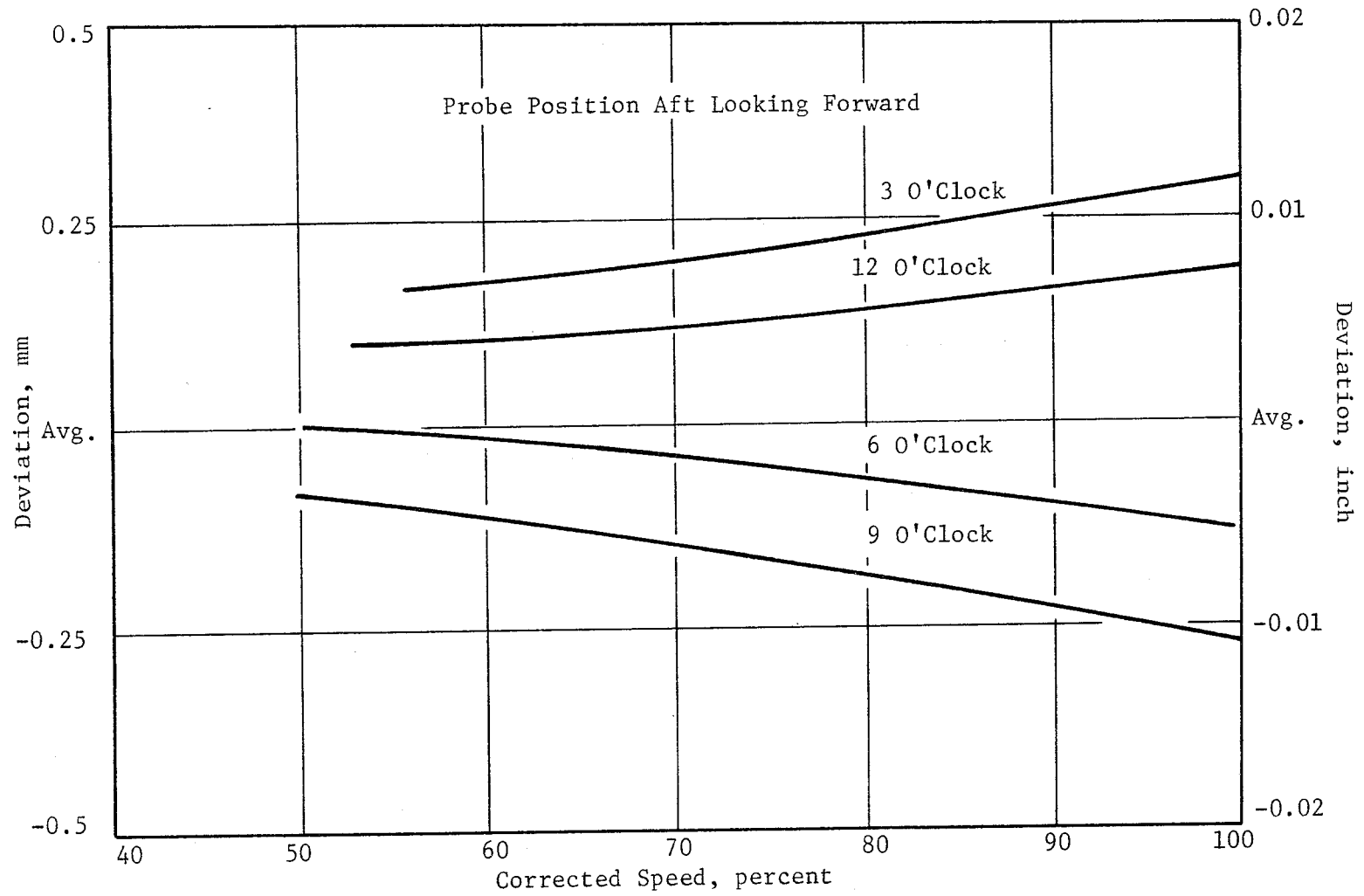


Figure 248. HP Turbine Stage 1 Blade Tip Clearance Active Clearance Control Effect.

Active Clearance Control

The HP turbine incorporates an ACC system. Several systems were considered, with fan air impinging on the outside of the turbine casing being chosen to achieve the required thermal response and produce the required clearance closure. During core engine testing, shop air was used to simulate fan discharge air. Design flow was a total of 0.3% W25 to both stages and evenly split to give 0.10 kg/s (0.225 lbm/s) flow to each stage.

The ACC system was less effective than anticipated. Figures 249 and 250 show blade tip clearance with and without ACC. The flow indicated was total flow to the system. The cooling flow was split evenly between Stage 1 and 2. Also shown is the predicted closure for 0.3% W25, as determined by a simplified performance analysis model.

A butterfly valve on each Stage 1 impingement manifold was designed to allow the cooling flow distribution to be shifted circumferentially on Stage 1 and also between Stage 1 and 2. Prior to DMS Reading 258 an effort was made to obtain more balanced clearances between Stage 1 and 2. The butterfly valves shown in Figure 251 were used to reduce the flow to Stage 1 while increasing the flow to Stage 2. The impingement air supply manifold pressure was also increased to a level that was higher than maximum design level. This resulted in a 40%/60% flow split between Stage 1 and 2. Stage 1 was maintained close to its maximum design value of 0.10 kg/s (0.225 lbm/s), while the flow to Stage 2 was nearly 50% above its maximum design value. This was done to help bring the clearances on Stage 2 down to a level comparable to the design value after the rub occurred, removing 0.75 mm (0.030 inch) from the blade tips.

An analysis, using DMS Reading 258, was conducted to explain the disparity between actual and predicted clearance closure. Conditions existing during this reading included maximum flow in the ACC system and maximum external cooling from the test cell entrainment phenomenon described earlier in this section.

The measured data from DMS Reading 258 are shown in Figure 252 and show the reduction in outer ring temperature below those presented in Figures 239 and 240 with no ACC cooling. To accomplish a data match of DMS Reading 258,

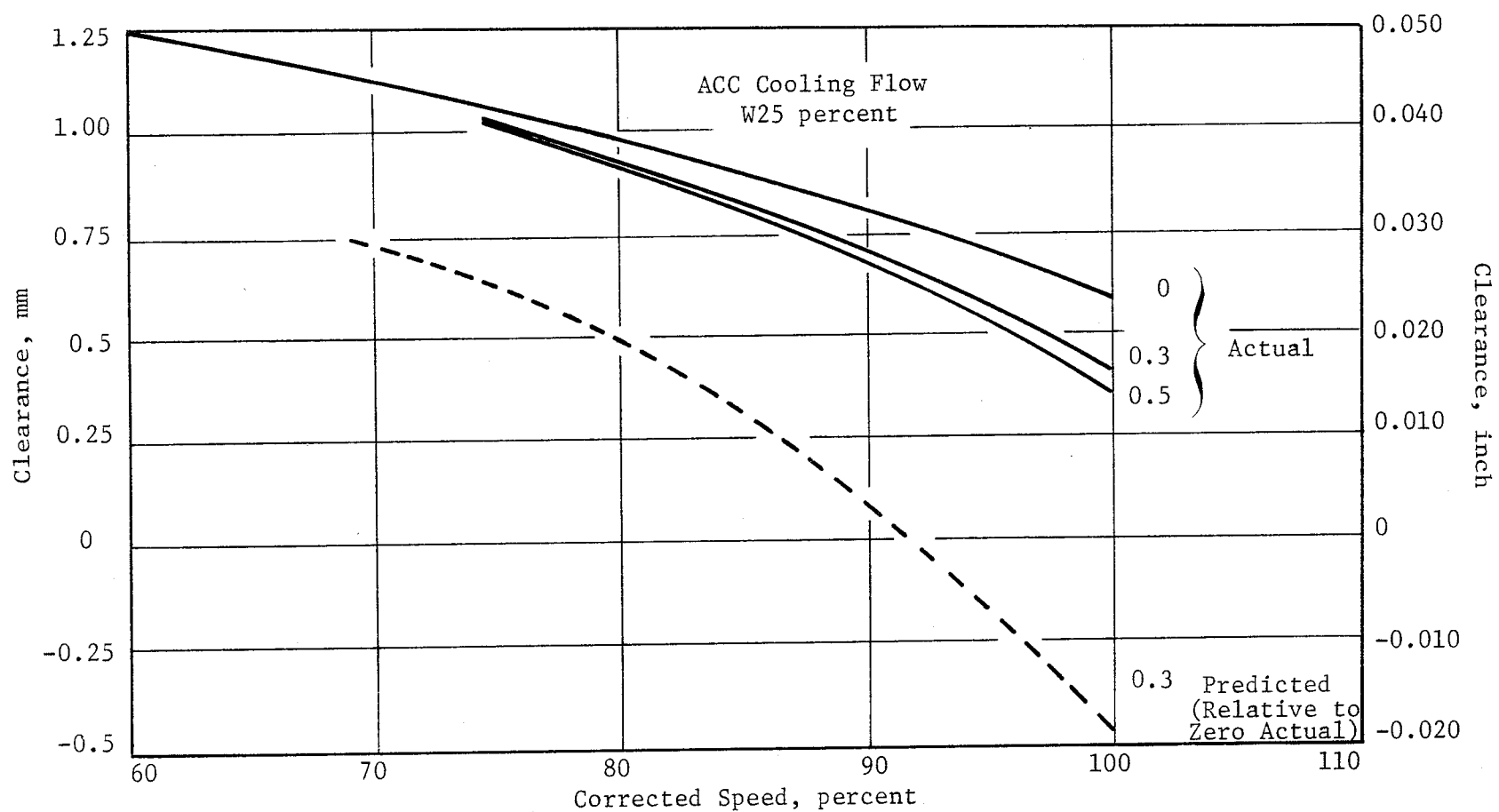


Figure 249. HP Turbine Stage 1 Blade Tip Clearance Active Clearance Control Effect.

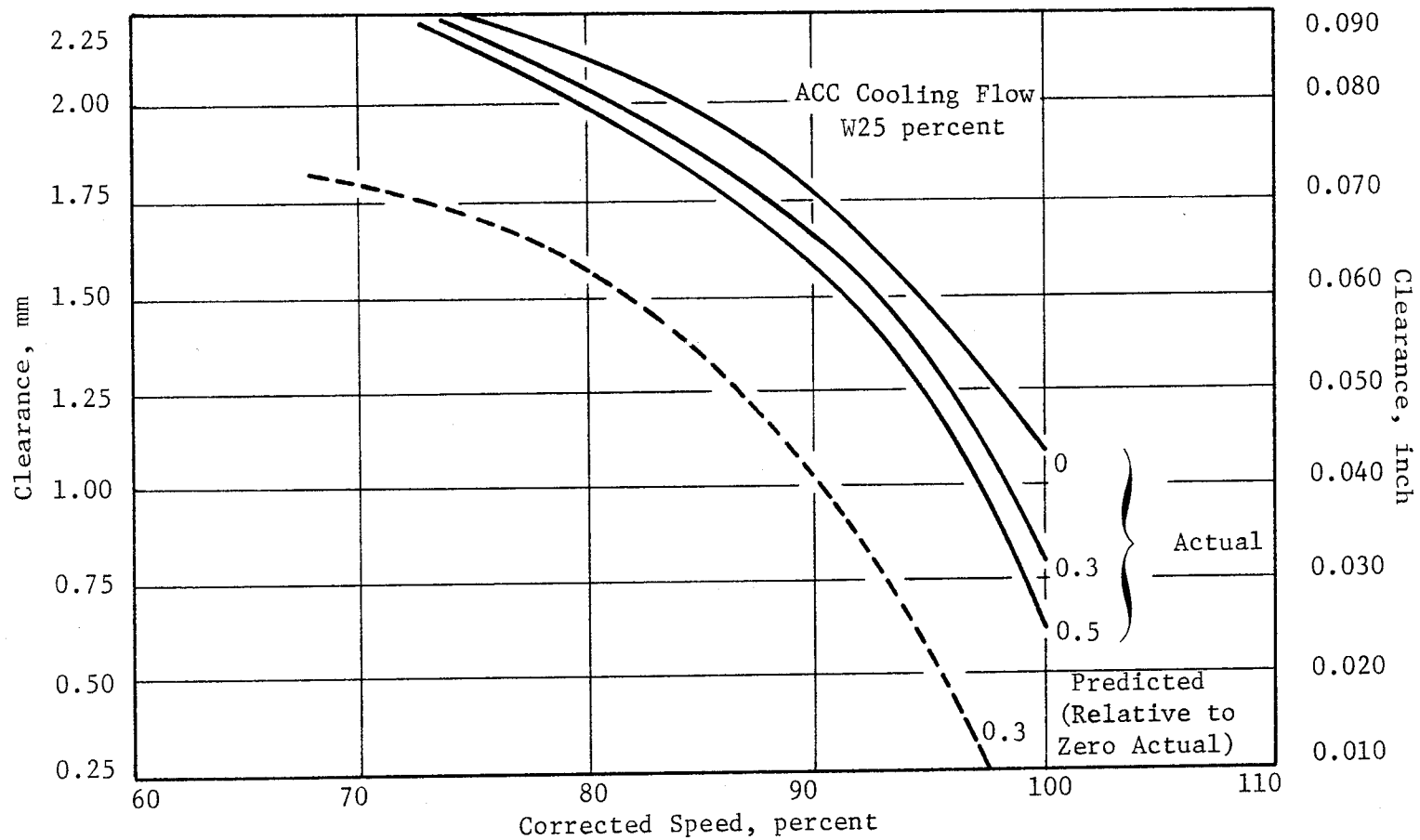
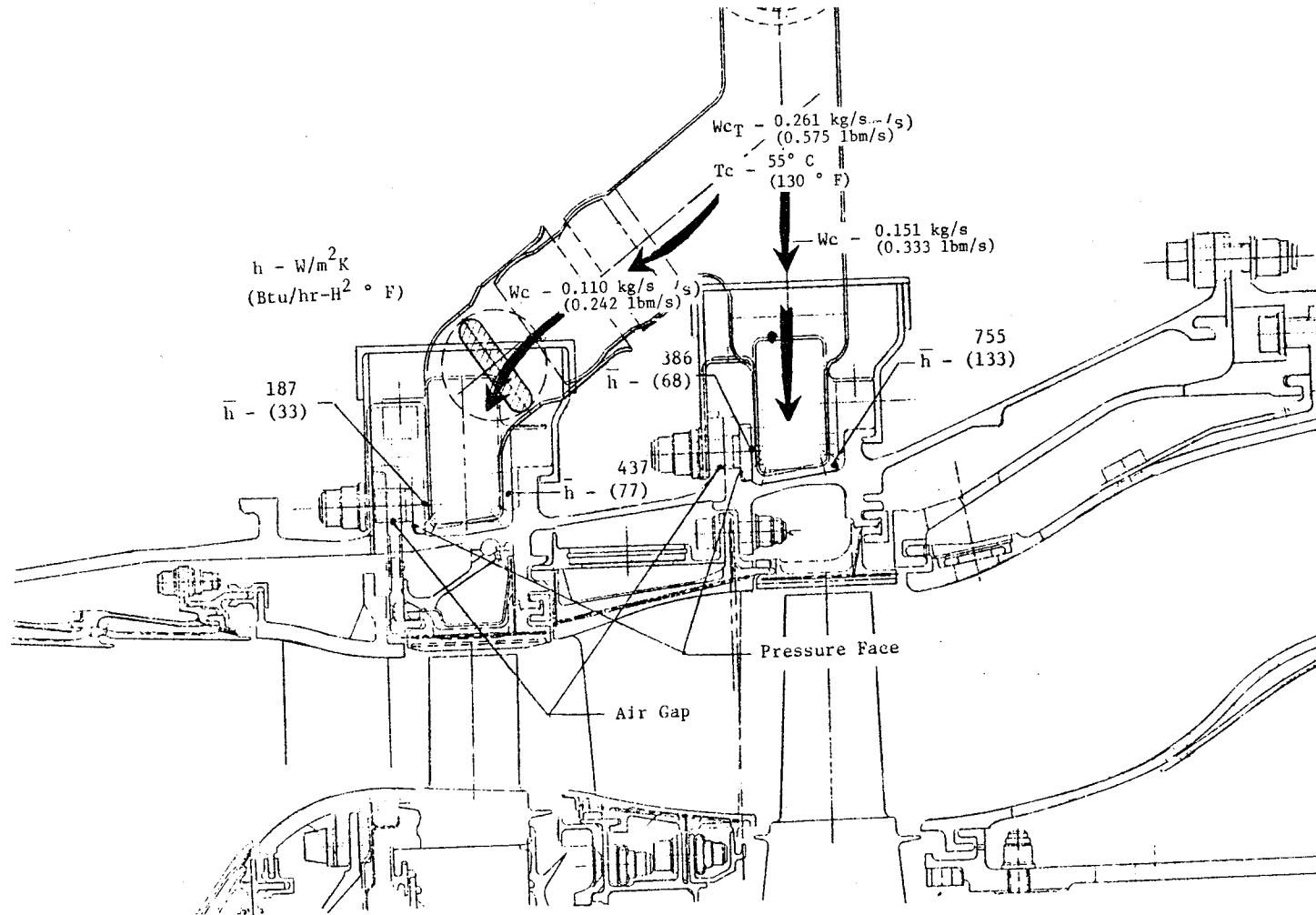


Figure 250. HP Turbine Stage 2 Blade Tip Clearance Active Clearance Control Effect.



ORIGINAL PAGE IS
OF POOR QUALITY

Figure 251. HP Turbine Casing Data Match for Reading 258 Flow and Heat Transfer Coefficient.

- All Temperatures are ° C (° F)

T41 1363° C (2485° F)

T3 509° C (949° F)

T_{Meas} Measured Metal Temperatures

T_{Avg} Average of T_{Meas} Temperatures

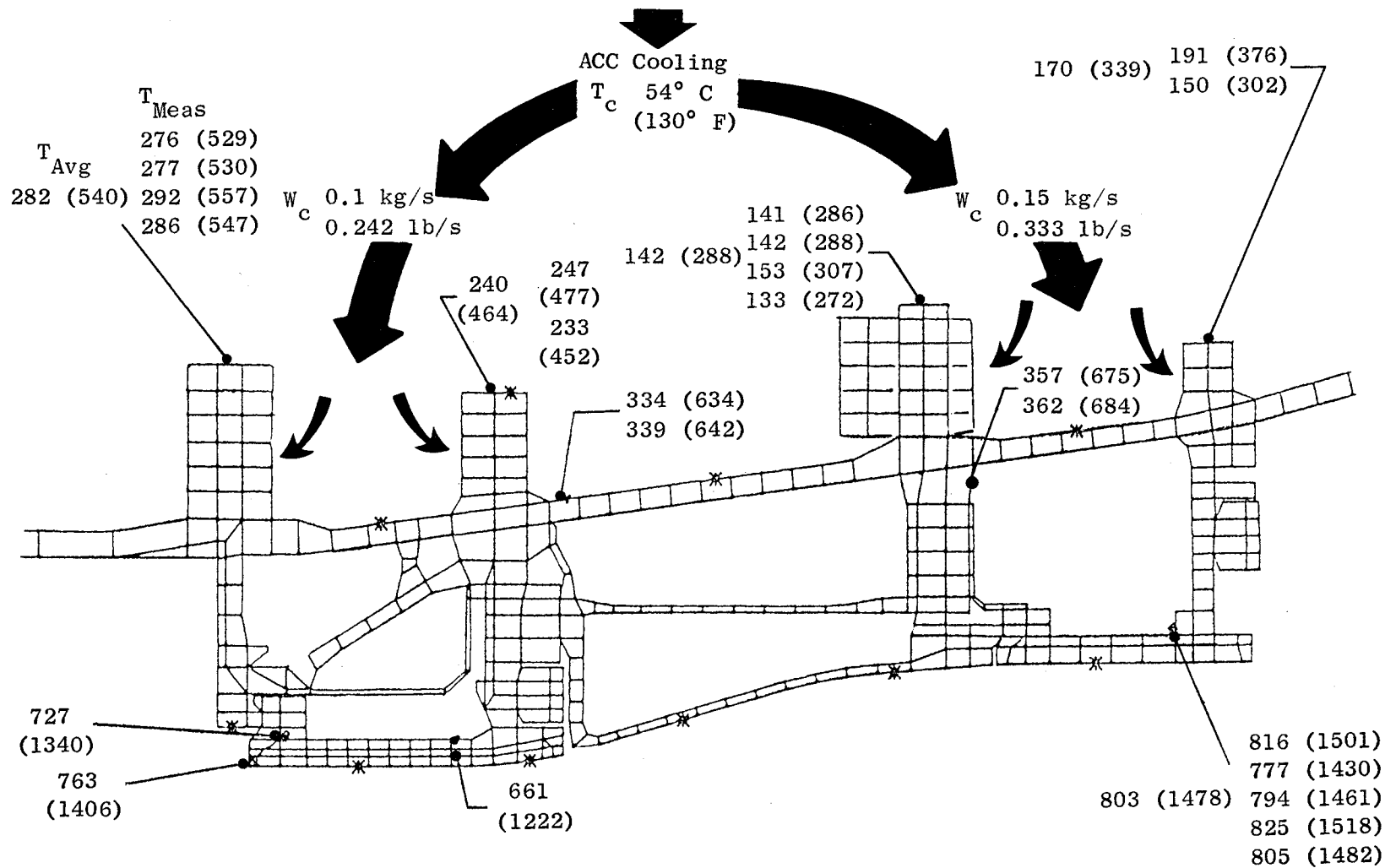


Figure 252. HP Turbine Casing Measured Temperature From Reading 258 (Maximum ACC Cooling).

the heat transfer coefficients and ambient temperature on the exposed portions of the casing (not covered by impingement manifolds) were kept at the same level as presented in Figure 240. The ACC cooling impingement heat transfer coefficients were varied until the calculated temperature matched the measured metal temperatures of DMS Reading 258. This data match is shown in Figure 253.

It is significant to note that the data-matched heat transfer coefficients resulting from the manifold flow are larger on the aft side of the manifold than on the front. This is true for both Stage 1 and 2. The coefficients on the aft side of the manifolds are close to the anticipated values, whereas the forward side coefficients are substantially lower than anticipated. The corresponding impingement flow and heat transfer coefficients for the ACC cooling system during DMS Reading 258 are presented in Figure 251. The total impingement flow was defined by using the pressure ratio/flow correlation established during a pretest flow check of each individual impingement manifold. Instrumentation in each manifold confirmed that cooling flow was being distributed uniformly around the casing.

From the data match, the heat transfer coefficient on the aft ring Stage 1 was $755 \text{ W/m}^2 \text{ K}$ ($133 \text{ Btu/hr-ft}^2 \text{ }^\circ \text{ F}$), which was close to the anticipated value for this flow. The indicated heat transfer on the forward bolt flange of Stage 2 was half the level of the aft ring, even though the cooling configuration of the manifold and the cooling flow were identical. A similar condition existed on the forward and aft rings of Stage 1. The aft ring heat transfer for Stage 1 was also close to the design level, while the heat transfer to the bolted flange was significantly lower.

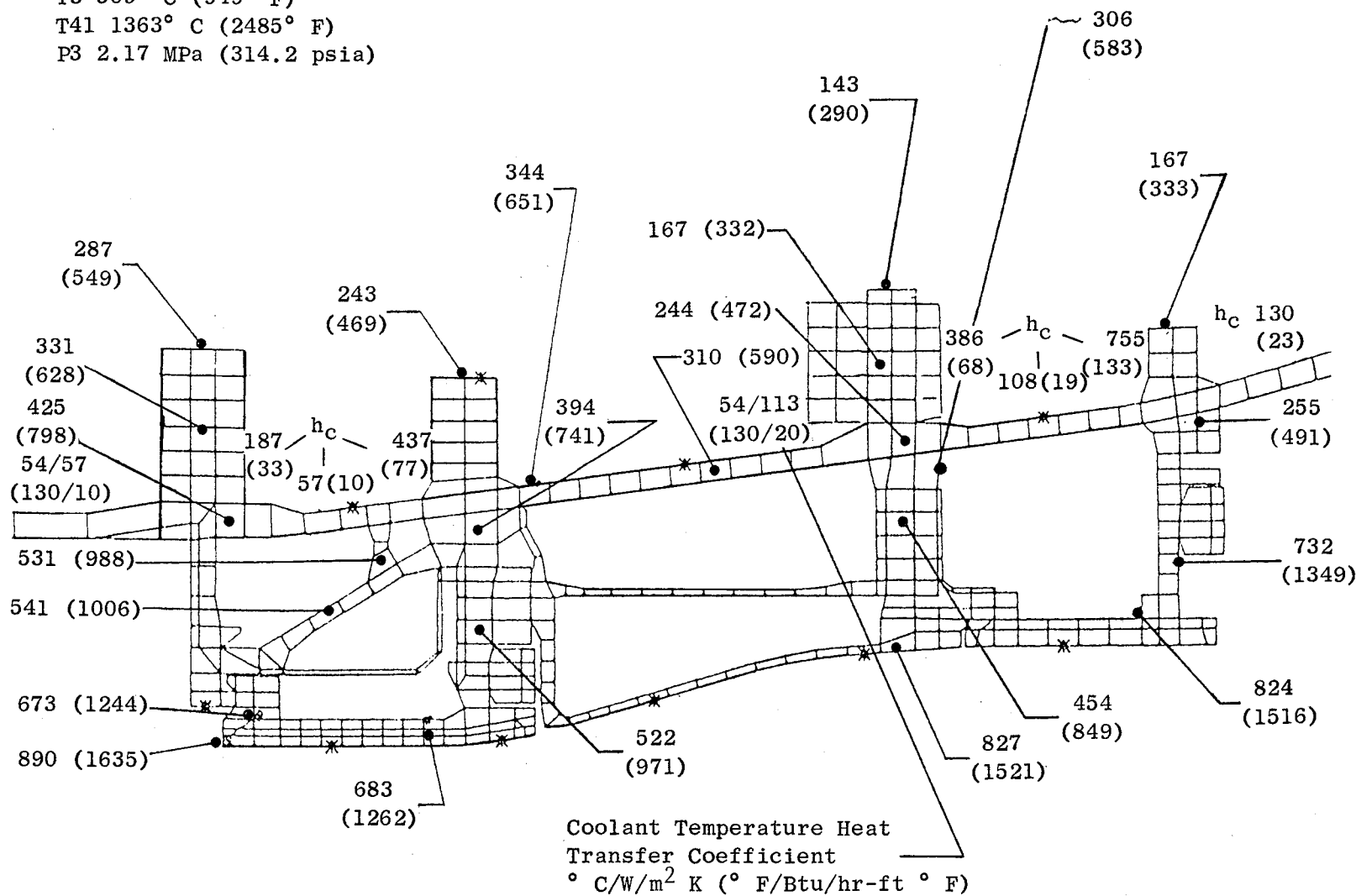
In comparing the thermal model with the actual hardware, an effort was made to understand and possibly account for the lower than anticipated heat transfer to the forward bolted flanges. The thermal model assumed identical heat transfer conditions on both forward and aft rings. Approximately 50% of the forward impingement jets on both stages were directed toward the bolt-heads where the only solid contact with the flange was at the clamping surface. There was a design diametral clearance of about 0.76 mm (0.030 inch) between the bolt shank and the flange bolthole. Therefore, the boltheads acted as a thermal resistance between the impingement jets and the flange

- All Temperatures are °C (° F)

T3 509° C (949° F)

T41 1363° C (2485° F)

P3 2.17 MPa (314.2 psia)



ORIGINAL PAGE IS
OF POOR QUALITY

Figure 253. HP Turbine Casing Data Match of Reading 258 (Maximum ACC Cooling and Test Cell Air Entrainment).

since the heat conduction could occur only at the small bolthead/flange interface. Also, the jets that were impinging between boltheads on the flange surface were 3.56 mm (0.140 inch) farther away than assumed due to bolthead thickness. The increased distance caused a reduction in the heat transfer.

The small contact area between the boltheads and the flange accounted for approximately 25% lower heat transfer than assumed. The greater-than-assumed distance of the impingement jets between boltheads accounted for another 25% reduction in the assumed heat transfer. A combination of these two effects was the most likely cause of the effective reduction in ACC impingement heat transfer to the bolted ACC casing flanges.

Because of the substantial rub, which occurred early in the test (due to the SRTC pipe flange failure reported earlier), the clearances were significantly larger than anticipated for the measured casing temperatures. During DMS Reading 258, with maximum flow in the ACC system, Stage 1 rubbed locally and Stage 1 had a minimum clearance of from 0.25 to 0.36 mm (0.010 to 0.014 inch). The average clearance for Stage 1 was 0.56 mm (0.022 inch) and for Stage 2 it was 0.86 mm (0.034 inch). Had the early rub not occurred, there would have been the potential for rubs of approximately 0.38 mm (0.015 inch) and 0.46 mm (0.018 inch) on Stage 1 and 2 respectively, with maximum ACC air during DMS Reading 258. To prevent such a rub, it would have been necessary to shut off the ACC cooling to the bottom of the turbine.

In order to compare the original ACC analytical model with the measured thermal performance, the analytical model was run to the conditions of DMS Reading 258. Cooling flow was assumed to be 0.10 kg/s (0.225 lbm/s) to each stage. The model did not include exhaust flow entrainment effects. The resulting temperature distribution is shown in Figure 254. This distribution is what would have been predicted for DMS Reading 258 cycle conditions using design ACC cooling flows and originally predicted heat transfer coefficient on the outside of the casing. Figure 238 similarly shows the temperature distribution that was predicted for maximum speed conditions using no ACC cooling flows and the corresponding predicted heat transfer coefficients on the outside of the casing. The resulting bulk average ring temperatures caused by the ACC system and the corresponding clearance change calculated by using those temperatures are shown in the following tabulation:

- All Temperatures are ° C (° F)

T3 509° C (949° F)

T41 1360° C (2485° F)

P3 2.17 MPa (314.2 psia)

W_c 0.20 kg/s (0.45 lb/s)

T_c 54° C (130° F)

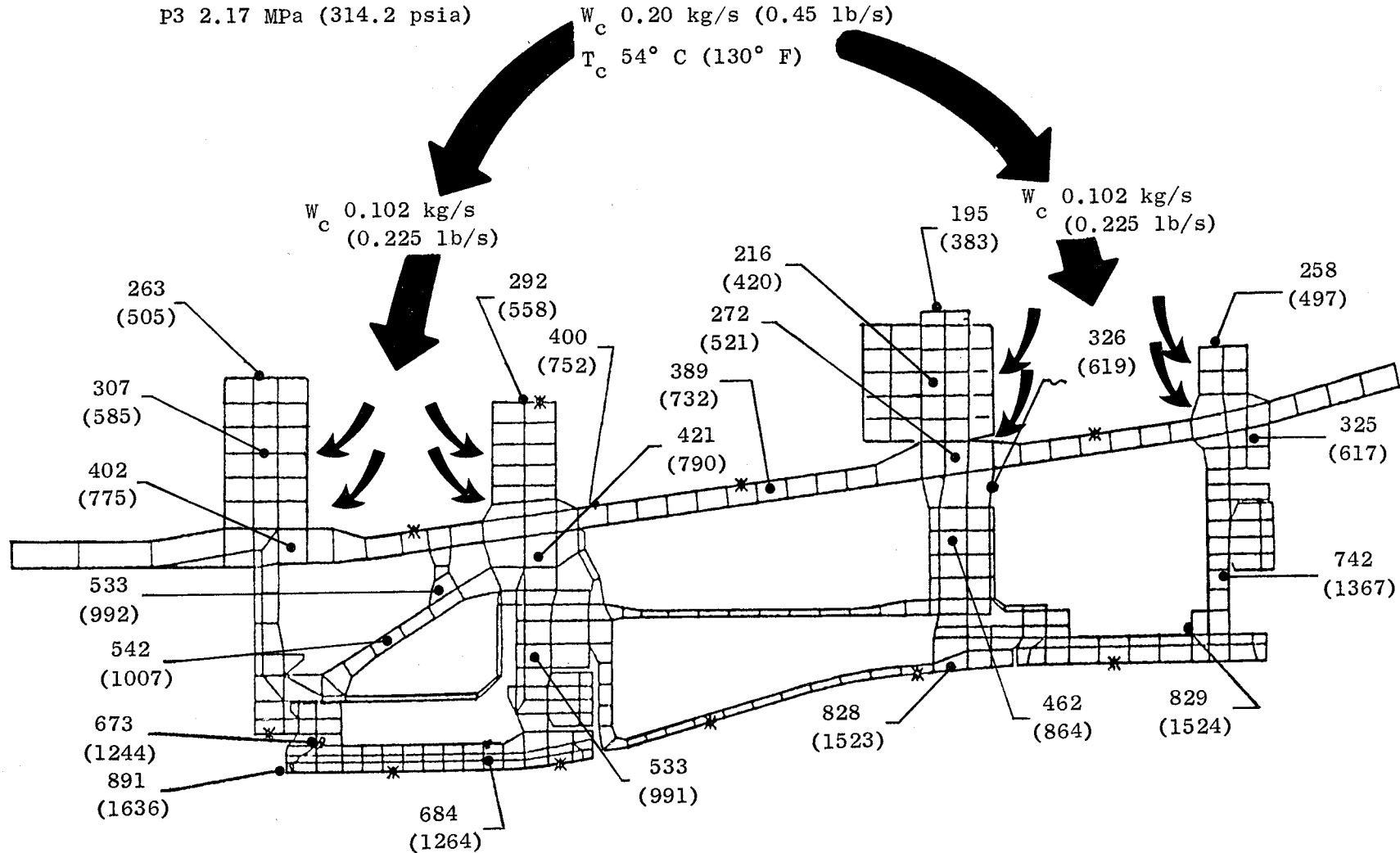


Figure 254. HP Turbine Casing Expected ACC Cooling on Casing for Reading 258 Cycle Conditions (Maximum Cooling and No Test Cell Air Entrainment).

	<u>Stage 1</u>	<u>Stage 2</u>
Anticipated Average Ring Temperature (No ACC Cooling, No Entrainment), ° C (° F)	516 (961)	464 (868)
Anticipated Average Ring Temperature (With Max ACC Cooling, No Entrainment), ° C (° F)	407 (765)	338 (641)
ACC Cooling Flow, kg/s (lbm/s)	0.1 (0.225)	0.1 (0.225)
Anticipated Average Ring Temperature Reduction Due to ACC (No Entrainment), ° C (° F)	109 (196)	126 (227)
Anticipated Clearance Reduction, mm (inch)	0.71 (0.028)	0.84 (0.033)

These data can then be compared to that actually obtained from the data match of the measured metal temperatures shown in the following tabulation:

	<u>Stage 1</u>	<u>Stage 2</u>
Data Match Clearance Reduction Due to Test Cell Air Entrainment (No ACC Cooling), mm (inch)	0.43 (0.017)	0.69 (0.027)
Data Match Additional Clearance Reduction Due to Max ACC Cooling, mm (inch)	0.40 (0.016)	0.48 (0.019)
Cooling Flow, kg/s (lbm/s)	0.11 ((0.242)	0.15 (0.333)
Data Match Average Total Clearance Reduc- tion, mm (inch)	0.84 (0.033)	1.17 (0.046)

When the data match clearance reductions are compared with the anticipated clearance reductions they agree within 0.13 mm (0.005 inch) and 0.33 mm (0.013 inch) for Stage 1 and 2, respectively. What this shows is that the original thermal model reasonably matched the actual test temperatures. However, this occurred only because of compensating differences between the model and the core engine. The exhaust entrainment effect cooled the casing, thereby reducing the amount of cooling available to the ACC system. Also, the flange bolts interfered with cooling. These reductions in ACC effectiveness were nearly balanced by the temperature reduction due to entrainment effects and the increase in the ACC cooling flow rate to Stage 2.

A comparison can now be made between clearance reduction deduced from data matches of measured temperatures and clearance reduction directly

measured by laser probes. The clearance reduction deduced from measured temperatures was determined by comparing the data match for no ACC (Figure 242) with the data match for maximum ACC (Figure 240). The data match average ring temperatures were compared to show the temperature reduction and corresponding calculated clearance reduction:

	<u>Stage 1</u>	<u>Stage 2</u>
Data Match Indicated Bulk Average Ring Temperature Without ACC, ° C (° F)	449 (841)	359 (679)
Data Match Indicated Bulk Average Ring Temperature With ACC, ° C (° F)	387 (729)	283 (542)
Data Match Ring Temperature Reduction, ° C (° F)	62 (112)	76 (137)
Calculated Clearance Reduction, mm (inch)	0.41 (0.016)	0.48 (0.019)

This data was not consistent with the indicated clearance reduction as measured by the laser clearance probes. The average clearance reduction was 0.23 mm (0.009 inch) on Stage 1 and 0.43 mm (0.015 inch) on Stage 2 as indicated from laser probe clearance measurements at DMS Readings 256 and 257.

The following may explain why the measured clearance reduction was only 56% in Stage 1 and 79% in Stage 2 of the reduction projected from measured temperature changes. The laser clearance probe support brackets for both stages prevented the ACC cooling jets from impinging directly on the aft flange over the length of the bracket. The support bracket covered three inches of the flange at each of the laser probe ports. Also, there was no flange cooling for 15 mm (0.6 inch) on either side of the laser probe port centerline. This 30 mm (1.2 inch) circumferential gap between adjacent manifold segments was required to provide space for the laser probes. These conditions represent a nonaxisymmetric feature that could not be included in the original analytical model and would cause the aft flange to be warmer than calculated at the clearanceometer port, thus causing the casing to go out-of-round slightly. The amount of out-of-roundness is difficult to determine, but the trend would be toward increasing the clearance at the clearanceometer ports.

6.7 HIGH PRESSURE TURBINE AERODYNAMIC PERFORMANCE

Analyses of the data from the core test show turbine performance to be in good agreement with component test results and core engine pretest predictions. This is evidenced primarily in the efficiency levels and flow capacity attained during the core test. The data and results that form the basis for the subsequent discussion were taken along the sea level operating line during the final performance calibration.

Core turbine performance results to be discussed cover the range of core engine operation from 76.5% to 98.1% corrected speed. All points are with double-annular combustion and with ACC on. Final performance data are the result of a balanced cycle calculation. (Details of this calculation are presented in Section 6.1.) Turbine exit pressure was corrected for a measurement error in the arc rake located at the lowest radial position. Turbine efficiencies have been corrected to a blade tip clearance of 0.041 cm (0.016 inch) on both stages, using the clearance derivative obtained in the component test for Stage 1 and a modified derivative for Stage 2 based on the core test (see HP Turbine Performance in Section 6.1.3).

Turbine performance at 98.1% core corrected speed is compared to pretest prediction in Table XXIX. Note that the flow function is as predicted, but the turbine pressure ratio is lower than expected. The latter is due to the effective area of the engine exhaust nozzle being smaller than intended. This reduced area was identified as being due to distortion of the exhaust nozzle. Turbine efficiency is observed to agree well with the map value.

A summary of the points along the operating line is presented in Table XXX. These data are compared to component test data in Figure 255. It is observed that the test points at high power settings show good agreement with the rig map. The low power point (76.5% speed) shows the most deviation from the map, 0.7 points. This is believed to be due to the inlet temperature profile from the combustor, since the profile was not simulated in the component test. The rig design point is also shown in Figure 255 for reference and to illustrate that the core turbine operated at a lower pressure ratio than design intent. This is a consequence of the exhaust nozzle area being smaller than intended.

Table XXIX. Core Turbine Operating Parameters Compared to Pretest Cycle.

	Core Test Data	Pretest Prediction
% N_c (corrected)	98.1	98.1
$W/\sqrt{T}/P, \frac{\text{gm } \sqrt{K}}{\text{s Pa}} \left(\frac{\text{lbm } \sqrt{^\circ R}}{\text{s psia}} \right)$	0.900 (18.36)	0.899 (18.33)
$N/\sqrt{T}, \frac{\text{rad}}{\text{s } \sqrt{K}} \left(\frac{\text{rpm}}{\sqrt{^\circ R}} \right)$	31.97 (227.6)	32.4 (230.6)
$\Delta h/T, \frac{\text{Joules}}{\text{kg K}} \left(\frac{\text{Btu}}{\text{lbm } ^\circ R} \right)$	341.2 (0.0815)	341.7 (0.0816)
P_4/P_{42}	4.60	4.75
η_T	0.923 ⁽¹⁾	0.922 ⁽²⁾

(1) By means of balanced cycle, corrected to 0.041 cm (0.016 in.) tip clearance

(2) By means of rig map

Table XXX. Core Turbine Parameters Along Operating Line.

% Nc (Corrected)	76.5	84.7	88.6	92.2	95.4	97.2	98.1
$w\sqrt{T}/P,$ $\frac{\text{gm } \sqrt{K}}{\text{s Pa}}$ $\left(\frac{\text{lbm } \sqrt{^\circ R}}{\text{s psia}} \right)$	0.910 (18.57)	0.915 (18.65)	0.903 (18.42)	0.911 (18.58)	0.905 (18.47)	0.904 (18.43)	0.900 (18.36)
$N/\sqrt{T},$ $\frac{\text{rad}}{\text{s } \sqrt{K}}$ $\left(\frac{\text{rpm}}{\sqrt{^\circ R}} \right)$	32.46 (231.0)	33.89 (241.2)	33.79 (240.5)	33.16 (236.0)	32.39 (230.5)	32.22 (229.3)	31.97 (227.6)
$\Delta h/T,$ $\frac{\text{Joules}}{\text{kg K}}$ $\left(\frac{\text{Btu}}{\text{lbm } ^\circ R} \right)$	287.1 (0.069)	319.7 (0.076)	330.4 (0.079)	335.1 (0.080)	336.2 (0.080)	339.4 (0.081)	341.2 (0.082)
$T_{41},$ K $(^\circ R)$	937 (1687)	1056 (1901)	1187 (2137)	1340 (2411)	1502 (2704)	1580 (2843)	1636 (2944)
P4/P42	3.830	4.403	4.573	4.592	4.596	4.607	4.596
$\eta_T,$ at running clearances	0.877	0.896	0.902	0.908	0.907	0.912	0.916
Clearance, Stage 1 cm (in.)	0.089 (0.035)	0.080 (0.031)	0.071 (0.028)	0.068 (0.027)	0.061 (0.024)	0.055 (0.022)	0.059 (0.023)
Clearance, Stage 2 cm (in.)	0.198 (0.078)	0.178 (0.070)	0.152 (0.060)	0.132 (0.052)	0.104 (0.041)	0.086 (0.034)	0.079 (0.031)
$\eta_T,$ at 0.041 cm (0.016 in.) Clearance	0.902	0.917	0.918	0.922	0.917	0.919	0.923

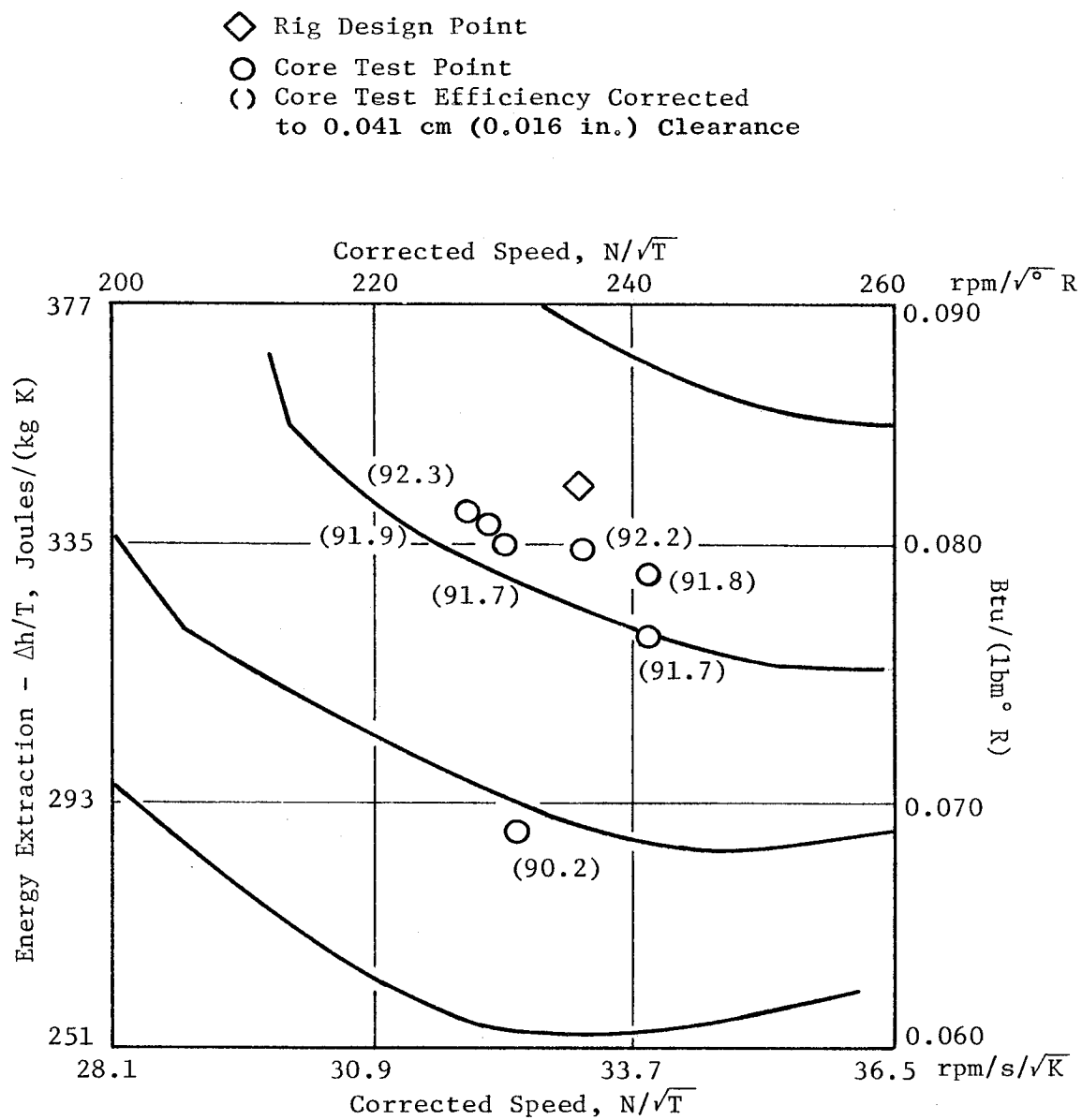


Figure 255. Core Turbine Efficiency Shown on Rig Efficiency Map.

As tested, the core turbine would produce an efficiency of 92.5% if operated at the design point cycle parameters of a production flight engine. This is 0.6% above the goal for the core hardware and 0.1% above the goal for a fully developed flight engine turbine.

Turbine flow function is compared to pretest prediction in Figure 256 for the seven points on the operating line. The total variation is 1.6 percent. Overall, the trend indicates that the turbine flow function is 0.8% higher than intent. This is in good agreement with prediction and is better than expectations.

The HP turbine exit pressure profiles are shown in Figure 257. This figure shows the profile development with corrected compressor speed and compares the profile based on arc rake data to that from the radial rakes. This figure also shows the nature and magnitude of the discrepancy between rakes near the inner annulus radii. This difference is seen to increase with increasing speed. A visual inspection of the turbine exit duct after the core test revealed a ridge of weld material along the inner duct wall. This ridge is underneath the radial rakes and upstream of the arc rakes. The flow disturbance caused by this protuberance is evidenced in the arc rake pressure being erroneously low at the innermost immersion.

The innermost arc rake pressures were corrected based on radial rake data. The resulting profiles are presented in Figure 258. These data are considered to be a reasonable representation of the turbine exit pressure profile. A comparison of the core engine data to the rig data is shown in Figure 259 where exit total pressure has been normalized by the turbine inlet total pressure. Core data are at the 98.1% speed point. The rig data have been adjusted in level to that of the core data. This figure also shows the correction made to the core engine arc rake at the innermost immersion. The core engine profiles are in good agreement with the rig data.

Turbine exit temperature profiles are shown in Figure 260 for various speeds along the operating line. All of these points are with double-annular combustion. The shape of the exit profile reflects the shape of the predicted combustor profile coming into the turbine. The effects of the turbine radial

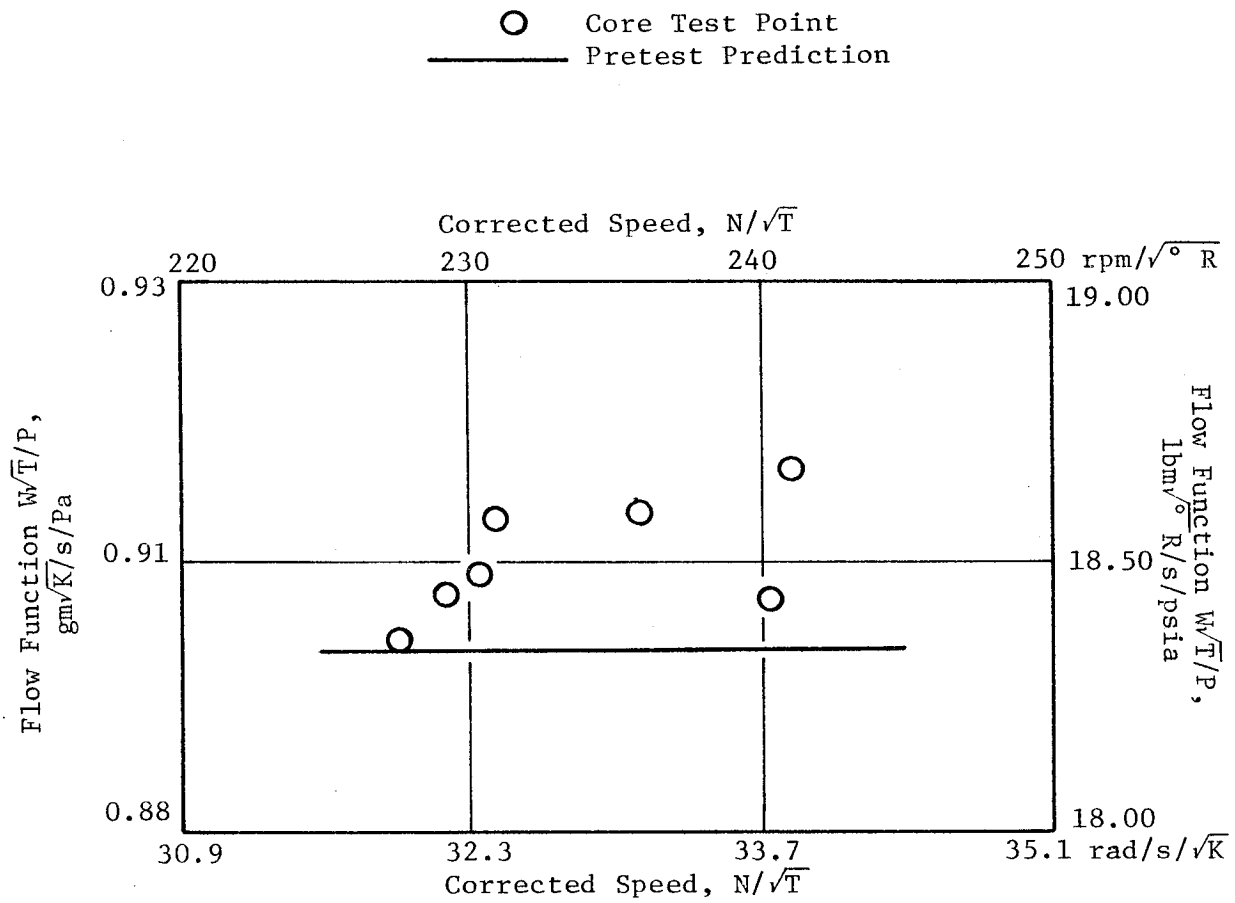


Figure 256. Core Turbine Flow Function Versus Turbine Corrected Speed.

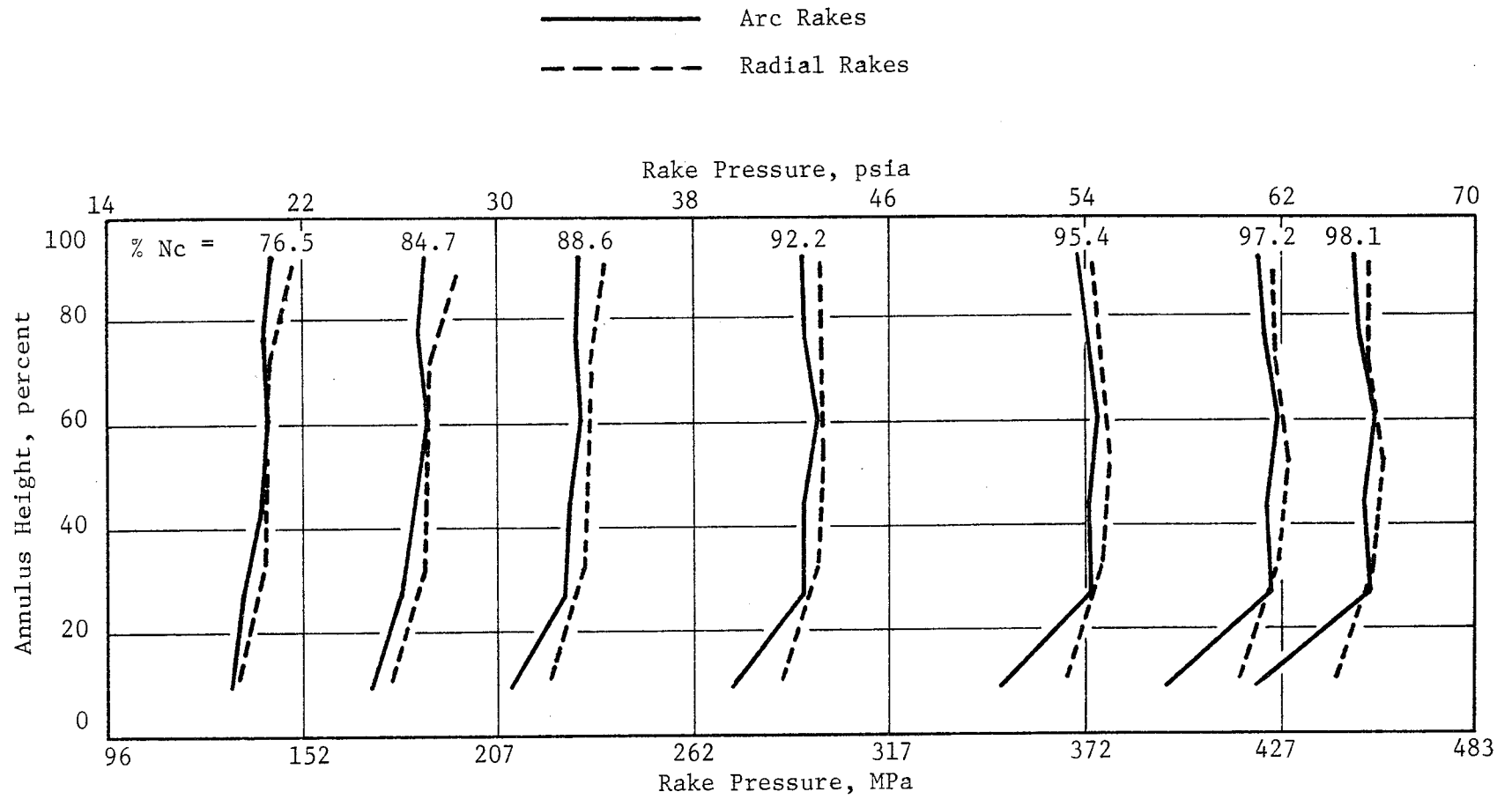


Figure 257. Turbine Exit Pressure Profiles With Speed, Arc Rake Pressure as Measured.

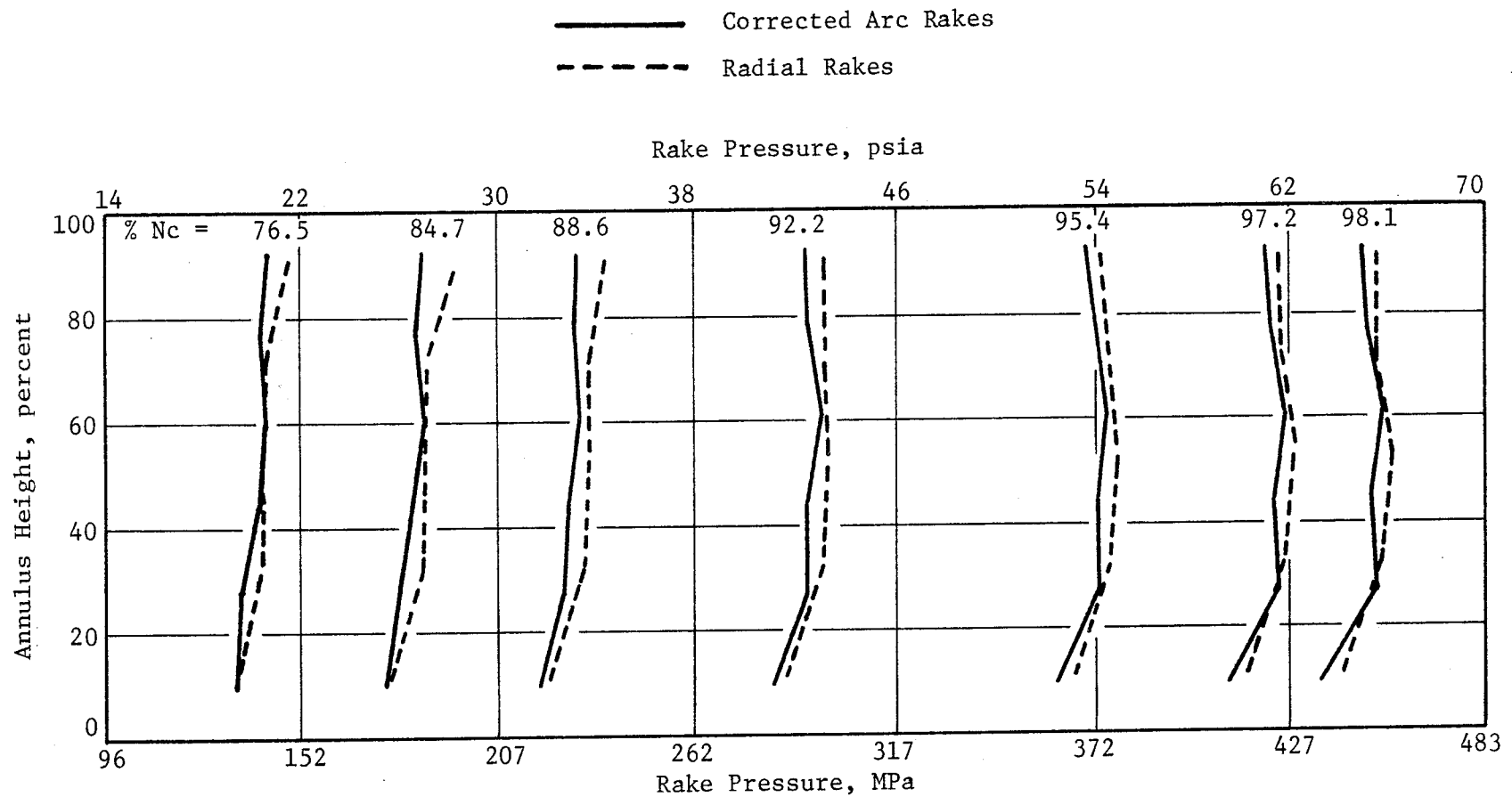


Figure 258. Turbine Exit Pressure Profiles with Speed and Corrected Arc Rake Pressure.

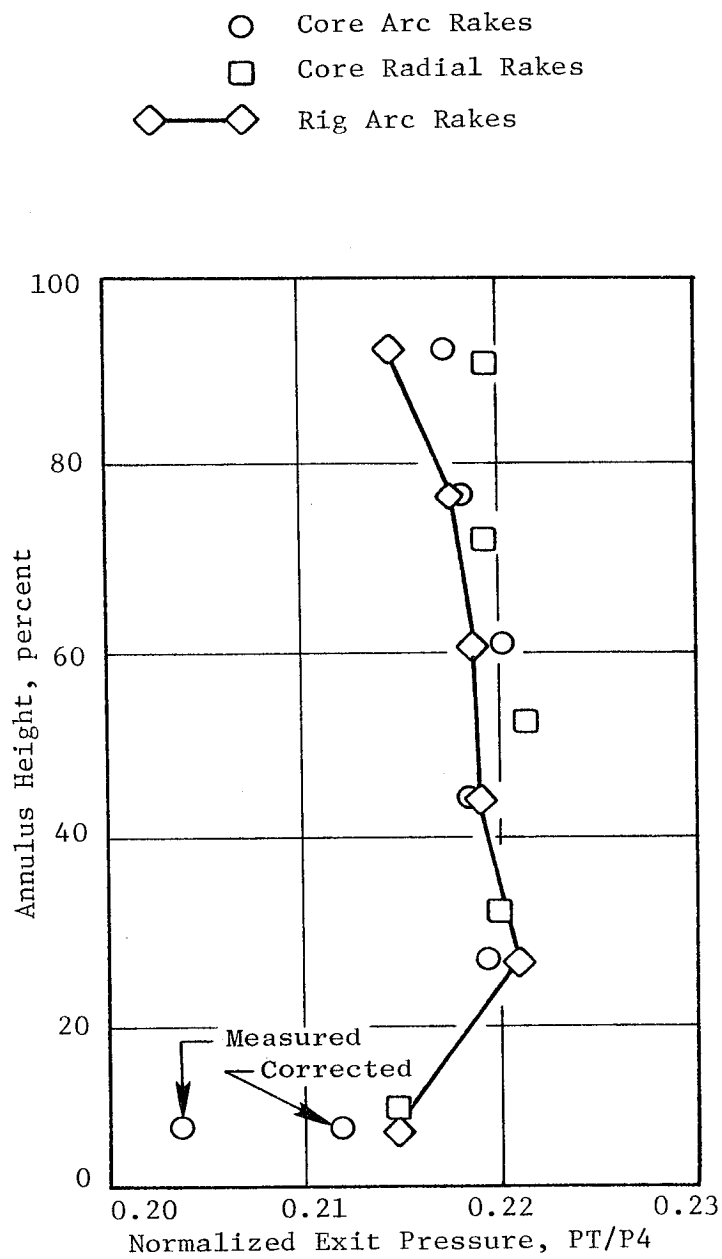


Figure 259. Comparison of HP Turbine Exit Pressure Profiles, Core Versus Rig.

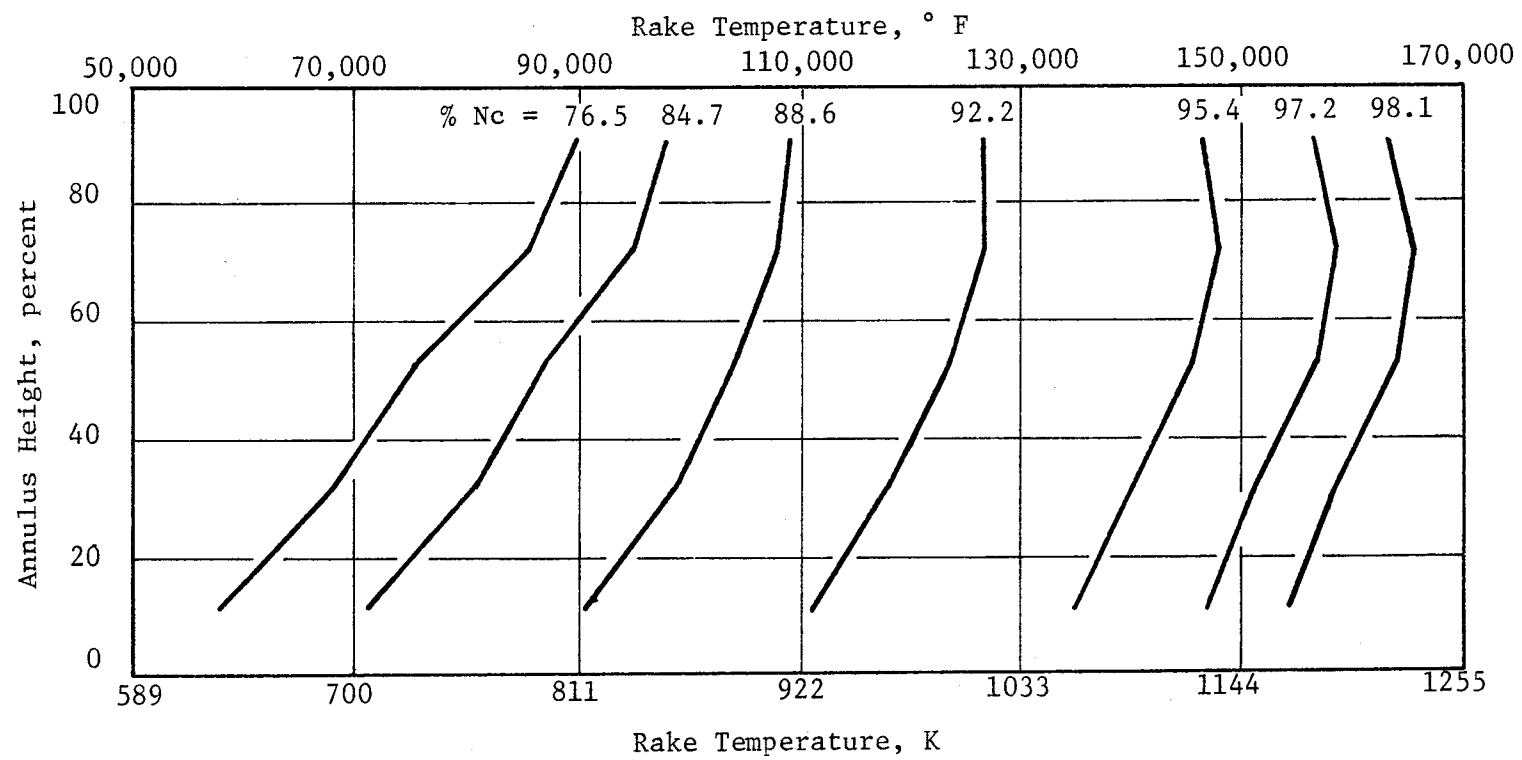


Figure 260. Core Turbine Exit Temperature Profiles.

work distribution and coolant dilution have had only a minor effect on the exit profile compared to the combustor profile.

The axial static pressure distribution through the turbine is presented in Figure 261 for the 98.1% speed point. The design intent distribution and that from the rig test are also shown. The pressure from the core test at the Stage 1 exit is higher than design intent. Some of this is due to the Stage 1 blade being cut back, but the core data show a greater difference than expected. A vector diagram calculation was generated to match the static pressures behind each row of airfoils. This analysis indicated that the Stage 1 blade effective flow area was larger than expected and the Stage 2 vane effective flow area was smaller than expected. The implications of this are lower reaction and lower work extraction on Stage 1. This latter item results in a higher temperature into Stage 2. The design intent work split was 57/43. Going into the core test, it was estimated that the split would be 53/47 due to the various differences in the core build (+4% A41, cutback blade, more cooling flow, etc.). Based on the static pressure data of the core test, it is estimated that the work split was 52.5/47.5. The work shift to Stage 2 meant that the more efficient stage did a larger portion of the work, and thereby increased the efficiency of the two-stage group. This accounts for a small amount of the increase in efficiency over the two-stage rig. The FPS design will retain the original work distribution because of cooling air backflow considerations for the Stage 2 vane leading edge.

In summation, the operation of the HP turbine in the core engine build agreed very well with that of the rig test. This was evidenced by the core turbine efficiency levels being at least equal to or slightly better than the component test levels at high power operating points. Turbine flow function was as intended. Exit pressure profiles were in good agreement with rig test results.

6.8 SUMPS, DRIVES, GEARBOX, AND PIPING PERFORMANCE

All components in the sumps, drives, gearbox, and piping functioned well during testing of the core engine. Each area is described in detail in the following paragraphs.

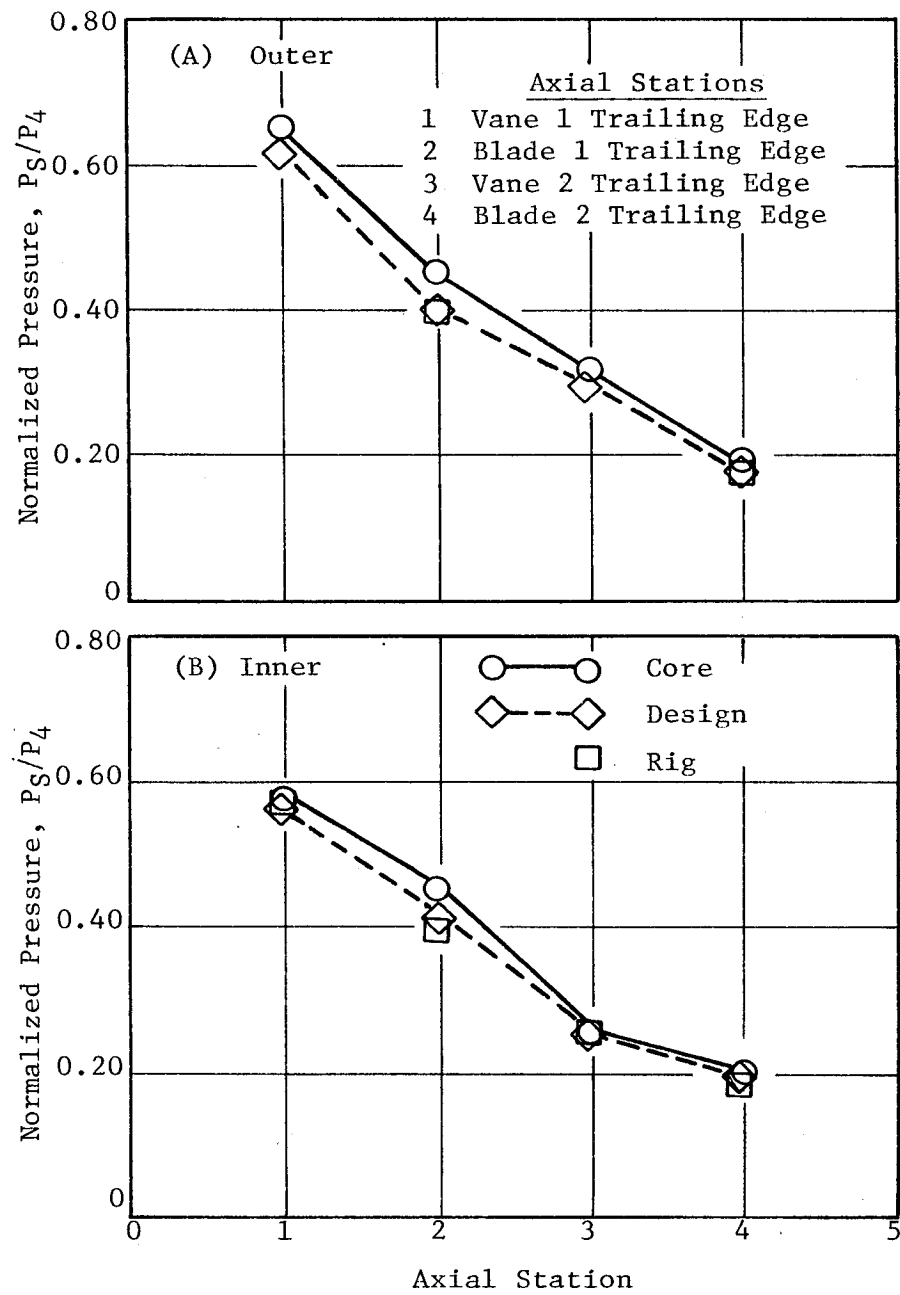


Figure 261. Turbine Static Pressure Distribution.

6.8.1 Forward Sump

Figure 262 shows the thrust bearing temperature versus core engine speed. Both outer and inner race temperatures were measured. The maximum outer race temperature was 137.8° C (280° F) which was well below the test limit temperature of 204.4° C (400° F). The bearing inner race ran 25° C (45° F) lower than the outer race. The design analysis utilized 148.9° C (300° F) for the outer race temperature with the inner race 13.9° C (25° F) cooler. These calculations were made with an 82.2° C (180° F) oil temperature. The difference between the calculation and the actual measured temperatures was not of a magnitude to have a detrimental effect on the performance of the bearing. At inspection teardown of the core engine, the bearing was found in excellent condition and will be used in the ICLS engine.

An axial proximity probe, sensing the bearing inner race axial movement, indicated the bearing was always thrust in a forward direction, as predicted.

Proximity probes to sense radial movement of the core thrust bearing were installed on the core engine. Figures 263 and 264 show the double-amplitude deflection measured by these probes in the horizontal and vertical plane, respectively, for the complete speed range of the engine.

The forward sump pressure was maintained at approximately 68.9 kPa (10 psia) for ambient inlet conditions and approximately 82.7 kPa (12 psia) at an inlet pressure of 151.7 kPa (22.0 psia). A posttest inspection indicated no oil leakage through the labyrinth seals.

The damper functioned well throughout the test and the leakage rate had not changed when posttest flow-checked. At disassembly, both piston rings were found installed backwards. This will be corrected for ICLS.

6.8.2 Aft Sump

Figure 265 shows the aft roller bearing inner and outer race temperatures along with the predicted temperatures. The indicated roller bearing temperatures were higher than predicted. Specifically, at the high-speed point the outer race was about 33° C (60° F) higher than calculated, and the inner race

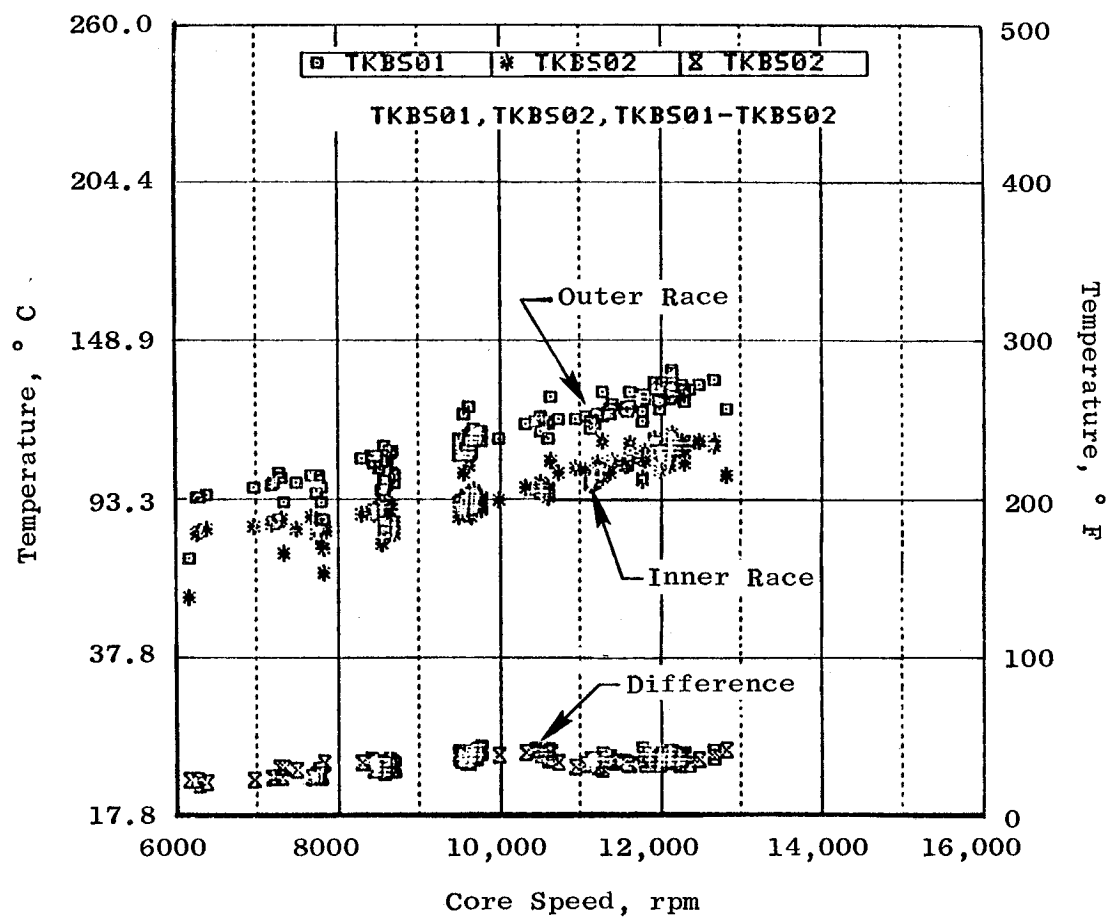


Figure 262. Thrust Bearing Temperature.

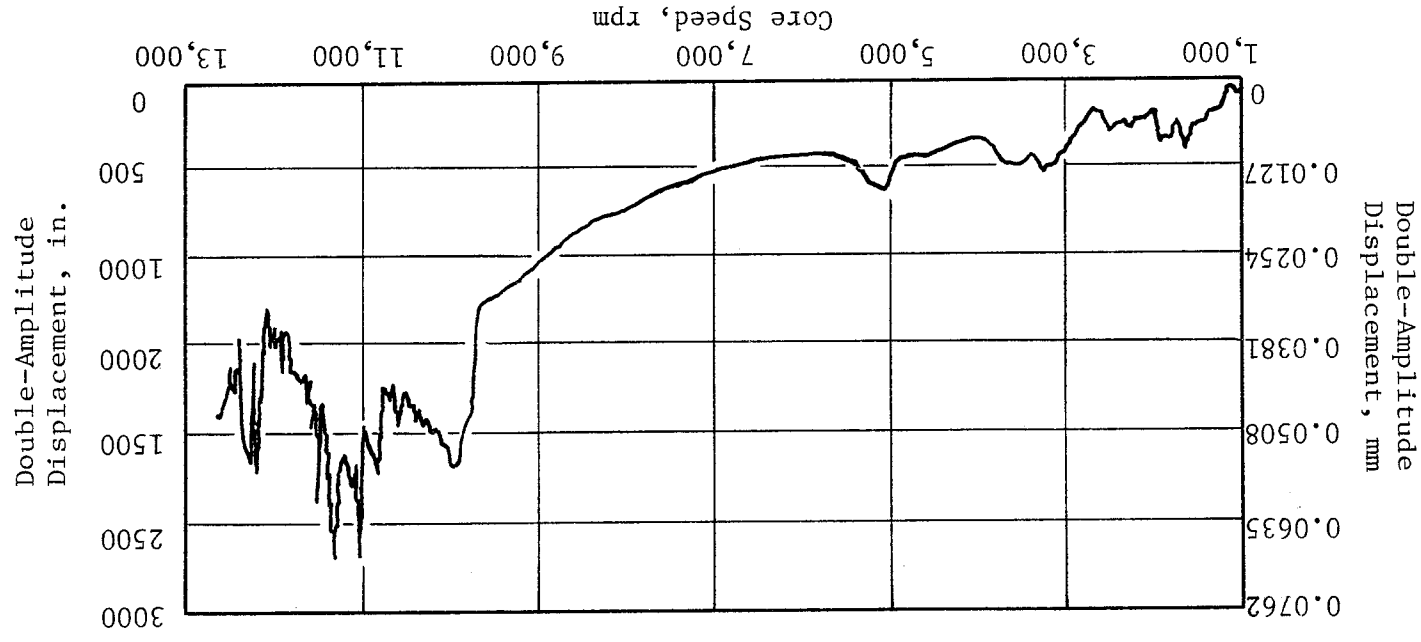


Figure 263. Thrust Bearing Proximity Probe Output Sensing Radial Motion (Horizontal Plane).

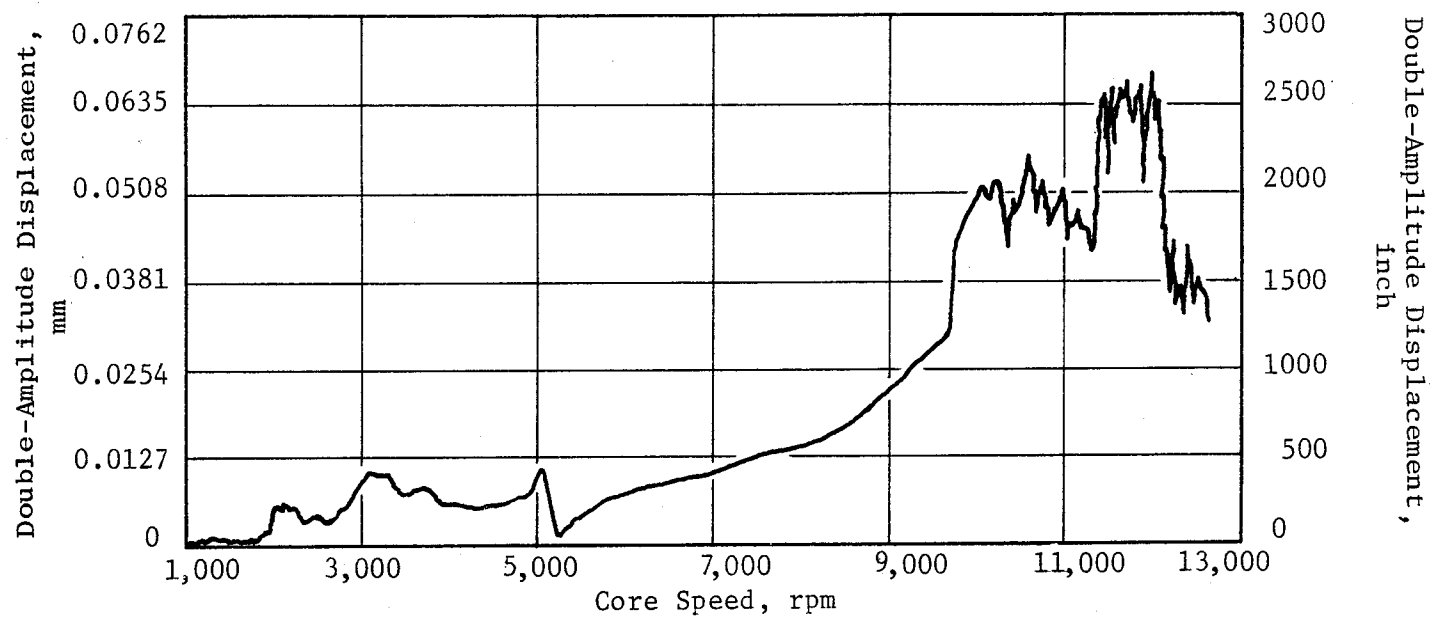


Figure 264. Thrust Bearing Proximity Probe Output Sensing Radial Motion (Vertical Plane).

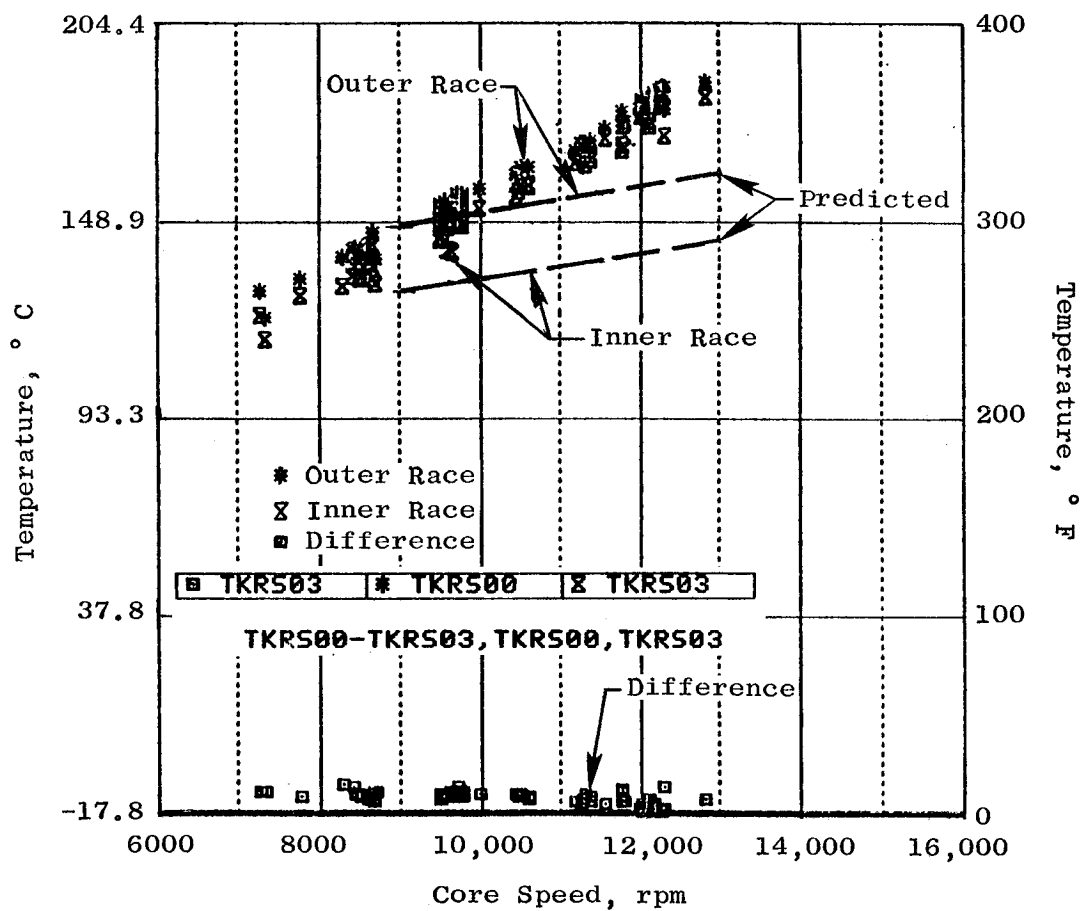


Figure 265. Aft Roller Bearing Performance Temperature.

was about 39° C (70° F) higher than predicted. The bearing inner and outer races ran at almost the same temperature which indicates that the internal clearances were only affected by rotation. This isothermal operation did help to prevent roller skidding by minimizing the thermal effects. The absolute temperature level recorded for the bearing did not exceed the test limits or capability of the bearing.

Sump pressures and pressurization flows were as predicted, and no oil loss was detected in the aft sump region.

The performance of the aft roller bearing during the core testing was a concern prior to the test. The primary concern was whether this roller bearing would exhibit skidding due to its high speed and being lightly loaded. Figure 266 shows the expected bearing speed. To reduce the possibility of skidding, bearing and mating component fits were adjusted to values calculated to achieve this objective.

To monitor the bearing for skidding, GE had developed a method of determining cage speed during engine testing. This is done as follows: Slots are cut axially in the outer race and are made wide enough that deflections, generated as rollers pass under it, can be measured as elastic strain by strain gages. The output of the strain gage gives a dynamic readout of roller passing frequency, hence, cage speed. If the rollers are not skidding, they will pass the strain gages at a passing frequency corresponding to the cage epicyclic speed. Skidding occurs when the rollers are passing at less than or more than the theoretical epicyclic speed. The roller passing frequency is given by the following equation:

$$f_T = \frac{Z}{120} \times [1 - \alpha] \times [N_i - N_o] \text{ (peaks/second or cycles/second)}$$

where

D = roller ϕ

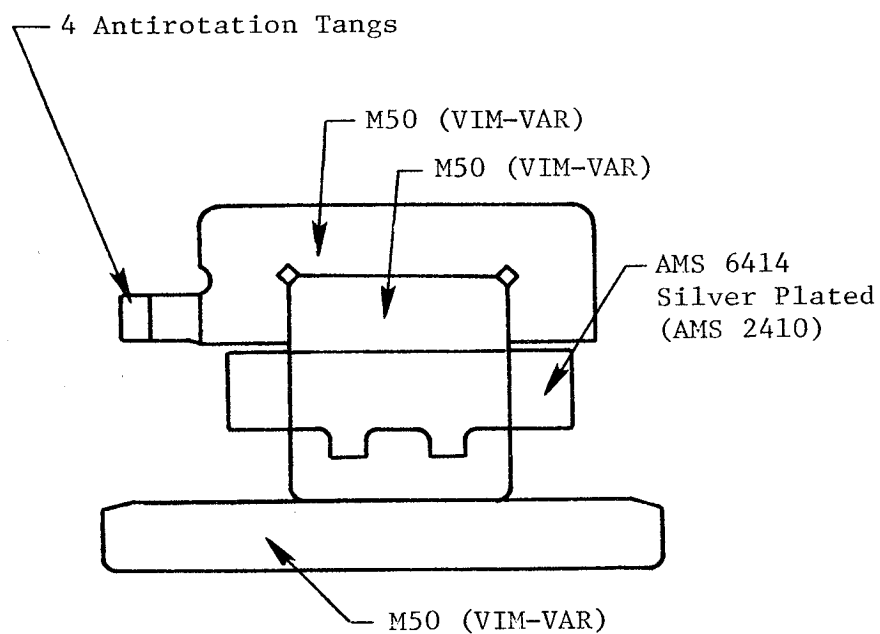
dm = pitch ϕ

Z = number of rollers

N_i = inner race rpm

N_o = outer race rpm

α = D/dm



Bore Diameter, mm (inch)	174.1	(6.856)
Mean Diameter, mm (inch)	196.9	(7.751)
Outside Diameter, mm (inch)	220	(8.660)
Element Size, mm (inch)	14 x 14	(0.5512 x 0.5512)
Number of Elements	---	28
Maximum Speed, rpm	---	13,300
DN, 10 ⁶	---	2.31
Load, kN (lbf)	3.643	[819 (Rotor 1G)]

Figure 266. Aft Roller Bearing.

For the E³ Core roller bearing

$$N_o = 0, d_m = 7.751, D = 0.5512, Z = 28 \text{ rollers}$$

$$f_T = \frac{Z}{120} \times \left[1 - \frac{D}{d_m} \right] \times N_i = \frac{28}{120} \times \left[1 - \frac{0.5512}{7.751} \right] \times N_i$$

$$f_T = 0.2167 (N_i) \text{ (cps)}$$

During testing, output of the strain gages was plotted on a Campbell diagram which shows the roller passing frequency versus core speed. Figure 267 shows the output from the strain gages. The result of the strain gage output on the Campbell diagram shows that the roller passing frequency (strain gage output) is consistent with theoretical cage speed; hence, no skidding has been detected. Posttest inspection verified that no roller skidding was indicated.

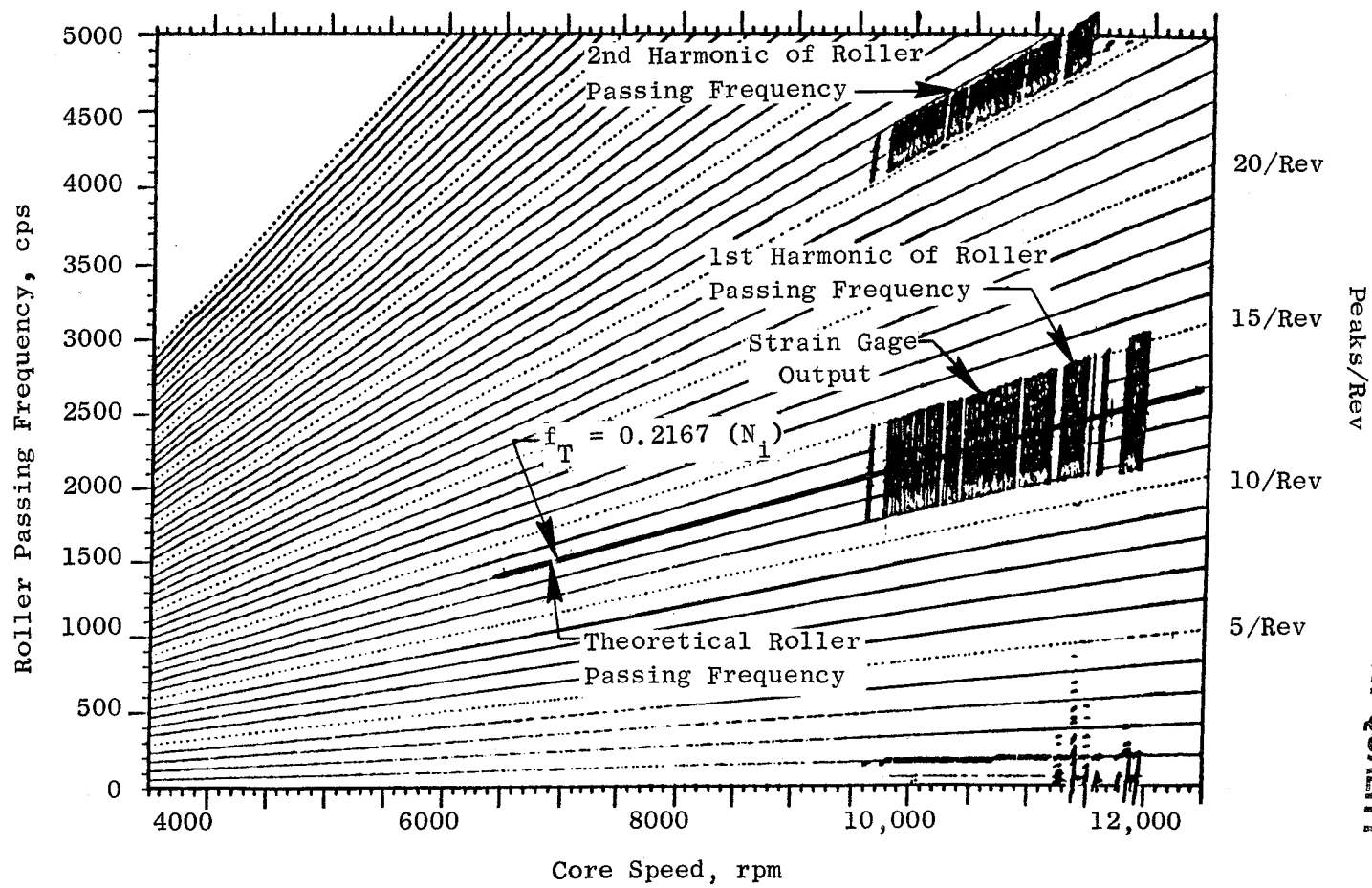
6.8.3 Accessory Drive System

All aspects of the drive system functioned well throughout the testing. During the start, as well as during the run mode, the level of vibration and oil scavenge temperature stayed below test limits. There were no signs of oil leakage from the gearbox. No signs of abnormal wear were detected by the magnetic chip detector. The AGB scavenge system performed without problems during all speed ranges.

A partial teardown of the gearbox has been completed, and all hardware is in excellent condition and ready to be rebuilt for ICLS testing.

6.8.4 Configuration

Due to the starting characteristics of the 10-stage compressor, there was a chance that it may have been necessary to bleed large quantities of seventh-stage air in order to obtain adequate stall margin in the subidle range. In this operating regime, compressor interstage pressures would not be sufficient to ensure proper cooling flow to the HP turbine. A start range turbine cooling (SRTC) augmentation system was installed to provide CDP air, with its



ORIGINAL PAGE IS
OF POOR QUALITY

Figure 267. Aft Roller Bearing Roller Passing Frequency.

inherently greater pressure, instead of fifth- and seventh-stage air during the subidle operating range. The valve was to be scheduled closed by the FADEC by the time ground-idle rpm was obtained.

During core engine mechanical checkout, it was noted that the SRTC valves did not close properly at idle. No valve position feedback signal was available, but system air temperatures and pressures indicated that CDP air, rather than seventh- and fifth-stage air, was being supplied to the turbine case cavities. Turbine temperatures were low enough at these engine speeds that it was deemed appropriate to continue the mechanical checkout until turbine Stage 2 vane temperatures became limiting.

Between DMS Readings 47 and 48, a substantial decrease in the left SRTC pipe pressure was noted (Figure 268). The ensuing inspection revealed that the left side SRTC pipe was disengaged at the flexible joint next to the SRTC valve (shown in Figure 269).

It is theorized that due to valve leakage, pressures in excess of design caused the two portions of the line to separate enough for the flexible joint to move out of the cylindrical section and into the chamfer area and become partially disengaged. When the pressure was relieved, the parts moved toward each other in such a way as to push the flexible joint out of its socket and jam it between the two ends of the pipe (Figure 270).

The decision was made to remove the damaged SRTC system and blank off the ports and pipes at the compressor and turbine cases, respectively, because seventh-stage bleed had not been required for core vehicle starts. Consequently, without the need for seventh-stage bleed, there was no need for SRTC augmentation, and the system could be removed from the vehicle.

6.8.5 Lube System

All lube system parameters functioned well throughout the test. Figure 271 shows the lube pump discharge pressure as a function of core engine speed. Oil pressures were maintained as predicted with the maximum pressure being 517.1 kPa (75 psia). No resizing of the bypass orifice described in Section 3.6 was required to maintain the proper flow distribution indicated by the lube discharge pressure.

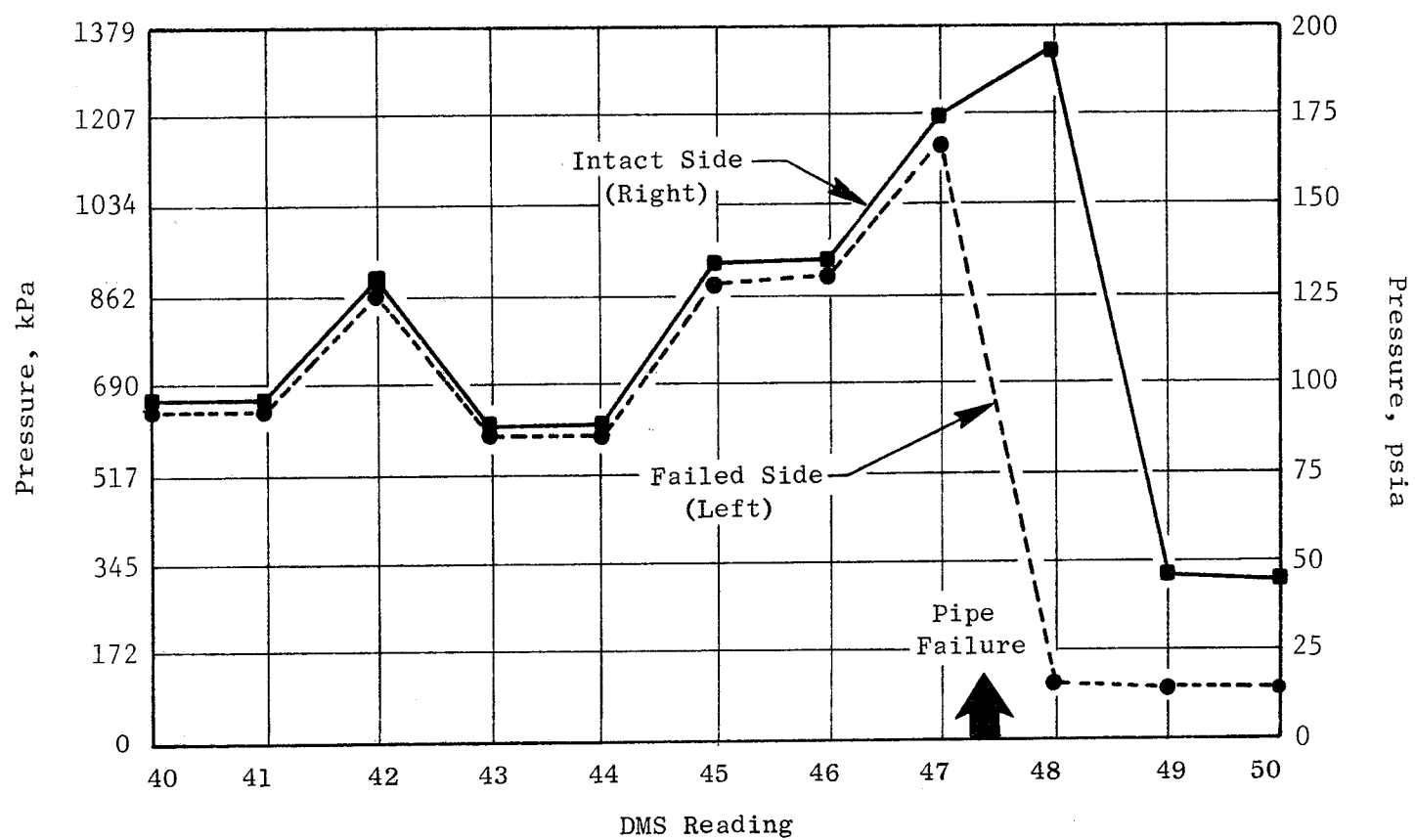


Figure 268. Start Range Turbine Cooling Pressure.

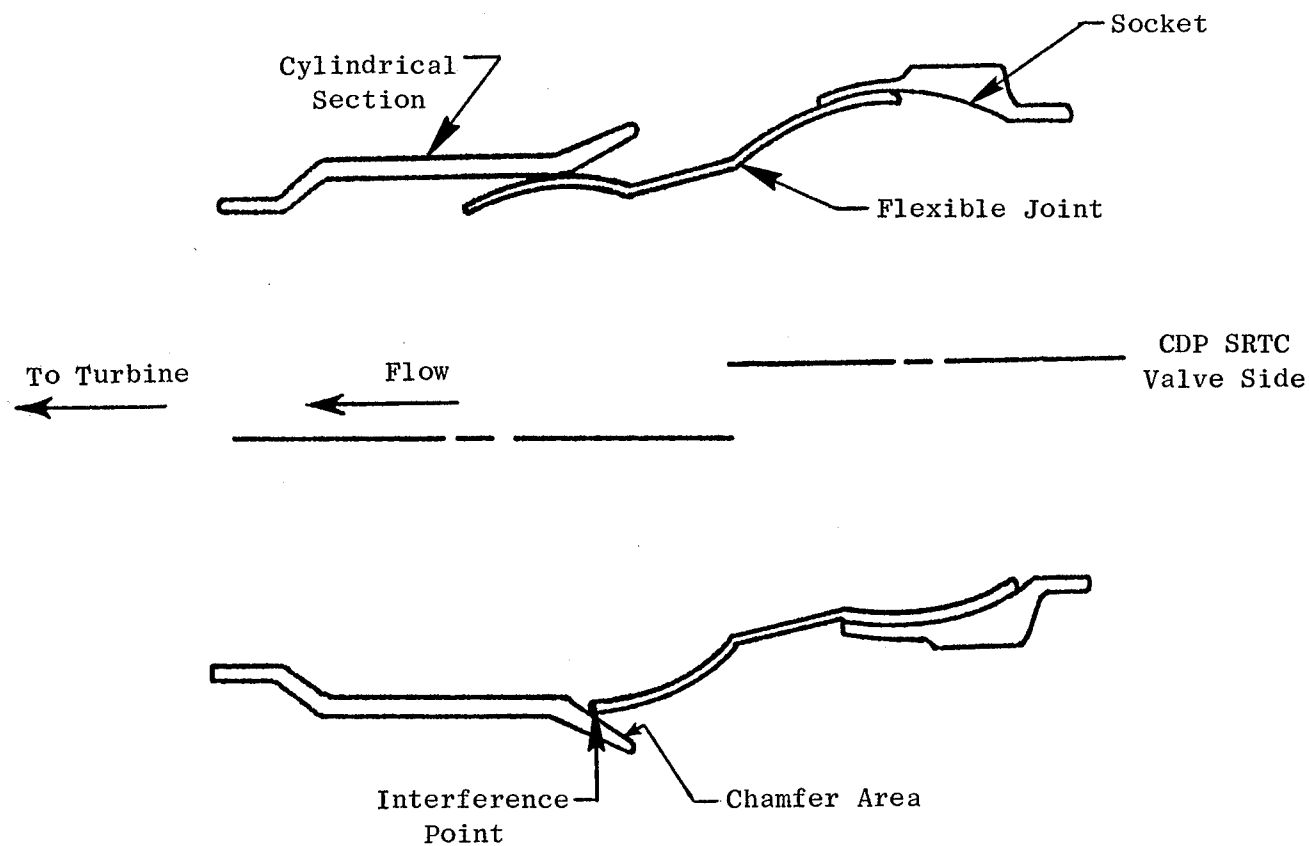
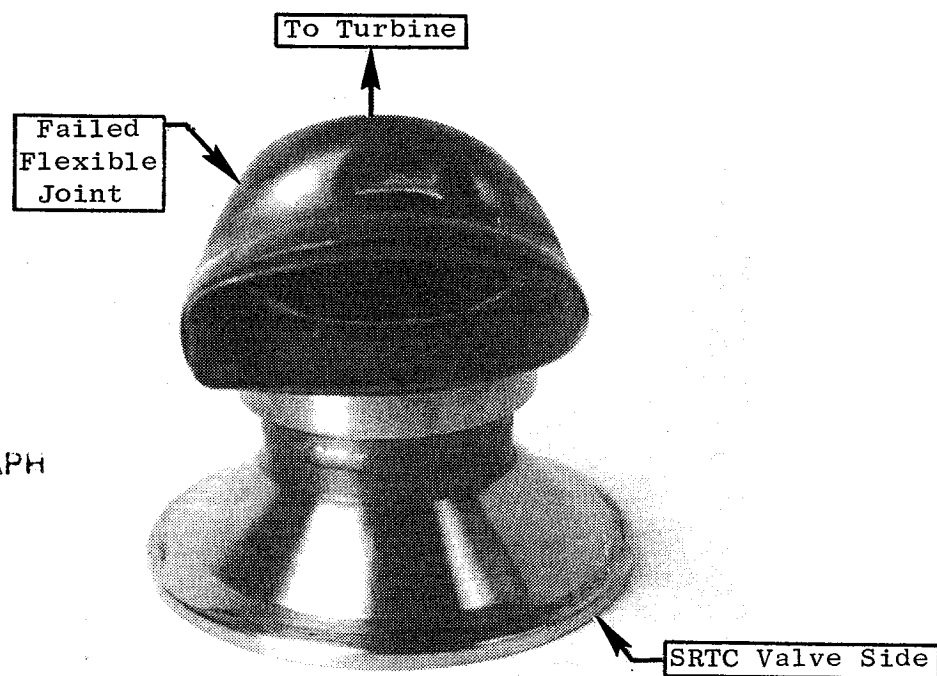
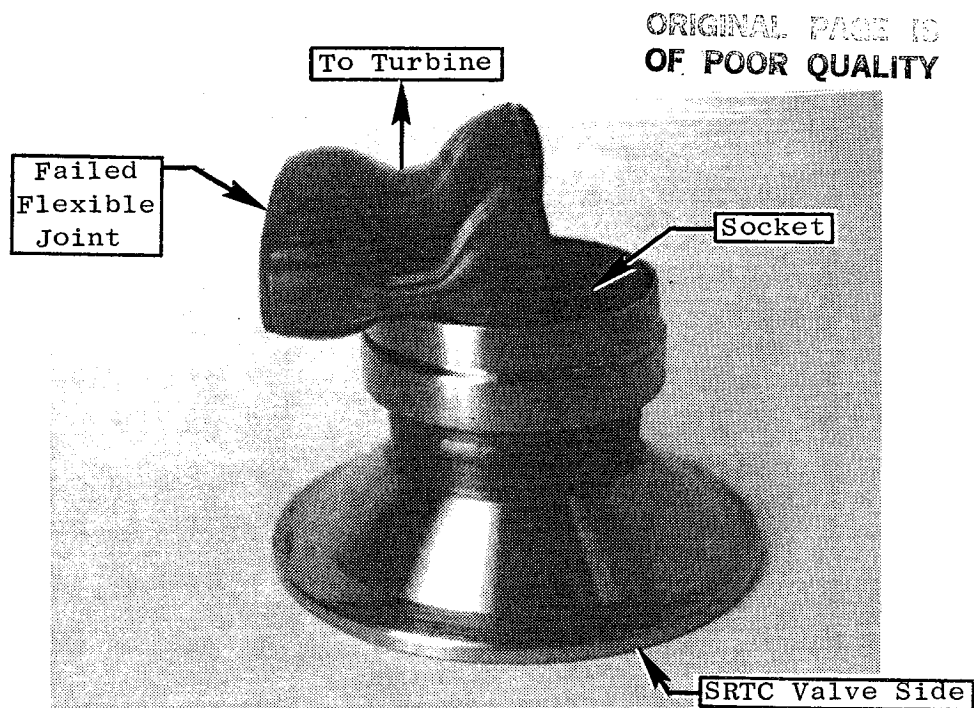


Figure 269. Flex Joint Adjacent to Start Range Turbine Cooling Valve.



ORIGINAL PAGE
BLACK AND WHITE PHOTOGRAPH

Figure 270. Failed Flex Joint in Start Range Turbine Cooling.

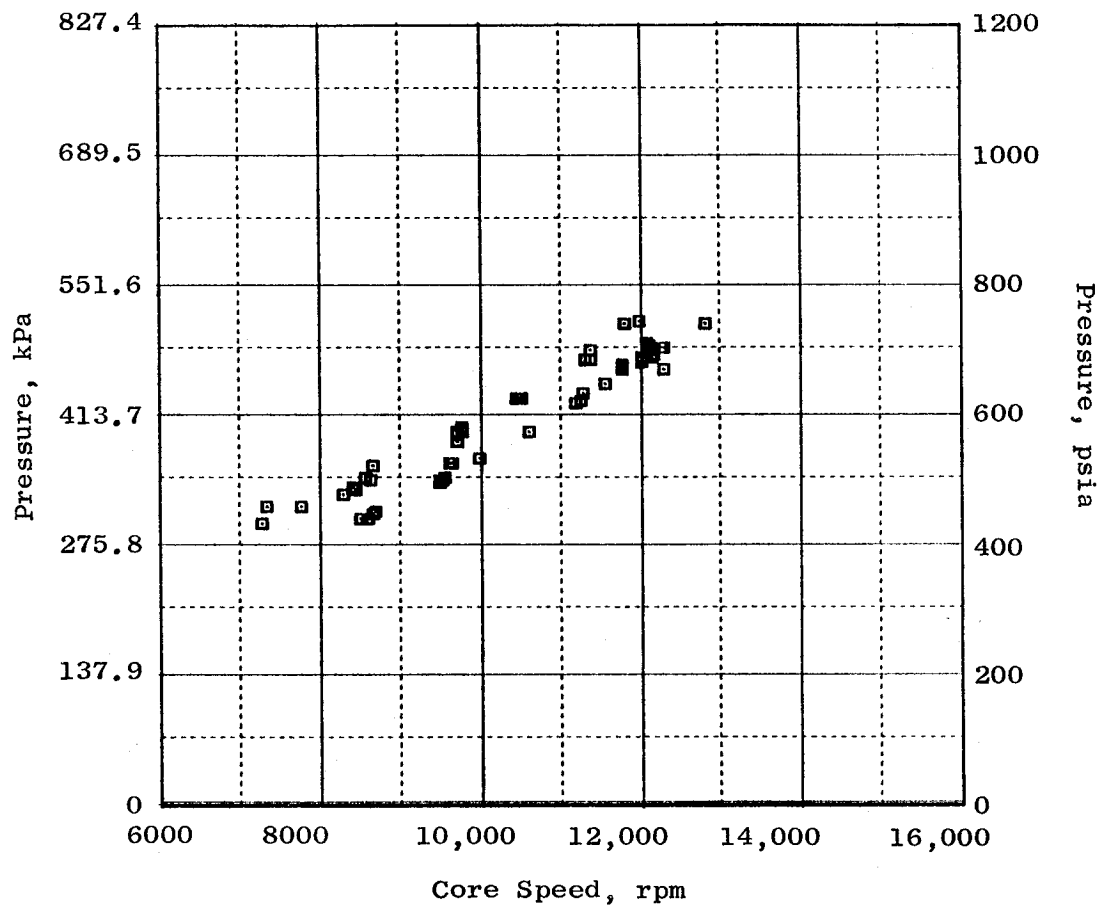


Figure 271. Lube Pump Discharge Pressure.

The lube supply temperature and the combined scavenge temperature are shown in Figure 272. The maximum lube inlet temperature was 79.4° C (175° F) and the maximum combined scavenge temperature was 101.7° C (215° F), which was well within the expected limits.

During mechanical checkout of the engine, a large facility filter was used to clean the overall lube system. This filter was used in the scavenge system.

Throughout the engine test there was no apparent oil loss when the engine was running at a steady-state condition. Measurements after shutdown did indicate some oil loss which probably occurred during transients.

The heat generated in the lube system was measured by determining the heat added to the fuel at the heat exchanger. The calculation made using measured test data is as follows:

$$Q = WC (TD - TU)$$

where

- W = The corrected measured fuel flow
- C = Specific heat of fuel as a function of temperature
- TD = Measured temperature of fuel leaving heat exchanger
- TU = Measured temperature of fuel entering heat exchanger.

Figure 273 shows this calculated heat load as a function of engine speed. The maximum heat generated was 40.4 kW (2300 Btu/minute) which is comparable to other GE Core engines.

During the initial fill-up of the oil tank it was noted that the system was requiring excessive oil. Analysis of the system indicated that oil was bypassing the antileak valve through the bypass orifice. This problem was easily resolved by placing a check valve in the system as shown in Figure 274.

6.8.6 Core Thrust Bearing Load Analysis

Pretest predictions of the axial load on the core thrust bearing were made by using computer techniques developed for engine rotor thrust analysis.

ORIGINAL PAGE IS
OF POOR QUALITY

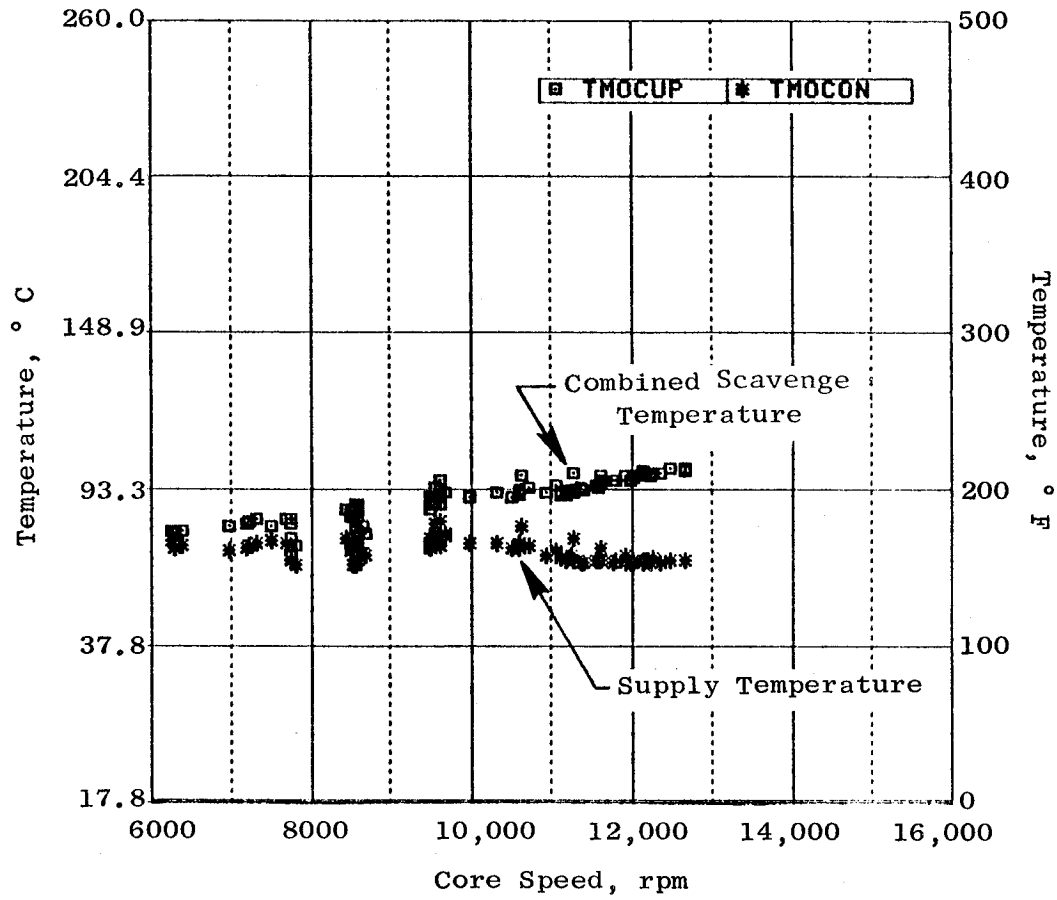


Figure 272. Lube Supply and Combined Scavenge Temperatures.

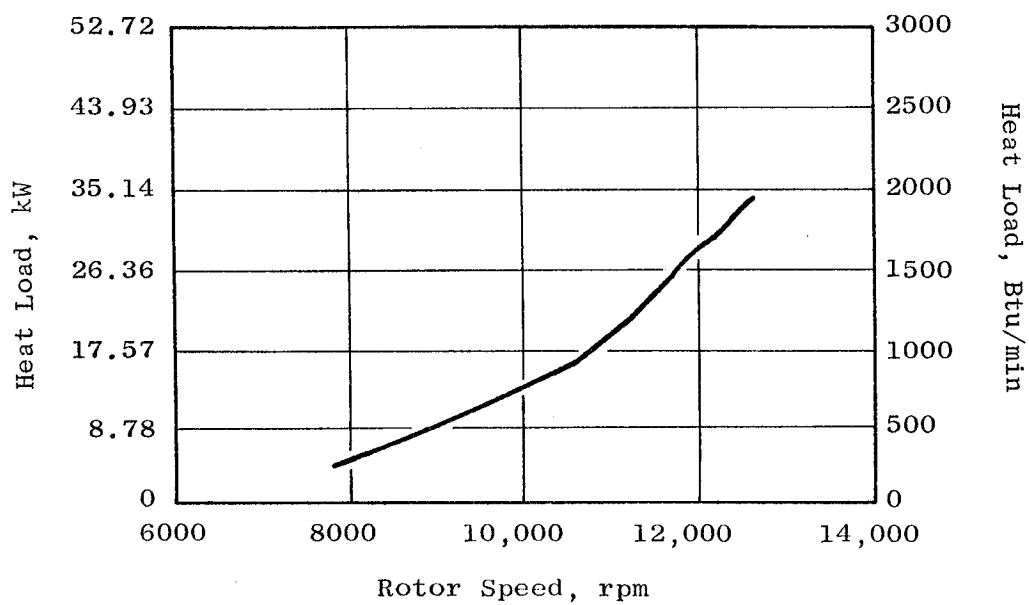


Figure 273. Lube System Heat Load.

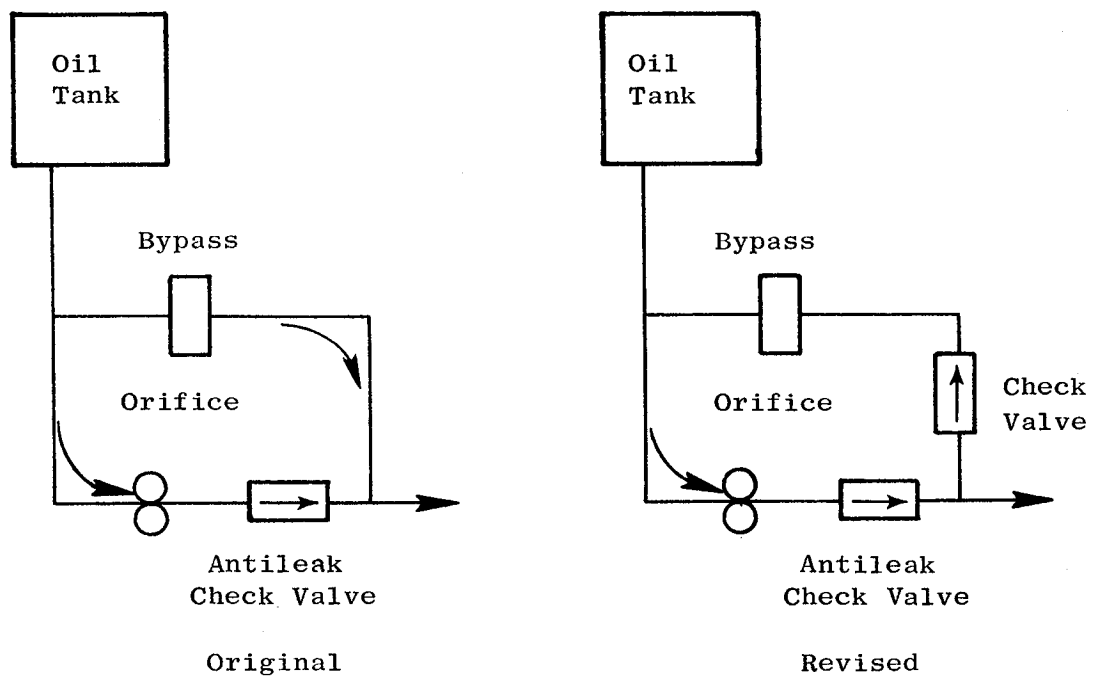


Figure 274. Schematic Showing Addition of Check Valve.

As part of substantiating these calculations, the bearing thrust load was calculated for each DMS reading using preprogrammed equations and actual test data.

Figures 275 and 276 show the predicted rotor thrust versus the test results for minimum and maximum A8, respectively.

Referring to the minimum A8 results shown in Figure 275, it will be noted that there is almost a constant difference between the predicted and the actual test results. This difference is the result of changing the balance piston cavity pressure from the original 344.7 kPa (50 psia) to 213.7 kPa (31 psia). This was done to minimize adverse cooling of the HP turbine disk due to cooler air leaking across the balance piston labyrinth seal.

Figure 276 shows a comparison of the predicted versus the test results for the maximum A8 condition. As can be seen, the difference between the predicted and test results increases at the higher corrected speed.

In order to evaluate the difference, a check was made at the 100% corrected speed point where the difference was most pronounced. The investigation revealed that the pressure on the aft side of the turbine was 107.9 kPa (15.65 psia) greater than predicted. This increase in pressure caused less aft force on the turbine blades and increased the forward force on the aft side of the turbine disk. These two forces account for the difference between the predicted and the test results.

For the maximum A8 condition, a balance piston pressure of 344.7 kPa (50 psia) was used; the load varied between 27.6 and 32.5 kN (6200 and 7300 lbf) and was always in a forward direction.

6.9 CORE SYSTEM DYNAMIC PERFORMANCE

The core engine test program was successfully completed without encountering any engine vibration problems. Synchronous vibration response levels were acceptable throughout the speed range, and the frequency response characteristics correlated well with the pretest analysis. The maximum physical speed obtained was 12,811 rpm. The isolated rotor and high load damper system performed very well throughout the test program. Results from the core test indicate that the ICLS test should be free of core synchronous vibration problems.

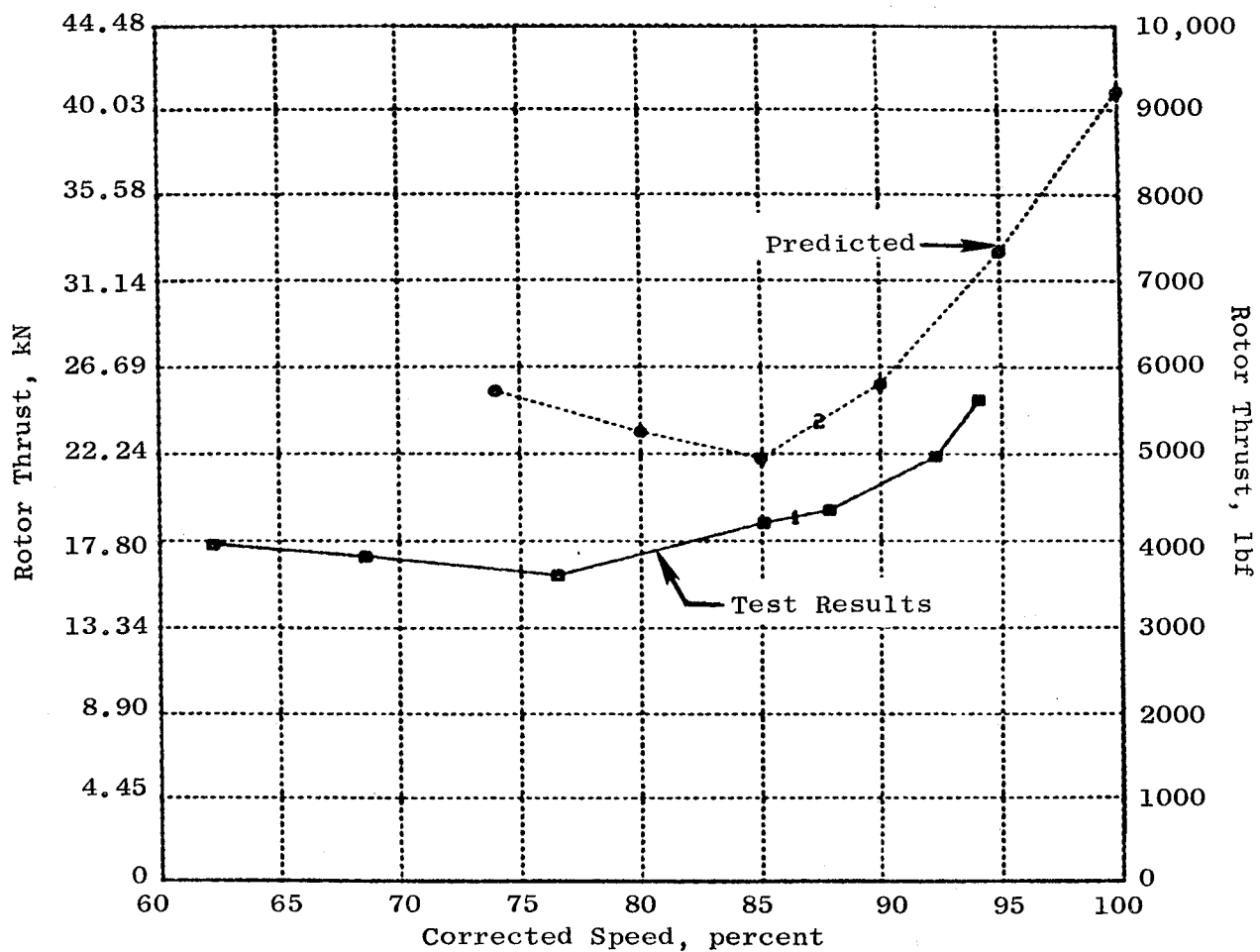


Figure 275. Core Thrust Bearing Load Minimum Exhaust Nozzle Area.

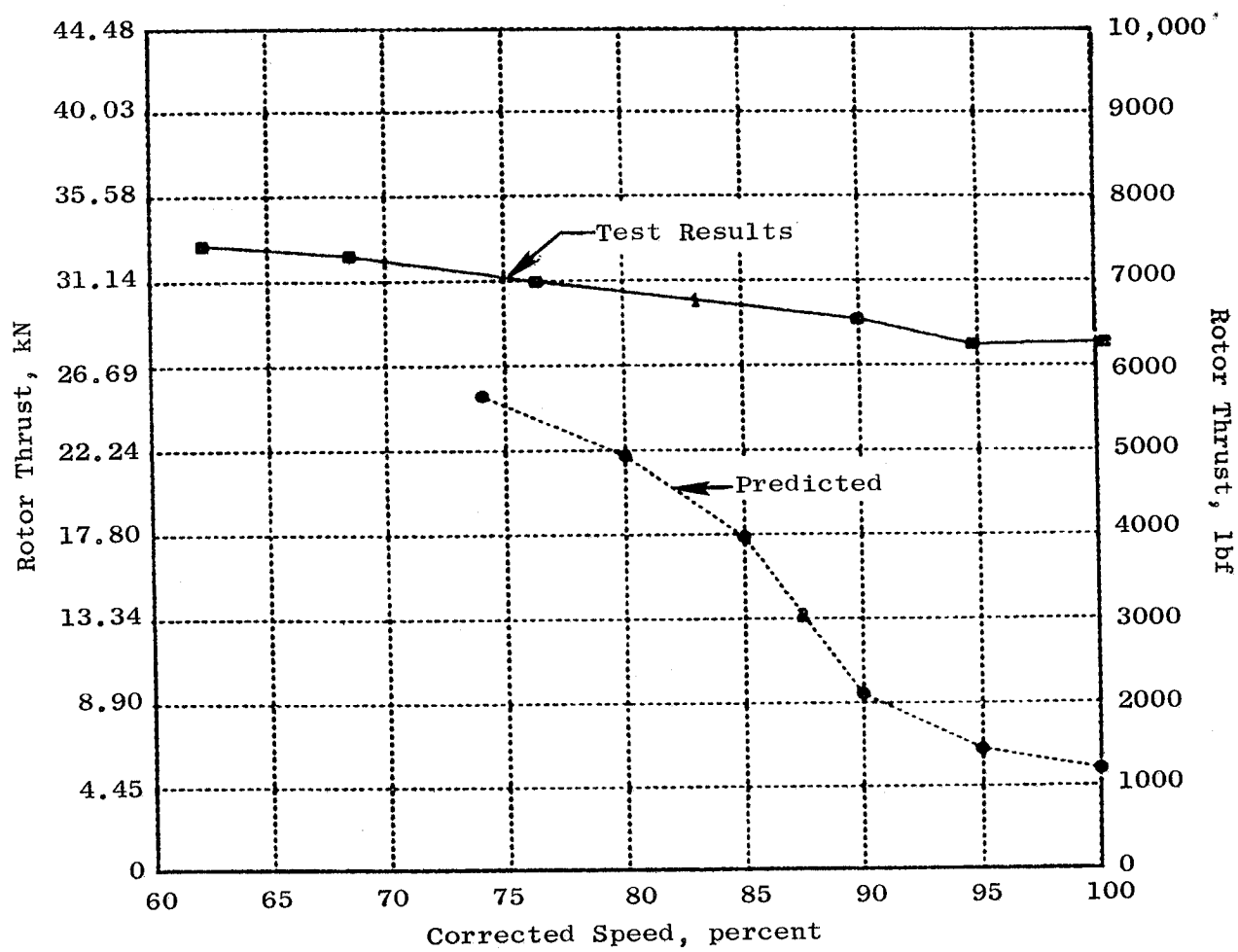


Figure 276. Core Thrust Bearing Load Maximum Exhaust Nozzle Area.

The maximum synchronous vibration level was between 0.127 and 0.152-mm double amplitude (0.005 and 0.006-inch double amplitude) at the No. 4 bearing sensor (soft side of the aft sump squirrel cage). These response levels occurred between 11,000 and 21,000 rpm following a gradual synchronous vibration level buildup that started at approximately 9,000 rpm and then leveled off at approximately 10,000 rpm with no distinct peak. Figure 277 illustrates the No. 4 bearing accelerometer 1/rev response for the decel from 12,660 to 9,700 rpm and the subsequent shutdown that occurred between 0008 and 0026 hours on 25 August 1982. This vibration response level was directly reflective of the rotor motion since the accelerometer was located on the soft side of the squirrel cage centering spring. The maximum No. 4 bearing load amplitude was 2.67 to 3.11 kN (600 to 700 lbf) based on the measured radial clearance change, 0.0635 and 0.076-mm single amplitude (0.0025 to 0.0030-inch single amplitude) at the No. 4 bearing and squirrel cage spring rate. The highest static structure 1/rev vibration response of 0.0762 to 0.1010-mm double amplitude (0.003 to 0.004-inch double amplitude) occurred on the bullet nose at 11,300 rpm. All casing, frame, bearing sump, and slipring 1/rev levels were 0.0254-mm double amplitude (0.001-inch double amplitude) or less throughout the operating speed range for the entire test program. Figures 278 through 281 illustrate the 1/rev vibration levels recorded at the bullet nose, compressor casing, turbine frame, and the hard side of the No. 3 bearing (forward sump) accelerometers during the decel from maximum speed referenced above.

The core system dynamic characteristics illustrated in Figures 277 through 281 represent the vibration levels typical of the entire test program. The broad response buildup at the soft side of the aft squirrel cage indicated substantial system damping as expected from the multishim squeeze film damper. In addition, there was an absence of subsynchronous whirl, indicating no rotor stability problems.

The rotor support and squeeze film damper system used for the core test was the same configuration designed for the FPS/ICLS engine system. This configuration was optimized to limit secondary damage due to unbalance associated with the loss of two HP turbine Stage 2 airfoils in an FPS application. The design consisted of a soft-mounted rotor by means of squirrel cage centering springs at both bearings and a high load multishim squeeze film damper at

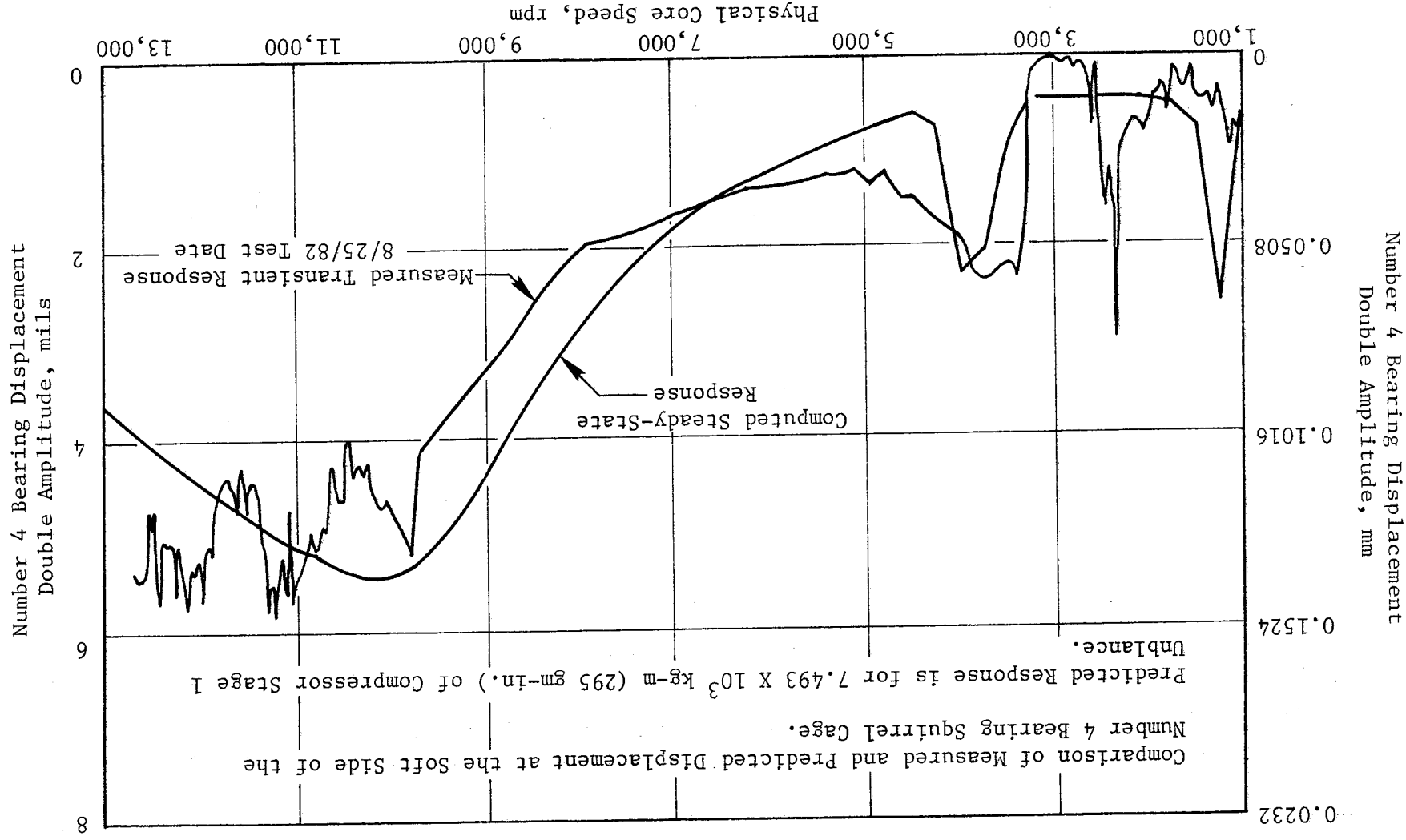


Figure 277. Core System Synchronous Vibration Response.

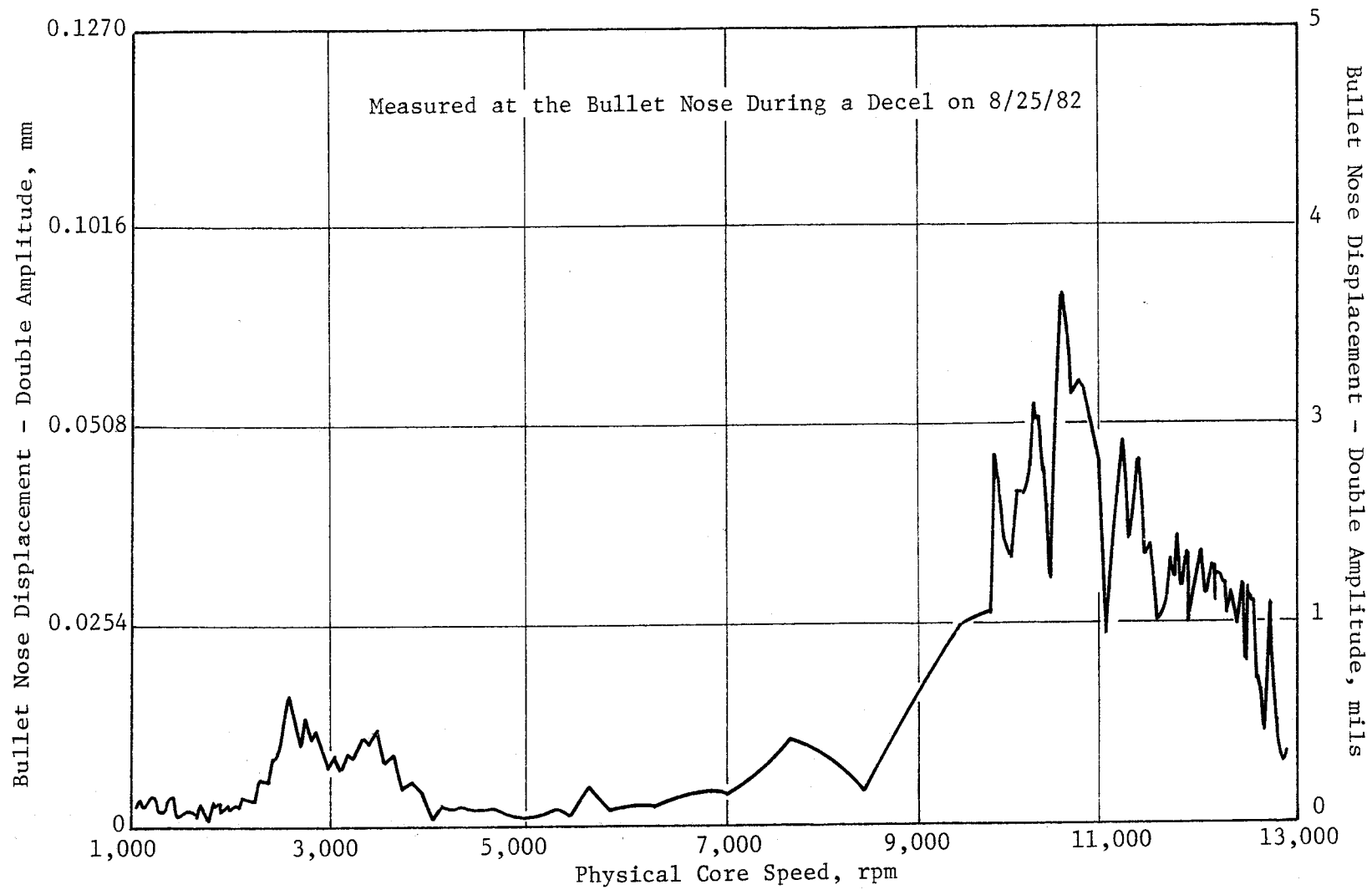


Figure 278. Core System Transient Vibration 1/Rev Displacement.

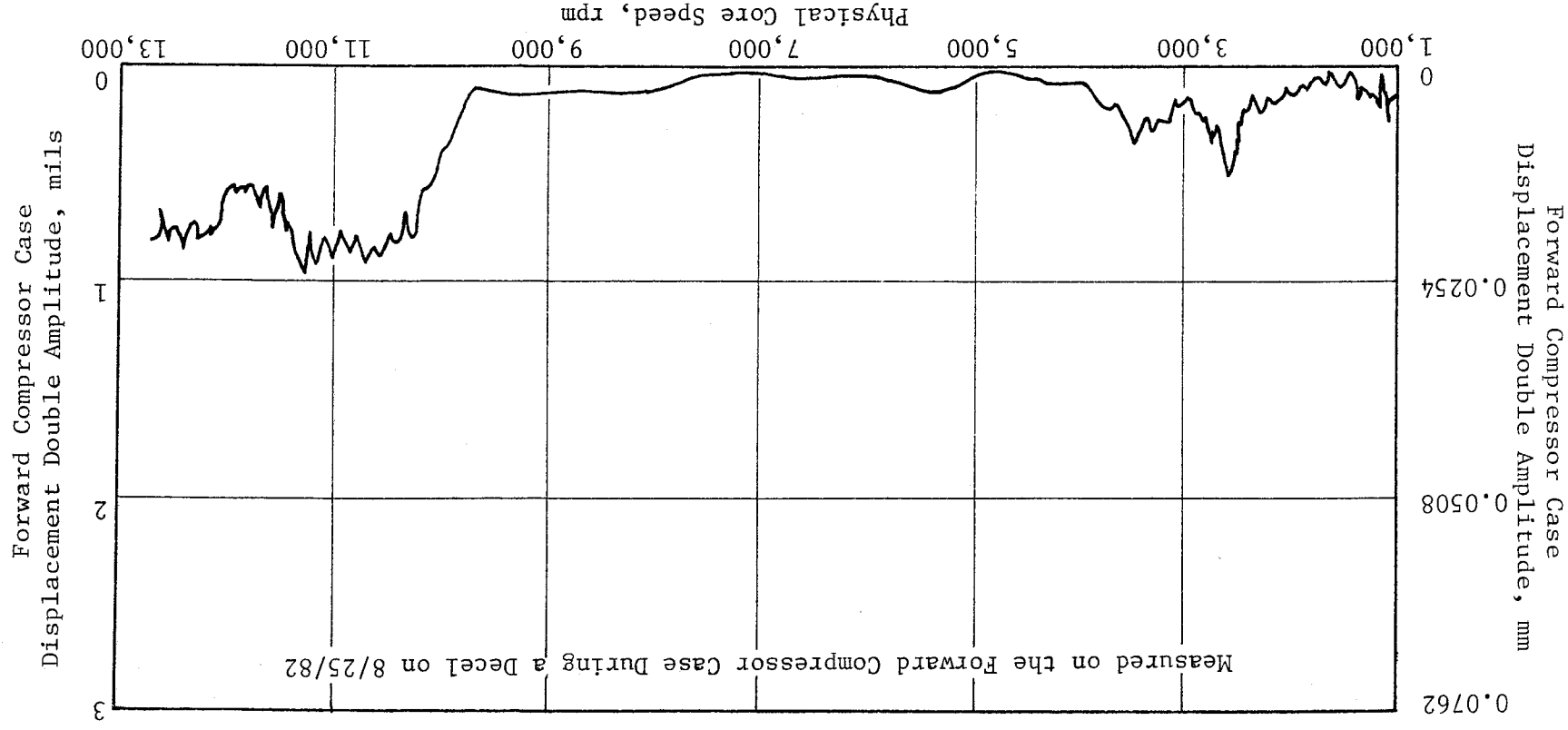


Figure 279. Core System Transient Vibration 1/Rev Displacement.

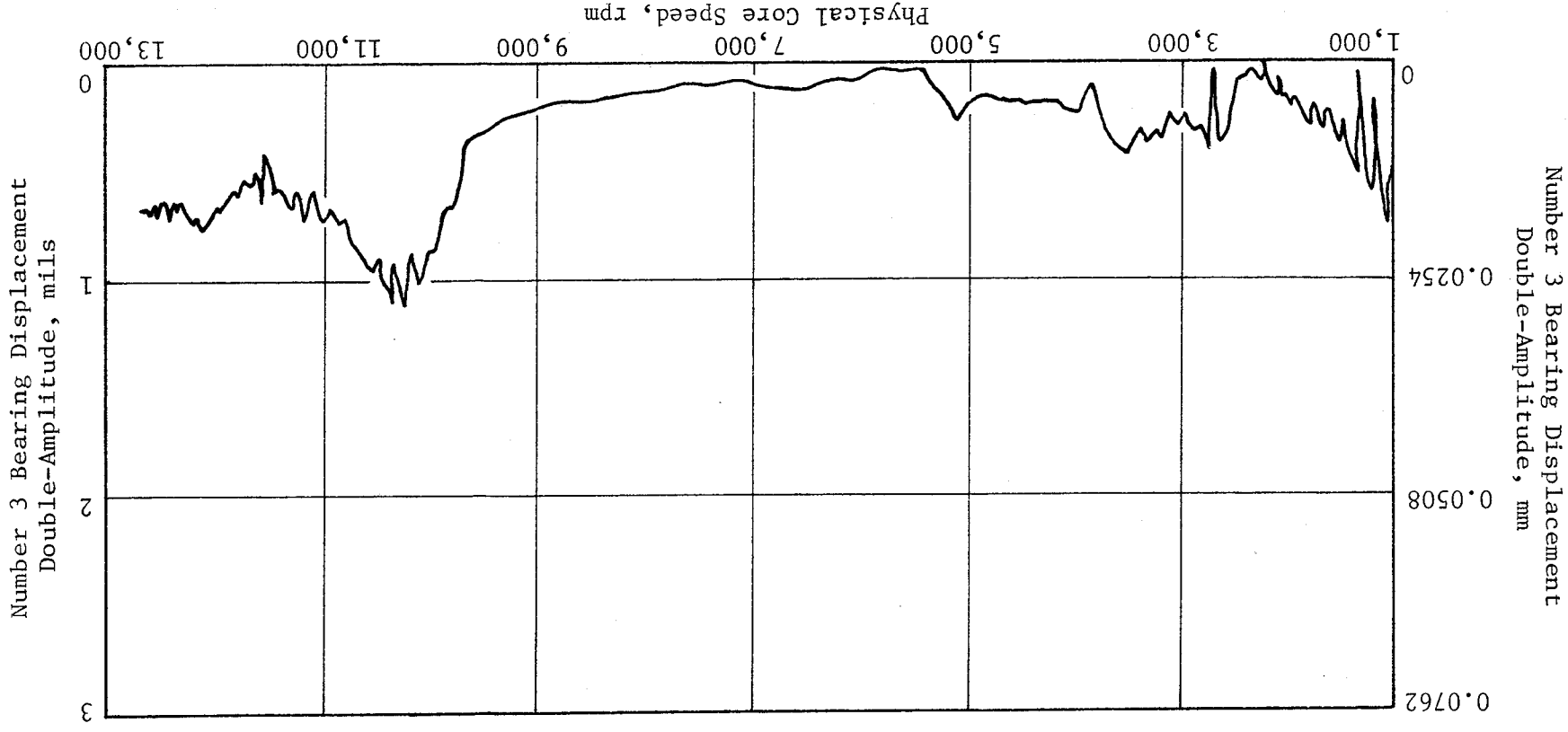


Figure 280. Core System Transient Vibration 1/Rev Displacement, Number 3 Bearing.

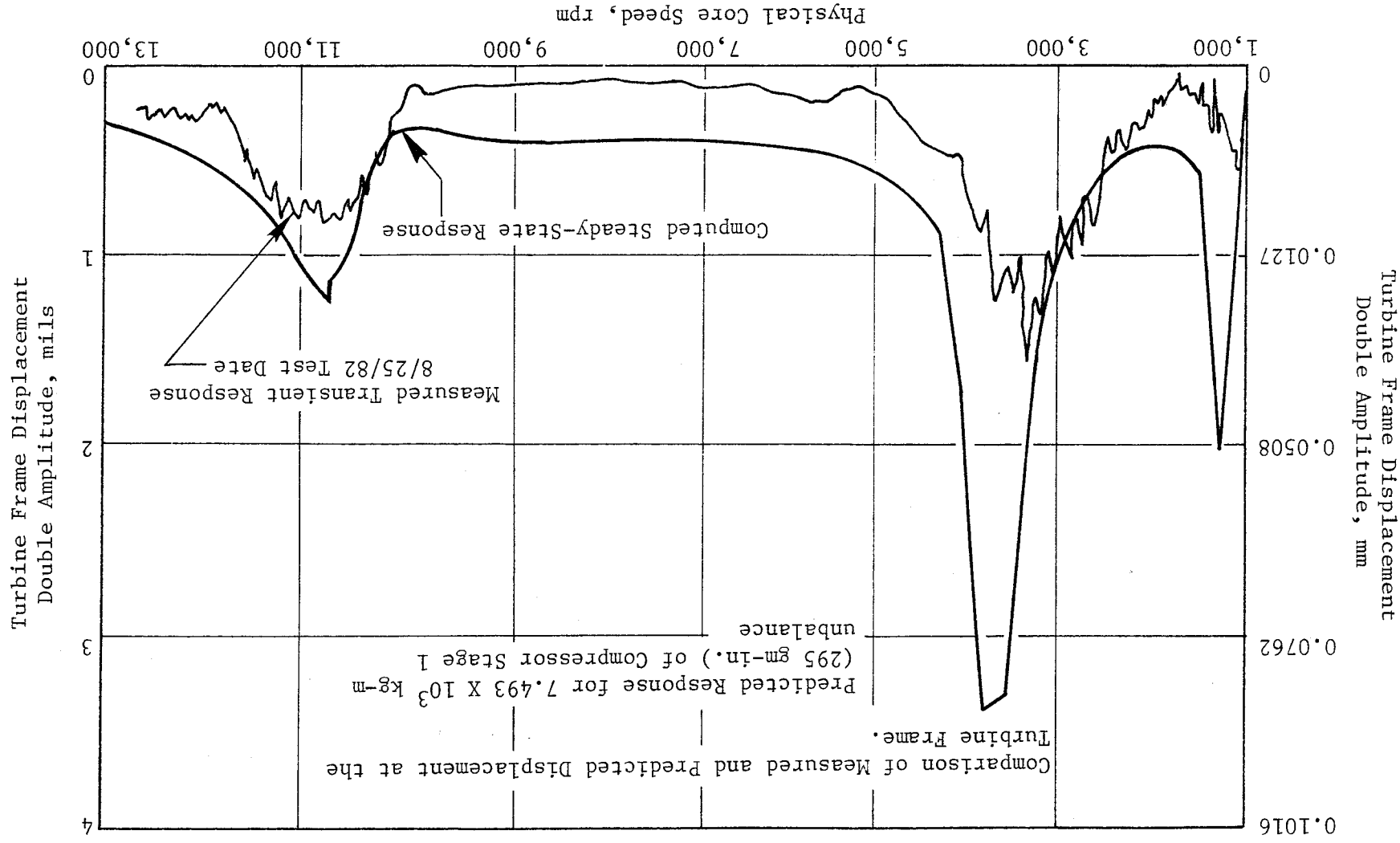


Figure 281. Core System Synchronous Vibration Response.

the forward bearing. The soft mount suspension system provided for rotor vibration isolation, and the squeeze film damper was utilized to dissipate the vibration energy associated with the rigid body modes. The system was designed to operate supercritical to the rigid body modes. The soft mounts allowed the rotor to run in a dynamically stiff configuration; that is, rotor bending did not occur over the operating speed range. The combined effect of the soft suspension system and the squeeze film damper resulted in a rotor that had a very low sensitivity to unbalance, as intended. Vibration response could have been further reduced if the rotor suspension system and damper had been uniquely optimized for the core engine. However, the ICLS damper suspension system design was incorporated in the core engine to allow for evaluation of the hardware design (squirrel cages, shim pack, and piston ring end seals) under actual engine operating conditions prior to the ICLS test. Results from the core test indicate that the rotor support and damper hardware performed as intended, and no core vibration problems are expected for the ICLS test. Figure 282 shows the configuration of the forward bearing damper and centering spring.

The core vibration test data were correlated with the design analysis to quantify the analysis procedure and to evaluate the test data. A planar finite-element analysis was used to determine critical speeds and the associated undamped mode shapes along with the potential (strain) and kinetic energy distribution. Figure 283 shows the finite-element model in schematic form. Figures 284 and 285 illustrate the rotor rigid body modes that involved mass coupling of the rotor with strain energy in the suspension system. The squeeze film damper characteristics (oil film spring and damping rates) were determined through the use of a component mode analysis. Figure 286 describes the subsystems and connecting elements used for the damper evaluation. Results from the component mode analysis verified that the peak response would occur at speeds considerably higher than 6900 rpm, the most responsive critical speed referenced in Figure 285. This is due to the damper stiffness and damping load paths which act in parallel with the squirrel cage load path at the forward rotor support. A cooler-than-anticipated damper oil inlet temperature resulted in a greater than predicted shift in the responsive rotor speeds because of the increased oil viscosity. Pretest damper system performance predictions

Forward Squirrel Cage, $K = 4,875,234 \text{ kg/m}$ (273,000 lb/in.)
Aft Squirrel Cage, $K = 4,285,920 \text{ kg/m}$ (240,000 lb/in.)
Squeeze Film Overall Radial Clearance = 0.127 cm (50 mils)

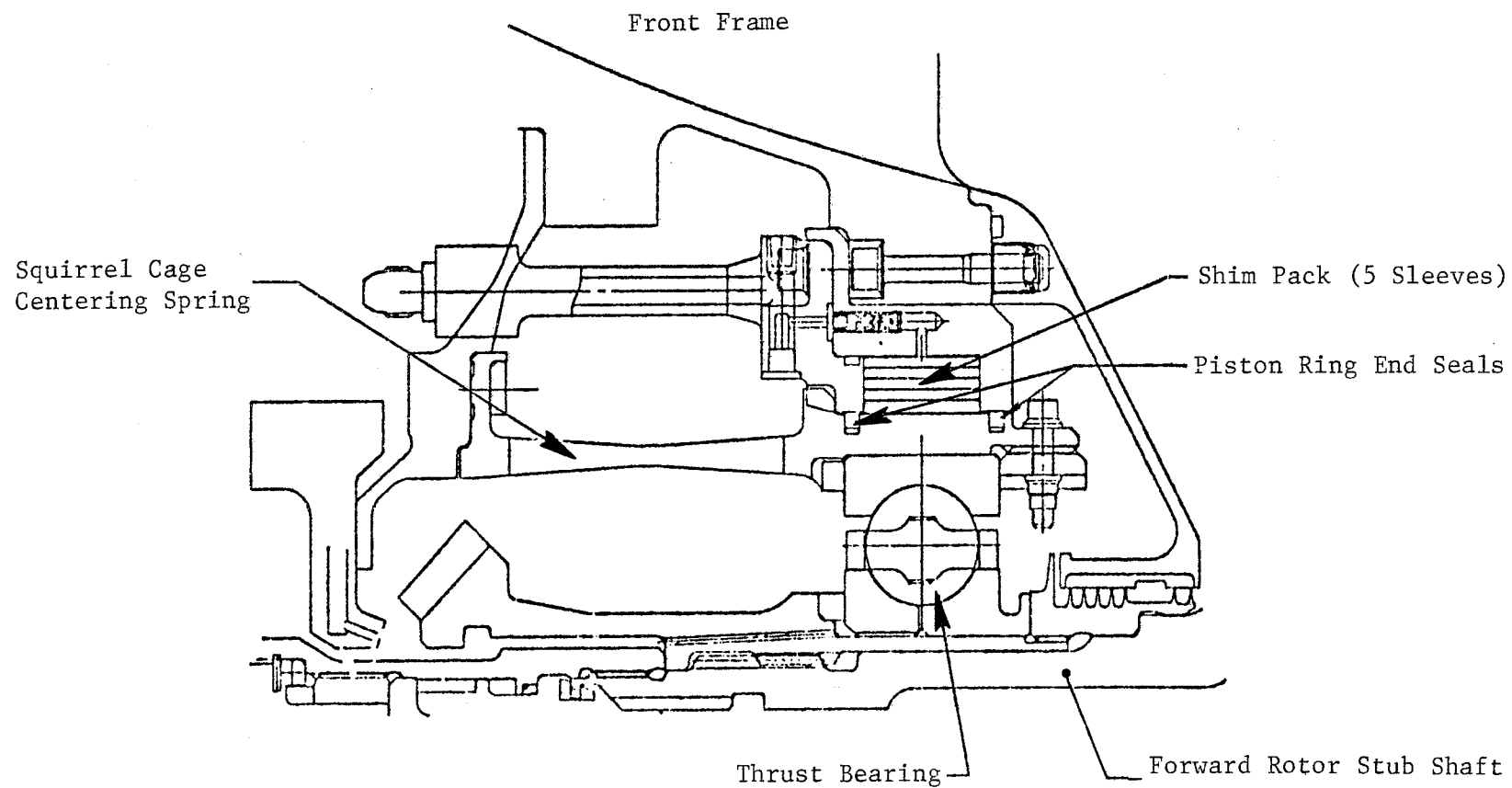


Figure 282. Forward Rotor Support and High Load Squeeze Film Damper.

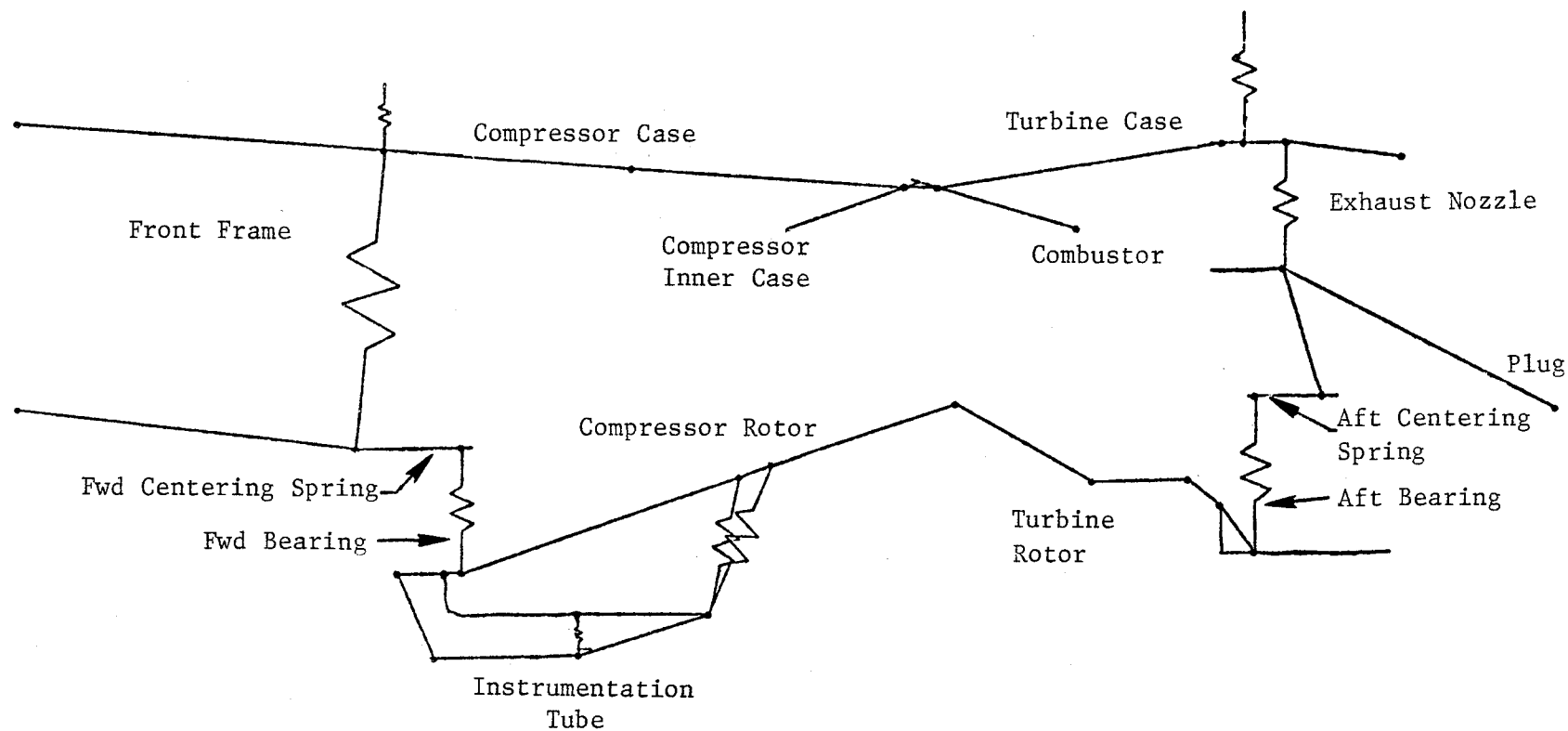


Figure 283. System Dynamic Analysis Computer Model Schematic.

Rotor Rigid Body Mode Involving Mass Coupling of Rotor with
Strain Energy in Soft Suspension System.

Number 1 Bearing = 3% Potential Energy
Number 2 Bearing = 3% Potential Energy
Fwd Squirrel Cage = 12% PE

Rotor Bending = 8% Potential Energy
Rotor Bending = 38% Kinetic Energy
Aft Squirrel Cage = 20% PE

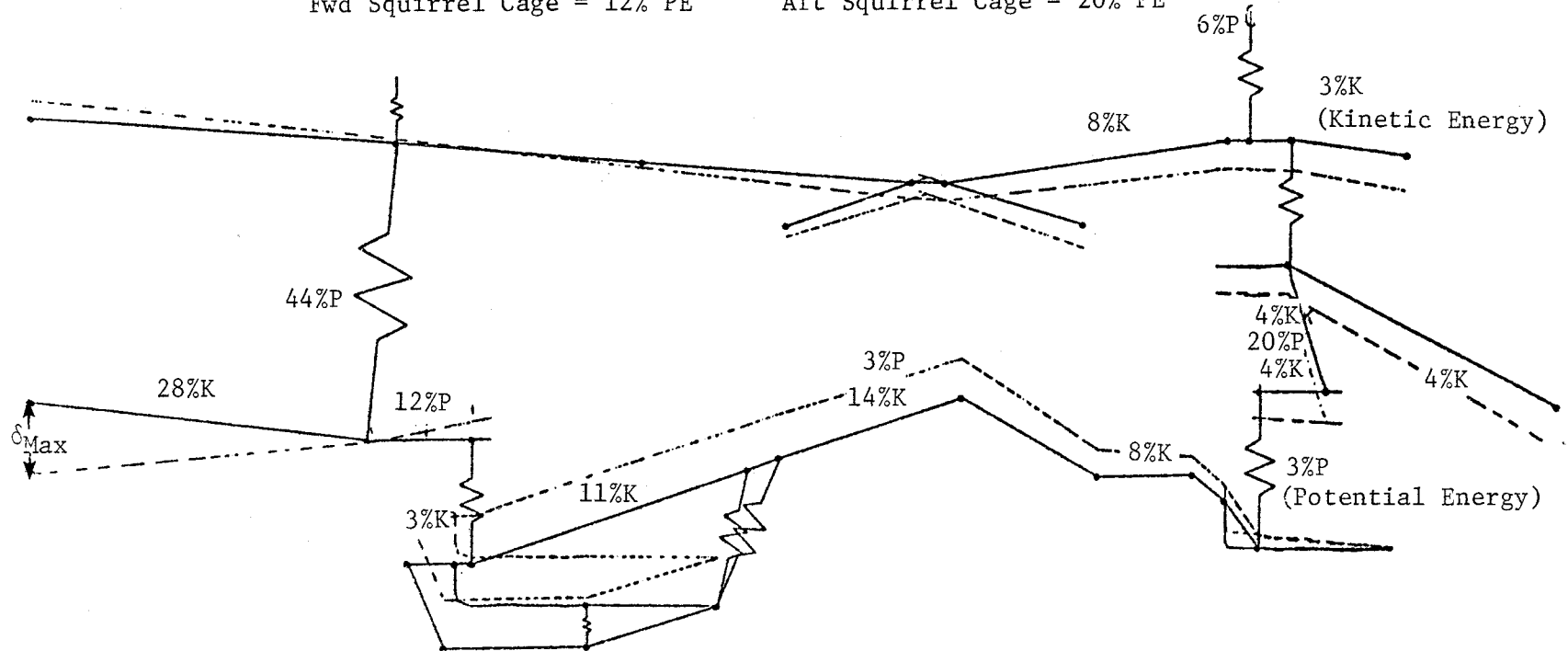


Figure 284. Modal Deflection for Critical Speed at 3469 RPM.

- Rotor Rigid Body Mode Involving Mass Coupling of Rotor With Strain Energy in Soft Suspension System
- No. 1 Brg = 13% PE, No. 2 Brg = 2% PE
- Forward Squirrel Cage = 49% PE, Aft Squirrel Cage = 15% PE
- Rotor Bending = 11% PE (Potential Energy), Rotor = 69% KE (Kinetic Energy)

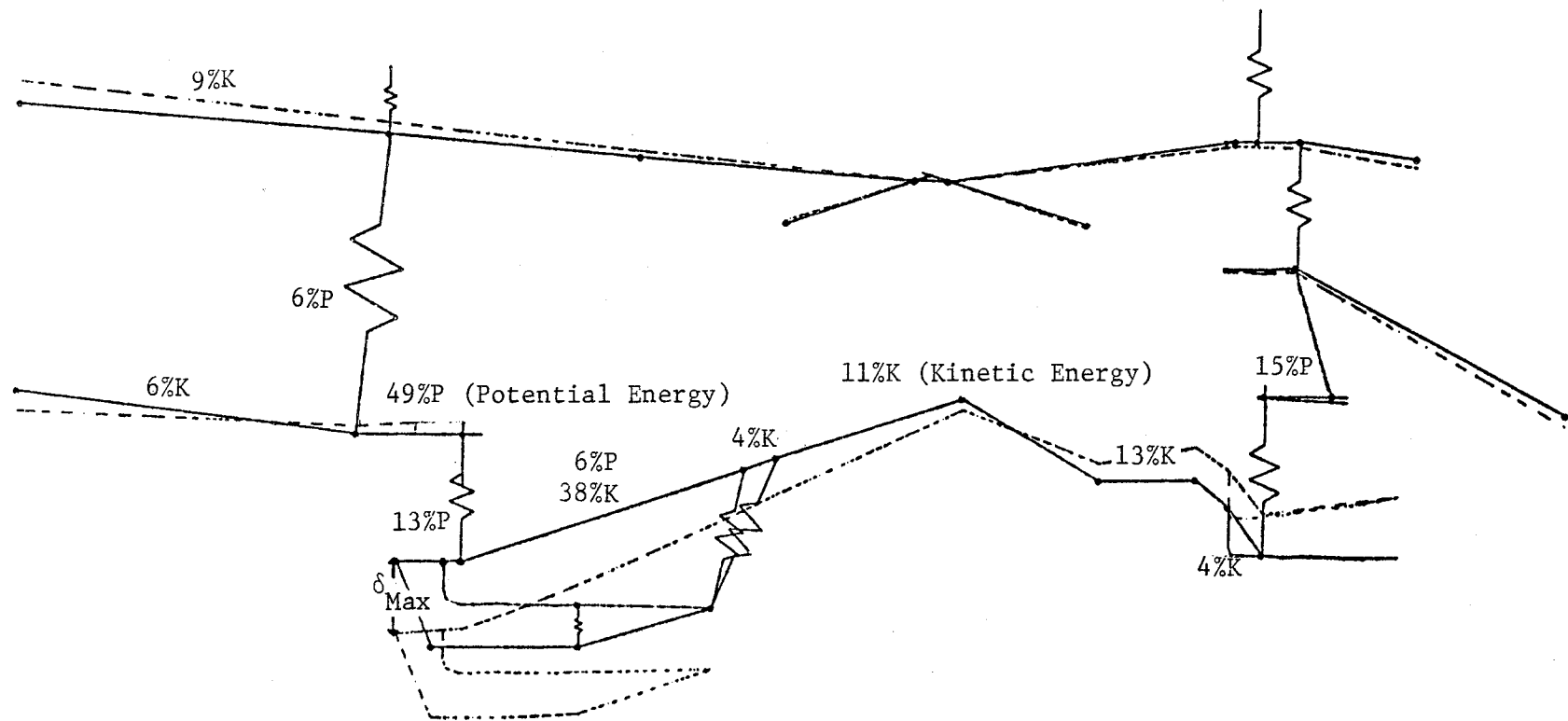


Figure 285. Modal Deflection for Critical Speed at 6911 RPM.

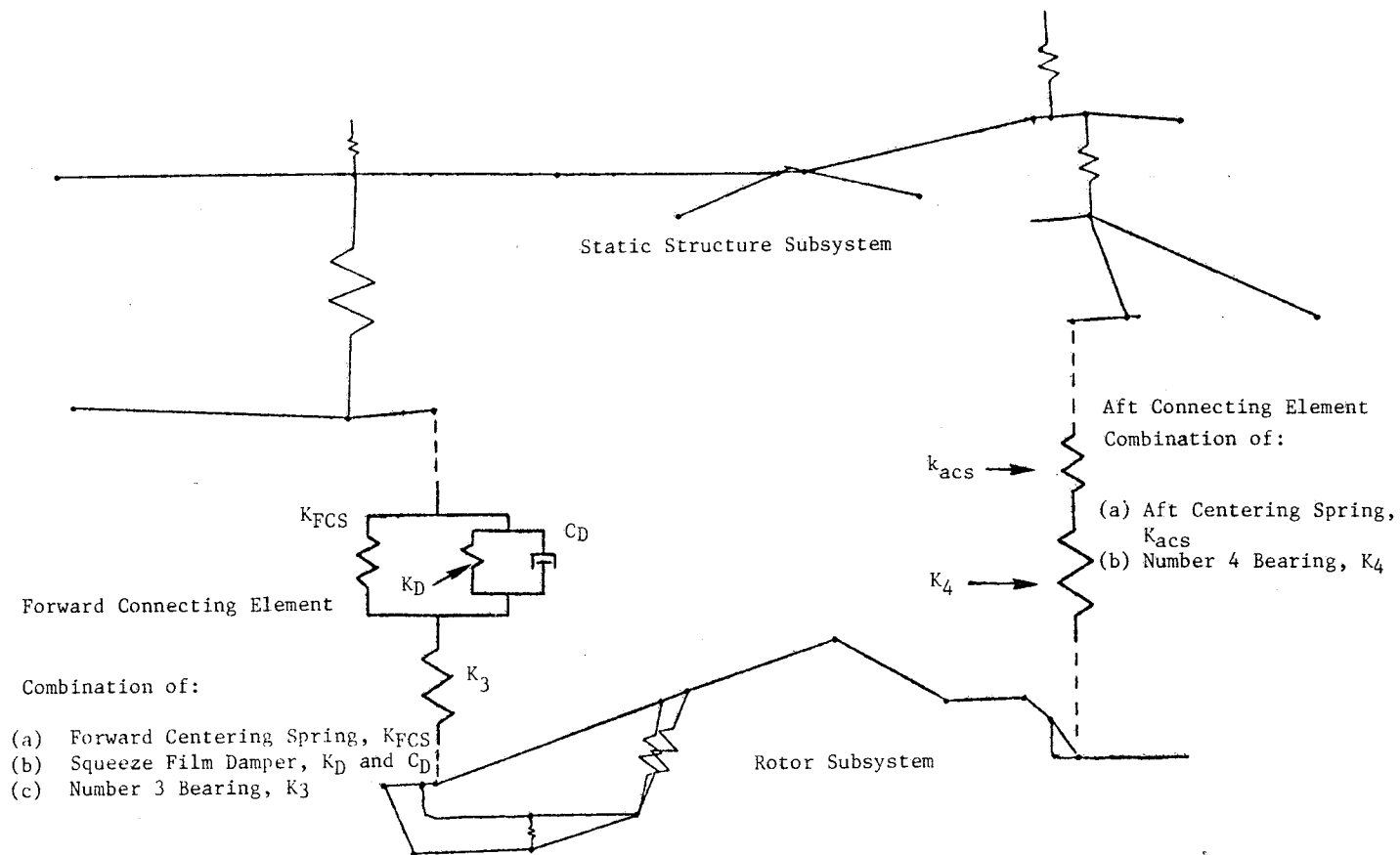


Figure 286. Core Engine Subsystems and Connecting Elements Used for Component Mode Analysis of Squeeze Film Damper System Characteristics.

had been based on assumed damper oil supply temperatures in the range 82.2° to 93.3° C (180° to 200° F). Figure 287 illustrates the sensitivity of the response characteristics to damper oil temperature.

The heat energy generated by the damper was calculated with the component mode analysis for several unbalance levels using a damper oil flow rate of $1.893 \times 10^5 \text{ m}^3/\text{s}$ (0.30 gpm), which is consistent with bench test flow check measurements made for the damper assembly before the core test. It was established that a 4.4° C (10° F) temperature rise in the damper and an unbalance of $7.493 \times 10^3 \text{ kg-m}$ (295 gm-inch) in the forward region of the rotor would provide agreement between the predicted and measured response levels and characteristics.

The damper spring and damping coefficients corresponding to the 4.4° C oil temperature rise and the $7.493 \times 10^3 \text{ kg-m}$ unbalance level and obtained from the component mode analysis were used in the planar finite-element model to obtain the direct damped solution for the engine system. Figures 277 and 281 compare the direct solution with test results, and Figures 288 and 289 show the calculated bearing loads.

6.10 CORE CONTROL SYSTEM PERFORMANCE

The full authority digital electronic control (FADEC) system on the core test vehicle performed well, providing the flexibility necessary for thorough exploration of engine characteristics. Areas of particular note are defined in the following sections.

6.10.1 Speed Governing

The FADEC provided the accurate speed governing necessary for orderly exploration of variable stator effects, compressor bleed, and ACC.

A mild governing instability (up to 30 rpm peak-to-peak at 0.2 to 1.0 Hz) was initially present. However, a PROM change (new program memory for the digital electronic control) was made, allowing the metering valve position loop gain to be increased and the core speed governing gain to be decreased. These gains were then adjusted to minimize the effects of the instability and permit good data acquisition.

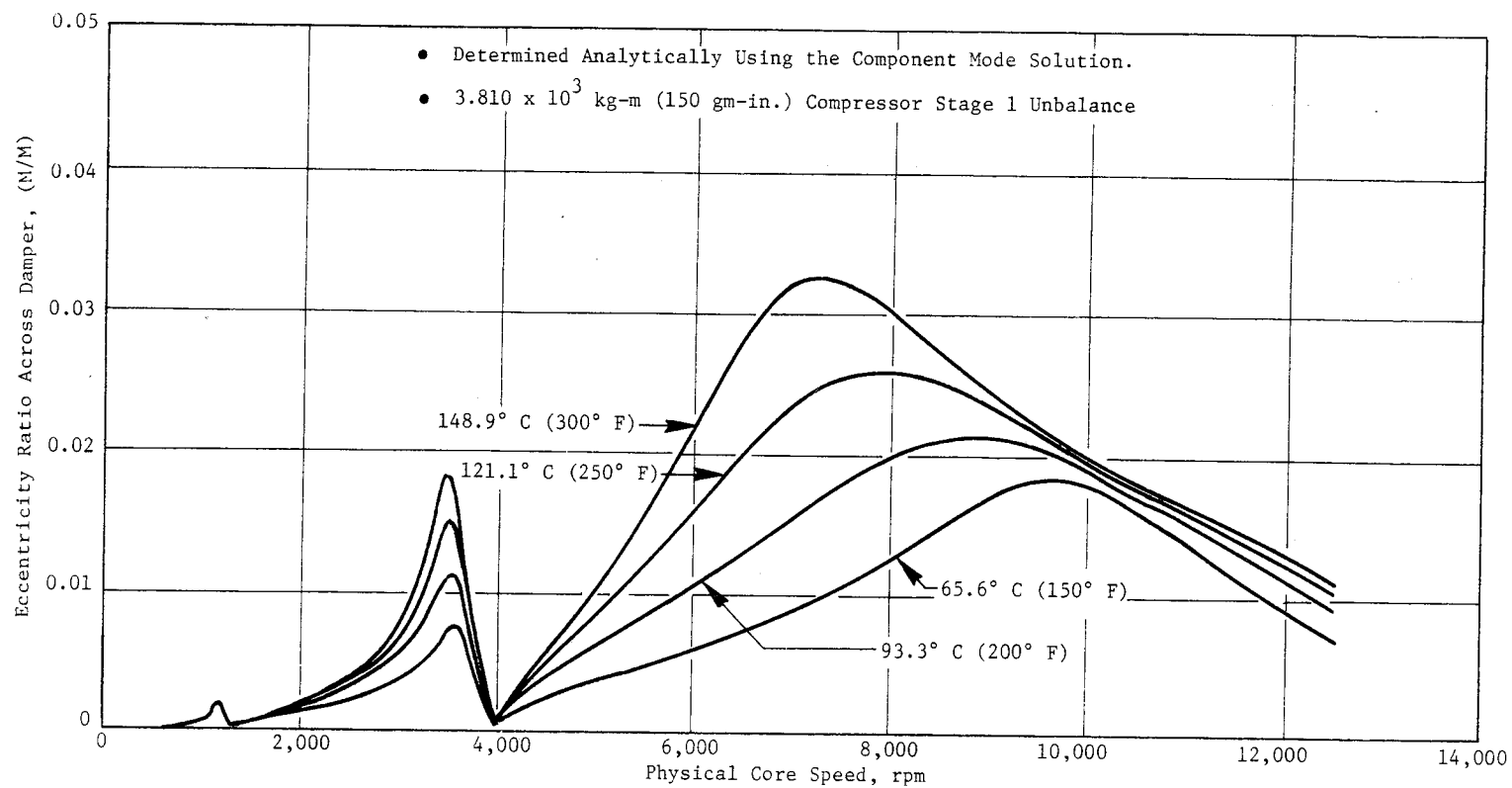


Figure 287. Core System Dynamics Response Sensitivity to Damper Oil Film Temperature.

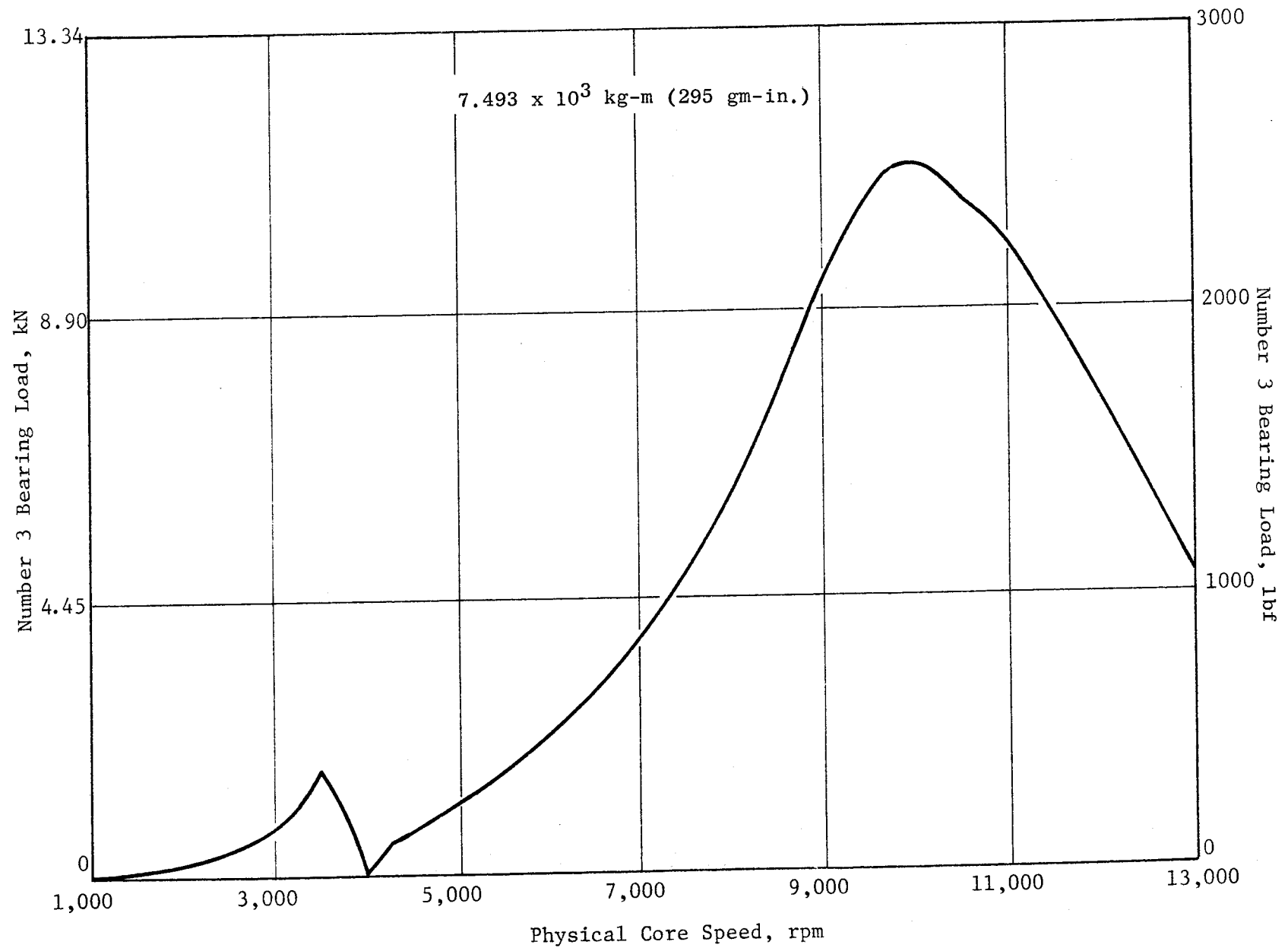


Figure 288. Number 3 Bearing Load Computer for Compressor Stage 1 Unbalance Using Direct Damped Solution.

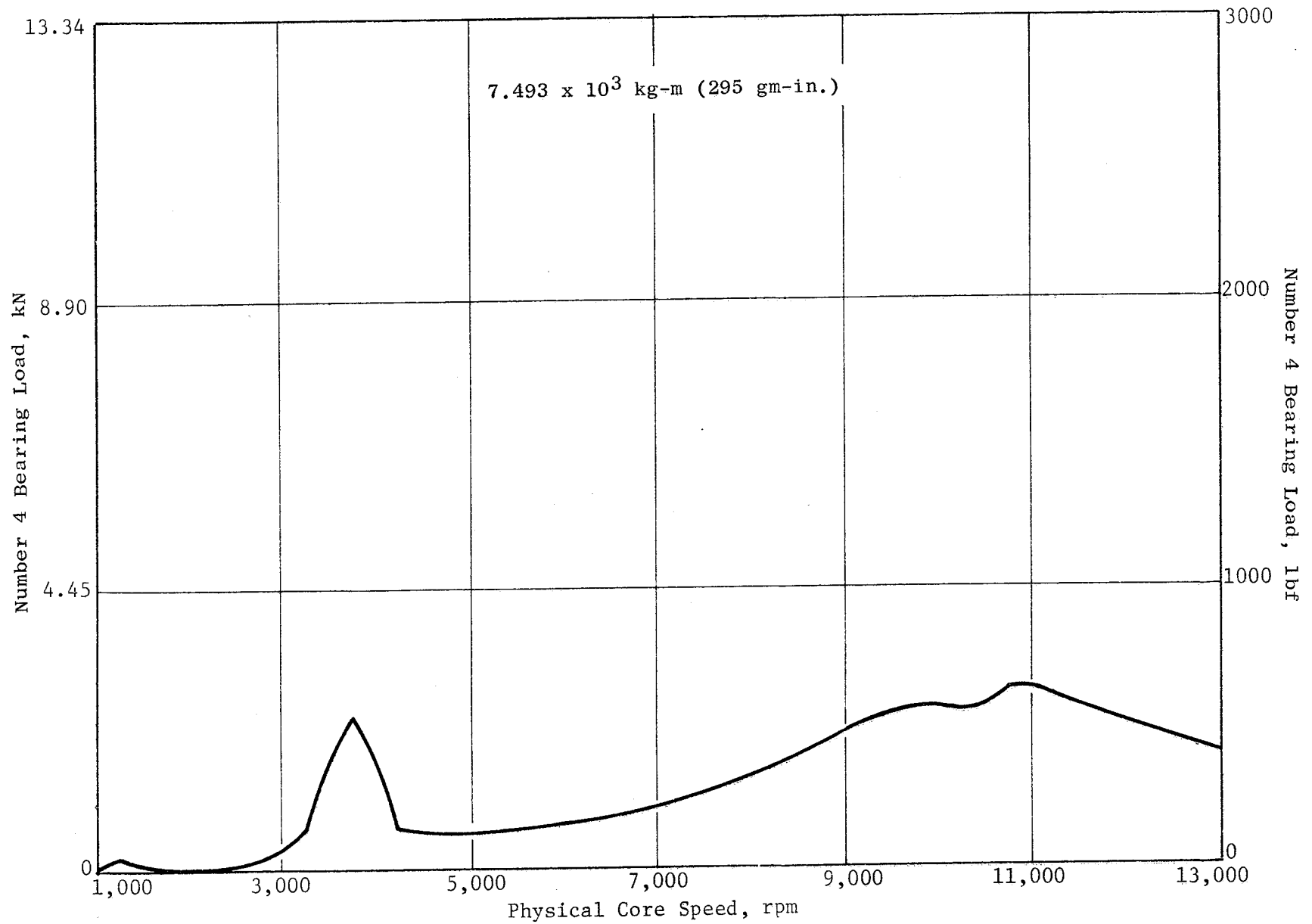


Figure 289. Number 4 Bearing Load Computed for Compressor Stage 1 Unbalance Using Direct Damped Solution.

This instability, following the PROM change, is shown in Figure 290. Fuel flow, torque motor current, and speed derivative signals are greatly expanded for evaluation purposes. The sawtooth waveform of torque motor current, together with the flattened-off fuel flow waveform, indicates that instability was caused by a combination of torque motor and servovalve dead band (and/or hysteresis) coupled with the software compensation network.

ICLS software will have the adjustable gains and an adjustable compensation network that will be fine-tuned during the control systems test to minimize this instability.

6.10.2 Fuel Leak

Fuel was observed leaking from the fuel control during the wet motoring posttest inspection. The fuel control was removed from the engine and taken to a component test cell where the leak was confirmed. The control cover was removed and an O-ring was found to be defective. The defective O-ring was replaced and the control returned to the engine. No further leakage was observed during engine test.

6.10.3 Double-Annular Combustor Control

As discussed in Section 6.5, transition from single-to double-annular combustion initially proved only partly successful because of leaky fuel nozzle check valves which allowed manifold drainage and resulted in delayed initiation of main zone fuel injection while the manifold refilled. It was necessary to utilize the manual fuel split control mode capability to allow complete main manifold filling and achieve successful transitions to double-annular combustion. Figure 291 shows a successful transition. Note the long main zone manifold fill-time prior to closing the pilot zone valve and fully opening the main zone valve.

ICLS control strategy is being modified to automatically transition from single-to double-annular combustion by the addition of adjustable timing of pilot zone reset valve and main zone shutoff valve sequencing.

ORIGINAL PAGE IS
OF POOR QUALITY

RECORD NO.		PRINTED IN U.S.A.
0		
Core Speed,		
rpm		
15,000		
0		
Power Lever Angle, degrees		
150		
4540 (10,000)		
Pilot Fuel Flow,		
kg/h (lbm/h)		
0		
6800 (15,000)		
Total Fuel Flow,		
kg/h (lbm/h)		
0		
0		
Compressor Discharge Pressure,		
kPa (psia)		
3450 (500)		
204 (400)		
HP Turbine Discharge Temperature, ° C (° F)		
1316 (2400)		
0		
Main Zone Actuator Stroke, cm (inch)		
1.8 (0.7)		
0		
Fuel Mode Control		
Core Speed		
Selected		
		1 sec

Figure 290. Speed Governing Instability.

ORIGINAL PAGE IS
OF POOR QUALITY

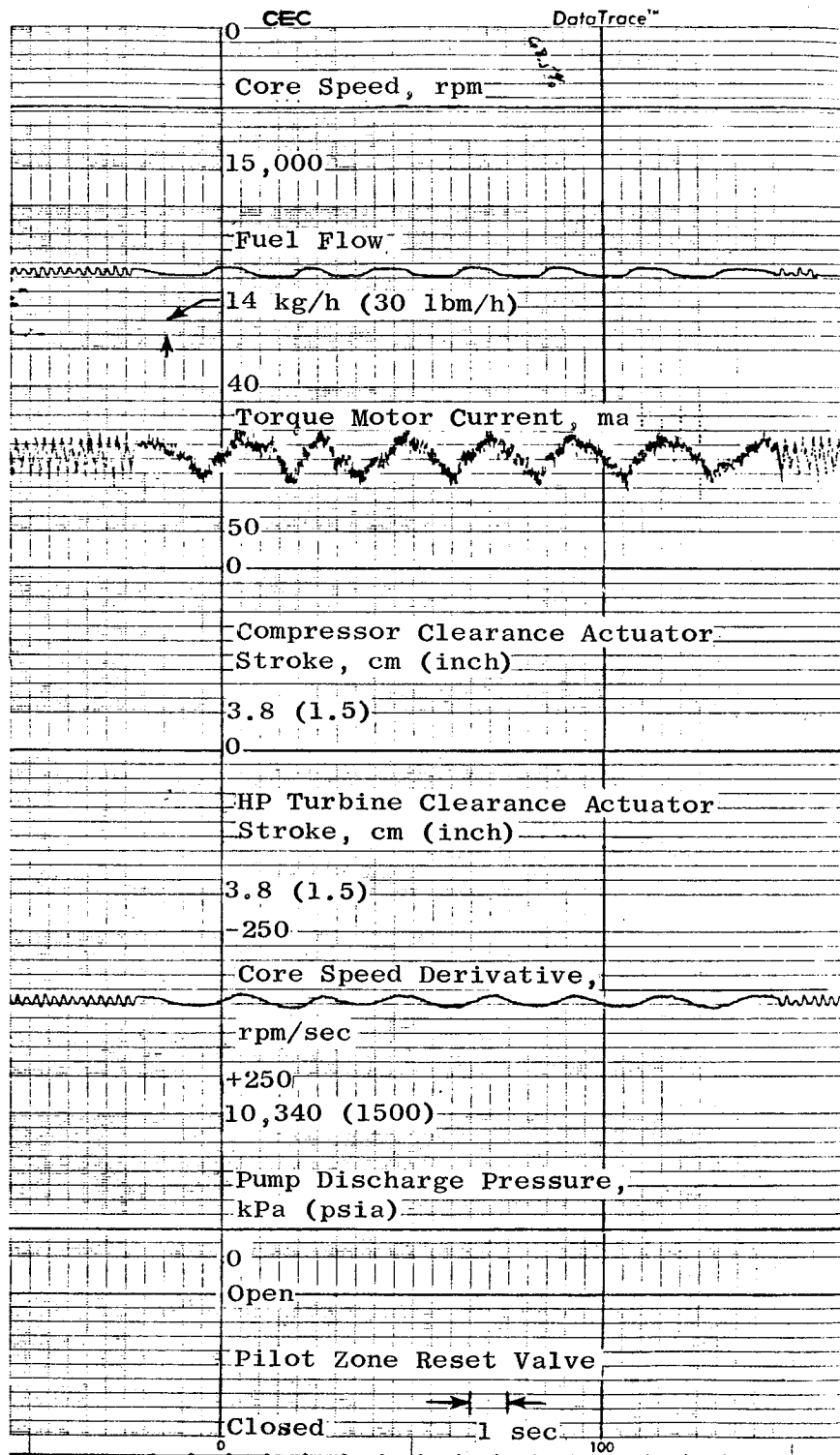


Figure 290. Speed Governing Instability (Concluded).

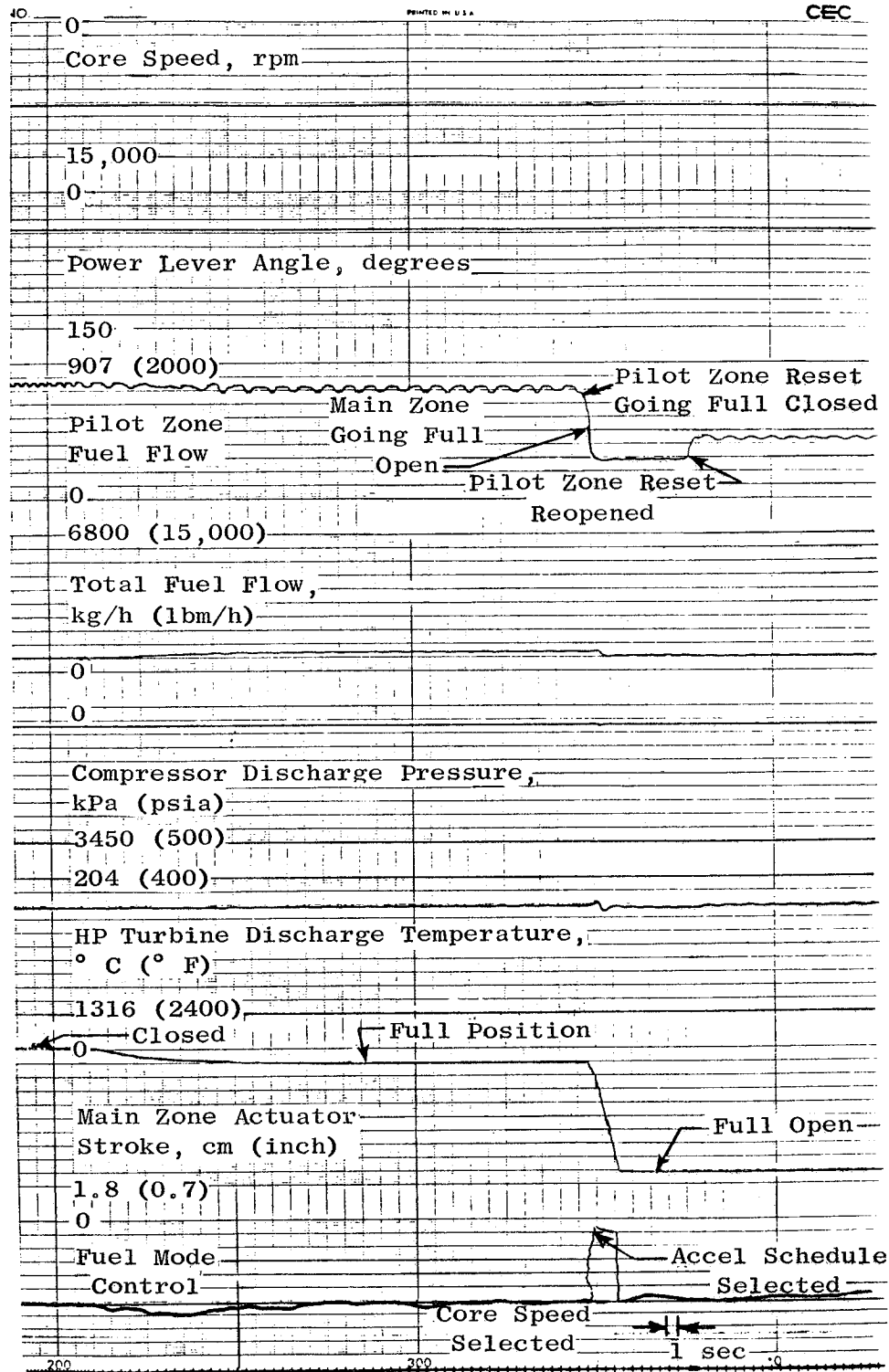


Figure 291. Switch From Single-to Double-Annular Combustion.

6.10.4 Active Clearance Control

The compressor and HP turbine clearance control features were thoroughly explored during core testing by utilizing manual control loops. Results of an application of clearance control air are covered in Sections 6.2 and 6.6 of this report. Casing thermocouples, intended for use for the automatic clearance control modes, proved to be incompatible with the FADEC. The core test thermocouples being used were grounded, while the FADEC required insulated thermocouples. These thermocouples will be insulated for ICLS testing. DMS data taken from core engine thermocouples in the same location will be used to design the casing temperature schedules for the ICLS control strategy.

6.10.5 Start Range Turbine Cooling System

The start range turbine cooling (SRTC) valves, which were supposed to be open during the use of start bleed and closed at idle and above, did not close as intended. The reason for this is unknown. The solenoid valve which ports either ambient or compressor discharge pressure to the SRTC valves was exercised during the controls system test and was functional. Both SRTC valves were tested by the supplier and again in a component test cell and found to be functional. The engine plumbing was installed as intended, and the solenoid would "click" when activated during a posttest investigation.

Successful starting without the use of seventh-stage bleed deleted the requirement for the SRTC system, so this system was removed from the engine early in the core test program.

6.10.6 Starting

Provisions were made for variable seventh-stage compressor bleed (up to 20%) and for simultaneous use of two large air turbine starters (Hamilton Standard PS600-3 starters). However, testing revealed that automatic starts could be made at simulated sea level static conditions using only one starter and without bleed. Light-off speed was progressively reduced from 35% to 20% speed, and the starting fuel schedule was progressively increased to the point that, with fixed fifth-stage compressor stator and no starting bleed, a measured start time of 46.5 seconds was achieved.

Note that the actual time from fuel initiation to governor cutback was 29 seconds. Starter air pressure was slowly raised resulting in a longer than necessary acceleration to the fuel initiation point. On an aircraft, starter pressure is brought up quickly so that a more realistic start time would be less than 40 seconds.

Figure 292 is a plot of start times showing the effects of fuel schedule increases and the changes in speed at which fuel is introduced into the combustor.

Figures 293 and 294 are transient plots of Starts 27 and 29 which show the relationship between core speed, corrected fuel flow, and corrected compressor discharge pressure. Figure 295 is the Sanborn recording for Start 27. Core speed must exceed 831 rpm (minimum FADEC detectable speed) before the speed derivative signal will respond. A lag in the core speed instrumentation causes Channel 1 (sensed speed) to continue to increase after fuel flow cutback. Figure 293 shows the correct representation of speed during automatic Start 27.

No evidence of compressor stall or turbine overtemperature was encountered during any core engine start.

Start times would have been less if actual starter output performance had been as expected and if starter pressure had been brought up more rapidly. For reasons unknown at this time, it is estimated that the performance of the starter was approximately 28.5% low in starter torque.

The conclusion that the starter had reduced output performance is based on the following analyses:

1. Core engine rotor unbalanced torque characteristics were calculated from unfired engine coast-down data as shown in Figure 296. The engine was motored with a Hamilton Standard PS600-3 starter (built for the RB211) to a stabilized maximum motoring speed point and the starter inlet conditions measured in order to calculate starter output torque using the pretest predicted starter performance curves shown in Figure 297. The calculated starter output torque at 4040 rpm core speed was much higher than the core engine unbalanced torque calculated from engine coast-down data, indicating that the actual starter output torque was approximately 28.5% lower than predicted from the estimated performance curves.
2. Additional analyses of engine and starter torque were made at the starter cutout region for Start 27. Starting data were sampled 10

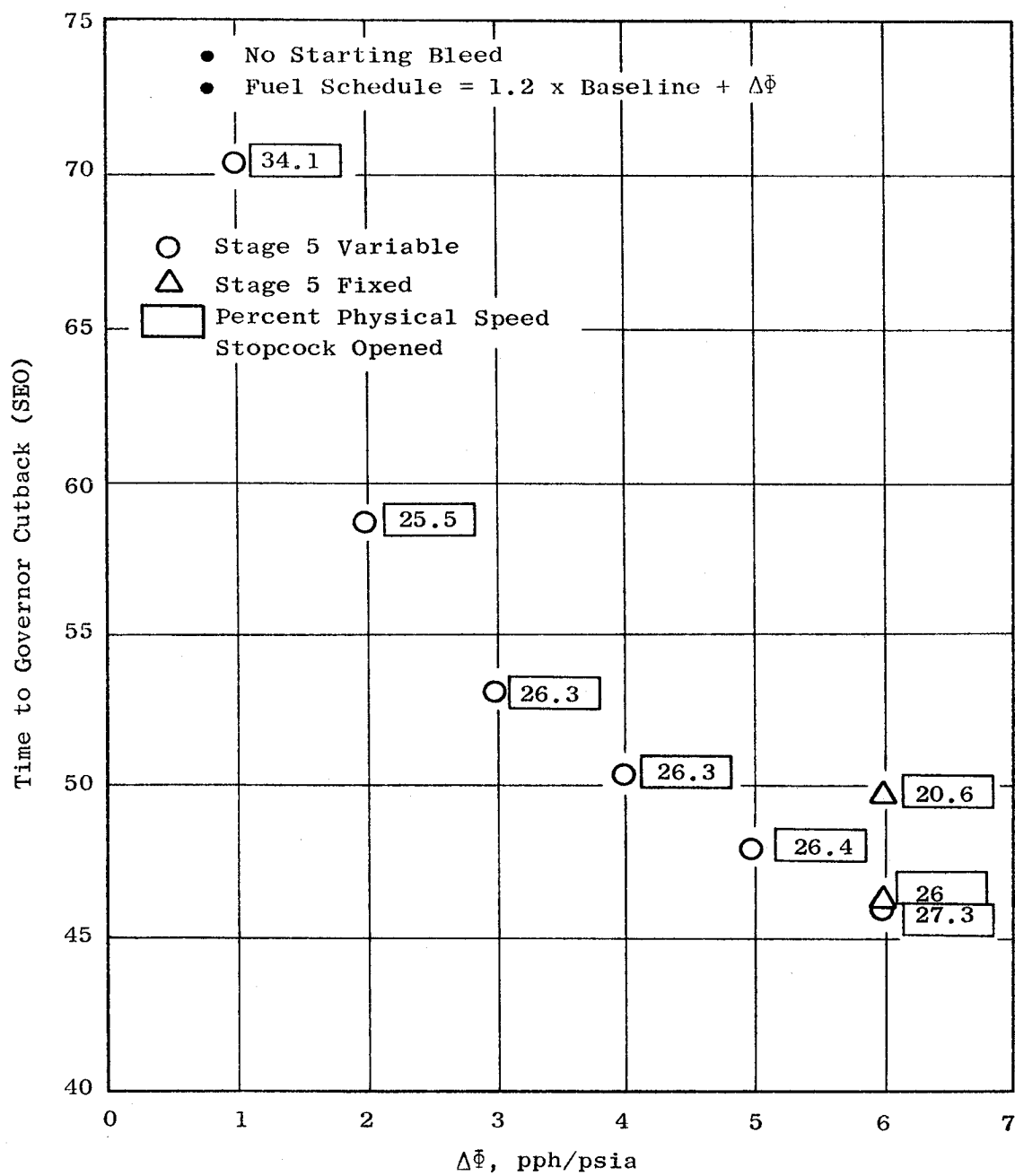


Figure 292. Start Time Investigation.

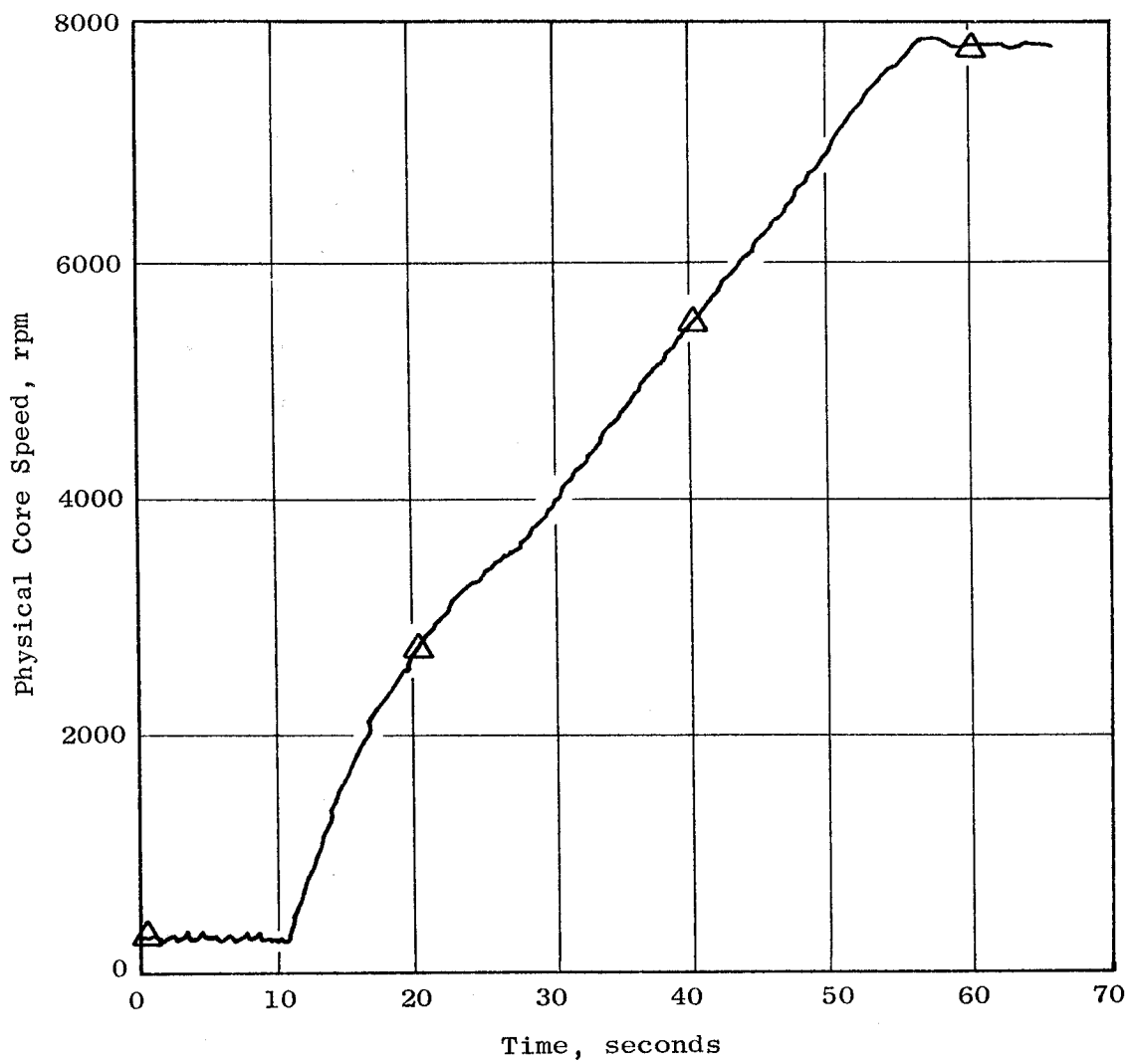


Figure 293. Start No. 27 - Transient Plot.

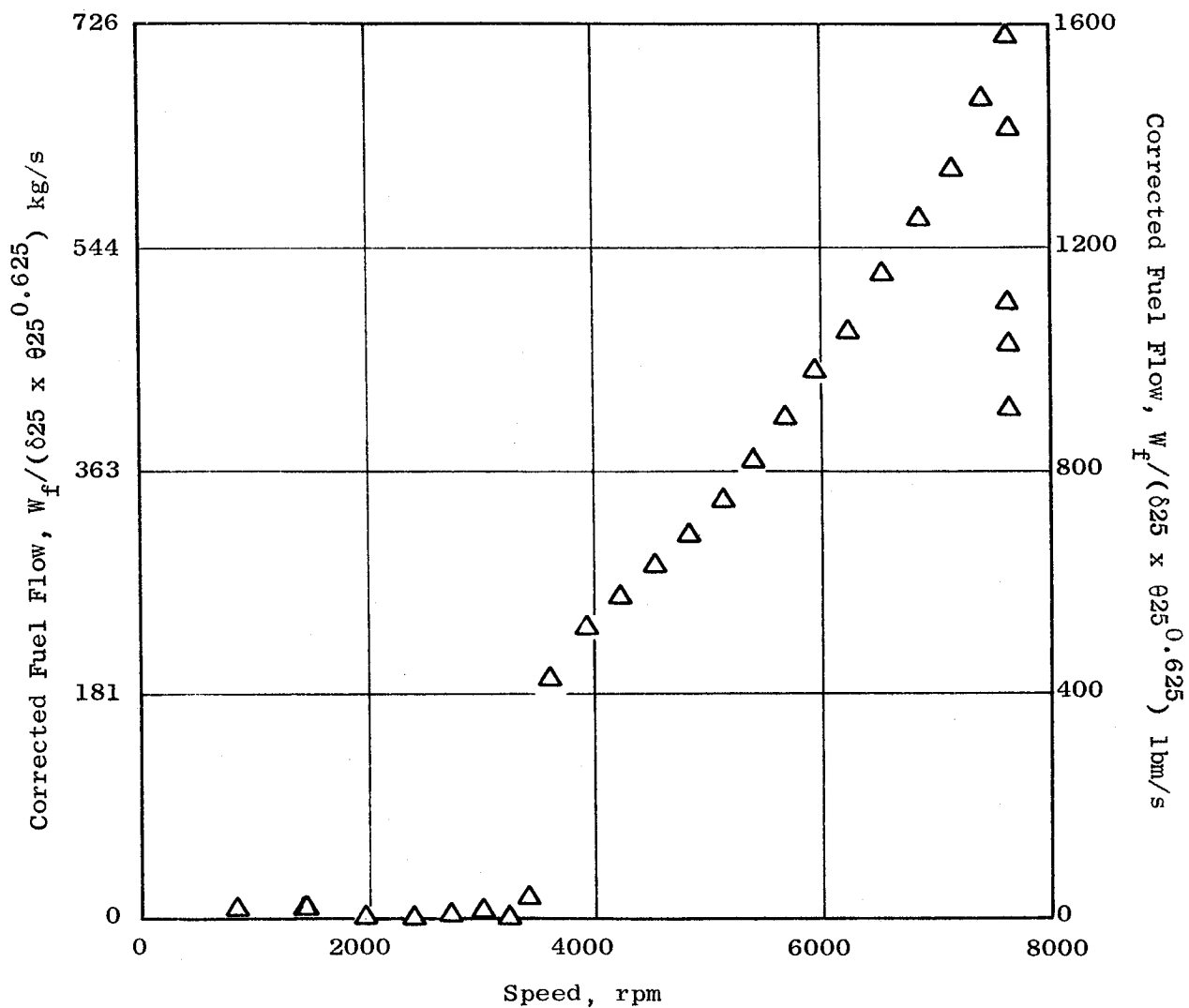


Figure 293. Start No. 27 - Transient Plot (Continued).

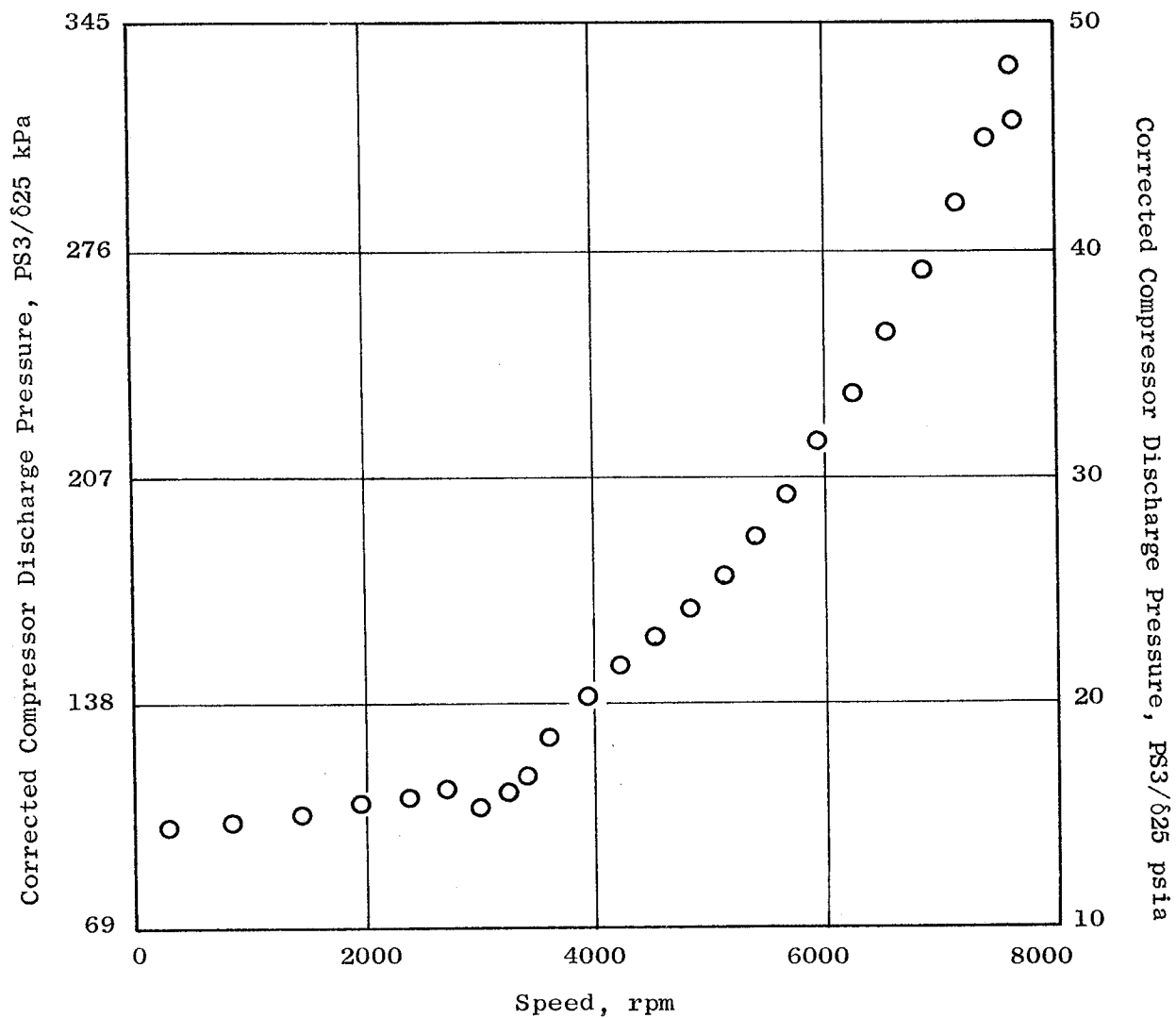


Figure 293. Start No. 27 - Transient Plot (Concluded).

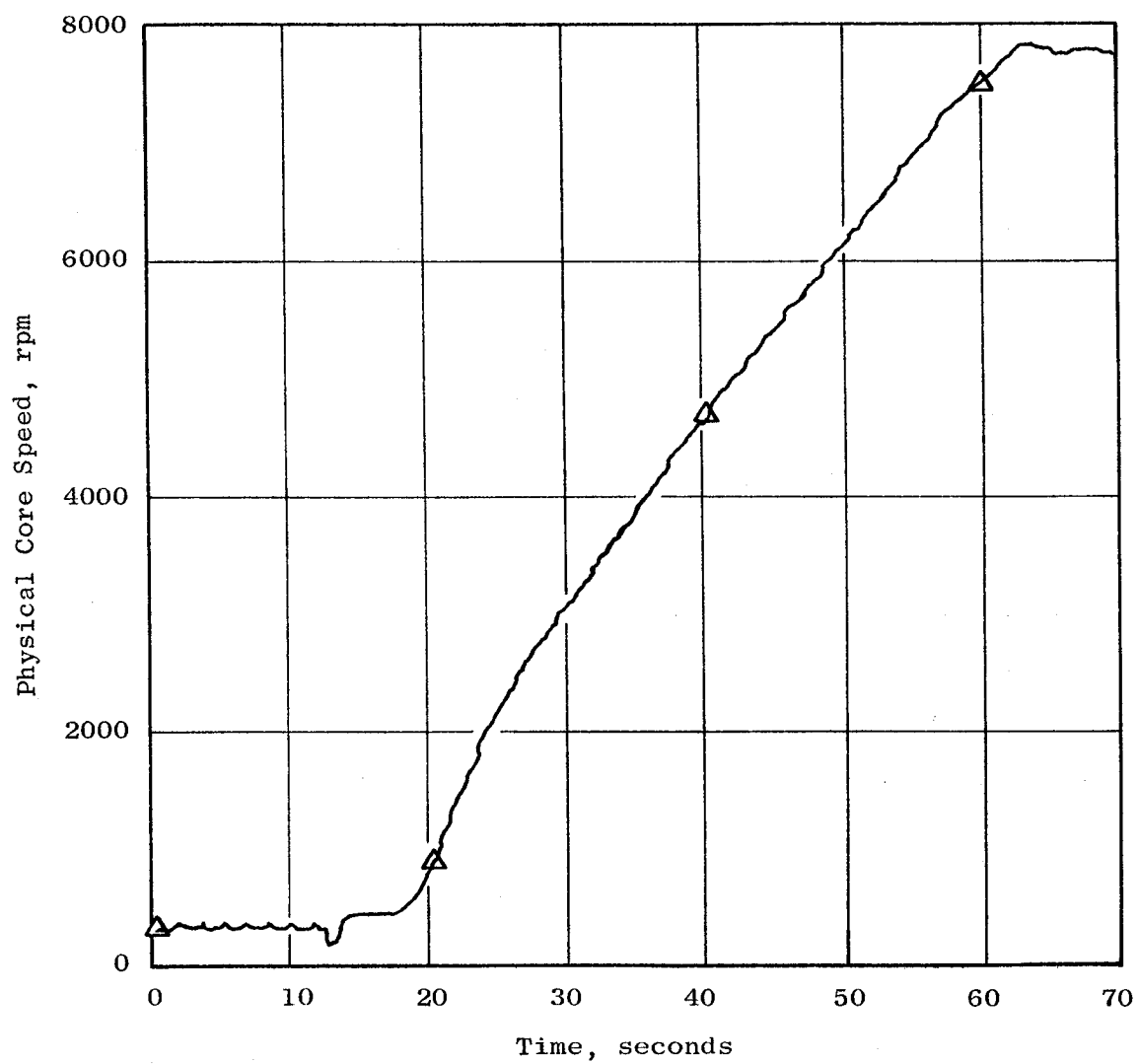


Figure 294. Start No. 29 - Transient Plot.

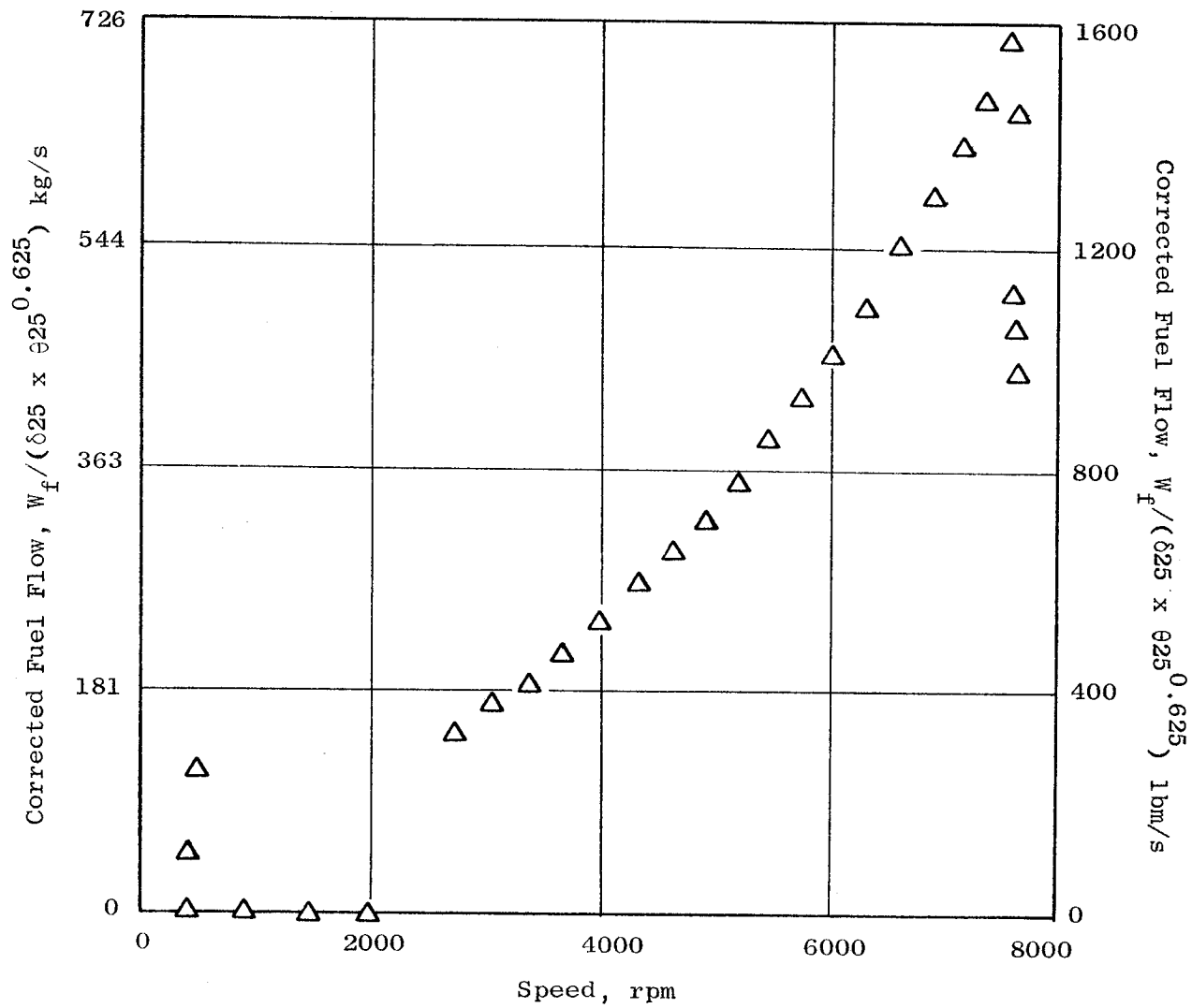


Figure 294. Start No. 29 - Transient Plot (Continued).

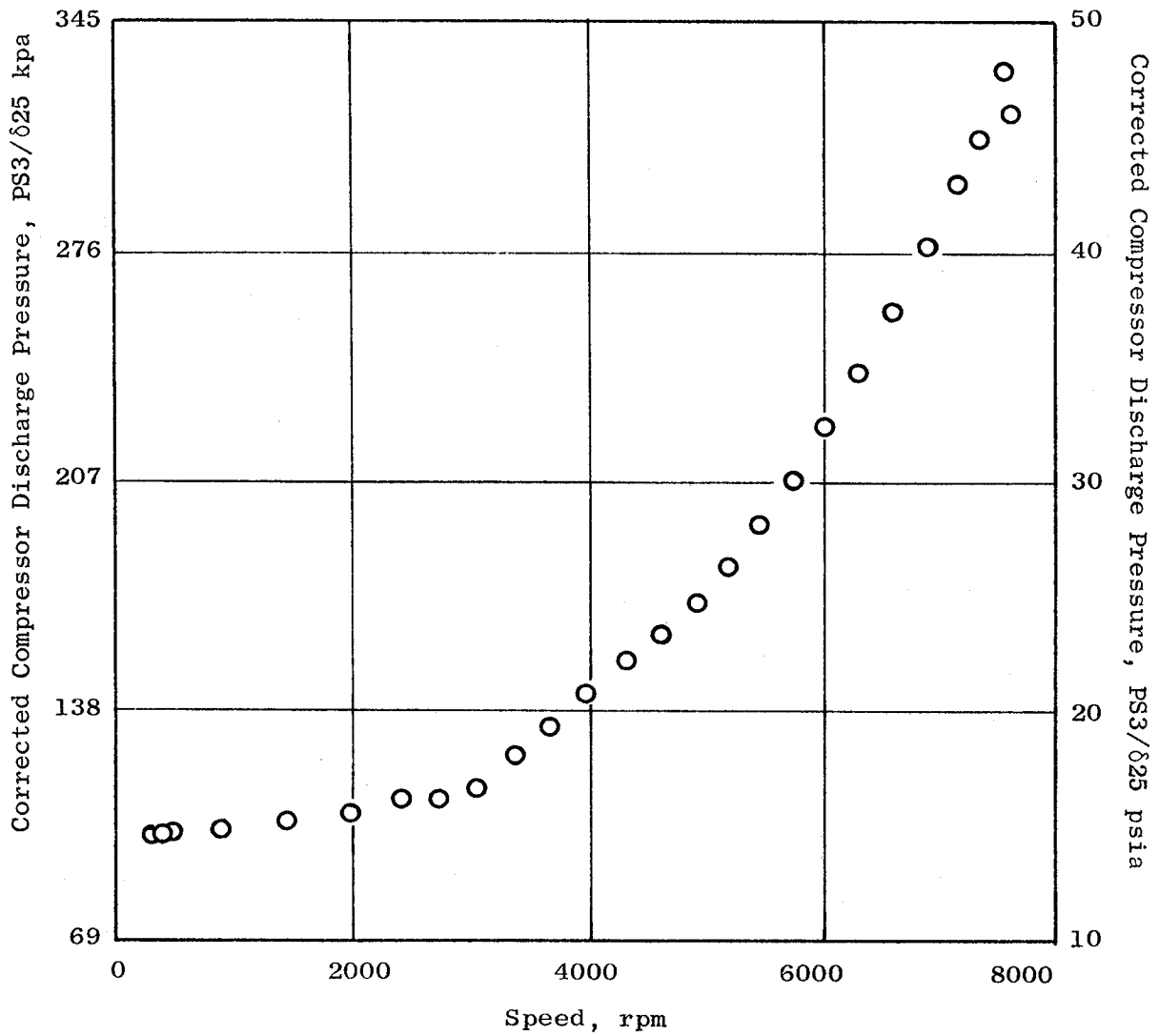


Figure 294. Start No. 29 - Transient Plot (Concluded).

ORIGINAL PAGE IS
OF POOR QUALITY

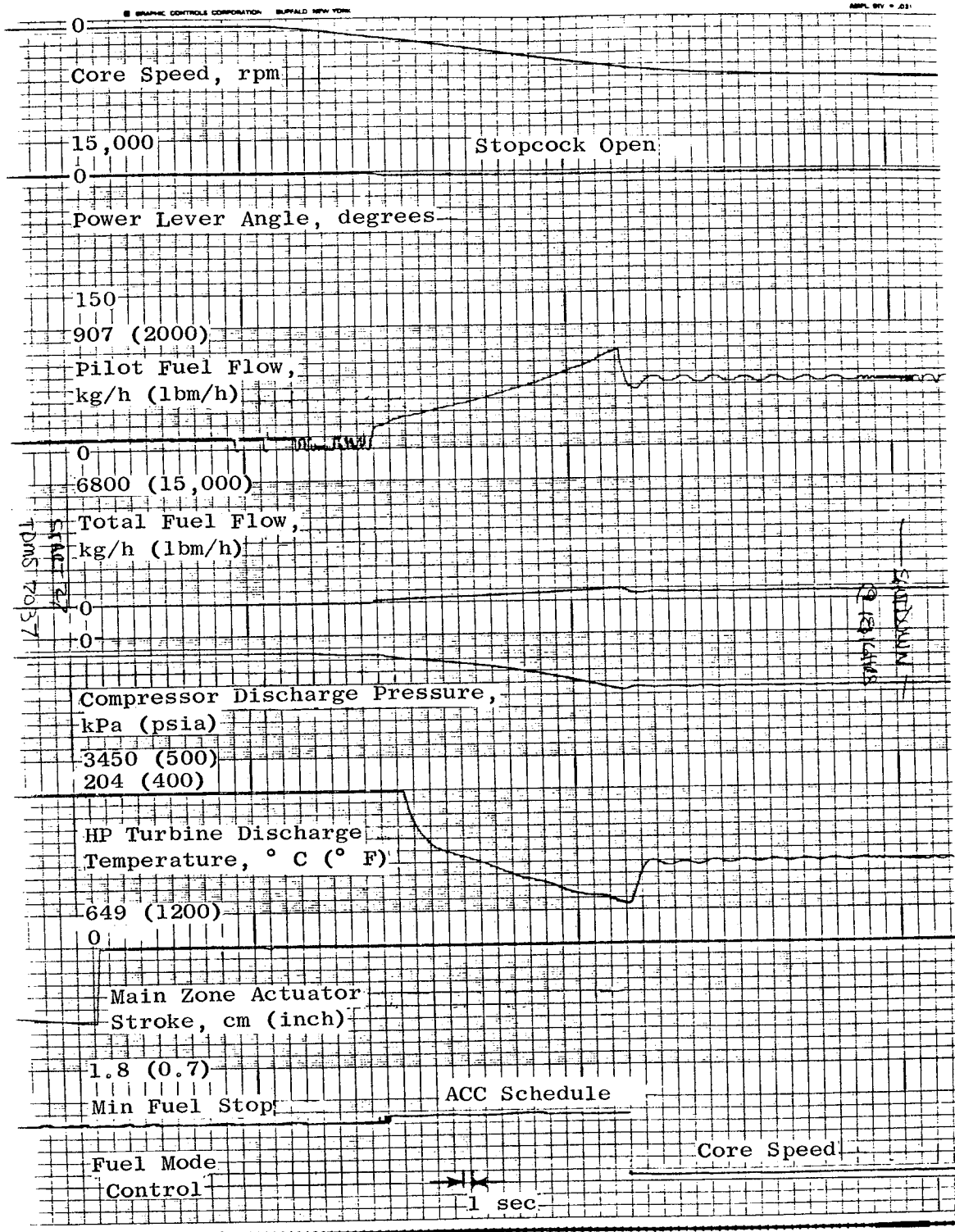


Figure 295. Start No. 27.

ORIGINAL PAGE IS
OF POOR QUALITY

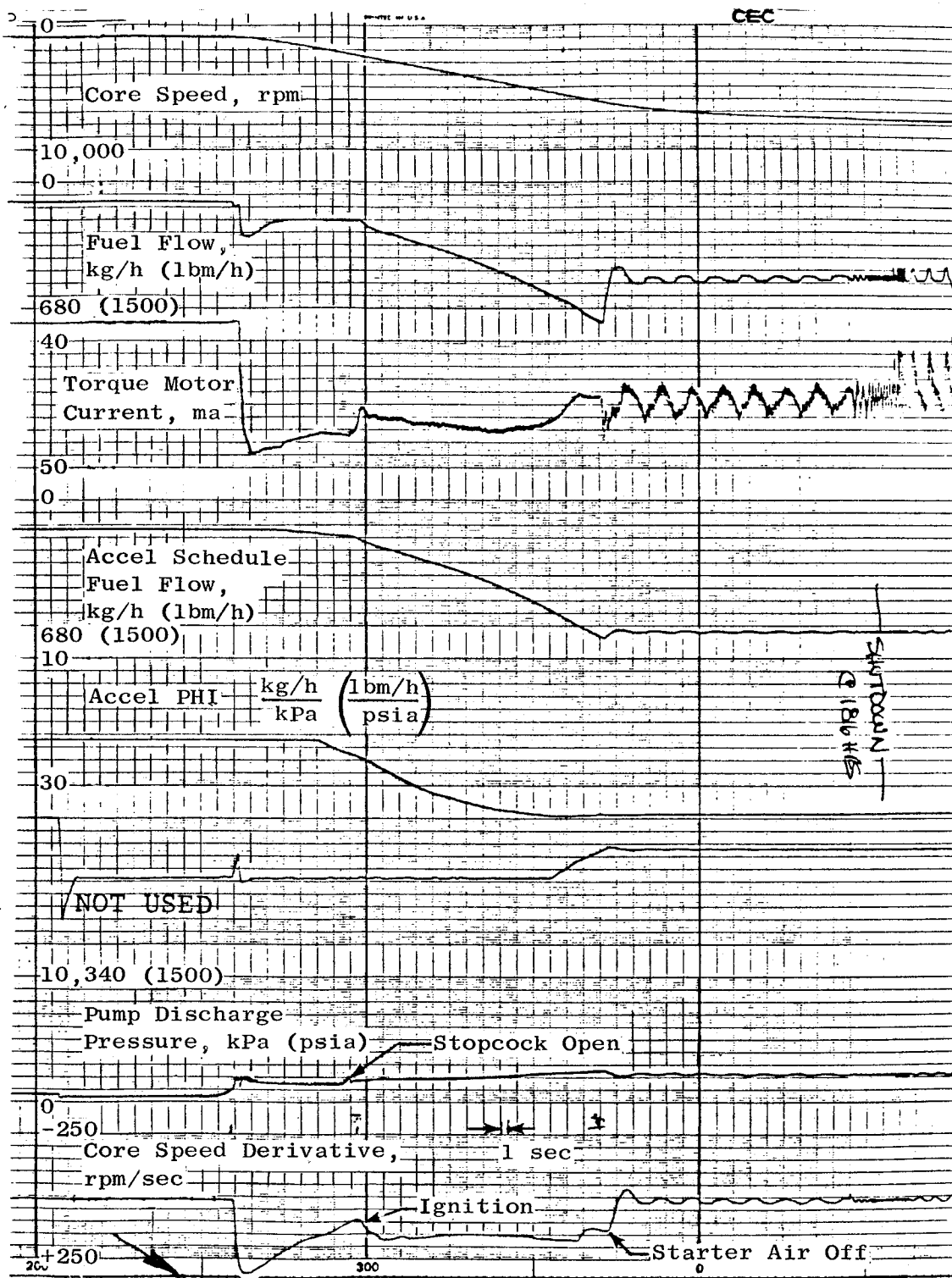


Figure 295. Start No. 27 (Concluded).

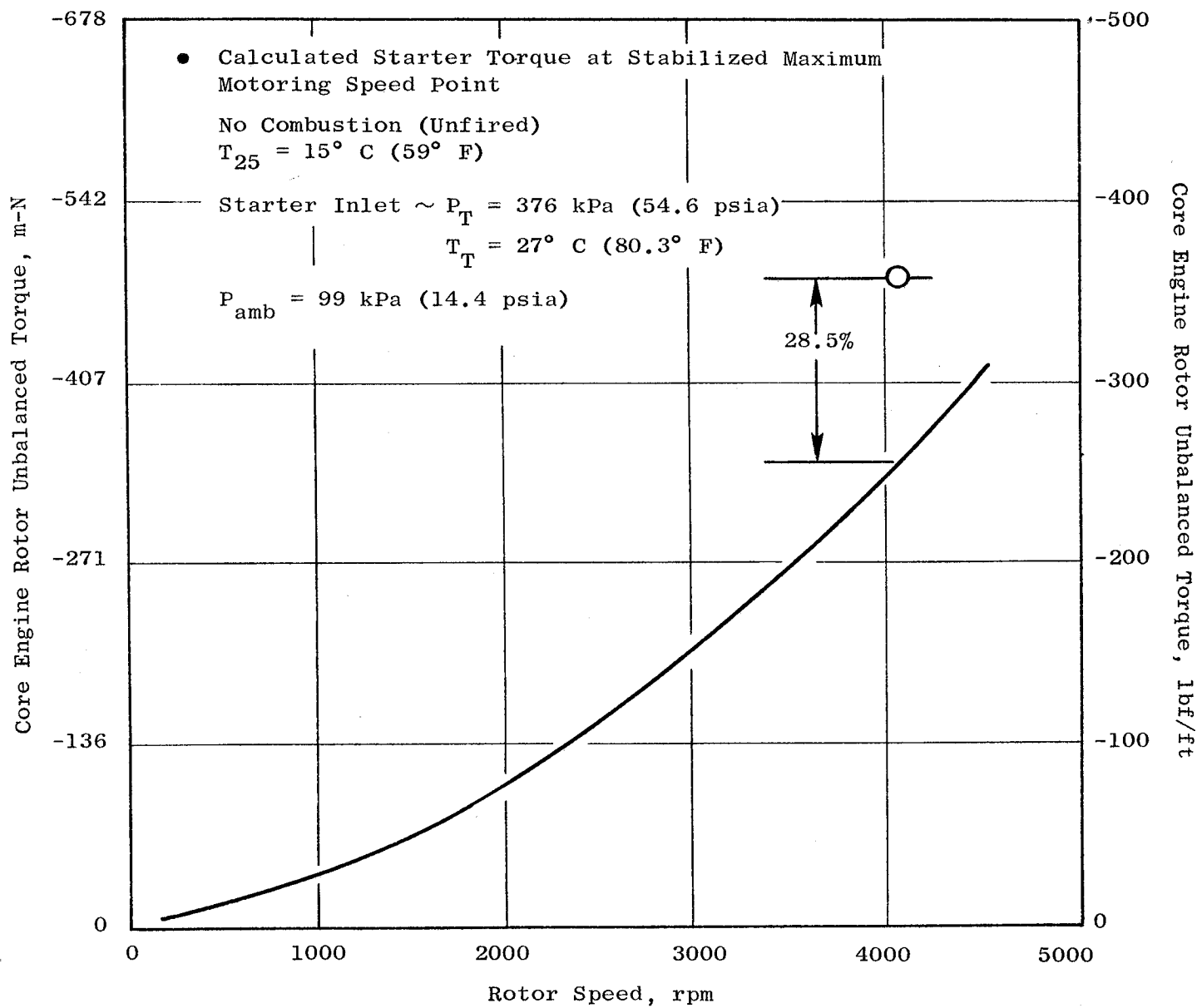


Figure 296. Core Engine Unbalanced Torque.

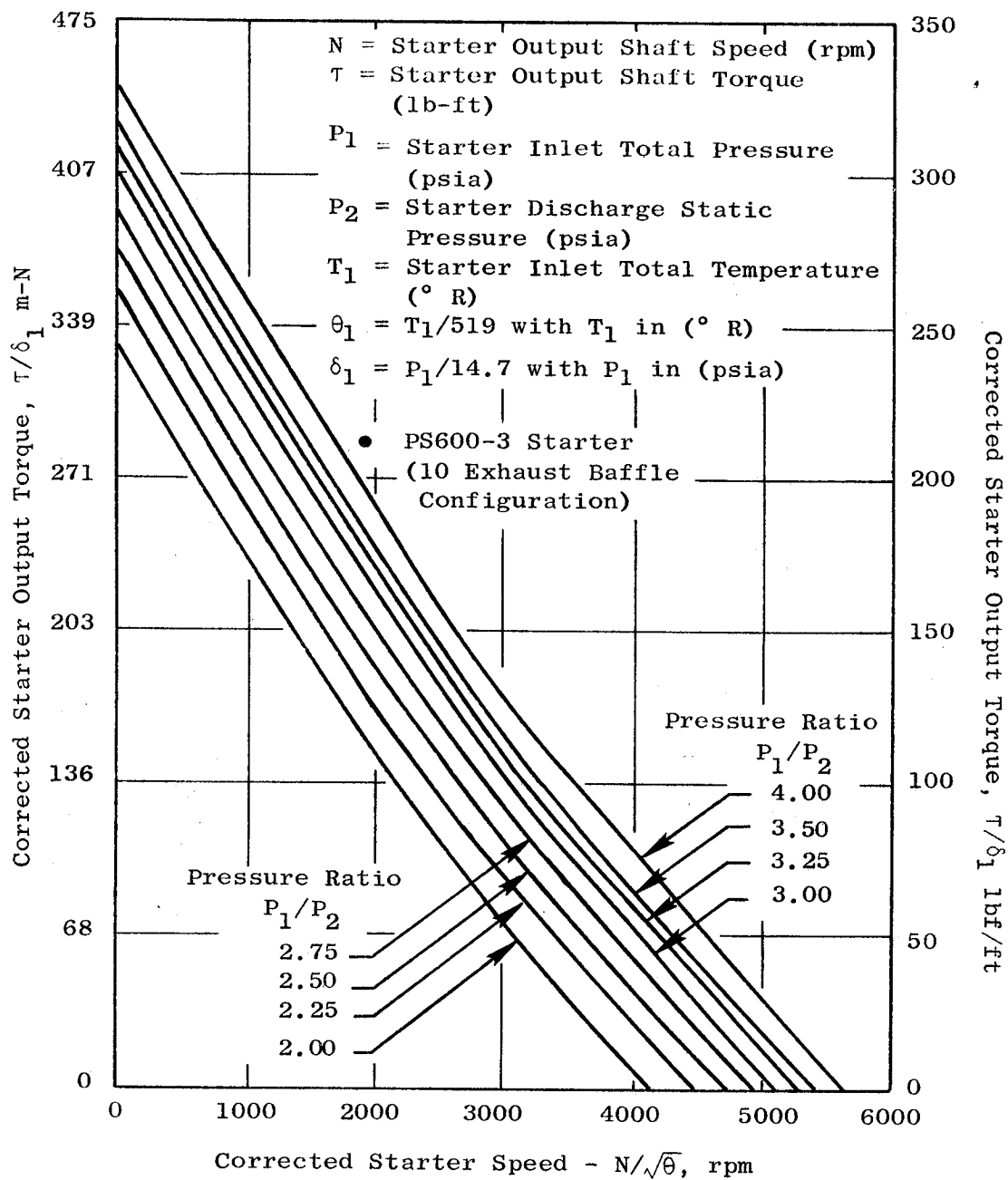


Figure 297. Pretest Predicted Starter Performance.

times each second, and an accurate calculation of net engine rotor torque was made based on measured acceleration rate and rotor characteristics. Corresponding calculations were made of starter torque based on starter inlet data and pretest predictions of starter performance. The difference between these two torque levels is the unbalanced torque between the turbine and compressor; it was plotted as shown in Figure 298. There should be no discontinuity in this unbalanced torque when the starter is cut off because there is no abrupt change in cycle variables affecting this torque, but the plot shows a step increase. This suggests that actual starter torque was lower than predicted. Figure 299 is a similar plot with the starter derated 28.5% below pretest predictions. The absence of an unbalanced torque discontinuity at the starter cutoff point supports the conclusion that starter torque was approximately 28.5% low.

The actual cause of the low starter torque is being investigated. The starter has been returned to Hamilton Standard for test, but no results are yet available.

The starting fuel schedule for the ICLS has been redesigned and incorporated into the ICLS control strategy. Redesign was necessary because the actual steady-state operating line (fuel flow/compressor discharge pressure versus speed) was substantially higher than the pretest predicted operating line in the start region. The steady-state pretest and actual operating line comparisons and the pretest core acceleration fuel schedule comparisons are shown in Figure 300.

For the same inlet conditions as during core engine testing, ICLS start times would be expected to be under 45 seconds. However, actual ICLS start times may be longer than this due to higher gearbox torques caused by increased oil viscosity at the lower ambient temperatures expected during ICLS testing.

6.10.7 Subidle Exploration

The FADEC manual fuel control mode provided precise, stable steady-state control of the engine in the subidle region, making it possible to gather valuable data relative to the start testing results reported above.

6.10.8 Sensor Accuracy

Control system sensing accuracy was assessed by comparing control system data on the following variables with corresponding data from the extensive performance instrumentation on the engine:

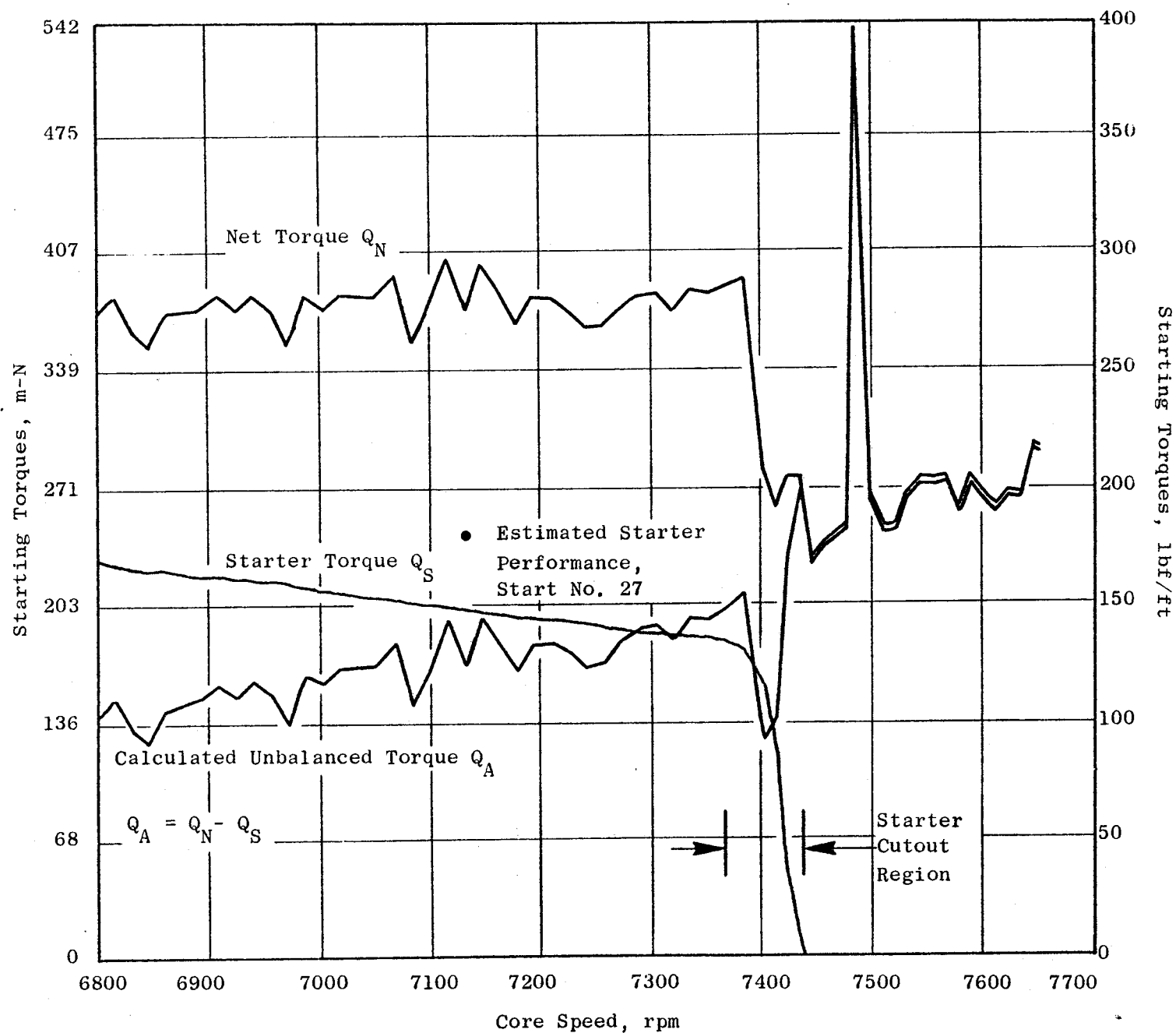


Figure 298. Core Engine Unbalanced Torque Characteristics.

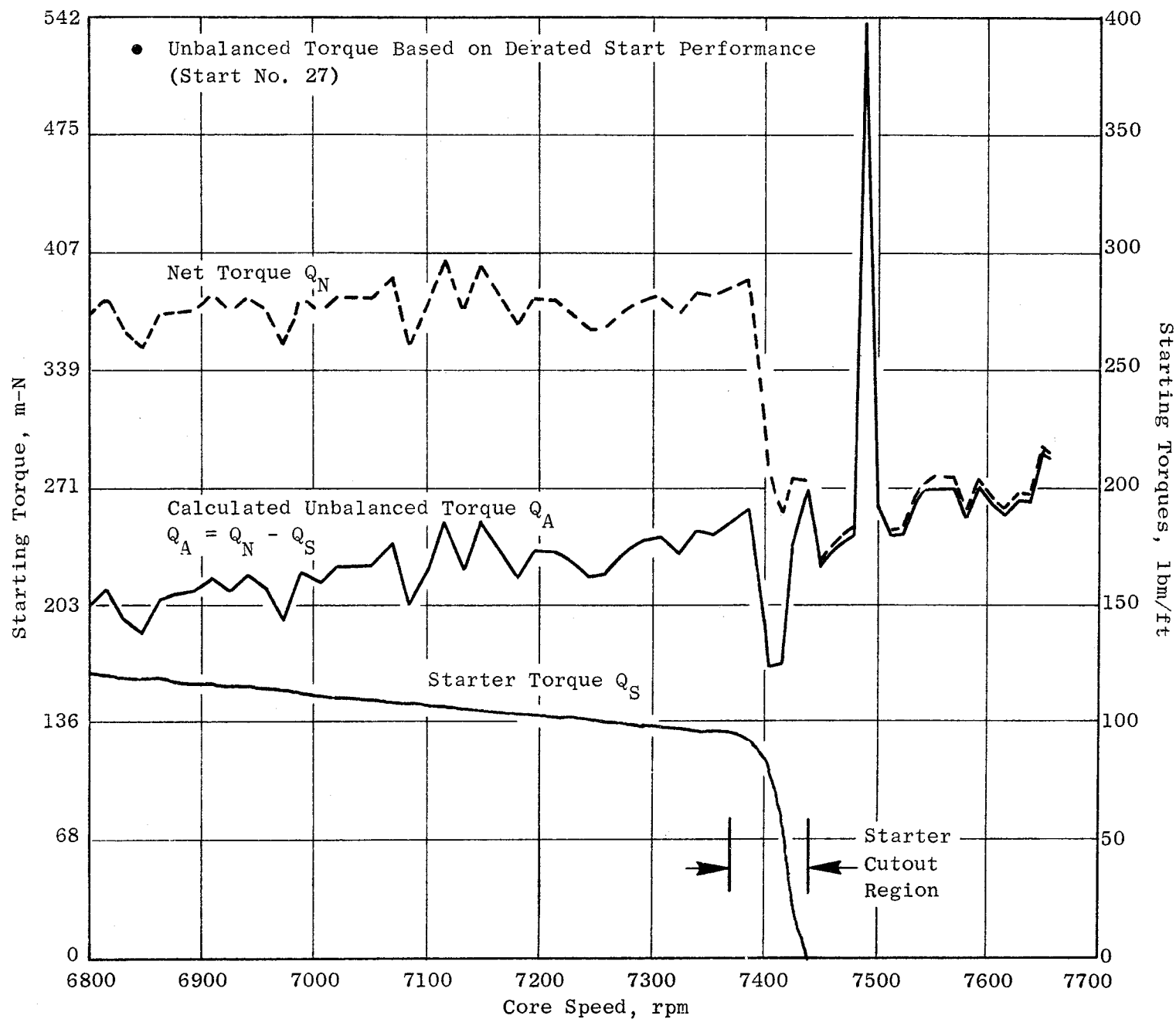


Figure 299. Estimated Starter Performance (Except Derated by 28.5%).

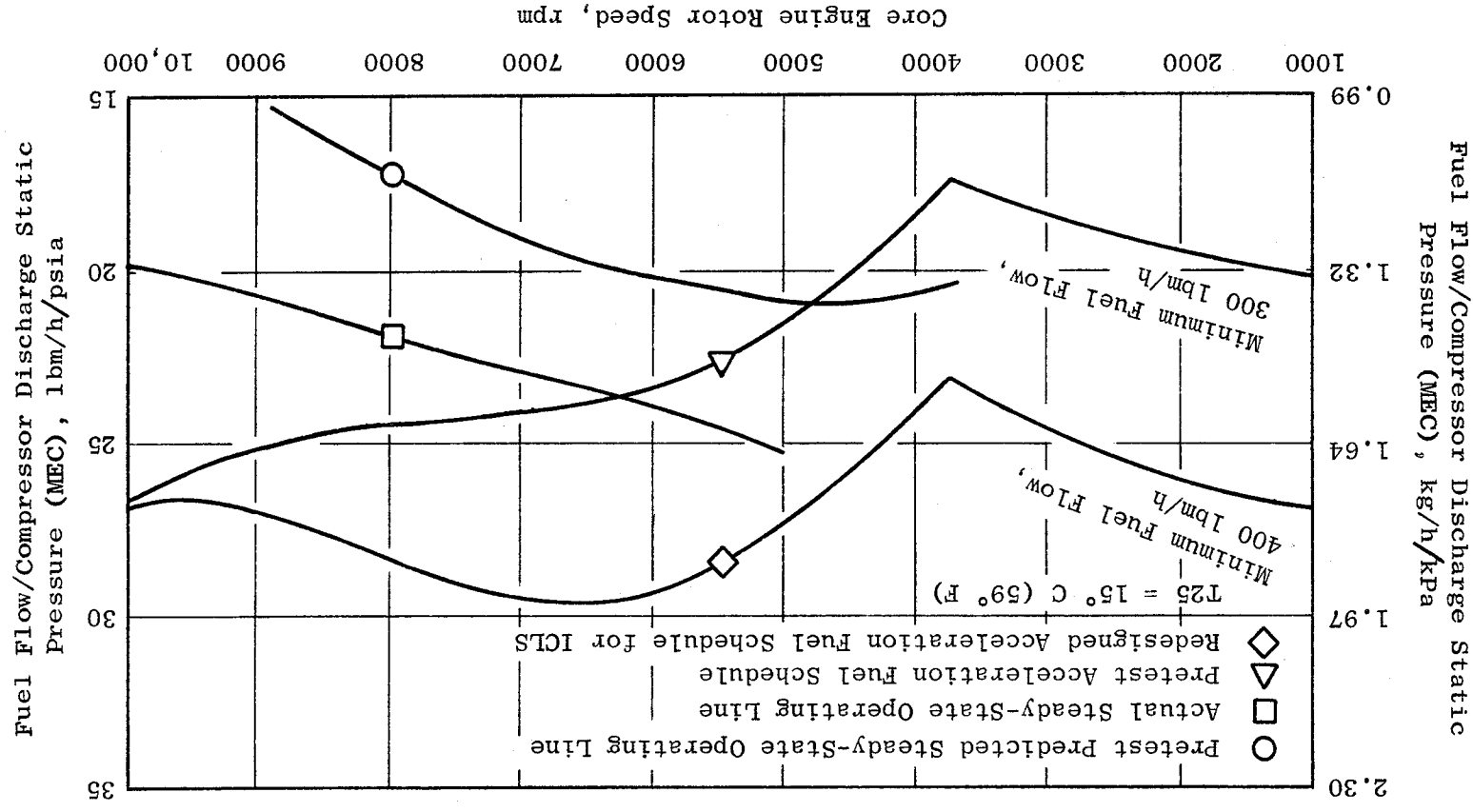


Figure 300. Starting Acceleration Fuel Schedule.

- Compressor inlet temperature (T25)
- Compressor discharge temperature (T3)
- HP turbine discharge temperature (T42)
- Compressor discharge pressure (PS3)
- Total fuel flow (WF36)
- Calculated HP turbine inlet temperature (T41)

The results of this comparison are given in Table XXXI. Inspection of this table indicates that all FADEC sensors are very close to cell instrumentation except for T42 in the low speed region. This is caused by the different temperature profile with single-annular combustion. The FADEC uses thermocouples in only three of the five radial locations sensed by the test instrumentation.

6.10.9 FADEC Configuration

The FADEC used for this core engine testing was control-room mounted. The same electrical design is being implemented in a newly designed on-engine configuration for the ICLS engine.

Table XXXI. FADEC Sensor Accuracy.

Reading	PCN25R, rpm	T25, K (° R)	ΔT25, % Δ Point	T3, K (° R)	ΔT3, % Δ Point	T42, K (° R)	ΔT42, % Δ Point
**235	62.15	294.28 (529.7)	-0.34	459.06 (826.3)	-1.97	775.67 (1396.2)	+9.07
**237	68.51	295.44 (531.8)	-0.28	491.61 (884.9)	-0.87	767.11 (1380.8)	+6.44
**238	76.54	295.56 (532.0)	-0.24	538.50 (969.3)	-1.24	767.61 (1381.7)	+4.26
242	85.01	295.83 (532.5)	-0.15	605.78 (1090.4)	-0.54	801.33 (1442.4)	+0.60
248	89.53	293.56 (528.4)	+0.07	643.11 (1157.6)	-1.07	842.06 (1515.7)	-1.58
251	92.30	300.11 (540.2)	+0.11	694.28 (1249.7)	-1.14	949.66 (1709.4)	-0.32
254	95.36	300.89 (541.6)	+0.37	742.94 (1337.3)	-1.15	1063.89 (1915.0)	-0.31
256	97.28	300.78 (541.4)	+0.57	768.44 (1383.2)	-1.53	1116.50 (2009.7)	-0.91
258	98.12	301.50 (542.7)	+0.64	782.61 (1408.7)	-1.67	1130.61 (2035.1)	-1.09

Reading	PS3, kPa (psia)	ΔPS3, % Δ Point	WF36, kg/h (pph)	ΔWF36, % Δ Point	T41, K (° R)	ΔT41, % Δ Point
235	300.21 (43.54)	-0.98	454.28 (1001.5)	-2.04	1000.28 (1800.5)	-2.95
237	368.47 (53.44)	-0.69	539.51 (1189.4)	-2.29	1010.89 (1819.6)	-2.61
238	507.33 (73.58)	-0.03	731.16 (1611.9)	-2.39	1047.83 (1886.1)	-2.60
242	766.66 (111.19)	+0.04	1122.43 (2474.5)	-0.93	1141.72 (2055.1)	+0.02
248	1070.24 (155.22)	-0.06	1662.58 (3665.3)	-0.84	1215.72 (2188.3)	-0.64
251	1314.67 (190.67)	-0.27	2278.48 (5023.1)	-0.12	1365.83 (2458.5)	+0.50
254	1664.66 (241.43)	-0.63	3237.57 (7137.5)	-1.30	1523.39 (2742.1)	+0.07
256	--	--	3871.98 (8536.1)	-2.40	1593.89 (2869.0)	-1.11
258	--	--	4116.43 (9075.0)	-2.47	1622.67 (2920.8)	-0.84

*FADEC T41 calculation adjusted by 135° to match test experience.

**Single-annular combustion

7.0 CONCLUSIONS

The General Electric E³ core engine was tested in a Company ram air test cell in Evendale, Ohio, during August 1982. The test provided an evaluation of thermodynamic performance and mechanical integrity. No limiting operational problems were encountered. No hardware refurbishment was needed for the following integrated core/low spool (ICLS) turbofan test engine.

The core engine was extensively instrumented. This provided detailed thermodynamic and mechanical information on the engine systems and on the components operating in the engine environment. The conclusions drawn from the test are presented below.

COMPRESSOR MECHANICAL PERFORMANCE

The compressor active clearance control (ACC) system worked as intended, achieving a 0.048 cm (0.019 inch) closure over Stage 10 blade tips compared to a predicted 0.041 cm (0.016 inch) closure. This system achieved 80% of Stage 10 closure within 60 seconds. Varying the bore cooling flow rate proved to be a means for controlling tip clearance. A 60% reduction in bore flow reduced clearances over Stages 3, 5, and 10 by 0.006 cm (0.0025 inch), 0.017 cm (0.0065 inch), and 0.028 cm (0.011 inch), respectively.

Rotor and stator vibratory frequencies closely matched predicted values: (1) One Stage 8 rotor blade strain gage indicated a high (76% of limit) three-stripe mode response at 12,600 rpm. This will not restrict ICLS testing since speeds will be lower. However, further investigations will be necessary in the event of future core testing. (2) One Stage 9 stator strain gage indicated dynamic stresses 33% above limits. Because other similarly located gages were inactive in this mode, it is suspected that the high reading was incorrect. This gage will be closely monitored during ICLS test.

No other high dynamic responses were found, and no operational limits to ICLS tests are forecast.

Compressor blade tips rubbed during a hot rotor restart, but running tip clearances were near design intent.

COMPRESSOR AERODYNAMIC PERFORMANCE

The core compressor efficiency exceeded the ICLS goal and was very near the final Flight Propulsion System (FPS) goal. Core compressor efficiency at the maximum cruise operating point, adjusted for interstage instrumentation, variable Stators 5 and 6, and Reynolds number effects, was 85.6% compared to the ICLS goal of 85.1%. The goal for a fully developed FPS is 86.1%.

Start characteristics of this high pressure ratio compressor proved satisfactory. Rapid starts were accomplished without using starting bleed and with fixed Stage 5 and 6 stators. The tests demonstrated that the final FPS compressor can be simplified by eliminating Stage 7 starting bleed.

COMBUSTOR MECHANICAL PERFORMANCE

Core combustor operating temperatures were below maximum limits and closely matched the predicted metal temperatures.

Light-off and staging from single-annular to double-annular combustion occurred smoothly with no excessive metal temperature excursions.

Borescope inspections at the conclusion of testing showed minor oxidation on splash-plate edges and sleeves and minor spallation of the thermal barrier coating on the centerbody. The combustor was in excellent condition for further testing.

COMBUSTOR AERODYNAMIC PERFORMANCE

The combustor achieved goal performance and operating characteristics. The combustor did not restrict core engine operation, and it is not expected to restrict ICLS operation.

The pressure drop was 5.4% at maximum power, slightly above the FPS goal of 5.0%. This was due to the higher discharge flow function of the compressor (unique to core and ICLS engines). Goal pressure drop is projected for FPS.

Efficiency was 99.9%.

Ignition, starting, and staging were accomplished smoothly and consistently. Full flame propagation during starting required 30% higher starting fuel flow than expected, but presented no problem.

Based on core and prior rig tests, FPS emissions goals will be met. Projected to FPS cycle conditions, the core engine combustor met carbon monoxide and hydrocarbon emissions goals. The goal for oxides of nitrogen was not met. However, prior rig testing established design changes which, if incorporated, would result in the oxides of nitrogen goal being met in the FPS. Based on measured levels, the ICLS is expected to produce no visible smoke.

HIGH PRESSURE TURBINE MECHANICAL PERFORMANCE

High instrumentation fatalities, 40% on the rotor and 17.5% on the stator, were incurred, but they did not impede the acquisition of sufficient data to determine the health and performance of the turbine.

No resonant blade responses were noted, and the blade systems appear to have excellent damping characteristics. Measured Stage 1 blade vibratory stresses extrapolated to hot day takeoff FPS conditions were 3% of scope limits. Stage 2 vibratory stresses, similarly extrapolated to FPS, were 46% of scope limits.

The maximum physical speed attained was 12,811 rpm, which will be the maximum speed limit for any future testing to protect against any unknown or larger response on the Stage 2 blades. The limit will remain in effect until additional instrumented rotor tests are performed.

Measured temperatures on Stage 1 and 2 blades were lower than anticipated. Scaled to turbofan conditions, the Stage 1 blade leading edge temperature was 32° C (58° F) lower than predicted; Stage 2 was 45° C (81° F) lower. Part of the reduction is due to lower pitch-line gas temperature, and part is suspected to be due to lower gas-side heat transfer coefficients in the E³ compared to prior experience.

As expected, the maximum rotor structure temperature observed was 772° C (1331° F) at the outer diameter of the Stage 1 aft blade retainer. All measured temperatures of the rotor structure were within design limits, with the

exception of the Stage 2 aft blade retainer which ran about 100° C (180° F) higher than predicted levels at high speed. The higher retainer temperature was attributed to a smaller-than-intended exhaust nozzle area and the omission of a "W" seal, both reducing purge flow adjacent to the retainer.

A reduction in life for the instrumented Stage 2 aft blade retainer can be expected due to the higher operating temperature, but adequate life still exists for safe ICLS operation. Restoration of the nominal turbine pressure ratio together with the proper "W" seal installation will allow the Stage 2 retainer to operate at design temperatures in the ICLS engine.

The rotor cooling system performed satisfactorily as evidenced by the recorded pressures, temperatures, and posttest blade condition. Instrumentation losses have made it difficult to exactly evaluate the cooling air supply system. Therefore, further analysis is postponed until after the rotor is removed and inspected following ICLS testing. Compressor rake thermocouples indicated that the pitch-line cooling supply source is providing the 21° C (38° F) temperature reduction expected from this unique design feature. Expander test results indicate that, although the flow was 0.3% low of compressor flow (W25), the rotor supply pressures and temperatures were performing at expected design values.

Small expander seal running clearances, due to the new condition of the core engine, resulted in an expander seal leakage of 0.56% W25. Design intent leakage is 1.38% W25 for a worn-in engine. However, the cavity was adequately purged and temperatures were under control.

Compressor discharge pressure seal leakage, calculated on the basis of continuity, was running at 0.55% W25 due to the tight clearances which, it is expected, will open up to flow 1.18% W25, as predicted, following some rapid transients.

The maximum Stage 1 vane airfoil temperature recorded was 966° C (1771° F) at the 60% span, suction side, trailing edge location. Leading edge temperatures, scaled to turbofan conditions, were 53° C (96° F) below design values; the posttest condition appears to be excellent.

Stage 2 nozzle leading edge temperatures ran close to design limits and became the temperature limiting item at 1035° C (1896° F). Leading edge temperatures were approximately 56° C (100° F) above design levels for a given speed point. This is mainly attributable to a low turbine pressure ratio, a transfer of work from Stage 1 to Stage 2, and an increase in cooling flows, all of which increases the gas temperature into Stage 2. Nozzle leading edge metal temperatures were within 20° C (36° F) of predicted peak design levels for a given gas temperature. Trailing edge metal temperatures operated about 143° C (257° F) cooler than predicted for a given gas temperature due to the additional 1% W25 flow through the oversize trailing edge cooling slots.

Temperature measurements on the Stage 1 disk aft face indicated that hot gas did not penetrate into the Stage 1 disk/interstage disk wheel space. The pressure data shows no discernible flow from the cavity under the Stage 2 vane through the forward side. A flow level of 0.28% W25 was predicted. Temperature measurements indicate higher than expected Stage 2 vane inner cavity temperatures, which ran to 703° C (1297° F). This level is acceptable for safe engine operation. The three pairs of air thermocouples in the interstage region were supplying conflicting information. The possibility exists that some thermocouples were picking up metal temperatures. Thus, the installation and operation of these thermocouples need to be examined during engine tear-down, which is not planned until after the ICLS test.

The shroud backside (metal substrate) temperatures for Stage 1 and Stage 2 were within predicted ranges. The localized rubs between rotor tips and shrouds occurred early in the test. Observation of the rubbed shroud surfaces indicated that all shrouds were in excellent condition, with no evidence of spalling or layer separation in the abradable material nor any cracks developing in the metal substrate.

The blade tip closures achieved with the ACC system were approximately one-sixth of the amount expected. This was due to bolthead interference with cooling air impingement on the casing flanges and also due to unexpected ambient air cooling of the casing. The ambient air cooling was caused by the exhaust jet entrainment of ambient air. Tip clearance closure due to ACC plus ambient cooling was close to the original intent, with 0.013 mm (0.005 inch)

more thermal closure than intended actually being achieved in Stage 1 and 0.33 mm (0.013 inch) in Stage 2. At the final high-speed point with ACC, a rub was achieved on Stage 1, and a minimum clearance of 0.25 to 0.36 mm (0.010 to 0.014 inch) was achieved on Stage 2.

HIGH PRESSURE TURBINE AERODYNAMIC PERFORMANCE

Turbine flow function, with the increased Stage 1 throat area, matched pretest predictions for that configuration. Core turbine efficiency was 92.3%, corrected to FPS tip clearances. The efficiency of the core engine turbine was consistent with earlier rig test results at medium and higher flight power levels.

Based on the agreement of the core test data with the component test results, it is projected that the core turbine would produce an efficiency of 92.5% if operated at design point conditions and design intent clearances. This is 0.6% better than the goal for the core hardware and 0.1% better than the goal for a fully developed flight engine turbine.

SUMPS, DRIVES, GEARBOX, AND PIPING

All components in the sumps, drives, and gearbox performed as intended, and the hardware is in good condition for use in the ICLS.

An external flexible joint in the left side start range turbine cooling piping circuit failed, thereby locally cooling the casing and causing a turbine blade tip rub. Laser clearance probe measurements indicated 0.38 mm (0.015 inch) and 0.76 mm (0.030 inch) of material was removed from the Stage 1 and 2 blade tips, respectively. This was substantiated by posttest inspections. Engine starting did not require start bleed and, therefore, start range turbine cooling was not necessary. The piping was removed for the remainder of the core test. Also, the circuit will be deleted from the ICLS.

CORE SYSTEM DYNAMICS

The core was tested to a maximum speed of 12,811 rpm. No engine vibration problems were encountered, and no core problems are forecasted for ICLS.

The isolated rotor and high load damper system performed as intended. Vibration response characteristics closely matched analytical predictions.

CONTROL SYSTEM

The digital electronic control system worked successfully in both automatic and manual modes. The necessary modifications to the control logic and schedules, determined during core testing, are being incorporated into the ICLS.

Early in the E³ program there were concerns that a very high pressure ratio core would be difficult to start. After exploring engine starting with the E³ core, a start time of only 46.5 seconds (29 seconds after opening of the fuel stopcock) to idle was achieved, without start bleed and with fixed fifth-stage compressor stators. Starting this high pressure ratio core was demonstrated to be no problem. Starter power output was 28% low. The reason has not been determined, but is being investigated.

8.0 REFERENCES

1. Johnston, R.P., et al., "Energy Efficient Engine - Flight Propulsion System Preliminary Analysis and Design," NASA-Lewis Research Center, NASA CR-159583, November 1979.
2. Stearns, E.M., "Energy Efficient Engine - Flight Propulsion System Preliminary Analysis and Design Update," NASA-Lewis Research Center, NASA CR-167980, July 1982.

DISTRIBUTION

NASA Headquarters

600 Independence Avenue, SW
Washington, DC 20546

Attention: RTP-6/R.S. Colladay
RTP-6/C.C. Rosen
RTP-6/J. Facey (2 copies)
RTM-6/L. Harris

NASA-Lewis Research Center

21000 Brookpark Road
Cleveland, OH 44135

Attention: D.L. Nored	MS 301-2
C.C. Ciepluch	MS 301-4 (18 copies)
J.W. Schaefer	MS 301-4
P.G. Batterton	MS 301-4
G.K. Sievers	MS 301-2
M.A. Beheim	MS 3-5
M.J. Hartmann	MS 3-7
R.A. Rudey	MS 86-5
W.C. Strack	MS 501-10
T.P. Moffitt	MS 77-2
R.E. Jones	MS 86-6
L.J. Kiraly	MS 23-2
D.C. Mikkelson	MS 86-1
A. Long	MS 500-305
J.F. Groeneweg	MS 54-3
W.M. Braithwaite	MS 500-208
J.C. Williams	MS 500-211
R.L. Davies	MS 106-1
R.H. Johns	MS 49-6
L.J. Kaszubinski	MS 86-2
J.F. Sellers	MS 100-1
J.R. Mihalow	MS 100-1
L. Reid	MS 5-9
D.W. Drier	MS 86-2
R.W. Niedzwiecki	MS 86-6
AFSC Liaison Office	MS 501-3
ARMY R&T Propulsion Lab	MS 302-2

NASA Ames Research Center

Moffett Field, CA 94035

Attention: 202-7/M.H. Waters

NASA Langley Research Center

Langley Field, VA 23365

Attention: R. Leonard
D. Maiden
L.J. Williams

NASA Dryden Flight Research Center
P.O. Box 273
Edwards, CA 93523
Attention: J.A. Albers

Department of Defense
Washington, DC 20301
Attention: R. Standahar 3D1089 Pentagon

Wright-Patterson Air Force Base
Dayton, OH 45433
Attention: APL Chief Scientist
E.E. Abell
H.I. Bush
E.E. Bailey (NASA Liaison)
R.P. Carmichael
R. Ellis
W.H. Austin, Jr.

Eustis Directorate
U.S. Army Air Mobility
R&D Laboratory
Fort Eustis, VA 23604
Attention: J. Lane, SAVDL-EU-Tapp

NAVY Department
Naval Air Systems Command
Washington, DC 20361
Attention: W. Koven AIR-03E
J.L. Byers AIR-53602
E.A. Lichtman AIR-330E
G. Derderian AIR-5362C

NAVAL Air Propulsion Test Center
Trenton, NJ 08628
Attention: J.J. Curry
A.A. Martino

U.S. Naval Air Test Center
Code SY-53
Patuxent River, MD 20670
Attention: E.A. Lynch

USAVRAD Command
P.O. Box 209
St. Louis, MO 63166
Attention: Robert M. Titus

Detroit Diesel Allison Div. G.M.C.
333 West First St.
Dayton, OH 45202
Attention: F.H. Walters

AFWAL/PS
ASD/YZE
AFWAL/POT
AFWAL/NASA
ASD/XRHI
ASD/YZN
ASD/ENF

Department of Transportation
NASA/DOT Joint Office of
Noise Abatement
Washington, D.C. 20590
Attention: C. Foster

Federal Aviation Administration
Noise Abatement Division
Washington, DC 20590
Attention: E. Sellman AEE-120

Rohr Corporation
P.O. Box 1516
Chuyula Vista, CA 92012
Attention: James C. Fuscoe

TRW Equipment
TRW Inc.
23555 Euclid Ave.
Cleveland, Ohio 44117
Attention: I. Toth

Federal Aviation Administration
12 New England Executive Park
Burlington, MA 18083
Attention: Jack A. Sain, ANE-200

Curtiss Wright Corporation
Woodridge, NJ 07075
Attention: S. Lombardo
S. Moskowitz

AVCO/Lycoming
550 S. Main Street
Stratford, CN 06497
Attention: H. Moellmann

Williams Research Co.
2280 W. Maple Road
Walled Lake, MI 48088
Attention: R. VanNimwegen
R. Horn

Teledyne CAE, Turbine Engines
1330 Laskey Road
Toledo, OH 43612
Attention: R.H. Gaylord

Pratt & Whitney Aircraft Group/UTC
Government Products Division
P.O. Box 2691
West Palm Beach, FL 33402
Attention: B.A. Jones

Boeing Commercial Airplane Co.
P.O. Box 3707
Seattle, WA 98124
Attention: P.E. Johnson MS 9H-46
D.C. Nordstrom MS-73-01

Brunswick Corporation
2000 Brunswick Lane
Deland, FL 32720
Attention: A. Erickson

Delta Airlines, Inc.
Hartsfield-Atlanta International Airport
Atlanta, GA 30320
Attention: C.C. Davis

Fluidyne Engineering Corp.
5900 Olson Memorial Highway
Minneapolis, MN 55422
Attention: J.S. Holdhusen

Massachusetts Inst. of Technology
Dept. of Astronautics & Aeronautics
Cambridge, MA 02139
Attention: Mames Mar

Detroit Diesel Allison Div. G.M.C.
P.O. Box 894
Indianapolis, IN 46202
Attention: W.L. McIntire

The Garrett Corporation
AIRsearch Manufacturing Co.
Torrance, CA 90509
Attention: F.E. Faulkner

The Garrett Corporation
AIRsearch Manufacturing Co.
402 S. 36 Street
Phoenix, AZ 85034
Attention: Library

General Electric Co./AEG
1000 Western Avenue
Lynn, MA 01910
Attention: R.E. Nietzel

Pratt & Whitney Aircraft Group/UTC
Commercial Products Division
East Hartford, CT 06108
Attention: W. Gardner (3 copies)
I. Mendelson

Douglas Aircraft Co.
McDonnell Douglas Corp.
3855 Lakewood Boulevard
Long Beach, CA 90846
Attention: R.T. Kawai Code 36-41
M. Klotzsche 36-41

AIRsearch Manufacturing Co.
111 South 34th Street
P.O. Box 5217
Phoenix, AZ 85010
Attention: C.E. Corrigan
(930120/503-4F)

American Airlines
Maint. & Engrg. Center
Tulsa, OK 74151
Attention: W.R. Neeley

Lockheed California Co.
Burbank, CA 91502
Attention: J.F. Stroud, Dept. 75-42
R. Tullis, Dept. 74-21

Grumman Aerospace Corp.
South Oyster Bay Road
Bethpage, NY 11714
Attention: C. Hoeltzer

